AOSTRA

Technical Handbook

on Oil Sands, Bitumens

and Heavy Oils

Edited by Loren G. Hepler and Chu Hsi

Alberta
OIL SANDS TECHNOLOGY
AND RESEARCH AUTHORITY

AOSTRA

Technical Handbook

on Oil Sands, Bitumens

and Heavy Oils

Edited by Loren G. Hepler and Chu Hsi

Alberta

OIL SANDS TECHNOLOGY
AND RESEARCH AUTHORITY

OTHER PUBLICATIONS IN THE AOSTRA TECHNICAL PUBLICATION SERIES

Syncrude Analytical Methods for Oil Sand and Bitumen Processing

The Thermodynamic and Transport Properties of Bitumens and Heavy Oils

Aquathermolysis: A Synopsis of Work on the Chemical Reaction Between Water (Steam) and Heavy Oil Sands During Simulated Steam Stimulation

Oil Sands Composition and Behaviour Research

A Review of Analytical Methods for Bitumens and Heavy Oils

AOSTRA TECHNICAL HANDBOOK ON OIL SANDS, BITUMENS AND HEAVY OILS

PUBLISHED BY

PUBLISHER'S NOTE

AOSTRA TECHNICAL PUBLICATION SERIES NUMBER 6

AOSTRA is pleased to publish this sixth book in a series of special publications by industry and academic authors. Like its predecessors, *Syncrude Analytical Methods for Oil Sand and Bitumen Processing, The Thermodynamic and Transport Properties of Bitumens and Heavy Oils, Aquathermolysis: A Synopsis of Work on the Chemical Reaction Between Water (Steam) and Heavy Oil Sands During Simulated Steam Stimulation, Oil Sands Composition and Behaviour Research* and *A Review of Analytical Methods for Bitumens and Heavy Oils,* this publication is designed to make available, research results, analytical procedures, and engineering data on the properties and behavior of Alberta petroleum resources that may otherwise not be available to the public.

Alberta Oil Sands Technology
and Research Authority

Edmonton, Alberta

October 1989

AOSTRA TECHNICAL HANDBOOK ON OIL SANDS, BITUMENS AND HEAVY OILS

EDITORS

Loren G. Hepler, University of Alberta
Chu Hsi, Alberta Oil Sands Technology and Research Authority

EDITORIAL BOARD

R.G. Bentsen, University of Alberta
T.R. Heidrick, Alberta Research Council
J.W. Kramers, Alberta Research Council
P.R. Kry, Esso Resources Canada Limited
J.K. Liu, Syncrude Canada Ltd.
D.A. Redford, Alberta Oil Sands Technology and Research Authority
J.D. Scott, University of Alberta
P.R. Tremaine, Alberta Research Council

PUBLICATION

D.B. Teppan, Alberta Oil Sands Technology and Research Authority

EDITING AND PROOFREADING

C.W. Gietz, Word Express

DISTRIBUTION

H. Petri, AOSTRA Library and Information Service

PREFACE

In 1984, the Alberta Oil Sands Technology and Research Authority (AOSTRA) published a technical report titled "The Thermodynamic and Transport Properties of Bitumens and Heavy Oils," sometimes informally called the "Robinson Compilation." This report has been useful in industry and also in university and government research laboratories as a convenient source of fundamental data on the thermodynamic and transport properties of bitumens and heavy oils. It has, however, been recognized by the authors of this report and by its users that a more comprehensive report would be even more useful.

As a result of research sponsored by AOSTRA's University Research Program and its Institutional Research Programs, and also as a result of industrial research, it became apparent to us a few years ago that many new experimental data were becoming available that should be included in an updated technical handbook. In addition, many of the researchers who were providing new experimental data were also developing correlations and predictive models, which permitted use of available data as a basis for estimating other data. Because both of us had been associated with several of AOSTRA's research programs and wanted to increase the use of results of these programs, we suggested that AOSTRA might sponsor the kind of technical handbook that would include a wide range of experimental data along with appropriate discussions of useful correlations and predictive methods. It was also intended that expert authors would provide information about methods used to obtain the tabulated experimental data and summaries of some methods of using such data. Finally, it was also intended that these expert authors would provide leading references to other sources of data and to further discussions of experimental methods, background theory, and practical applications.

We are pleased that AOSTRA decided to support publication of the proposed handbook and appointed an Editorial Board to assist us with detailed planning and with the selection of authors, all of which began in 1986. Now it is a pleasure to thank AOSTRA for its support, to thank the members of the Editorial Board for the useful advice, and especially to thank the expert authors without whose labors this handbook would not exist.

<div align="right">

Loren G. Hepler and Chu Hsi
Edmonton, Alberta

</div>

CONTENTS

1

GEOLOGY OF THE ALBERTA OIL SANDS DEPOSITS

D. Wightman
B. Rottenfusser
J. Kramers
R. Harrison

INTRODUCTION

The oil sands deposits of Alberta, Canada collectively represent one of the largest accumulations of hydrocarbons in the world [1]. The oil is contained in Lower Cretaceous sands and Upper Devonian to Mississippian limestones and dolomites. The Alberta Energy Resources Conservation Board currently groups these deposits into three geographic areas: Athabasca, Peace River, and Cold Lake (Figure 1). Table 1 provides a summary of the areal extent, mean pay, and in-place bitumen reserves for each deposit area, and Table 2 illustrates the primary bitumen-bearing horizons within the Cretaceous stratigraphic sequence. Table 3 gives the main geological attributes of the oil sands deposits. Of all these resources, less than 5% are deemed to be exploitable by open-pit mining. This surface-mineable area, defined by economic stripping ratio criteria, lies in the northern portion of the Athabasca oil sands area. Thus, the vast majority of Alberta's oil sands deposits will only be exploited through in situ technology.

The origin of the oil sands hydrocarbons has been the subject of much discussion and debate over the years, but it is now generally accepted that the bitumen was originally emplaced as a lighter hydrocarbon which has subsequently undergone significant in situ degradation following migration from some distant source area. While there is little dispute that this source area must have lain downdip in the more westerly portions of the basin, it has not been possible to identify clearly one or more specific source horizons. Late Cretaceous to Tertiary deformation, mountain building, and subsequent erosion in the western part of the basin have complicated the problem of source-rock identification. Earlier workers assumed that the hydrocarbons were originally sourced from Cretaceous sequences but other studies argue strongly for the possibility of several source horizons encompassing Devonian to Cretaceous strata. Current biomarker studies in progress at the Geological Survey of Canada's Institute of Sedimentary and Petroleum Geology have raised the possibility that the Cretaceous oil sands have one source horizon and the Paleozoic carbonates contain bitumen from two sources [2].
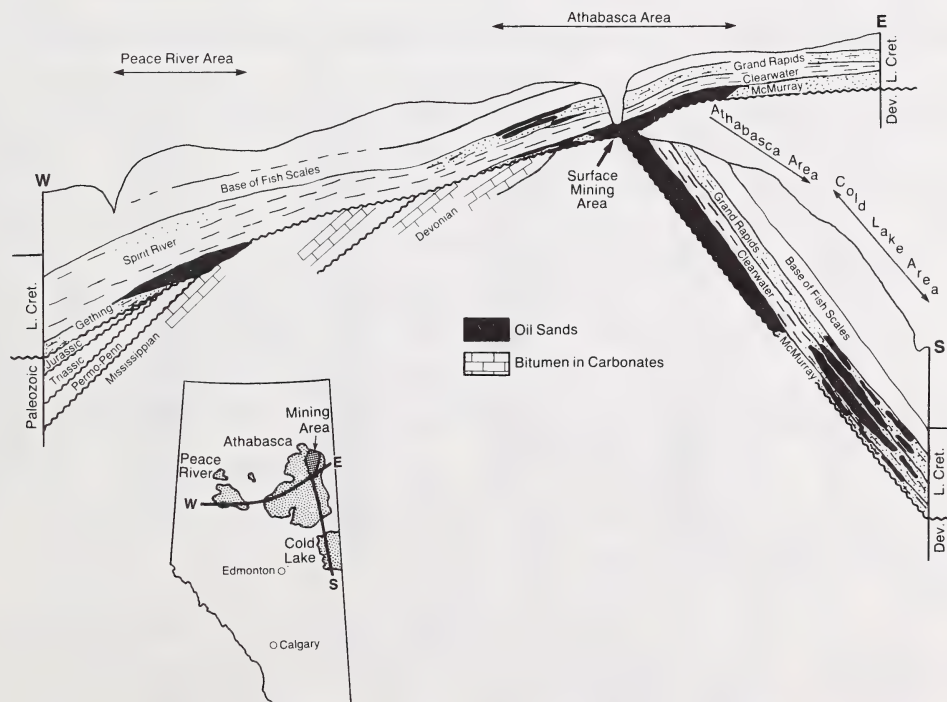
Figure 1. Generalized location map and stratigraphic relationships between the three oil sands deposit areas.

Table 1. Summary of bitumen reserves of Alberta as designated by the Alberta Energy Resources Conservation Board.

Area	Deposit	Areal extent (10³ ha)	Mean pay (m)	Bitumen in place (10⁹ m³)	(10⁹ bbl)
Athabasca	McMurray/Wabiskaw	4 680	34	144	906
	Grand Rapids	689	7	7	44
	Grosmont/Nisku	4 666	10	61	384
				212	1 334
Cold Lake	Grand Rapids	1 603	7	20	126
	Clearwater	561	12	11	69
	McMurray/Wabiskaw	666	5	4	25
				35	220
Peace River	Bluesky/Gething	987	14	12	76
	Debolt/Shunda	228	20	7	44
				19	120

Area	Deposit	Areal extent (10^3 ha)	Mean pay (m)	Bitumen in place (10^9 m^3)	(10^9 bbl)
Athabasca	McMurray/Wabiskaw	4 680	34	144	906
	Grand Rapids	689	7	7	44
	Grosmont/Nisku	4 666	10	61	384
				212	1 334
Cold Lake	Grand Rapids	1 603	7	20	126
	Clearwater	561	12	11	69
	McMurray/Wabiskaw	666	5	4	25
				35	220
Peace River	Bluesky/Gething	987	14	12	76
	Debolt/Shunda	228	20	7	44
				19	120

Table 2. Table of formations illustrating the primary oil sands and heavy oil horizons in Alberta.
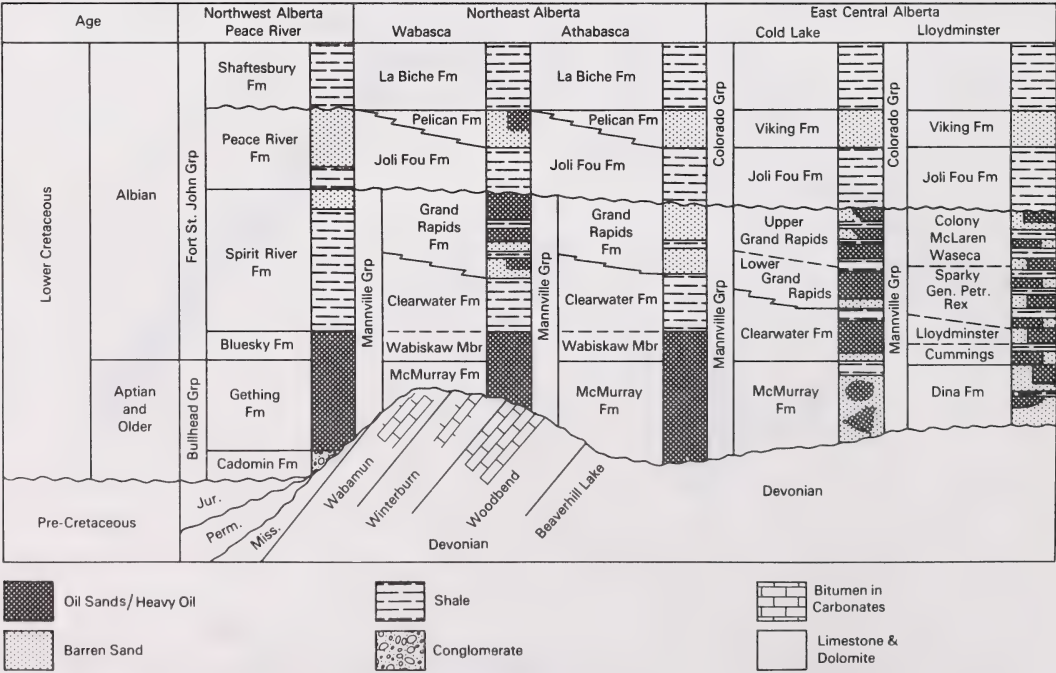
Deposit	Formation	Unit	Depth range (m)	Average pay thickness (m)	API°	Average porosity (%)	Depositional environment	Dominant grain minerals	Dominant clay minerals
ATHABASCA	Grand Rapids	Upper	200 - 400	9	8	30	Shoreline and Shallow Marine	Quartz Chert Feldspar Rock fragments	Kaolinite Chlorite Illite } Oil sands; Smectite Illite } Water sands
ATHABASCA	Grand Rapids	Middle	230 - 430	5	8	30	Shoreline and Shallow Marine	Quartz Chert Feldspar Rock fragments	Kaolinite Chlorite Illite } Oil sands; Smectite Illite } Water sands
ATHABASCA	Grand Rapids	Lower	270 - 470	6	8	30	Shoreline and Shallow Marine	Quartz Chert Feldspar Rock fragments	Kaolinite Chlorite Illite } Oil sands; Smectite Illite } Water sands
ATHABASCA	Wabiskaw/McMurray	Mineable	0 - 120	38	8 - 10	29	Continental to Marine Shelf	Quartz	Kaolinite Illite
ATHABASCA	Wabiskaw/McMurray	In Situ	80 - 750	19	8 - 10	28	Continental to Marine Shelf	Quartz	Kaolinite Illite
COLD LAKE	Grand Rapids	Upper	275 - 500	6	11 - 15	30	Continental to Marine Shoreline	Quartz Rock fragments Feldspar	Kaolinite Illite Smectite
COLD LAKE	Grand Rapids	Lower	325 - 525	12	9 - 12	31	Continental to Marine Shoreline	Quartz Rock fragments Feldspar	Kaolinite Illite Smectite
COLD LAKE	Clearwater		375 - 500	12	10 - 11	30	Marine Shoreline	Quartz Feldspar Rock fragments Altered grains	Kaolinite Illite Smectite
COLD LAKE	Wabiskaw/McMurray	Wabiskaw	425 - 600	5	10 - 12	25	Marine Shelf / Continental	Quartz Glauconite / Quartz	Kaolinite Illite
PEACE RIVER	Bluesky/Gething		460 - 760	14	9	24	Estuarine to Shallow Marine	Quartz Chert Rock fragments	Kaolinite Illite
CARBONATE DEPOSITS	Debolt		500 - 800	32	8 - 10	18	Open Marine	Limestone Dolomite	Not significant
CARBONATE DEPOSITS	Shunda		500 - 800	14	8 - 10	20	Tidal Flat to Open Marine	Limestone Dolomite	Not significant
CARBONATE DEPOSITS	Grosmont		260 - 350	16	7	16	Tidal Flat to Open Marine	Dolomite	Not significant

Table 3. Generalized geological attributes of the oil sands deposits.

ATHABASCA OIL SANDS AREA

McMurray deposit

The McMurray Formation is the primary Cretaceous reservoir horizon within the Athabasca area. The formation lies in direct contact with the underlying Paleozoic (Devonian) carbonates, and during the initial stages of deposition, was strongly influenced by relief on the Paleozoic surface [3–5]. Overall, the vertical sedimentological succession represents an evolution from predominantly continental, fluvial, and floodplain environments to a shoreline estuarine complex as a result of rising sea level. An erosional contact separates the McMurray Formation from the glauconitic sands of the overlying Wabiskaw Member (Clearwater Formation) which was deposited during the transgression of the boreal sea [6–8]. The McMurray Formation ranges typically between 40 and 80 m in thickness [9] and has been subdivided into three informal stratigraphic units (lower, middle, and upper McMurray). Where it lies close to the present-day surface, the formation constitutes the orebody being exploited by the Syncrude and Suncor mining operations.

Compared to other oil sands deposits, the sediments of the McMurray Formation in the Athabasca area have a very uniform, mature mineralogy [10]. The sediments consist of uncemented, very fine to coarse-grained quartz sand (quartz arenites and sublitharenites) with subordinate associated shale, silt, and thin coal beds. The continental nature of the formation gives rise to discontinuous reservoirs, in contrast to other Lower Cretaceous units such as the more continuous shoreline deposits of the Grand Rapids Formation. Where McMurray Formation sands are well sorted with little clay content (channel sands), excellent reservoir characteristics are displayed: porosities between 30 and 40% and oil saturations of 10 to 18 wt%. These reservoirs are commonly relatively narrow but due to vertical stacking (amalgamation of channel sands) thicknesses of up to 70 m may occur, with net pay zones on the order of 20 to 40 m [11,12].

Wabiskaw deposit

Wabiskaw Member sediments are more uniformly marine in character and generally consist of lower to upper shoreface and offshore sands, silts, and shales. The uncemented quartz sands (quartz arenites to sublitharenites) are generally fine to very fine grained and occur as laterally persistent, though relatively thin, reservoirs.

Grand Rapids deposit

The reservoir sands for the three Grand Rapids Formation sand units (Grand Rapids A, B, and C sands) were deposited in a high-energy, wave-dominated shoreline setting along a low-relief coastal plain, which was roughly oriented northeast to southwest [13]. The three sand units overstep each other basinward to the northwest. The depositional setting for the reservoir rocks encompassed nearshore shallow marine (to the limit of mean storm wave base), and shore-attached beach complexes with minor barrier islands and lagoons. Deposition in this setting has resulted in excellent reservoir continuity parallel to the regional northeast to southwest depositional strike. Locally the reservoirs may be interrupted by sand- or shale-filled channel deposits cutting through the shoreline zone at a high angle to regional strike. Because of the original high-energy depositional environment, reservoirs tend to be clean and have good permeability and porosity. Within each of the three Grand Rapids Formation sands, vertical reservoir continuity is good, but may be interrupted on a local scale by thin but areally extensive calcite or siderite cemented beds or zones of calcareous concretions. Bitumen pore-space saturation ranges from 40 to 70%, distributed through zones of net pay which vary from 5 to 25 m in thickness and lie at depths of 200 to 470 m.

In contrast to the McMurray Formation sands in the Athabasca area, the Grand Rapids Formation sands are mineralogically complex. Framework grain components are quartz, chert, feldspar, and rock fragments of mainly volcanic and sedimentary origin. Cements are dominantly clays: kaolinite and chlorite in the oil-saturated sands, and smectite and interlayered clays in the water sands, with illite in both.

PEACE RIVER OIL SANDS AREA

Bitumen within the Peace River deposit area is trapped in an updip pinchout of the Cretaceous Gething and Bluesky formations against Mississippian carbonates which form a high on the sub-Cretaceous unconformity [14]. These sediments were laid down in continental to marginal marine settings along the southeastern edge of a seaway which advanced from the north and northwest. Specific depositional environments ranged from shoreline and shallow marine, through tidal flat and tidal channel, to lacustrine and fluvial. Continental sediments were the first

deposited and infilled relief on the sub-Cretaceous unconformity; then as the transgression advanced, brackish tidal flat sediments succeeded by shoreline sediments gradually covered the area. Tidal channels are superimposed on the upper portions of the sequence.

Within the Peace River oil sands deposit, the thickest and most continuous oil sands are found in tidal channel complexes, but high oil saturations (77% pore volume) are also found in widespread shoreline and shallow marine sands. Laterally equivalent tidal flat sequences of interbedded oil sands and shale also contain bitumen but form less attractive reservoirs because of the interbedded shale. The reservoir is relatively deep (460 to 760 m) with zones of net pay up to 30 m thick. The reservoir sands have a mixed mineralogy, dominated by quartz, chert, rock fragments, carbonate grains, and minor feldspar. Clay minerals are primarily kaolinite, illite, and minor montmorillonite and chlorite. Within the oil leg of the reservoir, hydrocarbon emplacement appears to have halted or inhibited diagenesis relative to the underlying water-bearing sands in which authigenic clays (especially kaolinite) are much more abundant.

COLD LAKE OIL SANDS AREA

Bitumen in the Cold Lake area is distributed through four main stratigraphic intervals over a depth range of 275 to 600 m. In ascending order the key deposits are the McMurray-Wabiskaw, the Clearwater, and the Lower and Upper Grand Rapids.

McMurray-Wabiskaw deposit

This interval has the smallest reserves in the Cold Lake oil sands area. The McMurray Formation reflects the initial sedimentation on the underlying Paleozoic carbonates, and depositional environments range from fluvial to lacustrine. These quartzose continental deposits infill many or all of the low topographic areas on the unconformity surface. At the end of McMurray time, the boreal sea transgressed into the area and the Wabiskaw Member (Clearwater Formation) represents the transitional deposits between the underlying continental McMurray Formation and the marine sediments of the remainder of the overlying Clearwater Formation. The bulk of the bitumen is in the thinner (5 to 10 m) sands at the top of this interval, as the thick (10 to 50 m) channel deposits in the McMurray Formation are dominantly water bearing.

Clearwater deposit

This formation contains the second largest bitumen reserves in the Cold Lake area but is the smallest in areal extent and is restricted to the northern portion of the oil sands area [15,16]. The large reserves are due to the greater thickness of the oil sands (up to 60 m of net pay) and this, along with good lateral reservoir continuity, has resulted in the Clearwater being the focus of extensive thermal recovery activity. Sand type is nonquartzose and varies from litharenite to a feldspathic litharenite, with the sediment derived from a western source area [17,18]. Kaolinite, illite, and smectite clay minerals are present, as well as various forms of authigenic chlorite. Depositional environments are predominantly marine shoreline with associated continental deposits. The marine nature of the Clearwater Formation is a result of the transgression of the boreal sea at the end of McMurray time. The thick sands in the northern part of the deposit are interpreted to be part of a major deltaic system. Distributory channel and distributory mouth bar deposits of this system form the highest grade oil sands in the Cold Lake area. Trapping of the bitumen is partly stratigraphic, as the sands shale out to the north, and partially structural, as the removal of salt from the underlying Devonian evaporites has caused a reversal in dip (to the east) on the east side of the deposit.

Lower Grand Rapids deposit

This horizon contains the largest reserves of bitumen in the Cold Lake area. The nature of the reservoir sand (litharenites) is similar to that of the Upper Grand Rapids, with depositional environments exerting some control over variations in mineralogy. Depositional environments were predominantly marine shoreline with associated continental deposits. The deposit is not as areally extensive as that of the Upper Grand Rapids, but the oil sands are more continuous, reflecting the better-developed lateral persistence of marine shoreline facies.

Upper Grand Rapids deposit

Sands within this horizon vary from sublitharenites to feldspathic litharenites, and depositional environments range from continental to marine, with the marine influence increasing in the northern and eastern portion of the deposit [19]. Although the Upper Grand Rapids Member is areally extensive, the oil sands are often relatively discontinuous and thin (5 to 10 m), reflecting the continental aspect of this stratigraphic interval. Individual sand reservoirs, however, can attain a thickness of up to 30 m in channel deposits.

CARBONATE DEPOSITS

In addition to the relatively well known Cretaceous deposits, there is another immense but much less studied oil sands resource: bitumen contained along the eastern, updip margin of the Paleozoic formations which subcrop beneath the Cretaceous deposits [20,21]. The Alberta Energy Resources Conservation Board has undertaken detailed resource estimates for only four horizons within this carbonate trend: the Upper Devonian, Grosmont, and Nisku formations (Athabasca area) and the Mississippian, Shunda, and Debolt formations (Peace River area). Of these four formations, industry attention to date has primarily been focussed on the Grosmont Formation.

The Grosmont Formation is an immense, multistage, shallow-marine carbonate platform underlying the McMurray Formation of the Athabasca oil sands area. The main reservoir horizons, 25 to 50 m in thickness, lie at depths of approximately 250 to 300 m and are dolostones with average porosity as high as 20% and bitumen saturations averaging approximately 70% or more of the available pore space. In contrast to the overlying Cretaceous deposits, the Grosmont reservoir is a well-lithified dolostone with a heterogeneous dual-porosity fabric. The main reservoir horizons consist of a spectrum of rock types representing original depositional environments ranging from relatively deep water (platform-slope to basin transition), through variable carbonate sand, mud, and patch reef accumulations within a platform interior, to restricted-marine shorelines and tidal flat settings. Overall, the vertical succession of fabrics reflects a series of shallowing-upward depositional cycles with excellent lateral continuity but having a highly-variable vertical reservoir pore fabric.

SUMMARY

The oil sands deposits of Alberta differ substantially in terms of the environmental conditions under which they were deposited. This variability is in turn reflected by differences in reservoir geometry, lateral and vertical continuity, internal fabric, and mineralogic composition. These elements influence the relative distribution and saturation of reservoir fluids, and most importantly, the degree to which the reservoir responds successfully to various thermal stimulation processes. Since the early 1970s it has become increasingly recognized that

geology must be an integral part of oil sands resource assessment, reservoir analysis, and exploitation strategy. The accompanying list of references [22–31] provides a selection of articles which give more specific insight into the geological attributes of the Alberta oil sands and heavy oil deposits.

SELECTED REFERENCES

1. Alberta Energy Conservation Board, Atlas of Alberta's crude bitumen reserves, 85–38 (1985).
2. P.W. Brooks, M.G. Fowler and R.W. Macqueen, Implications of biomarker geochemistry to the origin of oil sands/heavy oils, Western Canada Basin, Forum 89 Geological Survey of Canada (1989) 60.
3. P.D. Flach, Oil sands geology — Athabasca deposit north, Alberta Research Council Bulletin 40 (1984).
4. D.W. Keith, J.R. MacGillivray, D.M. Wightman, D.D. Bell, T. Berezniuk and H. Berhane, Resource characterization of the McMurray/Wabiskaw deposit in the Athabasca Central region of northwestern Alberta, AOSTRA/ARC/AE internal report (1987).
5. G.D. Mossop, Geology of the Athabasca oil sands, Science, 207 (1980) 145.
6. P.D. Flach and G.D. Mossop, Depositional environments of the lower Cretaceous McMurray Formation, Athabasca oil sands, American Association of Petroleum Geologists Bulletin, 69 (1985) 1195.
7. G.D. Mossop, Facies control on bitumen saturation in the Athabasca oil sands, Canadian Society of Petroleum Geologists Memoir 6 (1980) 609.
8. G.A. Stewart, Athabasca oil sands, First UNITAR Conference on the Future of Heavy Crude Oils and Tar Sands, McGraw-Hill, New York (1981) 208.
9 J.R. MacGillivray, D.M. Wightman, D.A.W. Keith, B.D. Bell, H. Berhane and T. Berezniuk, Resource characterization of the central region of the Lower Cretaceous McMurray/Wabiskaw deposit, Athabasca oil sands area, northeastern Alberta, Paper no. 129, Fourth UNITAR/UNDP Conference on Heavy Crude and Tar Sands (1988).
10. G.D. Mossop, J.W. Kramers, P.D. Flach and B.A. Rottenfusser, Geology of Alberta's oil sands and heavy oil deposits, First UNITAR Conference on the Future of Heavy Crude Oils and Tar Sands, McGraw-Hill, New York (1981) 197.
11. D.A.W. Keith, D.M. Wightman, S.G. Pemberton

J.R. McGillivray, T. Berezniuk and H. Berhane, Sedimentology of the McMurray Formation and Wabiskaw Member (Clearwater Formation), Lower Cretaceous, in the central region of the Athabasca oil sands area, northeastern Alberta, Canadian Society of Petroleum Geologists, Memoir 15 (1988) 309.

2. D.A.W. Keith, D.M. Wightman, S.G. Pemberton, J.R. MacGillivray, T. Berezniuk and H. Berhane, Fluvial, estuarine and shallow marine sedimentation in the Lower Cretaceous McMurray Formation and Wabiskaw Member (Clearwater Formation) in the Athabasca oil sands area, Alberta, Paper no. 130, Fourth UNITAR/UNDP Conference on Heavy Crude and Tar Sands (1988).

3. J.W. Kramers and A.W. Prost, Oil sands resources of the Grand Rapids Formation in the Wabasca deposit, AOSTRA/ARC internal report (1986).

4. B.A. Rottenfusser, Peace River oil sands — Regional geology, AOSTRA/ARC internal report (1985).

5. D.M. Wightman and T. Berezniuk, Resource characterization of the Clearwater Formation, Cold Lake oil sands deposit, east-central Alberta, AOSTRA/ARC Internal Report (1985).

6. D.M. Wightman and T. Berezniuk, Resource characterization and depositional modelling of the Clearwater Formation, Cold Lake oil sands deposit, east central Alberta, U.S. Dept. of Energy Tar Sands Symposium, Wyoming (1986) 20.

7. M.E. Prentice and D.M. Wightman, Mineralogy of the Clearwater Formation, Cold Lake oil sands area: Implications for enhanced oil recovery, AOSTRA/ARC/AE Internal Report (1987).

8. Sedimentology Research Group, The effects of in situ steam injection on Cold Lake oil sands, Bulletin of Canadian Petroleum Geology, 29 (1981) 447.

9. D.M. Wightman, S.G. Pemberton and C. Singh, Depositional modelling of the Upper Mannville (Lower Cretaceous), east central Alberta: implications for the recognition of brackish water deposits, Society of Economic Paleontologists and Mineralogists, Spec. Publ. 40 (1987) 189.

0. R.S. Harrison, Regional geology and resource characterization of the Upper Devonian, Grosmont Formation, northern Alberta, AOSTRA/ARC internal report (1986).

21. R.S. Harrison, The bitumen-bearing Paleozoic carbonate trend of northern Alberta, American Association of Petroleum Geologists Studies in Geology 25 (1987) 319.

22. R.S. Harrison, The AOSTRA-ARC joint oil sands geology programs: Regional resource studies of the Alberta oil sands deposits, U.S. Dept. of Energy Tar Sands Symposium, Wyoming (1986) 11.

23. T.R. Lennox, The impact of geology on the design and performance of in situ projects, AOSTRA conference on Advances in Petroleum Recovery and Upgrading, Calgary, May (1981).

24. B.A. Rottenfusser, J.E. Palfreyman and N.K. Alwast, Geology of the AOSTRA Underground Test Facility site, Paper no. 115, Fourth UNITAR/UNDP Conference on Heavy Crude and Tar Sands (1988).

25. J.W. Kramers, S. Bachu, D.L. Cuthiell, M.E. Prentice and L.P. Yuan, A multidisciplinary approach to reservoir characterization; the Provost Upper Mannville B Pool, J. Can. Pet. Tech., 28 (1989) 48.

26. J.W. Kramers, S. Bachu, D. Cuthiell, A.T. Lytviak, J.E. Hasiuk, J.J. Olic, M.E. Prentice and L.P. Yuan, The Provost Upper Mannville B Pool; an integrated reservoir analysis, Paper no. 60, Fourth UNITAR/UNDP Conference on Heavy Crude and Tar Sands (1988).

27. L.P. Yuan and J.W. Kramers, Characterization of pore images in a heavy oil reservoir and its applications, Paper no. 67, Fourth UNITAR/UNDP Conference on Heavy Crude and Tar Sands (1988).

28. S.C. O'Connell, The geology and resource characterization of the Lower and Mid-Mannville formations of the South Lloydminster heavy oil trend, Alberta, AOSTRA/ARC internal report (1985).

29. S.C. O'Connell and G.W. Benns, The geology of the mid-Mannville subgroup in the west-central Lloydminster heavy oil trend, Alberta, Alberta Research Council Open File Report 1988-1 (1988).

30. G.T. MacCallum, Geology of Lloydminster play, Alberta, First UNITAR Conference on the Future of Heavy Crude Oils and Tar Sands, McGraw-Hill, New York (1981) 223.

31. R. Lefebvre and I. Hutcheon, Mineral reactions in quartzose rocks during thermal recovery of heavy oil, Lloydminster, Saskatchewan, Canada, Applied Geochemistry, 1 (1986) 395.

2

ANALYTICAL METHODS

Joseph K. Liu

Contributors
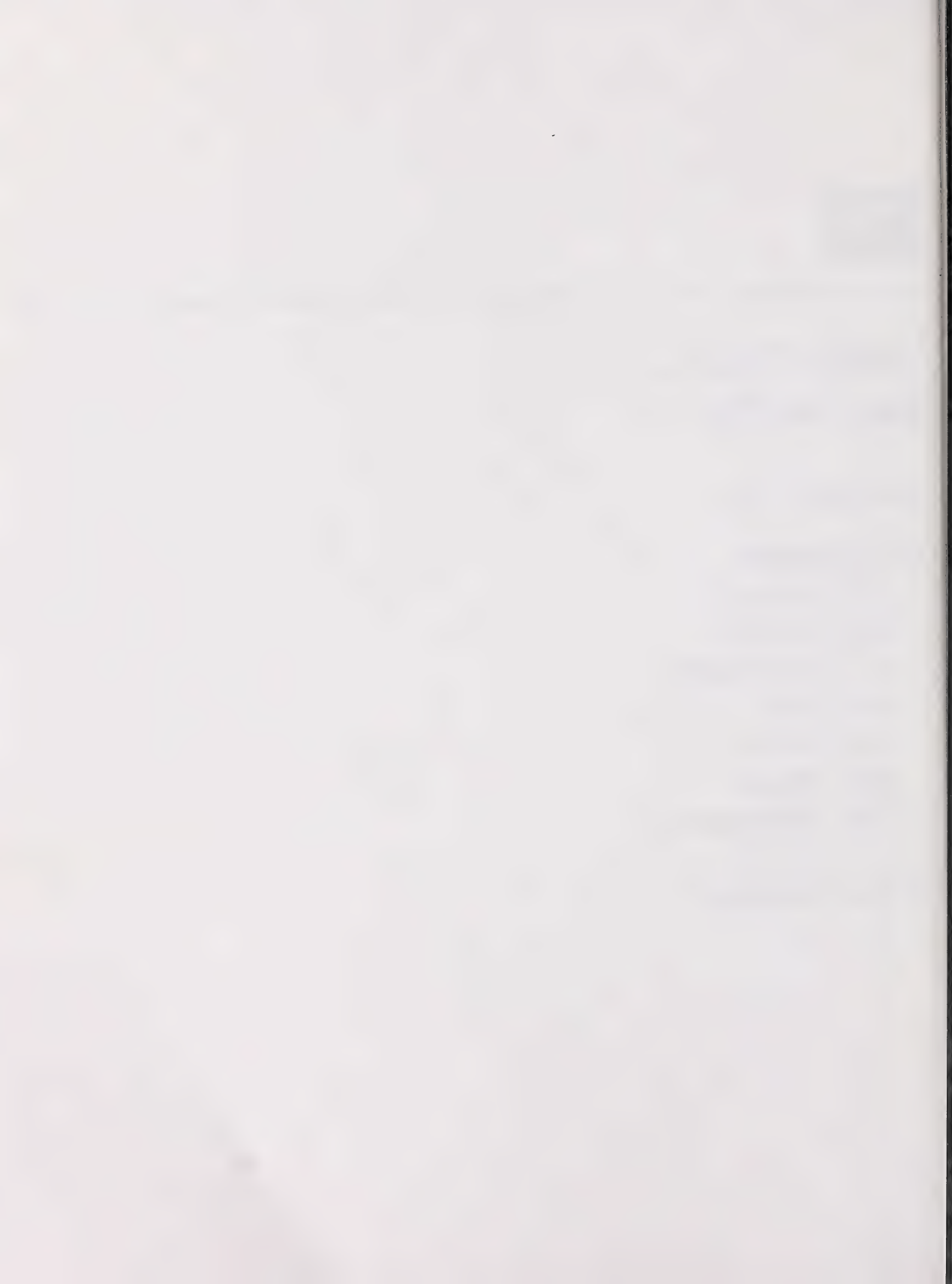 J. T. Bulmer
  J. M. Cooley
  B. D. Crickmore
  R. H. Hall
  R. E. Hoyle
  R. C. Shaw
  G.R. Thompson

Syncrude Canada Ltd.

INTRODUCTION

Oil sands research and oil sands plant operation require a wide range of analytical techniques to measure the various grades of ore and process streams. A number of analytical methods have been developed to meet the special requirements of an oil sands hot water extraction plant, particularly as they refer to the oil sand itself. These methods are:

- usually not used outside the oil sands industry,
- not standard methods established or accepted by the oil sands operators, and
- not included in the ASTM books of standards.

However, other process streams, particularly in the areas of upgrading, and water and metals analysis, may be measured using established or adapted methods. All these techniques are the subject of this chapter.

The aim of the oil sands industry is to economically produce synthetic crude oil, a relatively inexpensive commodity yet one which requires the handling of very large amounts of oil sand. It has been a challenging task for the analytical chemist to obtain representative samples from the huge, inhomogeneous streams of the hot water extraction processes. The resolution capability of a given analytical method is generally better than the uniformity of samples provided by the available subsampling procedures. Therefore, the effect of subsampling on the precision of analytical methods is critical and is discussed in depth in this chapter.

Analytical methods are used in oil sands plants to estimate the quality and quantity of the ore reservoir, monitor the processes, and to provide information for auditing the overall production performance of the plant. However, to realize effective process control, real-time process information is required from on-line analyzers. To illustrate developments in this area, a Wright and Wright on-line oil sands grade analyzer is introduced.

Methods related to the processibility of oil sands of various qualities, and product quality of hot water extraction processes are also discussed in this chapter.

SUBSAMPLING PROCEDURES FOR OIL SAND

General

Large quantities of oil sand obtained from the Athabasca deposit are widely used in pilot-scale and laboratory studies of extraction and in situ bitumen recovery processes. Accurate and precise estimates of the bitumen, water, and solids contents of the material are required.

Because of equipment limitations, consumables costs, and the desire for analytical expediency, laboratory procedures for oil sand assay determination are designed to be performed on relatively small samples. Unfortunately, methods used for withdrawing representative bulk samples from the parent population of material typically result in a sample exceeding the size requirements stipulated for direct analysis. In most instances, the gross sample collected and submitted to the laboratory for inspection must be reduced in size such that the analytical subsample reflects the composition and properties of the original bulk material. Representative subsampling is thus an important preliminary step in the analytical sequence.

Experience has shown that much of the variability among replicated sample analyses performed on a given bulk quantity of material can be attributed to subsampling uncertainty. The situation is particularly acute for oil sands wherein the bitumen, water, and solid components are invariably distributed in a segregated and heterogeneous fashion. Wallace and Kratochvil [1] have reported, that for bulk samples on the order of 325 kg, as many as 20 120-g subsamples must be collected and analyzed to hold sampling uncertainties to less than three times the analytical standard deviation. Subsampling variability data are summarized in Table 1. It was concluded from this study that effort spent on enhancing the precision of analytical measurements for component assay is misdirected. Considerably more emphasis should be placed on improving sampling techniques.

Coning and quartering

The most common approach used to reduce subsampling error resulting from bulk sample inhomogeneity involves particle size reduction and blending operations.

Shaw [2] has investigated the application of a manual chopping, coning, and quartering method for preparing 30-g subsamples from a 6-kg bulk sample of oil sand. Procedural details are documented in reference [3]. The bulk sample examined in this study consisted of a stratified mixture of oil sand containing equal proportions of low-, medium-, and high-grade (7, 11, and 14% bitumen) ores. It was determined that three coning and quartering operations resulted in subsampling uncertainties of approximately 0.5% for bitumen and solids and 0.2% for water for an oil sand having an average composition of 11% bitumen, 1%

Table 1. Subsampling variability data for bitumen-water-solids components of oil sand. Data obtained from Reference [1].

Grade of oil sand and month collected		Number of analyses	Bitumen mean (%)	Standard deviation	Relative standard deviation (%)	Overall variance s_o^2	Variance due to sampling[a] s_s^2	Range
Summary of bitumen determinations								
high-grade	Nov 76	233	14.9	0.6	4	0.36	0.34	12.5–16.7
	Dec 80	80	13.8	0.8	6	0.64	0.62	8.9–14.9
	Nov 81	94	14.8	1.2	8	1.44	1.42	9.4–17.3
medium-grade	Nov 76	49	11.7	0.6	5	0.36	0.34	3.6–12.8
	Nov 76	49	12.2	1.2	10	1.44	1.42	8.7–13.9
	Dec 80	30	12.3	1.4	11	1.96	1.94	8.5–14.5
	Nov 81	15	12.3	0.4	3	0.16	0.14	11.5–13.3
low-grade	Nov 76	48	6.8	1.7	25	2.89	2.87	3.8–12.7
	Nov 81	13	8.2	1.3	16	1.69	1.67	6.1–10.5
Summary of water determinations								
high-grade	Nov 76	233	1.1	0.5	46	0.25	0.23	0.1–3.8
	Dec 80	80	3.5	1.3	37	1.69	1.67	1.2–7.7
	Nov 81	94	3.4	1.5	44	2.25	2.23	0.7–10.6
medium-grade	Nov 76	49	6.2	1.5	24	2.25	2.23	3.5–15.8
	Nov 76	49	4.0	1.4	35	1.96	1.94	1.5–7.6
	Dec 80	30	3.8	1.7	45	2.89	2.87	1.7–8.8
	Nov 81	15	4.2	0.7	17	0.49	0.47	2.5–5.4
low-grade	Nov 76	48	7.4	2.0	27	4.00	3.98	3.0–13.6
	Nov 81	13	6.8	1.3	19	1.69	1.67	4.6–8.6
Summary of solids determinations								
high-grade	Nov 76	233	83.1	0.6	0.7	0.36	0.34	81.0–84.9
	Dec 80	80	82.8	1.0	1.2	1.00	0.98	79.4–85.7
	Nov 81	94	81.5	1.5	1.8	2.25	2.23	74.6–84.8
medium-grade	Nov 76	49	80.9	1.2	1.5	1.44	1.42	78.9–82.9
	Nov 76	49	82.8	1.0	1.2	1.00	0.98	78.5–84.4
	Dec 80	30	84.1	0.7	0.8	0.49	0.47	82.8–85.7
	Nov 81	15	83.3	0.6	0.7	0.36	0.34	82.3–84.4
low-grade	Nov 76	48	84.8	1.1	1.3	1.21	1.19	81.1–86.2
	Nov 81	13	84.9	0.7	0.8	0.49	0.47	83.4–85.7

[a] Calculated as overall variance minus variance due to analysis of a test portion ($s_a^2 = 0.02$).

water, and 88% solids.

Data obtained for a variety of other bulk samples have demonstrated that particle size reduction is essential for reducing subsampling variance. In this context, particle size refers to the size of the lumps of material produced by chopping the oil sand with a knife edge. The general relationships between oil sand particle size and subsampling error is shown in Figure 1. Results indicate that there is little economic reason for continuing the manual comminution and blending process beyond the 5-mm nominal diameter particle size range. Moreover, oil sand is prone to dehydration when exposed to the atmosphere in a finely divided state, as illustrated in Figure 2 for a medium-grade ore.

Mechanical subsamplers

The manual chopping, coning, and quartering procedure for blending and subdividing bulk quantities of oil sand is laborious and time consuming. Mechanical devices for grinding samples of ore have been considered as a means for improving the efficiency of subsampling operations.

Wallace and Kratochvil [4] have examined the application of a bench-scale mill and spinning riffler for collecting representative subsamples from 1-kg quantities of various grades of oil sand. The bulk samples were cooled to 3°C prior to treatment. Results indicated that subsampling-plus-analytical variabilities in the range 0.10 to 0.14% absolute can be assigned to a single bitumen, water, or solids determination for both low- (9% bitumen) and high-grade (14% bitumen) oil sand. Water loss due to evaporation and the selective retention of bitumen on the internals of the mill were shown, however, to contribute a systematic bias in assay results.

Syncrude Canada Ltd. has described the operation of a cryogenic grinder for homogenizing oil sand [3]. Statistical evaluations to assess subsampling variability, however, have not been published. A potential source of error at low temperatures is condensation of water on the oil sand, leading to erroneous results in water analyses.

Sampling constants

The literature cites numerous studies that suggest an inverse relationship between subsample size and subsampling variance. The effect of increasing subsample size on the subsampling uncertainty associated with the bitumen assay for a homogenized
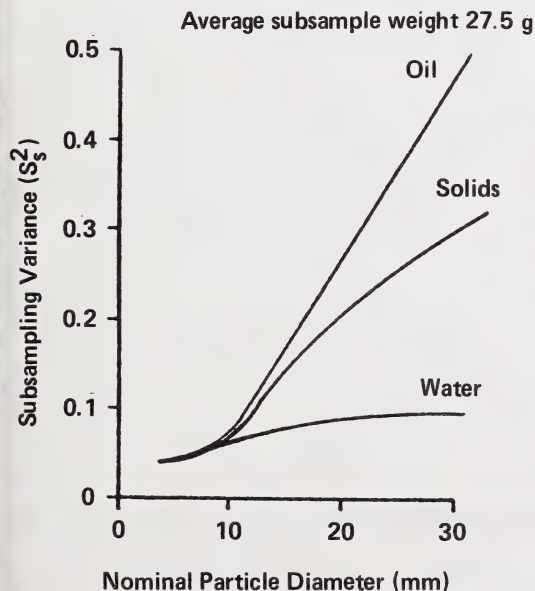

Figure 1. Relationship between oil sand particle size and subsampling variance for bulk samples prepared using the chopping, coning, and quartering procedure. Data obtained from Reference [2].
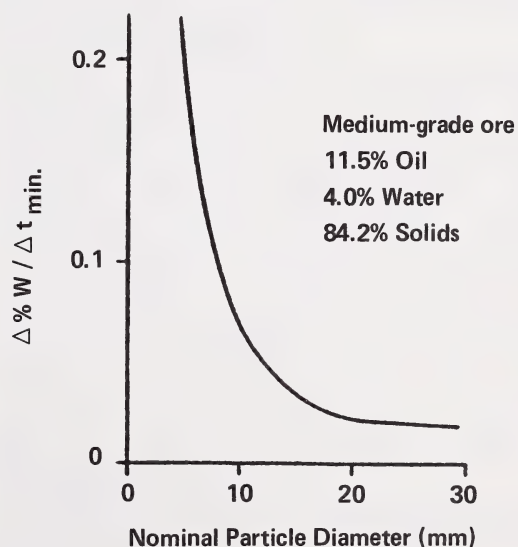

Figure 2. Rate of water loss as a function of oil sand particle size. Data obtained from Reference [2].

5-kg bulk sample of medium-grade oil sand (prepared in accordance with the chopping, coning, and quartering procedure) is shown in Figure 3. The data indicate that subsampling errors can be minimized by selecting the largest practical subsample for analysis. Ingamells and Switzer [5] have defined a sampling constant, K_s, that specifies the weight of a single subsample to be taken from a well-mixed quantity of bulk material to ensure a subsampling standard deviation, s_s, no greater than 1% relative at the 68% confidence level. The relation is

$$K_s = wR^2 = w(100\, s_s/\bar{x})^2 \qquad (1)$$

where w is the average subsample weight giving a relative standard deviation, R, in percent. Sampling constants calculated for the assay components of a medium-grade oil sand are summarized in Table 2.

The application of a single sampling constant for estimating the size of subsample to be retrieved from a bulk sample of oil sand, so as not to exceed a predetermined level of sampling variability, is only valid for well-mixed quantities of material. For larger bulk samples of ore where it becomes impractical to homogenize and subdivide the material effectively, other

Table 2. Subsampling variability data for bitumen-water-solids components of oil sand. Data obtained from Reference [2].

Assay component	$K_s(g)$	Standard error of $K_s(g)$
Oil	91.5	8.3
Water	18 803	1 598
Solids	28.6	2.3

sampling protocols must be considered. Wallace and Kratochvil [6] have discussed sampling plans for oil sand that take into account the effect of heterogeneity due to segregation. The approach, based on Visman's general theory of sampling [7], treats subsampling variance as the sum of two variances: one the variance due to local random distribution of the component of interest, A, which can be reduced by increasing either the size or the number of subsamples taken, and the other due to segregation, B, which can be reduced by increasing the number of subsamples collected. The function relating the sampling variance to these two sources of variability is

$$s_s^2 = (A/wn) + B/n \qquad (2)$$

Here w is the weight of the individual subsample and n is the number of subsamples selected at random from the bulk material. The authors conclude from their study that subsamples in the range of 50 to 250 g are optimal for determining the bitumen, water, and solids content of drum-sized lots of mined oil sand. The reduction of sampling uncertainties to 1% relative would require collection of fewer than 10 subsamples for solids, on the order of 100 for bitumen, and on the order of 1000 for water. Subsamples could be composited, blended, and further subdivided to provide an appropriately sized analytical sample.

OIL, WATER, SOLIDS

The oil-water-solids content of Athabasca oil sands is used to assess the extent and quality of bitumen reserves present in the deposit. Thus, it is used extensively by those in operating plants as well as by other lease holders and researchers. The methods that have been used for evaluation of the oil-water-solids
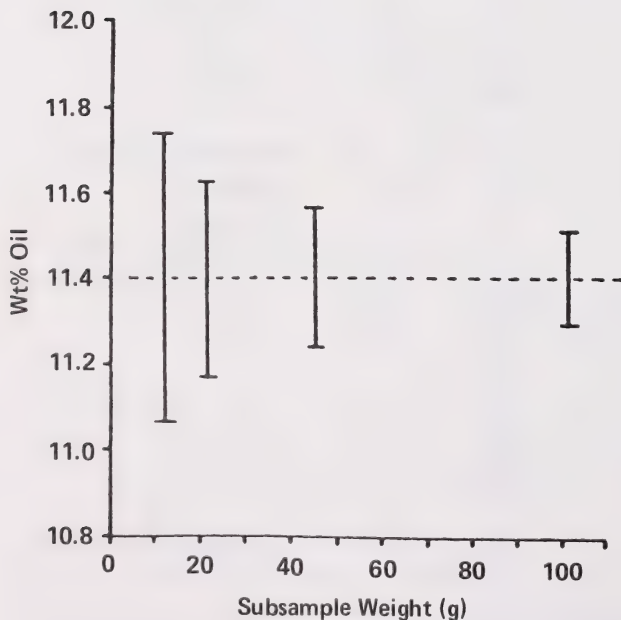

Figure 3. Effect of subsample size on sampling uncertainty. Average subsample weight 27.5 g. Data obtained from Reference [2].

content have had to be developed specifically for the Athabasca oil sand due to its unique nature. The results obtained are method dependent. There are no primary reference standards and hence the accuracy of the method cannot be defined.

In 1955 Draper et al. [8] compared three analytical methods for determining the bitumen content of bituminous sands. This work was undertaken to provide a basis for comparing the amount of bitumen analyzed by these methods and reported in the 1940s and early 1950s. One of their methods, the toluene extraction method, which was developed by the Calvan Consolidated Oil and Gas Company Limited, is an early version of the method now accepted by the oil sands industry:

The toluene extraction method consisted of the simultaneous extraction of the water and bitumen from the bituminous sand with toluene as the solvent. The determination was made in a modified extraction apparatus using a paper extraction thimble. The amount of silt that passed through the extraction thimble was again determined and applied as a correction to the bitumen content. The water in the sample was distilled out of the boiling flask with the toluene vapour, and condensed and collected in a graduated trap for estimation. The bitumen content was then calculated on a dry basis.

The carbon tetrachloride extraction method, devised by the staff of the Fuels Division, Department of Mines and Technical Surveys, was similar to the toluene extraction method, except that it used carbon tetrachloride and a second subsample to determine the water content using dilution naphtha as solvent as specified in ASTM standard D95. This second method was therefore not as rapid as the toluene extraction method.

The density method, devised by W.J. Dyck of the Fuels Division, consisted of the determination of the density and the water content of the sample. This third method was much less precise and was only intended as a rapid field method of assaying the bitumen content.

The study to compare these three methods used six oil sands samples (2 to 15% bitumen) and showed that the results were method dependent. The toluene extraction method gave results which were, on the average, 0.7% lower in bitumen than the carbon tetrachloride method. This was mostly attributed to the

higher water content determined by the toluene method. The toluene method, however, was found to give "the most uniform and accurate results" and also was faster than the carbon tetrachloride extraction method. The density method was not recommended as a laboratory method.

In 1974 the CPA Tar Sands Council reported [9] on the methods being used for oil-water-solids assay and the results from a round-robin study of the analytical procedures of various laboratories on assay analysis of Athabasca oil sands. A concern had been raised that different laboratory procedures might be yielding different results. This study of three oil sands samples (10 to 15% bitumen) compared results from four commercial laboratories and four oil industry in-house laboratories. It examined the consistency of the assay techniques and laboratory methods, and found generally good agreement amongst all laboratories. It was noted, however, that different companies require different degrees of "accuracy" in their analyses. The Tar Sands Council noted that sampling errors were probably significant.

Most laboratories used a version of the Dean-Stark analysis for the oil-water-solids analysis. These methods were similar to the toluene extraction method except that no fines correction was made. In the earlier study [8] the fines correction averaged 0.2% for the toluene extraction method.

A so-called Modified Dean-Stark method was also used in this second round-robin. Its advantage was that all three components, the bitumen, water, and solids were measured, and hence a mass balance could be calculated. In each of the earlier methods, the bitumen was calculated by difference. The Modified Dean-Stark method for bitumen determination was to evaporate most of the toluene and weigh the bitumen. A residual toluene correction was determined using infrared measurement. The Modified Dean-Stark method also incorporated a fines correction. Fine solids that passed through the thimble were measured after a centrifugation step. While this method was more time-consuming and hence more costly, the advantages of a mass balance and fines correction were realized.

The 1974 CPA Tar Sands Council study discussed other methods that were in existence but not widely used. These included the Retort and Pressure Elusion-Fisher Titration methods. All of these methods are documented [9].

The report discussed the errors involved in many of the steps of the analyses. Guidelines were given for

performing the Dean-Stark analysis. Considerable attention was drawn to the problem of the loss of water during the sampling and analysis steps. One of the Tar Sands Council's recommendations was that continuing research into bitumen analysis was needed.

During the following years, two commercial oil sands plants started production and many more laboratories began performing oil-water-solids assays. It was not until the 1980s that further round-robins were conducted in the industry. During the intervening years many of the laboratories in the 1974 study changed their methods or stopped doing this type of analysis. An Oil, Water, Solids Subcommittee was one of the first active groups of ACOSA, the Alberta Committee on Oil Sands Analysis. The subcommittee was open to any laboratory interested in oil-water-solids analysis of oil sand. Over the years, three round-robins were completed by this group. The subcommittee facilitated the exchange of methods among laboratories as well as a comparison of different methods. As with the earlier study, it was found that most laboratories used a version of the Dean-Stark or Modified Dean-Stark methods. The subcommittee recognized that no method was absolute but it did agree upon the ACOSA reference method:

The sample is separated into bitumen, water and solids by refluxing with toluene in a modified Dean-Stark extractor. Condensed solvent extracts the bitumen from the solids. The water azeotropically distills with the toluene and collects in the Dean-Stark trap. The water may be determined either gravimetrically or volumetrically. The solids in the thimble are oven dried and weighed. The toluene-bitumen bottoms are transferred into a volumetric flask and made up to volume. An aliquot is taken and placed on a glass fibre filter paper, the toluene is evaporated and the bitumen is weighed.

The main difference between the ACOSA reference method and the earlier Modified Dean-Stark method is in the determination of bitumen. This method is less time-consuming and less costly than the earlier bitumen determination method. Several laboratories analyzed for bitumen by placing the bitumen-in-toluene extract in an oven for several hours to remove the toluene. The round-robin results showed that procedure tended to yield low bitumen results, likely because of the loss of bitumen light ends during the drying step.

The ACOSA subcommittee documented the results from the round-robin studies. Table 3, taken from the ACOSA reference method, summarizes the precision of the oil sand analysis procedures.

While a type of Dean-Stark analysis is used in most laboratories, several novel methods have been reported over the years. These methods are not as universally accepted as the Dean-Stark method. In general, they were developed to meet specific needs.

Patel [10] reported a method in which toluene is pumped through a column of oil sand. The bitumen is determined spectroscopically by measurement at 530 nm and use of a calibration plot.
While the method has some advantages, its disadvantage is that any variations in bitumen composition would necessitate a new calibration graph. Bitumen composition has been reported to change with depth in the formation [11].

Syncrude Canada Ltd. developed a different method for oil sand assay. The summary of this Syncrude procedure [11,3] is:

A solvent blend of 74% toluene and 26% isopropyl alcohol extracts both the bitumen and the water from the solids producing a homogeneous liquid phase. The bitumen is determined gravimetrically on an aliquot of this solution. A Karl Fischer titration is used to measure the water concentration. Solids are measured gravimetrically.

The bitumen measurement step in this procedure is now used in the ACOSA reference procedure and also replaces the more time-consuming procedure used earlier by Syncrude Canada Ltd. in its Modified Dean-Stark method [3].

In the Gulf Canada Resources Ltd. method [12]:

The bitumen and water in the sample are extracted using tetrahydrofuran with subsequent determination of the bitumen using visible spectrophotometry and of the water using infrared spectrophotometry. The solids may be calculated by difference or measured gravimetrically.

The Petro-Canada Inc. method [13] to determine the bitumen-water-solids content of oil sand samples is as follows:

Table 3. Precision of oil-water-solids analyses.

		Oil sand grade		
		High	Medium	Low
% Bitumen	Mean	14.64	11.62	8.87
	SD[a]	0.32	0.20	0.42
	RSD (%)	2.2	1.7	4.7
% Water	Mean	1.45	3.63	4.65
	SD	0.17	0.26	0.27
	RSD (%)	11.7	7.2	5.8
% Solids	Mean	84.22	84.96	86.72
	SD	0.36	0.47	0.29
	RSD (%)	0.4	0.6	0.3
% Mass balance	Mean	100.31	100.21	100.24
	SD	0.36	0.47	0.42

Note: These values were determined from an interlaboratory round-robin in which each laboratory analyzed 10 replicate samples of each grade of oil sand. The standard deviation includes the variance due to subsampling the oil sand.

[a] SD = standard deviation. RSD = relative standard deviation.

The sample is received in a glass jar which becomes the distillation flask for a subsequent Dean-Stark extraction. The separated water is weighed. Solids are removed from the resulting toluene/bitumen solution by filtration. Bitumen is measured gravimetrically with a gas chromatographic measurement of residual toluene.

All of the above methods have been used with Athabasca oil sand. Oil-water-solids analysis of samples from other leases may require procedure changes. For example, oils containing significant light ends are not amenable to determination by the ACOSA reference method. Other methods, such as that of Gulf Canada Resources Ltd., must be used.

Oil sand is not the only type of bitumen-containing sample that is analyzed for its oil-water-solids content. Other process samples, for example, froth, middlings, and tailings, can be analyzed with only small changes in the oil sand method [3].

DETERMINATION OF PARTICLE SIZE DISTRIBUTIONS

Operators of oil sand processes have concerns about the particle size distribution of the solids in their material, for two reasons: operation of the hot water extraction process is significantly influenced by the amount of fine solids suspended in the water in the extraction cell; and, these fine solids are the most difficult to remove from recovered oil.

Particle size distribution (PSD) measurements have many applications in the mining and hot water extraction of oil sand:

• The fines content (<44 μm fraction) of an oil sand is one of the most significant variables in determining processability. Consequently, the particle size distribution is measured during coring programs as an indicator of the quality of reserves. Similarly, the scheduling of oil sand feedstocks to the extraction plant and the addition of caustic to improve recovery may be controlled by the PSD measurement.

Frequently the fines content and oil content are inversely related. This correlation is not sufficiently reliable for plant use.

- Optimal conditions for processes in which particle size and density separations dominate are determined by monitoring the process streams with PSD measurements. This applies to hot water extraction, tailings oil recovery, and froth treatment processes.
- Geotechnical behavior of natural soils, reject material, tailings, and settled fines may be predicted on the basis of PSD measurements.

The measurement of particle size distributions for oil sand process streams is subject to a number of difficulties which have led to considerable diversity in the methods used. The most important of these difficulties is the presence of bitumen, which, if not removed, interferes with the instrumental methods currently employed. Second, the dispersion of solids must be consistent with the application of the data, creating a difficulty in determining when an appropriate dispersion has been achieved. Third, each size-measuring technique provides a different measure of particle size for nonideal particles. Fourth, instrumental methods tend to use small samples with resulting subsampling problems. Finally, the particle sizes of interest range over about four orders of magnitude from the submicron level upward.

Bitumen removal

The usual method of removing bitumen from oil sands and process streams is the addition of solvent (e.g. a blend of toluene and isopropanol) to the sample to dissolve the bitumen, followed by centrifugation to separate the solids from the bitumen-laden solvent [3]. Repeated cleaning of the sample in this manner exhaustively removes the bitumen. The procedure however requires quite large amounts of solvent, is time consuming, and leaves a concern about the potential loss of very fine material during the centrifuging and solvent removal steps. In order to water wet the solids for analysis in water, the solvent washings are generally followed by washing with alcohol and water.

In the case of coring programs where many samples are analyzed, the time-consuming and expensive nature of this approach has led to the expedient of analyzing the cleaned solids from the thimble of the Dean-Stark oil-water-solids determination. The potential loss of fines in the thimble does not appear to degrade the PSD results relative to the solvent-washing/centrifuging technique. This sample preparation is inappropriate for

samples in which very fine particles are dispersed in large amounts of bitumen or water.

The degree to which the oil must be removed is method-sensitive, since some methods such as the Sedigraph are affected by even small amounts of oil, while others are quite oil tolerant. Clearly the most desirable characteristic for a PSD method would be a technique capable of determining the particle size distribution in the presence of bitumen.

Dispersion

The methods of sample dispersion are also critical to the results obtained. Coarse, discrete silica particles present no methodological difficulties, but this is not the case with clays, shales, and sandstones. It is often unclear whether a large lump of hard clay should be treated as one particle or a collection of very fine particles, and at what stage in the transition from a soft, easily dispersed clay to a shale, the sample should be considered as a single large particle. There is no hard and fast answer.

If a very fine sample dispersed in water is dried, it frequently forms lumps that are very difficult to redisperse. For coarse samples, it may be acceptable to wash and dry them, and then proceed to the analysis. For very fine particles, once they are cleaned of oil, it is better to maintain them in the wet suspended state until they have been separated or measured. However, if dried samples are encountered, wetting agents and sonification may effect dispersion. Each sample type has to be handled according to its particular requirements, and the suitability of the procedure should be verified by comparison to different handling procedures. In the end, the sample dispersion method should be appropriate for the planned use of the PSD data.

Measurement

All methods can be exact for ideal spherical particles of uniform density. The nonspherical nature of most real particles makes them act differently from spherical particles of equal volume. Each method responds differently to the nonspherical nature of the particles, and to differences in particle density. The result is disagreement between methods, which for ideal particles, may have been shown to be in full agreement.

Syncrude Canada Ltd. has used three PSD measurement methods for most process samples: screens, Sedigraph, and Microtrac [3]. These methods are described below; their advantages and disadvantages are summarized in Table 4.

Table 4. Comparison of particle size distribution methods.

	Advantages	Disadvantages
Screens	• low capital cost • widely accepted • portable • simple • measures wt%	• repeatability very operator-dependent • slow, especially below 45 μm • small sample size • needlelike particles measured on minimum size • platelike particles measured on maximum size
Sedigraph	• readings directly and accurately translate into settling properties of sample • measures all particles properly suspended at start of run • most operational problems (except proper initial suspension) are easily detected • direct reading in "wt% finer" • simple operation	• high capital cost • complex to service • requires sample screened to 45 μm • size reading may be in error due to density errors • size readings may be too small for clays • slower than microtrac • occasional coagulation problems • cell difficult to rebuild properly • poor sample suspension system (difficult to properly suspend larger solids)
Microtrac	• measures 176 to 1.9 μm in single measurement • rapid • highly repeatable • relatively operator-insensitive • large sample size • simple to operate • good sample suspension system	• high capital cost • complex to service • blind to particles larger or smaller than limits • vol% rather than wt% • overestimates volume of plate and needles • measures oil drops or air bubbles as solids • more difficult to detect problems • sample overloading results in size errors • size of plates and needles between maximum and minimum

Screens. The sample, either wet or dry, is placed on a screen in which the openings are of a known size, and those particles which cannot pass through are weighed to determine the portion larger or smaller than the opening size on the screen. While this is the simplest procedure, it is difficult to perform repeatedly and accurately. The screen must be monitored for wear from time to time. Larger particles tend to close off the openings and prevent small particles from passing through, while some larger particles may find holes larger than the nominal size and pass through. Workers need to review the screen specifications from time to time to be reminded of what portion of the openings are larger than the nominal screen size. Wet screening is the preferred technique for samples high in fines content.

Sedigraph. A sample, from which particles larger than 45 μm have been removed by screening or another method, is suspended in water. The sample is transferred to a small cell, and then allowed to settle. The settling of the solids is monitored using an X-ray densitometer and interpreted by applications of Stokes' law. A plot directly indicating the portion of the solids smaller than a so-called equivalent settling diameter is

drawn. These data accurately predict settling properties of the material, but may deviate significantly from other particle size measurements, especially for clays and similar particles which are thin, flat plates.

Microtrac. The sample is suspended in a recirculating water medium, and passed through a cell. The instrument measures the diffraction pattern produced by the particles when a laser beam is passed through the cell. This diffraction pattern is interpreted to provide the particle size distribution of the particles in a printed tabular form. Critical to the application of this instrument is the realization that it is totally blind to particles significantly outside its range. For example, the normal range of one commonly used Microtrac model is 1.8 to 176 μm. This means that samples with significant quantities of very fine (<1 μm) particles will show data errors because the instrument totally ignores the very small particles. Similarly, the instrument does not respond to particles coarser than the upper limit. Owing to the broad range of particle sizes present, the sample is screened to 150 μm and the Microtrac is used to characterize the –150 μm material. For appropriate samples, the Microtrac provides a wide range of data quickly and with little need for operator intervention.

CONTINUOUS MONITORING OF OIL SAND OIL CONTENT

Laboratory analyses of oil sand oil-water-solids content are valuable in determining the feed grade of material in the formation or in stockpiles, but for plant operations Syncrude Canada Ltd. has found it difficult to predict the timing and extent of feed grade changes using data on the oil sands grade in the windrows. Laboratory analyses of actual feed material cannot be produced with sufficient speed to control the plant operation, since it has been found that critical changes in feed grade may occur over periods as short as 15 to 20 min. As a result, Syncrude Canada Ltd. has developed an on-line instrument capable of monitoring the oil content of the oil sand feed as it flows into the plant on conveyor belts.

This section will describe the monitor in general terms, its location, the limitations and problems experienced by the unit, and some comments regarding its use.

The monitor, referred to as a Wright and Wright monitor, is a near-infrared reflectance instrument. It is made up of three major parts:

- A 250-watt tungsten-halogen light source housed in a reflector spotlight assembly. This unit uses 130-volt lamps, operated at 120 volts to obtain long life from the lamps. Typical lifetime is six to eight months. The light from the lamp is concentrated into a circle about 30 cm in diameter when operated at a distance of 140 cm.
- An optical-electronic measuring head containing:
  - an infrared-transmitting lens, to focus light from the measurement area onto the detector,
  - an indium arsenide photo-detector and preamplifier, to measure incident light, and convert this measurement to a useful signal,
  - a motorized filter wheel, that alternately places each of two narrow-band near-infrared optical filters between the lens and the detector,
  - a system for detecting which filter is in place, and routing the detector output to either a reference or measure signal integrator-amplifier,
  - appropriate amplifiers and power supplies.
- An electronic interface that receives voltage signals from the measuring head for the measure and reference beam intensities, and converts the signals to a current loop signal proportional to the oil content of the oil sand.

The light source and measuring head are those found in a slightly modified infrared oil film monitor, model E-250, manufactured by Wright and Wright, Inc. of Oak Bluffs, MA. Syncrude Canada Ltd. installs the appropriate filters and adds the interface box. This is a custom Syncrude design. The system as a whole is described in some detail in Canadian and US patents [14,15].

The basis of operation of the monitor is the existence of an oil absorption band at 2.2 μm in the near-infrared. Two filters are used: one specified for 2.22 $\pm$ 0.01 μm centre wavelength, 0.08 to 0.11 mm band width, and the other specified for 2.33 $\pm$ 0.02 μm centre wavelength, with the same band width. These filters serve to measure the reflectance of the oil sand just to one side of, and within, the oil absorption band. The stronger oil band at shorter wavelengths shows interference by bands from certain minerals in the oil sand.

The ratio of the measure and reference signals from the instrument provides a measure of the extent to which oil in the sample has absorbed the measure wavelength of light. Through comparison of the ratio to that for oil sands of known oil content, a calibration is obtained.

The electronics are adjusted to provide an output signal changing from 4 to 20 mA as the oil sand oil content changes from 5 to 15%. The reference signal compensates for variations created by the changing particle size, packing density, and profile of the material.

Oil sand is fed from up to four apron feeders, onto a small cross-conveyor that feeds the main conveyor where the measurement is taken. The instrument is set up with the light source and measuring head suspended above the oil sand on the conveyor belt. The light source and lens are targeted on the same area, with a sensitive area 10 to 12 cm in diameter. The interface is housed nearby, and connected by cables. In this location the ambient conditions are quite stable.

A critical factor is the ability of the instrument to operate at a sufficient height above the moving oil sand that it is not damaged by the passage of rocks or mounds of oil sand on the conveyor. The Wright and Wright system appears to do this well, although the signals are lower than ideal. The height requirement forced the development of this hardware. Commercially available instruments all seemed to operate only at very short distances.

This system, of course, is not ideal. The instrument sees only a thin layer of oil sand on the top, and in the centre, of the conveyor belt. If this portion is not representative of the whole, the result will be invalid, even if the instrument response is ideal.

In practice the instrument signals are integrated to produce an average over 30 s, resulting in the response being the average of that for a strip of oil sand 10 cm wide and about 76 m long. This averaging considerably reduces the problem of ensuring that the instrument response is an average for the whole of the feed. It is not, however, the complete answer.

It is possible to have the material from one apron feeder deposited onto the surface of the main belt selectively, and if that feed is not of the same composition as the feed from the other feeders, the response will not be correct. In addition, empty spots on the belt, when they occur, are averaged in as zero oil. This was found to be a major problem when trying to place an instrument on the conveyor belt in the mine area, since there are frequent short intervals when the belt runs empty.

In general, however, the instrument response has been reasonably good. The major difficulty has been in calibrating it properly, maintaining the calibration, and obtaining valid grab samples to evaluate its response. Experience has shown that it is extremely difficult to obtain representative samples from large, fast moving, highly loaded conveyors such as those used by Syncrude Canada Ltd. This fact has made it impossible to define the accuracy and precision of the instrument. An example of the recorder tracing from one of the instruments is shown in Figure 4.

The degree of agreement between the on-line monitor and laboratory analysis ranges from excellent to fair, depending upon the care exercised in sampling for the laboratory comparison sample, and the care being taken to maintain the instruments in calibration. A weekly calibration check is recommended.
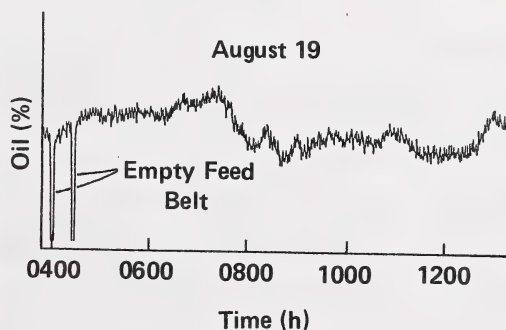
Figure 4. Recorder tracing from Wright and Wright instrument.

These instruments have been operating on all four feed conveyor belts to the Syncrude Canada Ltd. extraction plant since the summer of 1980. While they do not always agree as closely as wished with laboratory assays, they have provided a valuable immediate indication of the feed grade being provided, and a good indication of trends in the feed grade. As such they have become one of the key process monitors in the Syncrude Canada Ltd. extraction system.

BITUMEN ANALYSIS

Bitumen [16] (Table 5) differs from conventional crude in many regards but most notably it is characterized by:
- High molecular weight (low volatility), about 50% is sufficiently volatile to vacuum distill without thermal cracking;
- High sulfur content;
- High nitrogen content;
- High carbon:hydrogen atomic ratio.

Table 5. Typical Athabasca bitumen elemental analyses.

Element	Analysis (wt%)
Carbon	83.1
Hydrogen	10.6
Nitrogen	0.4
Sulfur	4.8
Conradson carbon (not ash corrected)	13.5
Oxygen	1.1
Carbon:hydrogen ratio	7.8

Bitumen is often classified according to region; for example, in Alberta, Canada where large deposits of bituminous sands are being developed, some typical kinds include Athabasca, Cold Lake, Peace River, and Wabasca. Detailed analysis reveals that there are differences in bitumen composition depending on source and method of separation from the parent material (oil sand). It is well known from detailed chemical composition studies (gas chromatography, mass spectroscopy, and others) that bitumen is a very complex mixture of numerous hydrocarbons. The oil sand industry's most commonly-used chemical definition of bitumen relates to the laboratory method of measuring bitumen concentration. An earlier section of this chapter discusses the oil-water-solids methods of analyzing oil sand. The most widely used technique is the extractor method, and as a consequence, the most widely used analytical definition of bitumen is "that portion of the oil sand hydrocarbon that is extracted by hot toluene under the conditions of the Modified Dean-Stark extractor method of analyses."

There are numerous sample types from which one can extract bitumen. The potential for different bitumen compositions is a direct function of the number of geological facies that are used to classify an oil sand deposit. Also, the many different bitumen-containing process streams generated by commercial hot water processes and in situ processes can result in differences in bitumen composition, dependent on process conditions and isolation methods. Therefore, one should be very careful to consider the bitumen source when comparing bitumen properties. The following is a review of several laboratory analytical procedures that are routinely used by the oil sand industry to characterize bitumen.

Sulfur

Much has been published on methods to determine sulfur in petroleum and petroleum-related products such as bitumen [17]. These laboratory methods can be grouped as combinations of combustion (sulfur is converted to sulfur dioxide), gravimetry or combustion, and titration. X-ray fluorescence is also a commonly used instrumental technique. Most of these methods have repeatabilities in the 0.1 to 0.2% range for samples containing 4 to 5% sulfur. For example, one method commonly used is the Leco combustion procedure (ASTM D1552) which claims a repeatability of 0.24% for samples containing sulfur at the levels expected in bitumen. The literature reports that, based on an interlaboratory statistical study [17], none of the many methods in use gives data that are significantly different. Syncrude Canada Ltd. reports the use of X-ray fluorescence and oxidative microcoulometry methods for measuring sulfur in bitumen-like samples. Their standard research practice for bitumen analysis is to use the Dohrmann microcoulometric titration system MCTS-30 (Dohrmann Division of Envirotech Corporation, Scott Boulevard, Santa Clara, CA) [3]. Quantification is based on comparison with the electrical current required to titrate the sulfur dioxide produced by combustion of an *n*-butyl sulfide standard. The technique is particularly useful, having broad application to the many different sample types of differing sulfur concentrations. Syncrude Canada Ltd., Research Department also determines sulfur in bitumen, coke, and coked sand using the Fisher model 470 sulfur analyzer (Fisher Scientific Co., 711 Forbes Avenue, Pittsburgh, PA). This is a combustion-titration technique with special advantages due to microprocessor control. A relative standard deviation of 2% is achieved.

Nitrogen

Total nitrogen (0.3 to 0.6 wt%) like total sulfur can be measured in bitumen by a number of different laboratory methods. The procedure traditionally used by bitumen testing laboratories is based on the classical Kjeldahl digestion technique (ASTM D3228). A brief survey of the literature revealed that there are three major method groupings: the Kjeldahl digestion based methods, the standard elemental combustion instrumental methods, and the method(s) based on chemiluminescence detection of nitric oxide after combustion in an oxygen-rich atmosphere. This latter technique is the most recent method applied to nitrogen

analyses. It is the approach that Syncrude Canada Ltd. uses in its Research Department Laboratory [3]. A recent round-robin laboratory study reports an overall mean of 0.44 wt% total nitrogen in Athabasca bitumen (Suncor coker feed bitumen) [17]. Eighteen different laboratories participated in the study.

DENSITY DETERMINATION

Density is a characteristic of interest for most petroleum fluids. Bitumen is no exception. Density is a process parameter in the separation of bitumen from oil sand, a means of converting mass to volume, and a fundamental physical property used to characterize bitumen.

Several techniques are in use for determining the density of bitumen:
- ASTM D70, pycnometer,
- ASTM D71, displacement,
- ASTM 4052, digital density meter,
- ASTM D1298, hydrometer,
- use of the above methods to find the densities of a series of bitumen/solvent mixtures and back-calculation of bitumen density.

The first four methods listed are measurements that are directly related to the density of the bitumen; no assumptions about the nature of the sample are made. Density determinations using bitumen/solvent mixtures, however, assume that solution nonidealities are totally accounted for in the calculation procedure; if this is not the case, some bias will be introduced into the determination.

Several problems can interfere with the accurate determination of bitumen density:
- Residual solids remain in the bitumen, even after Dean Stark extraction.
- Residual solvent may remain with the bitumen if an extraction step is used to isolate the bitumen.
- Light ends may be lost from the bitumen during the isolation step (or during storage).

Clearly, each of these problems could have an observable effect on the measured density of a bitumen sample.

A typical value for the density of Athabasca bitumen is 1.01 g/cm^3 at 15°C. The variation of bitumen density with temperature is reasonably well modelled by the API petroleum tables.

CARBON RESIDUE

Carbon residue levels have long been used in the characterization of conventional petroleum fluids. They are similarly applicable in bitumen characterization. The amount of carbonaceous residue left after the evaporation and pyrolysis of a petroleum fluid provides an indication of the relative coke-forming propensity of that fluid. There are three standard methods for assessing the amount of carbonaceous residue: Ramsbottom Carbon Residue (RCR) ASTM D524, Conradson Carbon Residue (CCR) ASTM D189, and Micro Carbon Residue (MCR) ASTM D4530.

Conradson Carbon Residue determination has been, until recently, the method of choice for bitumen characterization. At present, Micro Carbon Residue determinations are being used in preference to CCR determinations. The MCR determination is carried out in a microprocessor-controlled combustion chamber while the CCR determination is carried out using a Meker burner. This difference leads to the superior precision of MCR determination owing to improved control of combustion parameters. Both methods do, however, generate equivalent results. A typical MCR/CCR for Athabasca bitumen is 12.6% by weight.

Although Ramsbottom Carbon Residue determinations are possible with bitumen samples, they are operationally more difficult than either Conradson Carbon Residue determinations or Micro Carbon Residue determinations. A typical Ramsbottom Carbon Residue value for Athabasca bitumen is 10.6% by weight.

No satisfactory one-to-one correlation exists, for Athabasca bitumen, between RCR values on the one hand, and CCR/MCR values on the other.

An additional complicating factor for carbon residue determinations on bitumen arises from the unavoidable presence of inorganic solid material in bitumen samples. These solids are included in the residue determined. It is usual therefore, to report both carbon residue values and ash values for bitumen samples. Some laboratories may report a carbon residue value as "ash corrected." This involves additional analysis of the residue in the case of CCR, or of a separate subsample in the case of MCR or RCR.

Methods used for ash determination are numerous. Both the duration and temperature of the ashing procedure affect the result obtained. A typical ash value

for Athabasca bitumen is ~0.5% by weight.

DISTILLATION

Bitumen is subjected to distillation on a laboratory scale for two main reasons — simulation of distillation under plant conditions and characterization of the range of hydrocarbon species present in the bitumen. The distillation of bitumen presents several difficulties:
- Pot temperatures above 360°C lead to cracking of the bitumen (at atmospheric pressure, only ~10% of the bitumen typically distills before cracking).
- Excessive frothing is encountered when bitumen is degassed.
- Poor heat conduction through the bitumen can lead to localized overheating resulting in bumping or cracking.

A large number of bitumen distillation methods have been developed. There is no concensus among the laboratories that analyze bitumen as to which method is best. However, ASTM D1160 is most widely used for the distillation of bitumen and bitumenlike samples.

Methods for bitumen distillation include:
- ASTM D1160. The distillation is carried out at 1.0 mm Hg (0.13 kPa) with a separation equivalent to one theoretical plate. Material is distillable up to approximately 550°C atmospheric equivalent temperature (AET).
- Vacuum Pot-still HIVAC (proposed ASTM Committee D02.08C). This still operates at 0.2 to 0.3 mm Hg (0.03 to 0.04 kPa) with a separation equivalent to one theoretical plate. This method will distill material up to approximately 550°C AET.
- ASTM D2892 (also called TBP or 15/5). The distillation is carried out at 2 mm Hg (0.27 kPa) with a separation equivalent to 14 to 18 theoretical plates (nominally 15). A reflux ratio of 5:1 is used. Material is distillable up to about 450°C AET.
- Spinning band distillation. [3] The distillation is done at 0.6 mm Hg and achieves a separation comparable to a large number of theoretical plates (nominally 30). A reflux ratio of 3:1 is used and material distills off up to approximately 500°C AET.
- Short path distillation. [18] This is a proposed ASTM method for molecular distillation. The separation is carried out at 0.001 mm Hg (1.3 x 10^{-4} kPa) to approximately 650°C AET. The boiling ranges of fractions generated by short path are usually determined using another distillation method.
- Simulated distillation by gas chromatography. This is a proposed ASTM method (ASTM D-2 Proposal P167) that determines the boiling range distribution of a sample up to 538°C. The amount of sample boiling above 538°C is estimated by means of an internal standard.
- Thermogravimetric analysis [19] has been suggested as a form of simulated distillation that can correlate well with ASTM D1160.

Of the above methods, the first four are more useful for predicting the results of bitumen distillation on a commercial or pilot plant scale. The last three methods are more suitable for characterization of a bitumen sample in terms of boiling range.

The data generated by each of the techniques are not directly comparable since the basis of separation for each technique is different. Distillation results using ASTM D1160 for a typical bitumen sample are given in Table 6.

Table 6. Distillation results for a topped Athabasca bitumen using ASTM D1160.

Volume distilled (%)	AET (°C)
5	325
10	360
20	400
30	450
40	510
cracking	540

FILTRATION

The filterability of upgrading process streams is of interest as an indicator of process operability and as a measure of potential downstream fouling. Dry sludge may be defined as the material separated from the bulk of an oil by filtration and which is insoluble in heptane [20]. *Existent* dry sludge is the dry sludge in the original sample as received. This material is distinguished from the *potential* dry sludge obtained by aging the sample at an elevated temperature. The existent dry sludge test was originally developed in the early 1950s to measure the cleanliness of residual fuel oils. One implementation of the test is the Shell Hot Filtration Test [20]. In this test, the undiluted oil is heated to 100°C and filtered at

that temperature through a Whatman 50 filter by applying pressure (500 kPa) and pulling a vacuum (13 kPa). The material retained on the filter is washed with heptane, dried, weighed, and reported as a percentage of the sample weight.

In recent years, the hot filtration technology has undergone several modifications to adapt it to new applications [21,22]. The changes include replacement of the Whatman 50 filter with Whatman GF/A filter to improve filterability, and the inclusion of a second filter under the first filter to provide a correction for oil adsorption to the filter. There has also been some movement away from the use of pressure by providing instead the capability of varying the filtration temperature.

Of particular interest is the ability to distinguish between the hydrocarbon and extraneous components (e.g. clay, silt, sand, rust, coal, coke, fiber, catalyst fines) of the filterable material. Literature reports the use of ASTM D473 for this purpose [21]. An alternative is the use of the hot filtration apparatus at room temperature to filter samples diluted five- or ten-fold in toluene. In the case of bitumen feed, this extraneous matter may be of the order of 1%. Typically, a relative standard deviation of 1 to 2% is obtained using filtration to determine extraneous matter. On the other hand, the existent dry sludge precision varies with the sample type. Relative standard deviations may be similar to those for the extraneous material, or they may be degraded substantially, depending on the filterability of the sample.

WATER ANALYSIS — ANIONS

Water is an important component in the operation of an oil sand plant based on the hot water extraction process. For example, the Syncrude Canada Ltd. plant processes about 2.3×10^6 L of potable water and 2×10^8 L of process water each day. Although the volume of water is impressive, the quality of that water is also of great significance:
- About half of the process water is used for steam generation and requires cleanup to a high level of purity.
- The composition of aqueous plant streams permits monitoring of process effectiveness, for example, residence-time studies, carryover between streams, maximization of water recycle.
- Water quality may also be understood in terms of the

corrosivity, and the need for corrosion control to extend plant life.
- Numerous aqueous samples also arise as part of the environmental monitoring program.

Dissolved anions play an important role in all aspects of water quality [23,24]. The anions commonly measured include chloride, sulfate, cyanide, sulfide, thiocyanate, and carbonate/bicarbonate. Of lesser interest are phosphate and nitrate. Chloride and sulfate are present at significant levels in natural waters. Sulfide, cyanide, and thiocyanate are added to aqueous streams during the upgrading of bitumen. Carbonate/bicarbonate and chloride are present at high levels in the depressurization wells while hydrogen gas treatment streams are particularly high in carbonate/bicarbonate.

The concentrations of the anions of interest cover a very wide range. Sulfide and its oxidation offspring may be present at the level of several percent in upgrading streams. Depressurization wells may contain 5000 mg/L chloride; connate waters can range from one to 20 mg/L chloride or from 10 to 700 mg/L sulfate. Cyanide may be present at the 10 to 100 mg/L level if an additive was not used to convert it to a less corrosive species. Finally, in high purity water produced for use as boiler feed water, anions have been reduced to the level of a few micrograms per litre.
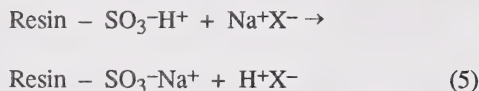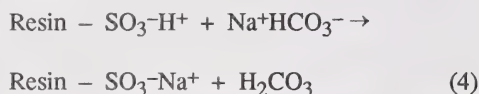
In recent years ion chromatography has become the dominant technique for determining anion concentrations in an industrial oil sand setting. It has displaced ion-selective electrodes which previously had provided a simple alternative for some analyses. The only remaining anions not routinely determined by ion chromatography are those where concentration levels are sufficiently high that titration is suitable. Examples include the determination of sulfide by silver nitrate titration and the determination of carbonate/bicarbonate by titration with hydrochloric acid.

Ion chromatography is a type of liquid chromatography in which ionic constituents are separated by ion exchange followed by eluent suppression and electrical conductivity detection. Eluent suppression refers to the substantial reduction in background conductivity by exchanging the cations of the eluent (the salt of a weak acid) for hydrogen ions. The process also converts the analytes to their acid form. Thus the analytes give a strong conductivity signal compared to the background and the same response independent of the associated cation in the original sample. In a typical ion chromatography analysis, dilute

$Na_2CO_3/NaHCO_3$ eluent separates sample anions (e.g. $X^- = F^-$, Cl^-, NO_2^-, PO_4^{3-}, Br^-, NO_3^-, SO_4^{2-}) by ion exchange on a separator column:

$$Resin - N^+HCO_3^- + Na^+X^- \Leftrightarrow Resin - N^+X^-$$

$$+ Na^+HCO3^- \qquad (3)$$
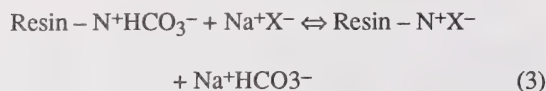
The suppressor reduces the background conductivity by changing carbonate and bicarbonate to carbonic acid and by converting the sample anions to their acid form:

$$Resin - SO_3^-H^+ + Na^+HCO_3^- \rightarrow$$

$$Resin - SO_3^-Na^+ + H_2CO_3 \qquad (4)$$

$$Resin - SO_3^-H^+ + Na^+X^- \rightarrow$$

$$Resin - SO_3^-Na^+ + H^+X^- \qquad (5)$$

In the early days of ion chromatography, suppression was accomplished with a packed column that required frequent acid regeneration. Presently, a micromembrane suppressor is available that provides continuous eluent suppression and regeneration.

The advantages of ion chromatography for the analysis of aqueous streams associated with an oil sand plant include:

- Provision of a multi-ion scan: Fluoride, chloride, nitrite, phosphate, bromide, nitrate, and sulfate can be detected on a single scan.
- Low detection limits: A common working range is 0.5 to 5.0 mg/L for chloride and 1.0 to 10.0 mg/L for sulfate. Dilution of more concentrated samples to this working range ensures a well-characterized working range, minimizes the potential for interferences, prevents column overload, and reduces maintenance requirements. This so-called dilute and shoot approach is well suited for most analysis in the oil sand industry. However, in the case of high-purity waters such as boiler feed water where anion concentrations have been reduced to the level of a few micrograms per litre, the typical 50 to 100 mL sample loop is replaced by a concentrator column. Sample is concentrated on this column to provide a well-detected amount in the analysis while ensuring that breakthrough does not occur during column loading.
- Good precision: The precision for measurements over a 0.5 to 5.0 mg/L chloride working range is typically

2% (relative standard deviation).
- Automation: Ion chromatography may be fully automated using an autosampler with computerized data handling. Similarly, on-line ion chromatography instrumentation is well developed and may be used to monitor water quality in oil sand plant utilities operations.

WATER ANALYSIS — CATIONS

The monitoring of cations in aqueous process streams is required in many areas throughout an operating oil sands plant. The supply of vast amounts of process and boiler feed water requires close monitoring to meet specification, especially in the latter case. The monitoring of boiler feed streams for cation content is directly related to the prevention of scale buildup in the lines and boilers.

The cation levels routinely monitored are in the parts per billion range, thus limiting the analysis techniques that can be used. Analyses at these low levels are most readily and traditionally carried out using a flameless atomic absorption spectrometer. The sample is injected, in microlitre quantities, onto a flameless carbon rod apparatus. A controlled temperature/time program effectively vaporizes the sample into the beam of a hollow cathode lamp, designed to emit light composed of wavelengths specific to the elements of interest. The intensity levels of the element-specific wavelengths are measured after passing through the sample vapor and are then related directly to concentrations through the use of calibration curves employing known standards.

The use of ion chromatography for the quantification of cations present in an aqueous stream is very recent technology and also provides the appropriate sensitivity and selectivity required. The use of an ion chromatograph is also amenable to monitoring the levels in an on-line mode. Again comparison with a calibration curve employing known standards is used. The section on anion analysis provides a description of the instrumentation and theory employed in ion chromatography.

Cations of concern in the utilities area include the following: Na^+, K^+, Ca^{2+}, Mg^{2+}, Fe^{2+}, Cu^{2+}. All are maintained below the 10 ppb level in the utility areas.

The precision of the analysis using either atomic absorption or ion chromatography is typically better than 2% relative. The accuracy of the analysis is dependent

upon the calibration standards used.

Aqueous NH^{4+} originating in several process streams is also monitored at relatively high levels (down to 5 ppm) using an ion-selective electrode.

WATER ANALYSIS — TOTAL ORGANIC CARBON

Total Organic Carbon (TOC) analyses have two major areas of application in the oil sand industry:
• Environmental monitoring,
• Investigation of the role of organics during water treatment.

Environmentally, organic matter exerts a demand on oxygen, while in water treatment, organics foul the ion exchange resins used for demineralization. The analytical techniques normally referred to as TOC are not used for monitoring the hot water extraction process. Technologies referred to as oil-in-water and oil-water-solids analyses are employed for this process monitoring and are described elsewhere.

Samples for TOC analysis generally occur in the range of 1 to 100 mg/L TOC. Boiler feed water samples fall at the low end of this range; raw water has TOC levels around 10 mg/L and tailing pond water contains about 60 mg/L. Complicating the issue somewhat is the presence of inorganic carbon in samples, and the desire to distinguish among the types of organics which may be present. In the first case, most TOC analyzers now have the capability to distinguish between organic and inorganic carbon. Two injections may be used — the first is a combustion to determine total carbon, and the second, at low temperature in an acid environment, determines total inorganic carbon. On the other hand, the sample may be treated with acid and sparged to remove the inorganic carbon before the TOC determination. The second complication arises because organic materials may be added to inhibit utility plant corrosion. In this case, straightforward TOC analysis does not distinguish between the naturally occurring organics and the corrosion inhibitors.

Total organic carbon analyzers use a two-step process:
• Oxidation of organics to CO_2,
• Quantitative determination of CO_2.

Nondispersive infrared detection is by far the most common means of quantifying the CO_2. The last decade or so has seen several technologies for converting organics to CO_2 gain popularity and regulatory recognition. Combustion of microlitre-sized samples at 850 to 950°C has relatively high detection limits. On samples without particulates, precision of the combustion technique approaches 1 to 2% or 1 to 2 mg/L, whichever is greater [25]. Sampling particulate matter on unfiltered samples limits precision to about 5 to 10% relative. On the other hand, these instruments tend to require significant amounts of maintenance due to catalyst poisoning or solids buildup. The combustion method does, however, analyze samples with high particulate content better than succeeding technologies. Consequently, other instruments often include a so-called sludge module to provide combustion capability. In recent years, ultraviolet-promoted persulfate oxidation has gained popularity due to its lower maintenance and lower detection limits compared to the combustion approach. The risk of incomplete conversion of organics to CO_2 is higher and oxidation of particulates is not assured. Another variation of the persulfate oxidation is heating the sample chamber to 90°C to encourage the kinetics of the oxidation. These types of instruments claim detection limits between 4 and 100 mg/L and precision of the order 2% at levels well removed from the detection limits.

In water treatment work, measurement of the absorption at 254 nm has been used as a proxy for the TOC measurement. Exclusive use of this ultraviolet absorbance is misleading since it does not allow for variation in the types of organics present [26]. Ultraviolet absorbance can be used as a monitoring tool, provided results are calibrated with TOC values.

METALS ANALYSIS OF OIL SAND AND BITUMEN

Oil sand, and consequently bitumen, may contain a wide variety of metals, some very important to the process aspect of an oil sand plant operation, and others critical to the environmental considerations of the plant operation. Areas impacted by the metals content include: plant operating efficiency, product quality (customer requirements), and environmental quality (air, water, soil). The relative amounts of metals present and their groupings are usually indicative of the location and geological formation from which the sample is derived. The metals, potentially present in all phases, are found in a variety of forms:
• inorganic complexes, including clays, oxides, sulfides, carbonates;

- organo-metallic complexes;
- dissolved salts such as Na, K, Ca, and Mg salts;
- process accumulated metals such as Fe, Sn.

The solids found in oil sands typically comprise 80% of the sample and include sand, clays, metal oxides, sulfides, and carbonates. Clays, primarily kaolinite and illite, are defined on the basis of a particle size as being less than 4 µm in diameter. Due to their small size, clays and metal oxides can readily remain suspended in the bitumen throughout the extraction, settling, and centrifuging processes, and therefore may enter into the upgrading streams. This can be a problem from the standpoint of poisoning of catalysts, as well as the buildup in, or clogging of, catalyst beds thus limiting throughput. Table 7 indicates typical levels of some of the predominant metals found in Athabasca oil sand solids.

Table 7. Levels of metals present in typical Athabasca oil sand solids.

Metal	Content (%)	Metal	Range (%)
Si	39–45	Ca	0.0–0.88
Al	1.5–4.0	Fe	0.3–0.25
Ti	0.10–0.35	Ba	0.0–0.04
Mg	0.0–0.88	Zr	0.01–0.04

Note: Many other metals are found to be present at trace levels.

A number of the heavy metals such as Ni, V, Cu, Hg, and Fe can also be effectively bound in large organic molecules characteristic of those found in the asphaltenes (nonpentane-soluble portion of the hydrocarbons) and resins. Ni and V porphyrins are commonly found and show high thermal stability allowing them to pass through the extraction process into the upgrading process. Porphyrins are the major, but certainly not the only, organo-metallic complexes present. Metals may simply be entrapped or loosely bound in the very large molecules present in the asphaltenes and resins. Although Fe is present as an organo-metallic, it occurs mostly in the form of process-accumulated rust. Since catalysts are used extensively in upgrading and are readily poisoned by these heavy metals, it is important to know the amounts present. Significant levels typically found in Athabasca bitumen

include Ni, 50 to 100 ppm; V, 150 to 250 ppm; and Fe, 300 to 1000 ppm.

Environmental concerns over the levels of heavy metals result mainly from the metals carried into the tailings pond and gaseous emissions from the main plant stack. Of most concern are Ni, V, Fe, Pb, Hg, and Be owing to their toxicity.

Oil sand solids, bitumen, and environmental samples are routinely analyzed by one or more of the following techniques: atomic emission/absorption, X-ray fluorescence/diffraction, classical wet methods, and neutron activation.

The analysis technique should be selected depending on the sensitivity required, the compatibility of the sample matrix with the specific analysis technique, and the availability of facilities. Sample preparation, if required, can present problems. Significant losses can occur, especially in the case of organo-metallic complexes, and contamination of environmental samples is of serious concern. Both wet and dry ashing of samples can lead to significant losses of metals such as Hg and As. Preparation techniques should be carefully reviewed before use.

For very low level samples such as those typically found in environmental samples (parts per billion range) flameless atomic absorption is the most commonly used technique. Use of a combination plasma atomic emission/mass spectrometry technique will become future standard for this type of analysis.

For samples in an aqueous matrix at moderate levels (0.1 to 200 ppm) the plasma atomic emission technique is currently the most applicable. Analysis is achieved to monitor the emission intensity of the element-specific ultraviolet/visible radiation emitted as the sample is aspirated into the highly energetic plasma excitation source. Excitation through air/acetylene or nitrous oxide/acetylene flame sources may also be used for the analysis of the light alkali metals, especially potassium. Absolute concentration levels are determined through comparison with known standards analyzed in a similar matrix. Techniques employing excitation sources such as an arc or spark can also be used effectively for semiquantitative analysis.

Analysis for metals in an organic matrix is most easily accomplished using X-ray fluorescence or neutron activation techniques for quantitative analyses. These particular techniques are also applicable for the direct analyses of oil sand solids. Spark techniques can be used for qualitative analyses. The direct aspiration of metal-containing hydrocarbons into the plasma

instrument also provides quantitative information, with the assumption that particulates present are fully incorporated into the analysis.

The precision of the analysis depends on the technique selected, the matrix in which the metal is analyzed, and the particular metal in question. Relative standard deviations range from 1% to >20%. The accuracy of the analysis is largely dependent on the quality of the calibration standards employed.

REFERENCES

1. D. Wallace and B. Kratochvil, Sampling uncertainty in the determination of major components in Athabasca oil sand, AOSTRA J. Res., 1 (1984) 31.

2. R.C. Shaw, Subsampling bulk quantities of oil sand for oil, water, and solids analysis, Alberta Committee on Oil Sands Analysis Workshop, Lake Louise, Alberta (1983).

3. J.T. Bulmer and J. Starr, "Syncrude analytical methods for oil sand and bitumen processing," The Alberta Oil Sands Technology and Research Authority, Edmonton, Alberta (1979).

4. D. Wallace and B. Kratochvil, Use of a mill and spinning riffle for subsampling laboratory samples of oil sand, AOSTRA J. Res., 2 (1985) 37.

5. C.O. Ingamells and P. Switzer, "A proposed sampling constant for use in geochemical analysis," Talanta, 20 (1973) 547.

6. D. Wallace and B. Kratochvil, Evaluation of statistical sampling methods for Athabasca oil sand, AOSTRA J. Res., 2 (1986) 233.

7. J. Visman, A general sampling theory, Material Research Standards, 9 (1969) 8.

8. R.G. Draper, A. Yates and H. McD. Chantler, A comparison of three laboratory methods for determining the bitumen content of bituminous sands, Canada Department of Mines and Technical Surveys, Mines Branch, Report FRL-211, Fuels Division, Dec (1955).

9. Canadian Petroleum Association Tar Sands Council, J.R. Eade, Shell Canada Ltd., Chairman, Round-robin study of analytical procedures of various laboratories on assay analysis of Athabasca tar sands, Nov (1974).

10. S. Patel, Rapid and convenient laboratory method for extraction and subsequent spectrophotometric determination of bitumen content of bituminous

sands, Analytical Chemistry, 46 (1974) 794.

11. D. Lorne Ball, E.D. Cooke, J.M. Cooley, M. Coreen Hamilton and R. Schutte, A rapid method for the determination of bitumen, water and solids in oil sands, Can. J. Chem., 59 (1981) 1527.

12. D. Kulawic, J.E. Coffey, L.L. McCorriston and M.P. Hahto, Spectrophotometric determination of bitumen and water in heavy oil and tar sand, Abstracts, 28th Canadian Spectroscopy Symposium, Ottawa, Sept 28-30 (1981).

13. P.J. Williams and J. Duchowski, A technique for rapid separation of tar sands, American Laboratory, Aug (1983) 78.

14. G.R. Thompson, Canadian Patent 1,139,702, "Method and apparatus for on-line monitoring of bitumen content in tar sand," (1983).

15. G.R. Thompson, United States Patent 4,433,239, "Method and apparatus for on-line monitoring of bitumen content in tar sand," (1984).

16. Kirk-Othmer, "Encyclopedia of chemical technology," third ed., 22 (1973) p. 612, table 4.

17. D. Wallace, B. Kratochvil and D.L. Jo, Effects of sampling and analytical uncertainty on the determination of bitumen variability in oil sand as measured by sulphur content, AOSTRA J. Res. 1 (1984) 83.

18. C.J. Domansky, Short path distillation of Athabasca bitumen, AOSTRA J. Res., 2 (1986) 191.

19. F. Mondragon and K. Ouchi, New method for obtaining the distillation curves of petroleum products and coal-derived liquids using a small amount of sample, Fuel, 63 (1984) 61.

20. Shell Method Series, Existent and potential dry sludge contents of residual fuel oils - hot filtration test, SMS 742-83, Shell International Research Maatschappij B.V.

21. Shell Method Series, Existent and accelerated dry sludge contents of residual fuel oils - modified hot filtration test, SMS 2696-83, Shell International Research Maatschappij B.V.

22. C.P.G. Lewis, R. Quillet and T. Schreuder, Resid fuel-oil stability, cleanliness test improved, Oil and Gas J. (1985) 73.

23. J.T. Bulmer and R.E. Hoyle, Application of ion chromatography to process streams in an oil sand plant, 34th Pittsburgh Conference on Analytical Chemistry and Applied Spectroscopy, Atlantic City, NJ, Mar 7–12 (1983).

24. H. Small, T.S. Stevens and W.C. Bauman,

Analytical Chemistry, 47 (1975) 1801.

25. APHA-AWWA-WPCF, "Standard methods for the examination of water and waste-water," 15th Edition (1980) 471.

26. J.F. Selann, et al., Characterization vs identification of organics in boiler feed water treatment, 47th Annual Meeting International Water Conference, Pittsburgh, PA, Oct 27–29 (1986).

General references

1. B. Kratochvil, D. Wallance and J.K. Taylor, Sampling for chemical analysis, Analytical Chemistry, 56 (1984) 113R.

2 B. Kratochvil and J.K. Taylor, A survey of recent literature on sampling for chemical analysis, National Bureau of Standards Technical Note 1153, U.S. Department of Commerce, Washington, D.C. (1982).

3

BITUMEN AND HEAVY OIL CHEMISTRY

O.P. Strausz

Department of Chemistry
University of Alberta

INTRODUCTION

Major advances in the chemistry of heavy oil and extra heavy crude oils (bitumens) have been made since the early 1970s. Interest in these classes of crude oils has stemmed from their top-ranking position on the list of alternative fuels in many countries where availability and recovery prospects appeared favorable, and from the general worldwide recognition of their fundamental importance as the future source of liquid fuels. As a consequence, research in this field intensified in many countries and international cooperation has been effectively encouraged through the efforts of UNITAR and AOSTRA Library and Information Services.

The definitions of bitumen and heavy oil require some comments. The term petroleum has been recommended for the spectrum of solid, liquid and gaseous members of the common series [1]. The liquid members constitute crude oils and the gaseous members, natural gas. The solid members are variously called bitumen, asphalt, tar, or pitch. It has been recommended that pooled crude oils with API gravity of 10° or less, and having a viscosity of 10 000 cP or more under reservoir conditions, be called extra heavy oils. In all other cases where viscosities are 10 to 10 000 cP, the oil is termed heavy oil [2]. Since oils in this viscosity range would have an API gravity of 20° or less, they would be heavy oils if their viscosity is lower than 10 000 cP. These definitions, however, may lead to inconsistencies. As Tissot and Welte [3] point out, when comparing two reservoirs of different depths and temperatures but containing crude oils with the same physical properties, the one at the lower temperature could be termed extra heavy oil while the other, with the higher temperatures, could be regarded as heavy oil owing to decreasing viscosity with increasing temperature. The term extra heavy crude oil, however, may prove to be somewhat cumbersome and the simpler term bitumen may remain in common usage. A more detailed discussion of the characterization of heavy oils has been given by Yen [4].

Crude oils have been recognized as one of the most complex mixtures of organic compounds in nature, in spite of their relatively simple elemental composition. Heavy oils are even more complex because of their greater content of high molecular weight polymeric asphaltenes and resins, which form polydispersed micellar colloidal solutions, and also because they contain elevated levels of heteroatoms, nitrogen, oxygen, sulfur, metals, organometallic compounds, and some clay minerals. The range of elemental compositions and other properties of Alberta oil sands extra heavy oils are given in Table 1. Most other extra heavy oils show similar elemental properties, with a few notable exceptions.

Table 1. Range of elemental composition and other characteristics of Alberta oil sand bitumens.

Weight percent

C	81 – 84	S	4.6 – 5.6
H	10.0 – 11.0	V	160 – 300 (mg/kg)
N	0.3 – 0.6	Ni	60 – 100 (mg/kg)
O	0.8 – 1.6	Ash	0.5 – 1.0

H/C atomic ratio	MW	°API
1.46 – 1.50	490 – 620	6 – 13

Viscosity
1.8×10^4 to 10^6 cP, 15°C

Ramsbottom carbon
R.C. 0.3 x % asphaltene + 5.9, 10 – 13.7 wt%

Heat of combustion
41 000 – 42 600 kJ/kg

PROPERTIES OF ALBERTA OIL SANDS

The properties of Alberta oil sands and oil sands in general have been discussed in many excellent books [1–3,5–7], symposia proceedings [8–17], and reviews [18–20], during the past decade; consequently the emphasis here will be on more recent developments.

Alberta oil sands comprise up to ~20% bitumen; ~5% water; 75% sand, silts, and clays; and ~1% other particulate minerals — small amounts of organic materials which, unlike the bitumen, are insoluble in organic solvents, as well as gases and volatiles. The inorganic matrices of the Athabasca oil sands are 90% quartz with minor amounts of K-feldspar, muscovite, chert, and clay minerals. The clay minerals, which appear in the fines fraction (particle size <44 μm), are predominantly kaolinite and illite with lesser quantities of montmorillonite [21]. The in situ porosity is ~35% by volume, corresponding to 82 wt% minerals and 18 wt% bitumen-plus-water. The highest grade ores contain ~18 wt% bitumen. A broad correlation between bitumen, water, and fine content has been known to exist [22]: as the mineral content increases so do the fines and

water contents, at the expense of the bitumen. Ores with a bitumen content 10 wt% are rich oil sands and those with a bitumen content ≤6 wt% are lean oil sands. The general composition can be quite constant over large areas of the deposit but may also change abruptly. A gradual increase in the bitumen content of the oil sand as well as of the asphaltene content of the bitumen has been noted with increasing depth of the deposit [23].

The microscopic structure of the Athabasca oil sand has been studied extensively. According to the model of Takamura [24] the connate water which, in the case of high-grade ores is still about 2 to 3 wt%, is present in part as a 0.01–μm film covering the surface of the sand grains, and in part as pendular rings formed at grain-to-grain contact points. The presence of this aqueous film has long been thought to be responsible for the water-wet character and hot water separability of the bitumen. The film is stabilized by the electrical double-layer repulsive force acting between the negatively charged sand and bitumen surface. The estimated amount of water retained by the thin film represents <0.05% of the pore volume only, and thus the bulk of the water is tied up in the pendular ring structures. Yet 70% of the sand surface is covered by the thin aqueous film and 30% by the pendular ring structures.

In lower-grade oil sand, clusters of fine particles exist and these are saturated with water. Hence, the amount of connate water increases linearly with increasing fines content. The cluster size can vary from a few micrometres to greater than that of the coarse sand grains.

The process of hot water separation is governed by the magnitude of the interfacial tension between bitumen and water, the contact area between bitumen and sand, and the viscosity of bitumen.

The surface charge of the bitumen-water interface is thought to be due to the dissociation of carboxyl groups naturally present in the bitumen. Theory predicts that the dissociation behavior of carboxyl groups at the interface depends strongly on the electrolyte concentration in the aqueous solution. The empirically-known adverse effect of multivalent cations on water-based separation methods has been interpreted by Takamura [24] as being due to a net attraction between the bitumen and the solid surface. Low values of pH are also detrimental. In bench-scale hot water tests with oil sand samples from the Bemolanga (Venezuela) deposit, Carrigy and Wallace [23] found an inverse relationship between separability of the bitumen and the Ca^{2+}, Mg^{2+}, and SO_4^{2-} levels.

Zajic et al. [25] investigated some Athabasca oil sand samples using the freeze fracture electron microscopic technique and came to the conclusion that in some places water and bitumen are present in a water-in-bitumen emulsion, the bitumen forming the continuous phase, and the water forming droplets with a size distribution of 0.5 to 0.02 μm. For the thickness of the water layer adsorbed on the sand surface, the authors placed an upper limit of 0.01 μm, which does not contradict Takamura's model; however, the presence of water-in-bitumen emulsion would not be fully consistent with the model of Takamura (unless, of course, the observed "water droplets" are in fact gas bubbles).

Aerial oxidation processes occurring during storage of mined oil sands, affecting both mineral and organic components of the oil sand, can also impair hot water separability. Wallace and Henry [26] identified two potential mechanisms for the oxidation of the ubiquitous pyrite in Athabasca oil sands, one involving a direct reaction of O_2 with FeS_2, and the other catalyzed by bacteria. The former produces $FeSO_4$ and elemental sulfur, and the latter $Fe_2(SO_4)_3$ and H_2SO_4. The Fe^{2+}, Fe^{3+}, and H^+ ions can then release Ca^{2+} and Mg^{2+} from the clay minerals by exchange. The released Ca^{2+} and Mg^{2+} decrease the separability of bitumen. Schramm and Smith [27] investigated the effect of air exposure on aging of mined Athabasca oil sand, and in addition to the oxidation of FeS_2, they identified another complex process influencing separability in terms of the reactions of polyvalent metal ions produced in the aging with NaOH or with the carboxylate surfactants, to form insoluble species.

Cyclic organic sulfides present in significant quantities in the aromatic and resin fractions of the bitumen also react readily with molecular oxygen to yield highly polar sulfoxides which can influence separability. Oxygen uptake by the oxidation of alkyl fluorenes to form alkyl fluorenols and fluorenones has been shown to occur as well (*vide infra*).

Oil sands are typically devoid of kerogen and their organic component is nearly completely soluble in organic solvents. Recent studies of Athabasca oil sands, however, have shown that some of the organic matter is insoluble in organic solvents [28]. Because of its inherent importance and potential role in the separability of the bitumen in the hot water extraction process and also in in situ steam flood and water flood recovery processes, the nature and distribution of this material were examined in some detail.

CHEMISTRY OF THE ORGANIC INSOLUBLE MATERIAL IN THE ATHABASCA OIL SANDS

Two Athabasca oil sand samples were investigated for the bulk composition of the organic-insoluble matter. Both samples were from the Syncrude quarry, one of which was a high-grade oil sand (SHG) and the other a low-grade oil sand (Syncrude Beach Sand, SBS) with bitumen contents of 11.8 wt% and 6.1 wt%, respectively. The SHG sample had a fines content of 8% and showed good separability in bench-scale experiments, while the SBS sample's fines content was 36% and its separability was poor. The total insoluble organic matter amounted to 0.3 wt% in the SHG sample (2.5 wt% based on bitumen content) and 1.5 wt% of the methylene chloride-extracted sand (or 24 wt% based on bitumen content) in the SBS sample.

The chemical composition of the methylene chloride-insoluble organic fractions of the two oil sands appeared to be similar and they contained 27% humic acids; 6.7% fulvic acids; and three polar fractions: 6.7% Polar 1, 27% Polar 2, and 6.7% Polar 3. The rest of the organic matter, 26%, was completely insoluble. The elemental composition of these organic fractions is given in Table 2 [29].

The compositions of the humic and fulvic acids are quite different from those of the bitumen or its fractions. They are both rich in oxygen and nitrogen and their IR spectra suggest the presence of bonded carboxylic acids, polymeric phenols, alcohols, and chelated ketones. The fulvic acids have an average formula $C_{15}H_{20}N_2SO_9$ and showed the presence of carboxylic acids and phenolic groups.

The nonhumic polar fractions have compositions closer to that of the bitumen. Polar 1 consists of fatty acids, sulfoxides, and phenols; Polar 2, of diketones or α,β-unsaturated ketones; and Polar 3, of carboxylic acids.

To date, only the monocarboxylic acid content has been studied in detail, although preliminary studies of Polar 2 clearly showed that this fraction complexes readily with Lewis acids such as $FeCl_3$, possibly with titanium salts, and presumably with other metals present in the clay minerals. In any case, iron appears to play an important part in complexation with the polar compounds adsorbed on the mineral surface. The monocarboxylic acids comprise a complex mixture of C_{12} to C_{32} normal, iso, and anteiso alkanoic acids, mono- and diunsaturated alkenoic acids, cyclopropylalkanoic and dicyclic and tricyclic terpenoid carboxylic acids, along with trace quantities of dehydroabietic acid [30]. The last acid is of higher plant origin and indicates some terrestrial contribution. The terpenoid acids, which are present in these chemically bound acid mixtures in lesser quantities than the acyclic alkanoic acids, are also present in the bitumen, where they constitute the main component of the carboxylic acids [31].

The origin of these acids can best be explained by aerobic bacterial processes altering the oil. During the microbial degradation of oil, these acids were present in the oil and some of them reacted with the basic sites of the mineral surface, where they became chemically bonded. Thereafter, this bound fraction was protected from further decomposition by microorganisms, chemicals, and water washing. In the bitumen, only the most stable and abundant of them, the tricyclic terpenoid acids, survived. Weathered oil sand deposits contain an elevated concentration of bound acids, especially the cyclopropylalkanoic type (e.g. Abasand, Cities Services). The total concentrations of these acids in the SBS and SHG samples are in the same ratio (5:1) as the concentrations of the total insoluble organic matter in the two samples. The carbon preference index of the n-alkanoic acids in general is high, pointing to a relatively recent origin and a geothermally immature state for the

Table 2. Chemical composition of the organic-insoluble matter from dichloromethane-extracted SBS oil sand.

Fraction	Wt% of sand	% daf					, Ash (wt%)	H/C	MW
		C	H	N	S	O			
Humic acids	0.4	68.6	4.0	1.8	2.5	23.1	1.9	0.70	
Fulvic acids	0.1	44.1	5.0	8.4	8.0	34.5	–	1.36	400
Polar 1	0.1	76.1	8.5	1.1	6.7	7.7	1.0	1.34	740
Polar 2	0.4	81.6	9.4	0.4	0.9	7.7	1.7	1.38	550
Polar 3	0.1	75.9	8.5	1.2	6.2	8.2	1.5	1.35	1 300

carboxylic acids.

The significance of these humic and polar materials with regard to the hot water separability of the oil sand was tested using the laboratory-scale Syncrude Batch Extraction Test and subsequent wet sieving [29]. The results clearly and unequivocally established a direct relationship between chemisorbed organic content and hot water separability. Thus, a fairly reliable linear relationship was found to exist between the amount of chemisorbed organic matter and the amount of bitumen retained on the sand after hot water extraction. This phenomenon can be readily explained by the far greater wet strength of the bond between bitumen and the organic insoluble-coated clay and silt particles than that between bitumen and the uncoated particles.

From the work of Kotlyar et al. [32] it is now known that sodium pyrophosphate solutions are more effective than sodium hydroxide solutions or water for the isolation of the complexes formed between the humic substances and the inorganic matter from the solvent-extracted sand matrix. Also, a correlation has been shown to exist between the extent of separation of the above complexes and that occurring during aqueous bitumen extraction from oil sands. During solvent extraction of the bitumen, some of the oil-wet particles become embedded in the bitumen. The finer fraction of these solids (<38 μm) is composed of amorphous complexes of inorganic matter with toluene-insoluble organic matter, and the coarser fraction occurs as globules, composed of finely divided quartz and clay bound together by toluene-insoluble organic matter [33].

Schramm et al. [34] investigated the hot water processibility of binary mixtures of Athabasca oil sands and attributed the observed nonlinearity in recovery to the effect of the clay minerals present in the oil sands. See also Sanford's work on the hot water separation of bitumen, described in Reference [34].

The potential role played by the chemisorbed organic matter in the oil sand during various in situ recovery processes has not yet been fully investigated.

GASES AND VOLATILES IN ALBERTA OIL SANDS

Like conventional crude oils, heavy and extra heavy crude oils can be fractionated into four essential classes of chemical types which are the saturates (both acyclic and cyclic paraffins), aromatic hydrocarbons, resins (N, O, S, and organometallic compounds, molecular weight

from 400 to 6000), and solid asphaltenes (N, O, S, polycondensed aromatics, organometallic and organo-clay complexes, molecular weight from 1000 to 40 000 and higher). In addition, most extra heavy oils in the reservoir, and the oil sands, contain small quantities of gases and volatiles. Table 3 lists the composition of this volatile fraction for samples obtained from various Alberta oil sand deposits. The presence of acetaldehyde and, in some cases, of larger quantities of CO and CO_2, is indicative of an ongoing slow thermal alteration and oxidation by exposure to air, aerobic microorganisms, or oxidizing groundwater. In certain samples, neopentane is present in significant quantities as the main C_5 hydrocarbon. This is unusual since neopentane in conventional oils amounts to only a few tenths of one percent of the pentane fraction. This may suggest that neopentane or its immediate precursor may be the residue of microbial degradations which have taken place in the formation.

At elevated temperatures the concentrations of all the volatiles present in the deposit increase and additional molecules such as H_2, CH_3SH, CH_3OH, C_3H_7SH, propionaldehyde, furan, and methylfuran, appear.

The initial rates of formation of all the volatiles feature unusually low activation energies (<63 kJ/mol), pointing to the unstable nature of the precursor molecules and the catalytic effect exerted by the mineral matter present. With increasing conversion, as the labile precursors become depleted, the rates of formation of all the products decline and the activation energies increase.

In the presence of oxygen the rates of formation of all the products, especially those of carbon monoxide, carbon dioxide, acetaldehyde, propionaldehyde, and acetone, are markedly enhanced and the residue also shows an increase of ~50% in its asphaltene content. The activation energy for oxygen uptake is temperature-dependent, having values of about 54 kJ/mol between 24 and 85°C and 121 kJ/mol between 85 and 130°C [35]; a value of 64 kJ/mol has been reported for the rate of oxidation of Athabasca bitumen loaded onto a chromatographic support material, in the temperature range 155 to 210°C, using a calorimetric method [36].

The activation energies for the formation of hydrocarbons from the thermolysis of bitumens are in the 146 to 172 kJ/mol range, and for the formation of oxygen-containing products, are 42 to 105 kJ/mol. The corresponding activation energies for the thermolysis of asphaltene are slightly lower. However, when they are measured at temperatures in the 400 to 700°C range [37]

Table 3. Compositions of gases[a] from Alberta oil sands [35].

Temperature	5°C			130°C			210°		130°C Ath.
	C.L.	Ath.	P.R.	C.L.	Ath.	P.R.	C.L.	Ath.	+ 150 Torr O_2
Methane	12	114	3.3	191	252	908	3 800	2 970	450
Ethylene				40	15	198	450	177	314
Ethane				26	17		452	113	119
Propane	3.5	1.1		154	37	190		270	
Acetaldehyde	9	2.8	0.2	84	167	556	7	30	9 020
Propylene		0.3	0.6	68	36	344	494	270	370
Isobutane	3.5				8.4	114		11	10
Isobutene	25.6			62	4.4	277	104	17	141
n-Butane				80	19	120	246	67	152
i-Butene				152	15		521		42
Neopentane		134		250				447	
Pentanes + pentenes	1.3		94	37	430	935	231	840	204
CO			1.3	880	1 820	3 014	4 790	10 700	32 560
COS			0.2	28		176	195	104	232
CS_2					53			28	
H_2S				85	15		1 930	2 350	
SO_2								4 730	129
CO_2			787			147 400			310 200
C_6	2 860		40	4 450		209	4 960		814
C_7									63
Acetone									2 525
Methanol						110			

[a] 10^{-8} mol/kg oil sand 5.5 h heating time. C.L. = Cold Lake; Ath. = Athabasca; P.R. = Peace River.

they become higher, and under nonisothermal conditions [38] they vary with the thermal history of the sample.

It should be emphasized that the volatile contents show great variability with locale, and in the case of the Athabasca samples it was found that low-grade, poorly separable samples had a much higher volatile content, especially carbon monoxide and acetaldehyde, and they were void of neopentane.

The phenomena of gas and volatile evolution and the ready oxidizability of the oil sands with molecular oxygen have ramifications with regard to steam and fire flood displacements and the storage of the bitumen, and require detailed investigation.

CLASS ANALYSIS OF EXTRA HEAVY OILS

Class analyses of crude oils have been developed for their chemical characterization, the classification of their origin and geological history, as well as for determining their commercial value and establishing process conditions for their refinement. There are a large number of class analytical procedures reported in the literature ranging from highly simplified ones recommended for rapid screening of a large number of samples [39] to detailed, complex procedures such as the USBM API-60 [40]. Some data showing representative class compositions of Alberta and other heavy oils are given in Table 4. They should be viewed in light of the constraints discussed below. Unfortunately, there are no generally accepted standards and for this reason and because of the possibility of significant fluctuations in composition with lithostratigraphic locations, few of the published class compositional data are directly comparable. The main differences in the results appear in the aromatics and resins contents. Since it is impossible to isolate the purely aromatic hydrocarbons quantitatively from the

N, O, S compounds by chromatographic separation, the aromatics vis-à-vis resins content will depend on the relative carry-over of these two fractions. Thus, for example, in the API-60 procedure the diaromatic fractions of the aromatic classes of Athabasca and Cold Lake bitumens already contain ~3% sulfur, while the tri- to polyaromatic fractions contain 6 to 7% sulfur, 2% oxygen, and 0.14% nitrogen, and essentially constitute part of the resins class. The extent of cross-contamination among classes depends not only on the procedure but also on the composition of the particular crude oil and the kinds and amounts of compounds present, which in the case of a major reservoir, could change quite dramatically from one sample to the next. Also, simple chromatographic separations may not be applicable to all oils, and in themselves do not provide sufficient information with regard to optimizing process options. Problems associated with open-column chromatographic methods for class separation of bitumens have been discussed by Wallace et al. [41]. Some data showing representative class compositions of Alberta and other heavy oils are given in Table 4. They should be viewed in light of the constraints mentioned above.

The saturate fraction of Alberta extra heavy oils

Most oil sand bitumens are microbiologically degraded crude oils and since microorganisms preferentially metabolize acyclic alkanes (first the straight chain, then gradually the branched ones), their acyclic alkane content is usually low. Of the Alberta bitumens studied, the Cold Lake bitumen contains the highest concentration of acyclic alkanes, ~0.5%, including n-alkanes, and a series of isoprenoid alkanes (pristane, phytane, etc.). On the other hand, the Grosmont Carbonate bitumen is so severely biodegraded that it does not contain acyclic alkanes except for trace amounts which can only be recovered by the acid dissolution of the reservoir rock [46]. Their main components are again n-alkanes and isoprenoids.

The bulk of the saturate fraction of Alberta bitumens is composed of alkyl cycloalkanes ranging from one to five rings with smaller amounts of six-ring compounds (Table 5) as determined by field ionization mass spectrometric analyses. In both cases, the dicyclic compounds are the most abundant but in the Cold Lake sample, the acyclic, mono-, and dicyclic members are more abundant than in the Athabasca sample, owing again to the difference in the extent of biodegradation.

Table 4. Class compositions of bitumens.

Athabasca bitumens

	Sync. [42]	T&W [3]	API-60 [43]	SiO$_2$/A1$_2$/0$_3$ [43]	SiO$_2$/FIMS [44]	USBM [45]	Iatroscan [39]
Asphaltenes	17.2	22.3	16.6	16.6	17.0	38.5	36.2
Resins	44.8	28.6	>46.3	48.5	47.2		
Saturates	16.9	15.9	18.5	20.6	16.8	21.6	20.7
Aromatics	18.3	32.2	>12.9	13.0	~19	38.1	43.1

Oil sand bitumens

	Peace River	Wabasca	Cold Lake	Tar Sand Triangle [45]	P.R. Spring [45]	N.W. Asph. Ridge [45]	E. Venezuela [3]
Asphaltenes	20	19	16	42	46	40	22
Resins	44	48	44				38
Saturates	15	15	21	26	26	28	14
Aromatics	19	18	19	32	25	27	26

Table 5. Composition of the saturate fraction of the Cold Lake and Athabasca bitumens [44].

Component	Series	C.L.	Ath.[a]
		% of bitumen	
C_nH_{2n+2}	acyclic	~0.5	trace
C_nH_{2n}	monocyclic	4.82	1.68
C_nH_{2n-2}	dicyclic	5.94	4.27
C_nH_{2n-4}	tricyclic	3.85	3.72
C_nH_{2n-6}	tetracyclic	2.92	3.23
C_nH_{2n-8}	pentacyclic	1.72	1.92
C_nH_{2n-10}	hexacyclic	0.59	0.23
Total saturates		20.3	15.1

[a] Not including 1.7% nonvolatile saturates which brings the total to 16.8%.

The monocycloalkanes are more degradable than the higher di- and polycyclics.)

To illustrate the complexity of just one subfraction of a SARA (saturates-aromatics-resins-asphaltenes) class, a few figures are presented showing the GC/field ionization mass chromatograms of the thiourea adduct (TUA), and thiourea non-adduct (TUNA) fractions of the monocycloalkane series, and the TUNA fraction of the tricycloalkane series of the Cold Lake saturate fraction. There are at least 200 members of the monocyclic series discernible from Figures 1 and 2. The actual number should be larger since the isomeric resolution of the GC column used was not very high and some of the isomers would not be apparent. The mass chromatogram of the tricycloalkane TUNA fraction, Figure 3, indicates even greater complexity and the presence of one predominant isomeric homologous series of alkyl tricycloalkanes. This has been identified as a novel series of tricyclic triterpenoid hydrocarbons, which turned out to be present in all petroleums. Terpenoid compounds are synthesized by living organisms. They occur in recent and ancient sediments along with the many other molecules produced by living organisms, either in their original form or in slightly altered forms. They are called biological markers or geochemical fossils. The nature and distribution of these geochemical fossil molecules has yielded important insights into the origin and history of crude oils.

The saturate fractions of Alberta oil sand bitumens are rich in geochemical fossil molecules. Figure 4 shows two GC/MS cross-scans of the zeolite-adduction enriched concentrate of isomeric homologous series of bicyclic and tricyclic terpenoid hydrocarbons along with the C_{27} to C_{35} series of pentacyclic hopane and moretane isomers from an Athabasca saturate fraction. Similar GC/MS ion cross-scans for the isomeric homologous series of tetracyclic sterane-type biological markers in the Athabasca oil sand and Grosmont Carbonate bitumen saturate fractions are shown in Figures 5 and 6, respectively [46].

As an illustration of the distribution of the mono-through pentacyclic series of alkanes according to carbon number in the molecule, field ionization mass spectrometric results on the Athabasca saturate fraction are depicted in Figures 7 and 8 [44]. Each series extends up to C_{50} but in fact about ~10% of the fraction was nondistillable at 240°C and 10^{-3} torr (Figure 9) and therefore the end of the fraction corresponding to carbon number greater than 50 could not be analyzed. The maxima in the intensity versus carbon number plots correspond to the maxima of the known geochemical fossils in the series: bicyclic terpanes C_{15} and C_{19} tricyclic terpanes C_{19} and C_{23}, tetracyclic steranes C_{21}[a], >C_{27}, and C_{29}, and pentacyclic hopanes C_{30}. Therefore, the distribution of the saturate fraction appears to suggest that the individual members are isomers of the major known alicyclic geochemical fossils occurring in crude oils.
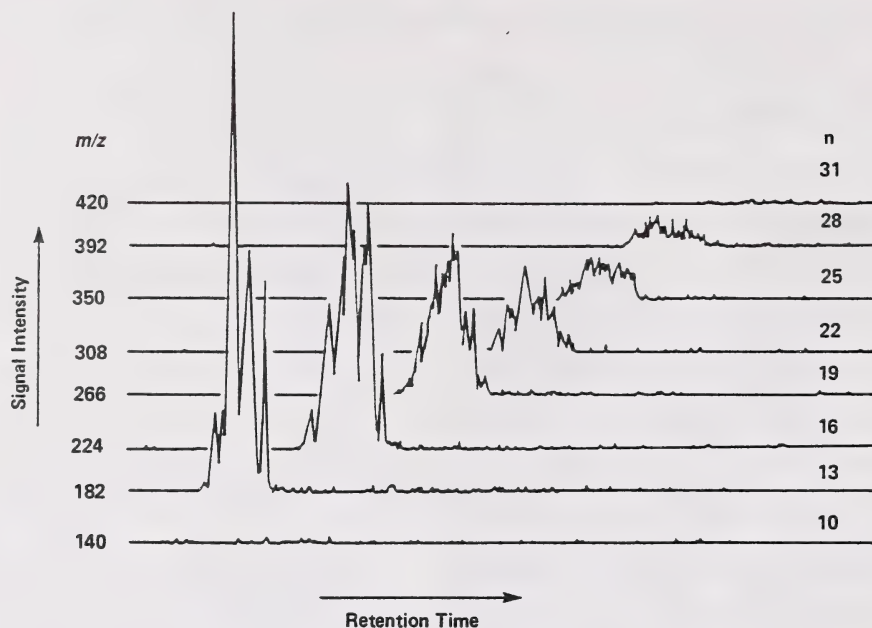
Structures are given in the appendix to this chapter.

Figure 1. FIMS scan of the C_n (n = 10, 13, 16, 19, 22, 25, 28, 31) monocyclic components of the TUA fraction.
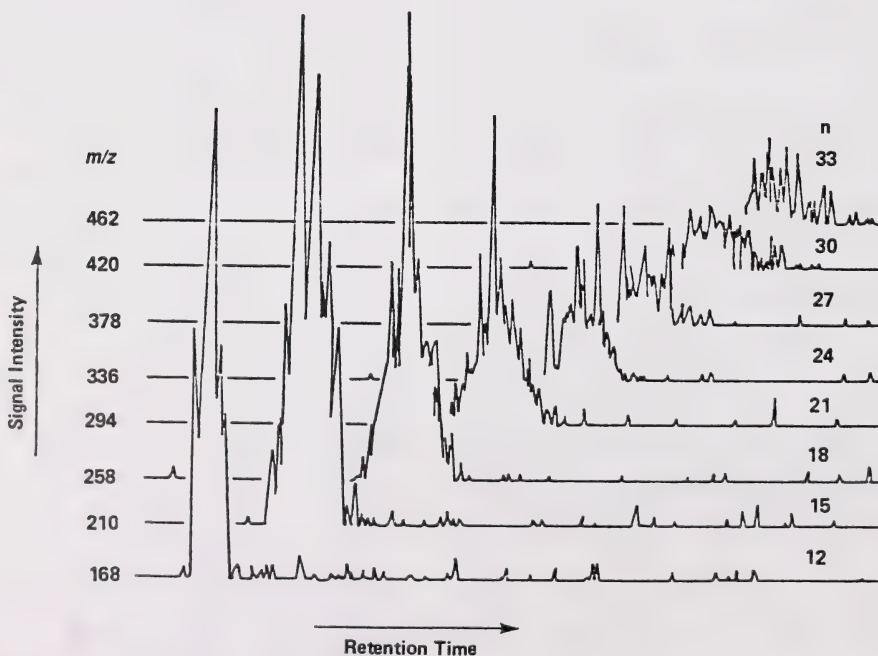

Figure 2. FIMS scan of the C_n (n = 12, 15, 18, 21, 24, 27, 30, 33) monocyclic components of the TUNA fraction.
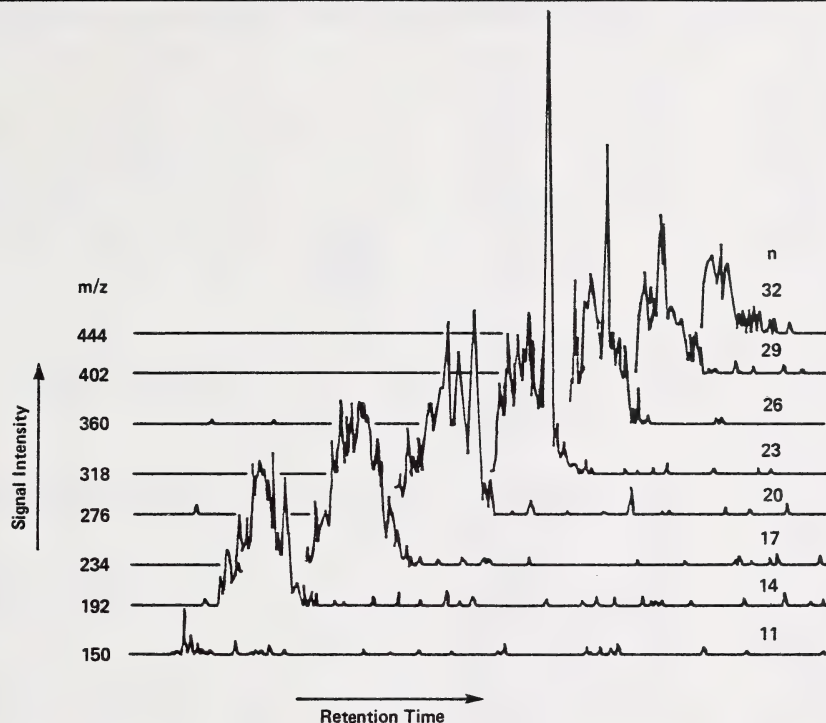
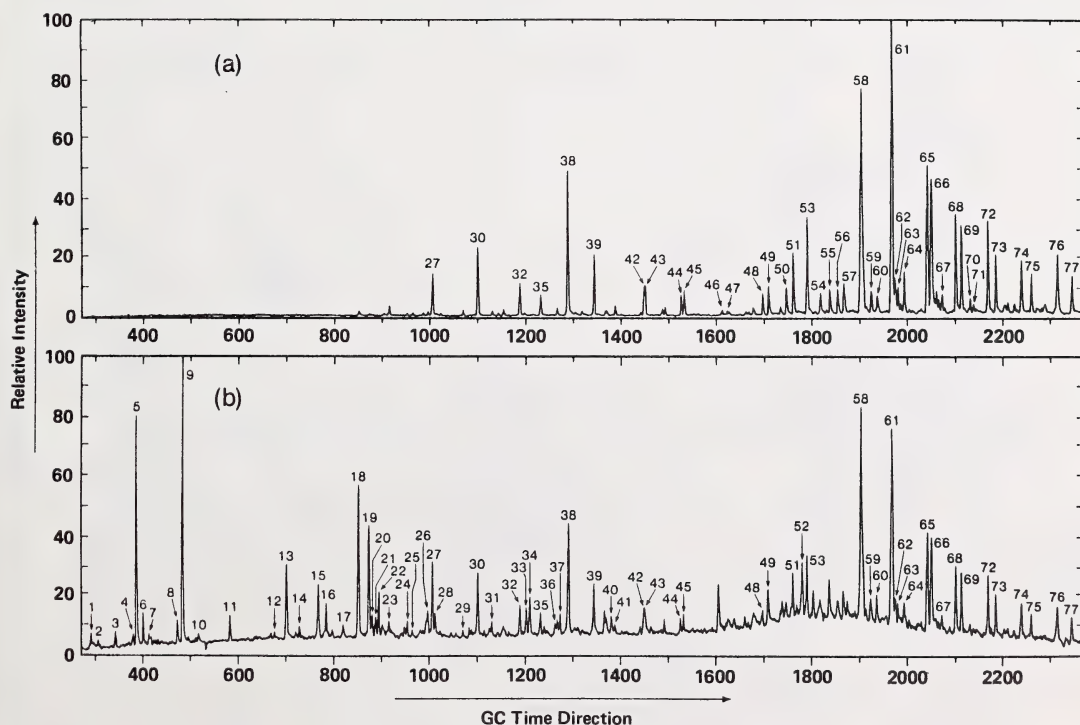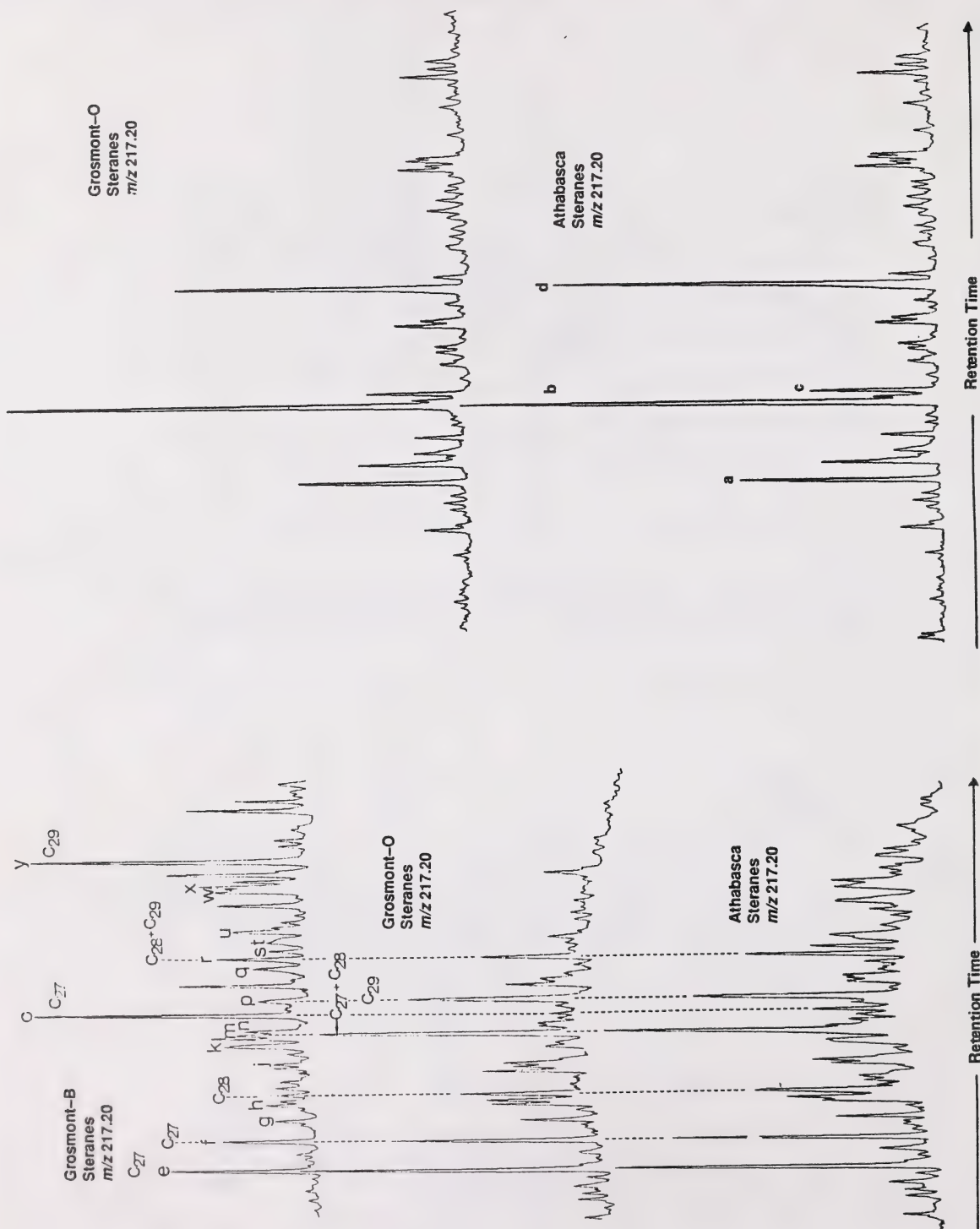**Figure 3.** FIMS scan of the C_n (n = 11, 14, 17, 20, 23, 26, 29, 32) tricyclic components of the TUNA fraction.

Figure 4. Cross-scans from the GC-MS analysis of the zeolite adsorbate fraction of the Athabasca saturates. (a) m/z = 191, (b) m/z = 123.

Figure 6. Distribution of C_{21} and C_{22} steranes in Grosmont and

Figure 5. Distribution of C_{27} to C_{29} steranes in
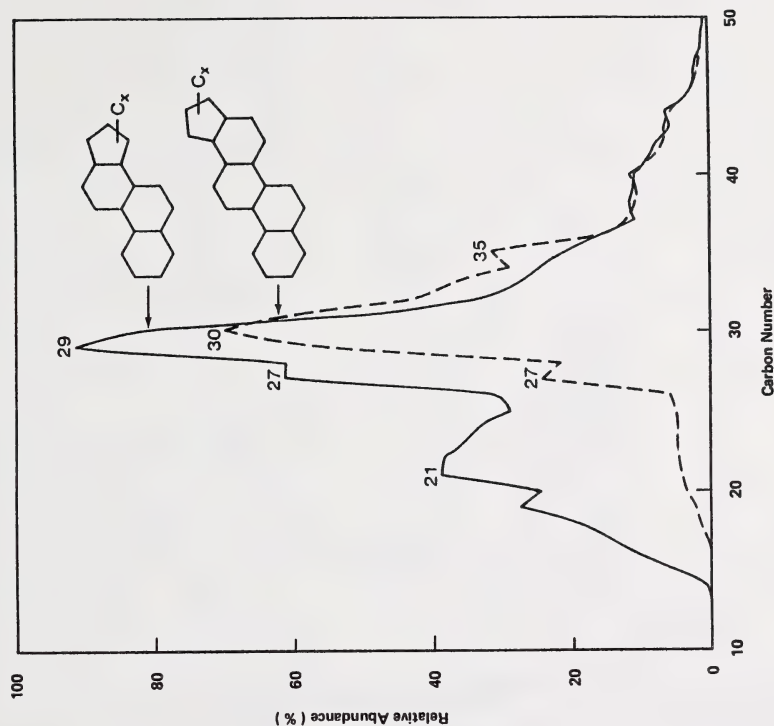
Figure 8. z-Plots for the homoglogous series of saturated hydrocarbons, C_nH_{2n-6} and C_nH_{2n-8} in Athabasca maltene. The plots display the relative abundance of 4 ring ($z = -6$), and 5 ring ($z = -8$) saturated hydrocarbons as a function of carbon number.
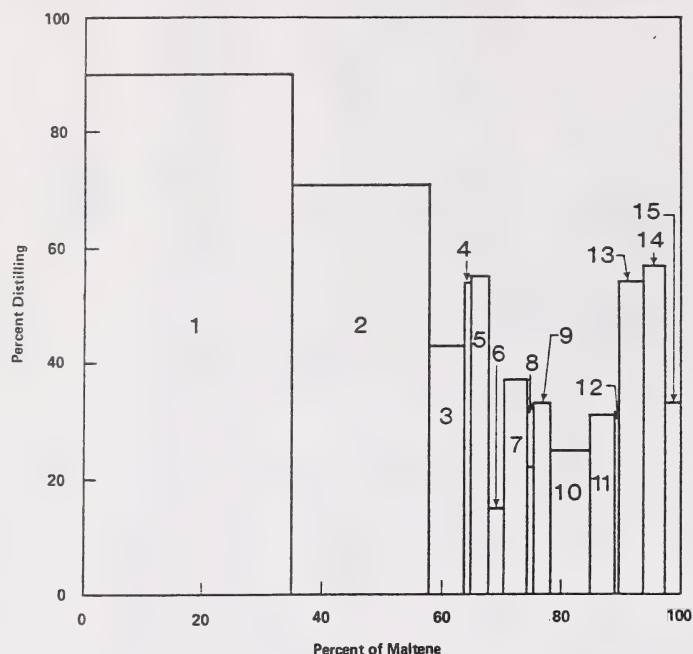

Figure 7. z-Plots for the homoglogous series of saturated hydrocarbons, C_nH_{2n+z} ($z = 0, -2, -4$) in Athabasca maltene. The plots display the relative abundance of 1 ring ($z = 0$), 2 ring ($z = -2$) and 3 ring ($z = -4$) hydrocarbons as a function of carbon number.

Figure 9. Distillation data from 15 fractions of Athabasca maltene obtained by elution chromatography. The plots show the percentage of each fraction distilling up to a maximum pot temperature of 240°C and 10^{-3} Torr for fractions 1 to 15. Compounds heavier than C_{50} do not distill under this condition [44].

The aromatic fraction of Alberta extra heavy oils

The monoaromatic subfraction makes up ~10% of the bitumen, and the distributions by number of naphthenic rings and carbon numbers for this subfraction are shown in Figures 10 and 11. The di- and higher nuclear aromatic hydrocarbons cannot be separated from the thiophenic compounds by chromatography and consequently their quantities can only be estimated. The combined amounts of dinuclear and trinuclear aromatic hydrocarbons are about ~9% of the Athabasca bitumen. The content of highly aromatic hydrocarbons with low H/C ratio is small. The sulfur is present in benzo-, dibenzo-, naphthobenzo-thiophenic form, in a short series of aromatic compounds containing two sulfur atoms, and the remainder in alicyclic sulfides with a high H/C ratio. The presence of nitrogen compounds such as alkylated benzoquinolines and carbazoles, along with their higher aromatic derivatives was also noted in the aromatic fraction.

The bulk of the aromatic fraction appears to have been derived from the aromatization and thermal maturation of the polycyclic lipids, di- and tricyclic terpanes, tetracyclic steranes, and pentacyclic hopanes. The thiophenes may be the degradation products of the asphaltene and may originate partly from the aromatization of the alicyclic sulfides.

In detailed studies of bitumens and heavy crudes, a large number of individual aromatic compounds have been identified by George and Beshai [47], Chemielowiec et al. [48], Coulombe and Sawatzky [49], and Poirier and Das [50].

The resin fraction of Alberta extra heavy oils

The resin fraction, the largest fraction of bitumen, is a highly complex mixture of heterocycles and carboxylic acids. Several homologous series of compounds have been identified in this fraction.

Among the oxygen-containing heterocycles identified was a series of methyl fluorenones with 1,4-dimethyl-fluoren-9-one, **1**[a], as the major component; a homologous series of alkyl benzofluorenones, **2**, identified by FIMS; a homologous series of 9-n-alkyl fluorene-9-ols, **3**, and their nuclear methylated derivatives where the n-alkyl chains extend from C_1 to C_8 [51,52]. The parent hydrocarbon fluorene, and 9-alkyl fluorene, can be easily oxidized to **1**, **2**, and **3** and the concentration ratios of **1**, **2**, and **3** to the parent hydrocarbons may serve as an indicator of the integral value of past redox conditions in the reservoir.

The carboxylic acids are made up of a novel homologous series of tricyclic terpenoid acids in the C_{20} to C_{26} range, the major components of which are the C_{21} and C_{24} members, **4** and **5**, the latter present in a pair of diastereoisomers, along with a series of pentacyclic hopanoid acids in the C_{30} to C_{47} range, **6** and with trace quantities of n-alkanoic acids [31]. The combined amount of carboxylic acids is not large, perhaps 1 to 2% of the bitumen (90% of which is made up of **4** and **5**), but as has been shown by Takamura [24], the carboxylic acids play a decisive role in determining the electric properties of the bitumen-water interface because the aqueous film which covers the sand surface is held in place by the electrical double-layer repulsive force acting between the negatively charged sand and

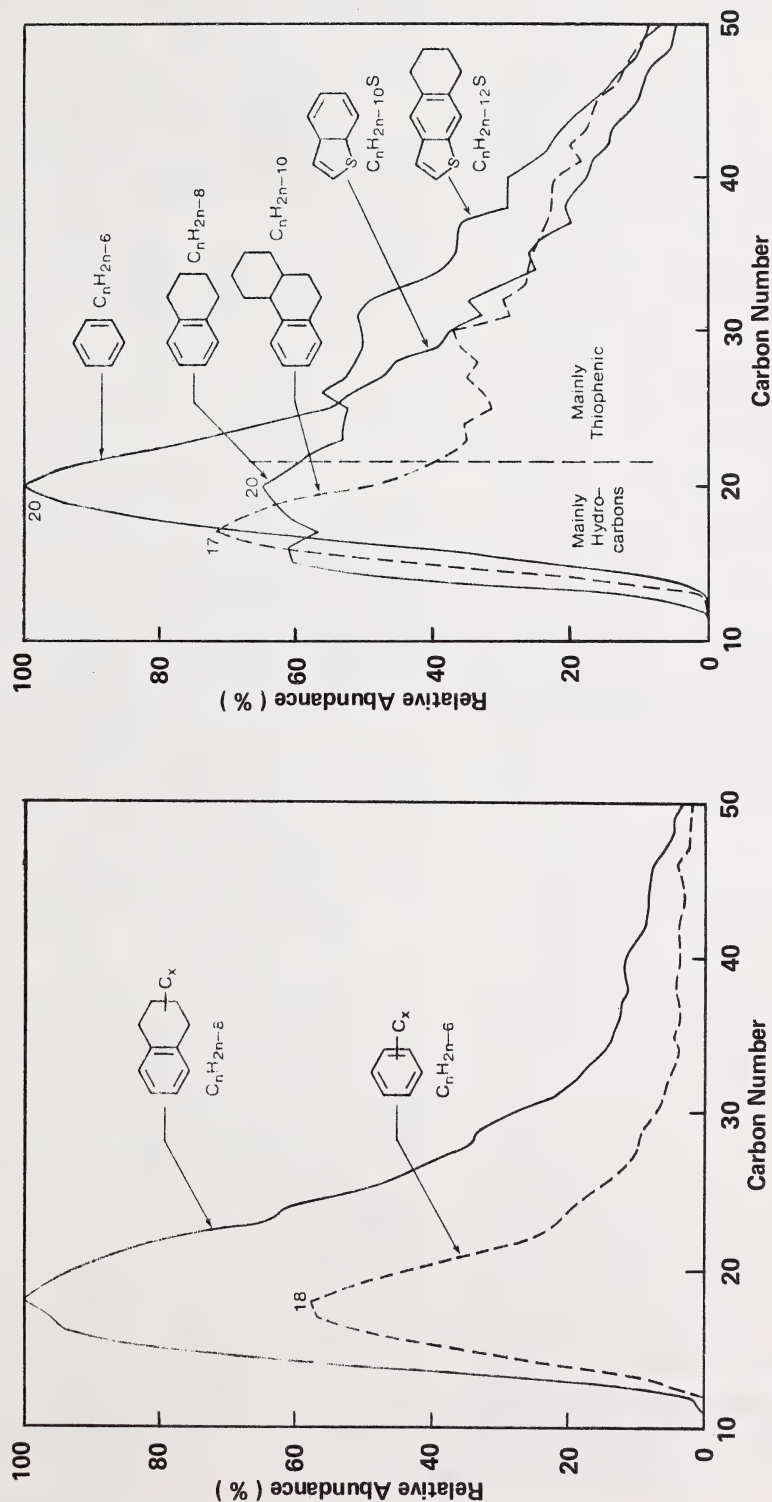---

[a] Structures are given in the appendix to this chapter.

Figure 10. (Left) z-Plots for the homogous series of monoaromatic hydrocarbons C_nH_{2n+6} (alkylbenzenes) and C_nH_{2n-8} from one subfraction of Athabasca maltene. (Right) z-Plots for the remaining homologous series in another subfraction. The $z = -8$ and $z = -10$ traces range up to $n = 20$ to 25. Above this carbon number range, the series are dominated by thiophenic sulfur compounds [44].
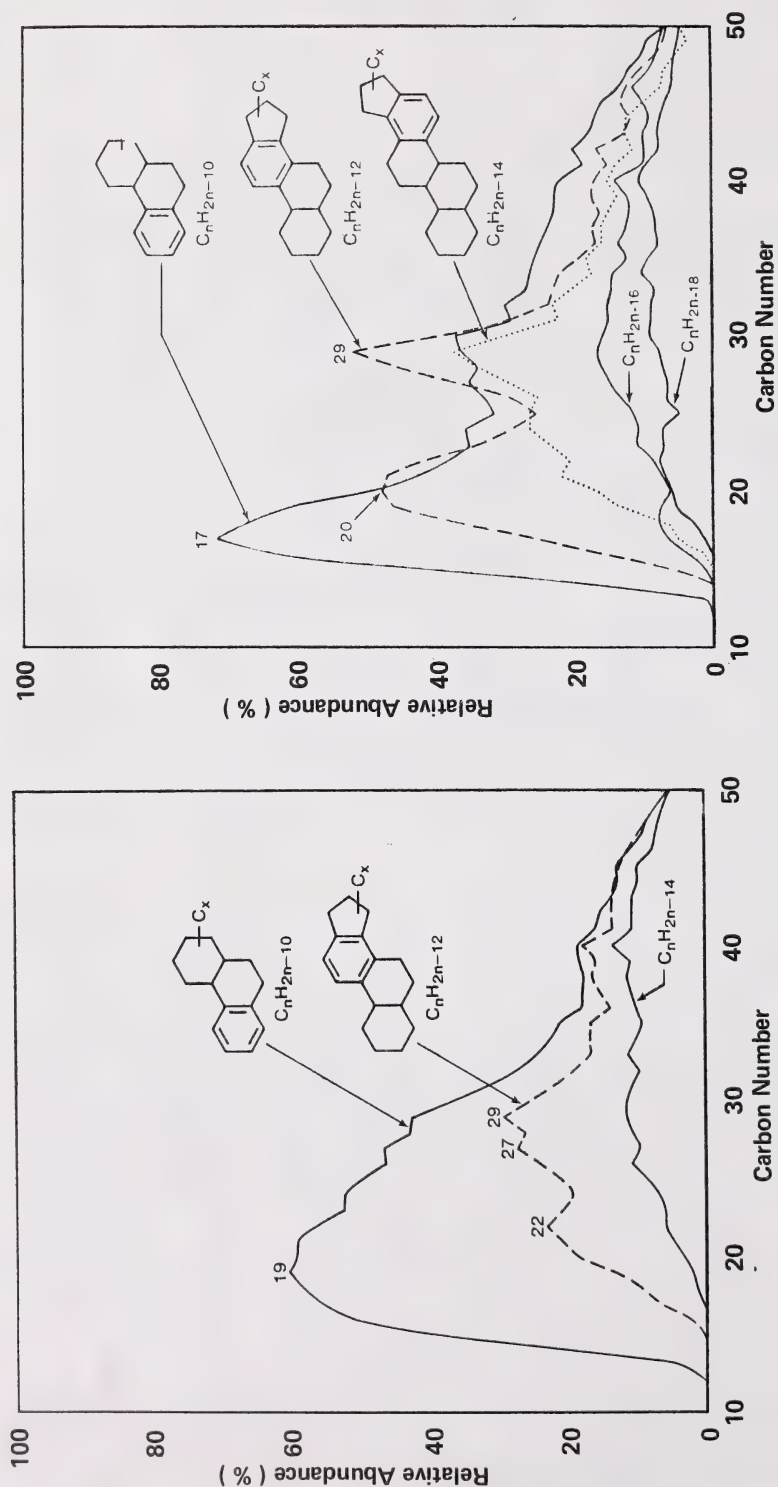
Figure 11. z-Plots for the homologous series of monoaromatic hydrocarbons C_nH_{2n-z} ($z = -10, -12, -14$) from two subfractions of Athabasca maltene [44].

bitumen surfaces. The negative charge of the bitumen surface is attributed to the dissociation of the surface carboxylic acids. There are, however, other types of acidic molecules present in the bitumen which could be involved in the creation of surface charges.

Other important classes of molecules present in all oil sand bitumen resins examined are the cyclic sulfides from which many new biological molecules having di-, tri-, tetra-, and hexacyclic terpenoid structures have been identified, together with their corresponding sulfoxides. The distribution of the dicyclic terpenoid sulfides by carbon number is in the C_{12} to C_{26} range with a maximum at C_{13}. The structure of only the C_{26} member, **7**, is shown here together with its corresponding sulfoxide, **8**. The lower members of the series arise by gradual loss of the isoprenoid side-chain end-carbon atoms [53].

The structure of the tricyclic terpenoid sulfide series has been established only tentatively, **9**. The carbon range for this series is 17 to 31 with maximum concentration at C_{18}. Chemically this series behaves somewhat differently from the other cyclic isoprenoid sulfides with respect to Raney nickel desulfurization. This series is the most resistant against desulfurization. The tetracyclic terpenoid sulfide series is in the C_{22} to C_{40} range with a maximum concentration at C_{23}, **10**.

The last of these series of new terpenoid sulfides identified was the hopanoid sulfide series having either or both structures **11** and **12**. Upon hydrodesulfurization the sulfides are converted to the hopanes with a concentration distribution somewhat different from that of the hopanes present in the saturate fraction of the bitumen.

As it turns out, these sulfur-containing biological marker molecules which were first discovered in Alberta oil sand bitumens occur not only in all Alberta oil sand bitumens, but also in conventional oils and other oil sand bitumens (e.g. from Venezuela and Argentina) — they are in fact ubiquitous components of all crude oils. The concentration of the total alicyclic sulfide fraction in the over two dozen samples studied falls into the 0.3 to 14% range, and in the Athabasca bitumens the average concentration is around 3 to 5%. The highest concentration, 14%, occurs in the Peace River bitumen in a sample taken from a depth of 558 m.

The concentration distribution of the sulfides varies with location even within a reservoir and depends on the thermal maturity and water washing of the formation. Consequently, the study of the distribution of these sulfides can give valuable information on the history of the deposit, and in particular, on the extent of geothermal heat and water washing to which the deposit was subjected.

All the cyclic sulfides are readily converted to their corresponding sulfoxides by aerial oxidation which may be catalyzed in the formation by the organic and inorganic matter present. Hence, the sulfide/sulfoxide concentration ratio of a fresh sample of bitumen provides an indicator, in addition to the fluorenone-fluorene system, for the evaluation of the redox conditions that have prevailed in the reservoir.

The analysis of a fresh Athabasca sample (17 m depth) indicated that ~10% of the sulfides were present in the form of sulfoxides, in agreement with other observations (e.g. presence of acetaldehyde, fluorenones, and fluorenols) pointing to mildly oxidative conditions in the deposit.

In the class of nitrogen-containing compounds detected were a series of alkyl carbazoles, **13**, with maxima corresponding to a side chain length of C_5–C_6; alkyl benzocarbazoles, **14**; alkyl quinolines, **15**; alkyl benzoquinolines, **16**; alkyl tetrahydrodibenzoquinolines, **17**; alkyl azafluoroanthrenes, **18**; or alkyl azapyrenes, **19**; and alkyl octahydrobenzoquinolines, **20**; or dibenzoquinolines, **21**. In the quinoline series, several compounds have isopropyl and ethyl groups in the 8 position; most molecules are polymethylated, and a few have an ethyl substituent [44,54]. The quinoline compounds are basic and tend to poison the hydrodesulfurization and hydrogenation catalyst, and they can cause polymerization and gum formation during storage of crude distillates. The carbazoles are nonbasic.

Nondistillable residues, of course, cannot be directly subjected to gas chromatographic or mass spectrometric analyses, and therefore, in order to gain an insight into their structural composition, they must be subjected to a mild, controlled, chemical degradation. One recently-developed approach along this line for petroleum residues involves Ru(VIII)-catalyzed oxidation, which permits the detection of the presence of alkyl side chains attached to aromatic rings, and polymethylene bridges between cyclic units (*vide infra*). By this method it was indeed possible to show the presence of these units in the Alberta oil sand resins: *n*-alkyl side chains up to C_{28}, and polymethylene bridges up to $\geq C_{12}$. Remaining were aromatic residues and a high molecular weight aliphatic core containing sulfide sulfur (oxidized to sulfone by the Ru(VIII)) and nitrogen [55,56].

The asphaltene fraction of Alberta extra heavy oils

Asphaltene is the highest molecular weight fraction of crude oils. The most extensively investigated asphaltene among Alberta oil sand asphaltenes is that from the Athabasca deposit. When precipitated from a benzene or methylene chloride solution of the bitumen by the slow addition of a 40- to 50-fold excess of *n*-pentane, Athabasca asphaltene appears as a shiny black amorphous solid.

This crude asphaltene may have a fairly high ash content (3.2%) which can be reduced with subsequent centrifugation (Table 6) [57].

Table 6. Clay removal from Athabasca asphaltene.

Asphaltene	No. of centrifugations[a]	Ash (wt%)
I	0	3.2
II	2[b]	2.3
III	8[b]	1.5
IV	11[c]	0.9
V	11[d]	0.5

[a] Duration of each centrifugation, 30 min.
[b] A-I centrifuged at 2500 rpm.
[c] A-I, 8 centrifugations at 2500 rpm followed by 3 centrifugations at 10 000 rpm.
[d] A-I, 11 centrifugations at 17 000 rpm.

The number average molecular weight of Athabasca asphaltene is ~3600. This asphaltene has been fractionated by gel permeation chromatography (GPC) according to molecular weight into five fractions (Table 7); 50% of the asphaltene had a molecular weight >13 000 [58]. The elemental composition does not show a significant change with molecular weight although the IR spectrum exhibits a small but systematic increase in the carbonyl absorption at 1700 cm^{-1} with decreasing molecular weight. Each fraction as well as the whole asphaltene has been examined in solution by high resolution ^{13}C and ^{1}H nuclear magnetic resonance (NMR) spectrometry [59]. Integration of the inverse gated decoupled spectra gave the aromaticity of each fraction (Table 7) as well as the relative number of carbon atoms responsible for well-resolved signals in the aliphatic portions of the spectra. A two-pulse spin-echo ^{13}C NMR sequence permitted the assignment of each aliphatic carbon signal to a methyl, methylene, or methine carbon; no quaternary aliphatic carbons were detected. The NMR spectra show that the aromatic core of the asphaltene is surrounded by *n*-alkyl chains with a mean length of 7.7 for the lowest molecular weight fraction, increasing to 12 for the highest molecular weight fraction. The aromaticity of the fractions ranged from 34 to 48%, exhibiting a gradual increase with decreasing molecular weight (Table 7). The degree of branching, featuring a methyl group in the alkyl side chain, also varied with the molecular weight and it was larger, ~1.0 (methyl per side chain) for the high molecular weight fraction than for the lowest molecular weight fraction (~0.33).
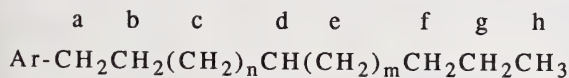
Significantly, the highest naphthenic carbon content was found in the high molecular weight fraction, and the lowest fraction was nearly devoid of such carbon. This latter fraction has a much higher aromaticity than the second lowest fraction and its overall composition (*vide infra*) and low molecular weight show that it is essentially a resin class material which precipitates upon adding *n*-pentane to the asphaltene solution. This resinous material apparently forms part of the asphaltene micelle, and presumably is responsible for the solubility of the higher molecular weight fraction of the asphaltene in the oil.

From the NMR data, one can also estimate the number of methyl groups in positions other than along the long alkyl side chains (attached to naphthenic rings, heteroatoms, etc.) and the H/C ratios for the remaining aliphatic structures (Table 7). That methyl groups are also attached to the aromatic systems was shown by further chemical studies.

The NMR spectra clearly show the presence of long alkyl groups attached to aromatic carbon in the asphaltene. However, the NMR spectra do not make it possible to differentiate between an alkyl side chain on an aromatic carbon or an alkyl bridge connecting two aromatic or one aromatic and one naphthenic ring systems. The answer to this, and other questions relating to structural features, such as the presence of alkyl chains attached to naphthenic rings, comes from chemical studies using Ru(VIII)-catalyzed oxidation of the asphaltenes by sodium metaperiodate in water tetrachloromethane-acetonitrile solvent systems at room temperature. Under these conditions the aromatic carbons are selectively oxidized to carbon dioxide leaving behind the aliphatic portion of the asphaltene structure, unaltered or only slightly altered, and thereby

Table 7. Molecular weight distribution, elemental composition, and NMR-derived structural features of Athabasca asphaltene [53].

GPC fraction	1	2	3	4	5	Whole
Yield (%)	22.5	30.5	13.6	11.1	20.8	asphaltene
Molecular weight	16 900	13 700	7 100	3 400	1 200	3 600
Elemental analysis (wt% daf basis)						
C	79.8	79.8	80.1	80.0	79.8	79.9
H	8.1	8.2	8.3	8.6	8.2	8.3
N	1.2	1.2	1.1	1.1	1.1	1.2
S	7.9	8.0	7.9	7.9	7.0	7.6
O	3.0	2.8	2.6	2.6	3.9	3.2
H/C	1.22	1.23	1.24	1.24	1.23	1.24
Number of carbon atoms per 100 C atoms of major types						
C aliphatic	65	66	61	59	52	57
C aromatic	35	34	39	41	48	43
Aliphatic carbon types per 100 C						
C(terminal)Me(h)	2	2	2	3	3	3
C(branch)Me(i)	2	2	1	1	1	2
$C\beta CH_2$(g)	2	2	2	3	3	3
C mid-chain CH_2(c e)	12	12	8	8	7	10
C other CH_2(a b f)	6	6	6	9	9	9
Average chain length	12	12	9.5	8.0	7.7	9.0
Branching	1.0	1.0	0.50	0.33	0.33	0.7
Proton types per 100 C						
H aliphatic	115	116	116	120	111	
H methyl	31	27	26	32	21	
H-CH_2, –CH	67	66	66	65	62	
H 2.1 – 5.0 ppm	17	22	25	22	28	
H aromatic	7	7	8	9	12	
H arom./C arom.	0.20	0.21	0.20	0.22	0.25	
Aliphatic carbon						
in side chain	26	26	20	25	24	
in other CH_3	6	5	6	8	3	
H/C in rest of aliphatics	<1.27	<1.34	<1.62	<1.80	<2.04	

```
        a    b    c    d    e     f    g    h
    Ar-CH₂CH₂(CH₂)ₙCH(CH₂)ₘCH₂CH₂CH₃
                    |
                   CH₃
                    i
```

$$\text{a} \quad \text{b} \quad \text{c} \quad \text{d} \quad \text{e} \quad \text{f} \quad \text{g} \quad \text{h}$$
$$Ar\text{-}CH_2CH_2(CH_2)_nCH(CH_2)_mCH_2CH_2CH_3$$
$$|$$
$$CH_3$$
$$\text{i}$$

^{13}C shifts: a, 37; b, 32; c, 30; d, 33; e, 30; f, 32; g, 23; h, 14; i, 20 ppm

bringing about the separation of the aliphatic components from the aromatic components of the asphaltene molecule. Alkyl side chains attached to aromatic carbons are converted to their carboxylic acid derivatives:
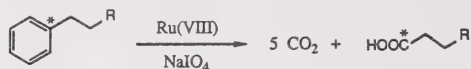
and polymethylene bridges between aromatic rings, are converted to α,ω-dicarboxylic acids:
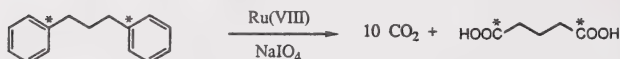
Condensed aromatic rings are oxidized to benzene di-, tri-, and tetracarboxylic acids and their methyl derivatives if the remaining ring, deactivated by the carboxylic groups against further oxidation, contains methyl substituents. For example, naphthalene gives benzenedicarboxylic (phthalic) acid, and tetralkyl anthracene could give benzenetetracarboxylic acid, respectively, upon Ru(VIII) oxidation:
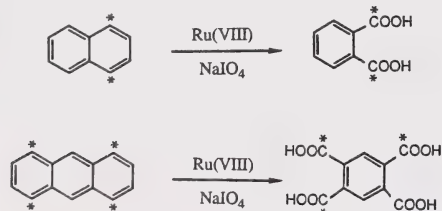

Experiments on Alberta oil sands and heavy oil asphaltene indeed yielded a series of n-alkanoic acids, α,ω-dicarboxylic acids and benzene di-, tri- and tetracarboxylic acids. After esterification with diazomethane, the methyl esters of these acids were analyzed by capillary GC/MS [60].

The homologous series of n-alkanoic acid esters from the oxidation of Athabasca asphaltene extends from C_2 to $\geq C_{26}$ with a concentration maximum at C_2, representing a methyl group on the aromatic carbon. The distributions of the n-alkanoic acid esters in other asphaltenes (from the Peace River oil sand, Grosmont Carbonate Triangle, and Lloydminster heavy oil deposit) are quite similar. These findings are in general agreement with the results of the NMR spectroscopic [59] and thermolysis [38,61,62] studies on asphaltenes.
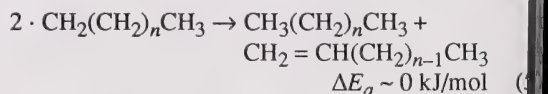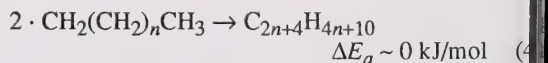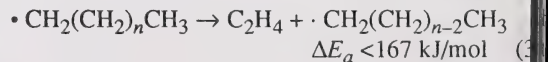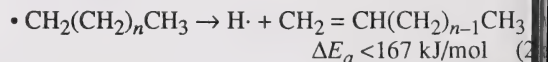
The thermolysis of asphaltenes yields, among a host of other products, a homologous series of n-alkanes and a homologous series of the corresponding 1-alkenes with similar relative distributions.

The carbon range of the dicarboxylic acids lies in the 4 to 24 interval, representing a C_2 to C_{22} chain length for the polymethylene bridges between aromatic moieties in the asphaltene structure with a maximum at ~C_3, C_4. The existence of a C_1 bridge could not be detected by the Ru(VIII)-catalyzed oxidation method.

The primary source of the n-alkane-1-alkene series in the thermolysis of asphaltene is thought to be the cleavage of the benzylic C-C bond in the alkyl side chains of aromatic nuclei of the asphaltene:
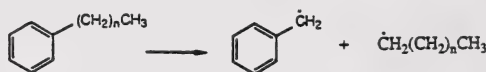
The benzylic radical is resonance-stabilized and its stability contributes to the lowering of the bond dissociation energy of the benzylic C-C bond by about 29 to 33 kJ/mol below the normal C-C bond dissociation energy. This renders the alkyl side chain thermally more reactive. The resultant n-alkyl radical can undergo hydrogen abstraction to give n-alkane, unimolecular loss of a hydrogen atom to give 1-alkene, unimolecular loss of ethylene to give a shorter chain alkyl radical, combination-disproportionation reaction with one another (or combination with other radicals in the system) to give n-alkane + 1-alkene:

$$R\text{-}H + CH_2(CH_2)_nCH_3 \rightarrow R \cdot + CH_3(CH_2)_nCH_3$$
$$\Delta E_a < \sim 42 \text{ kJ/mol} \quad (1)$$

$$\cdot CH_2(CH_2)_nCH_3 \rightarrow H\cdot + CH_2 = CH(CH_2)_{n-1}CH_3$$
$$\Delta E_a < 167 \text{ kJ/mol} \quad (2)$$

$$\cdot CH_2(CH_2)_nCH_3 \rightarrow C_2H_4 + \cdot CH_2(CH_2)_{n-2}CH_3$$
$$\Delta E_a < 167 \text{ kJ/mol} \quad (3)$$

$$2 \cdot CH_2(CH_2)_nCH_3 \rightarrow C_{2n+4}H_{4n+10}$$
$$\Delta E_a \sim 0 \text{ kJ/mol} \quad (4)$$

$$2 \cdot CH_2(CH_2)_nCH_3 \rightarrow CH_3(CH_2)_nCH_3 +$$
$$CH_2 = CH(CH_2)_{n-1}CH_3$$
$$\Delta E_a \sim 0 \text{ kJ/mol} \quad (5)$$
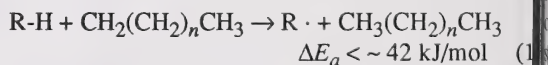
The relative importance of these steps will depend on the chemical composition of the material and the

reaction conditions. For this reason, and also because in thermolysis the polymethylene bridges and the alkyl side chains attached to naphthenic carbons in the asphaltene structure may also undergo cleaveage, thereby contributing to the alkane/1-alkene yield, it is believed that the alkanoic acids from the Ru(VIII)-catalyzed oxidation provide more reliable information on the alkyl side chain and polymethylene bridge distributions of the aromatic systems in the asphaltene structure than do the alkane/1-alkene products from the thermolysis of asphaltene.

Benzene, di-, tri-, and tetracarboxylic acids are produced in low yields (0.5 to 1.0%) in the Ru(VIII)-catalyzed oxidation reaction suggesting the presence of a relatively low concentration of highly polycondensed aromatic units. The relative concentration distribution of nine different acids in this group from five different Alberta asphaltene samples showed a close similarity, indicating that the nature and extent of aromatic condensation in the five samples examined cannot be drastically different [60].

An additional product of the oxidation of Athabasca asphaltene is a residue in about ~40 wt% yield. A fraction of this residue, ~28% based on the weight of asphaltene, is soluble in CH_2Cl_2 but insoluble in n-pentane. In this oxidized asphaltene, only ≤7% of the carbon is aromatic and its molecular weight distribution shows a broad envelope extending beyond 8000 amu. The existence of such large aliphatic core units in the asphaltene is a somewhat surprising result and requires some revisions of the earlier concepts of asphaltene structures. This oxidized aliphatic core, which is rich in oxygen (~20%) and contains ~4.7% sulfur is a potential source of further information regarding the original structure of the asphaltene. The aliphatic core molecules were originally attached to aromatic moieties in the asphaltene by covalent bonding. During oxidation the sites of attachment were converted to carboxylic groups anchored to the aliphatic core. On thermolysis, these may be cleaved from the core, yielding analyzable products. Also, if alkyl chains are attached to the aliphatic core, they too should yield suites of alkanes and alkenes.

Indeed, upon heating the oxidized aliphatic core after diazomethane treatment for esterification of the carboxylic groups in a flow reactor (300 to 375°C, 2 h), homologous series of n-alkanes and 1-alkenes (with distributions not unlike those from the asphaltene), homologous series of n-alkanoic acids and 1-alkenoic acid methyl esters, and a series of n-alkanoic acids were produced [60]. Thus, it can be concluded that the naphthenic ring systems of the asphaltene molecule also have alkyl side chain substituents. The n-alkanoic acids bound to the core via their terminal alkyl carbon atoms can be cleaved off and the resultant radicals, like the alkyl radicals, can undergo hydrogen abstraction or unimolecular loss of a hydrogen atom. The free carboxylic acids in turn could have arisen via molecular elimination from long-chain fatty acid esters to give an acid and an olefin, the latter remaining on the core. These esters could have been present in the asphaltene as such, or less likely, as the corresponding ethers, since alkyl ethers are known to be oxidized to esters in the Ru(VIII)-catalyzed oxidation. Finally, infrared spectroscopic examination of the oxidized nondistillable residue showed intense sulfone band absorptions. Since the core is nearly devoid of aromatic carbon (<7%) and contains 4.7% sulfur, the sulfones must be aliphatic, cyclic or acyclic sulfide sulfones. This observation provides unambiguous proof of the presence of aliphatic sulfide linkages in the Athabasca asphaltene. The core also contains some nitrogen, however, its functionality has not been established to date. In summary, the high molecular weight, oxidized aliphatic core residue consists of naphthenic ring systems to which are attached alkyl groups, long-chain carboxylic groups, long-chain fatty acid groups, and sulfides:
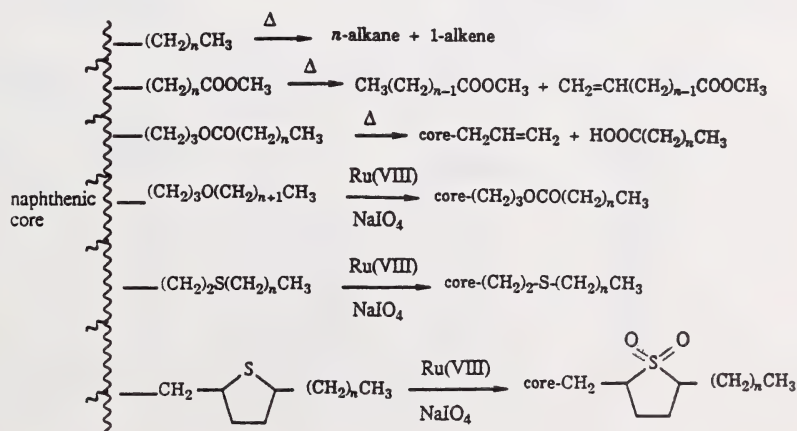
As noted above, the Ru(VIII)-catalyzed oxidation followed by thermolysis of the oxidized residue provides a powerful tool to probe into the structure of petroleum asphaltenes and establish some key structural features. Thus, for Alberta asphaltenes it has been shown that:

- both the aromatic and aliphatic systems of the asphaltene possess n-alkyl side chains from C_1 to $\geq C_2$ and C_1 to $\geq C_{30}$, respectively;
- n-polymethylene bridges, C_2 to $\geq C_{22}$ are present, connecting aromatic moieties;
- n-polymethylene bridges from at least C_{10} to $\geq C_{35}$ connecting aromatic units to naphthenic units are also present. Polymethylene bridges between naphthenic units should be present as well but only indirect experimental proof could thus far be obtained for them;
- part of the sulfur in the asphaltene is present in the form of nonaromatic sulfides;
- the aliphatic core shows a broad molecular weight distribution extending on the high side well beyond the number average molecular weight of the native asphaltene.

Like petroleum asphaltenes in general [63], Athabasca asphaltenes contain vanadyl porphyrins which give a more or less intense electron spin resonance spectrum of the VO^{2+} ion. In addition, they contain stable organic free radicals. The concentration of these organic radicals in the asphaltene is relatively high, of the order 10^{17} to 10^{18} radicals/g asphaltene. The origin, nature, concentration distribution and chemical reactivity of these radicals are of considerable importance with regard to the polymer, mesophase, and coke-forming propensity of the asphaltene. At elevated temperatures the stable radicals may become chemically active, undergoing charge transfer and addition reactions with sulfides and aromatics as well as other polymerization-initiating reactions.

The organic free radicals are associated with the aromatic fraction of the asphaltene. There may be two basic types of stable free radicals present, one which is neutral and one which carries an electrical charge. They are stabilized by aromatic delocalization or by strong steric hindrance of the unpaired electron site. Some simple illustrative examples are:

$\cdot C(Ar)_3$,
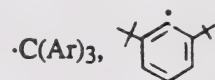
and radical ions with a polycondensed aromatic nucleus containing a large number of aromatic rings:
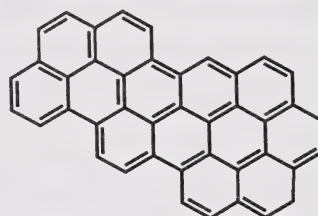
$(\stackrel{+}{\cdot})$ or $(\stackrel{\cdot}{\cdot})$

The ESR spectra of the organic free radicals present in the five different molecular weight fractions of Athabasca asphaltene (Table 7) were determined and the relevant data are summarized in Table 8 from which it may be concluded that:

- the radical concentration and the molecular weights of the radicals increase with increasing molecular weight of the asphaltene fraction;
- the concentrations of radicals and therefore of highly polycondensed large aromatic systems are relatively low, in agreement with the low yield of benzene carboxylic acids from the Ru(VIII) oxidation of asphaltenes;
- in addition to doublet state monoradicals, thermally excited triplet state radical pairs are also present at

Table 8. Free radicals in the five GPC fractions of Athabasca asphaltene [64].

Molecular weight	Wt% of asphaltene	g-Value	Rad./g asph. x 10^{17}	Rad. per molecule	% of triplet
16 900	22.5	2.002 90	10.2	1:35	23
13 700	30.5	2.003 05	8.3	1:53	20
7 100	13.6	2.003 10	8.7	1:98	18
3 400	11.1	2.003 25	6.0	1:297	7
1 200	20.8	2.003 30	5.6	1:897	5

T >50 K in thermal equilibrium with ESR-inactive singlet radical pairs. The concentration of triplets increases with increasing molecular weight of the asphaltene fraction;

• from the signal intensity enhancing effect of added oxygen on the ESR spectra it can be concluded that the steric density of packing of the asphaltene structures becomes gradually lower as the molecular weight decreases (in the separated solid asphaltene).

Recent results from two other independent studies on asphaltenes point in the same direction regarding asphaltene structure, namely, towards a smaller average size for the aromatic sheets. Thus, a study of the absorption, fluorescence, and excitation spectra of Athabasca asphaltene and its five GPC fractions led to the conclusion that the basic absorbing chromophores throughout the fractions are polynuclear aromatic units consisting, on the average, of three aromatic rings [65]. From a combination of magnetic susceptibility and ESR measurements [66], it was concluded that the average number of condensed aromatic rings in asphaltenes and other heavy petroleum fractions must be small and undoubtedly less than was previously assumed. Similar conclusions were reached from thermolysis studies of Athabasca asphaltene [67].

Considering the highest molecular weight fraction of the Athabasca asphaltene (16 900 amu), its carbon content (~80%), and aromaticity (~35%), the total number of aromatic carbons in the average molecule is ~400. Of this number, only a relatively small fraction appears to be present in large polycondensed units which, on stacking, could give doublet state monoradicals or carbocation-carbenion radical pairs

detectable in their excited triplet state by ESR spectroscopy. Nevertheless, it is clear (Table 8) that as the number of aromatic carbons in the molecule increases, the probability of stable free radical formation increases on both an absolute and a relative scale, per weight of sample and per molecule. Also, the relative proportion of the triplet versus the doublet state radicals increases with the number of aromatic carbons in the molecule.

Returning now to the chemical properties and composition of Athabasca asphaltene, the GPC fractions were subjected to low-temperature thermolysis (300°C, as used in in situ steam displacement) to investigate their polymer-forming propensity (Table 9) and the effect of clay minerals (Table 10) [58]. From the data in Table 9 it is seen that the polymer-forming propensity increases with increasing molecular weight of the fraction and that the lowest molecular weight fraction does not produce polymer (under the experimental conditions employed). Mixing of fraction 1 with fraction 5 (1:1) reduces polymer formation from fraction 1. Also, it is noteworthy that not the whole asphaltene yields polymer: on the contrary, thermal treatment results in some depolymerization, resulting in pentane-soluble maltene formation. The inhibiting effect of the low molecular weight fraction on polymer formation is probably due to its hydrogen-donating and consequent free-radical-scavenging ability.

Asphaltenes are capable of complexation with clay minerals and the higher the molecular weight of the asphaltene, the stronger its affinity for the clay. In turn, the clay seems to promote molecular aggregation of the

Table 9. Pyrolysis of Athabasca asphaltene and its GPC fractions at 300° C, 2 h.

Fraction no.	Wt% of asphaltene fraction on daf basis			
	Gas (by diff.)	n-C$_5$-soluble	n-C$_5$-insoluble-CH$_2$Cl$_2$-soluble	CH$_2$Cl$_2$-insoluble polymer
1	5.0	10.2	54.2	30.6
2	4.0	15.2	73.2	7.6
3	6.2	17.1	69.6	7.1
4	6.4	22.3	69.3	2.0
5	6.7	31.6	61.7	0.0
(1 + 5)[a]	5.3	17.3	75.4	2.0
Asphaltene	3.4	15.1	81.5	0.0

[a] Mixed in a ratio of 1:1.

Table 10. Effect of clay on the apparent molecular weight (MW) of Athabasca asphaltene.

Fraction No.	Ash (wt%)	MW in benzene	Ash (wt%)	MW in benzene	MW in CH₂Br₂
1	1.3	16 900	8.8	30 000	16 700
2	1.5	13 700	3.8	17 500	14 900
3	0.7	7 100	2.0	15 700	8 400
4	0.6	3 400	–	3 900	4 800
5	0.5	1 200	1.1	1 400	1 500

asphaltene and causes an increase in its molecular weight. The clay also induces polymerization during thermal treatment and this effect is larger, the higher the molecular weight of the fraction.

The removal of clay from the asphaltene can be effected by centrifugation (Table 6). The residual clay remaining in the asphaltene, ~0.5%, is the inherent clay. Empirical relations have been developed to estimate the percentage of clay and inherent ash present in the asphaltene fraction. The ash level, Y, of the asphaltene is related to the weight percent of clay, C_t, by the expression $Y = 0.872\ C_t + 0.582$. The ash level of the asphaltene is also correlated with the infrared absorbance, A, at 1032 cm^{-1}, which gives the approximate relation $A = 0.648Y + 0.294$. Greater accuracy at low ash levels can be achieved by measuring A at 1040 cm^{-1} above the base line, drawn from 960 to 1140 cm^{-1}. This results in the equation $A = 0.0709\ Y + 0.0124$ [57].

The clay separated from the asphaltene has been characterized by X-ray diffraction as a mixture of kaoline minerals, illite interstratified with <10% smectite and some quartz [57]. No evidence was found for the presence of discrete swelling clay minerals. With decreasing crystallinity and particle size, the clay has an increasing affinity towards organic matter, which makes the removal of clay progressively more difficult.

Trace elemental analysis of the inherent ash (Table 11) shows the major metallic constituents to be V, Ni and Fe; a host of minor components is also present.

The role, origin, and distribution of trace elements in Alberta bitumens and their fractions, including asphaltene, have been extensively studied by Filby [15] using the analytical method of neutron activation. The vanadium and nickel are present to a large extent in the form of porphyrin complexes [68–70]. Many of these metal complexes are volatile and would find their way into the distillate during upgrading and refining operations where their presence is highly undesirable because of their adverse effect on hydrogenation catalysts. Vanadium pentoxide is also corrosive to steel and catalyzes the oxidation of SO_2 to SO_3.

In the course of an investigation of the solubility of asphaltene, it was established that up to 21.7% of the n-pentane-precipitated asphaltene can be dissolved in acetone. This acetone-soluble fraction by and large corresponds to the lowest molecular weight fraction obtained by GPC separation (fraction 5, MW 1200, 20.8%). In this acetone extract it was possible to identify a large number of compounds for the first time in asphaltene chemistry.

Identified were four homologous series of

Table 11. Trace elements in asphaltene V[a] (mg/kg).

Na	41.6	Cu	18.0
K	52.8	Ag	0.8[b]
Be	0.2[b]	Zn	10.0
Mg	27.0	Cd	0.7[b]
Ca	89.0	B	0.5
Sr	1.7	Al	48.8
Ba	2.5	Si(SiO_2)	29.2
Ti	17.4	Sn	0.8[b]
V	604.0	Pb	3.0[b]
Cr	2.1[b]	P(PO_4)	17.5[b]
Mo	20.7	As	9.0[b]
Mn	6.0	Sb	4.3[b]
Fe	211.0	Bi	13.3[b]
Co	0.7[b]		
Ni	215.0		

[a] See Table 6.
[b] Within the detection limit.

carbazoles: 12 alkyl carbazoles, **13**; C_2H_5-C_8H_{17} substituted benzocarbazoles, **14**; dibenzocarbazoles, **22**, with up to C_6 substitution; and tetrahydrodibenzo-carbazoles, **23**, substituted with CH_3 to C_4H_9 in a combined amount corresponding to 0.4 wt% of the asphaltene [71].

It should be pointed out here that many different classes of nitrogen compounds have been identified recently by Holmes [72] in a Utah tar sand bitumen.

Another family of nitrogen compounds identified in smaller quantities (~340 ppm based on original asphaltene) was that of the vanadyl porphyrins: the DPEP, **24**; ETIO, **25**; and small amounts of RHODO, **26** variety with their carbon distribution in the 20 to 52 range [73].

Among the sulfur-containing compounds identified in the extract was the homologous series of sulfides and sulfoxides first detected in the resin fraction of the bitumen, the di-, tri-, and tetracyclic terpenoid sulfoxides and sulfides, and a short series of pentacyclic terpenoid sulfoxides, in a combined amount of 0.5% of the asphaltene. Other, higher molecular weight sulfur compounds (12% S, *MW* ~1100) were concentrated (3.1% of asphaltene) but have not yet been identified.

Several series of carboxylic acids were identified, comprising, with the sulfoxides, the most polar fraction of the acetone-soluble asphaltene in an amount of 2.2% of the asphaltene. The homologous series identified were: *n*-alkanoic acids (C_{14} to C_{28}), branched alkanoic acids (C_{12} to C_{15}), tricyclic terpenoid acids (C_{21} and C_{24} most prominent), unsaturated tricyclic terpenoid acids, alkylated anthracene carboxylic acids, a homologous series of alkylated dibenzothiophene carboxylic acids, and a homologous series of alkylated 9-carboxy-9-hydroxy fluorenones [74].

Some ketones and alcohols were also identified. These include a homologous series of alkylated dihydroxy phenanthrenes, a series of alkylated fluorenones, a series of alkylated substituted benzofluorenones, and a series of alkylated benzonaphthofluorenones. Among the alcohols were a series of alkyl fluorenols, a series of alkyl benzofluorenols, and a series of alkyl dibenzofluorenols.

The thermolysis of asphaltene is also a simple means of obtaining structural information. In a flow system at ~300°C Athabasca asphaltene may yield a pentane-soluble oil in yields of up to ~40% without coke formation. This oil is rich in biological markers which, as it turns out, are concentrated in the low molecular weight fraction of the asphaltene. This oil

also contains alicyclic sulfides and thiophenes along with the full complement of cycloalkanes, aromatics and resins. The sulfides are a mixture of the terpenoid sulfides **7**, **9**, **10**, **11**, **12** and *n*-alkyl-substituted five- and six-membered cyclic sulfides in which the substitution is characteristically in positions α,α to the sulfur,

strongly suggesting an *n*-alkane precursor which was cyclized by the incorporation of the bridgehead sulfur atom. On hydrodesulfurization these sulfides convert to a homologous series of *n*-alkanes. This finding is in keeping with the detection of aliphatic sulfones in the oxidized aliphatic core from the Ru(VIII)-catalyzed oxidation of the asphaltene (*vide supra*). Similarly, the thiophenes and benzothiophenes identified in the monoaromatic fraction of the pyrolysis oil show an analogous structural arrangement of the types:

and
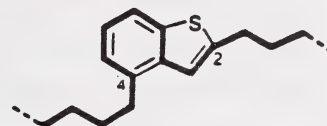
When this finding is considered in conjunction with the predominance of the *n*-alkyl-type side chains and polymethylene bridges present in the asphaltene, one is forced to conclude that part of the asphaltene aromatic structure (thiophenes at least) has arisen from the cyclization and aromatization of straight-chain alkanes. This is in sharp contrast to the bulk composition of the maltene which, apart from some of its aromatic components, appears to feature a branched, mainly isoprenoid, molecular framework, revealing distinctly different biotic source materials for the two fractions of the bitumen.

It has been recognized [75] that autochthonous marine organic matter contains abundant long-chain hydrocarbons, and that many oil-prone so-called herbaceous marine (type 2) kerogens contain long alkyl chains. Upon thermolysis they release homologous

series of *n*-alkanes and 1-alkenes in the obtained from the thermolysis of oil sand asphaltenes. Thus, it is probably not unreasonable to surmise that these asphaltenes may be related to such kerogens. This has, in fact, been suggested before [76] and the asphaltene has been proposed to be the thermal degradation product of the kerogen [77]. The branched, terpenoid-type saturate and resin fractions of the bitumen, on the other hand, could have originated mainly from the extensive microbiological activities that had taken place in the reservoir oil, and only to a lesser extent from the original biotic source material. The long alkyl chains in the asphaltene escaped destruction by microbial degradation because of the relatively large micelle structure of the asphaltene (and similarly the high molecular weight portion of the maltene) which provided protection against microbial attack.

From various studies, many aromatic molecules in the 1 to 4 fused ring range have been identified from asphaltene pyrolyzates [67,78].

Activation energies and preexponential factors have been measured for the decomposition of several oil sand asphaltenes by measuring these kinetic parameters for the appearance of some individual product [38] (C_1 to C_4 hydrocarbons, CO, CO_2, H_2S) or for the weight loss of the asphaltene [79]. The results are scattered and their interpretation is outside the scope of this chapter.

In a study of the structural changes which take place upon catalytic hydrocracking of the asphaltenes, Takeuchi et al. [80] followed the changes in elemental composition, molecular weight distribution, ESR, X-ray diffraction, and small-angle scattering. From the correlation of molecular

weight decrease in the course of conversion with the V/C and S/C ratios, along with the instrumental results, the mechanism illustrated in Figure 12 was proposed. According to these authors, disintegration of the large asphaltene micelles would start with the breakdown of the intermolecular forces exerted by the VON_4 moiety of the vanadyl porphyrin structures in the asphaltene, followed by further cleavages at the weak S-C bond sites. This micelle structure was originally proposed by Yen [81].

In contrast, Yoshida et al. [82] from an FTIR and high resolution ^{13}C and ^{1}H NMR study, concluded that Athabasca asphaltene is characterized by oligomers consisting of units of 1 or 2 aromatic rings highly substituted with C_3 to C_5 aliphatic chains and heteroatom-containing functional groups.

The changes in asphaltene properties during steam displacement of Cold Lake bitumen were investigated by Gould [83] who found an increase in the V and Ni content, a slight decrease in the H/C ratio, a large increase in aromaticity and some changes in the IR spectra of the treated asphaltene.

More detailed studies have shown that in laboratory aquathermolysis at 300°C, the asphaltene content of the bitumen shows a significant decrease after a few days and a commensurate increase in the maltene content, especially in the resin-plus-polyaromatic fraction.

MOLECULAR AGGREGATION

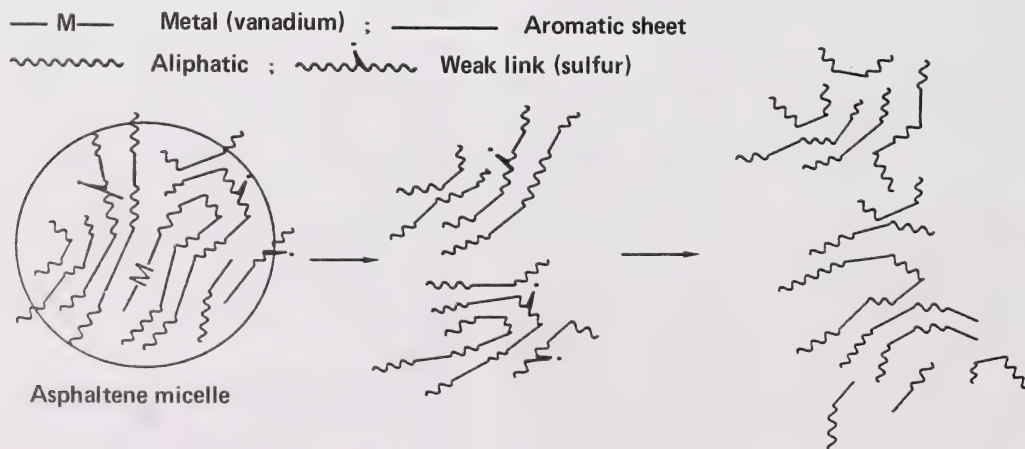One of the most important physical parameters of the bitumen from the standpoint of recoverability is the

Figure 12. Mechanism of Athabasca asphaltene cracking [80].

viscosity and its temperature dependence. On the other hand, gravity characterizes the chemical composition better than viscosity and gravity is a widely used basis for setting the price of oil. Viscosity and gravity, along with other important physical parameters such as rheological properties, colloidal state and micelle stability, solubility, and molecular weight, are governed by the chemical composition and molecular aggregation caused by noncovalent interactions such as hydrogen bonding, π-π interaction, charge transfer and van der Waals complexation of the polar constituent molecules.

The hydrogen bond may be represented as X-H$\cdots$Y, where X and Y are electronegative atoms such as oxygen, nitrogen, or sulfur. Atom Y is an electron-rich centre like the nitrogen in pyridine or quinoline (which has been detected in Athabasca bitumen) or a π base like an aromatic ring structure or a π bond, etc. The bonds are most favored when the X-H$\cdots$Y bond angle is nearly near and they operate over a distance of ~3Å between the electronegative atoms. Most hydrogen bond strength values lie in the 13 to 42 kJ/mol range, or about 1/10 that of a sigma bond. Hydrogen bonding represents an important mode of molecular aggregation in oil sand asphaltenes and resins, where the bonds are thought to involve phenolic or alcoholic OHs and pyrrole-type NH groups (carbazole, porphyrins) as hydrogen donors, and basic nitrogens and aromatic rings, the basicity of which increase with the number of condensed aromatic rings and carbonyl groups acting as hydrogen acceptors. However, the most acidic groups present are the carboxyl groups of carboxylic acids; the most basic compounds are the quinolines. Both should play a major role in hydrogen bonding.

The hydrogen-bonding interaction can be broken up by derivatization of the acidic X-H groups by silylation, alkylation, or acetylation which may then result in a decrease in the molecular weight. Like all intermolecular bondings, hydrogen bonding can be intra- as well as inter-molecular. The solubility of asphaltene in benzene, for example, is related to the weak hydrogen bonding ability of benzene. On precipitation with n-alkane, the solvent-solute hydrogen bonding is reduced and replaced by solute-solute hydrogen bonding, accompanied by the formation of a high molecular weight insoluble aggregate [84].

The larger aromatic π-electron systems are more basic and can participate in complexation with both protons and Lewis acids (electron deficient molecules).

The polyaromatic systems in bitumens have been demonstrated to undergo charge transfer complexation. The aromatic sheets can have either electron-donor or electron-acceptor properties depending on substitution, and charge transfer may take place to varying degree: in the extreme, it could result in the formation of radical ion pairs such as the triplet biradicals detected by ESR spectroscopy (vide supra), or it may result in two separate ions. Stacking of the aromatic structure in asphaltenes is primarily caused by π-π interaction. Substituents attached to the aromatic layers must be at the edge of the layers in order to avoid interference with parallel alignment of the plates. Alkyl side chains should be effective in preventing stacking and thereby in reducing the probability of polymerization and mesophase formation during heat treatment.

The viscosity of the bitumen is primarily determined by the molecular weight and the extent of hydrogen bonding with an average energy of 25 to 33 kJ/mol. Stacking of the aromatic plates is probably less important (owing to the entropy restriction on achieving parallel alignment). The magnitude of the hydrogen bonding energy is also compatible with the temperature-dependence of the viscosity.

The molecular weight of the Athabasca asphaltene is quite high, especially if appropriate allowance is made for the presence of the heavy resinous material which, from a structural point of view, does not form part of the asphaltene fraction. The high molecular weight and relatively high concentration of the asphaltene in the bitumen is one of the primary causes of the high viscosity of the oil sand bitumen.

The molecular weight of the asphaltene or of any fraction of the bitumen reported in the literature is generally the number average value determined by vapor pressure osmometry (VPO), and gives no information on the shape of the molecular weight distribution curve. An appreciation of this can be obtained from the plot of VPO molecular weights of fractions obtained by GPC separation of the material. Such plots for a number of Alberta asphaltenes and their deasphalted oil, the maltene, are shown in Figures 13 and 14, respectively [85]. The asphaltene and the maltene distribution curves of the various bitumens show some differences. One of the most striking aspects of the data is the presence of very high molecular weight materials, up to and beyond 6000 amu in the maltene fraction, which exceeds the VPO number average molecular weight of the native asphaltene (3600).
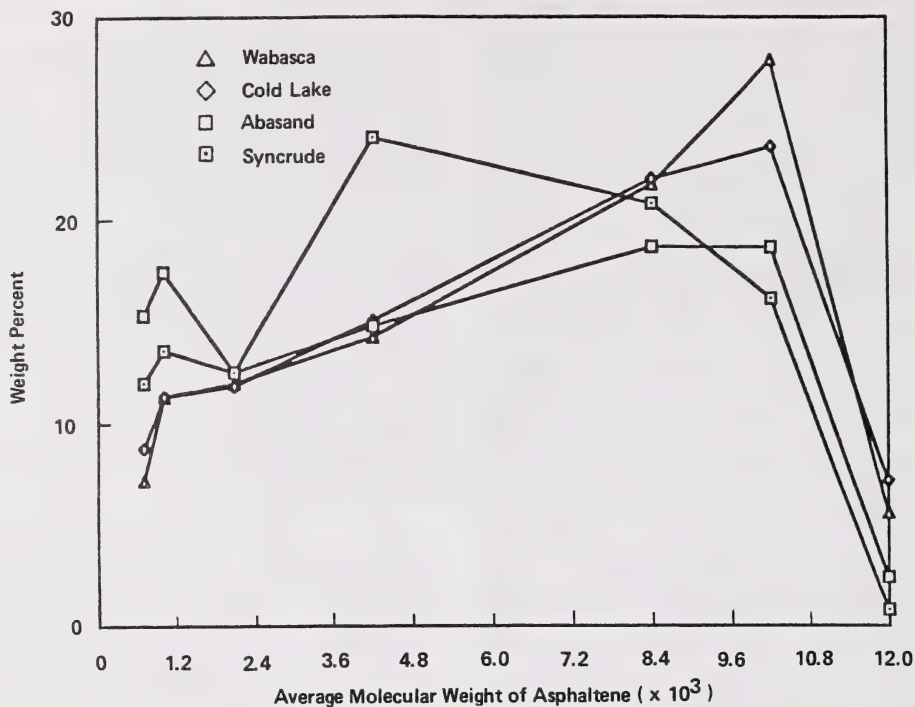
Figure 13. Distribution of the VPO molecular weights of the GPC fractions of Wabasca, Cold Lake, Abasand, and Syncrude asphaltenes.
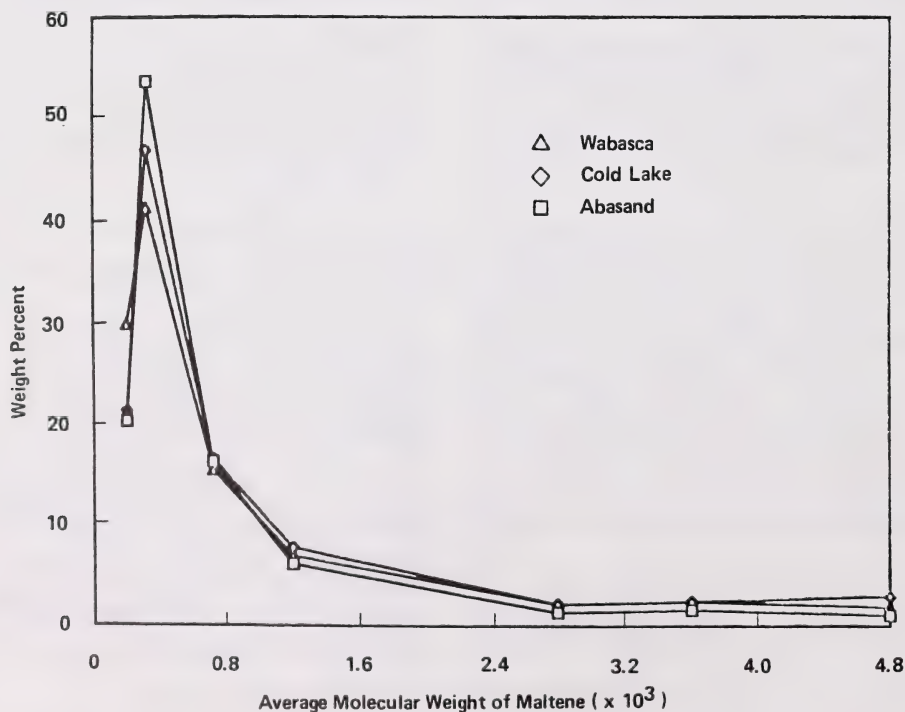

Figure 14. Distribution of the VPO molecular weights of Wabasca, Cold Lake, and Abasand maltene fractions.

CHEMICAL CHANGES IN OIL SAND BITUMENS

The chemistry associated with the exploitation of oil sand resources and the conversion of the bitumen to synthetic crude oil can be divided into two categories: (i) thermal treatment in the presence of the source rock either in the course of in situ steam or fire flood production of the bitumen or the dry retorting of the mined oil sand, and (ii) the upgrading of the separated bitumen. At present, the major use of oil sand bitumen is for synthetic crude oil production although its direct application to chemical feedstock manufacturing, such as benzene, has been considered. The prospects for using heavy crude visbreaking distillation residues for asphalt cement have been discussed recently by Poirier and Sawatzky [86].

The general concept of the bitumen upgrading process is simple, if not trivial: the molecular weight must be reduced, the H/C atomic ratio increased, either by rejection of carbon, addition of hydrogen, or both; and the heteroatoms (N, O, S, metals) and solids (fines, clays) must be removed. The process may or may not involve a catalyst. Visbreaking — a mild thermal cracking without a catalyst — is employed in the Suncor (delayed coking) process and in the Syncrude (fluidized bed) coking. Hydrovisbreaking is carried out in the presence of hydrogen and a donor solvent. The catalytic processes can also be carried out in the presence of hydrogen (hydroconversion) or without hydrogen (catalytic cracking) at ~400 to 420°C.

The overall chemistry involved in the four types of processes is quite complex but the underlying principles, the nature of thermal activation, the primary bond cleavages, the free radicals and their elementary reactions, appear to be closely similar.

One important aspect of the thermolysis of such complex systems as bitumens is that the thermolyses of the components are not independent of one another. One clear illustration, among others, of this facet is provided by the data in Table 9 for Athabasca asphaltene and by the detailed study of a vacuum residue in which the whole residue was subjected to a mild visbreaking industrially and in a microreactor [87] (with nearly the same results). Then, in subsequent experiments the four (SARA) class reactions, the C_5-maltene, and the C_7-maltene were pyrolyzed in the liquid phase under the same conditions [87]. The distribution of the products from the whole residue (SARA, C_{18}, unsaturates, coke) could not be reproduced well from those of the individual class fractions on the basis of simple additivity, according to partial concentration in the whole residue. The main conclusions that can be drawn from the accumulated experience may be summarized as follows:

- the highest coke yield comes from the asphaltene and resin, according to increasing molecular weight;
- the low molecular weight asphaltenes show a distinct inhibiting effect on polymer formation from the higher molecular weight fraction;
- the whole residue gives less coke and less cracked C_{18} than would be expected from the sum of the partial concentrations of the SARA fractions, because of the apparent inhibiting effect of the asphaltene and resin on the secondary cracking of the saturate and aromatic fractions;
- paradoxically, C_7 deasphaltened maltene yields slightly more coke than the whole residue and much more C_{18} cracked product;
- heavy resins convert to asphaltene;
- at low conversion rates, products are cracked with a kinetic order of close to unity and with an activation energy of ~159 kJ/mol.

The apparent fact that emerges, and which was not so well recognized before, is that asphaltene and/or heavy resin can serve as both sources and traps for free radicals.

The visbreaking of bitumen proceeds via several types of parallel, competing, and consecutive reactions including:
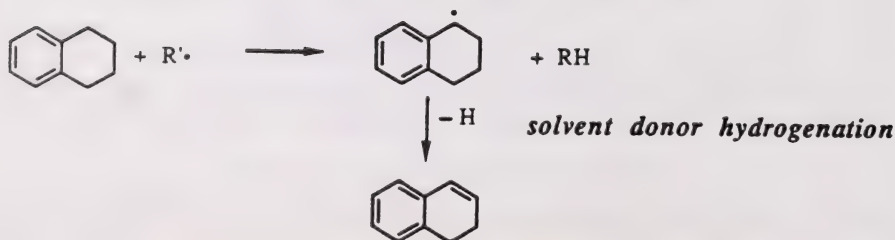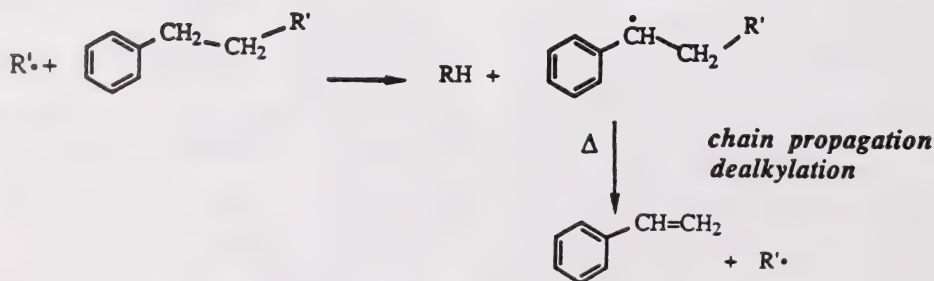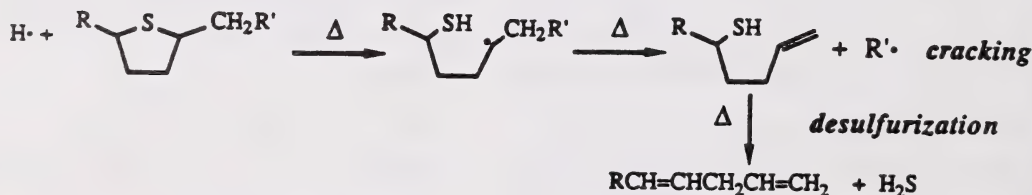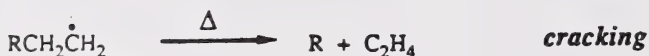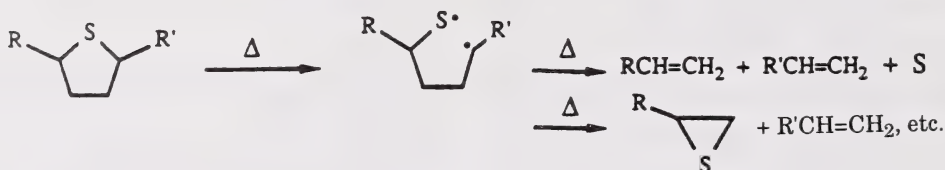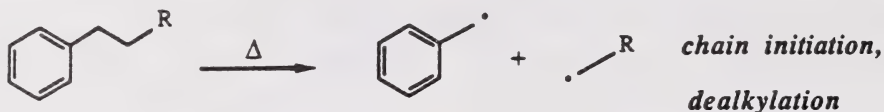
(a) *bond cleavages* producing free radicals; chain initiation, dealkylation;
(b) *hydrogen abstraction* by primary radicals, producing less reactive secondary radicals; chain propagation, donor hydrogen transfer;
(c) *decomposition* of primary and secondary radicals; chain propagation;
(d) *condensation* resulting in naphthenic and aromatic ring formation;
(e) *solvent donor hydrogen transfer*; aromatization;
(f) *combination and disproportionation* of radicals; chain termination;
(g) *molecular decompositions*; desulfurization;
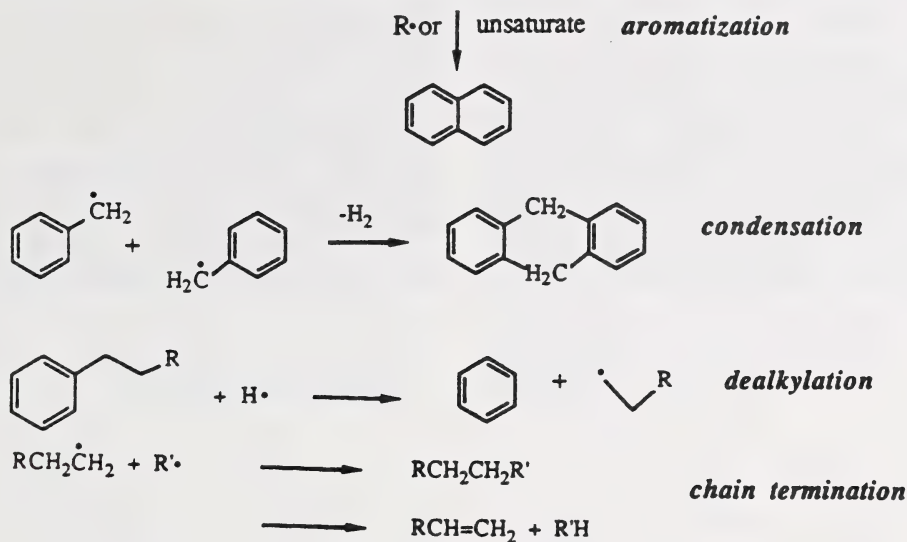(h) *dealkylation* by H-atom displacement.

In the thermal reactions of hydrocarbons, chain propagation of the decomposition is common. The chain-initiating radicals form in processes (a), (c), and (e) above, starting with the rupture of the weakest bonds in the molecules present. With Athabasca bitumen, decomposition proceeds at temperatures as low as 200°C,

yielding a plethora of products including CH_4 and n-alkanes, 1-alkenes, cycloolefins, cycloalkanes, acetaldehyde, acetone, methanethiol, CO, CO_2, COS, H_2S, benzene, and so on. The weakest major series of bonds known to be represented in the bitumen are the sulfide, C-S-C bonds having bond dissociation energies of 271 to 301 kJ/mol, and benzylic C-C bonds,
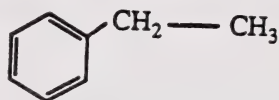
with 280 to 309 kJ/mol. These can undergo thermal decomposition giving rise to the formation of n-alkyl, benzyl, and sulfide radicals, for example,

R• or | unsaturate *aromatization*

(naphthalene structure)

condensation

$-H_2$

dealkylation

$+ H•$

$RCH_2\overset{\bullet}{C}H_2 + R'• \longrightarrow RCH_2CH_2R'$

chain termination

$\longrightarrow RCH=CH_2 + R'H$

Now, these are some of the main types of reactions occurring during visbreaking of bitumens and crude oils, and they can involve molecules of the saturate, aromatic, resin, and asphaltene fractions. The trace metals (V, Ni, Mo) naturally present in the bitumen and crude oil [68–70] may act as catalysts for some of these reactions.

As the visbreaking progresses, the aromatic molecules lose their alkyl side chains and the aromaticity increases owing to condensation and aromatization of alkyl and naphthoaromatic molecules. This in turn leads to an increase in the size of the aromatic clusters and to an increase in their compaction owing to a decrease in their void volume. The solute-solvent interaction with these large aromatic sheets gradually declines, and the sheets start to align themselves in a parallel position, maximizing the effect of intermolecular forces between sheets. As this action progresses, the solubility of the stacks decreases in the isotropic solvent and this is the prelude to the formation of mesophase, appearing as small droplets in the pitch. The droplets exhibit birefringence; that is, they possess two different indices of refraction depending on the direction, hence the terms mesophase and liquid crystals [88,89]. Mesophase droplets preferentially wet steel and tend to spread at the steel-pitch interface. Mineral matter also collects at the mesophase-isotropic pitch boundaries. In subsequent stages, as further dealkylation takes place, the distance between aromatic sheets decreases and a disc-shaped aromatic structure forms a dense mesophase coke relatively devoid of pores, while the isotropic pitch gives rise to more porous, amorphous coke. The liquid

crystallinity is determined by the shape of the aromatic clusters (discs, rods, platelets), the sum of the polar, aromatic and asphaltene contents of the oil, molecular weight, sulfur content, metallo-organic content, and so on.

In hydrovisbreaking, the chemistry involved and the products formed remain essentially the same; nevertheless, the product quality regarding flocculation threshold, density, and viscosity, improves. At the same time hydrogen is consumed; in visbreaking a very slight hydrogen loss occurs. In the hydrogenation process the trace metal salts (V, Ni, Mo, sulfides) and H_2S are suspected to play a catalytic role. Thermodynamic and kinetic considerations predict that condensation and cracking side reactions are reduced and these are then accompanied by a reduction in the yields of asphaltene, and ultimately pitch and light gas.

As in all thermal reactions, such kinetic parameters as residence time, extent of conversion, and extent of secondary reactions, can have a critical role in determining the outcome of the overall reactions and nature and yields of the products. Therefore, in the evaluation and comparison of the results of thermolysis reactions, these kinetic parameters have to be taken into proper account.

The catalyst in the catalytic processes (CANMET), iron sulfide + subbituminous coal (HDH VEBA-Combi), solid or colloidal group VI or VIII metals, may act by direct activation of the hydrogen or through the hydrogenation of pericondensed aromatic molecules. In the gas phase, the principal metathetical reaction is $R• + H_2 \leftrightarrow RH + H•$ and H atom reactions such as addition to olefins and aromatics, hydrodealkylation, dehydro-

genation of naphthenes, and so on, become more important [90].

Employing a metallic catalyst at 410 to 425°C, residence times of 1 to 2 h and hydrogen pressures of 2000 to 2500 psi, can give hydrogenated bitumens with slightly increased H/C ratios, significantly increased API gravity, lowered asphaltene, sulfur, and metal content, and only very low coke yields (~0.6%) with the coke having an ash content of 60 to 70% [91]. When this partially hydrogenated bitumen is subjected to delayed coking, the resultant liquid distillate has a higher yield, better quality, and lower metal content; and at the same time the combined gas and coke yield is lowered [92].

In the course of in situ recovery of the bitumen, the source rock containing the bitumen is heated to elevated temperatures where the bitumen viscosity would drop considerably and thus under the pressure of steam or hot combustion gases it would flow into production wells.

When steam is applied for this purpose the steam (at 200 to 325°C) and the condensed hot water interact
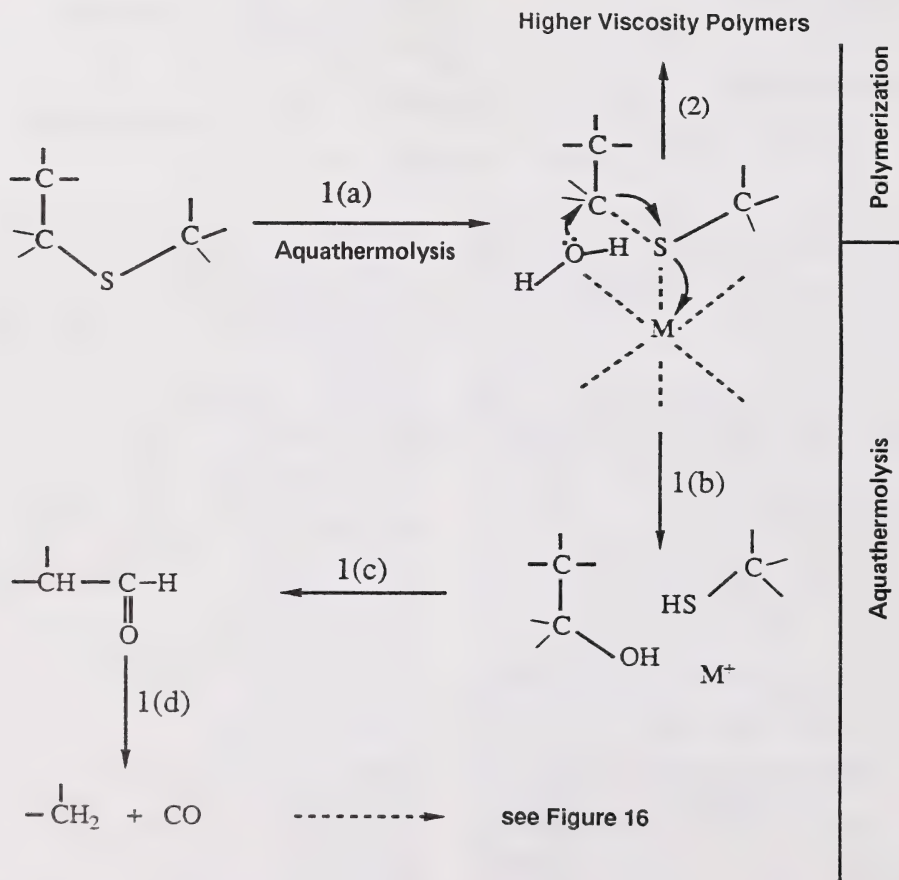

Figure 15. Mechanism of aquathermolysis. Evidence for metal complexation with sulfide sulfur has been found in the complexes between ruthenium salts and thiolane. NMR suggests intracomplex reactions. Intermediate thio production detected by potentiometric titration of SH. Enol rearrangement can yield aldehyde, detected by IR, and formation of 2,4-DNPH complex. Decarbonylation to yield CO shown possible by aquathermolyzing n-butyraldehyde under same conditions to yield CO [93].

chemically with the source rock and with the organic matter, the humic materials, and the bitumen. These steam and hot water reactions, called aquathermolysis, have been investigated extensively by Hyne and coworkers and recently were reviewed by Hyne [93].

The role of aquathermolysis is particularly important in the 200 to 325°C range where direct thermolysis of bitumen is thought to be relatively slow [93], yet the heating effect and consequent mobility increase of the bitumen is sufficient to induce and maintain production of the bitumen. However, direct thermolysis, even in the lower end of the aquathermolysis regime, cannot be neglected, especially over the weeks or months involved.

According to Hyne [93], the most important step in the aquathermolysis of bitumen involves the hydrolysis of the sulfide and thiophenic-sulfur bonds, which may be catalyzed by certain metal ions naturally present in the source rock and dissolved in the water. The principal reactions involved are shown in Figures 15 and 16 [93]. Cleavage of the S-C bond in sulfides may lead to a decrease in the molecular weight of the higher molecular weight molecules and to a decrease in asphaltene content which, in turn, results in a decrease in the viscosity of the bitumen. Under some conditions, owing to competing polymerization reactions, the viscosity may increase rather than decrease. The net effect,
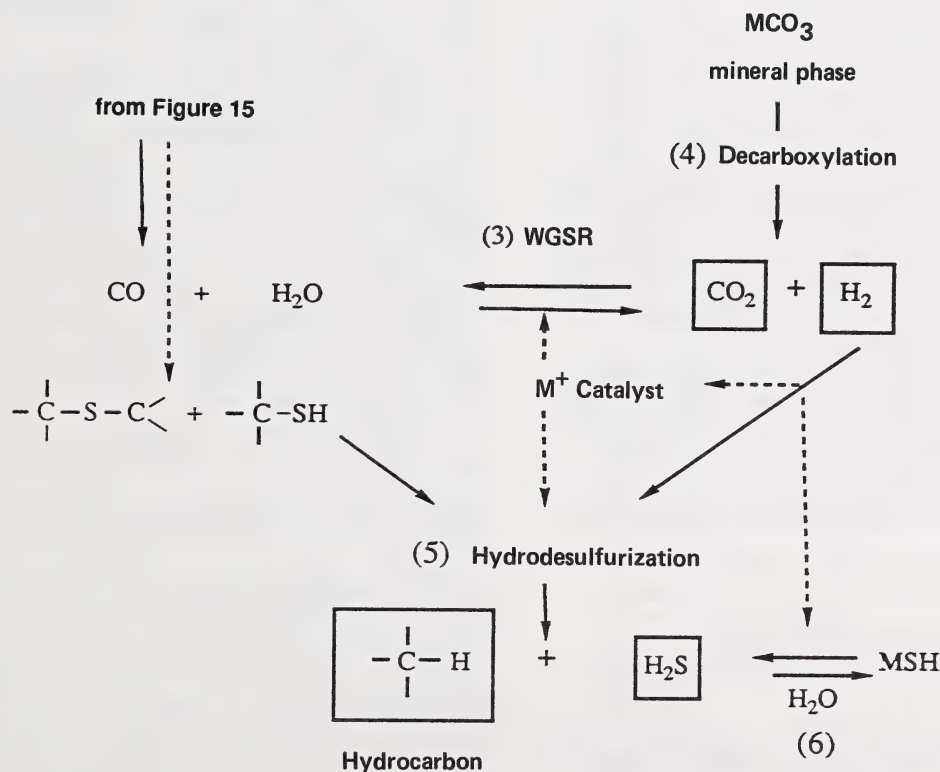

Figure 16. Other aquathermolysis reactions. Gases in boxes are principal components of gas phase, produced from aquathermolysis of both heavy oil sands and thiolane and thiophene. Metal ions from mineral phase or intentionally added act as catalysts for both WGSR and hydrodesulfurization, possibly in sulfide form through reaction with produced H_2S. Intermediate nature of CO explains transient appearance in produced gas [93].

demonstrated in laboratory experiments, depends on the experimental conditions: temperature, reaction time, composition of the oil sand, and so forth. The thiol produced in the aquathermolysis step may undergo H_2S elimination or secondary hydrolysis to yield H_2S. From thiophenes, the resultant alcohol rearranges to the aldehyde which readily decomposes to produce CO, which, with water, can enter into the water-gas shift reaction (WGSR). Again, this latter reaction may be catalyzed by some of the mineral components of the sand and, consequently, may proceed with high efficiency at the temperatures involved to yield hydrogen [93]. The hydrogen can bring about catalytic hydrodesulfurization and possibly some hydrogenation of other labile groups in the bitumen to produce hydrocarbons. Thus, during in situ steam displacement, a partial upgrading of the bitumen may be brought about by the aquathermolysis reactions, which would be manifested by a decrease in the viscosity, and the sulfur and asphaltene content of the produced bitumen. The overall effect can be amplified by the addition of extraneous CO (and trace amounts of metal ions, Fe^{2+}, MoO_4^{2-} and so on) to the system in order to drive the WGSR equilibrium in the $CO_2 + H_2$ direction, thereby producing more in situ hydrogen and introducing more hydrogen into the produced bitumen. The viscosity drop as well as the rate of H_2S formation can also be influenced by the presence of trace metals (Fe^{2+}, MoO_4^{2-}, and Tl^{3+}, respectively).

The humic materials (humic acids, fulvic acids, and humins) chemisorbed to the inorganic matrix hydrolyze and thermolyze in aquathermolysis between 200 and 325°C to release hydrocarbons, CO, and CO_2. The inorganic matrix itself may also release CO_2 from hydrolysis of iron carbonate (siderite) and other labile carbonates.

IN SITU COMBUSTION AND LOW-TEMPERATURE OXIDATION OF BITUMEN

An alternative in situ recovery technology to steam displacement is fire flooding, the partial combustion of in-place bitumen in air under pressure [94]. The propagation of the combustion front through the reservoir from the injection to production wells is maintained by the injection of air, and as the fire front moves through the reservoir, it vaporizes oil and the formation water, and also affects the composition of some minerals in the sand. The vapors are driven ahead

of the front and are condensed in cooler parts of the reservoir. The oil is ultimately forced to the surface through production wells. The fuel for the combustion is supplied by the residual coke.

Combustion can proceed in two directions [94]. In the more commonly used process the combustion zone advances in the same direction as the air flow (forward combustion) and in the other process the direction of the air flow is opposite to the advance of the combustion front (reverse combustion). Forward combustion burns the least desirable fraction of the oil, leaves a clean sand behind, and is an efficient heat generating process [94]. In wet combustion, water is injected with air to transport heat and to reduce the air requirement. This results in a significantly higher peak temperature and longer exposure of the oil to high temperature, leading to more thermal cracking and better quality produced oil. In dry combustion the maximum temperature is ~600°C and in wet combustion, it rises to ~800°C.

Results obtained in laboratory combustion tube tests have been compared with field pilots data and shown to be consistent with the displacement mechanism that is operating downhole [95].

Under elevated temperature conditions such as those associated with dry combustion, thermal cracking reactions are the dominant processes; however, oxygen may channel through the high-temperature combustion zone and react with the bitumen in the steam bank and in the low-temperature region downstream of the steam bank. Under superwet conditions, on the other hand, the low-temperature oxidation reactions become the dominant processes. Both the low- and high-temperature processes have been extensively investigated by Bennion, Moore, and co-workers during the past decade [94–96] in laboratory combustion tube experiments. Aspects explored included air and fuel requirement parameters; the effects of fire flooding temperature, air-fuel and water-air ratios on the combustion behavior of various core samples and reconstituted core samples, and on the quality of produced gas and liquid hydrocarbon streams; kinetics and kinetic parameters of the combustion processes; and the role of low-temperature oxidation. With regard to this latter process it was found that in the 220 to 275°C range the oxygen uptake did not obey Arrhenius's law, and the order with respect to oxygen pressure decreased with increasing temperature and reached zero at 175°C. Three reaction regimes were identified with transitions between them being characterized by the rapid formation of coke and the virtual disappearance of the

sphaltene fraction. It was also found that region I beys relatively simple kinetics and the experimental oke, asphaltene, and maltene yields can also be escribed by simple relationships [96].

The chemistry of the oxidation of hydrocarbons is xtremely complex and involves many short-lived eactive intermediates and chain processes [97,98]. Three distinct temperature regimes can be recognized. The first is the low-temperature regime ($T \leq 160°C$) where the important primary products are the hydroperoxides, R-O-O-H. Oxidation here can occur only via the agency of a catalyst. This regime is exothermic and an explosion may occur if no provision s made to remove the liberated heat. The hydroperoxides tend to undergo homogeneous, auto-atalytic, chain decomposition to produce predominantly lcohols and aldehydes [97]: $2R-CH_2-OOH \rightarrow CH_2OH + RCHO + O_2$; $RCHO + 1/2 O_2 \rightarrow RCOOH$.

The second regime is the so-called cool flame region (250 to 400°C). In this regime the gas-phase oxidation a slow process. The primary products are olefins and hydrogen peroxide: $RCH_2OOH + O_2 \rightarrow RCH = CH_2 + _2O_2$. This reaction is thermoneutral and there is no elf heating, but autocatalysis is important and therefore the initially slow reaction accelerates until substrate-epletion-caused deceleration takes over. Also haracteristic of this regime is the luminosity referred to s a cool flame. During passage of the flame the emperature rises by 100 to 200°C. Sometimes one ame can be followed repeatedly by others in short or ong time intervals. Their characteristics are highly ensitive to the nature of the hydrocarbons and the eaction conditions. The cool blue flames frequently ead to explosions, but generally they correspond to an xothermic reaction which turns itself off when it gets o hot.

The third temperature regime occurs above 450°C. is characterized by the absence of an induction period nd the products CO and CO_2. At higher temperatures it an lead to explosion.

In laboratory combustion-tube low-temperature xidation experiments both explosion and self-xtinguishing have been observed [99].

Among the low temperature oxidation products of lberta oil sands, acetaldehyde, propionaldehyde, etone, methanol, carbon disulfide, carbon monoxide, arbon dioxide, and so on have been detected. More ecently, over 300 other products have been observed nd many of them identified from a Saskatchewan heavy l [100]. The oxidation also causes changes in the composition of the residual bitumen, increasing the amount of asphaltene and its molecular weight, and increasing the oxygen content of asphaltene, maltene, coke, and THF-solubles. It also converts sulfur compounds to sulfoxides, sulfones, sulfinic-sulfonic acids, and eventually sulfuric acid, and produces significant quantities of carboxylic acids.

REFERENCES

1. F.K. North, "Petroleum geology," Allen and Unwin, Boston (1985) 9.
2. W. Rühl, Tar (extra heavy oil) sands and oil shales, in "Geology of petroleum," Ed. H. Beckman, 6, (1982).
3. B.P. Tissot and D.H. Welte, "Petroleum formation and occurrence," 2nd ed. Springer-Verlag, Berlin (1984) 470.
4. T.F. Yen in "The future of heavy crude and tar sands," R.F. Meyer, J.C. Wynn and J.C. Olson, Eds., Unitar (1982) 412.
5. D.R. Prowse, Ed., "Some physical properties of bitumen and oil sand," AOSTRA-ARC, Edmonton (1983).
6. D.A. Redford and H.G. Winestock, Eds., "The oil sands of Canada-Venezuela," Can. Inst. of Mining and Metallurgy (1977).
7. J.G. Speight, "The desulfurization of heavy oils and residua," Marcel Dekker, New York (1981).
8. O.P. Strausz and E.M. Lown, Eds., "Oil sand and oil shale chemistry," Verlag Chemie, New York (1978).
9. R.F. Meyer and C.T. Steele, Eds., "The future of heavy crude oils and tar sands," McGraw-Hill, New York (1981).
10. Second international conference on heavy crude and tar sands, Caracas, Venezuela, Feb. 7–17, 1982 McGraw-Hill, New York.
11. Third international conference on heavy crude and tar sands, Long Beach, CA, Jul 22–31, 1985, AOSTRA.
12. J.W. Bunger and N.C. Li, Eds., Chemistry of asphaltene, Symposia reprints, Am. Chem. Soc., Div. Petroleum Chem., 24 (1979).
13. J.W. Bunger and N.C. Li, Eds., Chemistry of asphaltenes, in Advances in chemistry series 195, Am. Chem. Soc. Washington, D.C. (1981).
14. H.C. Stauffer, Ed., Oil shale, tar sands and related materials, ACS symposium series 163, Am. Chem. Soc. Washington, D.C. (1981).

15. G.B. Grump, Ed., "Petroanalysis '81," John Wiley and Sons, Chichester (1982).

16. R.H. Filby, B.S. Carpenter and R.C. Ragain, "Atomic and nuclear methods in fossil energy research," Plenum Press, New York (1982).

17. Pan-Pacific synfuels conference, Vol.II, Jap. Pet. Inst., Tokyo (1982).

18. G. Deroo, T.G. Powell, B. Tissot, R. G. CcCrossan and P.A. Hacquebard, Geological Survey of Can. Bull., 262 (1977).

19. M.A. Carrigy and J. W. Kramers, Eds., "Guide to the Athabasca oil sands area," Alberta Res. Council, Edmonton (1973).

20. G.D. Mossop, Science, 207 (1980) 145.

21. G. Deroo, T.G. Powell, B. Tissot, R. G. CcCrossan and P.A. Hacquebard, Geological Survey of Can. Bull., 262 (1977) p. 94.

22. E.D. Innes and J.V.D. Fear, 7th World Pet. Congr. Proc., vol. 3 (1967) 633.

23. M.A. Carrigy and D. Wallace, New analytical results on oil sands from deposits throughout the world, Ref. 19, p.231.

24. K. Takamura, AOSTRA J. Res., 2 (1985) 1 and references therein.

25. J.E. Zajic, D.G. Cooper, J.A. Marshall and D.T. Gerson, Fuel, 60 (1981) 619.

26. D. Wallace and D. Henry, Engineering Foundation conference on the processing of energy minerals: shale, tar sands and coal, Henniker, New Hampshire (1984).

27. L.L. Schramm and R.G. Smith, AOSTRA J. Res., 3 (1987) 195, 215.

28. K. Al-Nuaimi, K.N. Jha, D.S. Montgomery and O. P. Strausz, Final progress report, AOSTRA Agreement 174, section B (1982).

29. T.M. Ignasiak, Q. Zhang, B. Kratochvil, C. Maitra, D.S. Montgomery and O.P. Strausz, AOSTRA J. Res., 2 (1985) 21.

30. T.D. Cyr and O.P. Strausz, Org. Geochem., 7 (1984) 127; D.D. McIntyre, D.S. Montgomery and O.P. Strausz, AOSTRA J. Res., 2 (1986) 223.

31. T.D. Cyr and O.P. Strausz, J. Chem. Soc., Chem. Commun. (1983) 1028

32. L.S. Kotlyar, B.D. Sparks and H. Kodama, AOSTRA J. Res., 2 (1985) 103.

33 L.S. Kotlyar, B.D. Sparks, H. Kodama and P.F. Grattan-Bellew, AOSTRA J. Res., 2 (1985) 121.

34. L.L. Schramm, R.G. Smith and J.A. Stone, AOSTRA J. Res., 1 (1985) 145.

35. K.N. Jha, D.S. Montgomery and O.P. Strausz,

Preprints, Div. Fuel Chem., ACS, 24 (1979) 260.

36. Z. Zhang, L.Barta and L.G. Hepler, AOSTRA J. Res. 3 (1987) 249.

37. M.M. Ekwenchi, E.M. Lown, D.S. Montgomery and O.P. Strausz, AOSTRA J. Res., 1 (1984) 127.

38. R.G.S. Ritchie, R.S. Roche and W. Steedman, Fuel, 64 (1985) 391; Chem. Ind. (London), 35 (1979) 25; Fuel, 58 (1979) 523.

39. B.J. Fuhr, L.R. Holloway and C. Reichert, AOSTRA J. Res., 1 (1985) 281.

40. U.S. Bureau of Mines, API RP-60, 1974. W.E. Haines and C.J. Thompson, Separating and characterizing high-boiling petroleum distillates: the USBM-API procedure, LERC/R1-75/5, and BERC/R1-75/2, Jul (1975).

41. D. Wallace, D. Henry, K. Pongar and D. Zimmerman, Fuel, 66 (1987) 44.

42. J.T. Bulmer and J. Starr, Eds., "Syncrude analytical methods for oil sand and bitumen processing," Syncrude Research, Edmonton, (1979) 123.

43. M.L. Selucky, Y. Chu, T. Ruo and O.P. Strausz, Fuel, 56 (1977) 369.

44. J.D. Payzant, A.M. Hogg, D.S. Montgomery and O.P. Strausz, AOSTRA J. Res., 1 (1985) 175, 183, 203.

45. J.W. Bunger, K.P. Thomas and S.M. Dorrence, Fuel, 58 (1979) 183.

46. C.F. Hoffmann and O.P. Strausz, Amer. Assoc. Pet. Geol. Bull., 70 (1986) 1113.

47. A.E. George and J.E. Beshai, ACS Symposium Div Pet. Chem., 182nd Natl. Meeting ACS, New York (1981) 23.

48. J. Chemielowiec, J.E. Beshai and A.E. George, Fuel 59 (1980) 838.

49. S. Coulombe and H. Sawatzky, Fuel, 65 (1986) 552.

50. M.A. Poirier and B.S Das, Fuel, 63 (1984) 361.

51. T.W. Mojelsky and O.P. Strausz, Org. Geochem., 9 (1986) 31, 39.

52. J.D. Payzant, T.W. Mojelsky, T.D. Cyr, D.S Montgomery and O.P. Strausz, Org. Geochem., 8 (1985) 177.

53. J.D. Payzant, D.S. Montgomery and O.P. Strausz Org. Geochem., 9 (1986), 357 and references therein

54. T.W. Mojelsky, D.S. Montgomery and O.P. Strausz AOSTRA J. Res., 3 (1986) 25.

55. T.W. Mojelsky, D.S. Montgomery and O.P. Strausz AOSTRA J. Res., 2 (1985) 131.

56. T.W. Mojelsky, D.S. Montgomery and O.P. Strausz AOSTRA J. Res., 2 (1986) 177.

57. T.M. Ignasiak, L. Kotlyar, N. Samman, D.S

Montgomery and O.P. Strausz, Fuel, 62 (1983) 353.

58. T.M. Ignasiak, L. Kotlyar, N. Samman, D.S. Montgomery and O.P. Strausz, Fuel, 62 (1983) 363.

59. N. Cyr, D.D. McIntyre, G. Toth and O.P. Strausz, Fuel, 66 (1987) 1709.

60. T.W. Mojelsky, D.S. Montgomery and O.P. Strausz, AOSTRA J. Res., 3 (1986) 43.

61. D.D. McIntyre, D.S. Montgomery and O.P. Strausz, AOSTRA J. Res., 2 (1986) 251.

62. J.G. Speight, Fuel, 49 (1970) 134.

63. T.F. Yen, J.G. Erdman, and A.J. Saraceno, Anal. Chem., 34 (1962) 694; T.F. Yen and D.K. Young, Carbon, 11 (1973) 33

64. P. Ragunathan, S. Niizuma, I. Safarik and O.P. Strausz (to be published).

65. T. Yokota, F. Scriven, D.S. Montgomery and O.P. Strausz, Fuel, 65 (1986) 1142.

66. S. El-Mohamed, M.A. Achard, F. Hardouin and H. Gasparoux, Fuel, 65 (1986) 1501.

67. J.G. Speight and R.J. Pancirov, Liquid Fuels Technology, 2 (1984) 287 and references therein; J.G. Speight, ACS Symp. Div. Pet. Chem., ACS Anaheim meeting (1986) 818; ACS Symp. Div. Pet. Chem., 32 (1987) 413; I. Rubinstein and O.P. Strausz, Geochim. Cosmochim. Acta 43 (1979) 1887.

68. T.F. Yen, Ed., "The role of trace metals in petroleum," Ann Arbor Science Publishers, Ann Arbor (1975); R.A. Hofstader, O.I. Milner and J.H. Runnels, Eds., Analysis of petroleum for trace metals, Advances in Chemistry Series 156 (1976).

69. F.S. Jacobs and R.H. Filby, Anal. Chem., 55 (1983) 74; F.S. Jacobs, F.W. Bachelor and R.H. Filby, 5th Intl. Conf. on Nuclear Methods in Environmental and Energy Research, Puerto Rico, Apr (1984).

70. J.A. Curiale, Distribution and occurrence of metals in heavy crude oils and solid bitumens: implications for petroleum exploration, in "Exploration, for Heavy Crude Oil and Bitumen," AAPG Res. Conf., Santa Maria (1984).

71. Z. Frakman, T.M. Ignasiak, D.S. Montgomery and O.P. Strausz, AOSTRA J. Res.,3 (1987) 131.

72. S.A. Holmes, AOSTRA J. Res., 2 (1986) 167.

73. Z. Frakman, T.M. Ignasiak, D.S. Montgomery and O.P. Strausz, AOSTRA J. Res., 4 (1988) 171.

74. Z. Frakman, T.M. Ignasiak, T.W. Mojelsky and O.P. Strausz (to be published).

75. B. Horsfield in "Advances in Pet. Geochem., 1," J. Brooks and D. Welte, Eds., Academic Press, N.Y. (1984), 247.

76. F. Behar, R. Pelet and J. Roucache, Org. Geochem., 6 (1984) 587.

77. F. Behar and R. Pelet, J. Anal. Appl. Pyrolysis, 7 (1984) 121.

78. P.E. Savage, M.T. Klein and S.G. Kukes, Ind. Eng. Chem. Process Des. Dev., 24 (1985) 1169; P.E. Savage and M.T. Klein, Preprints, ACS Pet. Chem., 30 (1985) 642.

79. K.C. Khulbe, A. K. Sachdev, R.S. Mann and S. Davis, Fuel Proc. Technol., 8 (1984) 259.

80. S. Asaoka, S. Nakata, Y. Shiroto and C. Takeuchi, Ind. Eng. Chem. Process Des. Dev., 22 (1983) 242.

81. S.A. Pollack and T.F. Yen, Anal. Chem., 42 (1970) 623 and references therein.

82. R. Yoshida, T. Yoshida, Y. Nakata, Y. Hasegawa and M. Hino, Fuel Proc. Technol., 7 (1983) 161.

83. K. A. Gould, Fuel, 62 (1983) 370 and references therein.

84. V.I. Stenberg, R.J. Baltisberger, K.M. Patal, K. Rannan and N.F. Woolsey, in Coal Science, M.L. Gorbarty, J.W. Larsen and I. Wender, Eds., 2 (1983) 125.

85. H.H. Chen, D.S. Montgomery and O.P. Strausz (to be published).

86. M.A. Poirier and H.Sawatzky, AOSTRA J. Res., 2 (1986) 185.

87. J.F. LePage, F. Morel, A.M. Trassard and J. Bousquet, Preprints, ACS Pet. Chem., 32 (1987) 470.

88. Y-D. Gu, V.A. Weinberg, M-A. Sadeghi and T.F. Yen, in Polymers for Fibers and Elastomers, J.C. Arthur, Jr., Ed., ACS Symp. Ser. 260 (1984) 263.

89. R.J. Diefendorf, ibid., 209.

90. J.W. Bunger, C-H. Tsai and C.P. Russell, Proceedings, 1986-DOE Tar Sand Symp., Jackson, Wyoming.

91. H.H. Chen, D.S. Montgomery and O.P. Strausz, AOSTRA J. Res., 4 (1988) 143.

92. H.H. Chen, D.S. Montgomery, Z.M. George and O.P. Strausz, AOSTRA J.Res., 5 (1989) 33.

93. J.B. Hyne, Synopsis Report No. 50, Aquathermolysis, AOSTRA Contracts No. 11, 103, 103B/C (1986).

94. D.W. Bennion, J.K. Donnelly and H.G. Moore, in Ref. 6, pp. 334 and 139.

95. R.G. Moore, J.P. Millour, D.W. Bennion and D.A. Best, paper presented at the 5th AOSTRA Conference on Advances in Petroleum Recovery and Upgrading Technology, Calgary, Alberta (1984).

96. J.P. Millour, R.G. Moore, D.W. Bennion, M.G.

Ursenbach and D.N. Gil, J. Can. Pet. Tech. (1987) 24.

97. S.W. Benson, Prog. Energy Combustion Sci., 7 (1981) 125.

98. S.W. Benson and P.S. Nangia, Accounts Chem. Res., 12 (1979) 223.

99. R.G. Moore and D.W. Bennion. Private communication.

100. N.A. Noureldin, D.G. Lee, F.M. Mourits and K.N. Jha, AOSTRA J. Res., 3 (1987) 155.

General references
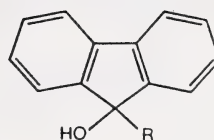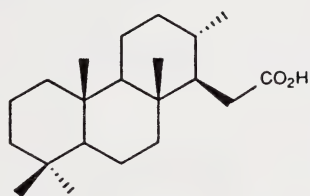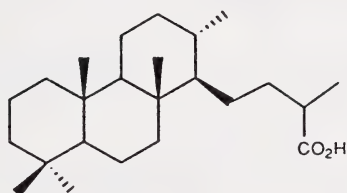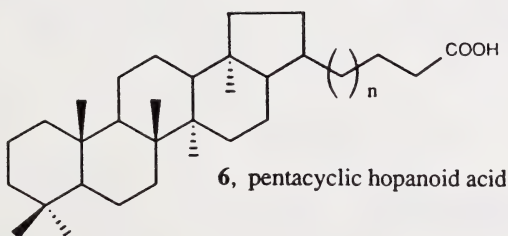
R.R.F. Kinghorn, "An introduction to the physics and chemistry of petroleum," J. Wiley & Sons, Chichester (1983).

J.M. Hunt, "Petroleum geochemistry and geology," W.H. Freeman & Co., San Francisco (1983).
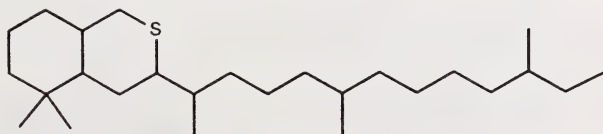
APPENDIX

Chemical formulas
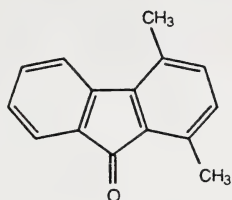
1, 1,4-dimethyl-
fluorene-9-one
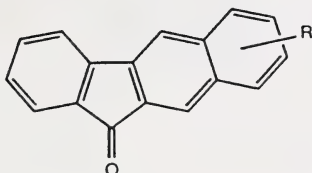
2, alkylbenzofluorenone

3, 9-*n*-alkyl fluorene-
9-ol

4, C_{21} tricyclic
terpenoid acid

5, C_{24} tricyclic
terpenoid acid

6, pentacyclic hopanoid acid

7, C_{26} dicyclic terpenoid sulfide
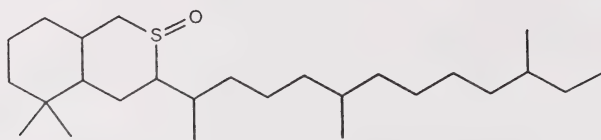
8, C$_{26}$ dicyclic terpenoid sulfoxide
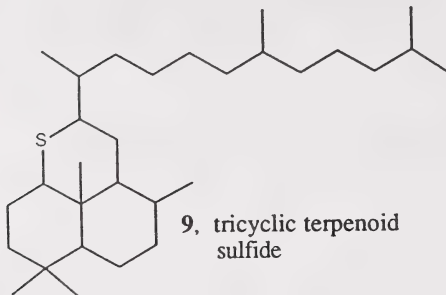
9, tricyclic terpenoid
sulfide
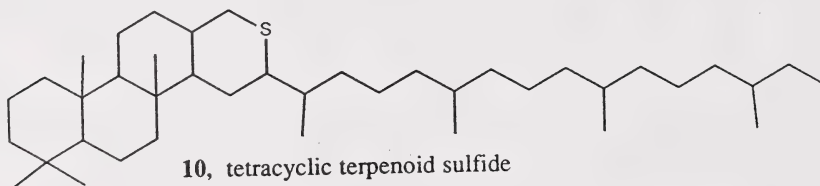
10, tetracyclic terpenoid sulfide
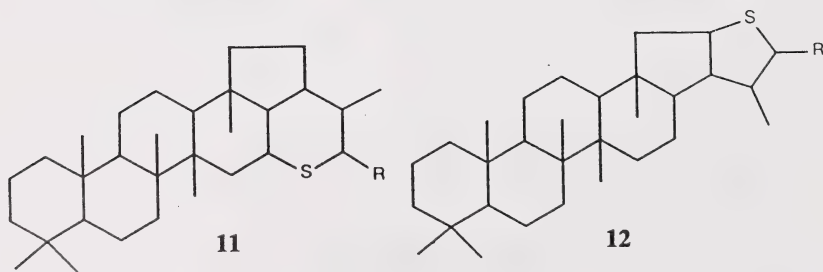
11   **12**

hopanoid sulfides
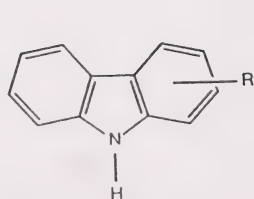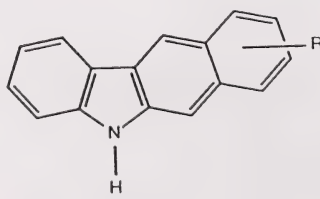
13, alkyl carbazole   **14,** alkyl benzocarbazole   **15,** alkyl quinoline
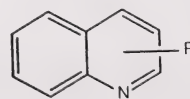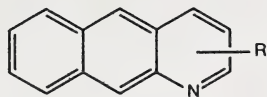
16, alkyl benzoquinoline
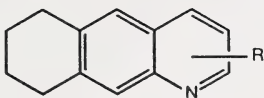
17, alkyl tetrahydro-
benzoquinoline
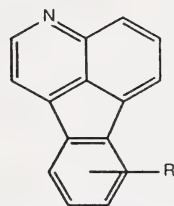
18, alkyl azafluoroanthrene
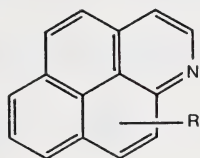
19, alkyl azapyrene
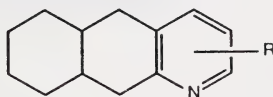
20, alkyl octahydro-
benzoquinoline
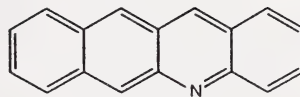
21, dibenzoquinoline
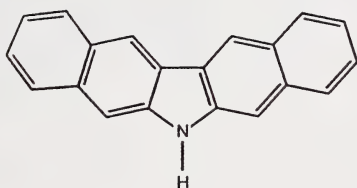
22, dibenzocarbazole
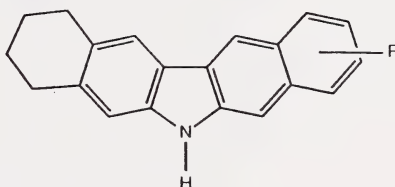
23, alkyl tetrahydrodibenzocarbazole
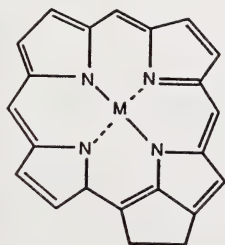
24, vanadyl porphyrin
DPEP
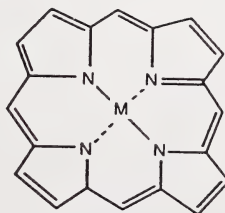
25, vanadyl porphyrin
ETIO
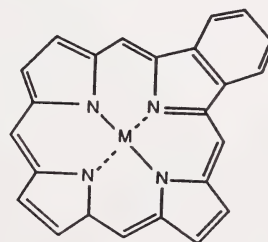
26, vanadyl porphyrin
RHODO

4
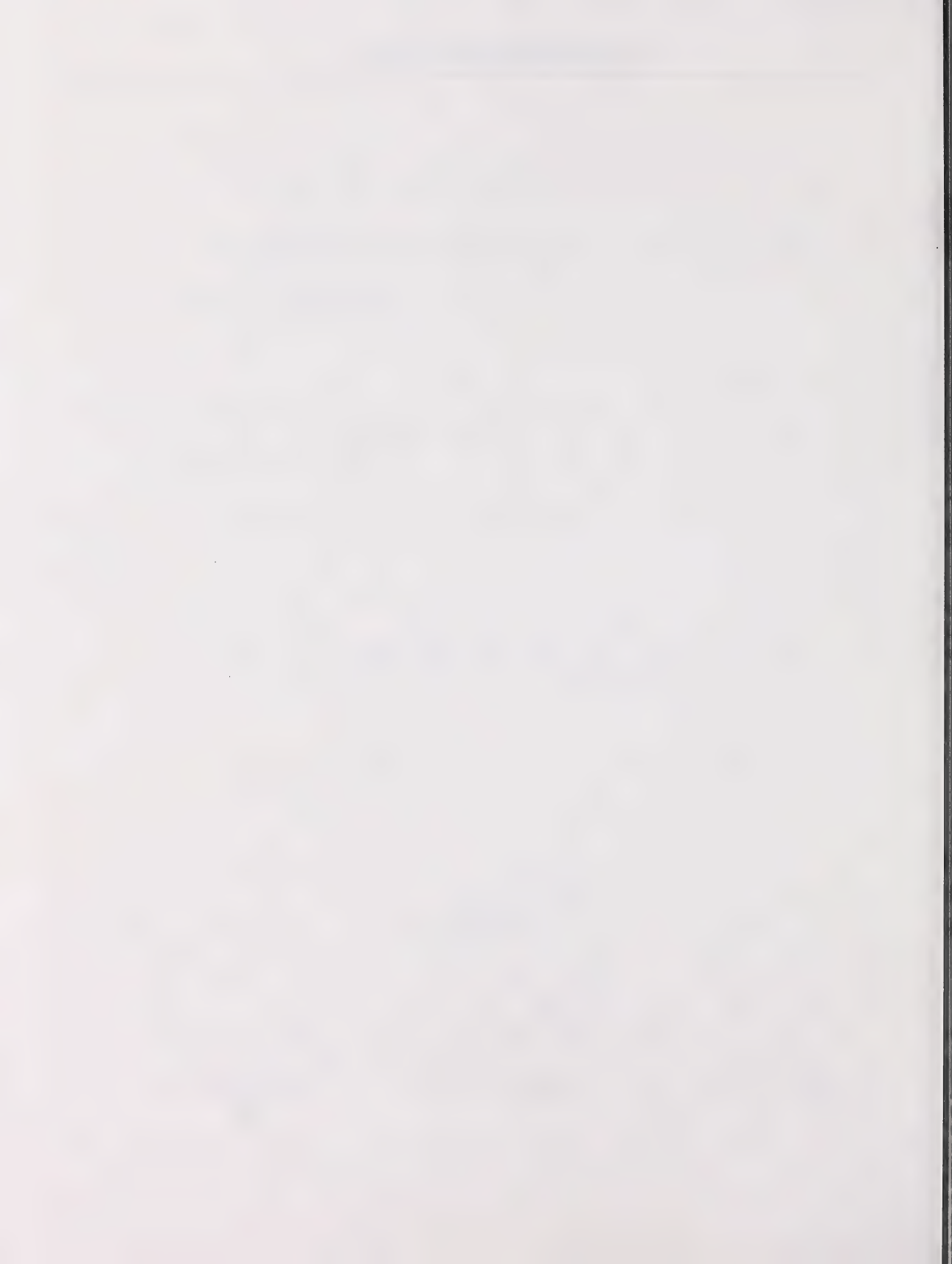
THERMOCHEMICAL
AND THERMODYNAMIC
PROPERTIES

Loren G. Hepler

Department of Chemistry and
Department of Chemical Engineering
University of Alberta

INTRODUCTION

The methods and data of thermochemistry and thermodynamics (sometimes specifically chemical thermodynamics) have been useful for many years in many ways in the production and processing of petroleum, and in such related areas as water treatment and pollution control. This chapter provides brief mentions (with references) of some of these uses, with particular emphasis on such uses in connection with oil (tar) sands and heavy oils. This chapter also includes tabulations of some kinds of thermochemical and thermodynamic data, with emphasis on those data that are specific to oil sands and heavy oils. Finally, this chapter contains an extensive bibliography of some of the pertinent technical literature, with particular emphasis on sources of useful thermodynamic data and guides to the uses of these data.

SOME USES OF THERMOCHEMICAL AND THERMODYNAMIC DATA

Bowman [1] and Leja and Bowman [2] provided two of the earliest accounts of applications of thermodynamics to production of bitumen from the Athabasca oil sands. The first [1] of these papers includes examples of applications of uses of thermodynamic properties in connection with chemical reactions of minerals with water or aqueous solutions, and the second [2] was focussed on applications of thermodynamics to the interfacial properties in relation to production of bitumen from the Athabasca tar sands by the Clark hot water process that is the basis for present commercial production by Syncrude Canada Ltd. and Suncor Inc.

Because the efficient use of heat is one very important component of all of the thermal methods that are used or that may be used for production of bitumen and heavy oils (and sometimes for enhanced recovery of light oils), applications of thermochemical and thermodynamic data have become increasingly common over the past two decades, as reviewed in the book *Thermal Methods of Oil Recovery* by Burger, Sourieau, and Combarnous [3].

It is well known that thermodynamic properties of hydrocarbons and some other substances are useful in the design and operation of petroleum processing operations. A recent summary [4] has been provided by Steele and colleagues at the National Institute for Petroleum and Energy Research (NIPER) in Bartlesville, OK. Many examples of such uses of thermodynamic properties have been provided in various textbooks devoted to chemical engineering [5] or more specifically to petroleum processing, sometimes with an emphasis on production of petrochemicals. Here it is appropriate to call particular attention to *The Chemical Thermodynamics of Organic Compounds* [6] by Stull, Westrum, and Sinke. In addition to containing one of the most useful collections of thermodynamic data, this book (in Chapter 7) presents illustrations of uses of these data in petroleum processing and other industries.

Now we turn to citation of a few publications that illustrate general or specific uses of thermochemical and thermodynamic data.

In addition to the book already cited [3], we call attention to three research papers [7–9] that provide early (still useful) accounts of investigations of *in situ* combustion and uses of thermochemical data. All efforts to carry out either mathematical or experimental modelling of *in situ* combustion processes make use of various kinds of thermodynamic data; here we cite just one such example [10]. We also note that efforts to use [11] knowledge of mineralogical transformations as indicators of combustion zone temperatures during *in situ* combustion would be aided by improved knowledge of thermodynamic properties of minerals and the thermodynamics of their chemical reactions with hot water (steam), oxygen, and chemical products of combustion.

We cite two papers [12,13] that have made use of thermodynamic data in modelling electrical heating processes for production of bitumen from oil sands, and two other papers [14,15] that are concerned with development of theory and modelling for steam-assisted production. These and other efforts to apply theoretical methods to modelling make direct and also indirect use of heat capacities to calculate desired values of thermal diffusivities from the more commonly measured thermal conductivities.

There are many needs for and uses of thermodynamic data for aqueous solutions. For example, thermodynamic calculations of equilibrium conditions in hot water-mineral systems can be useful in analyzing chemical reactions and possible formation damage associated with various steam-assisted production processes, as discussed in some recent research reports [16–18] and in Chapter 9 of this handbook. Mineral-water interactions have also been discussed in *Geochemical Thermodynamics* by

Nordstrom and Munoz [19]. Other applications of thermodynamics to aqueous systems have been reviewed in books titled *Thermodynamics of Aqueous Systems with Industrial Applications* [20] and *Gas Treating with Chemical Solvents* [21].

As pointed out by Filby, Flynn and Goldman [22], proper design and assessment of direct coking of mined oil sands can lead to a process that might have several potential advantages over other processes. Answers to questions about the heat required to bring the incoming oil sands to coking temperature and the heat that might be recovered from spent sands can be derived from knowledge of specific heats of minerals and their decomposition products. Detailed assessment also requires knowledge of heats of combustion of cokes, heats of vaporization of hydrocarbon products of coking, and heats of dehydration of clays.

Many of the references cited later as sources of specified kinds of thermodynamic data also contain statements or illustrations of uses of such data.

Meanings of various symbols used in the remainder of this chapter are given in Table 1, along with commonly used units and some comments about other symbols and units that are now used or have been used in other publications.

HEATS OF COMBUSTION

Heats of combustion provide direct measures of the heating values of oils, cokes, and combustible hydrocarbons. In addition, most of our standard enthalpies of formation ($\Delta_f H^\circ$) of organic compounds that are constituents of oils or products of processing are derived from heats of combustion.

Heats of combustion have been reported in various ways. For example, some results have been reported simply as "heats" (Q), without specification as to whether the results refer to combustion at constant volume or at constant pressure. Other results are reported as ΔU (heat at constant volume) values, while still others are reported as ΔH (heat at constant pressure) values. For fuel-value assessments of oils, cokes, pitches, and other combustible substances, the difference between ΔH and ΔU is usually too small to be important. Most reported heats of combustion refer to a total combustion process in which the H_2O produced is in the form of liquid water at the temperature of the measurement, usually 25 or 30°C, but it should be noted that some published results refer to a process in which the produced H_2O is in the form of water vapor or steam.

The McGraw-Hill Encyclopedia of Energy [23] lists heats of combustion (to form liquid water) for several typical fuels, and Speight [24] lists typical heats of combustion of several fuels and also heats of combustion of crude oils from many locations. Some of these heats of combustion are summarized in Table 2.

A considerable number of heats of combustion of bitumens and heavy oils have been reported, but many

---

Table 1. Some symbols, definitions, and units.

t	Temperature on the Celsius scale.	$c_{p,i}$	Specific heat of a mixture (oil sand or emulsion) or of a defined component of mixture. Subscripts *os, cs, fs, b, w, em,* and *o* indicate oil sands, coarse solids, fine solids, bitumen, water, emulsion, and oil, respectively.
T	Temperature on the kelvin scale, used in thermodynamic calculations.		
K	Symbol for the kelvin unit of temperature.		
K	Equilibrium constant for a chemical reaction.	f_i	Mass fraction of a defined component of mixture. See entry above for identification of subscripts.
J	Unit of energy, heat, or work (4.184 J = 1 cal = 3.966 Btu).		
Q	Heat.		
U	Energy (sometimes called "internal energy"); $\Delta U = Q$ at constant volume.	ΔH_{vap}	Enthalpy of vaporization.
		$\Delta_f H^\circ$	Standard enthalpy of formation, sometimes written ΔH_f° (kJ/mol)
H	Enthalpy; $\Delta H = Q$ at constant pressure.		
M	Molar mass or molecular weight (g/mol).	$\Delta_f G^\circ$	Standard Gibbs energy of formation, also sometimes called free energy of formation and written ΔG_f° (kJ/mol).
C_p	Molar heat capacity (J/K·mol).		
c_p	Specific heat (J/K·g).		

Table 2. Heats of combustion of typical fuels [23,24].

Fuel	Heat of combustion (exothermic) (kJ/g)
Anthracite	33 – 37
Bituminous coal	25 – 35
Sub-bituminous coal	18 – 28
Lignite	13 – 18
Charcoal	29
Gasoline	46 – 48
Kerosene	44 – 48
Fuel oil	40 – 47
Crude oil	40 – 51

All these reported heats refer to bitumens or heavy oils of unspecified composition. Most of these reports list the heats that are directly measured in a constant volume calorimeter (ΔU), but it should be recognized that such values are not well defined because of the unspecified states of some of the combustion products.

Here we cite just two pre-1980 reports of heats of combustion of bitumens. Clark's [25] results lead to 41.3 kJ/g and those of Bunger, Thomas, and Dorrence [26] lead to 41.2 kJ/g for the heat of combustion of Athabasca bitumen of specified composition. The latter authors [26] have also reported heats of combustion and compositions of bitumens from three other locations.

More recent measurements [27] have led to the heats of combustion listed in Table 3 for bitumens and heavy oils. Heats of combustion [28] of some other oils are listed in Table 4, while heats of combustion [27,28] of some substances (naphtha, coke, asphaltenes, maltenes, etc.) derived from Alberta bitumen/heavy oil are listed in Table 5. Elemental compositions of all these

substances are also listed in Tables 3, 4, and 5. It should be noted that all of these reported $\Delta U°$ values represent constant volume heats for combustion processes in which the products are in their thermodynamic standard states. An unbalanced chemical equation for the combustion processes is

$$\text{Substance combusted} + O_2(g) = CO_2(g)$$

$$+ H_2O(liq) + SO_2(g) + N_2(g) + ash \quad (1)$$
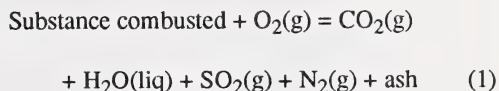
We emphasize that the $\Delta U°$ values cited here refer to combustion reactions in which the H_2O formed is in the liquid state.

An entirely empirical (no theory) equation has been found [27] to summarize reasonably accurately all of the results ($\Delta U°$ values and compositions) in Table 3 and the results for the last 10 substances listed in Table 5. This equation for $\Delta U°$ (expressed in kJ/g) is

$$\Delta U° = -0.3473(\%C) - 1.1696(\%H)$$

$$- 0.1507(\%S) + 0.1927(\%O + \%N) \quad (2)$$

Subsequent [28] comparisons of $\Delta U°$ values calculated using Equation (2) with other experimental values in Table 5 are satisfactory. The heats of combustion (with elemental compositions) that Bunger, Thomas, and Dorrence [26] reported for four bitumens in terms of Btu/lb have been converted to kJ/g and compared with values calculated using Equation (2); the average difference between calculated and experimental values is 0.3 kJ/g. It is therefore concluded that Equation (2) provides a useful means of estimating the standard state heats ($\Delta U°$) of combustion of bitumens, heavy oils, and various related substances.

Table 3. Heats of combustion and compositions [27] of bitumens/heavy oils. $\Delta U°$ values are constant volume heats for reactions represented by Equation (1), $T = 298.15$ K, and all substances in their thermodynamic standard states. Compositions are expressed as wt%.

Source of bitumen/ heavy oil	$\Delta U°$ (kJ/g)	%C	%H	%S	%N	%O	%Ash
Athabasca	−41.46	83.44	10.45	4.19	0.48	1.24	0.28
Peace River	−40.55	81.20	9.92	5.88	0.36	1.89	0.71
Cold Lake	−41.60	83.50	10.50	4.16	0.46	0.80	0.94
Madagascar	−42.73	86.29	11.33	0.61	0.73	1.66	0.08
Nigeria	−42.22	85.98	10.72	0.84	0.69	1.73	0.04
Asphalt Ridge, Utah	−42.68	85.75	11.43	0.49	0.88	1.82	0.05

Table 4. Heats of combustion and compositions of heavy and light oils [28]. $\Delta U°$ values are constant volume heats of reactions represented by Equation (1), $T = 298.15$ K, and all substances in their thermodynamic standard states. Compositions are expressed as wt%.

Oil	$\Delta U°$ (kJ/g)	%C	%H	%S	%(N+O)
Xinjiang, heavy #1	−43.53	86.37	12.14	0.30	1.19
Xinjiang #2	−44.29	85.62	12.25	0.30	1.81
Xinjiang #3	−44.42	86.89	12.32	0.23	0.51
Liaohe #1	−43.51	85.66	11.55	0.30	0.89
Liaohe #2	−43.22	87.72	11.36	0.27	0.76

Table 5. Heats of combustion and compositions of substances from bitumen/heavy oil [27,28]. $\Delta U°$ values are constant volume heats of reactions represented by Equation (1), $T = 298.15$ K, and all substances in their thermodynamic standard states. Compositions are expressed as wt%.

Substance	$\Delta U°$ (kJ/g)	%C	%H	%S	%(N+O)	%Ash
Syncrude gas oil #1	−44.50	87.46	11.91	0.28	0.35	
Syncrude gas oil #2	−44.52	87.51	11.78	0.35	0.36	
Syncrude synthetic crude oil #1	−45.81	87.36	12.05	0.42	0.17	
Syncrude synthetic crude oil #2	−45.54	86.90	12.56	0.36	0.18	
Syncrude naphtha #1	−44.71	85.59	13.38	0.15	0.18	
Syncrude naphtha #2	−44.65	85.80	13.21	0.17	0.82	
Syncrude naphtha #3	−46.11	83.45	13.79	0.29	2.32	
Syncrude naphtha #4	−46.41	83.70	13.92	0.21	2.03	
Syncrude H-oil pitch	−38.65	82.67	8.14	4.56	2.18	2.09
Asphaltenes from Athabasca bitumen, medium-grade ore	−37.02	78.52	7.83	7.62	2.87	2.32
Asphaltenes from Athabasca bitumen, high-grade ore	−36.82	78.71	8.12	7.75	3.74	0.86
Asphaltenes from Cold Lake	−37.79	80.83	7.79	7.54	2.84	1.04
Maltenes from Athabasca	−42.17	83.33	10.90	4.20	1.46	0.25
Suncor coke	−33.53	83.93	3.70	5.78	3.34	2.85
Syncrude coke #1	−29.70	78.72	1.76	6.55	3.68	8.53
Syncrude coke #2	−29.43	78.21	1.69	6.36	4.32	9.18
Syncrude coke #3	−28.91	76.49	1.66	6.59	5.82	8.57
Syncrude coke #4	−29.13	77.52	1.66	6.54	4.63	8.26

Smith, Lee-Bechtold, and Good [29] have reported thermodynamic properties (including heats of combustion) and elemental compositions of various materials (distillates and residues) derived from liquefaction of several coals. Most of the heats of combustion calculated using Equation (2) are in excellent agreement with the experimental values; the worst disagreements (only 1 to 3%) are for those coal liquids having relatively large (%O + %N) as compared with those substances considered in the derivation of Equation (2).

Lloyd and Davenport [30] have reviewed several earlier equations and have presented their own equation, similar to our Equation (2), for estimating heats of combustion of oils, coal liquids, etc. They have also provided some references to earlier reports of heats of combustion.

THERMODYNAMIC PROPERTIES OF ORGANIC COMPOUNDS

For many years researchers in the Bureau of Standards laboratory in Washington and in the Bureau of Mines laboratory in Bartlesville provided many of the thermodynamic data for pure organic compounds that are relevant to burning and processing oils. In recent years this work has been carried out in Bartlesville under the name of the National Institute for Petroleum and Energy Research (NIPER). A few other laboratories have also made important contributions to the thermo-dynamic data on organic compounds, as cited later.

There have been many very accurate measurements of heats of combustion of pure organic compounds. Results of most of these measurements have been used in calculating the useful standard enthalpies of formation $(\Delta_f H^\circ)$ values for organic compounds cited by Stull, Westrum, and Sinke [6]. Cox and Pilcher [31] have also provided a useful collection of heats of combustion and derived $\Delta_f H^\circ$ values.

Other thermodynamic properties (such as entropies, heat capacities, free energies, vapor pressures, and heats of vaporization) of organic compounds have been obtained in various ways, as summarized in the book by Stull et al. [6] and in other publications cited in this chapter.

Several publications [32–37] from NIPER contain recently determined thermodynamic data for organic compounds found in fossil fuels or derived from fossil fuels, along with descriptions of experimental methods, calculational procedures, and some illustrations of uses.

Scott and McCullough [38] have summarized the thermodynamic properties of 100 organic sulfur compounds in the gas state over the temperature range to 1000 K, and El-Sabban and Scott [39] have provided a similar summary for 25 more organic sulfur compounds; there are many references to earlier investigations, mostly at the Bureau of Mines laboratory in Bartlesville.

We cite a number of useful books and review articles [40–49] that list thermodynamic properties of organic compounds that are relevant in various ways to petroleum production and processing.

Finally, we call attention to a recent book [50] *Thermodynamic and Transport Properties of Coal Liquids* that contains useful data and references.

HEAT CAPACITIES AND SPECIFIC HEATS

Heat capacities of many pure organic compounds have been listed in several of the references cited in the preceding section. In this section we are concerned mostly with heat capacities or specific heats of pure minerals, reservoir minerals, bitumens, and heavy oils, and various substances (cokes, asphaltenes, etc.) that are derived from or separated from bitumens and heavy oils.

For pure chemical compounds of known molar mass (molecular weight), it has been common to report molar heat capacities (C_p) that are now usually expressed in terms of J/K•mol. On the other hand, for complicated mixtures such as bitumen or for substances such as coke for which there is no meaningful molecular weight, it is impossible to report molar heat capacities; in such cases specific heats (c_p) expressed in terms of J/K•g are reported and used. The relationship between molar heat capacity and specific heat is

$$c_p = C_p/M \qquad (3)$$

in which M (expressed as g/mol) represents the molecular weight of the substance.

Heat capacities and specific heats of minerals

The best single source of thermodynamic properties (including heat capacities) of minerals is the U.S. *Geological Survey Bulletin* [51] by Robie, Hemingway, and Fisher. This excellent book lists molar heat capacities (and other thermodynamic quantities) in tabular form and provides summarizing equations of the form

$$C_p = a + bT + cT^2 + dT^{-0.5} + eT^{-2} \qquad (4)$$

in which one or more terms are omitted for some substances.

Specific heats [52–54] of several minerals at several temperatures are listed in Table 6. Although the molar heat capacities of these minerals are very different from each other, the specific heats of all of these typical minerals are reasonably similar (difference between largest and smallest is about 25%), which means that it is often possible to estimate specific heats of minerals or mineral assemblages with useful accuracy.

Table 6. Specific heats of some minerals at several temperatures.

Mineral	c_p (J/K·g)					
	300 K	400 K	500 K	600 K	700 K	800 K
SiO_2 (quartz) [51]	0.743	0.889	0.990	1.073	1.148	1.219
$CaCO_3$ (calcite) [51]	0.835	0.969	1.044	1.098	1.141	
$CaMgCO_3$ (dolomite) [51]	0.855	0.995	1.095	1.169	1.229	
$MgCO_3$ (magnesite) [51]	0.904	1.074	1.185	1.274	1.352	
Kaolinite [52]	0.945	1.122	1.229	1.292	1.333	1.364
Kaolinite [53]	0.962	1.151	1.270	1.318	1.343	
Illite [53]	0.808	0.955	1.046	1.102	1.150	
Montmorillonite [53]	0.811	0.996	1.084	1.130	1.167	
$NaAlSi_2O_6$						
(dehydrated analcite) [51]	0.814	0.941	1.056	1.134	1.193	1.243
$NaAlSi_3O_8$ (analbite) [54]	0.782	0.914	1.004	1.067	1.112	1.146

Specific heats of oil sands and components of oil sands

Several investigations have established that the specific heats of mixtures of minerals can be represented accurately by equations of the form

$$c_p \text{ (mixture)} = \Sigma f_i c_{p,i} \qquad (5)$$

in which f_i and $c_{p,i}$ represent the mass (weight) fraction and specific heat of each mineral in the mixture. Equations of this type have been tested and found satisfactory [55,56] for minerals in the Athabasca oil sands and also for whole oil sands, for which we can write the specific equation

$$c_{p,os} = f_{cs} c_{p,cs} + f_{fs} c_{p,fs} + f_b c_{p,b} + f_w c_{p,w} \qquad (6)$$

in which f and c_p indicate mass fractions and specific heats of defined components and the subscripts os, cs, fs, b, and w indicate whole oil sands, coarse solids (mostly silica), fine solids (mostly clays), bitumen, and water, respectively. It has also been found [56] that specific heats of emulsions over the range 20 to 90°C can be represented by

$$c_{p,em} = f_w c_{p,w} + f_o c_{p,o} \qquad (7)$$

in which subscripts em, w, and o indicate emulsion, water, and oil, respectively.

Because equations of types (5), (6), and (7) can be used in calculating the specific heats of mixtures of minerals, of whole oil sands, and of emulsions from fractions of components and specific heats of these components, it is unnecessary to tabulate specific heats of the composite substances (of specified composition) that are frequently of greatest interest. Instead, it is more useful to have the specific heats of the components.

It has been found [56] that specific heats of components can be represented accurately by equations of the forms

$$c_p = a + bT + cT^2 \qquad (8)$$

and

$$c_p = a + bT + cT^{-2} \qquad (9)$$

Equations of type (8) are generally better than those of type (9) for extrapolating to temperatures lower than the specified range, while equations of type (9) are generally better than those of type (8) for extrapolating to temperatures higher than the specified range.

Specific heats of bitumens and heavy oils are summarized in Table 7 by means of the coefficients to be used in Equation (8) and in Table 8 by means of the coefficients to be used in Equation (9).

Specific heats of asphaltenes and cokes are summarized by means of the coefficients listed in Tables 9 and 10.

Specific heats of reservoir minerals are summarized in Tables 11 and 12. Specific heats of clays and dehydrated clays are summarized in Tables 13, 14, and 15.

Table 7. Specific heats [56] of bitumens/heavy oils summarized using constants for $c_p = a + bT + cT^2$. All c_p are expressed in terms of J/K•g and temperatures are kelvins (K).

Source	Temperature range	a	b	c
Athabasca, from Alberta Research Council, Petro-Canada, and Syncrude	300 – 600	0.055	6.818×10^{-3}	-4.464×10^{-6}
Cold Lake, Alberta, Esso Resources	300 – 600	−0.007	7.410×10^{-3}	-5.279×10^{-6}
Cold Lake, Alberta, BP	320 – 600	−0.067	7.232×10^{-3}	-4.260×10^{-6}
Lyehill-Lloydminster	300 – 600	0.404	5.294×10^{-3}	-2.644×10^{-6}
Primrose, Alberta, Phillips	320 – 600	0.537	4.595×10^{-3}	-1.638×10^{-6}
Peace River, early production, Shell Canada Resources	300 – 600	0.239	5.901×10^{-3}	-3.663×10^{-6}
Peace River, later production, Shell Canada Resources	300 – 600	−0.018	7.361×10^{-3}	-5.213×10^{-6}
Frosmont, Alberta, Union Oil	320 – 600	0.223	5.820×10^{-3}	-2.972×10^{-6}
Asphalt Ridge, Utah, Alberta Research Council	300 – 600	0.032	6.967×10^{-3}	-4.027×10^{-6}
Malagasy, Africa, Alberta Research Council	300 – 600	0.036	6.870×10^{-3}	-4.259×10^{-6}
Nigeria, Africa, Alberta Research Council	300 – 600	−0.078	7.375×10^{-3}	-4.933×10^{-6}
Zaire, Africa, Alberta Research Council	300 – 600	−0.141	7.678×10^{-3}	-5.532×10^{-6}
Venezuela, INTEVEP	300 – 600	0.256	6.087×10^{-3}	-3.536×10^{-6}

Table 8. Specific heats [56] of bitumens/heavy oils summarized using constants for $c_p = a + bT + cT^{-2}$. All c_p are expressed in terms of J/K•g and temperatures are kelvins (K).

Source[a]	Temperature range	a	b	c
Athabasca	300 – 600	1.763	1.542×10^{-3}	-4.884×10^{4}
Cold Lake, Esso Resources	300 – 600	2.055	1.108×10^{-3}	-6.021×10^{4}
Cold Lake, BP	320 – 600	1.655	2.068×10^{-3}	-5.301×10^{4}
Lyehill-Lloydminster	300 – 600	1.383	2.218×10^{-3}	-2.704×10^{4}
Primrose	320 – 600	1.181	2.635×10^{-3}	-1.929×10^{4}
Peace River, early	300 – 600	1.634	1.581×10^{-3}	-3.973×10^{4}
Peace River, later	300 – 600	1.980	1.196×10^{-3}	-5.725×10^{4}
Frosmont	320 – 600	1.379	2.286×10^{-3}	-3.436×10^{4}
Asphalt Ridge	300 – 600	1.596	2.175×10^{-3}	-4.539×10^{4}
Malagasy	300 – 600	1.659	1.848×10^{-3}	-4.619×10^{4}
Nigeria	300 – 600	1.817	1.535×10^{-3}	-5.441×10^{4}
Zaire	300 – 600	1.961	1.161×10^{-3}	-5.969×10^{4}
Venezuela	300 – 600	1.623	1.887×10^{-3}	-3.951×10^{4}

[a] More information about sources of samples is given in Table 7.

Table 9. Specific heats [56] of asphaltenes and cokes summarized using constants for $c_p = a + bT + cT^2$. All c_p are expressed in terms of J/K•g and temperatures are kelvins (K).

Substance [a]	Temperature range	a	b	c
Asphaltenes [b]	280 – 620	−0.593	8.079×10^{-3}	$−5.353 \times 10^{-6}$
Syncrude coke	280 – 720	−0.141	3.928×10^{-3}	$−2.108 \times 10^{-6}$
Suncor coke	280 – 720	−0.286	4.930×10^{-3}	$−2.733 \times 10^{-6}$

[a]   See Table 5 for compositions.
[b]   Specific heats of asphaltenes from Athabasca, Cold Lake, Peace River, and Nigeria are summarized by the coefficients listed here.

Table 10. Specific heats [56] of asphaltenes and cokes summarized using constants for $c_p = a + bT + cT^{-2}$. All c_p are expressed in terms of J/K•g and temperatures are kelvins (K).

Substance [a]	Temperature range	a	b	c
Asphaltenes [b]	280 – 620	1.444	1.748×10^{-3}	$−5.609 \times 10^{4}$
Syncrude coke	280 – 720	0.778	1.239×10^{-3}	$−2.739 \times 10^{4}$
Suncor coke	280 – 720	0.921	1.424×10^{-3}	$−3.647 \times 10^{4}$

[a]   See footnote a, Table 9.
[b]   See footnote b, Table 9.

Table 11. Specific heats [56] of reservoir minerals summarized using constants for $c_p = a + bT + cT^2$. All c_p are expressed in terms of J/K•g and temperatures are kelvins (K).

Substance , source	Temperature range	a	b	c
Athabasca coarse solids, mostly SiO_2, >325 mesh	300 – 700	0.168	2.442×10^{-3}	$−1.611 \times 10^{-6}$
Athabasca fine solids, mostly clays, < 325 mesh	320 – 680	0.342	1.873×10^{-3}	$−0.926 \times 10^{-}$
Cold Lake, Alberta, Esso Resources	300 – 700	0.128	2.692×10^{-3}	$−1.890 \times 10^{-}$
Peace River, Alberta, Shell Canada Resources	320 – 600	0.032	3.138×10^{-3}	$−2.392 \times 10^{-}$
Grosmont, Alberta, Union Oil	320 – 600	0.303	2.296×10^{-3}	$−1.438 \times 10^{-}$
Zaire, Africa, Alberta Research Council	300 – 700	0.047	2.894×10^{-3}	$−1.988 \times 10^{-}$
Asphalt Ridge, Utah, Alberta Research Council	300 – 700	0.170	2.425×10^{-3}	$−1.506 \times 10^{-}$
Malagasy, Africa, Alberta Research Council	300 – 700	0.158	2.630×10^{-3}	$−1.840 \times 10^{-}$
Nigeria, Africa, Alberta Research Council	300 – 700	0.041	3.022×10^{-3}	$−2.126 \times 10^{-}$

Table 12. Specific heats [56] of reservoir minerals using constants for $c_p = a + bT + cT^{-2}$. All c_p are expressed in terms of J/K•g and temperatures are kelvins (K).

Substance, source [a]	Temperature range	a	b	c
Athabasca, coarse solids	300 – 700	0.914	0.331 x 10^{-3}	–2.415 x 10^4
Athabasca, fine solids	320 – 680	0.787	0.644 x 10^{-3}	–1.559 x 10^4
Cold Lake, Alberta	300 – 700	0.986	0.244 x 10^{-3}	–2.774 x 10^4
Peace River, Alberta	320 – 600	0.997	0.243 x 10^{-3}	–2.961 x 10^4
Prosmont, Alberta	320 – 600	0.877	0.563 x 10^{-3}	–1.745 x 10^4
Zaire, Africa	300 – 700	0.955	0.313 x 10^{-3}	–2.946 x 10^4
Asphalt Ridge, Utah	300 – 700	0.825	0.512 x 10^{-3}	–2.017 x 10^4
Malagasy, Africa	300 – 700	1.024	0.205 x 10^{-3}	–2.906 x 10^4
Nigeria, Africa	300 – 700	1.024	0.243 x 10^{-3}	–3.230 x 10^4

More information about sources of samples is given in Table 11.

Table 13. Specific heats [56] of clays over the temperature range 300–700 K summarized using constants for $c_p = a + bT + cT^2$. All c_p are expressed in terms of J/K•g and temperatures are kelvins (K).[a]

Clay	a	b	c
Na-kaolinite	0.0885	3.8035 x 10^{-3}	–2.898 x 10^{-6}
Ca-kaolinite	0.0855	3.6576 x 10^{-3}	–2.670 x 10^{-6}
Na-montmorillonite	0.0911	3.1616 x 10^{-3}	–2.349 x 10^{-6}
Ca-montmorillonite	–0.1061	3.8274 x 10^{-3}	–2.819 x 10^{-6}
Illite	0.2322	2.4544 x 10^{-3}	–1.653 x 10^{-6}
Attapulgite	–0.0997	3.6783 x 10^{-3}	–2.803 x 10^{-6}

[a]   Constants for $c_p = a + bT + cT^{-2}$ for these clays are not reported because this equation does not fit the experimental data as well as $c_p = a + bT + cT^2$. See Reference [53] for further discussion of specific heats of these clays.

Table 14. Specific heats [56] of dehydrated clays over the temperature range 320–700 K summarized using constants for $c_p = a + bT + cT^2$. All c_p are expressed in terms of J/K•g and temperatures are kelvins (K).

Substance	a	b	c
Dehydrated kaolinite	0.256	2.090 x 10^{-3}	–1.224 x 10^{-6}
Dehydrated illite	0.242	2.156 x 10^{-3}	–1.478 x 10^{-6}
Dehydrated montmorillonite	0.255	2.136 x 10^{-3}	–1.380 x 10^{-6}

Table 15. Specific heats [56] of dehydrated clays over the temperature range 320–700 K summarized using constants for $c_p = a + bT + cT^{-2}$. All c_p are expressed in terms of J/K•g and temperatures are kelvins (K).

Substance	a	b	c
Dehydrated kaolinite	0.865	0.435×10^{-3}	-2.210×10^4
Dehydrated illite	0.957	0.186×10^{-3}	-2.517×10^4
Dehydrated montmorillonite	0.928	0.290×10^{-3}	-2.410×10^4

Several investigators have reported specific heats that can be compared with those cited in Table 6 and that can be calculated using equations of types (5) and (6) with the parameters given in Tables 7 through 15.

Clark [25] has measured the specific heat of a sample of high-grade Athabasca oil sand containing 17.1% bitumen and 0.9% water, and has also measured the specific heat of bitumen-free, dry mineral matter. By making use of the equivalent of our Equation (5), he has used these results in calculating the specific heat of bitumen at some unspecified temperature in the range 0 to 100°C. He also made one direct measurement (in this same temperature range) of the specific heat of bitumen. Clark's results lead to $c_p = 1.47$ J/K•g for Athabasca bitumen. Calorimetric measurements by Rajeshwar, Jones, and DuBow [57] have led to $c_p = 1.96$ J/K•g for Athabasca bitumen at 125°C (398 K). The specific heats summarized in Tables 7 and 8 are considerably larger than the value from Clark [25] and in fair agreement (2.06 versus 1.96 J/K•g) with the value from Rajeshwar, Jones, and DuBow [57].

Rajeshwar, Jones, and DuBow [57] have reported that the specific heat of a sample of Athabasca oil sands is 0.670 J/K•g at 125°C (398 K). Use of their composition data in Equation (6) with specific heats of components calculated using the coefficients listed in the tables in this chapter leads to a much larger $c_{p,os}$ for Athabasca oil sands at the specified temperature. Because the specific heat (of the composite oil sands) reported by Rajeshwar, Jones, and DuBow [57] is *smaller* than the specific heat of sand, which has the smallest specific heat of any component of oil sands, it is clear that their reported $c_{p,os}$ is too small. On the other hand, Cervenan, Vermuelen, and Chute [58] have measured specific heats of reconstituted Athabasca oil sands (specified compositions) and have obtained results over the temperature range 23 to 74°C (296 to 347 K) that are in satisfactory agreement with values calculated using Equation (6) and the summarizing coefficients

listed in this chapter. Clark's early measurements [25] led him to report the equivalent of $c_{p,os} = 0.91$ J/K•g for a high-grade oil sand at some unspecified temperature. If his specific heat was measured at some cool room temperature, it is in fair agreement with a value that can be calculated using Equation (6) and the specific heats of components as summarized in this chapter.

Rajeshwar, Jones, and DuBow [57] have reported specific heats of four samples of oil sands (specified compositions) from Utah. Most of these results are in poor agreement [55] with results summarized in this chapter.

Lindberg, Thomas, and Christensen [59] and Scott and Seto [60] have made measurements leading to thermal conductivities, thermal diffusivities, and specific heats of oil sands (from Utah and from Alberta, respectively). The specific heats reported by Scott and Seto [60] are in satisfactory agreement with the values that have been selected for this chapter, but there are substantial differences between the values summarized here and those reported by Lindberg, Thomas, and Christensen [59].

Saal, Heukelom, and Blokker [61] measured specific heats of asphaltic or distilled bitumens from Venezuela and Mexico and obtained results over the temperature range 0 to 300°C (273 to 573 K) that are in general agreement with the specific heats for other bitumens summarized in this chapter.

As expected on the basis of typical or average compositions, the specific heats of coarse and fine solids from Athabasca (summarized in Tables 11 and 12) are similar to specific heats at corresponding temperatures for silica [51] and for clays [52,53,56], respectively. Also, the specific heats of the mineral matter from the Grosmont (carbonate) deposit (summarized in Tables 11 and 12) are similar to specific heats at corresponding temperatures of dolomite [51].

Specific heats of cokes (Suncor and Syncrude) summarized in this chapter are comparable to specific

eats of coals and cokes [62–65] having similar compositions.

A number of other publications report specific heats of rocks [66], oil shales [67–70], and liquids produced from coals [29,50,71].

Finally, it is appropriate to call attention to one relatively new experimental method (differential scanning calorimetry, often called DSC) that has been much used recently for determination of specific heats (and heats of melting) of substances of interest to readers of this chapter. The DSC method is appealing in many fields because it permits reasonably rapid determinations over a considerable range of temperature. The method is also appealing in some fields because it permits measurements to be made using very small samples (0.05 g), but it should be recognized that use of such small samples can lead to misleading results when measurements are made on heterogeneous materials such as oil sands. Several investigations [52–56,64, 72–80] have shown that the DSC method can lead to usefully accurate results, and some of these investigations have provided results that are pertinent to the subject matter of this chapter. On the other hand, it should also be recognized that some DSC measurements leading to specific heats (already discussed in this chapter) have lead to results that are probably mistaken.

THERMODYNAMIC PROPERTIES OF ICE, WATER, AND STEAM

Thermodynamic properties of ice, liquid water, and steam have been summarized in two excellent compilations [81,82] and in a few more publications cited below.

Giauque and Stout [83] have made extremely accurate measurements of the heat capacities of ice down to very low temperatures. There is no simple algebraic expression that adequately summarizes all of their results, but it is possible to summarize their heat capacities (converted to specific heats) with useful accuracy over the temperature range –53 to 0°C (220 to 273 K) by means of the simple equation

$$c_p = 0.136 + 0.0072\,T \qquad (10)$$

in which c_p is expressed in terms of J/K•g and temperature is in kelvins.

The heat of melting of ice has been reviewed by Pitzer and Brewer [84], from whom we adopt

$$\Delta H \text{ (melting ice)} = 333.5 \text{ J/g} \qquad (11)$$

Osborne, Stimson, and Ginnings [85] have made accurate measurements of the heat capacity of liquid water over the temperature range 0 to 100°C (1 atm pressure). Over this range of temperature it is sufficient for many purposes to adopt an average specific heat of water as

$$c_{p,ave} \text{ (liquid water, 0–100°C, 1 atm)}$$

$$= 4.2 \text{ J/K•g} \qquad (12)$$

Calorimetric measurements [86] and vapor pressure measurements [87] at temperatures above 100°C have been made by Osborne et al. Results of these and other measurements on liquid and gaseous water at temperatures above 100°C and pressures above 1 atm have been reviewed and compiled in useful forms by Haar, Gallegher, and Kell [82].

Enthalpies (ΔH) of vaporization of water have been reviewed and listed [88] as follows:

$$H_2O(liq) = H_2O(g,\ saturation\ pressure)$$

$$\Delta H_{vap}\ (T = 273.16\ \text{K},\ p = 4.58\ \text{mm Hg}) = 2500\ \text{J/g}$$

$$\Delta H_{vap}\ (T = 298.15\ \text{K},\ p = 23.75\ \text{mm Hg}) = 2442\ \text{J/g}$$

$$\Delta H_{vap}\ (T = 373.15\ \text{K},\ p = 760\ \text{mm Hg}) = 2257\ \text{J/g}$$

Enthalpies (sometimes called latent heats) of vaporization at higher temperatures and pressures can be obtained directly [82,85–88] or can be calculated from data in steam tables.

Molar heat capacities (C_p) of gaseous water (ideal gas state, $p = 1$ bar $= 10^5$ Pa) have been summarized by Robie, Hemingway, and Fisher [51] by means of an equation of type (4), which is applicable up to $T = 1800$ K.

## THERMODYNAMIC PROPERTIES OF AQUEOUS SOLUTIONS

Some uses of thermodynamic data for aqueous solutions were mentioned briefly in the second section of this chapter, and three books [19–21] that deal with such uses were cited. Here it is appropriate to cite four more books [89–92] and one review article [93] that are

all concerned with uses of thermodynamic data for aqueous solutions.

Most of the uses of thermodynamic data for aqueous solutions involve calculation of the equilibrium properties of aqueous solutions, often in equilibrium with one or more solid phases. Such calculations may be done using equilibrium constants for the relevant chemical reactions, or by finding the chemical composition that corresponds to a minimum in the total Gibbs energy (also called free energy) of the system. Both approaches to calculating the equilibrium compositions of aqueous solutions and identifying the solid phases that are stable in contact with such solutions ordinarily begin with tabulated standard-state Gibbs energies of formation of the various substances under consideration.

The best and most extensive source of thermodynamic data for aqueous solutions is the compilation [94] from the U.S. National Bureau of Standards. This excellent compilation lists (for $T = 298.15$ K) standard Gibbs energies of formation $(\Delta_f G^\circ)$, standard enthalpies of formation $(\Delta_f H^\circ)$, and standard entropies (S°) for many inorganic substances (solid, liquid, gas, and in aqueous solution). These same thermodynamic quantities are also listed for many organic substances that contain only one or two atoms of carbon per molecule or ion. Molar heat capacities $(C_p{}^\circ)$ are also listed for many solid, liquid and gaseous substances (both inorganic and organic) for $T = 298.15$ K. Unfortunately, most of the work leading to this compilation was done several years ago, before many of the now available partial molar heat capacities of aqueous solutes were determined; it is therefore necessary to find values for these partial molar heat capacities (important in connection with calculations for high temperature solutions) elsewhere, as outlined later in this chapter.

Because of the important effects of acidity or basicity (often expressed as pH) of aqueous solutions on many chemical reactions that are related to the subjects treated in this handbook, it is necessary to have reliable information about the ionization of water as represented by
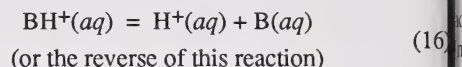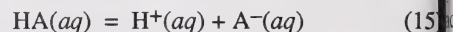
$$H_2O(liq) = H^+(aq) + OH^-(aq) \qquad (13)$$
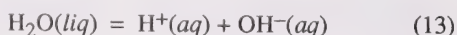
Many readers will remember from elementary chemistry that the equilibrium constant for the ionization represented by (13) is

$$K_w = [H^+][OH^-] \qquad (14)$$

in which brackets indicate the concentrations (molalities or molarities) of hydrogen ions and hydroxide ions. For $T = 298.15$ K and $p = 1$ atm, we have $K_w = 1 \times 10^{-14}$ ($pK_w = -\log K_w = 14$). The substantial dependence of this equilibrium constant on temperature and pressure has been summarized thoroughly [95–99].

Both inorganic and organic acids and bases are important in many aspects of aqueous solution chemistry. Acid-base equilibria of these substances are represented by reactions of types

$$HA(aq) = H^+(aq) + A^-(aq) \qquad (15)$$

$$BH^+(aq) = H^+(aq) + B(aq) \qquad (16)$$
(or the reverse of this reaction)

and

$$B(aq) + H_2O(liq) = BH^+(aq) + OH^-(aq) \qquad (17)$$

in which $HA(aq)$ represents an acid and $B(aq)$ represents a base. Cations of metals often exhibit acidic properties, as represented by reactions of type

$$M^{+n}(aq) + H_2O(aq) = M(OH)^{+n-1}(aq) + H^+(aq) \qquad (18)$$

Clear, useful, and reliable accounts of aqueous acid-base equilibria and pH are presented in two books [100,101], which also contain some thermodynamic data.

Equilibrium constants and other thermodynamic data for ionization of both organic and inorganic acids in aqueous solutions have been summarized in four books [102–105] and two reviews [106,107].

The aqueous solutions of interest in connection with such problems as mineral-water interactions, boiler water treatment, waste water treatment, and corrosion are often at temperatures other than $T = 298.15$ K and are often quite concentrated. It is therefore necessary to consider such complications as the temperature dependence of standard Gibbs energies and related equilibrium constants, and also to make use of activity coefficients for aqueous solutes (especially the ions). Methods of using tabulated thermodynamic data for calculations of Gibbs energies and equilibrium constants as a function of temperature are summarized in a review [93] and are illustrated in several other references cited in this chapter. Procedures for using activity coefficients are summarized in various textbooks of physical chemistry and chemical thermodynamics; these

ocedures are also discussed in books [20,84,89,90, 00–102] already cited here, in two useful textbooks [08,109], and in several papers (cited later in this apter) that deal with specific systems. Two of the oks [84] and especially [102] contain extensive bulations of activity coefficients for aqueous ectrolytes at $T = 298.15$ K. In addition, Goldberg, anley, and Nuttall [110] have provided a data base that cludes equations, computer programs, and references sources of data. We also have from Goldberg a paper 11] that describes methods of calculating and using tivity coefficients in various problems.

Sources of thermodynamic data for many specific ueous systems that are likely to be of interest are cited the next section of this chapter. References to the rtial molar heat capacities of aqueous solutes, which e needed for calculations of thermodynamic properties aqueous solutions at high temperatures are also cited the next section of this chapter.

DDITIONAL SOURCES OF THERMO-YNAMIC DATA

any sources of thermodynamic data for various well-fined chemical substances and also for more complex stems (rocks, minerals, bitumen, oil sands, etc.) have eady been cited in this chapter. Now we begin citing ditional sources by calling attention to six useful books 12–117] and one bibliography [118] of sources of data.

There are several useful methods of estimating ermodynamic properties of organic compounds, some which have already been cited and some of which ve been discussed by Cox and Pilcher [31]. Attention also called to three papers [119–121] that deal with timation of thermodynamic properties of organic bstances.

Pruden and Denis [122] have discussed thermal fects associated with hydrocracking of Athabasca umen.

Specific heats of several important minerals have eady been cited. Two books [19,51] are excellent neral references for other thermodynamic properties minerals and two other books [89,90] provide useful formation about the thermodynamic properties of nerals in relation to aqueous solutions.

Interactions of silica with water (aqueous solutions d steam) are of considerable importance in connection th thermal methods of production, scale formation, d treating boiler water. There have been many

investigations of the thermodynamics of silica-water systems; here we call attention to four papers [123–126] that provide useful data and many references to other sources of information.

As previously mentioned, thermodynamic properties of clays are important for several purposes, and some sources of thermodynamic data for clays have been cited. Two papers [127,128] provide thermodynamic data for ion exchange reactions by clays, along with references to other investigations.

Because thermodynamic data for some clays and other minerals that occur in petroleum and bitumen deposits are uncertain or unknown, estimation methods [129, 130] may be useful.

Complications related to internal consistency of thermodynamic data for different substances can be quite important, but have rarely been discussed. The book by Nordstrom and Munoz [19], (especially Chapter 12) is an admirable exception to this common neglect, with some specific discussion of kaolinite and related substances.

Marshall [132] has provided a useful review of aqueous inorganic phase equilibria at high temperatures. Other researchers [133–138] have provided thermodynamic data for several other important systems involving solids in equilibrium with aqueous solution, and also provide thermodynamic data that have other uses. Three of these papers [133–135] and one other [139] also provide data for the aqueous ions of iron that are relevant to some mineral-water interactions and to some corrosion problems.

As previously mentioned, there are several excellent collections of thermodynamic data (especially $\Delta_f H°$, $\Delta_f G°$, $S°$, and activity coefficients) for aqueous solutions at $T = 298.15$ K. Unfortunately, there are no comparable collections of often-needed thermodynamic data for aqueous solutions at much higher temperatures. Hence it is desirable here to provide references to recent accounts of investigations of several specific systems; these papers provide further references to accounts of earlier investigations. We also call attention to a review [93] of selected sources of thermodynamic data for aqueous solutions and uses of these data. In connection with use of existing tabulations of thermodynamic data for aqueous solutions at $T = 298.15$ K as the basis for calculations of desired thermodynamic quantities (especially equilibrium constants) for higher temperatures, heat capacities of solutions and the derived partial molar heat capacities of solutes are especially important. It is for this reason that many of

the following references are concerned with such heat capacities and their uses.

Recent references [140–189] listed approximately chronologically provide useful thermodynamic data for a variety of aqueous systems (salts, metal-EDTA complexes, acids and bases, surfactants, gases in brines, adsorption, etc.) and provide leads to accounts of earlier research that also provide useful data.

REFERENCES

1. C.W. Bowman, Molecular and interfacial properties of Athabasca tar sands, Proc. Seventh World Petroleum Congress, 3 (1967) 583.

2. J. Leja and C.W. Bowman, Application of thermodynamics to the Athabasca tar sands, Can. J. Chem. Eng. 46 (1968) 479.

3. J. Burger, P. Sourieau and M. Combarnous, "Thermal methods of oil recovery," Editions Technip, Paris (1985) 430 pp.

4. W.V. Steele, R.D. Chirico, W.B. Collier, R.H. Harrision and B.E. Gammon, Assessment of thermodynamic data needs, including their economic impact, for development of new fossil fuel refining processes, NIPER 159 (1986), National Institute for Petroleum and Energy Research, Bartlesville, OK.

5. M. Modell and R.C. Reid, "Thermodynamics and its applications," 2nd ed., Prentice-Hall, Inc., Englewood Cliffs, NJ (1983) 450 pp.

6. D.R. Stull, E.F. Westrum, Jr. and G.C. Sinke, "The chemical thermodynamics of organic compounds," John Wiley & Sons, Inc., New York (1969) 865 pp.

7. H.J. Tadema and J. Weidema, Spontaneous ignition of oil sands, Oil and Gas J., 14, Dec (1970) 77.

8. J.G Burger and B.C. Sahuquet, Chemical aspects of in-situ combustion — heat of combustion and kinetics, Soc. Petr. Eng. J., 12 (1972) 410.

9. J.G. Burger and B.C. Sahuquet, Laboratory research on wet combustion, J. Petroleum Techn., (1973) 1137.

10. A. Satman, M.Y. Soliman, M.R. Fassihi, A. Zolotukhin, S.K. Sanyal, W.E. Brigham and H.J. Ramey, Jr., Experimental and mathematical modelling of in-situ combustion oil recovery, chapter 46 in "The future of heavy crude and tar sands," R.G. Meyer and C.T. Steele, Eds, McGraw-Hill, New York (1981).

11. C. Perry and J.E. Gillot, Mineralogical transformations as indicators of combustion zone temperatures during in-situ combustion, Can. Petroleum Geol., 30 (1982) 34.

12. F.E. Vermuelen, F.S. Chute and M.R. Cervenan, Physical modelling of the electromagnetic heating of oil sand and other earth-type and biological materials, Can. Elec. Eng. J., 4 (1979) 19.

13. F.S. Chute, F.E. Vermuelen and L.G. Stevens, A study of the technical and economic feasibility of an electric preheat process for in-situ recovery from Athabasca oil sands, AOSTRA J. Res., 3 (1987) 139.

14. R.M. Butler and D.J. Stephens, The gravity drainage of steam-heated oil to parallel horizontal wells, J. Can. Petroleum Techn., 20, Apr–Jun (1981) 90.

15. R.M. Butler and C.T. Yee, A theoretical study of steam condensation in the presence of non-condensible gases in porous solids, AOSTRA J. Res., 3 (1986) 1.

16. J.A. Boon, T.W. Hamilton, L. Holloway and B.Wiwchar, Reaction between rock matrix and injected fluids in Cold Lake oil sands — potential for formation damage, J. Can. Petroleum Techn., 22, May–Aug (1983) 55.

17. J.A. Boon and B. Hitchon, Application of fluid rock reaction studies to in-situ recovery from oil sand deposits, Alberta, Canada — I. Aqueous phase results for an experimental-statistical study of water-bitumen-shale reactions, Geochim. Cosmochin. Acta, 47 (1983) 235.

18. J.A. Boon and B. Hitchon, Application of fluid rock reaction studies to in-situ recovery from oil sand deposits, Alberta, Canada — II. Mineral transformations during an experimental-statistical study of water-bitumen-shale reactions, Geochim. Cosmochim. Acta, 47 (1983) 249.

19. D.K. Nordstrom and J.L. Munoz, "Geochemical thermodynamics." Blackwell Scientific Publications, Palo Alto, CA (1986) 477 pp.

20. "Thermodynamics of aqueous systems with industrial applications," S.A. Newman, Ed., ACS Symposium Series 133, American Chemical Society, Washington (1980) 771 pp.

21. G.Astarita, D.W. Savage and A. Bisio, "Gas treating with chemical solvents," John Wiley and Sons, New York (1983) 493 pp.

22. J.E. Filby, P.C. Flynn and J.M. Goldman, Direct coking of Athabasca tar sand, Can. J. Chem. Eng. 58 (1980) 77.

3. "The McGraw-Hill encyclopedia of energy," 2nd ed., S.P. Parker, Ed., McGraw-Hill Book Co., New York (1977) pp. 315–317.

4. J.G. Speight, "The chemistry and technology of petroleum," Marcel Dekker, Inc., New York (1980) pp. 105–108.

5. K.A. Clark Some physical properties of a sample of Alberta bituminous sand, Can. J. Res. F, 22 (1944) 174.

6. J.W. Bunger, K.P. Thomas and S.M. Dorrence, Compound types and properties of Utah and Athabasca tar sand bitumens, Fuel, 58 (1979) 183.

7. H-k. Yan, Z.S. Kooner and L.G. Hepler, (to be published).

8. H-k. Yan and L.G. Hepler, China-Canada heavy oil technology symposium proceedings, Alberta Oil Sands Technology and Research Authority, Edmonton (1987); H-k Yan, J-r. Bian, J-g Gu and R-h. Hu, Acta Chim. Sinica, 45 (1987) 52; X-w. An, H-k. Yan and R-h. Hu, Acta Chim. Sinica, 40 (1982) 713.

9. N.K. Smith, S.H. Lee-Bechtold and W.D. Good, Thermodynamic properties of materials derived from coal liquefaction, DOE/BETC/TPR-79/2. U.S. Dept. of Energy (1980).

10. W.G. Lloyd and D.A. Davenport, Applying thermodynamics to fossil fuels: Heats of combustion from elemental compositions, J. Chem. Educ., 57 (1980) 56.

11. J.D. Cox and G. Pilcher, "Thermochemistry of organic and organometallic compounds," Academic Press, New York (1970) 643 pp.

12. R.D. Chirico, A. Nguyen, W.V. Steele, M.M. Strube, I.A. Hossenlopp and B.E. Gammon, Thermochemical and thermophysical properties of organic compounds derived from fossil substances: Chemical thermodynamic properties of organic oxygen compounds found in fossil materials, NIPER-135 (1986), National Institute for Petroleum and Energy Research, Bartlesville, OK.

13. W.V. Steele, R.D. Chirico, W.B. Collier, I.A. Hossenlopp, A. Nguyen and M.M. Strube, Thermochemical and thermophysical properties of organic nitrogen compounds found in fossil materials, NIPER-188 (1986), National Institute for Petroleum and Energy Research, Bartlesville, OK.

14. J.F. Messerly, S.S. Todd, H.L. Finke and B.E. Gammon, Thermodynamic properties of organic nitrogen compounds that occur in shale oil and heavy petroleum — topical report, NIPER-83 (1987), National Institute for Petroleum and Energy Research, Bartlesville, OK.

35. R.D. Chirico, I.A. Hossenlopp, A. Nguyen and W.V. Steele, Thermochemical and thermophysical properties of organic compounds derived from fossil substances: Thermodynamic studies related to the hydrogenation of anthracene, NIPER-239 (1987), National Institute for Petroleum and Energy Research, Bartlesville, OK.

36. R.D. Chirico, I.A. Hossenlopp, A. Nguyen, M.M. Strube and W.V. Steele, Thermodynamic studies related to the hydrogenation of phenanthrene, NIPER-247 (1987), National Institute for Petroleum and Energy Research, Bartlesville, OK.

37. W.V. Steele, D.G. Archer, R.D. Chirico and M.M. Strube, Comparison of thermodynamics of nitrogen and sulfur removal in heavy oil upgrading. Part 1. Acyclic and monocyclic compounds, NIPER-264 (1987), National Institute for Petroleum and Energy Research, Bartlesville, OK.

38. D.W. Scott and J.P. McCullough, The chemical thermodynamic properties of hydrocarbons and related substances: Properties of 100 linear alkane thiols, sulfides, and symmetrical disulfides in the ideal gas state from 0° to 1000°K, U.S. Bur. Mines Bull. 595 (1961).

39. M.Z. El-Sabban and D.W. Scott, The chemical and thermodynamic properties of hydrocarbons and related substances. II. Properties of 25 organic sulfur compounds in the ideal gas state from 0° to 1000°K, U.S. Bur. Mines Bull. 654 (1970).

40. F.D. Rossini, K.S. Pitzer, R.L. Arnett, R.M. Braun and G.C. Pimentel, Selected values of physical and thermodynamic properties of hydrocarbons and related compounds, American Petroleum Institute Program 44, Carnegie Press, Pittsburgh, PA (1953).

41. A.S. Brunjes, Section 12, Physical properties of hydrocarbons, in "Petroleum processing handbook," W.F. Bland and R.L. Davidson, Eds., McGraw-Hill Book Co., New York (1967).

42. E.S. Domalski, W.H. Evans and E.D. Hearing, Heat capacities and entropies of organic compounds in the condensed phase, J. Phys. Chem. Ref. Data, Supplement No. 1, 13 (1983) 1-286.

43. T. Boublik, V. Fried and E. Hála, "The vapour pressures of pure substances: Selected values of the temperature dependance of the vapour pressures of some pure substances in the normal and low

pressure region," 2nd revised ed., Elsevier, Amsterdam (1984) 972 pp.

44. V. Majer and V. Svoboda, "Enthalpies of vaporization of organic compounds: A critical review and data compilation," Blackwell Scientific Publications, Oxford (1984) 300 pp.

45. "Enthalpies of organic compounds," V. Majer and V. Svoboda, Eds., Chemical Data Series 32, Blackwell Scientific Publications, Pergamon Press, Oxford (1985) 304 pp.

46. J.B. Pedley, R.D. Naylor and S.B. Kirby, "Thermochemical data of organic compounds," Chapman and Hall Ltd., London (1986) 804 pp.

47. B.J. Zwolinski and R.C. Wilhoit, Handbook of vapor pressures and heats of vaporization of hydrocarbons and related compounds, API 44-TRC Publications in Science and Engineering, Thermodynamics Research Center, Texas A&M University, College Station, TX (1971).

48. R.C. Wilhoit and B.J. Zwolinski, Physical and thermodynamic properties of aliphatic alcohols, J. Phys. Chem. Ref. Data, Supplement No. 1, 2 (1973) 1–420.

49. TRC Thermodynamic Tables, Thermodynamics Research Center, The Texas A&M University System, College Station, TX, Volumes I–XI (Hydrocarbons) and Volumes I–VII (Non-hydrocarbons).

50. C. Tsonopoulos, J.L. Heldman and S-c. Hwang, "Thermodynamic and transport properties of coal liquids," John Wiley & Sons, New York (1986) 200 pp.

51. R.A. Robie, B.S. Hemingway and J.R. Fisher, Thermodynamic properties of minerals and related substances at 298.15 K and 1 bar (10^5 pascals) pressure and at higher temperatures, Geological Survey Bulletin 1452, U.S. Government Printing Office, Washington (1978). Reprinted with corrections, 1979.

52. B.S. Hemingway, R.A. Robie and J.A. Kittrick, Revised values for the Gibbs free energy of formation of [Al(OH)$_4^-$$_{(aq)}$], diaspore, boehmite and bayerite at 298.15 K and 1 bar, the thermodynamic properties of kaolinite to 800 K and 1 bar, and the heats of solution of several gibbsite samples, Geochim. Cosmochim. Acta, 42 (1978) 1533.

53. A. Skauge, N. Fuller and L.G. Hepler, Specific heats of clay minerals: Sodium and calcium kaolinites, sodium and calcium montmorillonites,

illite, and attapulgite, Thermochim. Acta, 6 (1983) 139.

54. B.S. Hemingway, K.M. Krupka and R.A. Robie, Heat capacities of the alkali feldspars between 35 and 1000 K from differential scanning calorimetry, the thermodynamic functions of the alkali feldspar from 298.15 to 1400 K, and the reaction quartz + jadeite = analbite, Am. Mineralogist, 66 (1981) 1202.

55. D. Smith-Magowan, A. Skauge and L.G. Hepler, Specific heats of Athabasca oil sands and components, J. Can. Petrol. Techn., 21, May–June (1982) 28.

56. R. Cassis, N. Fuller, L.G. Hepler, R.J.C. McLean, A. Skauge, N.S. Srinivasan and H-k. Yan, Specific heat capacities of bitumens and heavy oils, reservoir minerals, clays, dehydrated clays, asphaltenes, and cokes, AOSTRA J. Res., 1 (1985) 163.

57. K. Rajeshwar, D.B. Jones and J.B. DuBow, Thermophysical characterization of oil sands. 1. Specific heats, Fuel, 61 (1982) 237.

58. M.R. Cervenan, F.E. Vermuelen and F.S. Chute, Thermal conductivity and specific heat of oil sand samples, Can. J. Earth Sci., 18 (1981) 926.

59. W.R. Lindberg, R.R. Thomas and R.J. Christensen, Measurements of specific heat, thermal conductivity and thermal diffusivity of Utah tar sands, Fuel, 64 (1985) 80.

60. J.D. Scott and A.C. Seto, Thermal property measurements on oils sands, J. Can. Petroleum Techn., 25 Nov–Dec (1986) 70. A.C. Seto, Thermal testing of oil sands, M.Sc. thesis, University of Alberta (1985).

61. R.N.J. Saal, W. Heukelom and P.C. Blokker, Physical constants of asphaltic bitumens. Part I, J. Inst. Petroleum, 26 (1940) 29.

62. M. Gomez, J.B. Gayle and A.R. Taylor, Jr., Heat content and specific heat of coals and related products, U.S. Bur. Mines Rep. Inv. 6607 (1965).

63. A.A. Agroskin, V.B. Gleibaman, E.I. Goncharov and I.G. Zubilin, Specific heat of cokes made from hard coals, Coke & Chem., 8 (1973) 22.

64. E.I. Vargha-Butler, M.R. Soulard, H.A. Hamza and A.W. Neumann, Determination of specific heats of coal powders by differential scanning calorimetry, Fuel, 61 (1982) 437.

65. E. Melchior and H. Luther, Measurement of true specific heats of bituminous coals of different rank and of a high-temperature coke, in the temperature

range 30–350°C, Fuel, 61 (1982) 1071.

6. D.P. Lindroth and W.G. Krawza, Heat content and specific heat of six rock types at temperatures to 1000°C, U.S. Bur. Mines Rep. Inv. 7503 (1971).

7. R.J. Shaw, Specific heat of Colorado oil shales, U.S. Bur. Mines Rep. Inv. 4151 (1947).

8. R.L. Wise, R.C. Miller and H.W. Sohns, Heat contents of some Green River oil shales, U.S. Bur. Mines Rep. Inv. 7482 (1971).

9. K. Rajeshwar, R. Nottenburg and J. DuBow, Review: Thermophysical properties of oil shales, J. Materials Sci., 14 (1979) 2025.

0. D.B. Jones, K. Rajeshwar and J.B. DuBow, Specific heats of Colorado oil shales. A differential scanning calorimetry study, Ind. Eng. Chem. Proc. Des. Dev., 19 (1980) 125.

1. J.A. Gray, C.J. Brady, J.R. Cunningham, J.R. Freeman and G.M. Wilson, Thermophysical properties of coal liquids. 1. Selected physical, chemical, and thermodynamic properties of narrow boiling range coal liquids, Ind. Eng. Chem. Proc. Des. Dev., 22 (1983) 410.

2. K.C. Mills, Heat capacity of nickel and cobalt tellurides, J. Chem. Soc. Faraday Trans. I, 70 (1974) 2224.

3. M.G. Lowings, K.G. McCurdy and L.G. Hepler, Heats of melting of sodium nitrate and indium by differential scanning calorimetry: A suggestion for a new calibration substance, Thermochim. Acta, 23 (1978) 365.

. S.C. Mraw and D.F. Naas, The measurement of accurate heat capacities by differential scanning calorimetry. Comparison of D.S.C. results on pyrite (100 to 800 K) with literature values from precision adiabatic calorimetry, J. Chem. Thermodynamics, 11 (1979) 567.

. S.C. Mraw and D.F. Nass-O'Rourke, Thermodynamic properties of cyclohexane-D12: Low-temperature heat capacity and enthalpies of transition and fusion from accurate differential scanning calorimetry, and the entropy from spectroscopic results, J. Chem. Thermodyn., 12 (1980) 691.

. K.G. Zeeb, M.G. Lowings, K.G. McCurdy and L.G. Hepler, Heats of transition and melting of sodium nitrate by differential scanning calorimetry: Uses of indium and sodium nitrate as calibration substances, Thermochim. Acta, 40 (1980) 245.

. S.C. Mraw and D.F. O'Rourke, Accuracy of differential scanning calorimetry for heat capacities of organic compounds at high temperatures. New method for enthalpy of fusion by D.S.C., J. Chem. Thermodyn., 13 (1981) 199.

78. I. Dellien, A DSC study of the phase transformations of ammonium nitrate, Thermochim. Acta, 55 (1982) 181.

79. A. Skauge, N. Fuller, H-k. Yan, R. Cassis, N.S. Srinivasan and L.G. Hepler, Specific heat capacities of minerals from oil sands and heavy oil deposits, Thermochim. Acta, 68 (1983) 291.

80. J.E. Callanan and S.A. Sullivan, Development of standard operating procedures for differential scanning calorimeters, Rev. Sci. Instruments, 57 (1986) 2584.

81. N.E. Dorsey, "Properties of ordinary water-substance," Hafner Publishing Co., New York (1968) 673 pp., facsimile of 1940 edition, Reinhold Publishing Corp.

82. L. Haar, J.S. Gallegher and G.S. Kell, "NBS/NRC steam tables: Thermodynamic and transport properties and computer programs for vapor and liquid states of water in SI units," Hemisphere Publ. Corp., New York (1984) 320 pp.

83. W.F. Giauque and J.W. Stout, The entropy of water and the third law of thermodynamics. The heat capacity of ice from 15 to 273°K, J. Am. Chem. Soc., 58 (1936) 1144.

84. K.S. Pitzer and L. Brewer, "Thermodynamics," 2nd ed. (revision of 1st ed. by G.N. Lewis and M. Randall), McGraw-Hill, New York (1961) 723 pp.

85. N.S. Osborne, H.F. Stimson and D.C. Ginnings, Measurements of heat capacity and heat of vaporization of water in the range 0° to 100°C, J. Res. Natl. Bur. Standards, 23 (1939) 197.

86. N.S. Osborne, H.F. Stimson and D.C. Ginnings, Calorimetric determination of the thermodynamic properties of saturated water in both the liquid and gaseous states from 100° to 374°C, J. Res. Natl. Bur. Standards, 18 (1937) 389.

87. N.S. Osborne, H.F. Stimson, E.F. Fiock and D.C. Ginnings, The pressure of saturated water vapor in the range 100°C to 364°C, J. Res. Natl. Bur. Standards, 10 (1933) 10.

88. F.D. Rossini, D.D. Wagman, W.H. Evans, S. Levine and I. Jaffe, Selected values of thermodynamic properties, National Bureau of Standards Circ. 500, U.S. Government Printing Office, Washington (1952).

89. R.M. Garrels and C.L. Christ, "Solutions, minerals, and equilibria," Harper & Row, New York (1965)

450 pp.

90. W. Stumm and J.J. Morgan, "Aquatic chemistry: An introduction emphasizing chemical equilibria in natural water," John Wiley & Sons, New York (1970) 583 pp.

91. V.L. Snoeyink and D. Jenkins, "Water chemistry," John Wiley & Sons, New York (1980) 463 pp.

92. "Oil in freshwater: Chemistry, biology, countermeasure technology," J.H. Vandermeulen and S.E. Hrudey, Eds., Pergamon Press, New York (1987) 512 pp.

93. L.G. Hepler, Thermodynamic data for aqueous solutions and their uses, AIChE Symposium Series, 80 (1984) 84.

94. D.D. Wagman, W.H. Evans, V.B. Parker, R.H. Schumm, I. Halow, S.M. Bailey, K.L. Churney and R.L. Nuttall, The NBS tables of chemical thermodynamic properties: Selected values for inorganic and C_1 and C_2 organic substances in SI units, J. Phys. Chem. Reference Data, 11 (1982) Supplement No. 2, 392 pp.

95. F.H. Sweeton, R.E. Mesmer and C.F. Baes, Jr., Acidity measurements at elevated temperatures. VII. Dissociation of water, J. Solution Chem., 3 (1974) 191.

96. G. Olofsson and L.G. Hepler, Thermodynamics of ionization of water over wide ranges of temperature and pressure, J. Solution Chem., 4 (1975) 127.

97 R.H. Busey and R.E. Mesmer, The ionization of water in NaCl media to 300°C, J. Solution Chem., 5 (1976) 147.

98. W.L. Marshall and E.U. Franck, Ion product of water substance, 0–1000°C, 1–10 000 bars: New international formulation and its background, J. Phys. Chem. Ref. Data, 10 (1981) 295.

99. G. Olofsson and I. Olofsson, Empirical equations for some thermodynamic quantities for the ionization of water as a function of temperature, J. Chem. Thermodyn., 13 (1981) 437.

100. E.J. King, "Acid-base equilibria," Pergamon Press, Oxford (1965) 341 pp.

101. R.G. Bates, "Determination of pH: Theory and practice," John Wiley & Sons, New York (1973) 479 pp.

102. R.A. Robinson and R.H. Stokes, "Electrolyte solutions," 2nd ed., revised, Butterworths, London (1965) 571 pp.

103. J.J. Christensen, L.D. Hansen and R.M. Izatt, "Handbook of proton ionization heats and related thermodynamic quantities," John Wiley & Sons, New York (1976) 269 pp.

104. E.P. Serjeant and B. Dempsey, "Ionization constants of organic acids in aqueous solution," Pergamon Press, Oxford (1979) 989 pp.

105. C.F. Baes, Jr., and R.E. Mesmer, "The hydrolysis of cations," John Wiley & Sons, New York (1976) 489 pp.

106. L.G. Hepler and J.W. Larson, Heats and entropies of ionization, Chap. 1 in "Solute-solvent interactions," J.F. Coetzee and C.D. Ritchie, Eds., Marcel Dekker, New York (1969).

107. L.G. Hepler and H.P. Hopkins, Jr., Thermodynamics of ionization of inorganic acids and bases in aqueous solution, Rev. Inorg. Chem., 1 (1979) 303.

108. J.N. Butler, "Ionic equilibrium: A mathematical approach," Addison-Wesley Publ. Co., Inc., Reading, MA (1964) 547 pp.

109. G.M. Fleck, "Equilibria in solution," Holt, Rinehart and Winston, Inc., New York (1966) 217 pp.

110. R.N. Goldberg, J.L. Manley and R.L. Nuttall, GAMPHI — A database of activity and osmotic coefficients for aqueous electrolyte solutions, Natl. Bur. Stds. Tech. Note 1206 (1985).

111. R.N. Goldberg, An equilibrium model for the calculation of activity and osmotic coefficients for aqueous solutions, J.Res. Natl. Bur. Stds., 89 (1984) 251.

112. J.J. Christensen and R.M. Izatt, "Handbook of metal ligand heats and related thermodynamic quantities," Marcel Dekker, New York (1970) 324 pp.

113. D.A. Johnson, "Some thermodynamic aspects of inorganic chemistry," 2nd ed., Cambridge University Press, Cambridge (1982) 282 pp. (Includes example calculations.)

114. Y.A. Chang and N. Ahmad, "Thermodynamic data on metal carbonates and related oxides," The Metallurgical Society of AIME, Warrendale, PA (1982) 235 pp.

115. L.B. Pankratz, J.M. Stuve and N.A. Gokcen, "Thermodynamic data for mineral technology," Bureau of Mines Bull. 677, U.S. Government Printing Office, Washington (1984) 355 pp.

116. M.W. Chase, Jr., C.A Davies, J.R. Downcy, Jr., D.J. Frurip, R.A. McDonald and A.N. Syverud, JANAF thermochemical tables, 3rd ed. J. Phys.

Chem. Ref. Data (1985); Part I, pp. 1–196; Part II, pp. 927–1856.

7. "Standard potentials in aqueous solutions," A.J. Bard, R. Parsons and J. Jordan, Eds., Marcel Dekker, New York (1985) 834 pp.

8. D. Smith-Magowan and R.N. Goldberg, A bibliography of sources of data leading to thermal properties of binary aqueous electrolyte solutions, NBS Special Publication 537, U.S. Government Printing Office, Washington (1979).

9. M. Luria and S.W. Benson, Heat capacities of liquid hydrocarbons. Estimation of heat capacities at constant pressure as a temperature function, using additivity rules, J. Chem. Eng. Data, 22 (1977) 90.

0. M. Bures, V. Majer and M. Zabransky, Modification of Benson method for estimation of ideal-gas heat capacities, Chem. Eng. Sci., 36 (1981) 529.

1. O.V. Dorofeeva, L.V. Gurvich and S.J. Cyvin, On calculation of thermodynamic properties of polycyclic aromatic hydrocarbons, Thermochim. Acta, 102 (1986) 59. (Entropies of gases as function of temperature and review of some estimation procedures.)

2. B.B. Pruden and J.M. Denis, Heat of reaction and vaporization of feed and product in the thermal hydrocracking of Athabasca bitumen, CANMET Report 76–30, Energy, Mines and Resources Canada (1976).

3. B.A. Fleming and D.A. Crerar, Silicic acid ionization and calculation of silica solubility at elevated temperature and pH. Application to geothermal fluid processing and reinjection, Geothermics, 11 (1982) 15.

4. W.L. Marshall and C.-T.A. Chan, Amorphous silica solubilities — V. Predictions of solubility behaviour in aqueous electrolyte solutions to 300°C, Geochim. Cosmochim. Acta, 46 (1982) 289. (See several earlier papers by Marshall and colleagues for further information on solubilities of silica in various aqueous solutions.)

5. R.O. Fournier and R.W. Potter, II, An equation correlating the solubility of quartz in water from 25° to 900°C at pressures up to 10,000 bars, Geochim. Cosmochim. Acta, 46 (1982) 1969.

6. R.O. Fournier and W.L. Marshall, Calculation of amorphous silica solubilities at 25° to 300°C and apparent cation hydration numbers in aqueous salt solutions using the concept of effective density of water, Geochim. Cosmochim. Acta, 47 (1983) 587.

127. G.J. Ewin, B.P. Erno and L.G. Hepler, Clay chemistry: Investigation of thermodynamics of ion exchange reactions by titration calorimetry, Can. J. Chem., 59 (1981) 2927.

128. L.L. Schramm and J.C.T. Kwak, Thermochemistry of ion exchange and particle interaction in clay suspensions, Can. J. Chem., 60 (1982) 486.

129. J.O. Nriagu, Thermochemical approximations for clay minerals, Amer. Mineralogist, 60 (1975) 834.

130. Y. Tardy and R.M. Garrels, Prediction of Gibbs energies of formation of compounds from the elements — II. Monovalent and divalent metal silicates, Geochim. Cosmochim. Acta, 41 (1977) 87.

131. Y. Tardy and B. Fritz, An ideal solid solution model for calculating solubility of clay minerals, Clay Minerals, 16 (1981) 361.

132. W.L. Marshall, Aqueous inorganic phase equilibria at high temperatures. Some experimental, theoretical, and applied aspects, Pure & Applied Chem., 57 (1986) 283.

133. F.H. Sweeton and C.F. Baes, Jr., The solubility of magnetite and hydrolysis of ferrous ions in aqueous solutions at elevated temperatures, J.Chem. Thermodyn., 2 (1970) 479.

134. P.R. Tremaine, R. Von Massow and G.R. Sherman, A calculation of Gibbs free energies for ferrous ions and the solubility of magnetite in H_2O and D_2O to 300°C, Thermochim. Acta., 19 (1977) 287.

135. P.R. Tremaine and J.C. LeBlanc, The solubility of magnetite and the hydrolysis and oxidation of Fe^{2+} in water to 300°C, J. Solution Chem., 9 (1980) 415.

136. M.H. Lietzke and W.L. Marshall, Sodium sulfate solubilities in high temperature aqueous sodium chloride and sulfuric acid solutions — predictions of solubility, vapor pressure, acidity, and speciation, J. Solution Chem., 15 (1986) 903.

137. R.T. Pabalan and K.S. Pitzer, Thermodynamics of concentrated electrolyte mixtures and the prediction of mineral solubilities to high temperatures for mixtures in the system Na-K-Mg-Cl-SO_4-OH-H_2O, Geochim. Cosmochim. Acta, 51 (1987) 2429.

138. J.K. Hovey, L.G. Hepler and P.R. Tremaine, Thermodynamics of aqueous aluminate ion: Standard partial molar heat capacities and volumes

of Al(OH)$_4$⁻(aq) from 10 to 55°C, J. Phys. Chem., 92 (1988) 1323.

139. J.W. Larson, P. Cerutti, H.K. Garber and L.G. Hepler, Electrode potentials and thermodynamic data for aqueous ions: Copper, zinc, cadmium, iron, cobalt, and nickel, J. Phys. Chem., 72 (1968) 3695.

140. A.J. Read, The first ionization constant of carbonic acid from 25 to 250°C and to 2000 bars, J. Solution Chem., 4 (1975) 53.

141. S.R. Rao and L.G. Hepler, Equilibrium constants and the thermodynamics of ionization of aqueous hydrogen sulfide, Hydrometallurgy, 1 (1976/1977) 293. (There is continuing uncertainty and controversy about the second ionization of hydrogen sulfide; this uncertainty is important only for highly alkaline solutions.)

142. D. Langmuir, Techniques of estimating thermodynamic properties for some aqueous complexes of geochemical interest, ACS Symposium Series 93 (1979) 353.

143. G.C. Allred, J.W. Larson and L.G. Hepler, Thermodynamics of acid dissociation of aqueous bisulfite ion: $\Delta H°$, $\Delta C_p°$, and $\Delta V°$ at 298.15 K, Can. J. Chem., 59 (1981) 1068.

144. R.D. Deshmukh and A.E. Mather, A mathematical model for equilibrium solubility of hydrogen sulfide and carbon dioxide in aqueous alkanolamine solutions, Chem. Eng. Sci., 36 (1981) 355.

145. F-y. Jou, A.E. Mather and F.D. Otto, Solubility of H_2S and CO_2 in aqueous methyldiethanolamine solutions, Ind. Eng. Chem. Proc. Des. Dev., 21 (1982) 539.

146. S.D. Cramer, The solubility of methane, carbon dioxide, and oxygen in brines from 0° to 300°C, Bur. Mines. Rep. Inv. 8706 (1982).

147. G. Douheret and A. Viallard, Activity coefficients and micellar equilibria. 1. The mass action law model applied to aqueous solutions of sodium carboxylates at 298.15 K, Fluid Phase Equil., 8 (1982) 233.

148. C.S. Patterson, G.H. Slocum, R.H. Busey and R.E. Mesmer, Carbonate equilibria in hydrothermal systems: First ionization of carbonic acid in NaCl media to 300°C, Geochim. Cosmochim. Acta, 46 (1982) 1653.

149. J.W. Larson, K.G. Zeeb and L.G. Hepler, Heat capacities and volumes of dissociation of phosphoric acid (1st, 2nd, and 3rd), bicarbonate ion, and bisulfate ion in aqueous solution, Can. J. Chem., 60 (1982) 2141.

150. J.A. Barbero, K.G. McCurdy and P.R. Tremaine, Apparent molal heat capacities and volumes of aqueous hydrogen sulfide and sodium hydrogen sulfide near 25°C: The temperature dependence of H_2S ionization, Can. J. Chem., 60 (1982) 1872.

151. H.F. Holmes and R.E. Mesmer, Thermodynamic properties of aqueous solutions of the alkali metal chlorides to 250°C, J.Phys. Chem., 87 (1982) 1242.

152. C.J. Wormald, C.N. Colling and G. Smith, Thermodynamics of supercritical steam + carbon dioxide mixtures, Fluid Phase Equil., 10 (1983) 223.

153. C. Dobrogowska and L.G. Hepler, Calorimetric determination of the standard enthalpy of the first ionization of aqueous sulfur dioxide or "sulfurous acid" at 25°C, J. Solution Chem., 12 (1983) 153.

154. J.A. Barbero, L.G. Hepler, K.G. McCurdy and P.R. Tremaine, Thermodynamics of aqueous carbon dioxide and sulfur dioxide: Heat capacities, volumes, and the temperature dependence of ionization, Can. J. Chem., 61 (1983) 2509.

155. C.S. Paterson, R.H. Busey and R.E. Mesmer, Second ionization of carbonic acid in NaCl media to 250°C, J. Solution Chem., 13 (1984) 647.

156. A.H. Roux, G. Perron and J.E. Desnoyers, Capacités calorifiques, volumes, expansibilités et compressibilités des solutions aqueuses concentrées de LiOH, NaOH, et KOH, Can. J. Chem., 62 (1984) 878.

157. R.H. Busey, H.F. Holmes and R.E. Mesmer, The enthalpy of dilution of aqueous sodium chloride to 673 K using a new heat-flow and liquid-flow microcalorimeter. Excess thermodynamic properties and their pressure coefficients, J. Chem. Thermodyn., 16 (1984) 343.

158. B.E. Roberts and P.R. Tremaine, Vapour liquid equilibrium calculation for dilute aqueous solutions of CO_2, H_2S, NH_3, and NaOH to 300°C, Can. J. Chem. Eng., 63 (1985) 294.

159. R.N. Goldberg and V.B. Parker, Thermodynamics of solution of SO_2(g) in water and of aqueous sulfur dioxide solutions, J. Res. Natl. Bur. Stds., 90 (1985) 341.

160. L. Barta and D.J. Bradley, Extension of the specific interaction model to include gas solubilities in high temperature brines, Geochim. Cosmochim. Acta, 49 (1985) 195.

161. E.C.W. Clarke and D.N. Glew, Evaluation of th

thermodynamic functions for aqueous sodium chloride from equilibrium and calorimetric measurements below 154°C, J. Phys. Chem. Ref. Data, 14 (1985) 489.

2. J.K. Hovey and P.R. Tremaine, Thermodynamics of complexes of aqueous iron(III), aluminum, and several divalent cations with EDTA: Heat capacities, volumes, and variations in stability with temperature, J. Phys. Chem., 89 (1985) 554.

3. E.M. Woolley and T.E. Burchfield, Model for thermodynamics of ionic surfactant solutions. 3. Enthalpies, heat capacities, and volumes of surfactants, J. Phys. Chem., 89 (1985) 714.

4. E.M. Woolley and M.T. Bashford, Enthalpies of dilution of aqueous decyl-, dodecyl-, tetradecyl-, and hexadecyltrimethylammonium bromide + sodium bromide solutions at 10, 25, 40, and 55°C, J. Phys. Chem., 90 (1986) 3038.

5. G. Caron, N. Gelinas and J.E. Desnoyers, Effect of geometry on the thermodynamic properties of micellar systems: Trialkylamine oxides in water, Can. J. Chem., 64 (1986) 1573. (Also see many earlier papers by Desnoyers and colleagues about thermodynamics of micellar solutions.)

6. P.P.S. Saluja, J.C. LeBlanc and H.B. Hume, Apparent molar heat capacities and volumes of aqueous solutions of several 1:1 electrolytes at elevated temperatures, Can. J. Chem., 64 (1986) 926.

7. H.F. Holmes and R.E. Mesmer, Thermodynamics of aqueous solutions of the alkali metal sulfates, J. Solution Chem., 15 (1986) 495.

8. J.K. Hovey, L.G. Hepler and P.R. Tremaine, Thermodynamics of aqueous EDTA systems: Apparent and partial molar heat capacities and volumes of aqueous strontium and barium EDTA, J. Solution Chem., 15 (1986) 977.

9. K.S. Pitzer and R.T. Pabalan, Thermodynamics of NaCl in steam, Geochim. Cosmochim. Acta, 50 (1986) 1445.

10. P.P.S. Saluja, K.S. Pitzer and R.C. Phutela, High-temperature thermodynamic properties of several 1:1 electrolytes, Can. J. Chem., 64 (1986) 1328.

11. K.S. Pitzer and J.M. Simonson, Thermodynamics of multicomponent, miscible, ionic systems: Theory and equations, J. Phys. Chem., 90 (1986) 3005.

12. R.C. Phutela and K.S. Pitzer, Heat capacity and other thermodynamic properties of aqueous magnesium sulfate to 473 K, J. Phys. Chem., 90 (1986) 895.

173. L. Barta and L.G. Hepler, Densities and apparent molar volumes of aqueous aluminum chloride. Analysis of apparent molar volumes and heat capacities of aqueous aluminum salts in terms of the Pitzer and Helgeson theoretical models, Can. J. Chem., 64 (1986) 353.

174. J.K. Hovey and P.R. Tremaine, Thermodynamics of aqueous aluminum: Standard partial molar heat capacities of Al^{3+} from 10 to 55°C, Geochim. Cosmochim. Acta, 50 (1986) 453.

175. J.B. Rosenholm, R.B. Grigg and L.G. Hepler, Thermodynamic properties of aqueous solutions of surfactants: Molar heat capacities and volumes, J. Chem. Thermodyn., 18 (1986) 1153.

176. K. Sway, J.K. Hovey and P.R. Tremaine, Apparent molar heat capacities and volumes of alkylbenzenesulfonate salts in water: Substituent group additivity, Can. J. Chem., 64 (1986) 398.

177. D.G. Archer, Enthalpies of dilution from 50 to 225°C of aqueous decyltrimethlylammonium bromide, J. Solution Chem., 15 (1986) 581.

178. D.G. Archer, Enthalpy of dilution of aqueous sodium chloride from 76 to 225°C and aqueous dodecyltrimethylammonium bromide from 50 to 225°C, J. Solution Chem., 15 (1986) 727.

179. D.G. Archer, Enthalpies of dilution of aqueous tetradecyltrimethlylammonium bromide from 50–175°C, J. Solution Chem., 16 (1987) 347.

180. R.T. Pabalan and K.S. Pitzer, Thermodynamics of NaOH(aq) in hydrothermal solutions, Geochim, Cosmochim. Acta, 51 (1987) 829.

181. R.C. Phutela, K.S. Pitzer and P.P.S. Saluja, Thermodynamics of aqueous magnesium chloride, calcium chloride, and strontium chloride at elevated temperatures, J. Chem. Eng. Data, 32 (1987) 76.

182. E.M. Woolley and T.E. Burchfield, Model for thermodynamics of ionic surfactant solutions: Enthalpies, heat capacities, volumes, expansibilities, and compressiblities, in "Surfactants in solution," Vol. 4, K.L. Mittal and P. Bothorel, Eds., Plenum Press, New York (1987) pp. 55–67.

183. T.E. Burchfield and E.M. Woolley, Model for thermodynamics of ionic surfactants: Effect of electrolytes on osmotic and activity coefficients, in "Surfactants in solution," Vol. 4, K.L. Mittal and P.

Bothorel, Eds., Plenum Press, New York (1987) pp. 69–76.

184. L.V. Dearden and E.M. Woolley, Osmotic coefficients of alkylmethylammonium bromides in water and aqueous sodium bromide solutions at 55°C, J. Phys. Chem., 91 (1987) 2404.

185. L.V. Dearden and E.M. Woolley, Heat capacities of aqueous decyl-, dodecyl-, tetradecyl- and hexadecyltrimethylammonium bromides at 10, 25, 40 and 55°C, J. Phys. Chem., 91 (1987) 4123.

186. J.A. Gates, D.M. Tillett, D.E. White and R.H. Wood, Apparent molar heat capacities of aqueous NaCl solutions from 0.05 to 3.0 mol kg^{-1}, 350 to 600 K, and 2 to 18 MPa, J. Chem. Thermodyn., 19 (1987) 131.

187. D.E. White, A.L. Doberstein, J.A. Gates, D.M. Tillett and R.H. Wood, Heat capacity of aqueous $CaCl_2$ from 306 to 603 K at 17.5 MPa, J. Chem. Thermodyn., 19 (1987) 251.

188. J-H. Kim, C. Dobrogowska and L.G. Hepler, Thermodynamics of ionization of aqueous alkanolamines, Can. J. Chem., 65 (1987) 1726.

189. G.W. Woodbury and L.A. Noll, Thermodynamic model for surfactant adsorption, NIPER 223 (1987), National Institute for Petroleum and Energy Research, Bartlesville, OK.

5

INTERFACIAL PROPERTIES

K. Takamura*
E. E. Isaacs

Oil Sands and Hydrocarbon Recovery Department
Alberta Research Council

*Now with BASF Canada, Sarnia, Ontario

INTERFACIAL TENSION

Introduction

Surface or interfacial tension (γ) is the contractile force that exists in the boundary between two phases at equilibrium. As a consequence of surface tension there is a balancing pressure difference across any curved surface, the pressure being greater on the concave side (nonwetting phase). For a curved surface with principal radii of curvature r_1 and r_2 this pressure difference is given by the Young-Laplace equation

$$\Delta P = \gamma\left(\frac{1}{r_1} + \frac{1}{r_2}\right) \tag{1}$$

that reduces to $\Delta P = 2\gamma/r$ for a spherical capillary. This pressure difference is called capillary pressure P_c and is also a function of the wetting characteristics of the fluids:

$$P_c = \frac{2\gamma\cos\theta}{r} \tag{2}$$

where θ is the angle of contact, which defines the wetting preference to a fluid or wettability of the porous matrix. The role of capillary pressure in estimating reserves and predicting recovery and displacement efficiency from conventional oil reservoirs has been well covered in the petroleum literature. Both wettability and capillary pressure as they apply to bituminous reservoirs will be discussed in later sections of this chapter. In this section we examine the tension in the interface between four different pairs of phases: aqueous-vapor (AV), bitumen-vapor (BV) bitumen-aqueous (BA), and solid-fluid (SF). Surface tension and interfacial tension will be used to denote measurements at the liquid-vapor and liquid-liquid interfaces, respectively. A complete description of the various methods used to measure surface and interfacial tension is beyond the scope of this book; the reader is referred to several good references [1–5].

Liquid-vapor tension

The most common techniques used to measure liquid-vapor tensions for bituminous systems include ring tensiometry, the Wilhelmy plate method, and the maximum bubble pressure method. The maximum bubble pressure method is a dynamic method limited to aqueous-vapor tensions and is ideally suited to the measurement of surfactant content in aqueous

production streams from the hot water process [6]. Of the two force methods, the Wilhelmy plate method is somewhat more accurate, since unlike ring tensiometry, it causes less disturbance of the surface during measurement. The method is also more amenable to temperature scans involving bitumen and time dependence of the tension [7,8].

In the commercial hot water process, oil sand is slurried with water and sodium hydroxide. The role of the sodium hydroxide is primarily to neutralize the petroleum acids naturally present in the bitumen to yield salts that are surface-active in the aqueous phase. Figure 1, based on the data of Bowman [9], shows the effect of pH (adjusted with sodium hydroxide) on the aqueous-vapor tension γ_{AV} of an oil sand/aqueous slurry (ratio of 5:7).
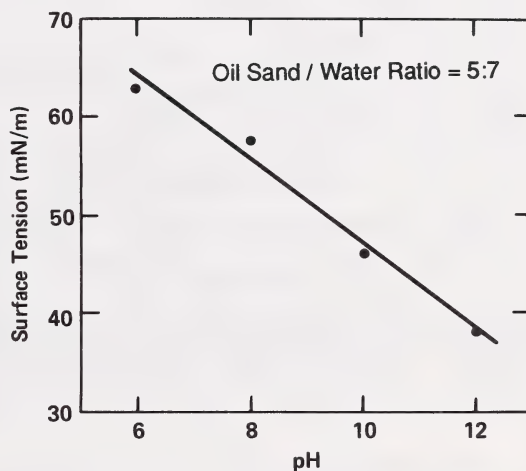

Figure 1. Effect of pH on the aqueous-vapor surface tension (γ_{AV}) of an oil sand/aqueous slurry (ratio = 5:7). The decline in γ_{AV} with increasing pH is indicative of the activation of surfactants naturally present in the bitumen.

A summary of data on the temperature dependence of the bitumen-vapor tension is given in Figure 2. Potoczny et al. [7] used the Wilhelmy plate method with centrifuged Athabasca bitumen samples, while Isaacs and Morrison [10] used the ring method with a commercially extracted sample (Suncor). Also in Figure 2 is the prediction of Mehrotra et al. [11] based on the principle of corresponding states. Data for surface tensions of bitumen extracted with various solvents not included in Figure 2 have also been published [7,8,10].

A common feature of the surface tension behavior of all bitumen samples is that the values are greater than those for most pure hydrocarbon solvents. This indicates, as Isaacs and Morrison [10] have noted, that the surface-active constituents naturally present in the bitumen are not adsorbed at the bitumen-vapor interface. Thus surface tension measurements are not suitable for characterizing changes in the bitumen due to processing or aging. This is also an indication of the hydrophilic character of the surfactants present in the bitumen, which do not absorb on the hydrophobic oil-vapor interface. For modelling purposes the bitumen-vapor interface can be treated as a pure hydrocarbon.
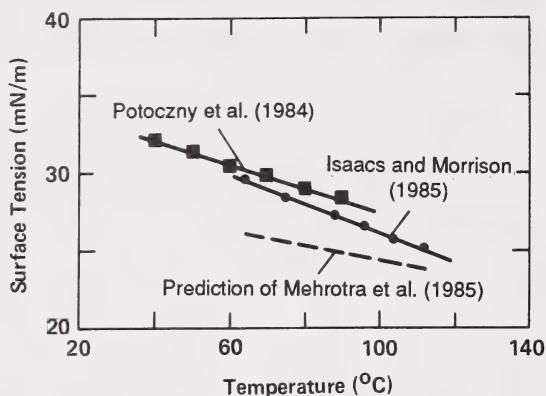
Figure 2. The influence of temperature on the surface tension of bitumen samples obtained by different methods.

Liquid-liquid tension

A serious objection to the application of the ring and Wilhelmy plate methods for liquid-liquid interfaces is the fact that contact angles of zero are very rare at the junction of the liquid-liquid interface with a solid. Therefore the equations used for calculations by these techniques may not apply. The use of the drop-weight method is also not recommended since at the moment of drop detachment new surfaces are forming rapidly, and except for pure liquids the surface may not satisfy equilibrium requirements.

The three shape methods, spinning drop, sessile drop and pendent drop, have been used for interfacial tension measurements involving heavy oil and bituminous systems. Large errors can occur with these techniques when drops are not well deformed by body forces due to the small difference in density between heavy oil and water. Interfacial tension values are

suspect for a density difference of less than about 0.05 g/cm^3, especially at high temperatures where the inaccuracy of density determinations and the mutual solubility of the two fluids also contribute to the error. To improve the reliability of interfacial tension values we recommend using heavy water (D$_2$O) instead of H$_2$O. The type of aqueous medium (H$_2$O or D$_2$O) is believed [12] to have no effect on the interfacial tension value. For measurements with produced water samples the procedure would involve evaporating the H$_2$O and redissolving the residue with the molar equivalent of D$_2$O.

The spinning drop method is the most suitable for low interfacial tension regimes (below about 1 mN/m) where knowledge of only one drop dimension is required. On the other hand the sessile and pendent drop methods are more accurate for high tensions (above about 1 mN/m).

Heavy crude oils in particular are sensitive to chemical [13] and photolytic oxidation [10] at the oil-water interface and great care must be taken to avoid laboratory artifacts during measurements. As an example, Figure 3 shows an irreversible change in the interfacial tension of a single sessile bitumen drop in D$_2$O measured in sequence at 50, 200, and 50°C [14]. Likely, interfacially active material degraded at the interface and could not be replenished from the bitumen bulk since the bitumen/water ratio was about 1:500. Since it is often convenient to measure tensions at several temperatures with a single drop, a good practice is to make sure that values at the initial temperature can be reproduced.
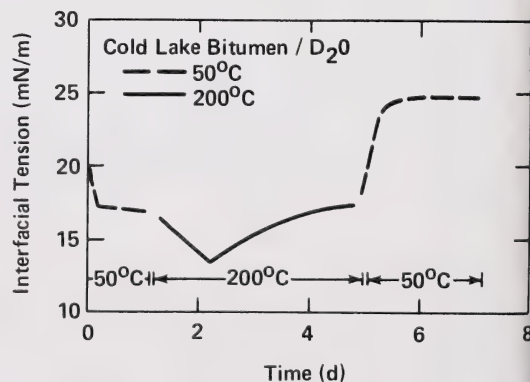

Figure 3. Evolution of interfacial tension for a bitumen drop in D$_2$O measured in sequence at 50°C, 200°C, and 50°C.

The interfacial tensions of crude oils from some western Canadian fields were measured in their respective produced water using the spinning drop technique [15]. The data are compared in Table 1 with values measured in deionized water. The densities of the crude oils used in the calculation of interfacial tension are plotted as a function of temperature in Figure 4.

Akstinat [16] observed that the temperature dependence of interfacial tension is strongly influenced by oil composition. High-naphthenic-content crudes showed a decrease in interfacial tension with increasing temperature while aromatic and paraffinic crudes were virtually unaffected. However, for heavy oils no systematic studies have been carried out to relate composition to interfacial tension behavior.

Temperature dependence data for Athabasca bitumen [12], and for Epping, Three Creeks, and Wainwright B crudes [13] are shown in Figures 5 and 6, respectively. The bitumen-D_2O tensions of Figure 5, measured using the spinning drop technique, were markedly influenced by both temperature and salinity. At a given salinity the interfacial tension decrease was of the order of 0.07 mN/m/°C. The value of 15.4 measured at 50°C in the absence of salt is identical to the value measured at the same temperature using the sessile drop technique [10].

The decrease in interfacial tension with temperature for 83 Epping and Three Creeks crudes in D_2O was about 0.06 and 0.01 mN/m/°C respectively (Figure 6). Wainwright crude in Battle River water showed an initial decrease (0.09 mN/m per °C) followed by an increase.

There are other examples of crude oils which have exhibited a minimum in their interfacial tension-temperature curves [13]. More experiments are needed before the trends can be ascertained.

Data for the interfacial tensions of Epping, Athabasca, and Lloydminster oils as a function of pH are shown in Figure 7. The observed shape of the curves is similar to that found for a large number of conventional crude oils contacted with NaOH [17], with interfacial tension minima at pH 12 to 12.5. Below a pH of about 11, the tensions are essentially unaffected by the presence of caustic.

The effect of brine addition is a shift in the interfacial tension minima to lower pH values and, in general, the minima are less pronounced. The degree of interfacial tension reduction is dependent on the dissociation of natural surfactants at the oil-water interface. The dissociation of the surfactants at the interface can be theoretically calculated using the interfacial electrochemistry of the system (see section on electric properties).

Interfacial tension versus pH measurements have also been carried out on natural surfactants isolated from heavy Venezuelan crudes [18] and fractions of Lloydminster crude [19].

Addition of commercial surfactants to brine can have a dramatic effect on interfacial tensions [12]. Figure 8 shows the effect of sodium chloride concentration on the bitumen-aqueous interfacial tension measured at 50°C for SunTech V, TRS 10-80, and sodium dodecyl sulfate (SDS). Both TRS 10-80 and SunTech V, which contain a mixture of many surfactant

Table 1. Comparison of interfacial tensions[a] of some crude oils in deionized water and in their produced water.

Crude oil	Interfacial tension (mN/m)	
	Distilled water	Produced water
Bonnie Glen	21.1	26.4
Wainwright	26.0	20.8
Epping	27.1	22.0
Chauvin	17.2	4.5
Lloydminster	26.8	15.4
Cold Lake-bailed	15.7	–
Cold Lake-produced[b]	15.0	7.4
Judy Creek	21.9	20.5
Athabasca[c]	15.0	–

[a]   Measured in a spinning drop apparatus at 23°C.
[b]   Measured at 40°C.
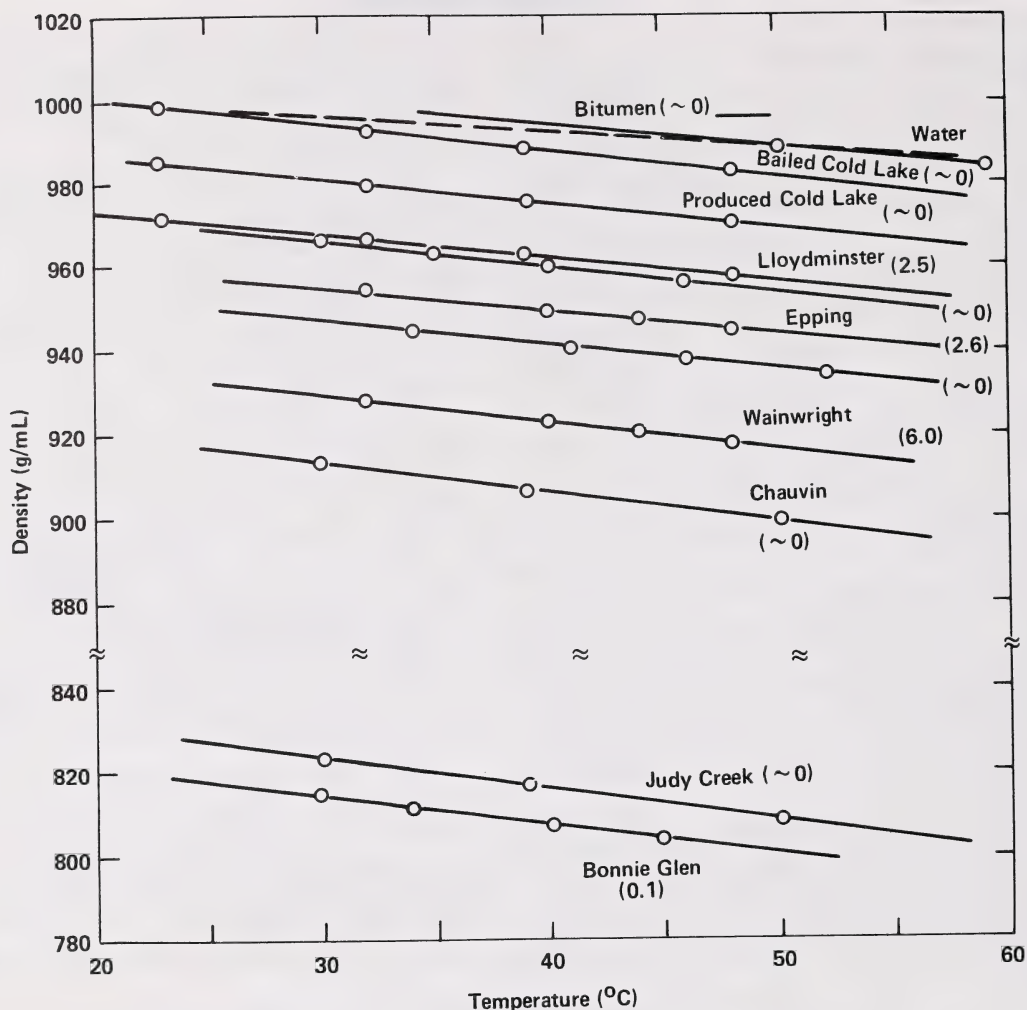[c]   Measured in D_2O at 50°C [12].

Figure 4. The effect of temperature on the density of some Western Canadian crudes. The densities were used to calculate interfacial tensions. Percent water in the crude is given in parentheses.
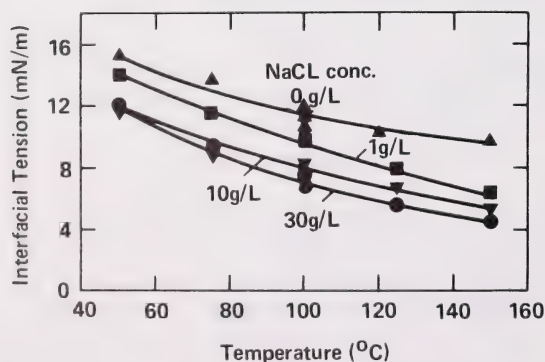

Figure 5. The influence of temperature and salinity on the interfacial tension of Athabasca bitumen and heavy water.
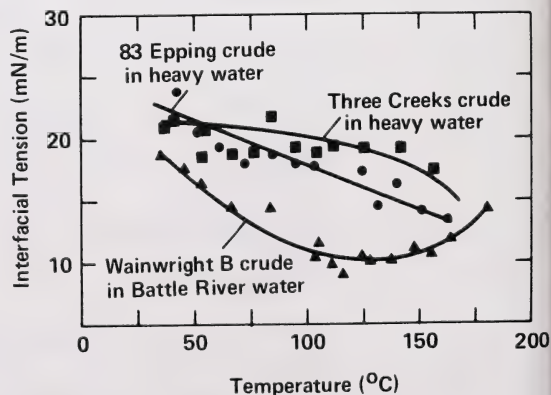
Figure 6. The influence of temperature on the interfacial tension of Epping, Three Creeks, and Wainwright B crudes against water.

ecies, displayed a tension minimum where the interfacial tension was reduced by 2 to 3 orders of magnitude. In the case of SDS, the bitumen-aqueous nsions were only slightly affected by salinity.

The low tensions (<0.1 mN/m) displayed by the ulfonate surfactant mixtures are often associated with the formation of a surfactant-rich third phase at the iumen-aqueous interface. Elevated temperatures tend to hinder the formation of this structured phase resulting in an increase in interfacial tension. Figure 9 shows the increase in interfacial tension with temperature for bitumen samples from Athabasca, Cold Lake, and Peace River against SunTech IV surfactant in the presence and absence of brine (10 g/L NaCl). The interfacial tensions at 200°C approach those expected in the absence of surfactant (Figure 5). In general, it is difficult to achieve low interfacial tensions at elevated temperatures especially given the range of reservoir salinities.
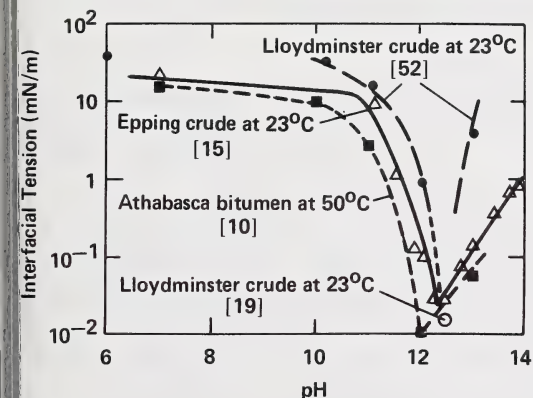

Figure 7. The effect of pH on the interfacial tension of Epping, Athabasca, and Lloydminster oils.
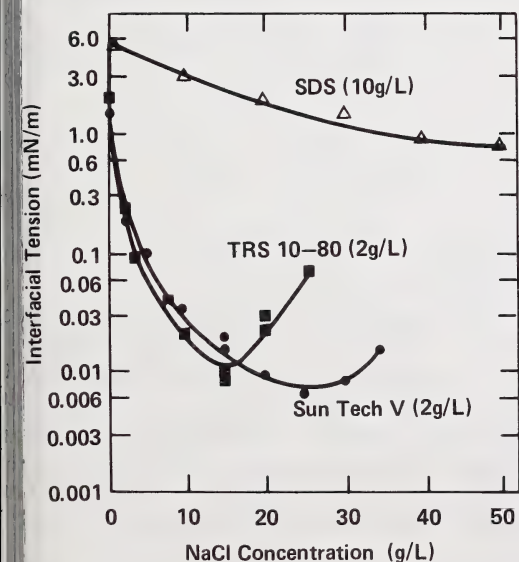

Figure 8. The effect of NaCl concentration on bitumen-aqueous interfacial tension for TRS 10-80, SunTech V and sodium dodecyl sulfate (SDS) at 50°C.
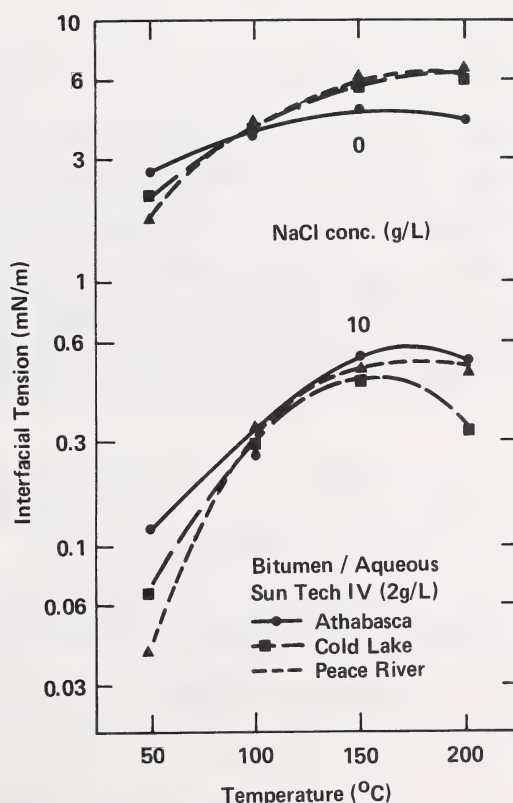

Figure 9. Interfacial tensions of the Athabasca, Cold Lake, and Peace River bitumen/D_2O systems as functions of temperature and NaCl concentrations.

Solid-fluid tension

Neumann and coworkers [20] have estimated values of the solid-vapor (γ_{SV}) and solid-aqueous (γ_{SA}) tensions for sand particles which were solvent-extracted from Athabasca oil sands. A technique known as the solidification front was used. In this method, solid particles are either engulfed or rejected by the solidification front of the melt material. Particles are engulfed when

$$\gamma_{SV} \text{ for the particle} < \gamma_{LV} \text{ for the matrix}$$

and rejected when

$$\gamma_{SV} > \gamma_{LV}.$$

Using several matrix materials with different γ_{LV}, the lower and upper bounds of γ_{SV} for the given sand particles were estimated. Values for γ_{SA} can be estimated in freezing-point experiments with water as the matrix material. More accurate values of γ_{SV} and γ_{SA} can be obtained from critical velocity measurements. This involves increasing the rate of solidification and increasing the hydrodynamic drag force opposing particle motion until at a critical rate, V_c, engulfment occurs. From the experimental values of V_c, the γ_{SV} can be calculated. The γ_{SA} can be calculated from the so-called equation of state relation:

$$\gamma_{SA} = \frac{\left[\left(\gamma_{SA} \right)^{1/2} - \left(\gamma_{LV} \right)^{1/2} \right]^2}{1 - 0.015 \left(\gamma_{SV} \gamma_{LV} \right)^{1/2}} \qquad (3)$$

Typical tension values for sand particles extracted with various solvents from Athabasca oil sands are:

$$\gamma_{SV} = 36 \text{ to } 38 \text{ mN/m}$$

$$\gamma_{SA} = 75 \text{ mN/m}$$

$$\gamma_{SB} = 88 \text{ to } 90 \text{ mN/m}$$

The γ_{SV} and γ_{SA} values were measured in Neumann's laboratory [20] and the solid-bitumen tension γ_{SB} was obtained from the Young-Dupre equation:

$$\gamma_{SB} - \gamma_{SA} = \gamma_{BA} \cos \theta \qquad (4)$$

assuming a value of 15 mN/m for the bitumen-water tension and a contact angle θ ranging from 0 to 30° (water-wet conditions).

The solid tension values given above should be considered preliminary since they were obtained on sands which had been solvent-extracted without further treatment to restore the wettability (see section on wetting behavior).

ELECTRIC PROPERTIES

Introduction

The electric properties of interfaces are governed mostly by phenomena occurring within an interfacial region of a few nanometres thickness, where both chemical and physical properties of a fluid change drastically as a function of distance. Small changes in physical properties such as surface roughness, or in chemical properties such as the presence of a trace amount of surface-active impurities or high-valence counter-ions become significant at the interface. Therefore, quantities determined experimentally are often applicable only to the specific system studied, even though the experiments are highly reproducible. Unfortunately, there are no thermodynamic constants which describe the reactions occurring at the interface, though some progress has been made recently. Lack of an appropriate experimental technique, and lack of theoretical understanding of complex phenomena controlling measured results are also obstacles to progress. For example, electrophoretic mobility and the zeta potential are often used as synonyms for the surface charge of the interface. Determinations of zeta potentials from measured mobilities are often very difficult, and estimates of changes in the surface charge density from the measured mobilities are impossible except under very ideal conditions.

In this chapter, the basic theory for the electric properties of interfaces is reviewed. Special care is taken to describe problems encountered during electrophoresis. Reported values of electrokinetic potentials and results of electrophoretic mobility measurements for bitumen, sands, and clay minerals are then discussed. All discussions are limited to experiments conducted using clean systems.

Origin of surface charge

Most interfaces, both liquid-liquid and solid-liquid, are electrically charged owing to the following possible

echanisms:

Ionization: dissociation of ionizable groups such as $-SO_3^-$, $-COO^-$ and $-NH_3^+$ on the surface. The ionization of the surface groups depends strongly on pH of the solution. The pH at which the net charge is zero is called the isoelectric point (iep).

Ion adsorption: unequal adsorption of oppositely charged ions, such as surfactants, on the surface. Ion adsorption may be positive or negative. For example, hydrocarbon droplets suspended in aqueous electrolyte solutions have a negative charge. This is explained in terms of negative adsorption of highly hydrated cations.

Ion dissolution: unequal dissolution of the oppositely charged ions of which compounds are composed, for example, AgI, $BaSO_4$, $CaCO_3$.

he diffuse double layer

Ions of opposite charge (counter-ions) are attracted wards the surface, and ions of like charge (co-ions) are pelled away from the surface. This, together with the ixing tendency of thermal motion leads to the rmation of an electric double layer. The surface arge is neutralized by the excess of counter-ions over -ions in the electric double layer. The ion distribution the double layer is described by the Boltzmann uation:

$$n_+ = n_o \exp\left[-\frac{ze\psi}{kT}\right] \tag{5a}$$

d

$$n_- = n_o \exp\left[-\frac{ze\psi}{kT}\right] \tag{5b}$$

here, n_+ and n_- are the densities of positive and gative ions at potential, ψ, n_o is the corresponding lk concentration of each ionic species, z is the valence ions, e is the electron charge, k is the Boltzmann nstant, and T is the absolute temperature.

Figure 10 illustrates distributions of Na+ and Cl− ar the negatively charged surface (surface potential = −160 mV) in a bulk liquid NaCl concentration −2 M at pH 7. Equation (5a) predicts that Na+ ncentration in the vicinity of the surface is proximately 5 M, whereas the Cl− concentration is ly 2 x 10−5 M. The curve for Na+ also describes the stribution of H+, and thus pH, as a function of stance from the surface. Although pH in the bulk lution is 7, it is only 4.3 at the surface. The pH in e vicinity of the surface, not pH in the bulk solution,
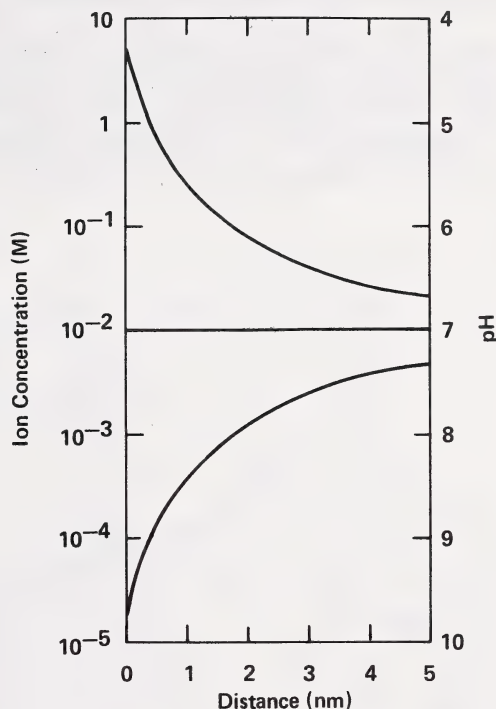

Figure 10. Distribution of Na+, H+ (pH), and Cl− near the negatively charged surface, surface potential −160 mV in 10^{-2} M NaCl solution at pH 7.

determines the dissociation of ionizable groups on the surface.

The effect of ion valences is illustrated in Figure 11 in the distribution of Na+ and Ca2+ near the surface having $\psi_o = -100$ mV in the solution containing 10^{-2} M NaCl and 10^{-4} M $CaCl_2$. Although the concentration of Ca2+ is only one-hundredth that of Na+ in the bulk solution, the concentrations of these two ions are very similar (0.25 and 0.5 M, respectively) in the vicinity of the surface.

Surface charge density

The surface potential (ψ_o can be related to the charge density (σ_o) at the surface by the Gouy-Chapman equation:

$$\sigma_o = (8 n_o \varepsilon kT)^{1/2} \sinh\left(\frac{ze\psi_o}{2kT}\right) \tag{6}$$

where ε is the permittivity of a medium. The surface potential depends both on the surface charge density and

on the ionic composition of the medium (through n_o and z). As seen in Figures 12a and 12b, ψ_o decreases sharply with increasing electrolyte concentration, and the valence of ions at a given σ_o (for example, $\psi_o = -260$, -200, and -145 mV for $\sigma_o = 320$ mC/m^2 (25Å^2 per charge group) in 10^{-3}, 10^{-2}, and 10^{-1} M electrolyte in which the valences of counter- and co-ions are 1:1).
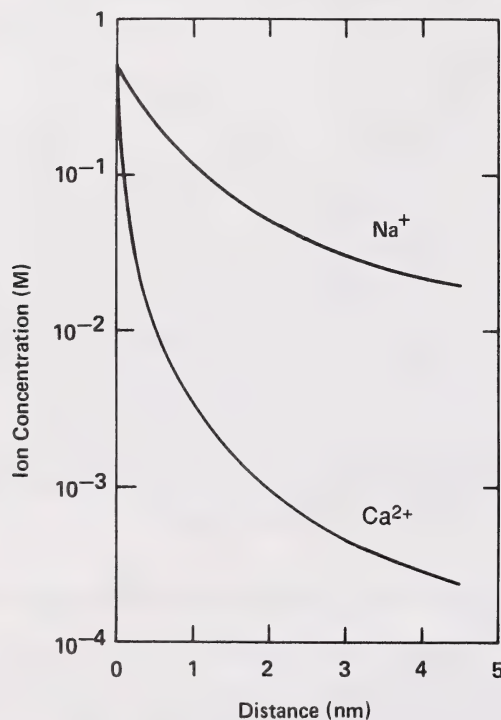

Figure 11. Distribution of Na$^+$ and Ca^{2+} near the negatively charged surface, surface potential -100 mV in 10^{-2} M NaCl and 10^{-4} M CaCl$_2$ solutions respectively, at pH 7.
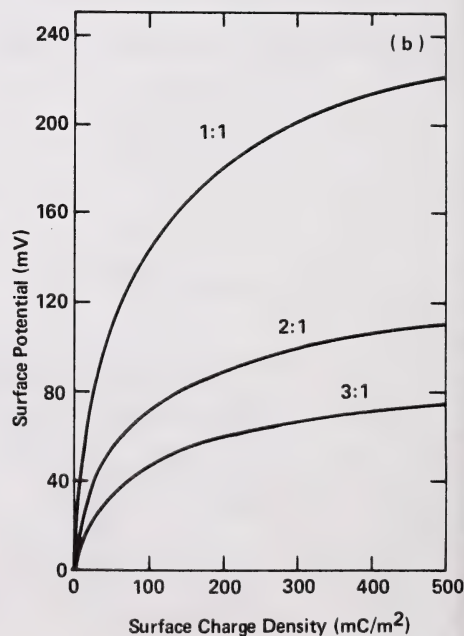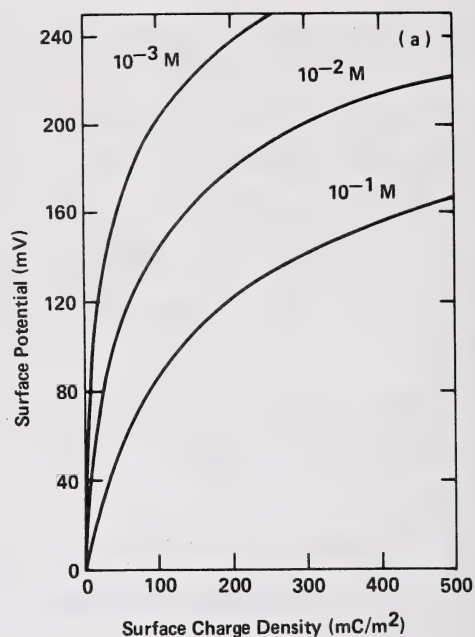

Figure 12. Relationships between surface charge density and surface potential for (a) 1:1 electrolyte 10^{-3}, 10^{-2}, and 10^{-1} M, and (b) for 1:1, 2:1, and electrolytes of 10^{-2} M.

ELECTROKINETIC POTENTIAL MEASUREMENT

Electrokinetic phenomena

Electrokinetic is the general term used to describe four phenomena which arise when attempts are made to tear off the mobile part of the electric double layer:

• *Electrophoresis*: the movement of a charged particle relative to a stationary liquid induced by an applied electric field.

• *Sedimentation potential*: the electric field which is created when charged particles move relative to a stationary liquid (the opposite of electrophoresis).

• *Electroosmosis*: the movement of liquid relative to a stationary charged surface induced by an applied electric field.

• *Streaming potential*: the electric field created when liquid is made to flow along a stationary charged surface (the opposite of electroosmosis).

Electrokinetic measurements can be interpreted to yield the electrokinetic or zeta potential (ζ), which represents a potential at the surface that separates the immobilized fluid layer surrounding the particle from the mobile fluid (the surface of shear or the shear plane). Although the precise location of the shear plane is not known, it lies within a couple of molecular diameters (0.5 to 1 nm) from the actual particle surface for smooth particles. Variation of potentials with a distance x from the surface for $\psi_o = -150$ mV are plotted in Figure 13 in 10^{-1}, 10^{-2}, 10^{-3}, and 10^{-4} M (1:1 electrolyte solutions). At high electrolyte concentration, ψ decreases sharply with distance near the surface. For example, ψ (0.6), the potential at $x = 0.6$ nm, is only 35% of ψ_o in 10^{-1} M. This means that the exact location of the shear plane becomes critical. Differences in the degrees of surface roughness of the particles or the adsorption of surfactants and high-molecular-weight polymer may result in appreciable variation in the location of the shear plane, and thus in zeta potential.

Adsorption of multivalent counter-ions or surfactant molecules within the shear plane may even result in the reversal of charge. This is illustrated in Figure 14 [21]. Although the inner part of the double layer is vastly different in the three cases, it results in the same zeta potential; that is, $\zeta_1 = \zeta_2 = \zeta_3$.

Case 1. High positive surface potential (ψ_{o1}) with moderately high supporting electrolyte concentration to

yield a thin double layer (Fe_2O_3 sol in 10^{-2} M KCl at pH 4.0).

Case 2. Lower surface potential but still positive (ψ_{o2}), and low electrolyte concentration so that there is considerable extension of the double layer (Fe_2O_3 sol in 10^{-4} M KCl at pH 7.0).
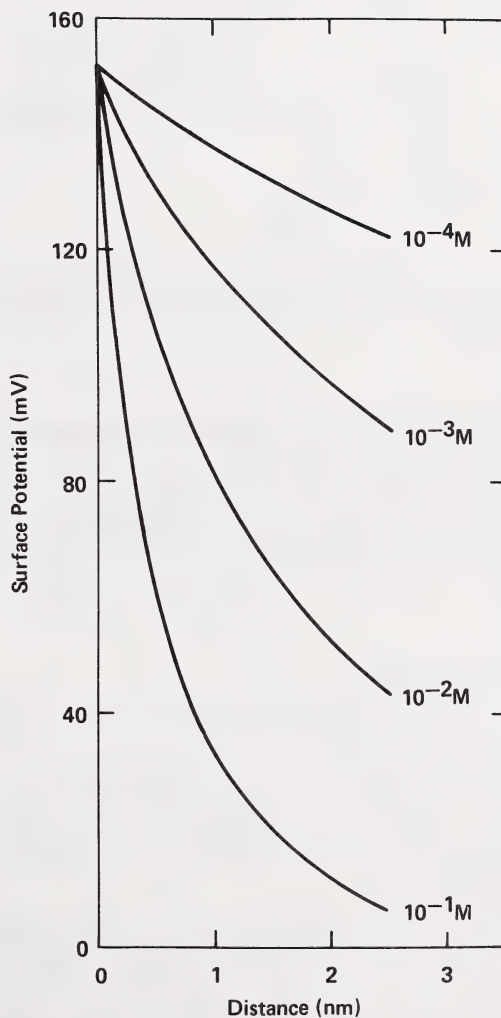

Figure 13. Variation of potentials with distance x from the surface for $\psi_o = -150$ mV in 1:1 electrolyte solution.
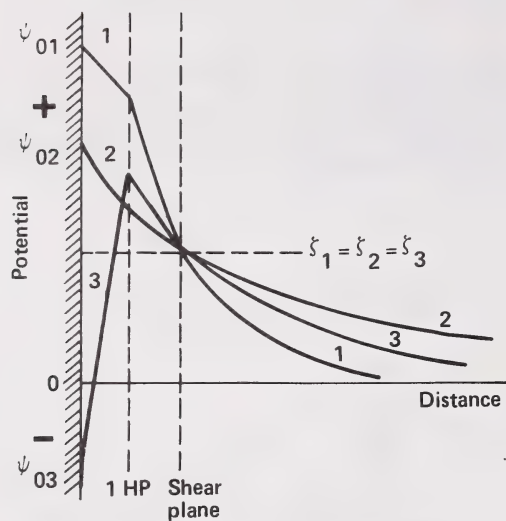
Figure 14. Three possible potential distributions leading to the same zeta potential [21]. For explanation see text.

Case 3. Negative but small surface potential (ψ_{o3}), strong adsorption of a cationic surfactant in the inner part of the double layer and moderate extension of the double layer; that is, moderate concentration of supporting electrolyte (Fe_2O_3 sol in 10^{-3} M KCl at pH 8.5 in the presence of 10^{-4} M long-chain ammonium salt).

Electrophoresis

A detailed description of electrokinetic measurements can be found in the literature [22]. Among the four electrokinetic methods discussed above, electrophoresis has been used extensively to study the electric properties of colloidal particles. Here we discuss the theoretical limitation of the electrophoresis measurement.

The complexity of electrophoresis arises from the fact that the electrophoretic mobility, U (m/s)/(V/m), is a complex function of both ζ and κa, where $\kappa = (2e^2 n_o z^2/\varepsilon\ kT)^{1/2}$ is the Debye-Hückel reciprocal double-layer thickness and a is the particle radius. Values of κ for several different electrolyte concentrations and valences are listed in Table 2. $U(\zeta,\ \kappa a)$ relations for spherical particles calculated using the O'Brien and White's computer solution [23] are shown in Figure 15 for various values of κa in

aqueous NaCl solutions at 25°C, and in Figure 16 for multivalent counter-ions at $\kappa a = 25$.

From Figure 15, U becomes a linear function of ζ (Smoluchowski equation) only at the limiting condition of $\kappa a = \infty$:

$$U = \frac{\varepsilon\zeta}{\eta} \qquad (7)$$

where η is the viscosity of the medium. Similar relations for $\kappa a < 1$ can be found in the literature [23]. $U(\zeta,\ \kappa a)$ relationships for different temperatures are shown in Figure 17 at $\kappa a = 15$. The increasing mobility at higher temperatures is mostly due to the reduction of the viscosity of water.

The complexity of the $U(\zeta,\ \kappa a)$ relation discussed above is the result of the electrophoretic relaxation effect: deformation of the double layer surrounding the particles by an externally applied electric field. The calculation of ζ from measured U becomes problematic unless the electric relaxation effect can be evaluated.
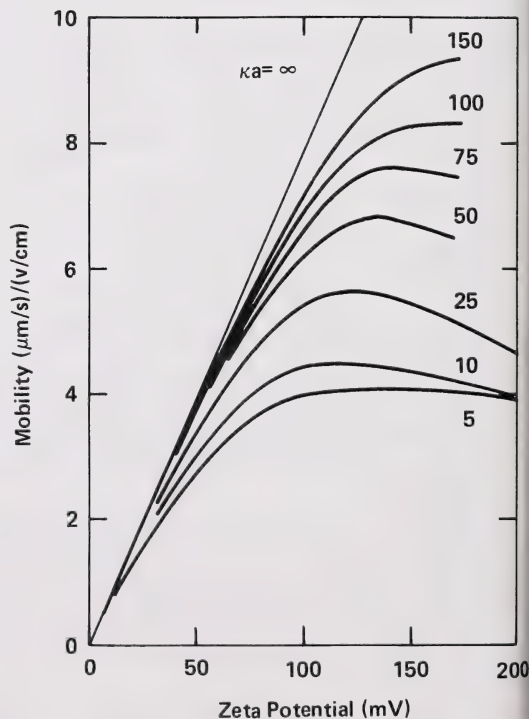

Figure 15. Mobility versus zeta potential relationship for spherical particles calculated using the O'Brien and White computer solution [23] at $5 < \kappa a < \infty$ and 25°C.

Table 2. Values of κ and κ^{-1} for several different electrolyte concentrations and valances with numerical formulas for these quantities also given for aqueous solutions at 25°C.

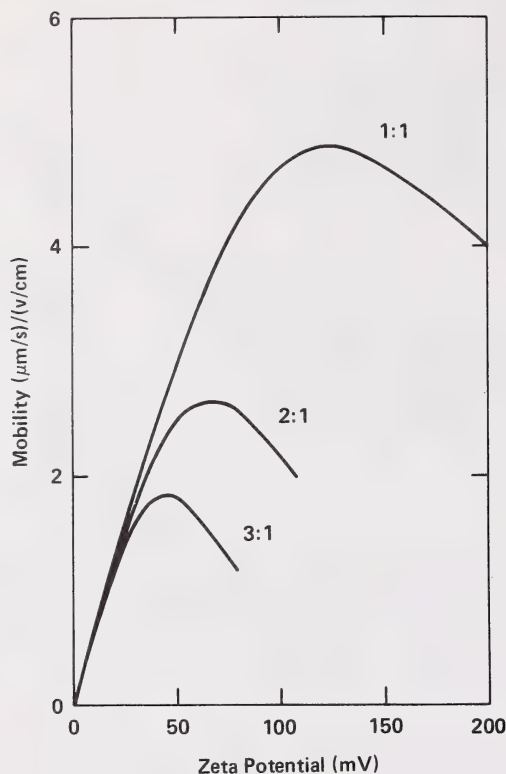| | | Symmetrical electrolyte | | | Asymmetrical electrolyte | |
		$\kappa(m^{-1}) = 3.29 \times$ $10^9 / z / M^{1/2}$	$\kappa^{-1}(m) = 3.04 \times$ $10^{-10} / z /^{-1} M^{-1/2}$		$\kappa(m^{-1}) = 2.32 \times$ $10^9(\Sigma_i z^2_i M)^{1/2}$	$\kappa^{-1}(m) = 4.3 \times$ $10^{-10}(\Sigma_i z^2_i M)^{-1/2}$
Molarity	$z_+ : z_-$			$z_+ : z_-$		
0.001	1:1	1.04×10^8	9.61×10^{-9}	1:2, 2:1	1.80×10^8	5.56×10^{-9}
	2:2	2.08×10^8	4.81×10^{-9}	3:1, 1:3	2.54×10^8	3.93×10^{-9}
	3:3	3.12×10^8	3.20×10^{-9}	2:3, 3:2	4.02×10^8	2.49×10^{-9}
0.01	1:1	3.29×10^8	3.04×10^{-9}	1:2, 2:1	5.68×10^8	1.76×10^{-9}
	2:2	6.58×10^8	1.52×10^{-9}	1:3, 3:1	8.04×10^8	1.24×10^{-9}
	3:3	9.87×10^8	1.01×10^{-9}	2:3, 3:2	1.27×10^8	7.87×10^{-10}
0.1	1:1	1.04×10^9	9.61×10^{-10}	1:2, 2:1	1.80×10^9	5.56×10^{-10}
	2:2	2.08×10^9	4.81×10^{-10}	1:3, 3:1	2.54×10^9	3.93×10^{-10}
	3:3	3.12×10^9	3.20×10^{-10}	2:3, 3:2	4.02×10^9	2.49×10^{-10}

Figure 16. Mobility versus zeta potential for 1:1, 2:1, and 3:1 electrolyte solutions at $\kappa a = 25$ and 25°C.
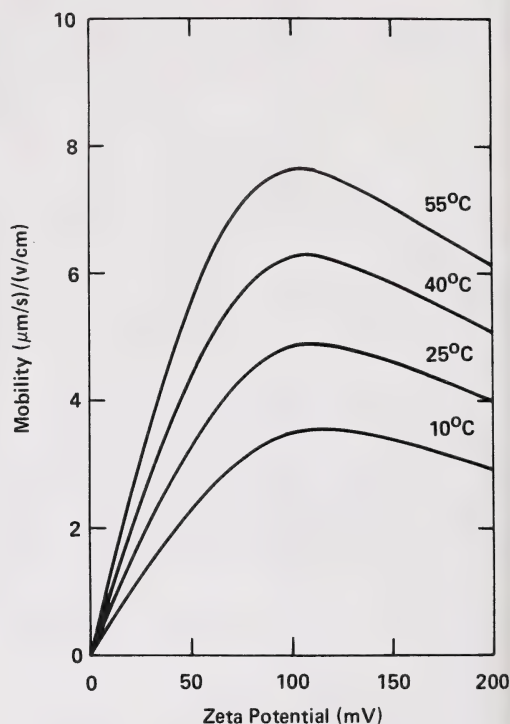

Figure 17. Mobility versus zeta potential for 1 electrolyte at 10, 25, 40, and 55°C.

precisely. This is demonstrated in Figures 18 and 19 by simulating the measured electrophoretic mobilities of bitumen-in-water emulsions having a (= 1 μm) as a function of pH at two different experimental conditions of varying and constant ionic strengths.

In Case 1, the pH of the solution was simply adjusted using a desired amount of HCl or NaOH, thus the concentration of counter-ions (H$^+$ or Na$^+$) varied during the measurement. The U vs pH relation for this case is indicated in Figure 18, and ψ_o, ζ, and σ_o vs pH relations are plotted in Figure 19. σ_o remained at small values of ~2 mC/m^2 at 2 < pH < 4, but ψ_o, ζ, and U increase with pH because of the reduction of the electrolyte (H$^+$) concentration (see Figure 11). Surprisingly however, the increase of σ_o, ψ_o, and ζ with pH at 4 < pH < 9 results in the reduction of U because of the electrophoretic relaxation effect at high ζ and low κa (here, it is assumed that 10^{-5} M 1:1 electrolyte is present in the water used for the experiment). Both ψ_o

and ζ decreased, even though σ_o increased sharp at pH > 9. Increasing counter-ion (Na$^+$) concentrati reduced ψ_o and ζ, but the reduction of the relaxati effect caused a sharp increase in U until pH 11.5. I important to notice that the measured mobilities 4 < pH < 9 merely reflect the degree of t electrophoretic relaxation effect, not the surface cha density of the bitumen emulsion. When polydispe samples are used, the exact particle size electrophoresis may not be known. Thus, the analysis measured U is practically impossible.

In contrast, when the ionic strength of the solut was maintained at 10^{-2} M by the addition of NaCl, measured U increased monotonically with pH as sho in Figure 18. Here, Equation (7) can be applied for entire experimental condition, because of a high valu κa (= 323). A detailed discussion of the elec properties of the bitumen-in-water emulsion may found in the next section.
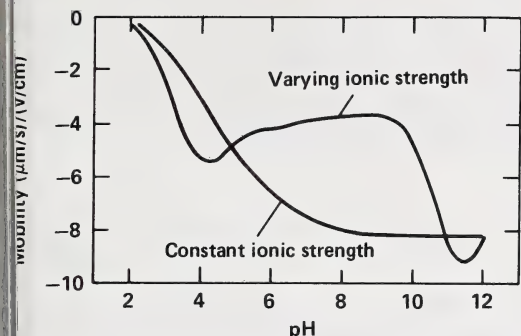
Figure 18. Mobility U vs pH relationships under the two different conditions of varying and constant ionic strength (10^{-2} M). For explanation see text.

Figure 19. ψ_o, ζ, and σ_o vs pH relationships under the condition of varying ionic strength.

The $U(\zeta, \kappa a)$ relations shown in Figures 15, 16, and 17 are only for spherical particles and the similar relations for irregularly shaped particles are expected to be more complex. Moreover, recent results by Chow and Takamura [24] using the bitumen emulsions indicate that the theory may overestimate the relaxation effect at low values of κa ($\kappa a < 100$).

ELECTRIC PROPERTIES OF MATERIALS IN OIL SANDS

Bitumen-water interface

Electric properties. The negative charge of the bitumen-water interface can be explained by the dissociation of carboxyl groups belonging to surfactants naturally present in bitumen [25]:

$$RCOOH \Leftrightarrow RCOO^- + H^+ \qquad (8a)$$
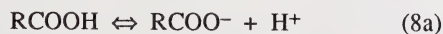
$$K_a = \frac{(RCOO^-)\ (H^+)_s}{(RCOOH)} \qquad (8b)$$

where K_a is the dissociation constant for the surface group and $(H^+)_s$ is the hydrogen ion concentration in the vicinity of the surface. As shown in Figure 10, hydrogen ions are preferentially accumulated near the bitumen surface due to the Coulombic interaction
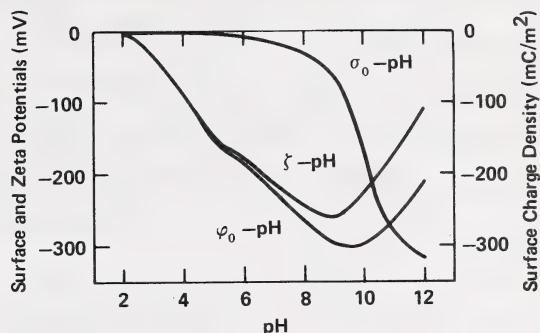
between positive hydrogen ions and the negatively charged surface. By using the relation

$$(H^+)_s = (H^+)_b \exp(-e\psi_o / kT) \qquad (9)$$

where $(H^+)_b$ is the hydrogen ion concentration in the bulk solution, Takamura and Chow [24,25] successfully explained the measured zeta potential of a bitumen-in-water emulsion using material constants of $N_s = 2 \times 10^{18}/m^2$, $pK_a = 4.5$, and $x = 0.6$ nm, where, N_s and x are the total surface density of carboxyl groups and the location of the shear plane, respectively. The measured and theoretically predicted zeta potentials are plotted as a function of bulk pH in Figure 20. The dissociation behavior of carboxyl groups has been illustrated in
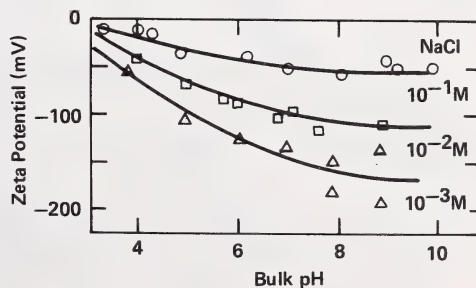

Figure 20. Comparison of zeta potentials calculated from measured mobilities (solid symbols) with those predicted (solid lines) for a bitumen emulsion using the Ionizable Surface-Group model.

Figure 21 by plotting the fraction of carboxyl groups dissociated, $-\sigma_o/eN_s$, as a function of bulk pH for conventional crude oil and heavy oil ($N_s = 2 \times 10^{17}$ m^{-2} and $N_s = 2 \times 10^{18}$ m^{-2}, respectively). These figures show that the dissociation behavior of carboxyl groups on the surface is complex and depends strongly on the value of N_s and on the electrolyte concentration in the aqueous solution. Figure 21 suggests that an optimum caustic concentration has to be found for each crude oil and reservoir for caustic flooding.

When a multivalent cation is present, the ion-binding between carboxyl groups and cations has to be included [25,26]. For example, the charge of the bitumen-water interface in an aqueous CaCl$_2$ solution can now be expressed by the combination of equations (8a) and (8b) together with

$$RCOO^- + Ca^{2+} \Leftrightarrow RCOOCa^+ \qquad (10a)$$

and

$$K_{Ca} = \frac{(RCOOH^-)\,(Ca^{2+})_s}{(RCOOCa^+)} \qquad (10b)$$

where K_{Ca} is the binding constant of Ca^{2+} with carboxyl groups, and the subscript s again refers to the concentrations of Ca^{2+} in the vicinity of the surface (see Figure 11 for the difference in Ca^{2+} concentration near the surface and bulk solution). The measured and 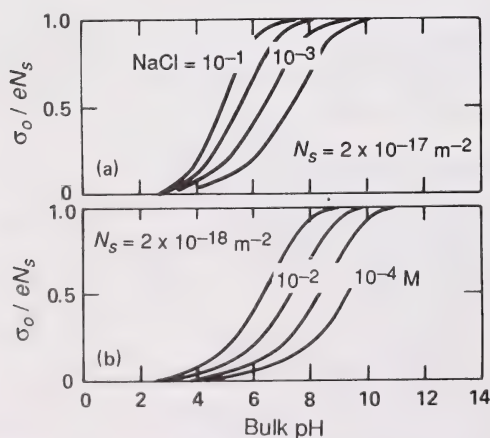calculated zeta potentials are shown in Figure 22 as a function of Ca^{2+} concentration in the presence of 10^{-2} M NaCl at pH 4, 7, and 10. Here, $pK_a = 0.5$ and $pK_{Ca} = 0.53$ (values for acetic acid) successfully explain the zeta potential calculated from measured mobilities, though there are some discrepancies in Ca^{2+} concentration below 10^{-3} M at pH 7 and 10.
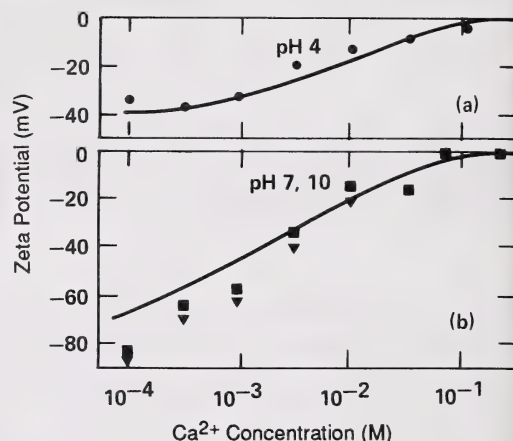
Figure 22. Measured mobilities (symbols) with those predicted (curves) as a function of Ca^{2+} concentration at pH 4(●), 7(■), and 10(▼) in the presence of 10^{-2} M NaCl.

Figure 21. Calculated fraction of dissociated surface groups, $-\sigma_o/eN_s$, as functions of pH in aqueous NaCl solutions at 25°C using (a) $N_s = 2 \times 10^{17}$ m^{-2} and (b) 2 $\times 10^{18}$ m^{-2}.

Stability diagram for bitumen-in-water emulsion
The stability of a bitumen-in-water emulsion can be predicted using zeta potentials calculated from the Ionizable Surface-Group model in conjunction with the DLVO theory [26]. First, the total potential energy, V_t, between a pair of bitumen droplets is calculated as a function of the separation distance, h, between the surfaces using the relation:

$$V_t = V_{rep}(h) + V_{attr}(h) \qquad (11)$$

where $V_{rep}(h)$ and $V_{attr}(h)$ are the double layer and van der Waals interactions. $V_{rep}(h)$ can be calculated using the zeta potential of the particles:

$$V_{rep}(h) = \frac{64\,\pi\,a n_o kT \gamma^2}{\kappa^2}\,\exp(-\kappa h) \qquad (12)$$

$$\gamma = \tan h\left(\frac{ze\zeta}{4kT}\right) \qquad (12b)$$

e retarded van der Waals attraction is best expressed

$$V_{attr}(h) = \frac{-Aa}{12h}\left[1-\frac{5.32h}{\lambda}\ln\left(1+\frac{\lambda}{5.32h}\right)\right] \qquad (13)$$

ere A is the Hamaker constant of 5.7×10^{-21} J for
men in water and λ is the London wavelength of
ghly 100 nm.

Figures 23a and 23b show examples of the
ulated $V_t(h)$ for bitumen particles in four different
centrations of NaCl and $CaCl_2$ at pH 6.0. The

particle radius was assumed to be 2.0 μm. The presence
of a deep secondary minimum of approximately –50 kT
for 3×10^{-1} M NaCl can be seen in Figure 23a.
Aggregates formed at the secondary minimum can be
redispersed with gentle agitation because of strong
repulsion at short distances. In contrast, agitation results
in the formation of tightly packed aggregates if there is
no energy barrier between particles (curves for 6×10^{-1}
M NaCl and 2×10^{-2} M $CaCl_2$).

By conducting similar calculations at various pHs
and electrolyte concentrations, the stability diagrams of
bitumen emulsions in NaCl and $CaCl_2$ solutions can be
constructed as a function of pH as shown in Figures 24a
and 24b. In the diagrams, the relative effects of the
valence and concentration of counter-ions, and the pH of
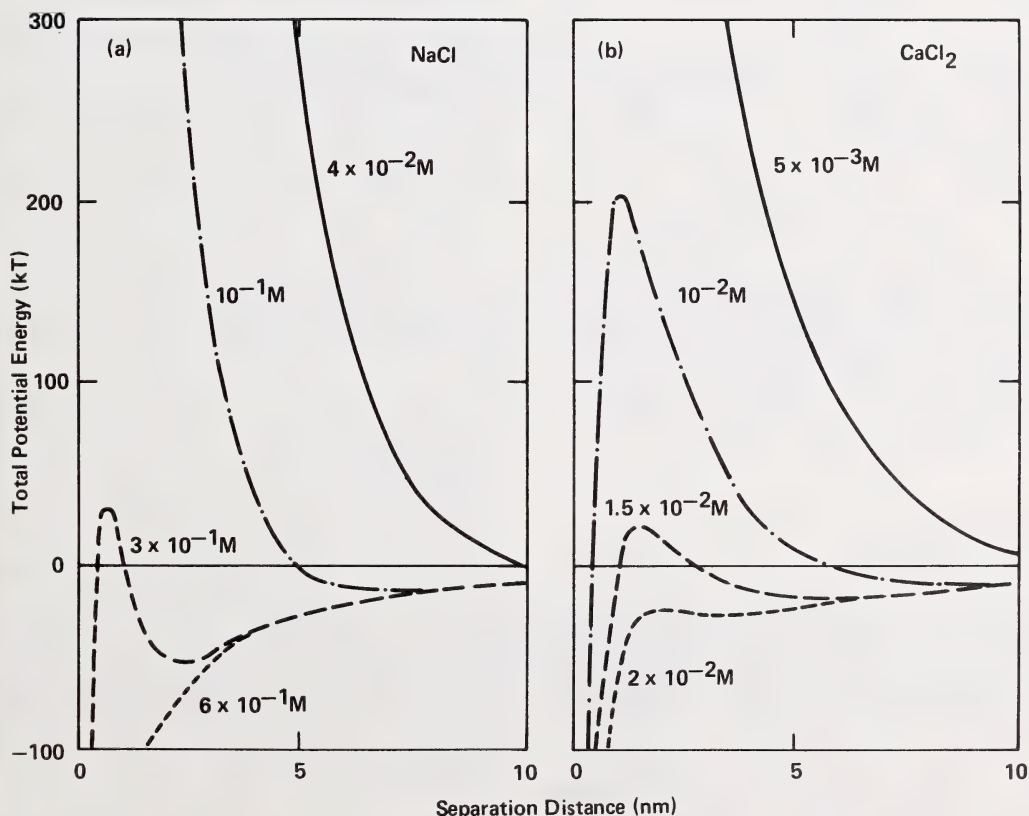the solution, on the emulsion stability can be clearly
seen.

Figure 23. Calculated total potential energy between bitumen droplets of 2 μm radius as a
function of the separation distance between the surfaces for NaCl (a) and $CaCl_2$ (b) solutions.

Results of experimentally determined coagulation behavior of bitumen emulsions in NaCl and CaCl$_2$ solutions were superimposed on the theoretical stability diagram in Figures 24a and 24b. Agreement between the measured and calculated stability of the bitumen emulsions is reasonable. The diagrams indicate the amount of acids or inorganic salts required to break the bitumen-in-water emulsion.
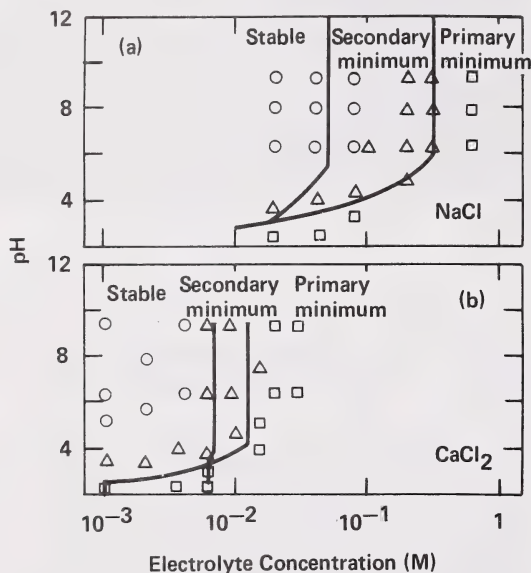

Figure 24. Theoretically predicted stability diagrams of the bitumen-in-water emulsions as functions of electrolyte concentration and pH in (a) NaCl and (b) CaCl$_2$ solutions. Symbols indicate the measured coagulation behavior of the emulsion: o – stable, Δ – weakly coagulated, ❏ – strongly coagulated.

Mineral-water interface

Silica. The electric properties of the mineral-water interface can be explained by the ionization of the surface groups [27]. For example, the silica surface becomes positively or negatively charged by one of the following surface ionization reactions:

$$-SiOH_2^+ \Leftrightarrow -SiOH + H^+ \qquad (14a)$$

and

$$-SiOH \Leftrightarrow -SiO^- + H^+ \qquad (14b)$$
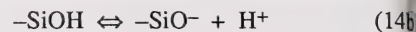
The two dissociation constants K_+ and K_- for these reactions are given by;

$$K_+ = \frac{(SiOH)\,(H^+)_s}{\left[SiOH_2\right]} \qquad (15a)$$

and

$$K_- = \frac{(SiO^-)\,(H^+)_s}{(SiOH)} \qquad (15b)$$

Figure 25 shows zeta potentials of silica in KNO$_3$ solutions reported by Wiese et al. [28]. The silica was cleaned with nitric acid and subsequently aged at 25 to 35°C for long periods of time in distilled water. Lines in the Figure demonstrate that the ζ vs pH relations can be adequately explained using the values of $pK_+ = -2.2$, $pK_- = 7.8$, and $N_s = 1 \times 10^{18}$ m^{-2} together with the relation of $x = -\log C$ (nm), where C is the concentration of electrolyte in mol/L.

Figure 25 indicates that the net charge of the silica surface is zero (point of zero charge, pzc) at pH 2.8. At pH values above pzc the surface has a net negative charge, while at pH values below pzc the surface has a net positive charge. Typical pzc values for clay minerals are given in Table 3 [29]. It is important to note that the values obtained are often affected by the presence of impurities, previous history including pretreatments, the method of storing and aging, and the extent of aging. For example, Figure 26 shows that the pzc of quartz can be raised from pH 2 to pH 6 by leaching it in hydrofluoric acid solution [29]. Upon aging the HF leached quartz in water, the pzc can be brought to its original value, but only over a period of several days. Washing the minerals with NaOH or hot aqueous solutions also produces similar long-term effects.

The effects of Ba^{2+} on zeta potentials for the silica surface are shown in Figure 27 [28]. Again, a pzc of about pH 2.8 indicates no chemical interaction of Ba with the silica surface at pH < 7 to 8. Wiese et al. [28] reported no significant adsorption of Ba^{2+} until pH 9 to 9.5. As shown in Figure 28, the presence of La^{3+} causes a shift in the pzc, indicating the chemisorption of La on the silica surface.

Carbonate. Zeta potentials calculated from measured mobilities for carbonate particles [30] are shown as
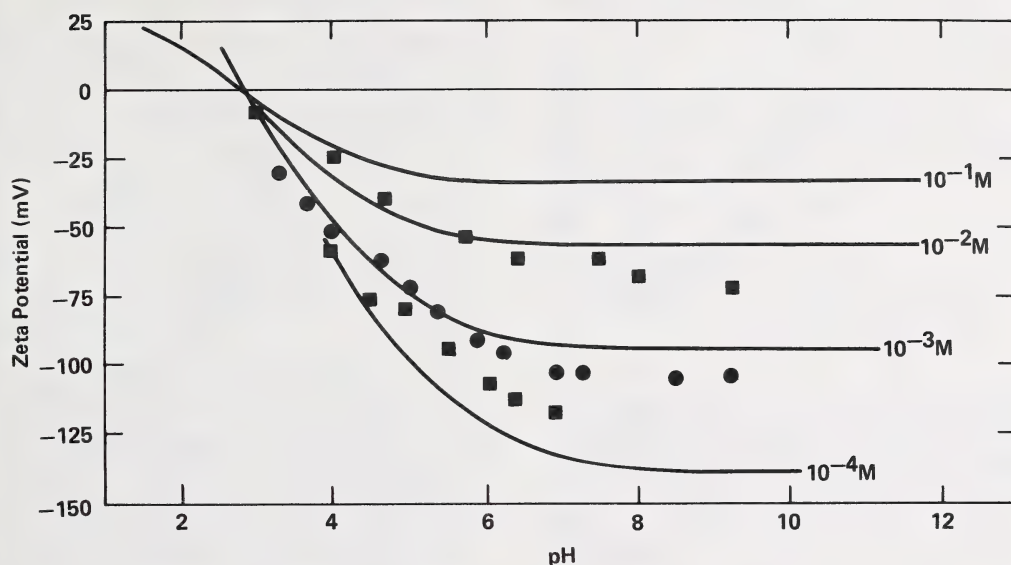
Figure 25. Zeta potentials of quartz capillary tube in KNO_3 solution calculated from measured streaming potential [28], and those predicted using Equations (12) and (13).

Table 3. Points of zero charge (pzc) or isoelectric points (iep) of various typical minerals.

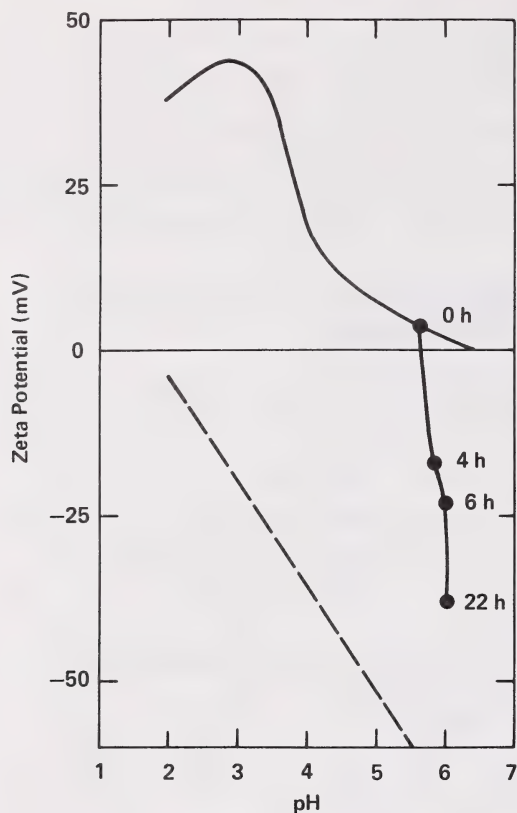| Minerals	pzc or iep
Quartz, SiO_2	pH 2-3.7
Rutile, TiO_2	pH 6.0
Corundum, Al_2O_3	pH 9.0
Magnesia, MgO	pH 12.0
Fluorapatite (natural), $Ca_5(PO_4)_3(F,OH)$	pH 6
Fluorapatite (synthetic)	pCa 4.4, pF 4.6, $pHPO_4$ 5.22
Hydrozyapatite, $Ca_5(PO_4)_3(OH)$, synthetic	pH 7-7.15, $pHPO_4$ 4.19-4.48
Calcite, $CaCO_3$	pH 9.5
Barite, $BaSO_4$	pBa 6.7
Silver iodide, AgI	pAg 5.6
Silver sulfide, Ag_2S	pAg 10.2

Figure 26. Zeta potentials of quartz treated with HF and then with hot NaOH solutions as a function of pH without aging, and at pH 6 after 4, 6, and 22 h of aging. Dashed line is for equilibrium values obtained for HNO_3^- treated with quartz, for comparison.

Figure 27. Same as Figure 25 but in $Ba(NO_3)_2$ solutions.
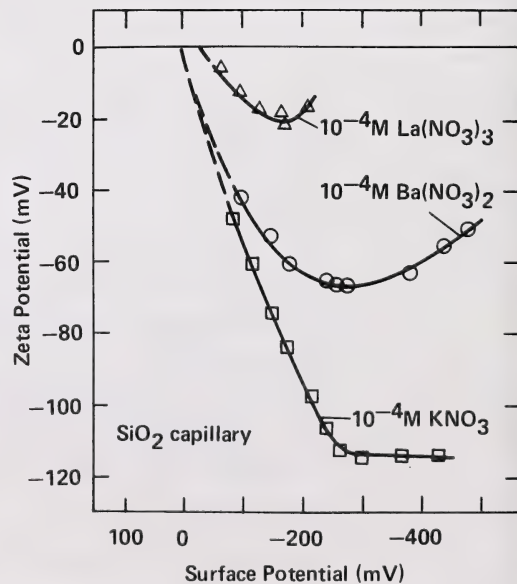
Figure 28. Same as Figure 25 but in $La(NO_3)_3$ solutions.

function of pH in 10^{-2} M NaCl in Figure 29 and as a function of $CaCl_2$ concentration in the presence of 10^{-2} M NaCl at pH 7.0 and 9.0 in Figure 30. For electrophoresis measurement, an oil-free core was dry-ground using a mortar and pestle to obtain particles between 1 and 10 μm diameter. In comparison, zeta potentials for Athabasca sand grains (which are over 90% quartz) [31] are also included in these figures. Although the carbonate-water interface is negatively charged at pH 6, the magnitude of the negative ζ is very small compared to those for the Athabasca sand-water interface. Zeta potentials for the carbonate particles become positive at $CaCl_2$ concentrations $>10^{-2}$ M at pH 7 and 2×10^{-3} M at pH 9. The results for the Athabasca sand grains show the zeta potential is negative even in 10^{-1} M $CaCl_2$.
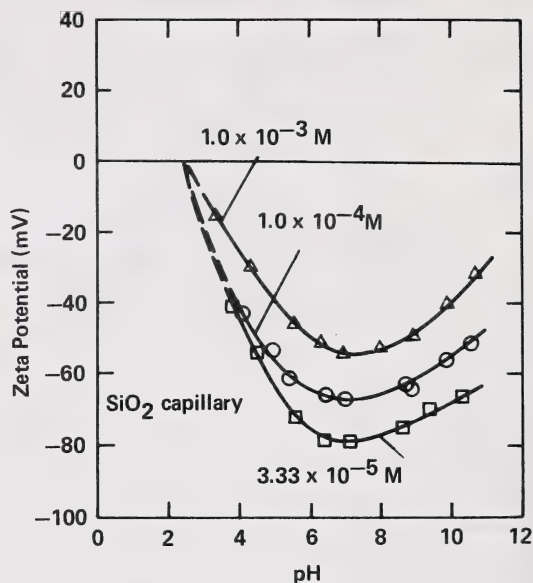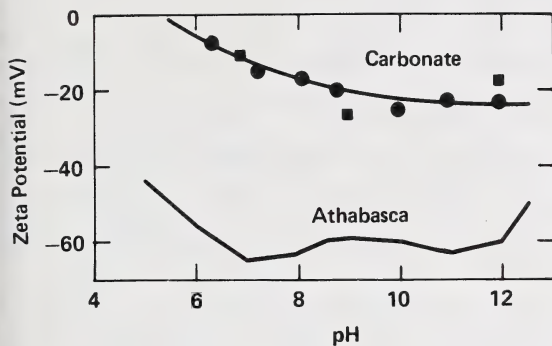
Figure 29. Zeta potentials of ground carbonate particles (solid circles) in 10^{-2} M NaCl as a function of pH. Solid squares indicate ζ obtained after treating the particles in an NaOH solution of pH 11.5 for 3 d [30]. Results of Athabasca sand grains measured under the same conditions are also included for comparison (no data).
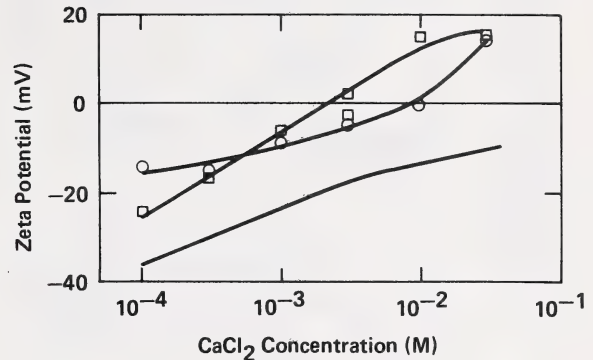

Figure 30. Zeta potentials of carbonate particles as a function of $CaCl_2$ concentration at pH 7 (circles) and pH 9 (squares) in the presence of 10^{-2} M NaCl [30]. The solid line (no data) is for Athabasca sand grains at pH 11.5.

Kaolinite. The edges and faces of kaolinite particles have distinctly different electric properties. According to Williams and Williams [32]:

• The edge is composed of exposed silica and alumina layers and is net positive at low pH and negative at high pH with a pzc in the range 5 to 8.

• The face is negatively charged throughout the pH range as a result of a small degree of isomorphous replacement of cations within the crystal.

Estimated zeta potentials for the edge of kaolinite by linear combination of quartz and α-alumina [32], are plotted in Figure 31; the measured ion adsorption from 5 x 10^{-3} M NaCl shown in Figure 32 [33] quantitatively agrees with the prediction. Electrophoretic mobilities of homoionic Na-kaolinite particles are shown in Figure 33 as a function of pH in 10^{-4}, 10^{-3}, and 10^{-2} M NaCl [32]. The preparation of the Na-kaolinite involved repeated washing of the clay in 1 M NaCl at pH 3, and washing with distilled water. At pH < 7 the faces and edge will be oppositely charged, and their contributions to the mobility of the particle depends on the axis ratio of the particles.

Mobilities of Na-kaolinite at pH 7.0 and Ca-kaolinite at pH 6.0 are shown in Figure 34 as a function of $CaCl_2$ concentration [34]. Ca-kaolinite was prepared by equilibrating the clay with 2 M $CaCl_2$ solution. Results indicate a strong interaction of Ca^{2+} with the kaolinite surface (ion-exchange).
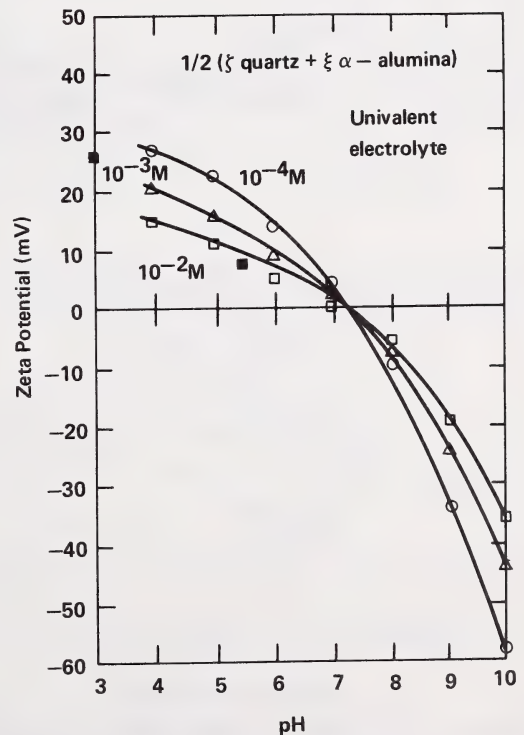

Figure 31. Estimated zeta potentials for edge of Na-kaolinite particles [32].
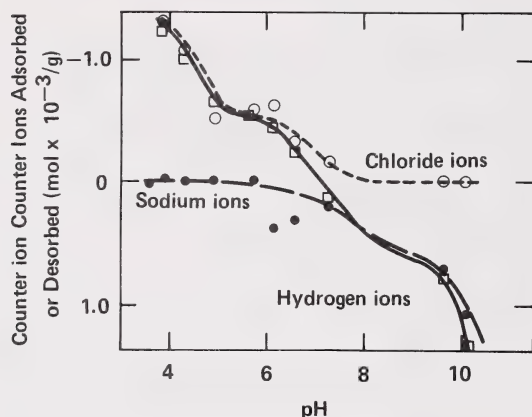
Figure 32. Ion adsorption on the edges of Na-kaolinite from 5 x 10^{-3} M NaCl solution over the pH range 4 to 10 [33].
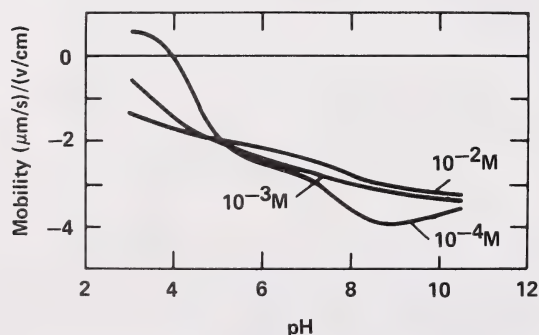

Figure 33. Electrophoretic mobilities of Na-kaolinite as functions of pH in 10^{-4}, 10^{-3}, and 10^{-2} M NaCl [32].
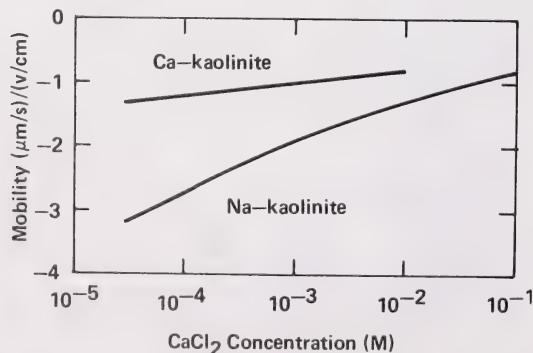
Figure 34. Electrophoretic mobilities of Ca-kaolinite at pH 6 and Na-kaolinite at pH 7 as functions of $CaCl_2$ concentration at 25°C [34].

Modes of particle association. When a suspension of clay particles flocculates, three different modes of particle association may occur: face-to-face (FF), edge-to-face (EF), and edge-to-edge (EE), depending upon pH and electrolyte concentrations. Modes of particle association in clay suspensions, and terminology are illustrated in Figure 35 [35]. The physical results of the three types of association are quite different. At low pH values (below the pzc of the edge surface of kaolinite) when the edges of the particles are positively charged, an electrostatic attraction is promoted between the edges and the negatively charged faces, leading to a voluminous card-house structure. At high ionic strengths all electrical double layers are compressed and coagulation is promoted. The system of lowest free energy is one in which the particles are associated in a face-face fashion to produce so-called card-pack aggregates. Under conditions of low ionic strength, at the pH value of the pzc of the edge surface of the kaolinite particle, the most favorable mode of particle-particle interaction would be an edge-to-edge association.

Figure 35. Modes of particle association in cla suspensions, and terminology used

Rheological and sedimentation properties. The rheological behavior of a kaolinite suspension depends strongly on particle association. Viscosit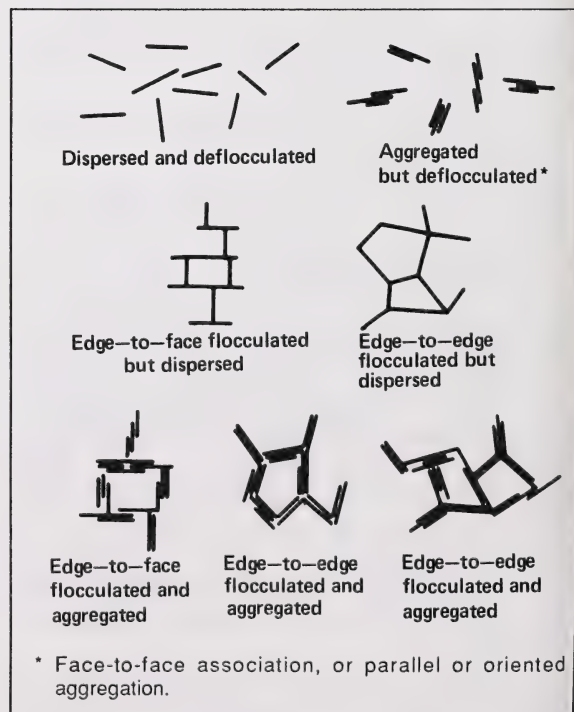y versus pH curves at a constant rate of shear for a 5 g/100 mL suspension of Na-kaolinite in 10^{-4} M NaCl [33] is shown in Figure 36. The viscosity reached a maximum at about pH 5.75 due to the formation of the card-house structure, and then decreased rapidly with increasing pH. The extrapolated regions of the curve at high pH values appear to approach a single point and indicate that the suspension becomes completely Newtonian at pH 11.5.

Changes in the Bingham yield stress of kaolinite suspensions as a function of pH at low ionic strength are schematically illustrated in Figure 37 in terms of the mode of particle interactions [36]. The effect of NaCl concentration on the measured Bingham yield stress [36] and sedimentation volume [37] of the kaolinite suspensions (9 wt%) is shown in Figures 38a and 38b. These results indicate that the face-to-edge coagulated structure of high apparent viscosity and sedimentation volume formed at pH < 7 changes into the face-to-face mode at NaCl concentrations 0.12 M.

The effects of NaCl, Na_2SO_4, $CaSO_4$, and $Ca(NO_3)_2$ on the Bingham yield stress of kaolinite suspensions (9 wt%) at pH 5.0 are compared in Figure 39 [37]. $CaSO_4$ and Na_2SO_4 have a more pronounced effect upon the reduction of the yield stress than NaCl or $Ca(NO_3)_2$ by converting edge-to-face structures into the face-to-face form (here, bivalent anions are counter-ions to the positively charged edges).

Montmorillonite. The measured mobilities of sodium montmorillonite particles [38] as a function of pH in various concentrations of NaCl are shown in Figure 40. Very little variation of mobility with pH was observed, suggesting that the edge sites do not make any substantial contribution to the charge on mont-morillonites, and that the electric properties are dominated by the charges on the face. This can be explained by the fact that montmorillonite particles are plate-like with a thickness of only about 1 nm, which is much smaller than the double-layer thickness. Thus, the negative electric field emanating from the particle face spills over into the edge region, especially at low electrolyte concentrations [39]. Kasperski et al. [40] explained the measured high viscosity of dilute montmorillonite suspensions in terms of the high degree of particle interactions.

Figure 41 shows mobilities of Na-montmorillonite/ Na-kaolinite mixtures (0.03 to 0.11 mass ratio in
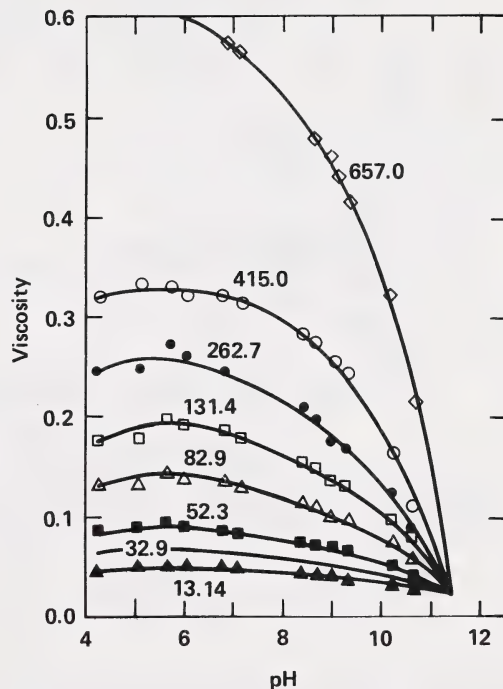
Figure 36. Viscosity versus pH for 5 g/100 mL of Na-kaolinite in 10^{-4} M NaCl solution at constant rate of shear (s^{-1}) [33].
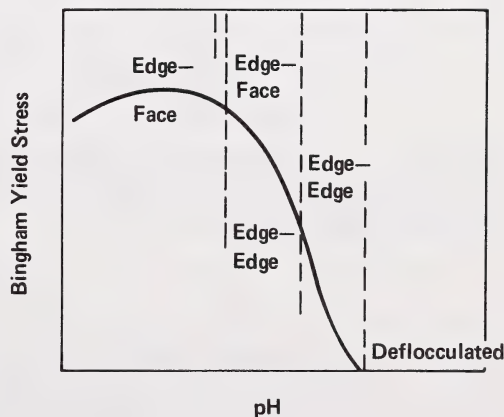
Figure 37. Interpretation of the effect of pH on the Bingham yield stress of kaolinite suspensions in terms of the mode of particle interactions [36].
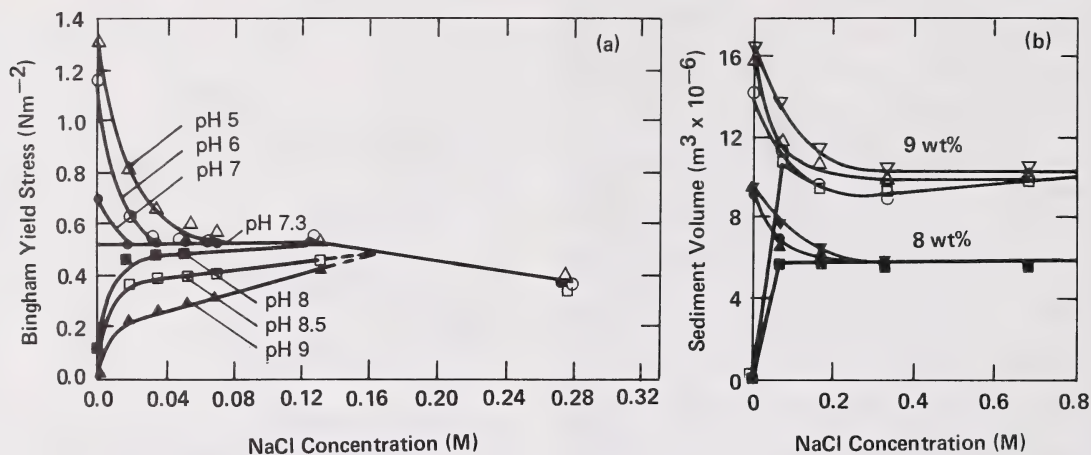
Figure 38. (a) Bingham yield stress (9 wt%) and (b) sedimentation volume of Na-kaolinite suspensions as functions of NaCl concentration at various pH [36,37].
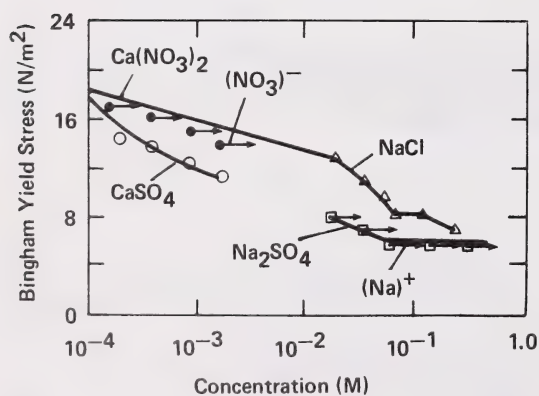
Figure 39. Comparison of the effect of NaCl, Na$_2$SO$_4$, CaSO$_4$, and Ca(NO$_3$)$_2$ on the Bingham yield stress of Na-kaolinite (9 wt%) at pH 5 [36].
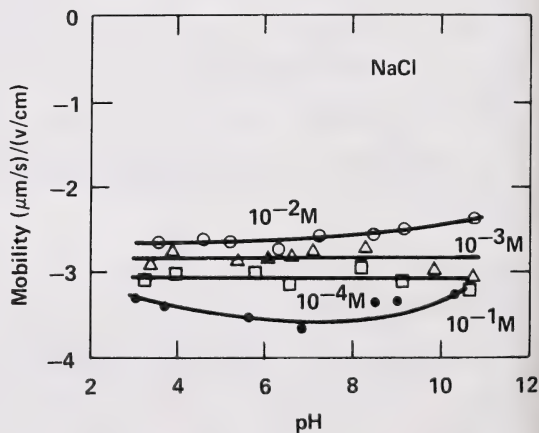
Figure 40. Electrophoretic mobilities of Na-montmorillonite particles as functions of pH in NaCl solution: □ – 10^{-4} M, ▲ – 10^{-3} M, ○ – 10^{-2} M, ● – 10^{-1} M.

suspensions) in 10^{-4} M NaCl as a function of pH [34]. Although the mixed suspensions consist mostly of Na-kaolinite, the measured mobilities are similar to those for pure Na-montmorillonite shown in Figure 40 rather than those for pure Na-kaolinite (see Figure 33). This is explained by adsorption of montmorillonite particles on kaolinite surfaces. Recent viscosity measurements of

Na-montmorillonite/Na-kaolinite mixtures by Kaspersk et al. [40] also support this explanation.

Illite. Very little is known of the electrokineti properties of other clay minerals. Figure 42 show mobilities for illite in 10^{-4} M NaCl as a function of pl as reported by Srinivasan [34].
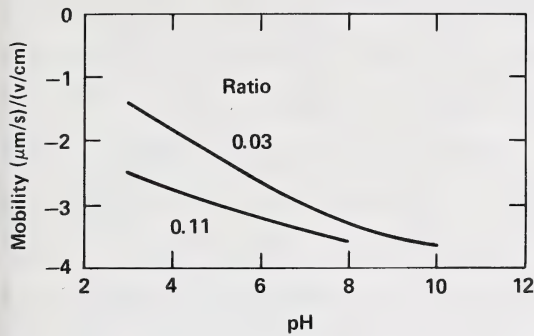
Figure 41. Electrophoretic mobilities of Na-montmorillonite/Na-kaolinite mixtures as functions of pH in 10^{-4} M NaCl [34].
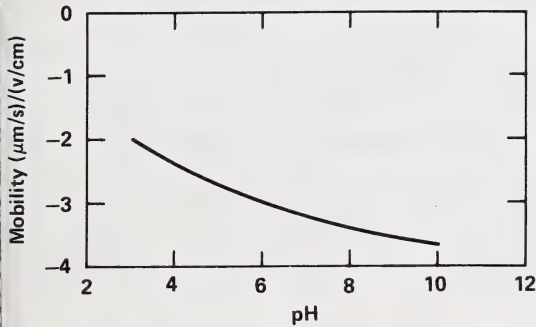
Figure 42. Electrophoretic mobilities of Na-illite as a function of pH [34].

WETTING BEHAVIOR

The determination of reservoir wettability and its effect on oil recovery are long-standing problems in reservoir engineering. Many researchers maintain that oil recovery is greatest under water-wet conditions, while others have maintained that wetting conditions other than strongly water-wet may be preferable. The fractional wettability concept assumes that reservoir mineral surfaces are composed of areas that are water-wet and areas that are oil-wet. Combinations of the oil-and water-wet areas result in surfaces of intermediate wettability. A second concept assumes reservoir surfaces to have a uniform wettability describable in terms of a contact angle according to the equation of Young-Dupre which relates the surface energies

$$\gamma_{os} - \gamma_{ws} = \gamma_{ow} \cos \theta_c \qquad (16)$$
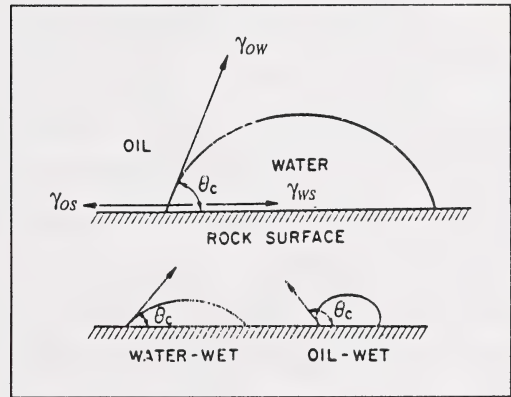
where γ_{os} = interfacial energy between the oil and solid, mN/m,

γ_{ws} = interfacial energy between the water and solid, mN/m,

γ_{ow} = interfacial energy (interfacial tension) between the oil and water, mN/m, and

θ_c = angle at the oil-water-solid interface measured through the water, degrees.

Contact angle measurement, usually on a smooth surface representing reservoir rock, is a common method of determining reservoir wettability. Contact angles less than 90° indicate a preferential water-wet condition, whereas contact angles greater than 90° indicate preferential oil-wet conditions. In theory, contact angle measurements can be used to quantify the degree of wetting of a reservoir surface. In practice, there are tremendous difficulties in reproducing contact angle measurements. Considering the added complexity that reservoir pore surfaces may not correspond well to carefully prepared smooth mineral surfaces used for measurements, it is unlikely that these measurements can be reliable as quantitative indicators for wettability.

Several types of laboratory tests have been described [41] which involve determining which fluid will displace the other from a representative reservoir sample by imbibition displacement tests. For bituminous sands we recommend a quick test involving the placement of a core sample in a test tube containing an aqueous medium representative of reservoir conditions. If the density of the oil is greater than H_2O, D_2O is used. The sample tube is then placed overnight in an oven at about 70°C. Preferential water-wet conditions are indicated if a portion of the oil is displaced and appears as a layer above the water phase.

Fines or solids which are wetted and displaced with the oil can usually be seen by microscopic examination of the oleic phase. The method can also be used with extracted sand. However, if solvents were used in the extraction process, restoration of the natural state is necessary. Ivory et al. [42] found that by heating sand from the Clearwater deposit at 300°C overnight, the water-wet characteristics could be restored. Cuiec [43] proposed the use of acidic and basic solvents for sandstone and limestone samples, respectively.

An alternate method of determining the wettability of bituminous samples has been described by Takamura and Chow [31]. In this method a thin layer of oil sand is placed on a microscopic slide equipped with a heating stage. Aqueous solution is then placed on the surface of the sand grains and the system is heated to about 70°C. If the sand is water-wet, the added water will displace oil from the surfaces of the sand grains and the oil will form in spherical droplets.

It has long been recognized that the single most fortunate aspect of the Athabasca sands is the aqueous film surrounding the sand grains. Recently, significant advances have been made in understanding the role of thin water films in oil sand separation [31]. Takamura [44] proposed a microscopic structure of oil sands, shown in Figure 43 [44] which quantified this picture and has a physico-chemical basis. Three types of aqueous domains were identified:

(a) Pendular rings of water at the grain-to-grain contact points. This accounts for more than 95% of the total amount of water in rich oil sands which contain virtually no fines.

(b) Water contained in fine clusters. The amount varies with fines content and mode of distribution.

(c) A ~10-nm water film separating the mineral grains from the bitumen. Less than 5% of the total water is contained in this film.

Since it is very likely that the reservoir sands were deposited in an aqueous environment, capillary forces prevented the displacement of type (a) and (b) water when oil invaded the reservoir. The stability of the thin water film is due to the disjoining pressure, which is a composite of electric double-layer repulsive forces and van der Waals attractive forces. A nuclear magnetic relaxation technique was used [45] to identify two types of water in oil sands and could in principle be used for determining the portions of the sand surface area that are preferentially water-wet or oil-wet.

CAPILLARY PRESSURE

In 1941, Leverett [46] introduced the concept of capillary pressure for oil industry use and proposed a dimensionless capillary pressure function, the Leverett J-function, as a method for normalizing capillary pressure data for porous media with similar lithology. The normalized capillary pressure, $J(S_w)$, is defined as:

$$J(S_w) = \frac{P_c}{\gamma \cos \theta} \cdot \sqrt{\frac{k}{\phi}} \qquad (17)$$

where P_c is capillary pressure, γ is the interfacial tension, θ is the contact angle, k is the absolute permeability, and ϕ is the porosity. Since questions will always remain as to the applicability of contact angle measurements for reservoir pore systems, rule-of-thumb values are often adequate. These values are: 40° for mercury-air, 0° for oil-air, 0° for water-air, and 30° for oil-brine (water-wet rock).

For intermediate wetting systems, the use of a contact angle of 30° for normalizing capillary pressure data is inadequate. Recently, Omoregie [47] suggested using both air-brine and oil-brine capillary pressure data on the same sample. Using a contact angle of 0° for normalizing the air-brine data, the contact angle needed to make the normalized oil-brine data equivalent to the air-brine data is calculated. The cosine of that contact angle can be used as a wettability index.
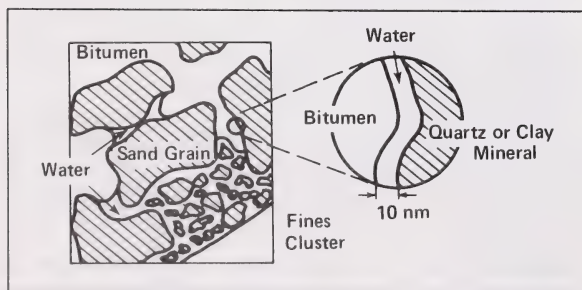

Figure 43. Schematic diagram showing a structural model of Athabasca oil sand. The water in the oil sand appears in three forms: as pendular rings at grain-to-grain contact points, as a ~ 10 nm thick film which covers the sand surfaces, and as water retained in fines clusters. The remaining void space is occupied by bitumen.

Reviews of the classical methods of capillary pressure measurement are available in the petroleum literature. The most commonly used methods are the centrifuge, mercury porosimetry, and porous plate (desaturation under pressure). Details of the experimental techniques are available elsewhere [47,48]. Capillary pressure properties depend on pore geometry, and data can be used to evaluate permeability, pore size distribution, differences in lithology, and formation damage. Samples of unconsolidated porous media present considerable experimental difficulties since they are subject to sample grain rearrangement during coring, packing, and application of overburden pressure.

For oil sand systems, only preliminary capillary pressure data are available. Figure 44 shows the capillary pressure versus saturation relationships representing the drainage of water (wetting-phase) from sand which is becoming saturated with bitumen. The centrifuge data [49] were obtained using solvent-extracted Cold Lake bitumen displacing 0.02 M NaCl in

D_2O at 90°C. The mercury porosimetry data [50] were obtained using a solvent-extracted high-grade Athabasca core, and plotted assuming:

$$\theta_{Hg\text{-}air} = 140° \text{ and } \gamma_{Hg\text{-}air} = 480 \text{ mN/m}$$

$$\text{and } \theta_{oil\text{-}water} = 30°$$

and

$$\gamma_{oil\text{-}water} = 13 \text{ mN/m at 90°C}$$

The assumption of interconversion of capillary pressure relationships between various pairs of wetting and nonwetting fluids is implied when using the Leverett function. Agreement between the two methods is good. However, there is poor agreement between the
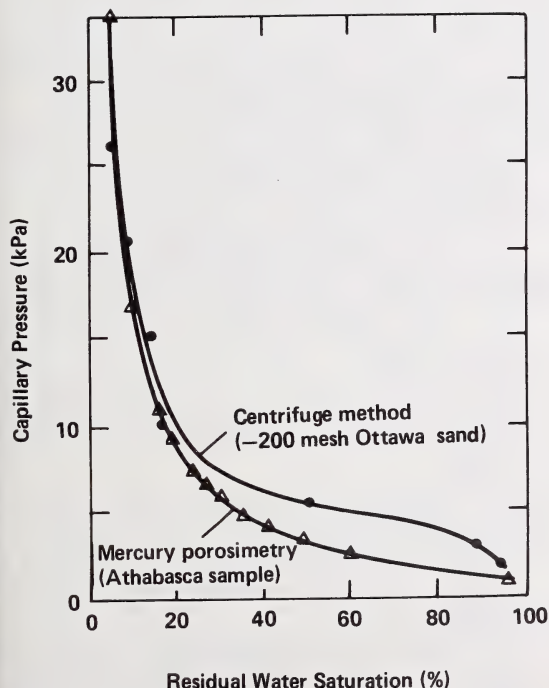

Figure 44. Capillary pressure versus saturation by wetting liquid during drainage for Dean-Stark extracted oil sand sample (+325 mesh), and −200 mesh Ottawa sand.
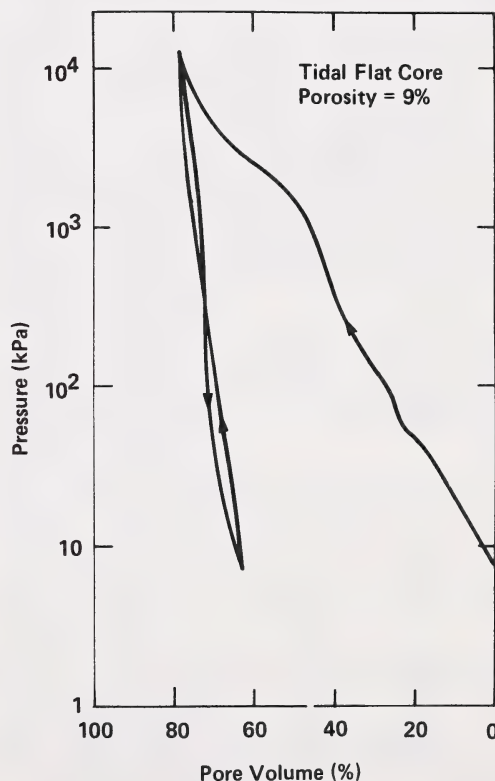
Figure 45. Mercury porosimetry capillary pressure curve for a carbonate core of relatively low matrix porosity.

results shown in Figure 44 and air-brine centrifuge data measured by Briggs [50] using –200 mesh silica sand. Conversion of the air-brine data to bitumen-water values results in drainage capillary pressure values that are lower about a factor of two.

A number of mercury capillary pressure injection tests on Grosmont carbonate rocks were conducted by Belanger-Davis [51]. Figures 45 and 46 show selected examples of the types of relationships obtained for a tidal flat core of low matrix porosity, and a shallow marine (shoal zone) core of higher porosity, respectively. Large hysteresis effects are observed between the first and second drainage curves, while hysteresis between the second drainage and imbibition curves is much smaller. The data can be converted to bitumen-water capillary pressure as described above and are shown in Figure 47 for the first drainage curve of Figure 46. An interfacial tension of 6 mN/m and contact angles of 30° and 60° were used to estimate conditions at 200°C.

Figure 47. Capillary pressure versus saturation during drainage by wetting liquid for carbonate sample; an interpretation from mercury porosimetry data of Figure 46.

Figure 46. Mercury porosimetry capillary pressure curve for a carbonate core of relatively low matrix porosity.

REFERENCES

1. A.W. Adamson, "Physical chemistry of surface," 3rd ed., Ch. 1, John Wiley, New York (1976).
2. P.C. Hiemenz, "Principles of colloid and surface chemistry," 2nd ed., Marcel Dekker, New York (1986).
3. D.J. Shaw, "Introduction to colloid and surface chemistry," Ch. 4, Butterworths, London (1979).
4. C.D. Manning, C.V. Peshek, J.E. Puig, Y. Secto,. H.T. Davis and L.E. Scriven, "Measurement of interfacial tension," DOE Report #DOE/BC/10116-12 Nov (1983).
5. J.F. Padday, in Surface and Colloid Science, E. Matigvic Ed., Wiley Interscience, New York, 1 (1969).
6   L.L. Schramm, R.G. Smith and J.A. Stone, A surface tension method for the determination of aniomic surfactants in hot water processing of Athabasca oil sands, Colloids and Surfaces, 11, (1984) 247.
7. A.M. Potoczny, E.I. Vargha-Butler, T.K. Zubovits and A.W. Neumann, Surface tension of bitumen I. Temperature dependence, AOSTRA J. Res., 1 (1984) 107.
8. Z.M. Potoczny, E.I. Vargha-Butler, T.K. Zubovits and A.W. Nuemann, Surface tension of bitumen II.

Solvent and fractionation effect, AOSTRA J. Res., 1 (1984) 118.

9. C.W. Bowman, Molecular and interfacial properties of Athabasca tar sands, 7th World Petroleum Congress, Mexico (1967).

10. E.E. Isaacs and D.N. Morrison, Interfacial films at the Athabasca bitumen/water interface, AOSTRA J. Res., 2 (1985) 113.

11. A.K. Mehrotra, C-K Yee and W.Y. Svrcek, Prediction of surface tension of Athabasca bitumen, Can. J. Chem. Eng., 63 (1985) 340.

12. E.E. Isaacs and K.F. Smolek, Interfacial tension behavior of Athabasca bitumen/aqueous surfactant systems, Can. J. Chem. Eng., 61 (1985) 233.

13. D.L. Flock, T.H. Le and I.P Gibeau, The effect of temperature on the interfacial tension of heavy crude oils using the pendent drop apparatus, J. Can. Pet. Tech., (1986).

14. E.E. Isaacs, Surfactants and foams in thermal recovery from oil sands, Assessment report to AOSTRA, Nov (1985).

15. T. Boogmans, D.L. Flock, H. Elmayergi, E.E. Isaacs, J. Quehl and H. Schroeder, A laboratory investigation of steam solvent extraction of heavy oils and bitumen for in-situ application, annual report to AOSTRA (Agreement no. 8), Mar (1978).

16. M.H. Akstinat, Surfactants for enhanced oil recovery processes in high-salinity systems — product selection and evaluation, Proceedings of the European Symposium on Enhanced Oil Recovery, Bournemouth, England, Sep (1981).

17. E. Rubin and C.J Radke, Dynamic interfacial tension minima in finite systems, Chem. Eng. Sci. 35 (1980) 1129.

18. I. Layrisse M. Rivas and S. Acvendo, Isolation and characterization of natural surfactants present in extra heavy crude oils, J. Disp. Sci. and Tech., 5 (1984) 1.

19. K.C. Khulbe, V. Hornof and G. Neale, Interfacial activity of heavy oil and its maltene constituents against caustic solutions, AOSTRA J. Res., 2 (1985) 95.

20. Z.N. Potoczny, "Determination of surface thermodynamic parameters of tar sand systems," M.A.Sc. thesis, Univ. of Toronto (1984).

21. D.W. Fuerstenau and T.W. Healy, Principles of mineral flotation, Ch. 6, in "Adsorptive bubble separation techniques," Academic Press, New York and London (1972).

22. R.J. Hunter, Measurement of electrokinetic parameters, Ch. 4, in "Zeta Potential in colloid science, principles and application," Academic Press, London, New York, Toronto, Sydney and San Francisco (1981).

23. R.W. O'Brien and L.R. White, Electrophoretic mobilty of a spherical colloidal particle, J. Chem. Soc. Faraday Trans. 2, 74 (1978) 1607.

24. R.S. Chow and K. Takamura, Electrophoretic mobilities of bitumen and conventional crude oil-in-water emulsions using the laser doppler apparatus in the presence of multivalent cations, J. Colloid Interface Sci. 125, 1 (1988) 212.

25. K. Takamura and R.S. Chow, The electric properties of the bitumen/water interface, Part II, Application of the ionizable surface-group model, Colloids and Surfaces, 15 (1985) 35.

26. K. Takamura, R.S. Chow and D.L. Tse, Prediction of electrophoretic mobilities and the coagulation behavior of bitumen-in-water emulsions in aqueous NaCl and $CaCl_2$ solutions using the Ionizable Surface-Group Model, Proc. Sym. on Flocculation in Biotechnology and Separation Systems, San Francisco, CA, Jul (1986).

27. T.W. Healy and L.R. White, Ionizable surface group models of aqueous interfaces, Adv. Colloid Interface Sci., 9 (1978) 303.

28. G.R. Wiese, R.O. James and T.W. Healy, Discreteness of charge and solvation effects in cation adsorptin at the oxide/water interface, Disc. Faraday Soc., 52 (1971) 302.

29. P. Somasundaran and E.D. Goddard, Electrochemical aspects of adsorption on mineral solids in "Modern aspects of electrochemistry," B.E. Conway and J.O'M. Bockris, Eds., Plenum, New York and London (1979).

30. E. Isaacs, K. Takamura, D. Maunder and R. Chow, Report for the Alberta Oil Sands Technology and Research Authority, Calgary (1986).

31. K. Takamura and R.S. Chow, A mechanism for initiation of bitumen displacement from oil sand, Can. J. Pet. Tech., 22 (1983) 22.

32. D.J.A. Williams and K.P. Williams, Electrophoresis and zeta potential of kaolinite, J. Colloid Interface Sci., 65 (1978) 79.

33. A.W. Flegmann, J.W. Goodwin and R.H. Ottewill, Rheological studies on kaolinite suspensions, Proceedings of the British Ceramic Society, Jun (1969).

34. N. Srinivasan, J.J. Spitzer and L.G. Hepler, Electrophoretic properties of oil sands tailings and

constituent clays in aqueous suspensions, J. Pet. Tech. (1982) 25.

35. H. van Olphen, "An introduction to clay colloid chemistry," Wiley, New York (1977).

36. B. Rand and I.E. Melton, Particle interactions in aqueous kaolinite suspensions, I. Effect of pH and electrolyte upon the mode of particle interaction in homoionic sodium kaolinite suspensions, J. Colloid Interface Sci., 60 (1977) 308.

37. I.E. Melton and B. Rand, Particle interactions in aqueous kaolinite suspensions, II. Sedimentation volumes, J. Colloid Interface Sci., 60 (1977) 331.

38. I.C. Callaghan and R.H. Ottewill, Interparticle forces in montmorillonite gel, Disc. Faraday Soc., 57 (1974) 110.

39. R.B. Secor and C.J. Radke, Spillover of the diffuse double layer on montmorillonite particles, J. Colloid Interface Sci., 103 (1985) 237.

40. K.L. Kasperski, C.T. Hepler and L.G. Hepler, Viscosities of dilute aqueous suspensions of montmorillonite and kaolinite clays, Can. J. Chem., 64 (1986) 1919.

41. W.G. Anderson, Wettability literature survey — Part 2: Wettability measurement, J. Pet. Tech., Nov (1986) 1246.

42. J. Ivory, W.D. Gunter, P. Mikkelsen, K.N. Chhom, J. Hruschak and B. Tilley, Development and testing of a synthetic Cold Lake oil sand, Paper 86-37-77 presented at the Petroleum Society of CIM Meeting, Calgary, Jun (1986).

43. L.E. Cuiec, Resoration of the natural state of core samples, Paper SPE 5634 presented at the 50th Annual Meeting, Dallas, Sep (1975).

44. K. Takamura, Microscopic structure of Athabasca oil sand, Can. J. Chem. Eng., 60 (1982) 538.

45. W.T. Sobol, L.J. Schreiner, L. Miljkovic, M.E. Helene, L.W. Reeves and M.M. Pintar, NMR line shape — relaxation correlation analysis of bitumen and oil sands, Fuel, 64 (1985) 583.

46. M.C. Leverett, Capillary behavior in porous solids, Trans. AIME, 142 (1941) 152.

47. Z.S. Omoregie, Factors affecting the equivalency of different capillary pressure measurement methods techniques, Paper SPE 15384 presented at the 61st Technical Conference, New Orleans, Oct (1986).

48. J.W. Amyx, D. Bass and R.L. Whiting, "Petroleum reservoir engineering," 2nd ed. McGraw-Hill, New York (1960).

49. J.P. Briggs, "Preliminary measurement of capillary pressure with a prototype centrifuge cell," Alberta Research Council, May (1985).

50. A. Mar, In-situ recovery project ARC/AOSTRA Semi-annual report Apr–Sep (1980).

51. C.E. Belanger-Davis, "Mineralogical and petrophysical changes after steam injection in carbonate rocks of the Grosmont Formation, Alberta," AOSTRA-University Access Program.

52. S.M. Faroug Ali, J.M. Figueroa, E.A. Azuaji and R.G. Farqhuarson, Recovery of Lloyminster and Morichal crudes by caustic, acid and emulsion floods, Paper 78-29-35 presented at 29th Petroleum Society of CIM, Calgary, June (1978).
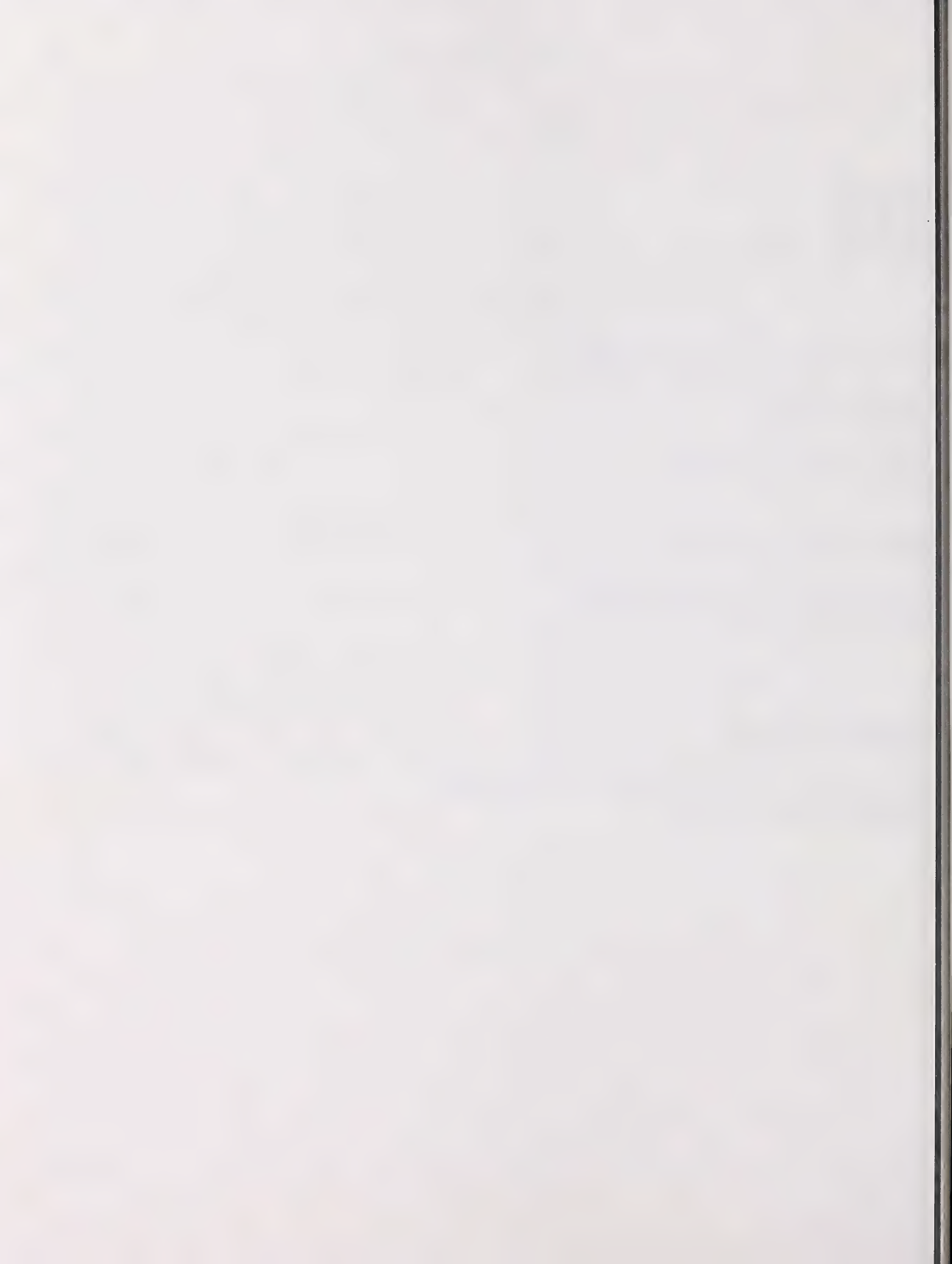
6

PHASE EQUILIBRIA AND PVT PROPERTIES

Benjamin C.-Y. Lu

Department of Chemical Engineering
University of Ottawa

Cheng-Tze Fu

Oil Sands and Hydrocarbon Recovery Department
Alberta Research Council

CONDITIONS OF EQUILIBRIUM

For phase equilibria, thermodynamics is concerned with the relations and differences between distinct equilibrium phases. The thermodynamic treatment of these properties is frequently carried out by means of equations of state, relationships between the pressure P, temperature T and volume V,

$$f(P, V, T) = 0.   \quad (1)$$

The treatment is applicable to the equilibrium properties, but not to the properties measured at the conditions of steady state, especially when the steady-state conditions are far removed from the equilibrium conditions. A suitable equation of state when combined with appropriate thermodynamic relations can be used to evaluate many properties of pure substances and mixtures, such as vapor pressure, liquid and vapor-phase densities, latent heat of vaporization, vapor-liquid equilibrium relations, isothermal changes in heat capacity, enthalpy, and entropy.

Considering a closed system at constant temperature T and pressure P, with P acting as the only external force, the Gibbs energy G of the system does not change in an infinitesimal reversible process. Hence, we have

$$dT = 0, \ dP = 0, \ dG = 0$$

at equilibrium. In other words, the criteria of equilibrium for a system containing different phases are thermal, mechanical, and chemical equilibrium. All phases must have the same temperature, the same pressure (provided they are not separated by a rigid barrier or by an interface of appreciable curvature), and the chemical potential of each chemical species in the system must be the same in all phases between which this species can freely pass. In terms of chemical potential μ, we have at equilibrium for π phases and N chemical species,

$$\mu_{i,\alpha} = \mu_{i,\beta} = \dots = \mu_{i,N} \quad (i = 1, 2, \dots N) \, (T, P). \quad (2)$$

The fugacity of a component in solution, $\hat{f}_i$, is defined by

$$\mu_i = \mu_i^o + RT \ln \hat{f}_i \quad (3)$$

where μ_i^o, the standard chemical potential of a pure component i at T, is a function of T only. An alternative expression,

$$\hat{f}_{i,\alpha} = \hat{f}_{i,\beta} = \dots = \hat{f}_{i,N} \quad (i = 1, 2 \dots N) \, (T, P) \quad (4)$$

may be used to replace Equation (2) as the criterion for phase equilibrium.

EXPERIMENTAL METHODS FOR MEASURING PHASE EQUILIBRIUM

An experimental determination of vapor-liquid equilibrium involves the measurements of T, P, and concentrations of both phases (vapor mole fraction y and liquid mole fraction x). It is necessary to separate samples of the liquid and vapor that are in true equilibrium. This approach of measuring T–P–x–y is required for systems involving heavy oils and bitumens.

The determination of the equilibrium compositions can be carried out at either isothermal or isobaric conditions. The frequently used methods include the recirculation method, the static method, the dew point and bubble point method, and the flow method. For bitumen-containing systems, internally consistent equilibrium values have been obtained by means of the recirculation and static methods at isothermal conditions.

In the determination of phase behavior of bitumens in the presence of gases and liquids, equilibrium is reached in the static method by mechanical mixing or by rocking the mixture in an equilibrium cell at constant temperature.

Lal et al. [1] used a two-litre Autoclave Model AFP 2005 as the equilibrium cell. Mixing of the fluids within the cell was achieved using a magnetic stirrer at a stirring rate of 900 rpm. The cell was usually left overnight to ensure that equilibrium was reached.

Robinson and Sim [2] used a stainless steel equilibrium cell with a maximum working volume of 200 mL. The bottom of the cell was closed by the piston of a Ruska-type positive displacement pump. The head at the top of the cell contained a stirring device and openings for pressure measurement, charging, and sampling. It was sealed by a glass-filled teflon (rulon) ring. Mixing within the cell was achieved using a belt-driven stirrer.

Fu et al. [3] used an equilibrium cell with mixing of its contents achieved through rocking the cell by means of a motor. A two-day period was required for the contents in the cell to reach equilibrium. In addition, Fu

et al. [3] used a vapor-recirculating apparatus for the determination of phase equilibrium values, reducing the time required to reach equilibrium.

Svrcek and Mehrotra [4] determined the solubility of gases in bitumen by means of a mixing cell, in which mass transfer between the gas and the circulating bitumen took place. A gear pump was used to draw bitumen from the bottom to the top of the cell.

A continuous-flow apparatus was presented by Radosz [5] for measuring high-pressure phase equilibria in systems containing supercritical gases and heavy hydrocarbons. Depending on the system, it took up to 30 min to reach a steady state with constant effluent stream compositions. The suitability of the apparatus for systems containing bitumen is being established.

Important features in the equilibrium studies include the design of the equilibrium cell, the degassing procedure in the charging step, the sampling techniques, the accuracy of phase composition analyses, the accuracy of temperature and pressure measurements, and the assurance that equilibrium conditions have been attained.

AVAILABLE SOURCES OF EXPERIMENTAL RESULTS

One of the enhanced oil recovery methods is to pump gas (for example, natural gas, carbon dioxide, or nitrogen) into the reservoir from an injection well. Some of the gas dissolves in the oil, causing it to flow more easily; the rest of the gas pushes the oil toward the production well. Application of this method to the in situ recovery of bitumen from oil sands has been considered by many researchers. Experimentally determined solubility data for gases in bitumen are of importance in this connection. Considerable work has been reported on solubility of pure gases, such as carbon dioxide, carbon monoxide, nitrogen, methane, and ethane, but solubility data reported for mixtures of gases are limited. The gas produced from the in situ combustion process can bring about the same desired benefits mentioned above, in addition to the increase of temperature that makes the bitumen less viscous.

In addition to solubility data, liquid density values are useful for the process design. The available sources of experimental results for these properties are summarized in this section.

Gas solubility data

The solubilities of gases in Alberta bitumens have been determined and reported in the literature. The experimental conditions and the number of data points reported up to 1985 are summarized in Table 1.

In addition, solubilities of hydrogen, carbon monoxide, and mixtures of hydrogen and carbon monoxide, in Athabasca bitumen have been determined by Lal et al. [1]. Numerical values [12] are presented in Table 2 as they were not included in the original publication.

Liquid densities

Bulkowski and Prill [13] reported the densities of four Athabasca bitumen samples with different treatment histories in the 273 to 423 K temperature range and developed the following linear relationship between temperature and density:

$$\rho_T = \rho_{T^\circ} - AT \qquad (5)$$

In Equation (5) ρ_T and ρ_{T° refer to the densities at temperatures T and T° (= 273 K), respectively. The quantity A is a constant and was assigned a value of 0.62 K^{-1}. The densities measured by Polikar [13] in the temperature range of 273 to 533 K for bitumen extracted from high-grade Athabasca oil sands can also be represented by Equation (5). A graphical representation of the data is shown in Figure 1.
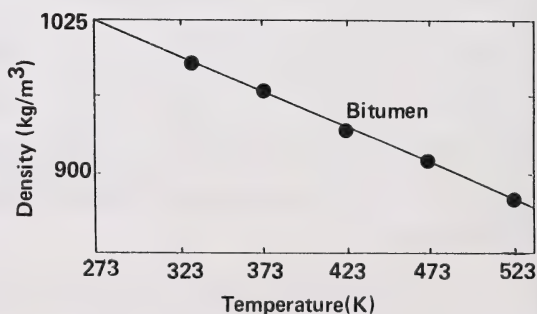

Figure 1. Athabasca bitumen density as a function of temperature [13].

The pressure effect on the density of Athabasca bitumen has been reported by Wallace [13] for a solvent extracted and a coker feed (hot water process) bitumen. The reported values are listed in Table 3. Over a wide

Table 1. A summary of reported experimental data for solubilities of gases in Alberta bitumen.

Bitumen	Gas	No. of data points	Temperature (K)	Pressure (MPa)	Reference
Athabasca	Nitrogen	7	403.2	4.069 – 11.454	[3]
		11	306.0 – 374.1	2.84 – 8.71	[4]
	Carbon monoxide	19	299.2 – 391.4	2.80 – 9.90	[6]
	Carbon dioxide	10	373, 423, 473	3.30 – 10.50	[2]
		6	373.2	4.974 – 8.136	[3]
		29	296.2 – 370.5	1.60 – 6.38	[4]
	Methane	30	299.4 – 373.9	0.88 – 9.77	[4]
	Ethane	6	373, 423, 473	3.22 – 10.54	[2]
		20	295.9 – 381.5	1.30 – 8.60	[6]
	Combustion gas (17% CO_2, 1% CH_4, 82% N_2)	22	300.2 – 372.9	1.94 – 10.01	[7]
Cold Lake	Carbon dioxide	9	373, 423, 473	3.489 – 10.372	[8]
Marguerite Lake	Carbon dioxide	31	284.7 – 377.7	1.37 – 6.70	[9]
Peace River	Nitrogen	15	295.8 – 372.7	3.02 – 9.1	[10]
	Carbon monoxide	12	296.2 – 373.7	3.03 – 9.35	[10]
	Carbon dioxide	21	295.4 – 380.2	1.54 – 6.21	[10]
	Methane	16	295.2 – 387.5	2.40 – 10.30	[10]
	Ethane	17	288.8 – 379.8	1.42 – 4.30	[10]
Wabasca	Nitrogen	13	296.4 – 370.2	3.08 – 10.20	[11]
	Carbon monoxide	11	296.2 – 375.0	3.02 – 9.67	[11]
	Carbon dioxide	18	294.6 – 423.2	1.36 – 6.62	[11]
	Methane	12	296.2 – 383.8	3.07 – 9.35	[11]
	Ethane	19	289.2 – 372.8	0.96 – 4.14	[11]

range of pressure (0.097 to 10.35 MPa), the maximum change in density is <2%.

The effects of temperature and pressure on Cold Lake bitumen have been determined by Fu et al. [13] for 373 to 473 K in the pressure range of 2 to 10 MPa. The reported values are listed in Table 4. The dependence of density on temperature can be described by Equation (5). The dependence of density on pressure is very slight as shown in Figure 2.

Nearly all the apparatus described earlier for the determination of gas solubilities in Alberta bitumens were equipped with provisions for density measurements. The densities of gas-saturated bitumens are available from the references listed in Table 1.

An attempt by Robinson [14] to correlate the effects of pressure and dissolved gas on the density of bitumen is illustrated in Figures 3 and 4, in which carbon dioxide in Athabasca bitumen was considered.
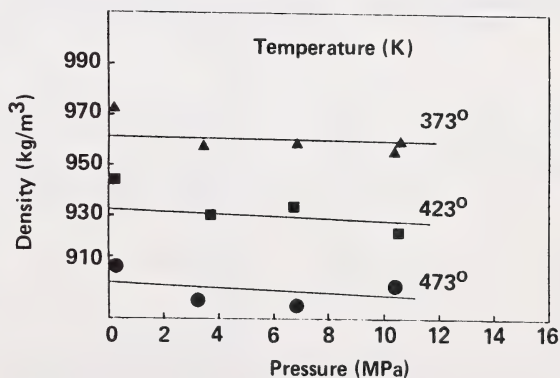

Figure 2. Liquid densities of Cold Lake bitumen [13].

Table 2. Experimental solubility values of hydrogen, carbon monoxide, and mixtures of hydrogen and carbon monoxide in Athabasca bitumen [12].

Solubility of hydrogen

Temperature (K)	Partial Pressure of H_2 (MPa)	Solubility of H_2 (wt%)	Temperature (K)	Partial Pressure of H_2 (MPa)	Solubility of H_2 (wt%)
473	4.896	0.0296	523	4.695	0.0321
	10.004	0.0562		8.713	0.0590
	13.733	0.0793		12.087	0.0819
	18.694	0.1076		14.794	0.1013
	22.996	0.1297		18.104	0.1242

Solubility of carbon monoxide

Temperature (K)	Partial Pressure of CO (MPa)	Solubility of CO (wt%)	Temperature (K)	Partial Pressure of CO (MPa)	Solubility of CO (wt%)
373	3.744	0.346	573	1.818	0.273
	6.893	0.610		3.470	0.515
	8.894	0.809		3.886	0.607
473	2.102	0.225		5.001	0.749
	2.931	0.288		5.312	0.784
	3.614	0.353		5.812	0.895
	4.593	0.478		6.148	0.868
	5.938	0.614		6.764	0.951
	6.851	0.722		7.946	1.158
	7.114	0.751		8.040	1.186
	7.990	0.825		8.774	1.231
	8.606	0.885		8.822	1.276
	8.678	0.876		8.960	1.290
	9.232	0.961		9.220	1.350
	10.305	1.061		9.244	1.305
	10.614	1.095		9.254	1.305
523	3.497	0.404		10.009	1.419
	6.652	0.792		11.468	1.640
	9.394	1.112		14.637	2.092
	11.763	1.385			

Solubility of hydrogen-carbon monoxide mixtures

Temperature (K)	Partial Pressure of H_2 (MPa)	Partial Pressure of CO (MPa)	Solubility of H_2 (wt%)	Solubility of CO (wt%)
473	2.523	6.871	0.0191	0.679
	2.547	4.298	0.0208	0.424
	2.680	5.514	0.0194	0.537
	4.475	7.123	0.0350	0.657
	5.262	3.000	0.0366	0.261
	5.451	4.842	0.0374	0.434
	7.381	4.870	0.0534	0.404
	7.416	6.678	0.0516	0.565
	7.529	4.768	0.0542	0.397
	9.660	7.093	0.0654	0.549
	9.960	4.664	0.0667	0.365
	12.432	7.161	0.0845	0.521
	12.851	3.093	0.0830	0.222
	14.839	7.200	0.0955	0.504
	15.073	3.021	0.0940	0.221
	17.504	3.389	0.1083	0.220

Table 3. Effect of pressure on the density of Athabasca bitumen [13].

Pressure (MPa)	Density (kg/m^3) at 288 K	
	Solvent-extracted	Coker feed
0.097	1005	999
0.690	1007	
1.275		1002
3.300		1003
3.450	1014	
6.725		1005
6.900	1017	
10.20		1006
10.35	1020	

Figure 3. Effect of pressure on the density of carbon-dioxide-saturated Athabasca bitumen [14].

Table 4. Effect of temperature and pressure on the density of Cold Lake bitumen [13].

Temperature (K)	Pressure (MPa)	Liquid (kg/m^3)
373.15	2.0	959.3
	4.0	961.8
	6.0	962.0
	8.0	962.8
	10.0	963.2
423.15	2.0	927.5
	4.0	928.2
	6.0	929.5
	8.0	930.8
	10.0	933.4
473.15	2.0	897.0
	4.0	898.8
	6.0	900.5
	8.0	902.1
	10.0	904.7
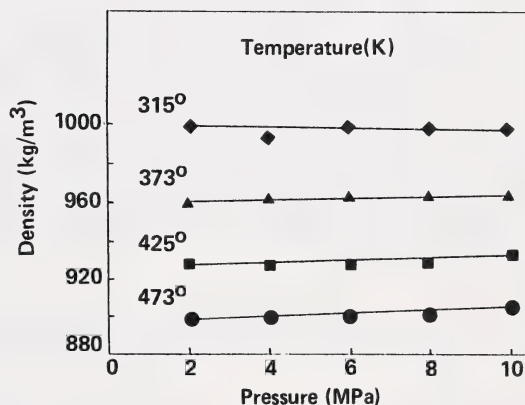
Figure 4. Effect of dissolved carbon dioxide on the density of Athabasca bitumen [14].

APPLICATION OF EQUATIONS OF STATE TO PHASE EQUILIBRIUM CALCULATIONS

Various cubic equations of state have been used in industry for calculating thermodynamic properties. There are two important factors for vapor-liquid equilibrium calculation: the reproduction of pure-component vapor pressures and the mixing rules for determination of the mixture parameters. For volumetric representation, another factor plays an important role, namely, the form of the equation. A generic expression for the currently popular cubic equations can be represented in the form of an extended van der Waals (VDW) equation [15]

$$P = \frac{RT}{V-b} - \frac{a}{V^2 + ubV + wb^2} \qquad (6)$$

The expression $(V^2 + ubV + Wb^2)$ replaces the term in the denominator of the original VDW equation. Equation (6) reduces to the original VDW equation with $u = w = 0$; to the Redlich-Kwong (RK) equation [16] with $u = 1$, $w = 0$ and $a = a'/T^{1/2}$; to the Soave form of the RK equation (SRK) [17] with $a = a(T)$; and to the

Peng-Robinson (PR) equation [18] with $u = 2$ and $w = -1$. A number of other equations are obtained when particular values are assigned to u and w of Equation (6). A number of special cases are listed in Table 5, in which some features of these equations are also included for comparison. The equation type indicated in the table refers to the total number of parameters and the number of temperature-dependent parameters. For example, the SRK equation contains two parameters, one of which (the parameter a) is treated as temperature dependent. It is designated as a 2P1T equation.

A suitable equation of state for the representation of phase equilibrium values must be able to reproduce first of all vapor pressures of pure components. The current practice is to treat the parameter a as temperature dependent and adjust its value by fitting the vapor pressures. A proper temperature function is also required. The other important feature to be considered is the mixing rules, making the constants of the equation of state a function of composition. The form of the equations of state appears to be of less importance for phase equilibrium calculations. There is evidence in the literature [31] that practically identical vapor-liquid equilibrium (VLE) values (T-P-composition) can be obtained from various cubic equations of state, and these results are frequently comparable to those obtained from more complex equations.

Expressions and generalized parameters of frequently used cubic equations

The most frequently used equations of state have been the SRK and the PR equations, both of which are of the 2P1T type. It has also been demonstrated [31] that the VDW equation is equally useful for calculating VLE values by treating the parameter a as temperature dependent. The parameter a of these equations is expressed in terms of the critical temperature and pressure by means of Equation (7):

$$a = \frac{\Omega_a R^2 T_c^2}{P_c} \qquad (7)$$

with Ω_a treated as temperature dependent and its coefficient generalized in terms of Pitzer's acentric factor ω. The generalized temperature functions for these equations are listed in Table 6.

For a pure component, the evaluation of the fugacity coefficient ϕ is given by

$$\ln \phi_{pure\ i} = \ln\left(\frac{f}{p}\right)_{pure\ i} = \int_o^p \left(\frac{Z_i - 1}{p}\right) dP \qquad (8)$$

which can be calculated by means of an equation of state.

Table 5. Features of some cubic equations of state of the van der Waals type.

Type	Equation	u	w	a	b	Fitted properties	Reference
2P0T	van der Waals (1873)	0	0	a_c	b_c	none	[15]
2P1T	Redlich-Kwong (1949)	1	0	$a_c/T^{1/2}$	b_c	none	[16]
	Soave-Redlich-Kwong (1972)	1	0	$a(T)$	b_c	P^v	[17]
	Peng-Robinson (1976)	2	-1	$a(T)$	b_c	P^v	[18]
3P1T	Harmens-Knapp (1980)	$1-w$	$f(\omega)$	$a(T)$	b_c	P^v, Critical isotherm	[19]
	Schmidt-Wenzel (1980)	$1-w$	$f(\omega)$	$a(T)$	b_c	P^v, V^l ($T_r = 0.7$)	[20]
	Patel-Teja (1982)	$1-w$	$f(\omega)$	$a(T)$	b_c	P^v, V^l($T_r \approx 0.6$ to 1.0)	[21]
	Adachi et al. (1983)	$f(\omega)$	0	$a(T)$	b_c	P^v, V^l	[22]
	Martin (1979)	$f(\omega)$	$u^2/4$	$a(T)$	b_c	P^v	[23]
	Translated SRK (1982)	$f(\omega)$	$(2u^2-u-1)/9$	$a(T)$	b_c	P^v, V^l	[24]
	Freze et al. (1983)	$f(\omega)$	$\approx(u^2-4u-4)/8$	$a(T)$	b_c	P^v, Z^l	[25]
4P1T	Adachi et al. (1983)	$f(\omega)$	$f(\omega)$	$a(T)$	b_c	P^v, Critical isotherm	[26]
2P2T	Hamam et al. (1977)`	1	0	$a(T)$	$b(T)$	P^v, V^l	[27]
3P2T	Heyen (1980)	$1-w$	$f(\omega,b)$	$a(T)$	$b(T)$	P^v, V^l	[28]
	Kubic (1982)	$f(\omega)$	$u^2/4$	$a(T)$	$b(T)$	P^v, B	[29]
3P3T	Fuller (1976)	$f(T)$	0	$a(T)$	$b(T)$	P^v, V^l, V^v	[30]

Table 6. Parameters of three cubic equations of the 2P1T type.

Equation	Temperature function for Ω_a $(= a\,P_c/R^2T_c^2)$	Ω_b (bP_c/RT_c)	Z_c $(= P_cV_c/RT_c)$
Modified van der Waals $$P = \frac{RT}{V-b} - \frac{a(T)}{V^2}$$	$\Omega_a = \Omega_{ac}\,10^{m\,(1-T_r)}$ $\Omega_{ac} = 27/64$ $m = 0.228165 + 0.791981\omega - 0.648552\omega^2 + 0.654505\omega^3$	1/8	3/8
Soave form of RK $$P = \frac{RT}{V-b} - \frac{a(T)}{V\,(V+b)}$$	$\Omega_a = \Omega_{ac}[1 + m\,(1 - T_r^{1/2})]^2$ $\Omega_{ac} = 0.42747$ $m = 0.480 + 1.574\,\omega - 0.17\omega^2, \ \omega < 0.5$ $m = 0.47978 + 1.57624\omega - 0.19394\omega^2 + 0.02779\omega^3$ $\quad - 0.0016577\omega^4 - 0.0001315\omega^5, \ \omega > 0.5$	0.086 64	1/3
Peng-Robinson $$P = \frac{RT}{V-b} - \frac{a(T)}{V\,(V+b)\,+\,b\,(V-b)}$$	$\Omega_a = \Omega_{ac}\,[1 + m\,(1 - T_r^{1/2})]^2$ $\Omega_{ac} = 0.45724$ $m = 0.37464 + 1.54226\omega - 0.26992\omega^2, \ \omega < 0.5$ $m = 0.37964 + 1.48503\omega - 0.16442\omega^2 + 0.1667\omega^3,$ $\quad 0.2 \le \omega \le 2.0$	0.077 80	0.307

All the cubic equations of state mentioned above are pressure explicit. Taking T, V, and composition as the independent variables, the thermodynamic relation for obtaining the fugacity coefficient of component i in the vapor phase, $\hat{\phi}_i^v$, by means of an equation of state is given by

$$RT\ln\hat{\phi}_i^v = RT\ln\left(\frac{\hat{f}_i^v}{Y_i\,P}\right)$$

(9)

$$= \int_v^\infty \left[\left(\frac{\partial P}{\partial n_i}\right)_{T,\,V,\,n_j} - \frac{RT}{V}\right] dV - RT\ln Z$$

Similarly, the fugacity coefficient of component i in the liquid phase $\hat{\phi}_i^l = \hat{f}_i^l / x_i P$ is obtained by replacing y_i of Equation (9) with x_i. The expressions obtained from Equation (9) for the modified VDW, the SRK, and the PR equations are listed in Table 7.

At given T and P, the equilibrium condition is that

$$\hat{f}_i^v = \hat{f}_i^l$$

(10)

Hence

$$y_i\hat{\phi}_i^v = x_i\hat{\phi}_i^l$$

(11)

Table 7. Expressions for obtaining fugacity coefficients ($a = \Sigma\Sigma y_i y_j a_{ij}$, $b = \Sigma y_i b_i$)

Equation of state	Fugacity coefficient for pure component i	Fugacity coefficient for component i in mixture
Modified van der Waals		
$P = \dfrac{RT}{V-b} - \dfrac{a(T)}{V^2}$	$\ln\phi = Z - 1 - \ln(Z-B) - \dfrac{A}{Z}$	$\ln\hat{\phi}_i = -\ln(Z-B) + \dfrac{b_i}{b}(Z-1) - \dfrac{A}{Z}\left(\dfrac{2\sum_j y_j a_{ji}}{a} - \dfrac{b_i}{b}\right)$
Soave-Redlich-Kwong		
$P = \dfrac{RT}{V-b} - \dfrac{a(T)}{V(V+b)}$	$\ln\phi = Z - 1 - \ln(Z-B) - \dfrac{A}{B}\ln\left(1+\dfrac{B}{Z}\right)$	$\ln\hat{\phi}_i = \dfrac{B_i}{B}(Z-1) - \ln(Z-B) + \dfrac{A}{B}\left[\dfrac{B_i}{B} - \dfrac{2}{a}\sum_j y_j a_{ji}\right]\ln\left(1+\dfrac{B}{Z}\right)$
Peng-Robinson		
$P = \dfrac{RT}{V-b} - \dfrac{a(T)}{V(V+b)+b(V-b)}$	$\ln\phi = Z - 1 - \ln(Z-B) - \dfrac{A}{2\sqrt{2}\,B}\ln\left(\dfrac{Z+2.414B}{Z-0.414B}\right)$	$\ln\hat{\phi}_i = \dfrac{B_i}{B}(Z-1) - \ln(Z-B) - \dfrac{A}{2\sqrt{2}\,B}\left[\dfrac{2\sum_{ij} y_j a_{ji}}{a} - \dfrac{B_i}{B}\right]$ $\times\ \ln\left(\dfrac{Z+2.414B}{Z-0.414B}\right)$
	$A = \dfrac{aP}{R^2 T^2},\quad B = \dfrac{bP}{RT}$	$A = \dfrac{aP}{R^2 T^2},\quad B = \dfrac{bP}{RT},\quad B_i = \dfrac{b_i P}{RT}$

or

$$K_i = \frac{y_i}{x_i} = \frac{\hat{\phi}_i^l}{\hat{\phi}_i^v} \qquad (12)$$

Thus, the equilibrium ratio K_i is obtained from the calculated $\hat{\phi}_i^l$ and $\hat{\phi}_i^v$ values, and can be used for VLE calculations (such as dew point, bubble point, and flash calculations).

In VLE calculations involving heavy oil and bitumen, the following conventional mixing rules have often been employed for the three cubic equations of state:

$$a = \sum_i \sum_j x_i x_j a_{ij} \qquad (13)$$

and

$$b = \sum b_i x_i \qquad (14)$$

These rules are referred to as the VDW random mixing rules, relating the parameters a and b of the mixture to the phase composition. Although Equations (13) and (14) are expressed in terms of the mole fractions of components i and j in the liquid phase, they can be applied equally well to the vapor phase composition by replacing x with y. The cross coefficient a_{ij} is frequently expressed as

$$a_{ij} = \left(a_{ii} a_{jj}\right)^{1/2} \left(1 - k_{ij}\right) \qquad (15)$$

The quantity k_{ij} is the so-called binary interaction coefficient, which is determined from binary data. In the calculation, $k_{ij} = k_{ji}$ and $k_{ii} = k_{jj} = 0$.

Characterization of bitumen

The application of an equation of state to the calculation of phase equilibrium properties for a mixture using the approach mentioned above requires characterization parameters for every constituent of the mixture. These parameters are the acentric factor ω, critical temperature T_c and critical pressure P_c. The composition of bitumen is complex. The critical properties of such complex large molecules cannot be experimentally determined without destroying their original structure. Whether bitumen is treated in terms of hypothetical fractions, chemical structures, or as a

pseudo-pure component, suitable correlation or estimation methods are required for obtaining T_c, P_c, and ω values to facilitate the calculations. The recommended correlations are briefly presented in the following section.

Correlations for critical properties, specific gravity, and molecular weight using only normal boiling points. Twu [32] correlated the critical temperature, critical volume, specific gravity, and molecular weight of n-alkanes from C_1 up to C_{100} using only the normal boiling point as follows:

- Critical temperature, T_c :

$$
\begin{aligned}
T_c^o = T_b \div \Big(& 0.296262 + 0.106121 \times 10^{-3}\, T_b \\
& + 0.240642 \times 10^{-7}\, T_b^2 - 0.048761 \times 10^{-10}\, T_b^3 \\
& + \frac{0.199790 \times 10^{37}}{T_b^{13}} \Big) \qquad (16)
\end{aligned}
$$

- Critical pressure, P_c (with the exception of methane):

$$
\begin{aligned}
P_c^o = \big(& 26.1219 + 8.15159\,\alpha^{1/2} + 237.734\,\alpha \\
& + 246.636\,\alpha^2 + 709.977\,\alpha^4 \big)^2 \qquad (17)
\end{aligned}
$$

- Critical volume, V_c :

$$
\begin{aligned}
V_c^o = \big[1 - \big(& 0.419869 - 0.505839\,\alpha - 1.56436\,\alpha^3 \\
& - 9481.70\,\alpha^{14} \big) \big]^{-8} \times 0.062428 \qquad (18)
\end{aligned}
$$

- Specific gravity, SG :

$$
\begin{aligned}
SG^o = \; & 0.843593 - 0.128624\alpha \\
& - 3.36159\alpha^3 - 13749.5\alpha^{12} \qquad (19)
\end{aligned}
$$

- Molecular weight, MW :

$$T_b = \left[\exp\left(5.71419 + 2.71579\,\theta - 0.286590\,\theta^2 \right.\right.$$

$$\left. - \frac{39.8544}{\theta} - \frac{0.122488}{\theta^2} \right) - 24.7522\,\theta \qquad (20)$$

$$\left. + 35.3155\,\theta^2 \right] \div 1.8$$

where

$$\alpha = 1 - \frac{T_b}{T_c^o} \qquad (21)$$

and

$$\theta = \ln MW^o \qquad (22)$$

As the correlation for MW is explicit in T_b, a trial-and-error procedure is required to determine molecular weight. In the above equations,

T_c = critical temperature (K),
T_b = normal boiling-point temperature (K),
P_c = critical pressure (kPa),
V_c = critical volume (L·g/mol),
SG = specific gravity (liquid component at 289 K/ water at 289 K),
MW = molecular weight,

and the superscript "o" denotes correlations specific to the n-alkanes.

Correlations using normal boiling points and specific gravities for critical properties and molecular weight. Twu [33] correlated the critical properties and molecular weights of petroleum and coal-tar liquids in terms of normal boiling points (up to 988 K) and specific gravities (up to 1.436). The proposed correlations using the same units as above are as follows:

- Critical temperature, T_c:

$$T_c = T_c^o \left[\frac{\left(1 + 2f_T\right)}{\left(1 - 2f_T\right)} \right]^2 \qquad (23)$$

$$f_T = \Delta SG_T \left[-\frac{0.270159}{T_b^{1/2}} + \left(0.0398285 \right.\right.$$

$$\left.\left. - \frac{0.706691}{T_b^{1/2}} \right) \Delta SG_T \right], \qquad (24)$$

$$\Delta SG_T = \exp\left[5\,(SG^o - SG)\right] - 1 \qquad (25)$$

- Critical volume, V_c:

$$V_c = V_c^o \left[\frac{\left(1 + 2f_v\right)}{\left(1 - 2f_v\right)} \right]^2, \qquad (26)$$

$$f_v = \Delta SG_v \left[\frac{0.347776}{T_b^{1/2}} + \left(-0.182421 \right.\right.$$

$$\left.\left. + \frac{2.24890}{T_b^{1/2}} \right) \Delta SG_v \right], \qquad (27)$$

$$\Delta SG_v = \exp\left[4\,(SG^{o2} - SG^2)\right] - 1 \qquad (28)$$

- Critical pressure, P_c:

$$P_c = P_c^o \left(\frac{T_c}{T_c^o}\right)\left(\frac{V_c^o}{V_c}\right)\left[\frac{\left(1 + 2f_p\right)}{\left(1 - 2f_p\right)} \right]^2 \qquad (29)$$

$$f_p = \Delta SG_p \left[\left(2.53262 - \frac{34.4321}{T_b^{1/2}} - 0.00230193 T_b \right) \right.$$

$$\left. + \left(-11.4277 + \frac{187.934}{T_b^{1/2}} + 0.00414963 T_b \right) \Delta SG_p \right] \qquad (30)$$

$$\Delta SG_p = \exp\left[0.5\,(SG^o - SG)\right] - 1 \qquad (31)$$

• Molecular weight, *MW:*

$$\ln MW = \ln MW° \left[\frac{\left(1 + 2f_M \right)}{\left(1 - 2f_M \right)} \right]^2, \qquad (32)$$

$$f_M = \Delta SG_M \left[|x| + \left(-0.0175691 + \frac{0.143979}{T_b^{1/2}} \right) \Delta SG_M \right], \qquad (33)$$

$$|x| = 0.123420 - \frac{0.244541}{T_b^{1/2}}, \qquad (34)$$

$$\Delta SG_M = \exp \left[5 \left(SG° - SG \right) \right] - 1 \qquad (35)$$

In these expressions, $T_c°$, $V_c°$, $P_c°$, $MW°$ and $SG°$ are evaluated from hypothetical *n*-alkanes having the same normal boiling point as the system of interest.

Correlations for ω. Kesler and Lee [34] proposed two acentric factor correlations in terms of T_{br} and K_w. These quantities are defined by

$$T_{br} = \frac{T_b}{T_c} \qquad (36)$$

and

$$K_w = \frac{(CABP)^{1/3}}{SG} \qquad (37)$$

where T_b denotes the molar average boiling point and *CABP*, the cubic average boiling point. For $T_{br} < 0.8$,

$$\omega = \left[-\ln \left(\frac{P_c}{14.7} \right) - 5.92714 + 6.09648 \, T_{br}^{-1} \right.$$

$$+ 1.28862 \ln T_{br} - 0.169347 \, T_{br}^6 \right] + \left[15.2518 \right.$$

$$- 15.6875 \, T_{br}^{-1} - 13.4721 \ln T_{br} + 0.43577 \, T_{br}^6 \right] \qquad (38)$$

and for $T_{br} > 0.8$,

$$\omega = -7.904 + 0.1352 \, K_w - 0.007465 \, K_w^2$$

$$+ 8.359 \, T_{br} + \frac{\left(1.408 - 0.01063 \, K_w \right)}{T_{br}} \qquad (39)$$

The units for pressure and temperature are psia and degrees Rankine, respectively.

Correlations based on carbon number, or boiling point, and hydrogen deficiency for critical properties. Black and Twu [35] developed correlations for the prediction of thermodynamic properties of true and pseudo components in heavy petroleum, shale oils, tar sands, and coal liquids. These correlations require characterization of fractions with regard to carbon number, hydrogen deficiency, and predominant type of molecule in the given fraction. Eleven families of compounds were considered in the development of these correlations. They are (1) *n*-alkanes, (2) *n*-alkyl cyclopentanes, (3) *n*-alkyl cyclohexanes, (4) *n*-alkenes, (5) *n*-alkyl naphthenoaromotics, (6) *n*-alkyl aromatics, (7) furans, benzofurans, dibenzofurans, etc., (8) phenols, naphthols, anthracols, etc., (9) pyrroles, indoles, carbazoles, etc., (10) pyridines, quinolines, acridines, etc., and (11) thiophenes, benzothiophenes, dibenzothiophenes, etc. The correlations for critical properties are expressed in terms of carbon number N, or normal boiling point T_b, hydrogen deficiency Z, and family type I. Hydrogen deficiency is defined as the value of Z in the formula $C_N H_{2N+Z}$ where C and H represent carbon and hydrogen atoms, respectively, and N is the number of carbon atoms in the molecule. The correlations for the critical properties and normal boiling point are as follows:

• Critical temperature, T_c:

$$T_c = T_b \left[A_1(I) + A_2(I) T_b - A_3(I)^{-6} T_b^2 \right.$$

$$+ A_4(I) 10^{-9} T_b^3 + A_5(I) \left(T_b \right)^{-0.5} + A_6(I) K_2 \right]^{-1} \qquad (40)$$

where

$$K_2 = \frac{(Z+6) + (-Z)^{3/4}}{\mu_2} \qquad (41)$$

and

$$\mu_2 = \frac{N}{\left(2 - \frac{2Z}{3}\right)} \qquad (42)$$

• Critical pressure, P_c:

$$\ln P_c = B_1(I) + B_2(I)Y^{1/3} - B_3(I)Y^{5/3}$$

$$+ B_4(I)Y + B_5(I)Y^2 + B_6(I)K_3 \qquad (43)$$

where

$$Y = \left(1 - \frac{T_b}{T_c}\right) \qquad (44)$$

$$K_3 = \frac{\frac{(Z+6)}{B_7(I)} + B_8(I)\ln(-Z)}{\mu_3} \qquad (45)$$

and

$$\mu_3 = \frac{N}{\left(2 - \frac{2Z}{3}\right)} \qquad (46)$$

• Critical volume, V_c:

$$V_c = \frac{RT_c}{P_c}\left[C_1(I) + C_2(I)Y + C_3(I)Y^3\right.$$

$$\left. - C_4(I)Y^5\right] + C_5(I)K_4 \qquad (47)$$

where

$$K_4 = \frac{(Z+6)}{e^{0.01}\mu_4} \qquad (48)$$

and

$$\mu_4 = \left[\ln\left(\frac{N}{2 - \frac{2Z}{3}}\right)\right]^5 \qquad (49)$$

• Normal boiling point, T_b:

$$\ln\left[T_b - D_6(I)x - D_7(I)x^2 - D_8(I)K_1\right] = D_1(I)$$

$$+ D_2(I)x - D_3(I)x^2 - D_4(I)x^{-1} + D_5(I)x^{-2} \qquad (50)$$

where

$$x = \ln(N + 0.5) \qquad (51)$$

$$K_1 = \frac{(Z+6)\left[\ln(-Z)\right]}{e^{0.01}\mu_1} \qquad (52)$$

and

$$\mu_1 = \ln\left[\frac{N}{\frac{1}{3}(11 - 2Z)}\right] \qquad (53)$$

The values of the coefficients have recently been modified by Fu et al. [36], and are presented in Tables 8 through 11.

Treatment of gas solubility data

When the solubilities of pure gases in bitumen obtained at isothermal conditions are presented on an $\ln(f_2/x_2)$ vs P plot, a smooth trend should be observed. The quantities f_2 and x_2 refer to the fugacity and mole fraction of the dissolved gas in bitumen, respectively. The quantity P is the system pressure. The Krichevsky-Kasarnovsky [37] equation,

$$\ln\frac{f_2}{x_2} = \ln K_H + \frac{\overline{V}_2^\infty(P - p_1)}{RT} \qquad (54)$$

is suitable for representing solubilities of sparingly soluble gases up to high pressures. In Equation (54), subscripts 1 and 2 refer to the solvent (bitumen) and the solute gas, respectively. The quantity $\overline{V}_2^\infty$ is the partial molar volume of the dissolved gas in bitumen at infinite dilution, and K_H is Henry's constant at the saturation pressure of bitumen p_1. A linear relationship can be expected on the above-mentioned plot when the solubilities are very low. However, when the solubility is appreciable, the Krichevsky-Ilinskaya [38] equation

Table 8. Critical temperature via normal boiling point and hydrogen deficiency.

	n-Alkanes (I = 1)	n-Alkyl Cyclopentanes (I - 2)	n-Alkyl Cyclohexanes (I = 3)	n-Alkenes (I = 4)	n-Alkyl Naphthenoaromatics (I = 5)	n-Alkyl Aromatics (I = 6)
$A_1(I)$	0.164 179	0.147 939	0.144 735	0.161 136	0.112 161	0.029 643 6
$A_2(I)$	0.001 139 67	0.001 241 89	0.001 262 84	0.001 139 48	0.001 441 36	0.001 404 66
$A_3(I)$	-0.600 463 E-06	-0.684 440 E-06	-0.698 280 E-06	-0.598 234 E-06	-0.832 601 E-06	-0.780 557 E-06
$A_4(I)$	0.108 763 E-09	0.129 271 E-09	0.132 014 E-09	0.107 850 E-09	0.162 806 E-09	0.148 785 E-09
$A_5(I)$	3.423 19	2.694 36	2.447 89	3.430 228	0.982 917	3.627 06
$A_6(I)$	0.0	0.096 309 9	0.096 309 9	0.007 472 72	0.037 682 5	0.061 504 5
$K_2(I)$		$Z/(-Z+6)^{3/4}$	$Z/(-Z+6)^{3/4}$	$Z/(-Z+6)^{3/4}$	$(Z+8)/(-Z-2)^{3/4}$	$(Z+6)/(-Z)^{3/4}$
$\mu_2(I)$		$\dfrac{N}{5-3Z/2}$	$\dfrac{N}{6-2Z}$	$\dfrac{N}{2-Z}$	$\dfrac{N}{1/3(11-2Z)}$	$\dfrac{N}{2-2Z/3}$

	Furans Menzofurans Dibenzofurans (I = 7)	Phenols Manhthols etc. (I = 8)	Pyrroles Indoles Carbazoles (I = 9)	Pyridines Quinolines Acridines (I = 10)	Thiophenes Benzothiophenes Di-Menzothiophenes (I = 11)
$A_1(I)$	0.147 939	0.910 346 E-01	0.127 925	0.028 705 5	0.047 874 7
$A_2(I)$	0.001 241 89	0.001	0.001 388 05	0.001 415 71	0.001 425 18
$A_3(I)$	-0.684 440 E-06	-0.837 367 E-06	-0.794 806 E-06	-0.779 422 E-06	-0.804 961 E-06
$A_4(I)$	0.129 271 E-06	0.163 582 E-09	0.154 727 E-09	0.146 329 E-09	0.155 790 E-09
$A_5(I)$	2.694 36	1.373 87	1.238 56	3.279 32	2.929 03
$A_6(I)$	0.098 649 9	0.026 265 1	(0.072 739 7)[b]	0.072 739 7	(0.098 649 9)[a]
$K_2(I)$	$(Z+4)/(-Z+2)^{0.75}$	$(Z+6)/(-Z)^{0.75}$	$(Z+3)/(-Z+3)^{0.75}$	$(Z+5)/(-Z+1)^{0.75}$	$(Z+4)/(-Z+2)^{0.75}$
$\mu_2(I)$	$\dfrac{N}{2/3(2-Z)}$	$\dfrac{N}{2-2/3Z}$	$\dfrac{N}{2-2/3Z}$	$\dfrac{N}{1/3(5-2Z)}$	$\dfrac{N}{2/3(2-Z)}$

N = Carbon number
Z = Hydrogen deficiency, C_NH_{2N+Z}
T_b = Normal boiling point (K)
T_c = Critical temperature (K)
a From furans
b From pyridines

$$T_c = T_b \left[A_1(I) + A_2(I)T_b + A_3(I)T_b^2 + A_4(I)T_b^3 + A_5(I)T_b^{0.5} + A_6(I)K_2(I) \right]^{-1}$$

Table 9. Critical pressure via T_b / T_c, carbon number, and hydrogen deficiency.

	n-Alkanes (I = 1)	n-Alkyl Cyclopentanes (I - 2)	n-Alkyl Cyclohexanes (I = 3)	n-Alkenes (I = 4)	n-Alkyl Naphthenoaromatics (I = 5)	n-Alkyl Aromatics (I = 6)
$B_1(l)$	6.601 87	6.465 00	6.450 65	6.596 37	6.435 29	6.435 21
$B_2(l)$	2.104 48	2.633 98	2.700 41	2.058 45	2.667 57	2.680 34
$B_3(l)$	-3.187 66	-6.938 46	-6.899 07	-0.038 590 1	-5.940 41	-5.771 22
$B_4(l)$	6.748 70	5.801 82	5.749 27	6.655 83	6.595 47	6.521 56
$B_5(l)$	2.582 10	9.058 63	8.594 47	1.319 93	6.427 71	5.809 02
$B_6(l)$	0.0	-0.119 005	0.006 00	-0.067 144 6	-0.003 637	-0.001 13
$B_7(l)$	0.0	2.134 59	-2.134 59	-1.741 57	-1.183 00	-0.584 30
$B_8(l)$	0.0	1.412 26	1.412 26	1.705 29	0.441 31	-0.302 80
$B_{add}(l)$	0.0	0.0	0.0	0.0	-0.051 43	0.058 10
$K_3(l)$	$[B_7(l)+B_8(l)\ln(-Z+6)]\mu_3(l)$	$[B_7(l)+B_8(l)\ln(-Z+6)]\mu_3(l)$	$[B_7(l)+B_8(l)\ln(-Z+6)]\mu_3(l)$	$[B_7(l)+B_8(l)\ln(-Z+6)]\mu_3(l)$	$[B_7(l)+A_8(l)\ln(-Z-2)]\mu_3(l)$	$[B_7(l)+B_8(l)\ln(-Z)]\mu_3(l)$
N	Z	Z	Z	Z	$(Z+8)$	$(Z+6)$
$\mu_3(l)$	$\dfrac{N}{5-\frac{3Z}{2}}$	$\dfrac{N}{6-2Z}$	$\dfrac{N}{6-2Z}$	$\dfrac{N}{2-Z}$	$\dfrac{N}{\frac{1}{3}(11-2Z)}$	$\dfrac{N}{2-\frac{2Z}{3}}$

	Furans, Menzofurans, Dibenzofurans (I = 7)	Phenols, Manhthols etc. (I = 8)	Pyrroles, Indoles, Carbazoles (I = 9)	Pyridines, Quinolines, Acridines (I = 10)	Thiophenes, Benzothiophenes, Di-Menzothiophenes (I = 11)
$B_1(l)$	6.512 47	6.398 90	6.430 74	6.455 09	6.366 81
$B_2(l)$	2.709 41	2.818 50	2.680 75	2.615 28	2.943 35
$B_3(l)$	-6.808 32	-6.017 56	-5.445 45	-5.118 76	-7.079 44
$B_4(l)$	5.811 41	6.370 70	6.571 99	6.493 68	6.060 94
$B_5(l)$	0.930 22	9.453 80	7.074 83	6.412 60	8.499 53
$B_6(l)$	0.004 68	-0.050 18	0.042 72	-0.005 97	(-0.180 93)[a]
$B_7(l)$	2.109 58	-2.109 58	(-2.226 29)[c]	2.145 00	(-2.109 58)[a]
$B_8(l)$	-2.109 58	-1.42 498	(-1.38 131)[c]	1.052 00	(1.424 98)[a]
$B_{add}(l)$	0.0	0.0	0.0	0.089 00	0.0
$K_3(l)$	$[B_7(l)+B_8(l)\ln(-Z+2)]\mu_3(l)$	$[B_7(l)+B_8(l)\ln(-Z)]\mu_3(l)$	$[B_7(l)+B_8(l)\ln(-Z+3)]\mu_3(l)$	$[B_7(l)+B_8(l)\ln(-Z+1)]\mu_3(l)$	$[B_7(l)+B_8(l)\ln(Z+2)]\mu_3(l)$
N	$(Z+4)$	$(Z+6)$	$(Z+3)$	$(Z+5)$	$(Z+4)$
$\mu_3(l)$	$\dfrac{N}{\frac{2}{3}(2-Z)}$	$\dfrac{N}{2-\frac{2Z}{3}}$	$\dfrac{N}{2-\frac{2Z}{3}}$	$\dfrac{N}{\frac{1}{3}(5-2Z)}$	$\dfrac{N}{\frac{2}{3}(2-Z)}$

T_b = Normal boiling point (K)
T_c = Critical temperature (K)
P_c = Critical pressure (MMHG)
[a] From furans
[b] From aromatics
[c] From pyridines

Table 10. Critical volume via T_b/T_c, T_c, P_c, N, and Z.

	n-Alkanes (I = 1)	n-Alkyl Cyclopentanes (I = 2)	n-Alkyl Cyclohexanes (I = 3)	n-Alkenes (I = 4)	n-Alkyl Naphthenoaromatics (I = 5)	n-Alkyl Aromatics (I = 6)
$C_1(I)$	0.154 943	0.154 643	0.154 643	0.152 361	0.153 261	0.153 697
$C_2(I)$	0.191 641	0.194 132	0.225 663	0.210 847	0.302 006	0.283 710
$C_3(I)$	2.325 150	1.776 810	1.326 060	1.837 540	1.396 290	2.438 160
$C_4(I)$	-8.508 170	-5.454 460	-3.989 440	-8.155 780	-13.197 600	-17.407 600
$C_5(I)$	0.0	42.858 200	42.858 200	6.399 670	4.204 000	6.405 000
$C_{add}(I)$	0.0	0.0	0.0	0.0	0.0	16.340 000
$K_4(I)$	$\dfrac{Z}{e^{0.01}\mu_4(l)}$	$\dfrac{Z}{e^{0.01}\mu_4(l)}$	$\dfrac{Z}{e^{0.01}\mu_4(l)}$	$\dfrac{Z}{e^{0.01}\mu_4(l)}$	$\dfrac{Z+8}{e^{0.01}\mu_4(l)}$	$\dfrac{Z+6}{e^{0.01}\mu_4(l)}$
$\mu_4(l)$	$\left[\ln\left(\dfrac{N}{5-\frac{3}{2}Z}\right)\right]^5$	$\left[\ln\left(\dfrac{N}{5-\frac{3}{2}Z}\right)\right]^5$	$\left[\ln\left(\dfrac{N}{6-2Z}\right)\right]^5$	$\left[\ln\left(\dfrac{N}{2-Z}\right)\right]^5$	$\left[\ln\left(\dfrac{N}{\frac{1}{3}(11-2Z)}\right)\right]^5$	$\left[\ln\left(\dfrac{N}{2-\frac{2}{3}Z}\right)\right]^5$

	Furans Menzofurans Dibenzofurans (I = 7)	Phenols Manhthols etc. (I = 8)	Pyrroles Indoles Carbazoles (I = 9)	Pyridines Quinolines Acridines (I = 10)	Thiophenes Benzothiophenes Di-Menzothiophenes (I = 11)
$C_1(I)$	0.165 052	0.155 581	0.152 451	0.152 814	0.153 810
$C_2(I)$	0.231 013	0.254 918	0.355 451	0.324 113	0.297 629
$C_3(I)$	1.822 950	4.424 040	1.988 440	2.533 890	2.071 450
$C_4(I)$	8.084 880	-37.646 500	-19.391 900	-19.739 600	-15.583 600
$C_5(I)$	55.160 000	17.995 500	(55.160 000)[a]	(55.160 000)[a]	(55.160 000)[a]
$C_{add}(I)$	0.0	0.0	0.0	0.0	0.0
$K_4(I)$	$\dfrac{(Z+4)}{e^{0.01}\mu_4(l)}$	$\dfrac{Z+6}{e^{0.01}\mu_4(l)}$	$\dfrac{Z+3}{e^{0.01}\mu_4(l)}$	$\dfrac{Z+5}{e^{0.01}\mu_4(l)}$	$\dfrac{(Z+4)}{e^{0.01}\mu_4(l)}$
$\mu_4(l)$	$\left[\ln\left(\dfrac{N}{\frac{2}{3}(2-Z)}\right)\right]^5$	$\left[\ln\left(\dfrac{N}{2-\frac{2}{3}Z}\right)\right]^5$	$\left[\ln\left(\dfrac{N}{2-\frac{2}{3}Z}\right)\right]^5$	$\left[\ln\left(\dfrac{N}{\frac{1}{3}(5-2Z)}\right)\right]^5$	$\left[\ln\left(\dfrac{N}{\frac{2}{3}(2-Z)}\right)\right]^5$

V_c = Critical volume(mL/g-mol)
[a] From furans
[b] From aromatics

$$V_c = RT_c/P_c\,[C_1(I) + C_2(I)Y + C_3(I)Y^3 + C_4(I)Y^5 + C_5(I)K_4(I)] + C_{add}(I)$$

Table 11. Normal boiling point via N and Z.

	n-Alkanes ($I=1$)	n-Alkyl Cyclopentanes ($I=2$)	n-Alkyl Cyclohexanes ($I=3$)	n-Alkenes ($I=4$)	n-Alkyl Naphthenoaromatics ($I=5$)	n-Alkyl Aromatics ($I=6$)
$D_1(I)$	4.078 16	3.702 67	3.707 03	5.716 74	3.849 81	3.796 64
$D_2(I)$	2.377 14	1.809 64	1.805 22	1.835 11	2.108 01	2.112 08
$D_3(I)$	-0.348 74	-0.251 99	0.252 19	-0.292 39	0.307 25	-0.301 82
$D_4(I)$	-16.486 80	-9.430 40	-9.327 12	-17.625 80	-13.250 00	-13.558 60
$D_5(I)$	14.863 70	10.720 80	10.582 90	14.575 30	15.287 50	14.539 50
$D_6(I)$	-164.243 00	-130.881 00	-131.177 00	-159.383 00	-158.792 00	-157.122 00
$D_7(I)$	-5.571 43	-10.144 50	-10.129 50	-6.133 95	-6.287 28	-6.483 39
$D_8(I)$	0.0	-1.647 27	-1.647 27	-2.060 66	-1.639 51	-2.126 61
$K_1(I)$	$\dfrac{(Z+4)\ln(-Z+2)}{e^{0.01}\mu_1(I)}$	$\dfrac{(Z)\ln(-Z+6)}{e^{0.01}\mu_1(I)}$	$\dfrac{(Z)\ln(-Z+6)}{e^{0.01}\mu_1(I)}$	$\dfrac{(Z)\ln(-Z+6)}{e^{0.01}\mu_1(I)}$	$\dfrac{(Z+8)\ln(-Z-2)}{e^{0.01}\mu_1(I)}$	$\dfrac{(Z+6)\ln(-Z)}{e^{0.01}\mu_1(I)}$
$\mu_1(I)$	$\left[\ln\left(\dfrac{N}{\frac{2}{3}(2-Z)}\right)\right]^5$	$\left[\ln\left(\dfrac{N}{5-\frac{3}{2}Z}\right)\right]^5$	$\left[\ln\left(\dfrac{N}{6-2Z}\right)\right]^5$	$\left[\ln\left(\dfrac{N}{2-Z}\right)\right]^5$	$\left[\ln\left(\dfrac{N}{\frac{1}{3}(11-2Z)}\right)\right]^5$	$\left[\ln\left(\dfrac{N}{2-\frac{2}{3}Z}\right)\right]^5$

	Furans Menzofurans Dibenzofurans ($I=7$)	Phenols Manhthols etc. ($I=8$)	Pyrroles Indoles Carbazoles ($I=9$)	Pyridines Quinolines Acridines ($I=10$)	Thiophenes Benzothiophenes Di-Menzothiophenes ($I=11$)
$D_1(I)$	3.788 57	3.449 52	4.562 77	3.871 10	1.728 66
$D_2(I)$	2.079 42	2.228 40	0.874 617	2.166 50	1.741 66
$D_3(I)$	-0.302 699	-0.308 527	-0.121 399 7	-0.314 819	-0.214 667
$D_4(I)$	-12.965 6	-13.262 9	-2.220 54	-13.435 2	-0.441 705
$D_5(I)$	14.194 9	19.442 1	3.130 23	17.170 5	3.133 02
$D_6(I)$	-161.610	-151.829	-81.564 6	-154.621	-128.792
$D_7(I)$	-5.927 26	-7.102 78	-15.453 0	-6.809 25	-9.979 10
$D_8(I)$	-1.451 90	-2.196 02	-1.617 63	-1.576 18	(-1.451 90)[a]
$K_1(I)$	$\dfrac{[(Z+4)\ln(-Z+2)]}{e^{0.01}\mu_1(I)}$	$\dfrac{[(Z+6)\ln(-Z)]}{e^{0.01}\mu_1(I)}$	$\dfrac{[(Z+3)\ln(-Z+3)]}{e^{0.01}\mu_1(I)}$	$\dfrac{(Z+5)\ln(-Z+1)}{e^{0.01}\mu_1(I)}$	$\dfrac{[(Z+4)\ln(-Z+2)]}{e^{0.01}\mu_1(I)}$
$\mu_1(I)$	$\left[\ln\left(\dfrac{N}{\frac{2}{3}(2-Z)}\right)\right]^5$	$\left[\ln\left(\dfrac{N}{2-\frac{2}{3}Z}\right)\right]^5$	$\left[\ln\left(\dfrac{N}{2-\frac{2}{3}Z}\right)\right]^5$	$\left[\ln\left(\dfrac{N}{\frac{1}{3}(5-2Z)}\right)\right]^5$	$\left[\ln\left(\dfrac{N}{\frac{2}{3}(2-Z)}\right)\right]^5$

T_b = Normal boiling point (K)
a From furans

$$\ln\{T_b - D_6(I)x - D_7(I)x^2 - D_8(I)K_1(I)\} = D_1(I) + D_2(I)x - D_3(I)x^2 - D_4(I)x^{-1} + D_5(I)x^{-2};\ x = \ln(N+0.5)$$

may be used for correlating the data. In this equation, an extra term involving the logarithm of the activity coefficient of the solute is added to the right-hand side of Equation (54). Since swelling is observed when gas is dissolved in bitumen, $\bar{V}_2^{\infty}$ should be positive. Thus, on a semilogarithmic plot of the ratio f_2/x_2 against P at constant T, a smooth curve with a positive slope is expected. For small values of x_2 or P, a linear relationship should be obtained from both equations.

In the calculation, fugacities of pure gases may be used instead of $\hat{f}_2$ because the concentration of bitumen is extremely small in the vapor phase. When scattering of the data points is observed, it is an indication that some of the solubility values are of doubtful quality.

Lu et al. [39] screened the solubility values of gases in Athabasca bitumen using this approach, and removed 33 data points out of 100 by this selection procedure. The selected solubility values are presented in Table 12.

Correlation of solubilities of gases in Alberta bitumen

Lu et al. [39] correlated the selected solubility data by means of simple cubic equations of state. The modified van der Waals equation, the Soave form of the Redlich-Kwong equation and the Peng-Robinson equation are found to be suitable. The selected data were used to determine the optimum k_{ij} values by means of the bubble point calculation procedure. These k_{ij} values were subsequently correlated by means of Equation (55):

$$k_{ij} = a_0 + \frac{a_1}{T} \qquad (55)$$

A typical set of a_0 and a_1 values together with the errors obtained from the correlation are presented in Table 13, in which the values are obtained using the Peng-Robinson equation.

APPLICATION OF EQUATIONS OF STATE TO PVT CALCULATIONS

The capabilities of the available simple cubic equations of state for representing volumetric properties vary from equation to equation, especially in the calculation of liquid volumes.

Yu et al. [40] studied Equation (6) and plotted deviation contours of saturated liquid volumes V^l of n-alkanes on a u–w plot. Such a plot is shown in Figure 5, in which the curves represent deviations of 1% in V^l in
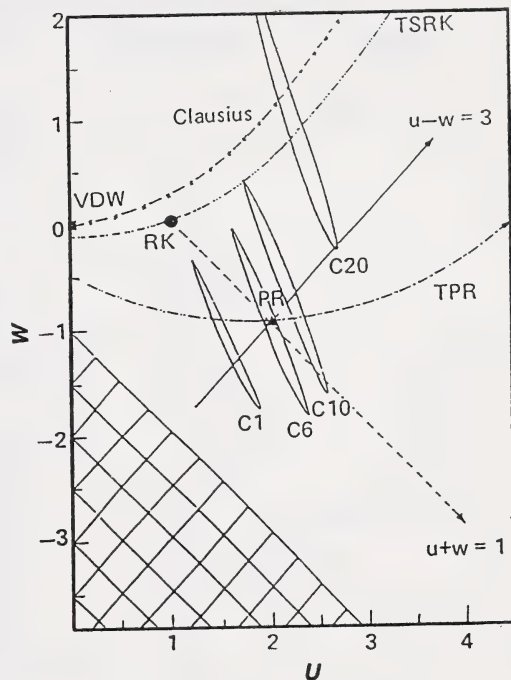

Figure 5. Relative positions of several cubic equations of state deviation and contours of V^l in the temperature range of $0.5 \le T_r \le 0.85$. Curves represent deviations of 1% in V^l.

the temperature range of $0.5 \le T_r \le 0.85$. Several cubic equations are also indicated in the figure and their inadequacy for representing saturated liquid volumes for pure n-alkanes is apparent. Yu et al. suggested that u and w of Equation (6) be related by $u - w = 3$. A new three-parameter cubic equation resulted:

$$P = \frac{RT}{V-b} - \frac{a}{V(V+c)+b(3V+c)} \qquad (56)$$

Let

$$a = \alpha(T_r, \omega)a_c = \frac{\alpha(T_r, \omega)\Omega_{ac}(\omega)R^2 T_c^2}{P_c}, \qquad (57)$$

$$b = \frac{\Omega_{bc}(\omega)RT_c}{P_c}, \qquad (58)$$

Table 12. Solubility data for pure gases in bitumen selected for correlation.

System	Data point no.	T (K)	P (Mpa)	Weight fraction of gas in bitumen
CH_4 – Bitumen	1	299.4	9.77	0.013 2
	2	299.6	8.25	0.010 6
	3	300.0	7.04	0.010 0
	4	300.7	5.79	0.007 9
	5	301.1	4.46	0.006 5
	6	300.7	3.32	0.004 5
	7	301.5	2.32	0.003 1
	8	301.4	1.59	0.002 3
	9	318.9	6.39	0.007 6
	10	317.8	8.18	0.009 6
	11	316.6	5.09	0.006 3
	12	319.0	3.18	0.003 9
	13	342.2	9.65	0.010 3
	14	341.1	8.60	0.009 3
	15	340.7	7.47	0.008 4
	16	340.2	6.29	0.007 2
	17	340.4	5.10	0.005 7
	18	373.0	9.44	0.009 5
	19	373.4	7.82	0.008 2
	20	373.4	5.79	0.006 7
CO_2 – Bitumen	21	297.0	4.01	0.054 5
	22	296.2	4.67	0.061 6
	23	298.7	4.08	0.055 0
	24	298.8	3.01	0.038 7
	25	314.9	2.92	0.030 5
	26	315.0	4.03	0.045 0
	27	315.1	4.81	0.048 9
	28	313.8	6.18	0.064 9
	29	315.5	4.99	0.052 9
	30	315.2	2.94	0.031 5
	31	335.6	2.83	0.025 1
	32	336.0	4.96	0.042 0
	33	336.1	6.09	0.052 0
	34	336.1	3.06	0.026 4
	35	373.15	8.136	0.442 9[a]
	36	373.15	7.134	0.397 0[a]
	37	373.15	6.994	0.393 8[a]
	38	373.15	6.158	0.345 4[a]
	39	373.15	5.268	0.315 3[a]
	40	373.15	4.974	0.316 8[a]
	41	373	3.45	0.021 8
	42	373	6.82	0.051 4
	43	423	3.63	0.018 4
	44	423	6.78	0.041 4
	45	423	10.50	0.061 8
	46	473	3.30	0.014 8
	47	473	6.91	0.032 7
	48	473	10.41	0.050 7
N_2 – Bitumen	49	326.6	8.71	0.004 6
	50	325.9	5.94	0.003 9
	51	325.4	2.88	0.002 1
	52	349.2	8.50	0.004 5
	53	347.9	5.92	0.003 8
	54	347.2	2.97	0.002 0
	55	403.15	4.069	0.057 2[a]
	56	403.15	6.123	0.080 0[a]
	57	403.15	8.929	0.106 0[a]
	58	403.15	9.925	0.121 2[a]
	59	403.15	10.744	0.122 5[a]
	60	403.15	11.293	0.128 6[a]
	61	403.15	11.454	0.130 6[a]
C_2H_6 – Bitumen	62	373	3.22	0.277
	63	373	10.48	0.107 0
	64	423	3.33	0.021 2
	65	423	6.97	0.045 2
	66	473	7.07	0.034 1
	67	473	10.54	0.054 4

Points 1–34 and 49–54 from Reference [4]; 35–40 and 55–61 Reference [3]; 41–48 and 62–67 Reference [2]. [a] Mole fraction as originally reported.

Table 13. Correlation of solubilities of gases in Athabasca bitumen using the Peng-Robinson equation.

Characterization parameters of bitumen:

T_c = 824 K
P_c = 1.267 MPa
ω = 1.231
Molecular weight = 544 g/mol

System	Data points	a_0	a_1	$\lvert\Delta P/P\ \text{exp}\rvert_{\text{avg}}$ x 100%	$\lvert\Delta x\rvert_{\text{avg}}$
CH_4–bitumen	20	– 0.077 13	27.86	4.03	0.006 1
CO_2–bitumen	28	– 0.208 59	96.51	4.20	0.010 8
N_2–bitumen	13	0.038 35	5.09	5.73	0.004 2
C_2H_6–bitumen	6	– 0.118 06	40.28	5.50	0.015 5
Average				4.56	0.008 5

and

$$c = \frac{\Omega_{cc}(\omega)RT_c}{P_c},\qquad(59)$$

with

$$\Omega_{cc}(\omega) = w\,\Omega_{bc}(\omega)\qquad(60)$$

The generalized expressions in terms of T_r and ω are determined [41] using the properties of n-alkanes as follows:

$$\Omega_{ac}(\omega) = 0.468630 - 0.0378304\,\omega$$
$$+ 0.00751969\,\omega^2,\qquad(61)$$

$$\Omega_{bc}(\omega) = 0.0892828 - 0.0340903\,\omega$$
$$- 0.00518289\,\omega^2,\qquad(62)$$

$$u = 1.70083 + 0.648463\,\omega + 0.895926\,\omega^2,\qquad(63)$$

and

$$\log_{10}\alpha = m(\omega)(A_0 + A_1 T_r + A_2 T_r^2)(1 - T_r)\qquad(64)$$

Two acentric factor ranges are used in the application of Equation (64). For $\omega \leq 0.49$,

$$m(\omega) = 0.406846 + 1.87907\,\omega - 0.792636\,\omega^2$$
$$+ 0.737519\,\omega^3,\qquad(65)$$

$$A_0 = 0.536\ 84,$$
$$A_1 = -0.392\ 44,$$
$$A_2 = 0.265\ 07.$$

For $0.49 < \omega \leq 1.0$

$$m(\omega) = 0.581981 - 0.171416\,\omega + 1.84441\,\omega^2$$
$$- 1.19047\,\omega^3\qquad(66)$$

$$A_0 = 0.793\ 55$$
$$A_1 = -0.534\ 09,$$
$$A_2 = 0.372\ 73.$$

Equations (56) through (66) complete the description of the proposed equation. Its usefulness for asymmetric mixture density calculations has been demonstrated for systems such as CO_2–C_{19} and C_1–C_{10}.

One way to improve an existing cubic equation of state, such as the Peng-Robinson equation, for representing liquid volumes is to apply a volume-translation technique to change it from a two-parameter equation to a three-parameter equation, without affecting its Ω_a value at the critical point. Such a translation has been made by Yu and Lu [41]. The proposed expressions together with a recent modification of the expression for Ω_{bc} [42], are given below:

$$P = \frac{RT}{V-b} - \frac{a(T)}{V^2 + \left(\left[2 - \frac{4c}{b}\right]\right)bV + \left(\frac{2c^2}{b^2} - 1\right)b^2}\qquad(67)$$

$$\frac{c}{b} = \frac{(2-u)}{4} \tag{68}$$

$$u = 1.5251 + 1.1146\omega + 1.1538\,\omega^2, \tag{69}$$

$$b = \frac{\Omega_{bc} RT_c}{P_c} \tag{70}$$

$$\Omega_{bc} = \frac{0.3112}{(2+u)} \tag{71}$$

$$a = \alpha a_c = \frac{\alpha \Omega_{ac} R^2 T_c^2}{P_c} \tag{72}$$

$$\Omega_{ac} = 0.45724, \tag{73}$$

$$\alpha = [1 + m(\omega)(1 - T_r^{1/2})]^2, \tag{74}$$

For $\omega \leq 0.2$

$$m = 0.37464 + 1.54226\,\omega - 0.26992\,\omega^2,$$

For $0.2 \leq \omega \leq 2.0$

$$m = 0.37964 + 1.48503\,\omega \tag{75}$$

$$- 0.16442\,\omega^2 + 0.01667\,\omega^3 \tag{76}$$

Equations (67) through (76) complete the description of the volume-translated Peng-Robinson equation.

REFERENCES

1. D. Lal, A.E. Mather and F.D. Otto, Solubility of CO, H_2 and $CO-H_2$ mixtures in Athabasca bitumen, Proc. 34th Can. Chem. Eng. Conf., Sep 30–Oct 3 (1984) pp. 510–513.
2. D.B. Robinson, H. Kalra and S.-K. Sim, Behavior of bitumen-water-gas systems, Final report on AOSTRA research agreement 43 Sep (1980).
3. C.T. Fu, V.R. Puttagunta and G. Vilscak, VLE Properties for CO_2-Athabasca bitumen and N_2-Athabasca bitumen, AOSTRA J. Res., 2 (1985) 73.
4. W.Y. Svrcek and A.K. Mehrotra, Gas solubility, viscosity and density measurements for Athabasca bitumen, J. Can. Pet. Tech., 21, Jul–Aug (1982) 31.
5. M. Radosz, Continuous-flow apparatus for measuring phase equilibria in supercritical gas-heavy hydrocarbon systems, in "Supercritical fluid technology," J.M.L. Penniger, M. Rodoz, M.A. McHugh and V.J. Krukonis, Eds., Elsevier Science Publishers, Amsterdam (1985) pp. 179–190.
6. A.K. Mehrotra and W.Y. Svrcek, Viscosity, density and gas solubility data for oil sand bitumens, part I, Athabasca bitumen saturated with CO and C_2H_6, AOSTRA J. Res., 1 (1985) 263.
7. A.K. Mehrotra and W.Y. Svrcek, Correlations for properties of bitumen saturated with CO_2, CH_4, and N_2, and experiments with combustion gas mixtures, J. Can. Pet. Tech., 21, Nov–Dec (1982) 95.
8. D.B. Robinson and S.-K. Sim, The behavior of bitumen mixtures during *in situ* recovery, Progress report on AOSTRA agreement 184, Nov (1981).
9. A.K. Mehrotra and W.Y. Svrcek, Measurement and correlation of viscosity, density and gas solubility for Marguerite Lake bitumen saturated with carbon dioxide, AOSTRA J. Res., 1 (1984) 51.
10. A.K. Mehrotra and W.Y. Svrcek, Viscosity, density and gas solubility data for oil sand bitumens. part II: Peace River bitumen saturated with N_2, CO, CH_4, CO_2 and C_2H_6, AOSTRA J. Res., 1 (1985) 269.
11. A.K. Mehrotra and W.Y. Svrcek, Viscosity, density and gas solubility data for oil sand bitumen, part III: Wabasca bitumen saturated with N_2, CO, CH_4, CO_2 and C_2H_6, AOSTRA J. Res., 2 (1985) 83.
12. A.E. Mather, Private communication to B.C.-Y. Lu (1985).
13. Internal reports of Alberta Research Council: P. Bulkowski and G. Prill (1978), M. Polikar (1980), D.Wallace (1978–1983), C.T. Fu, V.R. Puttagunta and G. Vilscak (1985).
14. D.B. Robinson, AOSTRA technical report – The thermodynamic and transport properties of bitumens and heavy oils (1984).
15. J.D. van der Waals, "The continuity of the gaseous and liquid phases," Doctoral dissertation, Leiden, Holland (1873).
16. O. Redlich and J.N.S. Kwong, On the thermodynamics of solutions, V., An equation of state. Fugacities of gaseous solutions, Chem. Rev., 44 (1949) 233.
17. G. Soave, Equilibrium constants from a modified Redlich-Kwong equation of state, Chem. Eng. Sci., 27 (1972) 1197.
18. D.Y. Peng and D.B. Robinson, A new two-constant

equation of state, Ind. Eng. Chem. Fundam., 15 (1976) 59.

19. A. Harmens and H. Knapp, Three-parameter cubic equation of state for normal substances, Ind. Eng. Chem. Fundam., 19 (1980) 291.

20. G. Schmidt and H. Wenzel, A modified van der Waals type equation of state, Chem. Eng. Sci., 35 (1980) 1503.

21. N.C. Patel and A.S. Teja, A new cubic equation of state for fluid and fluid mixtures, Chem. Eng. Sci., 37 (1982) 463.

22. Y. Adachi, B.C.-Y. Lu and H. Sugie, Three-parameter equations of state, Fluid Phase Equilibria, 13 (1983) 133.

23. J.J. Martin, Cubic equations of state — which?, Ind. Eng. Chem., 18 (1979) 81.

24. A. Peneloux, E. Rauzy and R. Freze, A consistent correlation for Redlich-Kwong-Soave volumes, Fluid Phase Equilibria, 8 (1982) 7.

25. R. Freze, J.-L. Chevalier, A. Peneloux and E. Rauzy, Vapor-liquid equilibrium calculations for normal fluid systems using a new cubic equation, Fluid Phase Equilibria, 15 (1983) 33.

26. Y. Adachi, B.C.-Y. Lu and H. Sugie, A four-parameter equation of state, Fluid Phase Equilibria, 11 (1983) 29.

27. S.E.M. Hamam, W.K. Chung, I.M. Elshayal and B.C.-Y. Lu, Generalized temperature-dependent parameters of the Redlich-Kwong Equation of state for vapor-liquid equilibrium calculations, Ind. Eng. Chem. Process Des. Dev., 16 (1977) 51.

28. G. Heyen, Liquid and vapor properties from a cubic equation of state, Proc. 2nd Int. Conf. on phase equilibria and fluid properties in the chemical industry, DECHEMA, Frankfurt/Main (1980) pp. 9–14.

29. W.L. Kubic, Jr., A modification of the Martin equation of state for calculating vapor-liquid equilibria, Fluid Phase Equilibria, 9 (1982) 79.

30. G.G. Fuller, A modified Redlich-Kwong-Soave equation of state capable of representing the liquid state, Ind. Eng. Chem. Fundam., 15 (1976) 254.

31. Y. Adachi and B.C.-Y. Lu, Simplest equation of state for vapor-liquid equilibrium calculations. A

modification of the van der Waals equation, AIChE J., 30 (1984) 991.

32. C.H. Twu, Prediction of thermodynamic properties of normal paraffins using only normal boiling point, Fluid Phase Equilibria, 11 (1983) 65.

33. C.H. Twu, An internally consistent correlation for predicting the critical properties and molecular weights of petroleum and coal-tar liquids, Fluid Phase Equilibria, 16 (1984) 137.

34. M.G. Kesler and B.I. Lee, Improved prediction of enthalpy of fractions, Hydrocarbon Processing, 55 no. 3 (1976) 153.

35. C. Black and C.H. Twu, Correlation and prediction of thermodynamic properties for heavy petroleum, shale oils, tar sands and coal liquids, Paper presented at AIChE National Meeting, March 27–31, Houston (1983).

36. C.-T. Fu, R. Puttagunta, L. Baumber and C. Hsi, Pseudo-critical properties of heavy oils and bitumen, Fluid Phase Equilibria 30, (1986) 281.

37. I.R. Krichevsky and Ya.S. Kasarnovsky, Thermodynamic calculations of solubilities of nitrogen and hydrogen in water at high pressures, J. Am. Chem. Soc., 57 (1935) 2168.

38. I.R. Krichevsky and A.A. Ilinskaya, Zh. fiz. Khim. USSR, 19 (1945) 621. Quoted from J.M. Prausnitz, "Molecular thermodynamics of fluid phase equilibria," Prentice-Hall (1969) 360.

39. B.C.-Y. Lu, W.K. Chung, Y. Adachi and T. Boublik, Correlation and prediction of solubilities of gases in Athabasca bitumen, AOSTRA J. Res., 3 (1986) 139.

40. J.-M. Yu, Y. Adachi and B.C.-Y. Lu, Selection and design of cubic equations of state, ACS Symposium Series 300, Equations of state: Theories and applications, Eds: K.C. Chao and R.L. Robinson, Jr., Ch. 26, Am. Chem. Soc., Washington, D.C. (1986) pp. 537–559.

41. J.-M. Yu and B.C.-Y. Lu, A three-parameter cubic equation of state for asymmetric mixture density calculations, Fluid Phase Equilibria, 34 (1987) 1.

42. M.R. Margerum, A.S.-F. Cheung and B.C.-Y. Lu, Further evaluation of the volume-translated Peng-Robinson Equation proposed by Yu and Lu, University of Ottawa internal report (1988).

7

VISCOSITY

F. A. Seyer
C. W. Gyte

Department of Chemical Engineering
University of Alberta
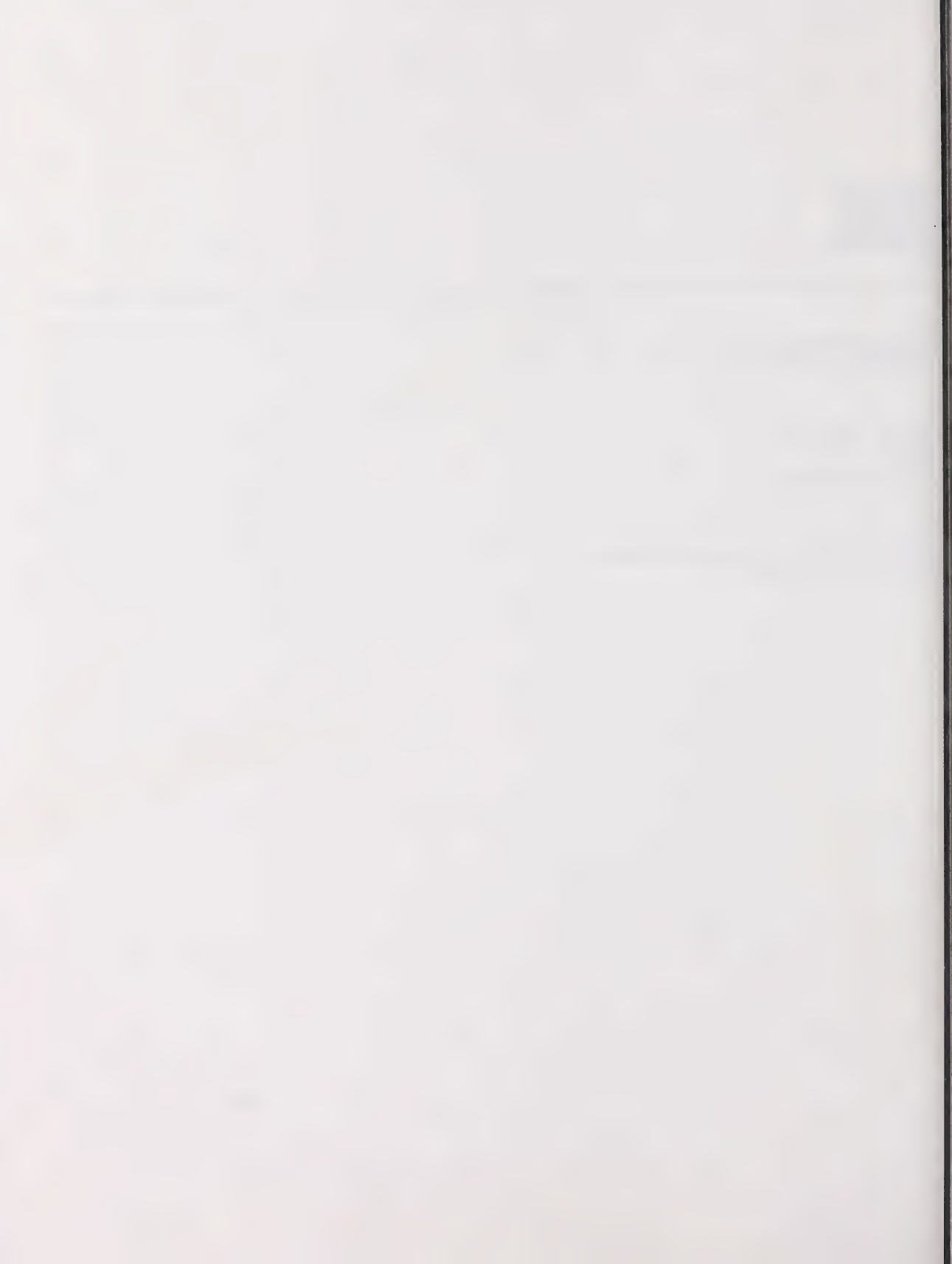
INTRODUCTION

Definition of viscous behavior

The viscosity, η, of a fluid reflects the resistance it offers to either the flow and deformation of itself, or to the flow of materials through it such as settling solids. In the simplest case the viscosity is a single constant at given pressure and temperature and the fluid is called Newtonian. The essence of Newtonian fluid behavior can best be illustrated by reference to Figure 1. In Figure 1 a fluid is contained between two parallel plates separated by a distance, d, and with area, A. The upper plate is pulled at a steady velocity, V, and the resultant steady force, F, is measured (In practice the independent and dependent variable roles of V and F may be reversed, depending on the design of the instrument.) For Newtonian materials Equation (1) is found to apply with η precisely constant as either V or d are varied at given temperature and pressure:

$$\frac{F}{A} = \eta \frac{V}{d} \tag{1}$$

Inspection of Equation (1) indicates the dimensions of viscosity are (Force x Time)/(Length)^2. In the SI system the accepted units are newtons, seconds, and metres so that

$$\eta \sim \frac{N \cdot s}{m^2} = \frac{kg}{m \cdot s} \quad \text{or} \quad Pa \cdot s$$

where $1\ Pa = 1\ N/m^2$. The units of mPa·s are numerically equal to the commonly used centipoise (cP) in the cgs system. Kinematic viscosity is defined as $\eta^1 = \eta/\rho$ where ρ is the fluid density in kg/m^3. Thus SI units are m^2/s. Correspondingly, in the cgs system the unit of kinematic viscosity is the centistoke obtained by dividing the viscosity in cP by density in g/cm^3 (1 centistoke = 1 m^2/s x 10^6).

In utilizing practical instruments or experiments, such as rotational cup-and-cylinder or capillary devices, it is necessary to generalize the variables to shear stress ($\tau = F/A$) and shear rate or velocity gradient ($\gamma = V/d$). Thus, a general definition of Newtonian behavior is:

$$\tau = \eta \gamma \tag{2}$$

in which η is independent of γ. At temperatures of interest for in situ recovery, or for upgrading, most heavy oils will exhibit Newtonian behavior.
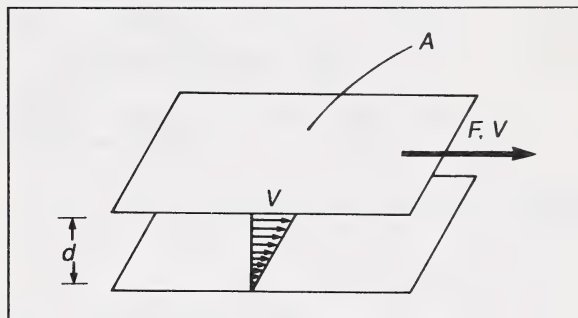

Figure 1. Viscosity determination by parallel plates.

The most common non-Newtonian behavior is manifest in a decrease of viscosity with increase of the shear rate. Both behaviors are illustrated qualitatively by Figure 2 where the slope gives viscosity for the material. As will be shown for heavy oils, deviations from Newtonian behavior are slight compared with temperature or solvent effects.
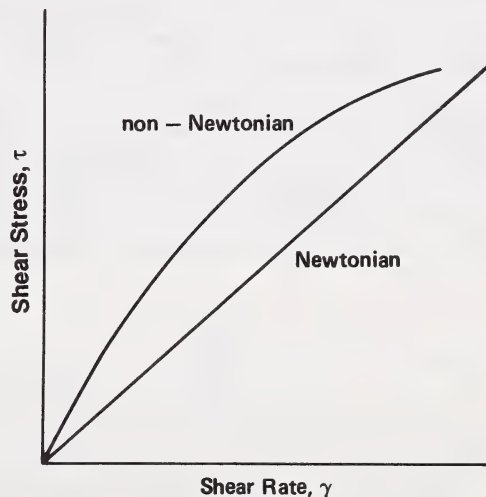

Figure 2. Types of behavior with shear rate.

More complicated behavior can occur, particularly when dealing with concentrated emulsions and slurries. For example, dependence of stress level on time of shearing and apparent yield stress may occur. In either case, care is required in the interpretation of measurements and in their application. Generally (except for cone-and-plate viscometers) a viscometric

equation of state or an analytical relation for the curve in Figure 2 is required in order to determine true shear stress-shear rate data from a given instrument. In the absence of true values, data obtained from instruments with different geometries will not superimpose, depending on how pronounced the non-Newtonian behavior is. Reference [1] provides a thorough discussion of techniques for measurement of Newtonian and non-Newtonian behavior.

Measurement techniques

There are numerous measurement devices that can be applied to the determination of shear stress, shear rate, and consequently viscosity of a sample. However, distinct techniques can be consolidated to four classes. Each of these has advantages depending on considerations of accuracy, data end-use, cost, convenience, sample size, and the ranges of pressure, temperature, and viscosity.

To determine shear stress, it is necessary to create shear in a geometry for which shear rate can be determined from measured values of speed or flow rate. Similarly, shear stress must be determinable from measured values of a force, torque, or pressure, depending on the instrument.

Linear flow. Devices with geometry such as that illustrated by Figure 1, while offering geometric simplicity, have no practical value for heavy oils. The list of disadvantages includes major problems in controlling or analyzing edge effects, and difficulty of instrumentation.

Rotational viscometers. In simple form, a cylinder is rotated within a concentric cup of the sample (Couette flow device). The schematic arrangement is illustrated by Figure 3. The inner cylinder has a rotational speed, ω; the torque, T, is measured on either the cylinder or the cup. Equations (3) and (4) are the working forms of equation for the geometry of Figure 3. Development of the equations is discussed in most textbooks on transport phenomena as well as books on rheology [1–3].

$$\eta = \frac{\tau_R}{\gamma_R} \tag{3}$$

$$\gamma_R = \frac{2\omega}{1 - \left(\dfrac{R}{R_o}\right)^2} \tag{4}$$

$$\tau_R = \frac{T}{2\pi R^2 L} \tag{5}$$

$$\eta = K\frac{T}{\omega} \tag{6}$$

Equations (3), (4), and (5) ignore the end effect caused by drag on the end of the cylinder, but in a properly designed instrument this will be negligible if the cylinder is hollow, or sufficiently long and slender. For a given instrument setup, all of the geometric factors in Equations (3), (4), and (5) are fixed so that in Equation (6) all of the fixed parameters can be incorporated in a constant K for the instrument. The constant K can be evaluated from measurements using a standard oil of known viscosity. Standard oils can be purchased from a number of sources such as instrument companies selling calibrated standards.
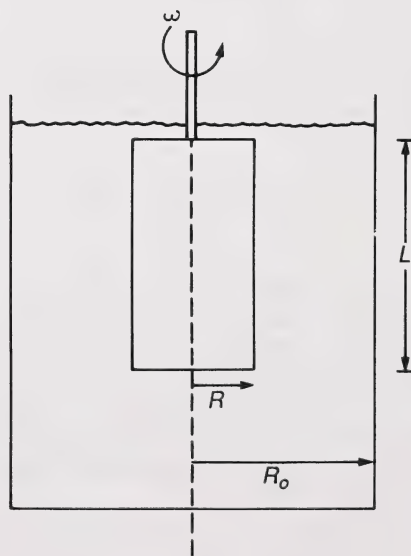

Figure 3. Concentric cylinder viscometer.

Equations (3), (4), and (5) show that a concentric cylinder instrument can be designed for a great deal of flexibility and essentially any range of liquid viscosity of interest. Additionally there is the advantage that the instrument can be totally enclosed for temperature and pressure control (see following sections).

If measurements on liquids with very low viscosity are required (e.g. water), very small gaps and relatively high rotational speeds will be required to generate accurate measurements of torque, but care must be taken in ensuring concentricity of the elements. In practice, a limit of rotational speed exists beyond which secondary or turbulent flows negate the analysis leading to Equations (3), (4), and (5). Speeds should be maintained below a critical value given in Reference [2]:

$$\omega_c = \frac{R_o}{R} \frac{\eta}{\rho R^2} \frac{41.3}{\left(1 - \dfrac{R}{R_o}\right)^{1.5}} \qquad (7)$$

If the outer cup is rotated, somewhat higher rotational speeds are acceptable.

As an example, in Equation (7) with Athabasca bitumen at 20°C, $\eta_o = 6000$ Pa·s, $\rho = 1000$ kg/m^3:

$R/R_o = 0.95$
$R = 1.2 \times 10^{-2}$ m
$\omega = 0.1$ rad/s (0.95 rpm)
$L = 3 \times 10^{-2}$ m.

Equation (7) is used to check whether the flow is steady:

$$\omega_c = \left(\frac{1}{0.95}\right) \times \left(\frac{6000\,\text{Pa·s}}{\left(1000\,\text{kg/m}^3\right)\left(1.5 \times 10^{-2}\,\text{m}\right)^2}\right)$$

$$\left(\frac{4\ 1.3}{(1 - 0.95)^{1.5}}\right) = 1.04 \times 10^8\ \text{s}^{-1}$$

Thus the experiment is operating far below the limit of critical speed. In fact it should be observed that critical speed will never be a problem with typical heavy oils.

Using Equation (4)

$$\gamma_R = \frac{2\,(0.1)}{1 - (0.95)^2} = \frac{2.05}{s}$$

and therefore with Equation (5) for shear stress

$$\tau_R = (6000)(2.05) = 12\,300\ \text{N/m}^2.$$

The torque to be measured is

$$T = 2\pi\,(1.5 \times 10^{-2})^2\,(3 \times 10^{-2})(12\,300)$$
$$= 0.522\ \text{N·m}.$$

The following two sections list several available commercial instruments as well as specialized designs. It will be seen that rotational instruments can be adapted for wide ranges of temperature and pressure. For high pressures, special seals are required and in some cases a magnetic coupling is used to rotate the cylinder. At extremes of temperature and pressure the viscosity range of a given instrument becomes somewhat restricted owing to mechanical considerations.

An advantage of the simplest commercial instruments is that only a relatively small sample is needed. Typically 10 to 15 mL of sample may be required. However, in specialized instruments much larger volumes may be required. In the gap between the cylinders, shear rate is not constant, which complicates interpretation of non-Newtonian behavior [1].

A variation of the rotational viscometer design referred to as the cone-and-plate viscometer is shown in Figure 4. In this viscometer a small sample of fluid is sheared between a flat plate and a shallow-angled cone (0.5 to 2°). Equation (6) is applicable with the appropriate value for the machine constant, K. In this case, in terms of the geometric parameters analogous to Equations (4), (5), and (6):
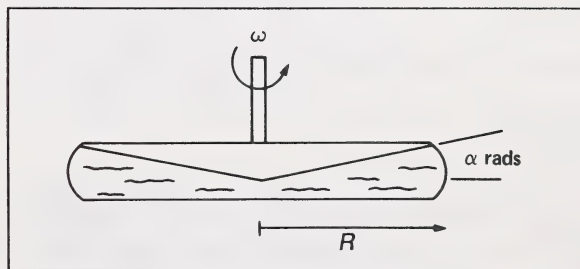

Figure 4. Cone-and-plate rotational viscometer.

$$\eta = \frac{\tau}{\gamma} = \frac{\dfrac{3T}{2\pi R^3}}{\dfrac{\omega}{\alpha}} \qquad (8)$$

Using the same fluid property parameters as in the previous example, and assuming the cone is $0.5° = 0.0087$ rad with $R = 0.025$ m, and $\omega = 0.1/s$:

$$\gamma = \frac{\omega}{\alpha} = \frac{0.1}{0.0087} = \frac{11.5}{s}$$

and the torque to be measured is

$$T = \frac{(6000)(11.5)(2)(0.025)^3}{3} = 2.3\,\text{N} \cdot \text{m}$$

The principal advantages of this instrument are its ability to rigorously define non-Newtonian behavior, and the extremely small sample size required. In the sheared space, shear rate is constant and reaches steady state in a fraction of a second. This results in measurements being made with limited viscous heating. Thus viscosity-shear rate-time profiles are readily determined without approximation.

There are several limitations related to the small spacing that must be accurately set between the cone and plate. Allowable size of emulsion or suspension particles is 50 to 100 μm depending on the cone angle. Particles that are too large result in contact between the cone and plate. On some machines, precise alignment of the cone and plate can be tedious and time consuming, depending on the skill of the operator. All commercial machines are limited to modest temperatures and cannot be operated above atmospheric pressure.

Equation (8) shows there is considerable flexibility of design and that a considerable range of viscosity can be measured. In practice, excessive rotational speeds will throw the fluid from the gap between the cone and plate. This situation is unlikely to be encountered with heavy oils.

Tube flow viscometers. Figure 5 illustrates the essential features of tube flow viscometers. Fluid flows from the inlet to the outlet of a round tube of known length, L, and radius, R. The volumetric flow rate is, Q, and the inlet and outlet pressures are P_1 and P_2 respectively. In practice the flow can be controlled by a positive displacement pump or alternatively, the pressures P_1 and P_2 can be controlled. The orientation of the tube is unimportant except in simple gravity drainage instruments where the driving force is determined solely by hydrostatic head. Equations (9) to (11) are the working equations [1].
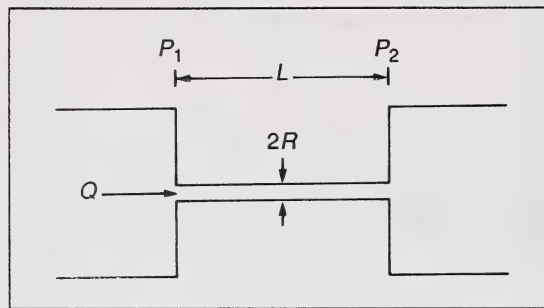

Figure 5. Tube flow viscometer.

$$\eta = \frac{\left(P_1 - P_2\right)\pi R^4}{8LQ} \tag{9}$$

and at the tube wall

$$\gamma = \frac{4Q}{\pi R^3} \tag{10}$$

$$\tau = \frac{\left(P_1 - P_2\right)R}{2L} \tag{11}$$

or in the form of Equation (6)

$$\eta = K\frac{\left(P_1 - P_2\right)}{Q} \tag{12}$$

In practice, entrance effects occur [1,3] as the fluid enters the tubing. If the viscometer is well designed (large L) the loss of pressure at the entrance will be a small fraction of the total pressure loss over the tubing. If dissolved gases are present, enough back pressure has to be maintained to avoid flashing at the exit.

Inspection of Equations (9), (10), and (11) shows there is considerable flexibility in design of tube flow instruments. In practice, operation must be limited to values of the group (Reynolds number) $2Q\rho/\pi\eta R$ less than approximately 2000, Equation (13). This is not a significant limitation given the high viscosity of heavy oils.

$$\left(\frac{2Q\rho}{\pi R\eta}\right)_{crit} < 2000 \tag{13}$$

Inspection of Equation (9) shows tubing radius must be known very accurately to determine accurate values of viscosity.

Miscellaneous devices. Various techniques exist to determine viscosity conveniently and at modest cost. These include a variety of devices which utilize steady-state gravity-induced motions of rods, spheres, or bubbles through a sample to determine the viscosity. A principal disadvantage is that these are not susceptible to rigorous analysis for shear rate and shear stress so that calibration must be done with Newtonian oils of known viscosity. Useful range is limited to modest viscosity (less than 10^5 mPa·s).

A falling ball device takes advantage of Stokes' law such that [4]

$$\eta = \frac{2R^2 \left(\rho_s - \rho_f\right) g}{V_t} \qquad (14)$$

ρ_s, ρ_f = sphere and sample densities
g = gravitational acceleration
R = radius of sphere
V_t = steady velocity of fall, distance divided by time.

For a falling sphere the shear rate experienced by the fluid cannot be defined uniquely as it depends on position around the sphere and also distance from the sphere. Nevertheless, the maximum is close to:

$$\frac{3}{2}\left(\frac{V_t}{R}\right) \qquad (15)$$

Equation (14) is valid at Reynolds number less than approximately 0.1 defined as:

$$R_e = \frac{2 R V_t}{\eta} \rho_f \qquad (16)$$

In practice, gravity devices are influenced by wall effects which have to be calibrated or corrected for. The corrections can be large if the sphere or other object is large compared with the radius of the container, R_c.

Commercial viscometers. The previous section discussed several viscometric geometries. The main types of viscometers are: rotational viscometers — controlled speed (shear rate) and controlled torque (shear stress)

types, and tube viscometers — controlled ram/screw speed (shear rate) and controlled pressure (shear stress) types. The most common design is the speed-controlled viscometer where the shear rate is fixed and the resulting shear stress is measured. A list of selected commercial rotational viscometers and some features is given in Table 1, whereas a few selected commercial tube viscometers are listed in Table 2 [1]. Reference [1] should be consulted for a much more thorough listing of manufacturers and features. It is also recommended that the manufacturers be approached for further details as their knowledge and experience in the use of their equipment can be invaluable.

During testing, the sample is subjected to both shear stresses and shear rates. Each of the instruments listed in Tables 1 and 2 is capable of providing estimates of stress and strain or strain rate. The tables include the instrument-controlled variables (e.g. speed, torque, ram/screw speed, or pressure) as well as the ranges of strain and stress.

Specialized instruments. Commercial viscometers may not be appropriate for the measurement of bitumen and heavy oil viscosities. A study by the Alberta Research Council on commercially available apparatus revealed that at high temperature and pressure, capillary tube and rolling ball viscometers tended to plug, causing an inconsistency in measurements [6]. Adaptations of these commercial viscometers may be used to perform the necessary measurements. Three of these specialized instruments are the ARC/AOSTRA viscometer, the JEFRI high-pressure fluid viscometer, and an apparatus designed by Jacobs [6–8].

The ARC/AOSTRA viscometer, illustrated in Figure 6, is an integral part of the apparatus which has the following specifications [6]:

- Leak-free operation at high temperature and pressure
- A mechanism capable of producing pressure variations which are independent of the vapor pressures of the compounds contained within the pressure vessel.
- A means of heating and maintaining constant temperature throughout the apparatus.
- A mechanism which ensures that all the added gas and/or volatile solvent is in solution (i.e. that the system is operated above the saturation pressure or bubble point).
- A mechanism for mixing a known quantity of additive in with the bitumen or heavy oil, to produce a mixture of a constant composition throughout the apparatus.
- For the case of emulsions which are unstable in the

Table 1. Commercial steady rotation viscometers.

Manufacturer	Name of instrument	Measuring heads	Controlled variable	Strained rate range (s⁻¹)	Stress range unit (Pa)	Temperature range (°C)
Brookfield	Synchro-Lectric	coax-cyl. or coni-cyl.	speed	2×10^{-3} to 100	[a]	100
	Wells Brookfield	cone-plate	speed	1×10^{-3} to 1.5×10^3	[a]	100
Contraves	Rheomat 15 (RM15)	coax-cy. or cone-plate	speed	1.3 to 4×10^3	[a]	80
	Rheomat 30 (RM30)	As RM15	speed	1.1×10^3 to 3.9×10^3	[a]	200
Ferranti	Ferranti-Shirley	cone-plate	speed	0.18 to 1.8×10^3	44 to 1.1×10^5	200
	Portable VL	coax-cyl.	speed	43 to 950	0.8 to 390	200
	Portable VM	coax-cyl.	speed	4.7 to 508	0.8 to 610	200
	Portable VH	coax-cyl.	speed	0.3 to 37	0.8 to 6.1×10^3	200
Sangamo	Weissenberg Rheogoniometer R19	cone-plate or par-plate	speed	7×10^3 to 9×10^3	1.9×10^3 to 1.2×10^6	–50 to 400

[a] Dependent on torque system and measuring head.

Table 2. Commercial tube viscometers.

Manufacturer	Name of instrument	Flow rate control (s)	Typical tube sizes (mm)		Flow rate measur.	Typical pressure range (Pa)	Overall ranges		Range	
			Diameter	Length			Strain rate (s⁻¹)	Shear stress (Pa)	Viscosity (Pa·s)	Temp (°C)
Gottfert	Rheograph 2000	ram speed or pressure	0.5 to 2	5 to 30	ram travel	1×10^6 to 2×10^8	0.7 to 6×10^5	2×10^4 to 1×10^7	3.5×10^2 to 1.4×10^7	20–400
	Rhograph 1000	ram speed	0.5 to 2	5 to 30	ram travel	1×10^6 to 1×10^8	0.7 to 3×10^5	2×10^4 to 5×10^6	7×10^{-2} to 7×10^6	20–400
	Extrusionmeter 45	screw speed	Tube or slit dies		–	–	10 to 1.8×10^5	80 to 8×10^5	to	20–400
Instron	Capillary rheometer 3211	ram speed	0.76 to 1.52	25 to 100	ram travel	3×10^5 to 2.8×10^8	0.4 to 1.1×10^4	5.7×10^{-2} to 4.3×10 to 6	5×10^{-2} to 1×10^7	40–350
Tinius Olsen	Seiglaff-McKelvey	ram speed or pressure	0.76 to 2	25.4	ram movement	1×10^5 to 1×10^7	0.2 to 7×10^5	5×10^3 to 1×10^7	7×10^{-3} to 5×10^7	50–426
Davenport	Extrusion rheometer	ram speed	1.0	20	ram movement	1.4×10^8	62 to 1.2×10^4	–	–	100–300
Monsanto	Automatic rheometer	pressure	1 to 2	8 to 16	ram movement	1.1×10^6	10^{-1} to 10^6	2×10^6	–	30–425
	Atkinson-Nancarrow	ram speed	1.5 to 3	18 to 25	ram movement	5×10^7	–	–	–	Amb. –200

absence of artificial surfactants, a mechanism of shearing to produce a constant state of dispersion.

The ARC/AOSTRA viscometer incorporates a positive displacement piston pump that eliminates the need for the apparatus to be pressurized with an inert hydraulic fluid, thus viscosity measurements may be made with bitumen and heavy oil which contains a known amount of additive.

The JEFRI high-pressure fluid viscometer, Figure 7, was designed specifically to measure the viscosity of high-pressure single-phase fluids [7]. One of the central features of this viscometer is the patented double-acting pump which displaces the sample at a very accurately known rate. The viscometer can be operated at much higher pressures than any rotational device and over much wider ranges of viscosity (gases to bitumens) by an appropriate choice of capillary. This viscometer is extremely accurate for laminar flow of Newtonian fluids. These accurate measurements are possible because of four important components:

- Constant-volume, controlled-flow, high-pressure pump.
- Sensitive pressure differential cell.
- Uniform-temperature air bath.
- Long, narrow capillary tube with consistent geometry.

The apparatus designed by Jacobs [8] consists of a gear pump, a mixing cell, and a Contraves DC44 viscometer. The apparatus, shown in Figure 8, is designed around a commercially available viscometer, densiometer, and pump in order to meet the following criteria:

- Temperature range of 20 to 300°C.
- Pressure range of atmospheric to 13.8 MPa.
- Anticipated viscosity range of 3.5 to 1.5×10^6 mPa·s,
- Specific gravity range of 0.75 to 1.10.

These three specialized viscometers show how an adaptation of a commercial viscometer can be used to meet certain required specifications. Depending on the fluid's application, these specialized instruments, and others, should be considered before selecting a commercially available viscometer.

Sample preparation/variability. Viscosity data suffer from sample variability and from the multitude of preparation techniques in use.

Gathering and preparation of samples invariably results in some modification of the natural feedstock. Produced oils may have been subject to high temperatures, solvents, steam, water, caustic, and other materials depending on the recovery scheme. They will
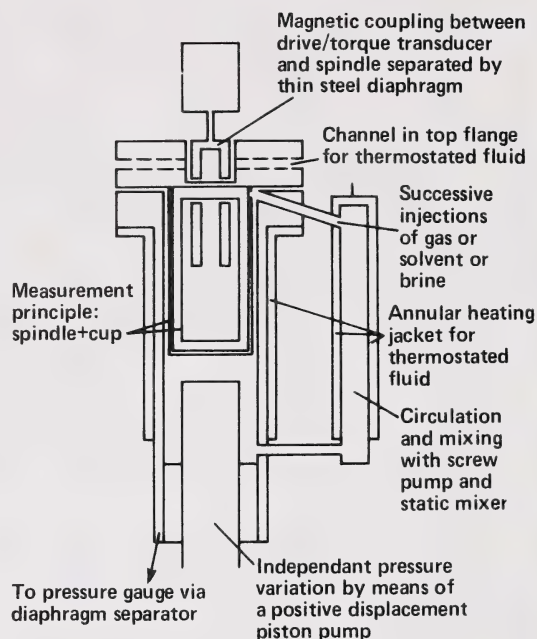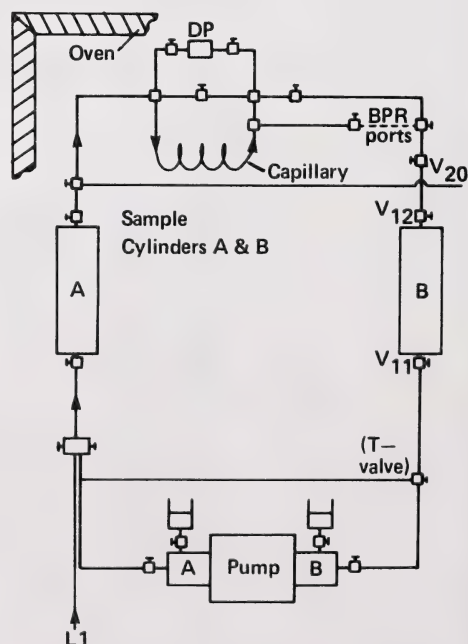

Figure 6. ARC/AOSTRA viscometer.

Figure 7. JEFRI viscometer assembly.

PI — Pressure indicator
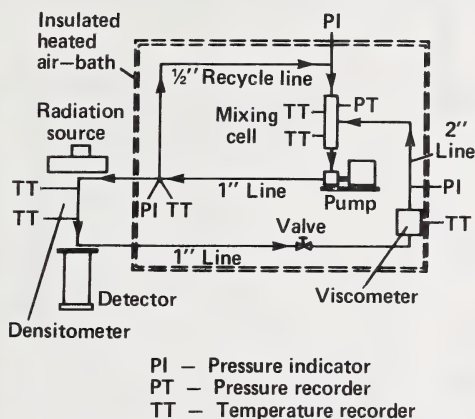PT — Pressure recorder
TT — Temperature recorder

Figure 8. Viscometer designed by Jacobs.

generally contain some mineral matter and varying amounts of water. Samples from cores or mined material must be subjected to an extraction procedure.

There is no single agreed-to procedure of sample preparation for viscosity determination. Vorndran et al. describe one procedure in detail [9]. Other descriptions are available [10,11].

The variety of effects of sample history or preparation are discussed in some detail [10,12]. Detailed conclusions are not possible because of use of different instruments and batches of sample by the various investigators. It is useful, however, to have some idea of the magnitude of uncertainty which may result from sample history. Specific effects such as residual solvent, water, and solids are discussed in the section on viscosity modification. Analytical methods are discussed in Chapter 2.

Viscous heating. Viscous heating of a sample during shear always creates uncertainty in viscosity at the reported temperature. References [1, 3] describe simplified analyses which can be used to check for the magnitude of sample temperature rise expected for either isothermal or adiabatic viscometer elements. Temperature rises of a few degrees Celsius can be expected at viscosities comparable to those of bitumens.

A very thorough review of available data and analyses is available [13]. Of significance is that the paper reports new data on the heating of a synthetic oil with very nearly the same viscosity and temperature

sensitivity as bitumen. It is shown that very large temperature gradients must exist within the fluid in order to conduct the generated heat from the viscometer. Thus, there may be locations within the fluid which are several degrees Celsius warmer than the reported temperature, depending on mechanical detail, point of measurement, shear rate, and so on. This is probably one of the major contributors to scatter in reported viscosity data.

VISCOSITY OF REGIONAL CRUDES — DEPENDENCE ON TEMPERATURE AND PRESSURE

The viscosity and specific gravity of heavy oils varies markedly from deposit to deposit and may vary significantly with location within a deposit [10]. Temperature is by far the most important variable affecting viscosity. Compared with temperature, pressure has only a minor influence on viscosity for natural samples. Pressure does play an important role where dissolved gases are involved, owing to the dependence of solubility on pressure.

An extensive compilation of most viscosity data available to 1984 has been published [10]. Sample handling, preparation, and age are all known to affect the absolute values of observed viscosity. To a lesser extent, sensitivity or slope of viscosity with temperature and pressure may also be affected. Generally there are many procedures of extraction, filtration, and centrifugation used to remove most particulate matter from the oil. The sample preparation invariably will result in some modification of the natural material depending on type and amount of residual solvent. Sample modification may include the loss of a portion of the light ends, and possibly structural modification if subjected to high temperatures. Thus, the most reliable data will result from consistent handling and preparation of samples. The accuracy of absolute values depends further on the accuracy of viscometer calibrations and measurements, particularly temperature. Consequently, there can be considerable discrepancy or scatter in data consolidated from a number of different sources. Obviously scatter in available data inhibits severe testing of the value of any proposed analytical relations.

Table 3 gives typical values of viscosity of the various bitumens of interest. All of these samples were solvent extracted to remove solids and water. Data are at 1 atm pressure.

Table 3. Typical viscosities by region.

Deposit	Viscosity (Pa·s)	
	24°C	65°C
Peace River	125–155	1.9–2.9
Athabasca		
Mildred Lake	17–18.6	–
Lease 86	6.9–265	0.6–5.3
Wabasca		
Wabiskaw	0.4–27.1	00.5–0.7
Carbonate		
Grosmont	–	5.1–8.3
Cold Lake		
Clearwater	20.6–176	0.7–3.1
Lloydminster	2.6–8.9	–

Athabasca bitumen viscosity

Dependence on temperature. Figure 9 is a mean curve for viscosity established from some 20 sets of data [10] at atmospheric pressure. Viscosity varies nearly five orders of magnitude over the temperature range from 20 to 200°C. While occasional data points (5 to 10 out of 200) show a large deviation from the mean curve, the bulk of the data are within ±15% of the curve. In view of the large range covered by the data, and the variety of experimental techniques and sample preparation, this scatter for most purposes is negligible. The curve in Figure 9 should be taken as the standard for Athabasca bitumen. Figure 10 is an extension of Figure 9 into a lower temperature range (< 20°C) [15]. As can be seen, the lower temperature data follow the original curve, enabling an extrapolation of data to less than 20°C.

One significant uncertainty in any data point is the reported value for temperature. At low temperatures, and depending on the detailed design of the viscometer as discussed in the first section of this chapter, viscous heating may bias the reported temperature as well as the assumed flow field for the viscometer. At higher temperatures viscous heating is much less of a problem owing to the low viscosities and decreased temperature dependence of viscosity. However, there is a strong temperature gradient between the apparatus and the ambient conditions, which can create uncertainty in the temperature reported for the sample. Again the magnitude of uncertainty depends on details of the equipment.
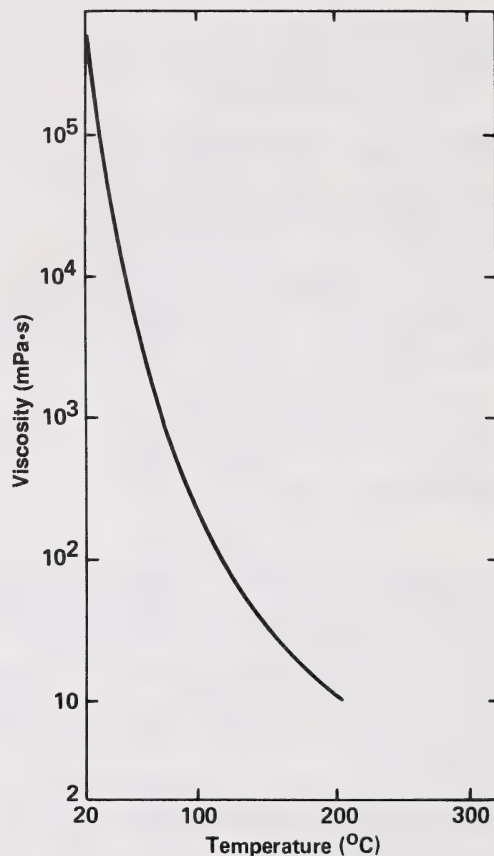

Figure 9. Mean viscosity of Athabasca bitumen.

Significant deviations from the curve, either absolute or qualitative, should be viewed with caution. Extremely thorough experimentation and analysis will be required to establish a significant (more than 15%) deviation from the curve for the average Athabasca bitumen.

Dependence on pressure. Several sets of data have been published to show how viscosity varies with pressure for natural samples. Mehrotra and Svrcek [16] present a consistent set of data, which are given in Table 4, for a sample of Alberta Research Council bitumen pressurized with N_2 at temperatures from 43 to 120°C.

Viscosity shows a consistent increase with pressure over the range from 1 to nearly 100 atm. The increase is very small compared with dependence on temperature.
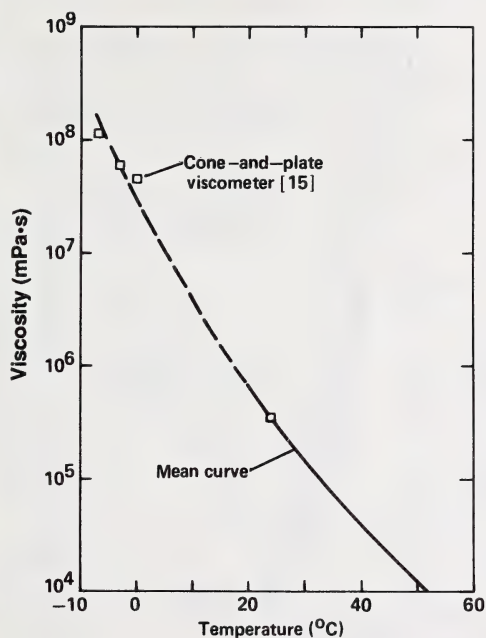
Figure 10. Mean viscosity of Athabasca bitumen (cold temperature data, < 20°C).

From Table 4 it can be seen that the rate of viscosity increase is slightly less at higher temperatures. The effect of pressurization with nitrogen is small since the gas is only slightly soluble. The section on viscosity modification presents data for gas-saturated samples.

Table 4. Viscosity of N_2-pressurized bitumen.

Gauge pressure (MPa)	Viscosity (Pa·s)	
	43°C	120°C
0.0	14.2	0.079
2.0	15.4	0.085
6.0	18.2	0.093
10.0	21.2	0.105

Alberta Research Council researchers have obtained similar viscosity measurements using mechanically pressurized samples of Athabasca bitumen [6]. In their work, consistent with molecular physics, they have fit the data using:

$$\frac{\eta}{\eta_0} = \exp B_T P \qquad (17)$$

in which B_T is a temperature-dependent coefficient, and η_0 is the viscosity at atmospheric pressure. Figure 11 shows the temperature dependence of the coefficient B_T. Superimposed on the figure is the constant value for B_T obtained by Mehrotra based on a least squares regression using their data. Over the more limited range of temperatures studied by Mehrotra, it can be seen that the two interpretations are consistent.

Chemical modifications. Tar sand exposed to air undergoes oxidation of certain components. Data are available showing the magnitude of viscosity change under oxidation accelerated by maintaining the samples in air at 100°C for four days [17]. Figure 12 gives reported values. These viscosities are very much larger than the viscosities leading to the mean curve. These data are of limited value to experimenters concerned with sample handling but do illustrate potential problems to be expected after reasonably severe conditions of oxidation. Similar effects can be expected under some in situ conditions.

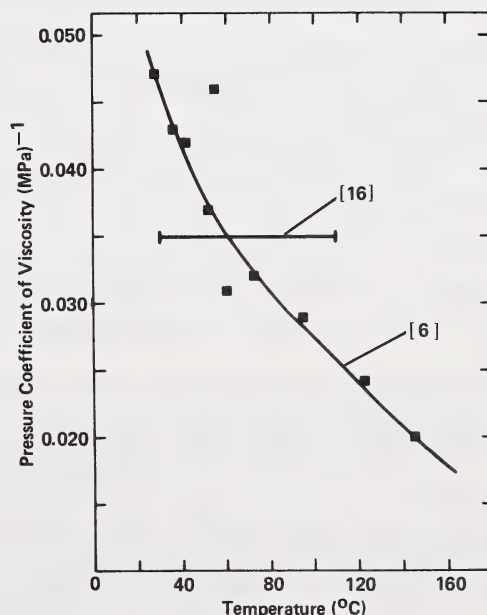**Dependence on location.** There is evidence that viscosity can vary considerably with location and depth

Figure 11. Pressure coefficient of viscosity as a function of temperature for Athabasca bitumen [6,16].
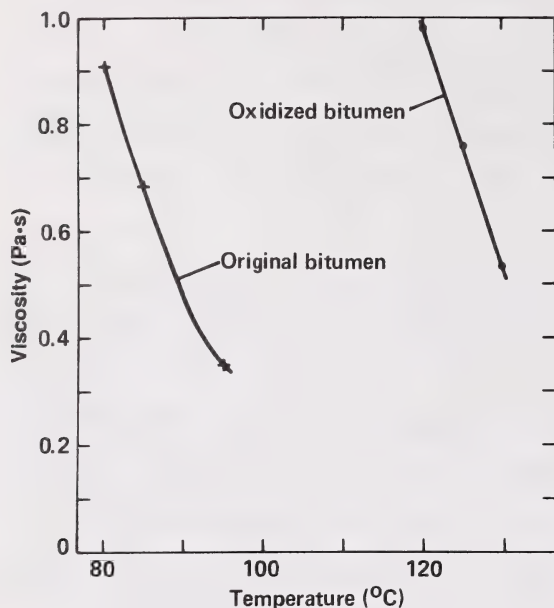
Figure 12. Effect of oxidation on viscosity of Athabasca bitumen.

Figure 13. Variation of viscosity with location, Athabasca bitumen.

within a region. Figure 13 reproduces Athabasca bitumen viscosities obtained for samples ranging from the far south at Abasand to more northerly samples from the Bitumount region [10]. Also included is the mean curve from Figure 9. At 25°C it is evident that the Abasand sample gives viscosity nearly an order of magnitude higher than the mean values. These data show that care must be exercised in setting a value for viscosity based on an isolated sample.

At Bitumount, samples were obtained from differing depths, however, the precision of the measurements does not allow definitive conclusions regarding dependence on depth.

Most evidence shows bitumen to contain higher fractions of asphaltenes near the top of the deposit. This suggests a decrease of viscosity from top to bottom of a deposit. In view of the inherent heterogeneity of tar sand, verification and generalization of any conclusions regarding dependence on location will require statistically sufficient numbers of rigorously consistent measurements.

For most purposes, if only one or two data points are available at a given temperature, it will be sufficient to interpolate or extrapolate with temperature, parallel to the mean curve.
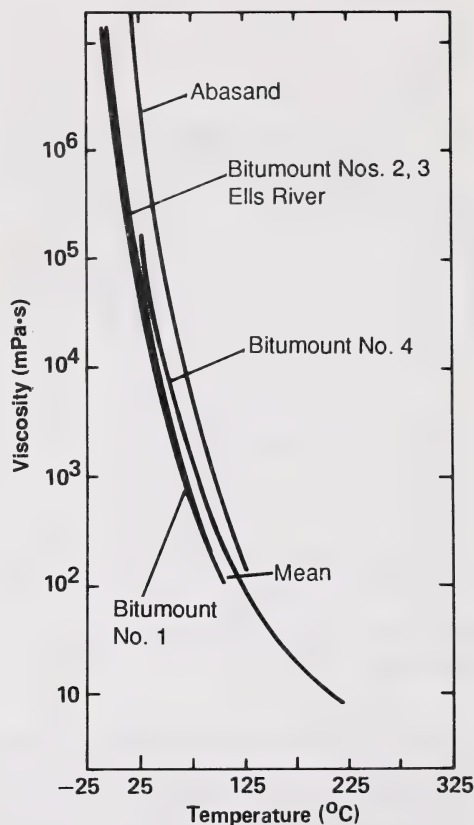
Cold Lake heavy oil viscosity

Dependence on temperature. Oil from the Cold Lake region is generally considered to be lighter and less viscous than Athabasca bitumen. However as shown by Table 3 there is a broad overlap of reported data. Figure 14 shows a bracket for data available from five investigators to 1983 [10]. There is a considerable range of observed viscosity, particularly at the lowest temperatures, compared with the data for Athabasca bitumen. This range reflects differences in samples from a variety of locations, differing preparation techniques, apparatus used, and some information on non-Newtonian behavior [10,18,19,15,20,21]. The non-Newtonian behavior should be viewed in light of the comments on viscous heating.
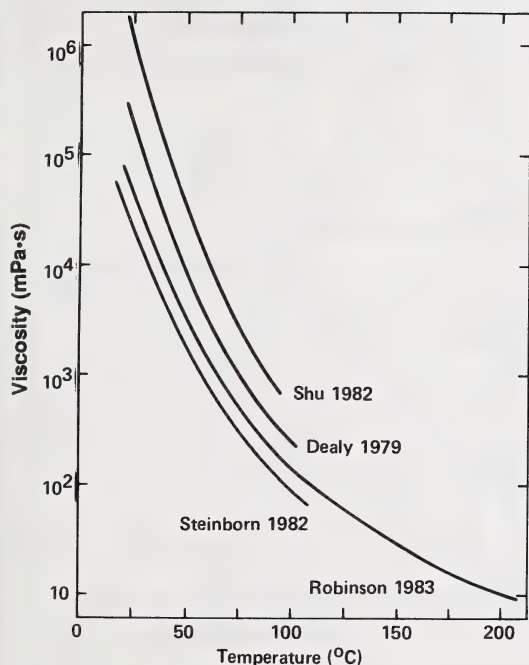
Figure 14. Cold Lake samples viscosity.

Figure 15. Cold Lake/Athabasca comparison.

The lowest values were obtained by a single investigator using rotational viscometers on samples produced by in situ steam stimulation samples [21]. There is insufficient discussion to categorize sample history. Highest values were obtained with a cone-and-plate viscometer on a sample extracted from a core and rotary-evaporated at 38°C to remove residual solvent [18]. This procedure would result in loss of light ends.

New data [6,12,22] for gas-free bitumen should be considered in light of the older data. In Figure 15 data are compared with the bank of data in Figure 14 published earlier. These are within the band occupied by earlier published data and below the mean curve for Athabasca bitumen. It is suggested that the curves of Figure 15 are most representative of Cold Lake samples. The Research Council data [6] can be represented by the equation:

$$\ln \eta = \ln \left[2.303 \left(\frac{6.66}{\left(\frac{1+T}{135} \right)^{1.36}} - 1.2 \right) \right] + 0.435 \, P \, e^{-0.0065T}$$
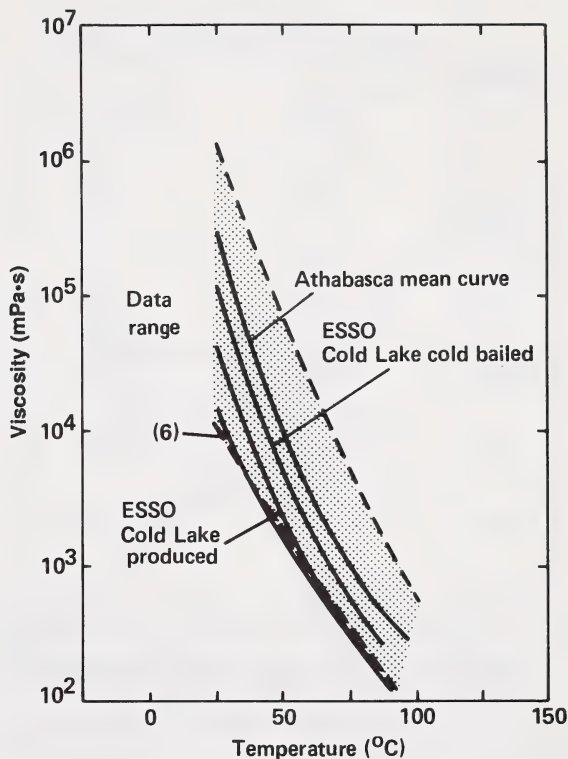
$$(18)$$

T = temperature in °C; P = pressure in MPa.

It is in close agreement with slopes found by other investigators and lies in the lower half of the band. Sample history and handling which minimized loss of light ends are consistent with this observation.

An alternative least squares correlation of similar form has been supplied courtesy of Esso Resources [22]. Equation (19) is a plot of the indicated lines

$$\log_{10} \log_{10} (\eta + 0.8) = C - D \log_{10} (1.8T + 492) \qquad (19)$$

$C = 11.57$, $D = 3.98$ for cold bailed samples and $C = 11.41$, $D = 3.94$ for produced samples in Figure 15. There is generally good agreement with the Research Council curve.

Dependence on pressure. Data have been correlated recently showing the slight effect of pressure on viscosity [6,16]. These are the most comprehensive data available for gas-free Cold Lake samples.

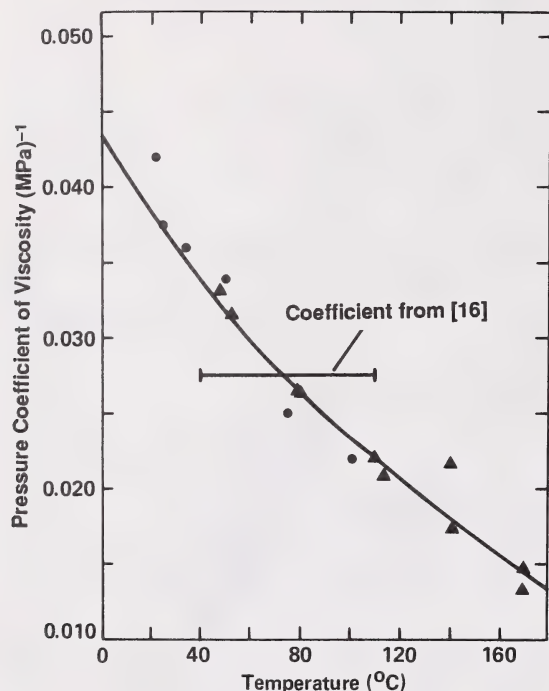Figure 16 shows the pressure coefficient of

Figure 16. Pressure coefficient of viscosity as a function of temperature for Cold Lake bitumen [12].

Figure 17. Peace River bitumen viscosity.

viscosity, B_T, as a function of temperature (Equation (17)) . As with Athabasca bitumen, one set of data is best-fit with a constant coefficient [16]. In either case the dependence on pressure is less than for Athabasca bitumen.

Dependence on location. In light of all of the uncertainties in sample history there are few consistent data to portray dependence on location. Data from samples from the same well [10] suggest an increase of viscosity with depth, however, this is small and hardly conclusive or systematic in view of other uncertainties in the data.

Peace River bitumen viscosity

Reservoir conditions in the Peace River area are approximately 17°C temperature and up to 3.6 MPa pressure [17].

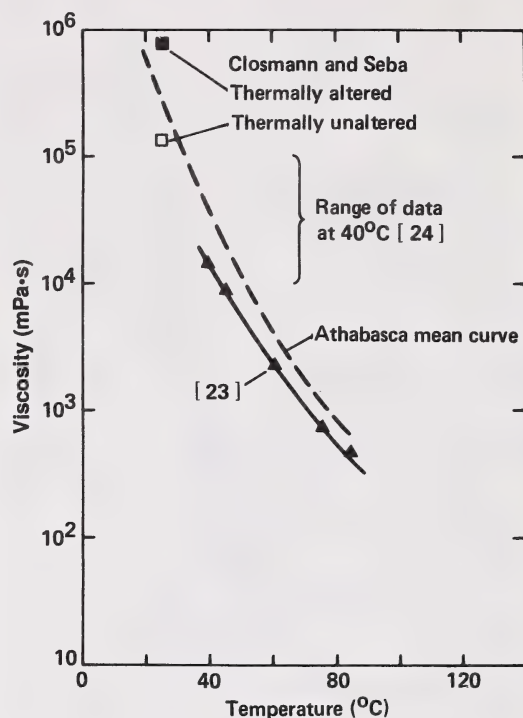**Dependence on temperature.** Peace River bitumen viscosity lies between values for Athabasca and Cold

Lake bitumens at reservoir conditions. Figure 17 shows available data from earlier references, [10] and Mehrotra [23]. The data points essentially cover the range of available data for this material. Evidently the temperature dependence can be taken as equal to that for Athabasca bitumen. Some adjustment of constants is required, however, to reflect the lower value of viscosity for the average Peace River sample. Included are data supplied by Closmann [24] on unaltered and thermally altered samples from the area.

Dependence on pressure. There is negligible dependence of viscosity on pressure up to pressures in excess of 9 MPa. This can be inferred indirectly by extrapolating the available data for N_2-saturated samples [23]. Further consideration is given to the effect of dissolved gases in the section on viscosity modification.

Wabasca bitumen viscosity

The viscosity data for Wabasca bitumen vary over a wide range. Figure 18 shows the range reported in [10]

based on several samples. The data reported in [23] may not be typical of the region as they lie far below any values previously reported. Temperature dependency is consistent among the data sets. Any effect of pressure is negligible in view of the wide range of reported viscosities.
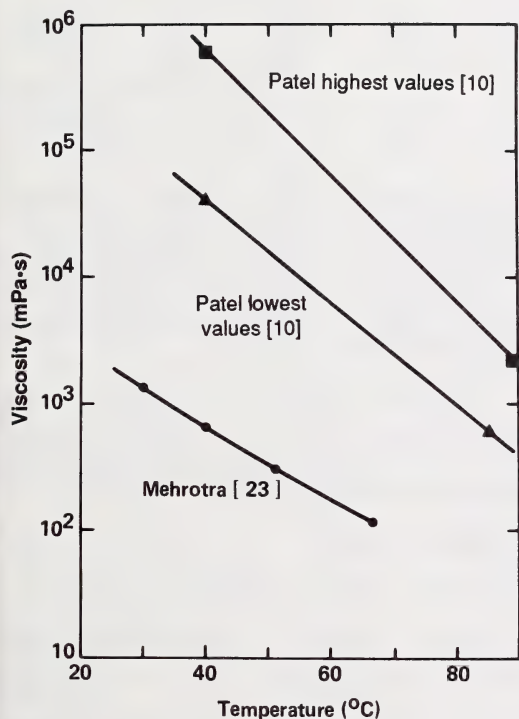

Figure 18. Wabasca bitumen viscosity.

VISCOSITY OF PURE COMPONENTS AND HEAVY OIL DERIVATIVES

Viscosity data for pure components over wide ranges of temperature and pressure is available in numerous references of which the most comprehensive is the International Critical Tables. Perry [4] has conveniently summarized data for numerous pure components in the form of tables and monographs.

Gases

Table 5 gives the viscosity of selected gases of interest in refining and in situ operations [4].

Table 5. Viscosities of selected gases.

Component	η (mPa·s x 1000)	
	20°C	100°C
H_2	8.7[a]	10.2
O_2	18.3	22.0
N_2	17.2	20.8
air	17.8	21.0
CO	17.8	21.0
CO_2	14.2	17.5
SO_2	12.1	14.8
CH_4	10.5	12.9
C_2H_6	9.0	11.2
C_3H_8	8.0	9.8

[a] $\eta_{20°C} = 8.7 \times 10^{-3}$ mPa·s.

Dependence on pressure is negligible up to reduced pressures of approximately 0.5 (reduced pressure equals actual pressure divided by pressure at the critical point). Except for the two heavier hydrocarbons, this is a safe approximation up to at least 1.0 MPa (10 atm). At higher pressures, reduced charts or other sources should be consulted [2,4].

The temperature dependence of viscosity can be safely interpolated by assuming that viscosity depends on the 0.65 power of absolute temperature, T_A. That is

$$\frac{\eta_1}{\eta_2} = \left(\frac{T_{A,1}}{T_{A,2}}\right)^{0.65} \tag{20}$$

Using CO_2 as an example from Table 5, the viscosity at 100°C is predicted assuming the viscosity is known at 20°C. Therefore, using Equation (20):

$$\eta_{100} = 0.0142\left(\frac{100 + 273}{20 + 273}\right)^{0.65} = 0.0166 \text{ mPa·s}$$

compared with 0.0175 mPa·s from the table. Extrapolation to temperatures much beyond 100°C should be carried out with established and more rigorous functions [2] which give a somewhat higher dependence on temperature.

Viscosity of light gas mixtures can be adequately estimated by a semi-empirical equation [2]. For a mixture

$$\eta_{mix} = \sum_{i=1}^{n} \frac{x_i \eta_i}{\sum_{j=1}^{n} x_j \phi_{ij}} \qquad (21)$$

where by definition

$$\phi_{ij} = \frac{\left[1 + \left(\dfrac{\eta_i}{\eta_j}\right)^{1/2}\left(\dfrac{M_i}{M_j}\right)^{1/4}\right]^2}{2.83\left(1 + \dfrac{M_i}{M_j}\right)^{1/2}} \qquad (22)$$

and in which

n = number of species in mixture,
M_i = molecular weight of species i,
x_i = mole fraction of species i.

For a two-component system of species labelled 1 and 2, Equation (21) would expand to

$$\eta_{mix} = \frac{x_1 \eta_1}{x_1 \phi_{11} + x_2 \phi_{12}} + \frac{x_2 \eta_2}{x_1 \phi_{21} + x_2 \phi_{22}}$$

Light hydrocarbon solvents and water

Table 6 lists viscosities for selected light hydrocarbon solvents [4] as well as water. These are of interest in sample preparation and in some cases for in situ or surface recovery of bitumen. At pressures of interest the viscosity of liquids can be safely assumed to be independent of pressure.

The viscosity of these liquids varies exponentially with temperature. For the range of temperatures shown by Table 6, and to somewhat lower temperatures, the simple two-parameter Andrade equation [2,3,10] can adequately represent the viscosity

$$\eta = A e^{B/T} \qquad (23)$$

In Equation (23) A and B are empirical constants for a particular liquid. Note that two data points are

Table 6. Viscosity of selected solvents and water.

Component	η (mPa·s)		Boiling point (°C)
	20°C	40°C	
pentane	0.24	–	36
methylene chloride	0.47	–	40
benzene	0.67	0.52	80
toluene	0.60	0.48	111
xylene	0.62	0.51	139
water	1.01	0.67	100

required to evaluate A and B, although crude methods may be used if only one point is available [2,4].

For miscible liquid mixtures of two components there are few general correlations which can be used over wide ranges of composition and viscosity. An estimate can be obtained from [4]:

$$\eta_{mix}^{1/3} = x_1(\eta_1)^{1/3} + x_2(\eta_2)^{1/3} \qquad (24)$$

provided the individual component viscosities are reasonably close, like those in Table 6.

Heavy oil derivatives

Heavy oils can be fractionated, extracted, or processed into a variety of derivatives. Selected data will be used to illustrate the viscosity of the major fractions including naphtha, kerosene, light gas oil, heavy gas oil, and fractionation bottoms. Properties of the fractions which are most commonly used to describe its nature with regard to viscosity are boiling range, gravity, and averaged molecular weight as determined by osmotic pressure measurements.

Table 7 gives properties for a variety of selected derivatives from Suncor [25]. It should be noted that any one of the derivatives can have markedly different properties depending on boiling range and the processing it has been subjected to.

Similar data have been provided courtesy of Shell, Scotford refinery [26], and Syncrude Canada Research [27]. These are given in Tables 8 and 9. Syncrude's data provide the most thorough characterization available.

Figure 19 shows some of the available viscosities plotted versus temperature on an ASTM chart. Viscosities vary widely with gravity. Generally, the figure shows that parallel temperature dependence on
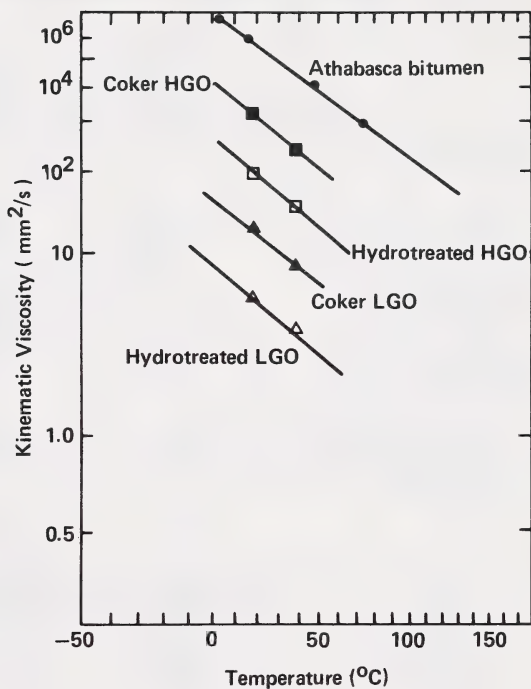
Table 7. Viscosity of Suncor derivatives.

	Temperature (°C)	Density (kg/m³)	Viscosity (mPa·s)
Coker distillates			
kerosene	38	877	1.7
	58		1.3
gas oil	38	963	20.4
	58		3.6
Hydrotreated compounds			
kerosene	25	842	2.8
gas oil side stream	25	859	2.2
	38		1.8
gas oil	25	922	32.0
	38		17.2
heavy naphtha	25	810	–
	38		1.1
synthetic crude [8]	26	827	4.6

Table 8. Viscosity at 21°C of synthetic crude cuts received at Shell Scotford refinery.

Crude tower cut	Density (kg/m³)	Viscosity (mPa·s)
light straight run	667	0.41
heavy straight run	755	0.83
light gas oil	851	3.22
heavy gas oil	889	8.32
feed (synthetic crude)	858	3.74
bottoms	925	69.0

Figure 19. Kinematic viscosity (mm²/s).

these charts is a reasonable approximation. Thus one data point can be extrapolated several degrees Celsius with some certainty.

A useful correlation of viscosity with molecular weight has been obtained for a very wide range of viscosities and molecular weights of fractions [24]. Figures 20 and 21 give the data for $\eta > 10^5$ and $\eta < 10^5$ respectively, all at 25°C. Table 10 presents the basic data. The distillates and residual fractions were obtained by bubbling nitrogen through the samples at the indicated temperatures. Molecular weights of subsamples were determined by vapor pressure osmometry with toluene as the solvent.

There is a significant scatter at lower viscosities, but in view of the wide range covered, the overall correlation is remarkably good. Equations have been developed to fit the data. In these, density has been accounted for implicitly by correlating it with molecular weight.

Equation (25) represents high viscosities, $\eta > 18\ 300$ mPa·s, (molecular weight, $M = 483$):

$$\ln \eta = 0.0482\ M - 13.44 \qquad (25)$$

Equation (26) should be used for the lower viscosities, $\eta < 18\ 300$:

$$\ln \eta = -2.807 + 0.0204\ M - 3.95940 \times 10^{-5}\ M^2 + 9.903 \times 10^{-8}\ M^3 \qquad (26)$$

Table 9. Properties of Athabasca bitumen-derived distillates and their hydrotreated products provided by Syncrude Canada Research [27].

|	Coker LGO	Coker CGO	Coker HGO	Hydrotreated LGO	Hydrotreated HGO
Feeds					
Density, 20°C (g/cm^3)	0.9447	0.9830	1.0045	0.8686	0.9402
Refractive I., 20°C	1.5302	1.5547	1.5718	1.4854	1.5288
Sulfur (wt%)	3.67	4.29	4.64	0.66	1.52
Nitrogen (mg/kg)	1 443	2 915	3 910	1 355	2 850
Carbon (wt%)	85.07	84.63	84.16	87.41	86.70
Hydrogen (wt%)	10.88	10.15	9.88	12.38	11.37
Kinematic viscosity					
20°C (mm^2/s)	17	191	1 768	4.7	109
40°C (mm^2/s)	7.9	50	249	2.9	34
ASTM D2887					
IBP	175	194	230	142	291
5%	236	260	309	182	319
10%	255	283	334	202	330
30%	292	341	385	245	359
50%	317	385	423	276	382
70%	344	429	461	303	408
90%	393	480	508	334	448
95%	425	499	528	347	469
FBP	501	529	567	378	522
Hydrotreated products, typical operating conditions					
Density 20°C (g/cm^3)	0.8891	0.9027	0.9233	0.8479	0.9091
Refractive I., 20°C	1.4949	1.5013	1.5162	1.4691	1.5051
Sulfur (mg/kg)	1 120	479	1 430	35	936
Nitrogen (mg/kg)	102	173	798	4.6	501
Carbon (wt%)	87.16	87.82	88.10	87.45	87.63
Hydrogen (wt%)	12.53	12.39	11.62	13.16	12.32
Kinematic viscosity					
20°C (mm^2/s)	10	24	67	4.3	56
40°C (mm^2/s)	5.1	11	23	27	20
ASTM D2887					
IBP	123	87	100	127	132
5%	201	190	213	174	282
10%	224	230	261	193	307
30%	272	299	335	236	345
50%	302	345	380	267	371
70%	331	393	424	295	399
90%	384	456	482	328	441
95%	421	482	507	341	463
FBP	519	530	555	372	524
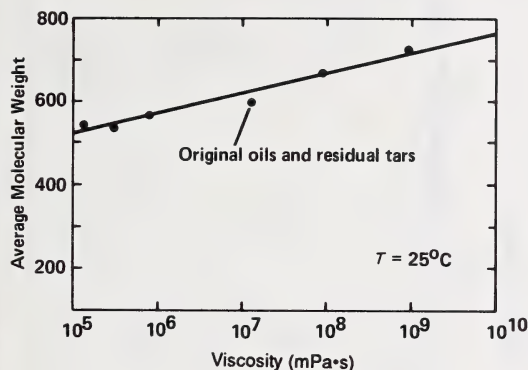
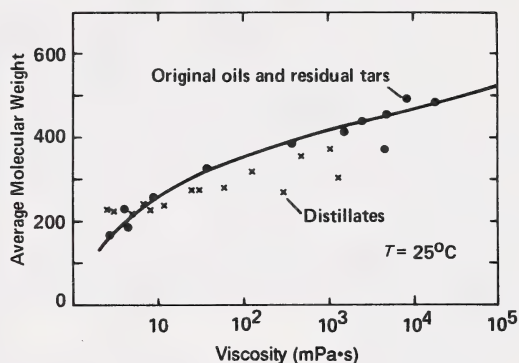**Figure 20.** Viscosity versus molecular weight for various bitumens and fractions at 25°C, (high range).

Figure 21. Viscosity versus molecular weight for various bitumens and fractions at 25°C, (low range).

Table 10. Viscosity, density, and molecular weight for various Peace River oils and fractions.

Sample	Molecular weight	Density (kg/m^3)	Viscosity ($mPa \cdot s$)
Athabasca	532	1 001	300 000
Peace River (thermally altered)	563	1 023	800 000
Peace River (cold bailed)	537	1 013	137 200
Peace River (maltenes)	453	–	5 000
Peace River:			
154°C 310 residual	594	1 052	1.3×10^7
191°C 375 residual	665	1 072	8.8×10^7
223°C 434 residual	718	1 093	9.5×10^8
273°C 523 residual	755	1 128	1.7×10^{10}
303°C 578 residual	969	1 270	[a]2.5×10^{11}
			[a]6.0×10^{11}
			[a]1.2×10^{12}
154°C 310 (1)[a] distillate	222	869	3.0
154°C 310 (2) distillate	221	981	5.0
191°C 375 (1) distillate	227	919	8.3
191°C 375 (1) distillate	239	920	11.8
223°C 434 (1) distillate	277	943	31.2
223°C 434 (2) distillate	280	957	60.1
273°C 523 (1) distillate	322	963	129
273°C 523 (2) distillate	272	973	291
303°C 578 (1) distillate	359	976	396
303°C 578 (2) distillate	374	988	1 050
303°C 578 (3) distillate	306	989	1 290
154°C 310 distillate	228	884	2.5
191°C 375 distillate	241	938	6.8
223°C 434 distillate	276	961	24.9
273°C 532 distillate	386	1 128	17.8

[a] Extrapolated to 25°C.

VISCOSITY MODIFICATION

The viscosity of natural bitumen and heavy oils can be reduced dramatically by blending with light distillates such as naphtha, with pure organic solvents, or by solution of light gases at high pressure. The solubility of natural materials with the light fractions and organic solvents is infinite. Weight fractions as high as 50:50 are of interest in surface extraction of tar sands, including sample preparation. Diluent ratios are somewhat less in transportation applications. In analytical sample preparation, the effects of trace quantities of solvent are of interest since these can cause significant error in viscosity determination.

Dissolved gases have limited potential for viscosity reduction because of limits to their solubility at a given temperature and pressure. Thus the upper limit of interest will be generally limited by the reservoir pressure and temperature.

Mixtures with gases

Some of the common gases have been listed in Table 5. Solubility of gases is discussed in Chapter 6 of this handbook. Several studies have reported viscosity as a function of temperature and pressure for mixtures saturated with various gases [6,8,10,12,14,23]. One of these includes measurement and correlation for subsaturation concentrations [12].

With these systems there can be considerable discrepancy between data from different laboratories or even between data from the same source [10]. In addition to all of the experimental complications discussed in the first two sections, complications can occur because of uncertainty about the true equilibrium composition of the sample mixture. It should be noted that a bias in composition may not be constant with temperature and pressure.

Despite the uncertainties, comparison of the various sets of data shows there is consistent agreement of the shape (or slope) of viscosity-temperature-pressure curves for a given solute. The major disagreements lie with absolute values reported. With consistency of shape the uncertainty of extrapolating from one or two data points is greatly reduced. As a consequence, where possible, this section will limit comparison to data from a single source.

Figure 22 shows the viscosity reduction for Athabasca bitumen at fixed temperature and pressure for solutes of various molecular weights [6]. This sample with no solute has a viscosity close to that of Figure 9.
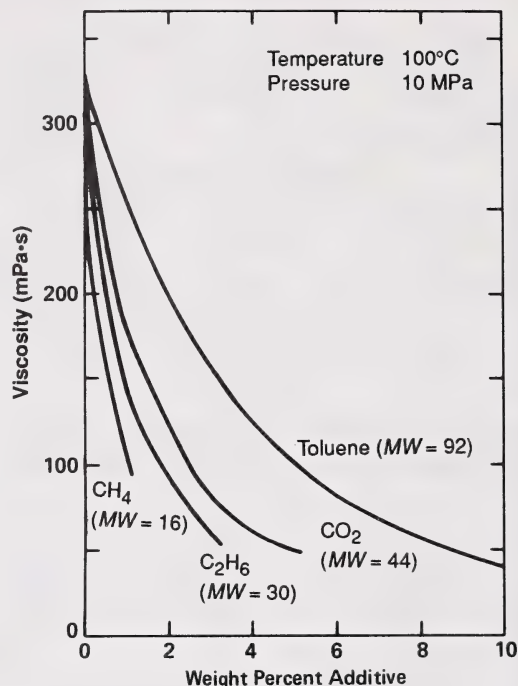

Figure 22. Effect of various additives (subsaturated) on the viscosity of Athabasca bitumen.

On a weight percent basis, materials with lower molecular weights are evidently the most effective in viscosity reduction.

Figures 23a and 23b show similar data for Cold lake bitumen at 25 and 100°C. These show the general similarity of shape, the dominant effect of temperature, and the relative effectiveness depending on molecular weight of solute. A proposed generalization of Figures 23a, b is given in Figure 27.

Several sets of data exist for Athabasca bitumens saturated with N_2, CH_4, C_2H_6, CO, and CO_2 [8,10,23]. Figures 24a through 24e show viscosity-pressure isotherms for each of the solutes. The viscosity of the gas-free bitumen is in close agreement with the curve of Figure 9.

In these experiments there is uncertainty in the actual quantity of gas at saturation, or the composition of gas in contact with the bitumen at a given pressure and temperature. The system is brought to steady state by mixing the bitumen with the pressurized solute at a given temperature [8,23]. Subsequently, a sample of the
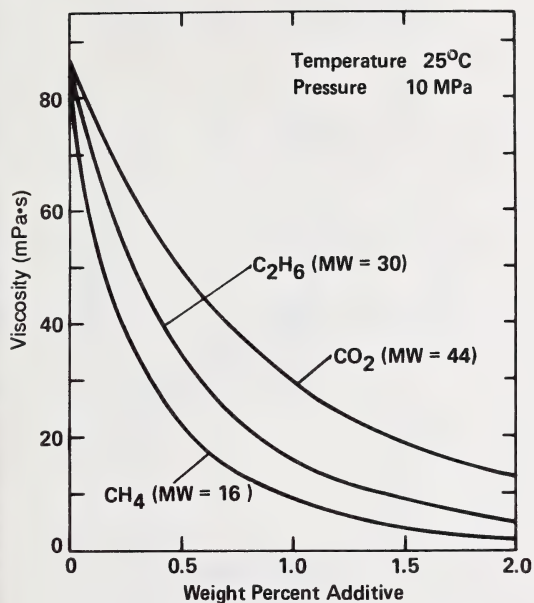
Figure 23a. Effect of various additives on the viscosity of Cold Lake Bitumen.
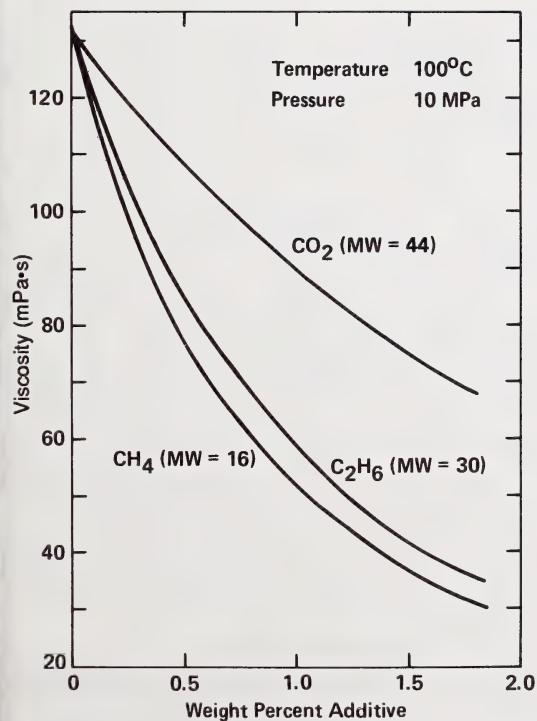

Figure 24a. Viscosity of Athabasca bitumen saturated with N_2.

Figure 23b. Effect of various additives on the viscosity of Cold Lake bitumen.
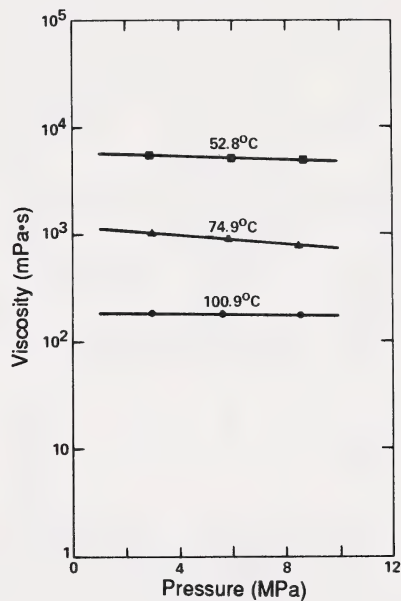

Figure 24b. Viscosity of Athabasca bitumen saturated with CO.
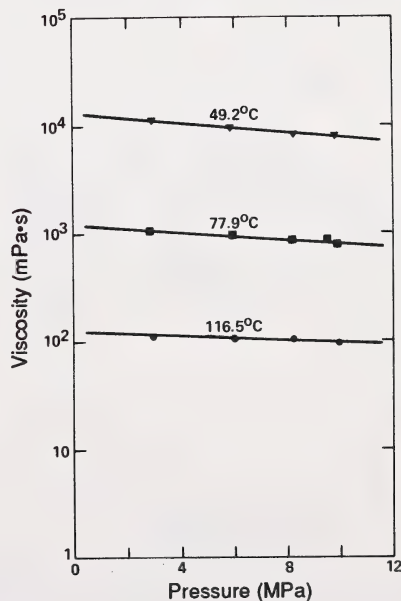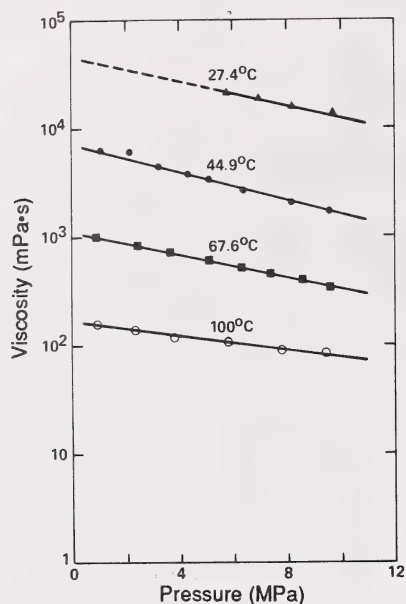
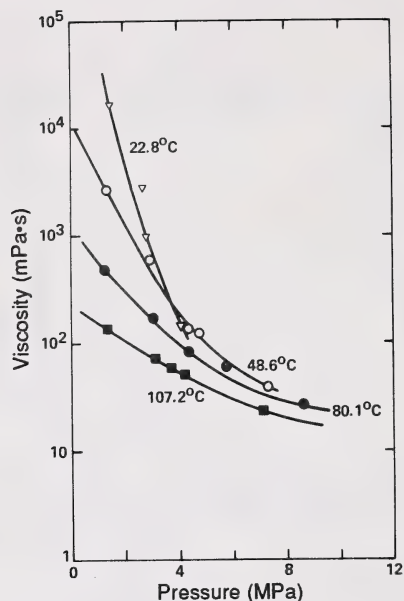**Figure 24c**. Viscosity of Athabasca bitumen saturated with CH_4.

Figure 24e. Viscosity of Athabasca bitumen saturated with C_2H_6.
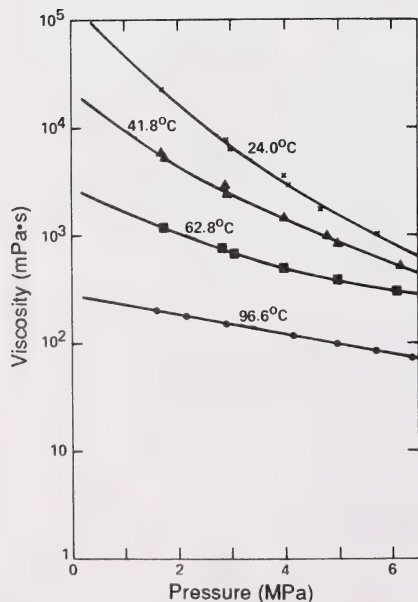
Figure 24d. Viscosity of Athabasca bitumen saturated with CO_2.

liquid mixture is heated to 100°C and depressurized to determine the volume of dissolved gas. At high pressure, with a solute such as ethane, there is the possibility of the presence of a second liquid phase.

The viscosity reduction of Peace River bitumen is similar to that presented for Athabasca bitumen by Figures 24. The viscosity-pressure isotherms are plotted in Figures 25a through 25e for various solutes [23]. The viscosity of the gas-free bitumen is given by Figure 17.

Limitations of the data are the same as those discussed above for the Athabasca bitumen.

For both the Athabasca bitumen and the Peace River bitumens the reduction in viscosity follows the order N_2 < CO < CH_4 < CO_2 < C_2H_6 based on a given volume (number of moles) dissolved. If comparisons are made as in Figures 22 and 23 based on a given weight percent, the effectiveness orders as CO_2 < C_2H_6 < CH_4.

Wabasca bitumen viscosities with dissolved gaseous species are given by Figures 26a through 26e [23]. Generally similar trends are observed as for the Cold Lake data set.

A major problem with the data is the uncertainty concerning the sample characteristics. As pointed out by the authors, the viscosity of the gas-free bitumen is much lower than previously observed for Wabasca

Figure 25a. Viscosity of Peace River bitumen saturated with N_2.

Figure 25c. Viscosity of Peace River bitumen saturated with CH_4.

Figure 25b. Viscosity of Peace River bitumen saturated with CO.

Figure 25d. Viscosity of Peace River bitumen saturated with CO_2.

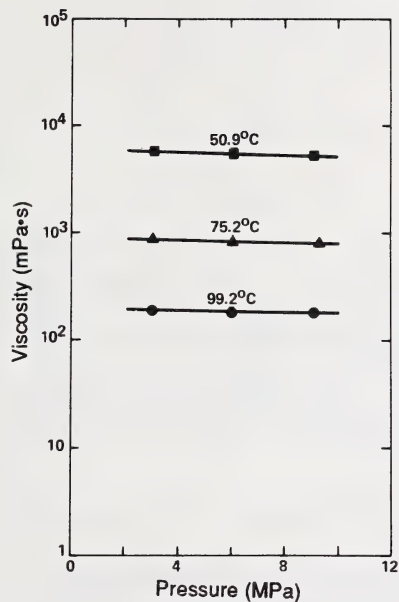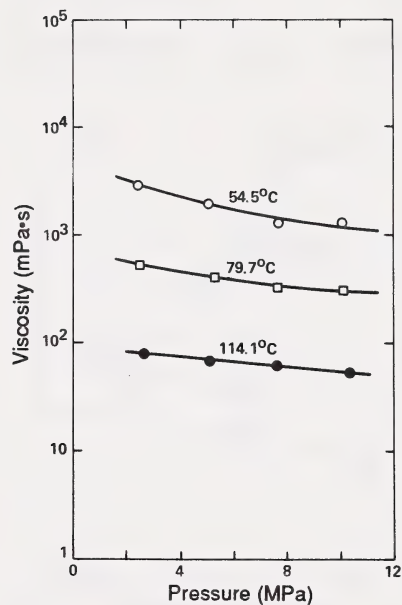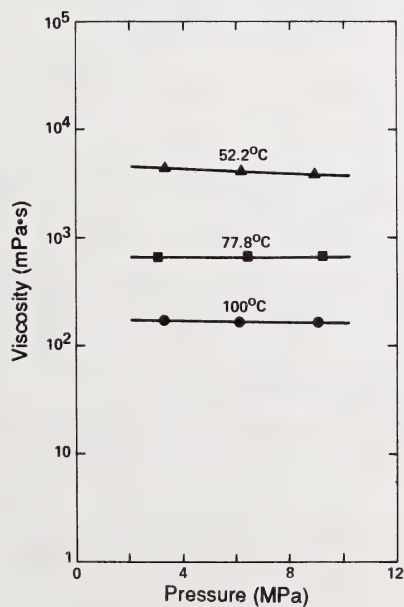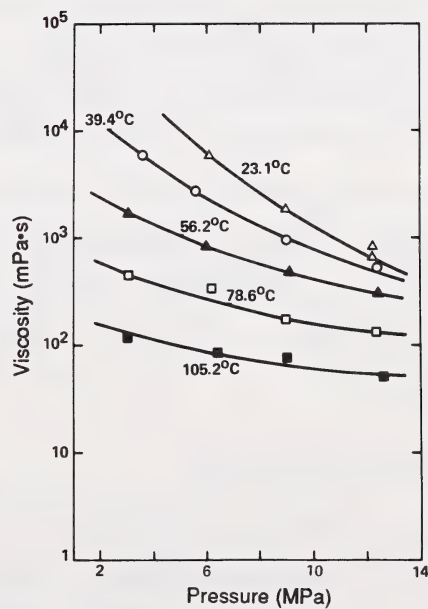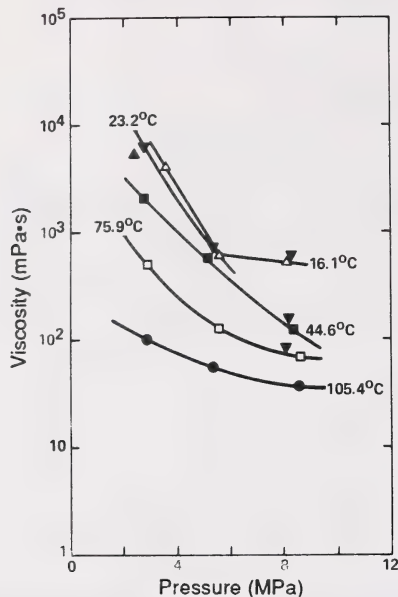**Figure 25e**. Viscosity of Peace River bitumen saturated with C_2H_6.

$$\ln \eta_0 = 2.303 \left[\frac{b}{\left(1 + \frac{T}{135}\right)^s} \right] - 1.2 \qquad (27b)$$

$$B_T = B_0 \exp [-DT] \qquad (27c)$$

$$C_T = C_0 \exp [-ET] \qquad (27d)$$

where b and s are constants determined for dead oil and B_T, C_T are parameters which appear to depend only on temperature since D and E, empirical parameters, were found to be constant. Thus, as illustrated by Figure 27, the entire behavior can be mapped based on very few data points. Although data points have been omitted, the correlation appears to work very well for the Research Council data.

Mixtures with solvents and liquid derivatives or diluents

Figure 28 indicates the viscosity reduction at 25°C for Athabasca bitumen with several solvents [29,30]. Note the data using methylene chloride are from a different investigator than those for the other solvents. Figure 29 is a similar plot showing the effect of molecular weight for the homologous series of aliphatic hydrocarbons starting with pentane. A similar data set [10], but at 38°C, is available for some solvents in Cold Lake bitumen and is shown in Figure 30.

It is evident on a weight percent basis that straight-chain hydrocarbons are more effective in viscosity reduction than are the aromatics. Effectiveness decreases with larger molecular weights as shown by Figure 29. Over the range of composition in Figures 28 and 29 the viscosity reduction with weight percent is largely linear on the semilog coordinates. It should be noted that linearity cannot be maintained over the entire range of solvent composition up to pure solvent. Although some extrapolation is required, the figures show the important effect of residual solvent on solvent-extracted samples of bitumen.

An equation proposed by Crago can be used to correct for the effect of residual solvent [10,14].

samples. In this study, the measured value at 43°C was 50 mPa·s. This should be contrasted with the viscosity range shown by Figure 18 and is clearly well out of the range of any previous work. Thus, only the qualitative features of the data should be considered usable at this time.

The viscosity reduction achieved with CO_2 for a sample of Marguerite Lake bitumen (Cold Lake) is shown by Figure 27. This gas-free sample also had a low viscosity compared with the viscosity range of previous measurements and should be compared with the band of data given by Figure 14 or Figure 15. It is lower than the lower bound shown by Figure 14 by at least an order of magnitude.

Viscosity-solubility correlation

It is of interest to consolidate the viscosity-temperature- pressure-gas solubility information for various bitumens. A novel approach [6] to map the entire behavior is based on modifications to the Roeland equation. A minimal number of empirical constants are required. Thus

$$\ln \eta \ (P,T,x) = \ln \eta_0 \ (0,T,0) + B_T P - C_T x \qquad (27a)$$

$$\ln \eta_{mix} = -9.904 + \left[\frac{x_1}{\ln \eta_1 + 9.904} + \frac{x_2}{\ln \eta_2 + 9.904} \right]^{-1} \qquad (28)$$

where η_{mix} = viscosity of mixture of liquids, (Pa·s),
        x = weight fraction of pure liquids, 1 and 2,
        η = viscosity of the pure liquids, (Pa·s).
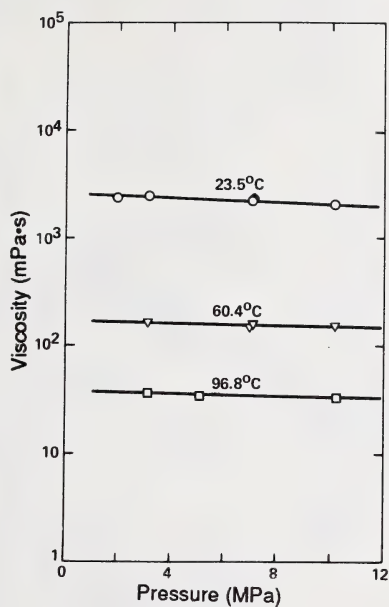
Figure 26a. Viscosity of Wabasca bitumen saturated with N_2.
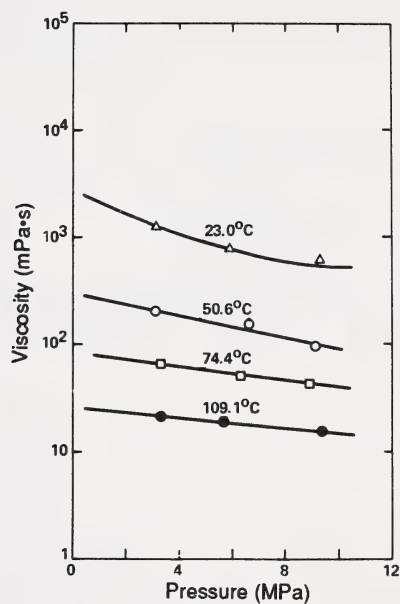
Figure 26c. Viscosity of Wabasca bitumen saturated with CH_4.
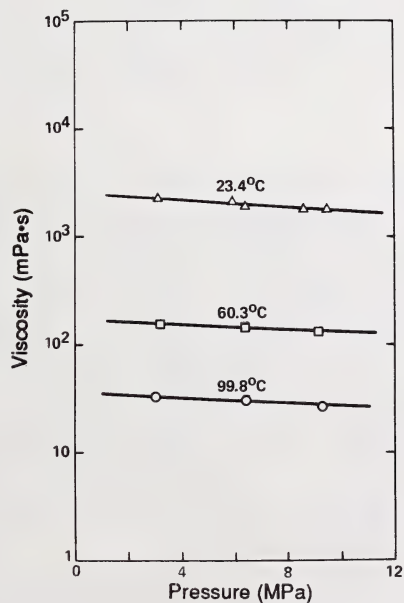
Figure 26b. Viscosity of Wabasca bitumen saturated with CO.
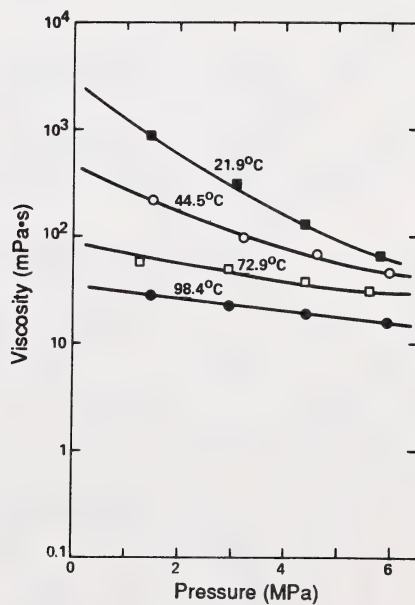
Figure 26d. Viscosity of Wabasca bitumen saturated with CO_2.
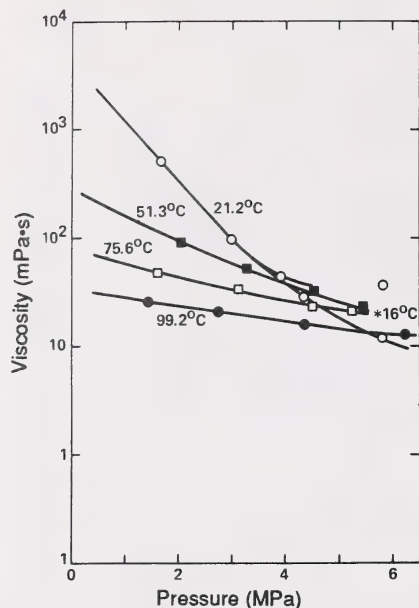
Figure 26e. Viscosity of Wabasca bitumen saturated with C_2H_6.
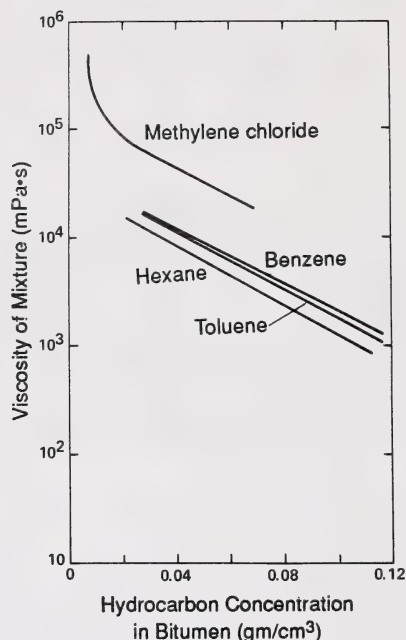
Figure 28. Reduction of viscosity by miscellaneous solvents, Athabasca bitumen.
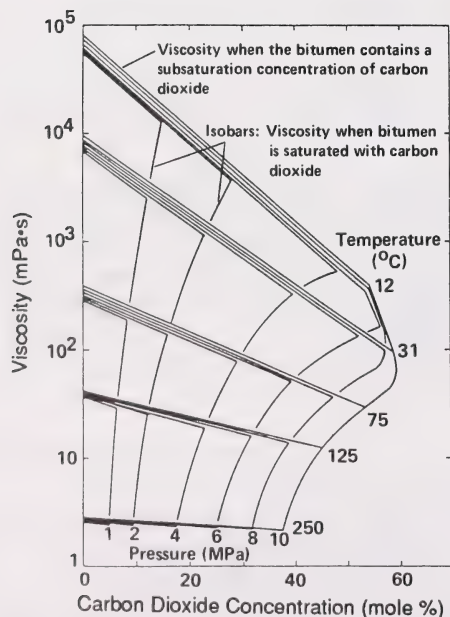
Figure 27. Viscosity-pressure-temperature correlation for Cold Lake bitumen and CO_2.

Dilution with process naphtha is of importance to a number of processes. Figure 31 shows the most comprehensive set of viscosity data available as a function of temperature and naphtha content [31]. It should be noted that the undiluted bitumen viscosity (curve 1) in this investigation is significantly lower than those reported by some other investigators [8,20]. Samples were obtained from Syncrude Canada's commercial Mildred Lake plant. High-range viscosities were measured with a concentric cylinder rotational Haake Rotovisco viscometer. Low-range viscosities (high naphtha ratios) were measured with Ostwald capillary viscometers.

The curves through the data points represent best fits using the Andrade equation (23). Good fit is evident over the entire range of data. Table 11 lists the parameters determined.
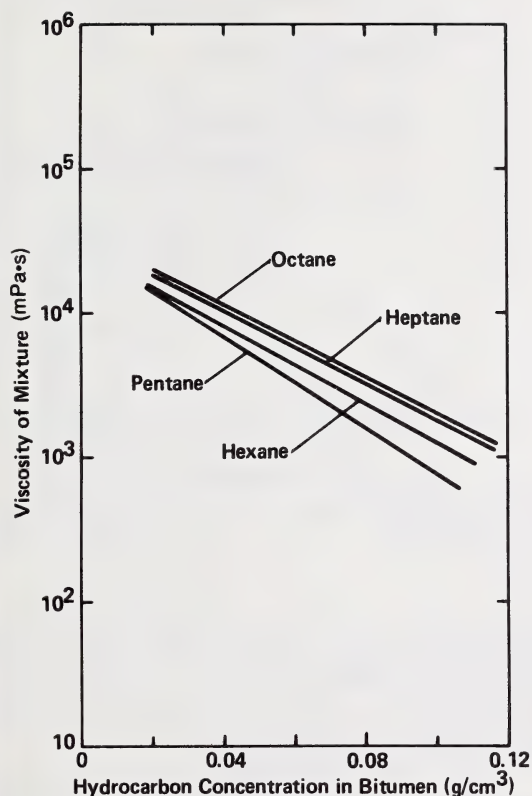
Figure 29. Reduction of viscosity by aliphatics of molecular weight.
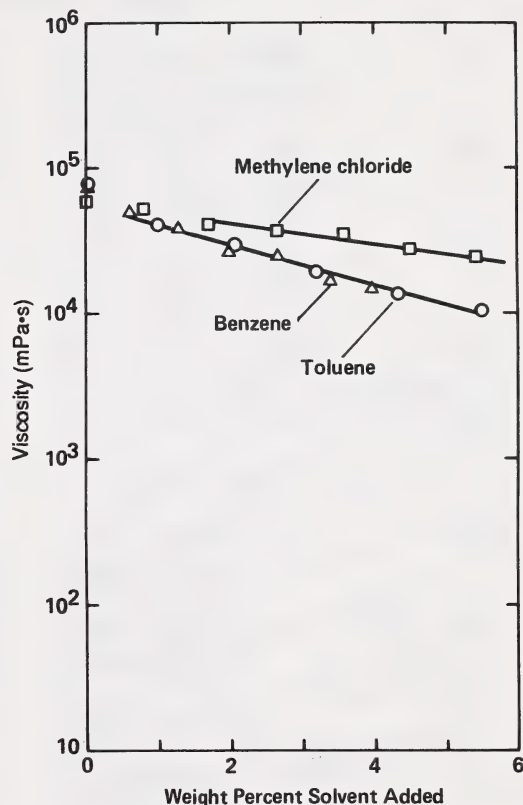
Figure 30. Reduction of viscosity by miscellaneous solvents, Cold Lake bitumen.

Table 11. Andrade parameters for mixtures of bitumen and naphtha.

Naphtha (wt%)	A (mPa•s)	$B \times 10^{-3}$ (K)
0	10.0×10^{11}	10.2
10	6.2×10^{7}	6.6
15	1.3×10^{5}	5.4
20	9.1×10^{6}	5.1
30	1.6×10^{2}	2.5
37.5	1.2×10^{2}	2.3
44.4	1.6×10^{2}	2.1
50	5.8×10^{4}	2.7
60	1.2×10^{2}	1.6
80	5.7×10^{3}	1.5
90	1.3×10^{2}	1.2

VISCOSITY OF PHYSICAL MIXTURES

Physical mixtures are encountered in virtually every heavy oil process or recovery operation. Reported viscosities may be significantly influenced by coalescence, heterogeneity, and particle migration within the shear field. Apparent non-Newtonian behavior may appear. Consequently, interpretation of data should be subject to question, and application of data to other situations may lead to large errors, particularly with concentrated suspensions [32]. This section will present a few data to illustrate the magnitude of effects which may occur.

Bitumen-water suspensions

Figure 32 shows typical data for oil-in-water emulsions. Data were obtained with rotational viscometers [21]. Photographs of these emulsions show

Naphtha N/B	% w/w	Curve
0.00	0.0	1
0.11	10.0	2
0.18	15.0	3
0.25	20.0	4
0.43	30.0	5
0.60	37.5	6
0.80	44.4	7
1.00	50.0	8
1.50	60.0	9
4.00	80.0	10
9.00	90.0	11
–	100.0	12
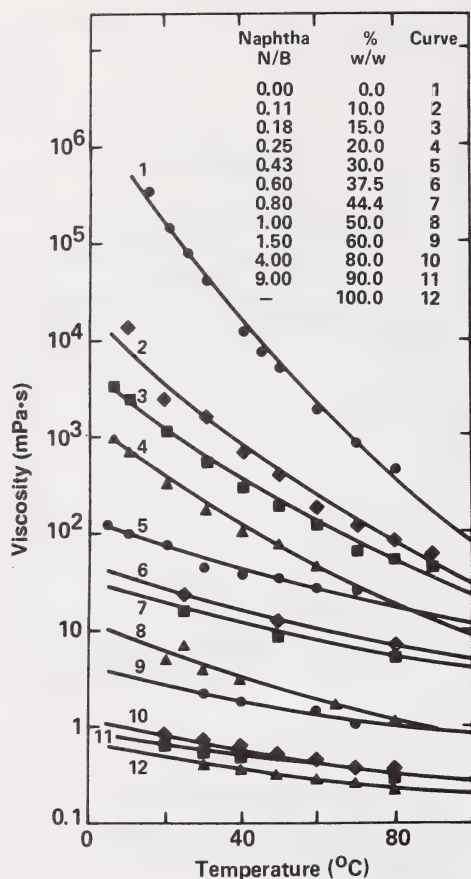
Figure 31. Viscosity reduction by naphtha.
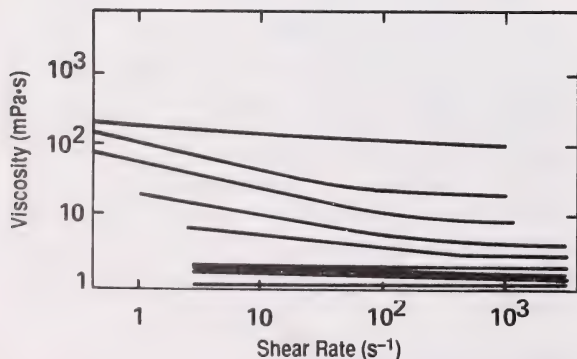
Figure 32. Viscosity of Cold Lake oil-in-water emulsions, 20°C.
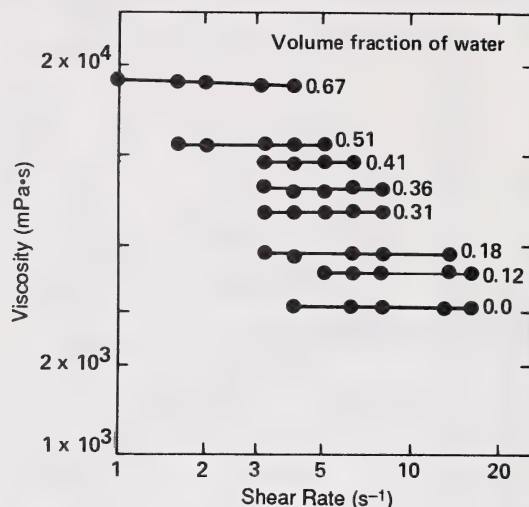
Figure 33. Viscosity of Cold Lake water-in-oil emulsions, 53°C.

complicated changes with oil content. Two of the intermediate curves show a large apparent non-Newtonian effect. This may be an artifact of the experiment. The original reference should be consulted for details of the experimentation.

A similar set of data is shown by Figure 33 for water-in-oil dispersion. These also increase with the amount of disperse phase. The increase over the range is not as large as that shown in the previous figure and non-Newtonian behavior is shown. The range of shear rate, however, is much smaller than that shown in Figure 33.

Hot water extraction process froth

Bitumen produced by hot-water extraction is a mixture of bitumen, water, solids, and vapor if it is fresh. Thus, its viscosity will be a complicated function of composition, temperature, time, and no doubt the experimental technique. Recent data are available which illustrate some of the sensitivities and the magnitude of viscosity [31].

Figure 34 shows the viscous behavior of samples which contain little if any vapor, versus naphtha content and temperature. the lines are plots of the Andrade equation through the data and can be compared with curves for pure bitumen (curve 1) and pure naphtha (curve 12). Plots of the data over shear rates from 0 to 250 s^{-1} suggest the samples are Newtonian. The
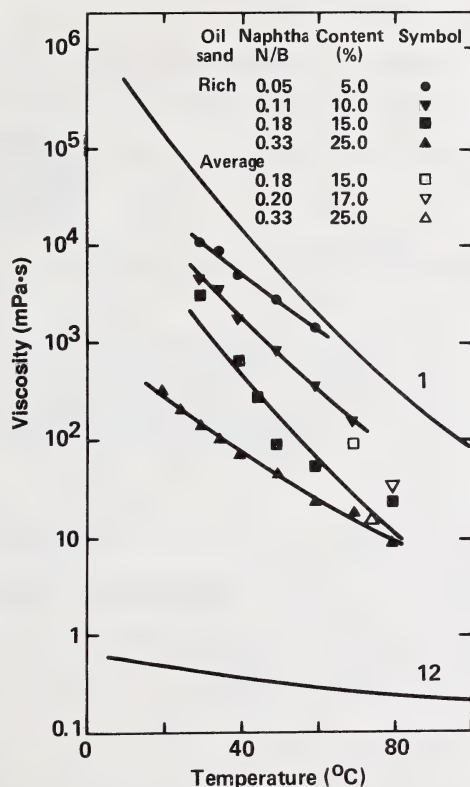
Figure 34. Viscosity of froth samples diluted with naphtha.

composition of the froth samples was approximately 60% bitumen, 18% water, and 22% solids. The rich oil sand had composition 13%, 2%, 85% oil:water:solids with 15% of the solid as fines. The average oil sand had composition 9%, 5%, 86% oil:water:solids with 37% fines.

Measurements using froths collected immediately from the flotation unit were time dependent. Some were moderately stable with time while others were highly time dependent, probably due to differences in rate of escape of entrained air. Viscosities of fresh samples were typically 4 to 6 times higher than the viscosity of pure bitumen. All were apparently non-Newtonian. Low-shear viscosities observed ranged from 600 to 6000 mPa•s. These observations cannot be compared directly with Figure 34 since differing tar sands were used and the samples were produced from different flotation units.

LIST OF SYMBOLS

A	area, constant in Andrade equation
B	constant in Andrade equation
C	empirical constant
C_p	specific heat
D	distance or empirical constant
E	empirical constant
d	distance
F	force
g	gravitational acceleration
K	machine constant
L	length of cylinder or tubing
M	molecular weight, (also referred to as MW)
n	number of species in mixture
P	pressure
Q	volumetric flow rate
R	radius
R_c	radius of container
R_e	Reynolds number
R_o	radius of viscometer
T	torque, temperature
T_A	absolute temperature
T_o	room temperature
V	velocity
V_t	steady velocity of fall, distance divided by time
x	mole fraction
α	angle of cone, radians
γ	shear rate
η	viscosity
η'	kinematic viscosity = viscosity/density
η_0	viscosity at atmospheric pressure, no dissolved gas
ρ	fluid density
τ	shear stress
ω	angular velocity

REFERENCES

1. R.W. Whorlow, "Rheological techniques," John Wiley and Sons, distributor, Rexdale, Ontario (1980).
2. R.B. Bird, W.E. Stewart and E.N. Lightfoot, "Transport phenomena," John Wiley and Sons, New York (1960).
3. S. Middleman, "The flow of high polymers," Interscience, New York (1968).
4. R.H. Perry, C.H. Chilton and S.D. Kirkpatrick,

"Chemical Engineers' Handbook," 4th ed., McGraw-Hill (1963).

5. N. Heywood, Selecting a viscometer, in The chemical engineer, Jun (1985).

6. AOSTRA/ARC, Viscosity assessment report no. 8586-30, Oct (1985).

7. JEFFRI manual, courtesy of D.B. Robinson and Associates, and S.-K. Sim and C.-J. Chen, Behavior of bitumen mixtures during in situ recovery, AOSTRA agreement 184, Final Report, Jul (1983).

8. F.A. Jacobs, Viscosity of gas-saturated bitumen, J. Can. Pet. Tech., Oct–Dec (1980)46.

9. L.D.L. Vorndran, A. Serres, J.K. Donnelly, R.G. Moore and D.W. Bennion, Bitumen separation for experimental use, Can. J. Chem. Eng., 58 (1980) 580–587.

10. AOSTRA technical report, Thermodynamic and transport properties of bitumens and heavy oils, Jul (1984).

11. S.H. Ward and K.A. Clark, Determination of the viscosities and specific gravities of the oils in samples of Athabasca bituminous sand, Research Council of Alberta report no. 57, Mar (1950).

12. J.P. Briggs, V.R. Puttagunta and N.B. Khiamel, viscosity of heavy oil and bitumen which contain subsaturation concentrations of CO_2, WRI-DOE Tar Sand Symposium, Vail, CO, Jun (1984).

13. P.C. Sukanek and R.L. Laurence, An experimental investigation of viscous heating in some simple shear flows, AIChE J., 20 (1974) 474.

14. D.R. Prowse, Ed., Some physical properties of bitumen and oil sand, ARC/AOSTRA industry access report no. 8384-40, Rev.2, Sep (1983).

15. F.A. Seyer, private communication, May (1987).

16. A.K. Mehrotra and W.Y. Svrcek, Viscosity of compressed Cold Lake bitumen, Can. J. Chem. Eng., 64 (1986) 844, 65 (1987) 672.

17. F.A. Jacobs, "Viscosity of carbon dioxide saturated bitumen," M.Sc. thesis, Univ. of Calgary, Alberta, (1978).

18. M.S. Patel, Determination of viscosities of oils from Mannville Formation oil sand, Alberta Research Council, Edmonton, Oct (1973).

19. W.R. Shu, A viscosity correlation for mixtures of heavy oil, bitumen and petroleum fractions, SPE paper no. 11280, Aug 4 (1982).

20. J.M. Dealy, Rheological properties of oil sand bitumens, Can. J. Chem. Eng., 5 (1979) 677.

21. R. Steinborn and D.L. Flock, Rheology of heavy crude oils and their emulsions, J. Can. Pet. Tech., 2,
no. 5, Sep–Oct (1983) 38–52;
and
R. Steinborn, "The Rheological behavior of heavy crude oils and their emulsions," M.Sc. thesis, Univ. of Alberta (1982).

22. Esso Resources Research Department, Correlation for viscosity of cold bailed Cold Lake bitumen, private communication, Aug (1986).

23. A.K. Mehrotra and W.Y. Svrcek, Viscosity, density and gas solubility data for oil sand bitumens, Part I: Athabasca bitumen saturated with CO and C_2H_6, AOSTRA J. Res. 1(1985)263, Part II: Peace River bitumen saturated with N_2, CO, CH_4, CO_2, and C_2H_6, AOSTRA J. Res. 1(1985) 269, Part III: Wabasca bitumen saturated with N_2, CO, CH_4, CO_2, and C_2H_6, AOSTRA J. Res. 2 (1985) 83.

24. P.J. Closmann and R.D. Seba (courtesy Shell Development Co.), On a correlation of viscosity and molecular weight, Bellaire Research Center, Houston, TX, Apr (1985).

25. Courtesy of Suncor Resources Development Division, Viscosity of miscellaneous upgrading streams, Calgary, Alberta, Feb 5 (1986).

26. Courtesy of Shell, Scotford refinery, Mar (1987).

27. S.M. Yui and E.C. Sanford, Kinetics of hydrogenation of aromatics determined by carbon-13 NMR for Athabasca bitumen-derived middle distillates, Symposium on Advances in Hydrotreating, American Chemical Society, Denver, CO, Apr 1987, private communication, Oct (1987).

28. W.Y. Svrcek and A. Mehrotra, Gas solubility, viscosity, and density measurements for Athabasca bitumen, J. Can. Pet. Tech., Jul–Aug (1982) 31.

29. B.C.H. Fu and C.R. Phillips, Plasticizing effectiveness of hydrocarbons in Athabasca bitumen, Fuel, 58 (1979) 554.

30. C. Reichert, B.J. Fuhr, J.A. Koots, and D. Wallace, Problems in the analysis and characterization of bitumen and heavy oils, 3rd International Conference on Heavy Crude and Tar Sands, Long Beach, CA, Jul (1985).

31. L.L. Schramm and J.C.T. Kwok, The rheological properties on an Athabasca bitumen and some bituminous mixtures and dispersions, J. Can. Pet. Tech., Feb (1988); private communication with L.L. Schramm, Oct (1987).

32. C.A. Schook, Experiments with concentrated slurries of particles with densities near that of the carrier fluid, Can. J. Chem. Eng., 6 (1985) 861.

8

GEOTECHNICAL
PROPERTIES

P.R. Kry
J.M. Gronseth

Esso Resources Canada

N.R. Morgenstern

Department of Civil Engineering
University of Alberta

INTRODUCTION

What are geotechnical properties?

Geotechnical properties are concerned primarily with the mechanical behavior of earth materials — their deformation and strength characteristics. An understanding of geotechnical behavior also requires knowledge of the properties and flow characteristics of pore fluids and heat transfer characteristics of the earth materials. These properties are discussed elsewhere in this volume and will not be referred to further in this chapter. The study of geotechnical behavior begins with the knowledge of the state of stress in the ground. While not truly a material property, the evaluation of this reference state will be considered here.

Geotechnical properties are of interest in oil sand development because there is an interaction between the recovery process and the mechanical behavior of the oil sand. For extraction by surface mining, this is obvious. The stability of slopes and hence the risk associated with alternate mining schemes is dominated by the shearing resistance of material composing the high wall. In recent years, research into geotechnical properties of oil sands has produced an extensive body of literature on the subject, for example, Dusseault [1], Dusseault and Morgenstern [2,3], and Fair and Lord [4]. Much valuable experience has been accumulated in the context of resource recovery by surface mining.

The level of geotechnical detail utilized for the ongoing evaluation of slope stability is now very high and has become a matter of specialized experience. This chapter will not address further those properties used to assess slope stability in oil sands, but will draw on this data base wherever it is relevant to in situ recovery processes.

Geotechnical engineering in the in situ extraction of bitumen from oil sands involves studying the stresses and deformations that occur in a formation due to changes in stress, pore fluid pressure, and temperatures. The geotechnical response of an oil sands reservoir to fluid pressure changes or to temperature changes results in stresses and deformations that affect hydraulic fracture propagation, formation shearing, production containment, well casing performance, the stability of underground openings (uncased wells, tunnels and shafts), and the magnitude of surface heave. Analytical procedures used to model these mechanisms require a number of parameters that should be representative of the composition and structure of the particular oil sand and should be measured under conditions representative of the specific production technique. As will be noted in subsequent sections, this ideal is seldom met.

A minimum requirement for a representative specimen for geotechnical testing is that it be undisturbed with regard to the composition, density, and arrangement of the grains and fluids. This requirement is quite restrictive in conventional geotechnical testing but even more so when oil sands are to be tested. While samples that are representative in composition are readily obtained by conventional drilling and coring, it is extremely difficult to avoid density reduction when sampling. Moreover it is not possible to reestablish the fabric of oil sands in the laboratory, and hence, results from any testing on reconstituted oil sands are at best only illustrative of geotechnical characteristics in situ. Geotechnical properties reported for oil sands must always be scrutinized carefully with regard to the quality of the samples utilized in the testing. In conventional geotechnical engineering, some of the problems associated with sample disturbance are overcome by conducting geotechnical tests in situ. For oil sands, comparable progress has not been made because of technical difficulties and cost of in situ geotechnical testing.

When a fully saturated porous substance is subjected to a stress change $\Delta\sigma$ under conditions of zero drainage, a pore fluid pressure change Δu results. The resulting stress difference, $\Delta\sigma'$, is known as the effective stress:

$$\Delta\sigma' = \Delta\sigma - \Delta u$$

where σ' denotes the effective stress
σ denotes the total stress
and u denotes the pore fluid pressure.

As has been demonstrated both theoretically and experimentally for porous materials like oil sands, the effective stress is a fundamental stress-state variable and both strength and deformation properties must be expressed in terms of effective stress. Pore pressure changes and hence effective stress changes result not only from changes in applied total stress, but also from changes in temperature. Experimental information on the coupling of these effects will be summarized.

Reservoir engineers are familiar with the concept of effective stress used in calculations of stress and reservoir response, making use of the theory of poroelasticity, for example, Geertsma [5] and Jaeger and Cook, [6].

Sampling oil sands

During core sampling from boreholes, in situ confining stresses and pore pressures are reduced rapidly and gas exsolution from the bitumen and water may occur. This formation of gas bubbles, when there is weak cohesion between sand grains due to a lack of cementation, results in expansion of the oil sand microfabric. The sample disturbance caused by core expansion affects the geotechnical properties of oil sands. Agar [7] observed a 25% decrease in maximum shear strength for Athabasca oil sands, corresponding to an initial porosity difference of only about 1%. The reduced shear strength was attributed to very subtle, possibly localized, microfabric disturbance.

Present preferred core sampling techniques utilize core barrels with a nonrotating inner barrel containing a PVC liner to collect the core sample. The inner barrel precludes washing of the sample with drilling fluid and the development of rotational shear within the sample. After the core barrel reaches the surface the PVC liner containing the oil sand core is sealed and the sample is immediately frozen. Freezing the core aids in preserving the structure of the oil sands by considerably increasing the viscosity of the bitumen and thus greatly reducing the rate of gas exsolution, and by causing bitumen shrinkage which reduces the pore fluid pressures. Even this procedure involves some structural disturbance, particularly if there is significant water content in the oil sand.

Prior to preparation, the oil sands core samples are stored in a cold room at –25°C. When an oil sands sample is required for testing, a piece of core is taken and sealed in an airtight metal container in dry ice (approximately –78°C) for several hours. The core sample is then trimmed to test-specimen dimensions in a lathe situated in the cold room. To preclude structure expansion, the specimen is not allowed to thaw until it is under sufficient confining stress (normally 500 kPa or greater) in the laboratory test cell. It is generally good practice to conduct tests under stress levels comparable to those in situ.

Factors influencing geotechnical properties.
Laboratory measurements have shown that the geomechanical characteristics of uncemented sands also depend on the sand grain mineralogy, geological environment of deposition, and geological history (see Chapter 1). As a result, these properties vary from deposit to deposit, and in some cases, within the deposit, as the grain composition and arrangement and geological stress history change. Meaningful measurements of strength, compressibility, and deformation modulus can only be obtained by testing specimens in which the integrity of the sand matrix has been preserved. Test measurements show that small disruptions of the sand matrix caused by gas evolving from the bitumen during coring and sample preparation have a major effect on these mechanical properties. The bitumen also has a controlling influence on in the rate of pore pressure dissipation and therefore on the magnitude of shear deformations. In addition, gas exsolution has a major influence in maintaining pore fluid pressures, as a decrease in confining stress or increase in temperature allows the formation of gas bubbles which retards the dissipation of pore pressures.

Experimental results to be presented show that the geotechnical properties of Cold Lake (Clearwater Formation) oil sands differ significantly from those of the oil sands of the Athabasca (McMurray Formation) deposit. This is not meant to imply that all Cold Lake sands or all Athabasca sands have similar properties; in fact samples collected from within each area can have mineral and fabric differences that lead to different geotechnical behaviors. Cold Lake oil sands are generally weaker and contain some minerals which are more susceptible to physical breakdown from shear strains, especially at elevated temperatures and pressures.

Test procedures

At room temperature, the geotechnical properties of oil sands can be determined using conventional geotechnical test equipment for the triaxial and oedometer tests [8]. These tests allow substantial independent control of both stress and drainage. Direct shear tests can be used to evaluate strength but have severe limitations for the study of other properties. No standard equipment or procedures exist for testing at higher temperatures and with hot-water or steam injection.

The geotechnical oil sands test facility at the University of Alberta includes triaxial cell systems, oedometer systems, and hot-water or steam injection systems. Schematics of the high temperature and pressure triaxial and oedometer systems are shown in Figures 1 and 2. The triaxial cell can be used to measure the compressibility and shear strength of oil sands and associated strata (shale, limestone) under confining stresses up to 27 MPa and temperatures up to 315°C. Loads up to 440 kN can be applied to shear the sample.
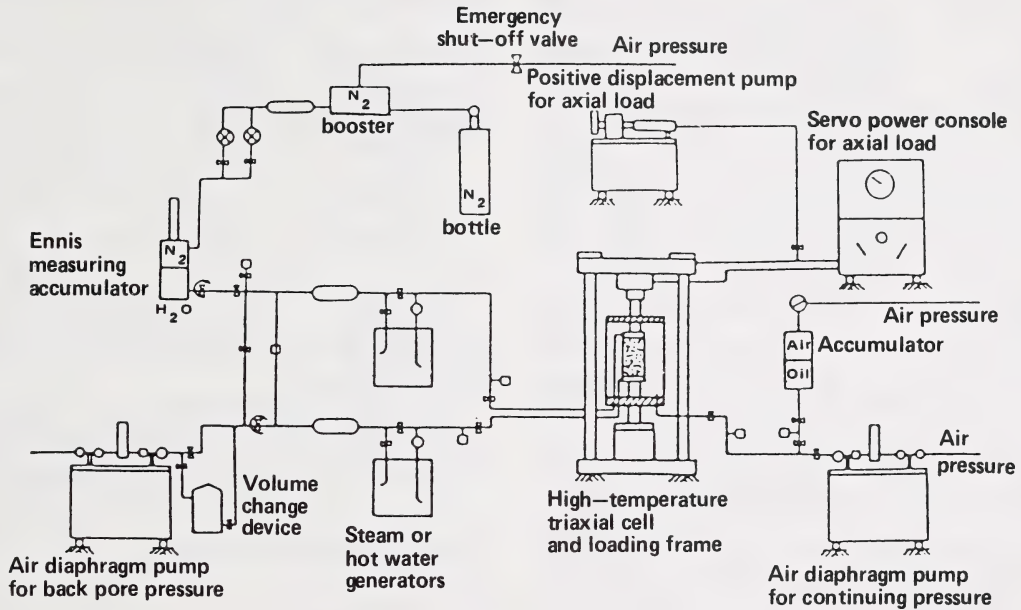
Figure 1. High-temperature triaxial system for measuring geomechanical properties.
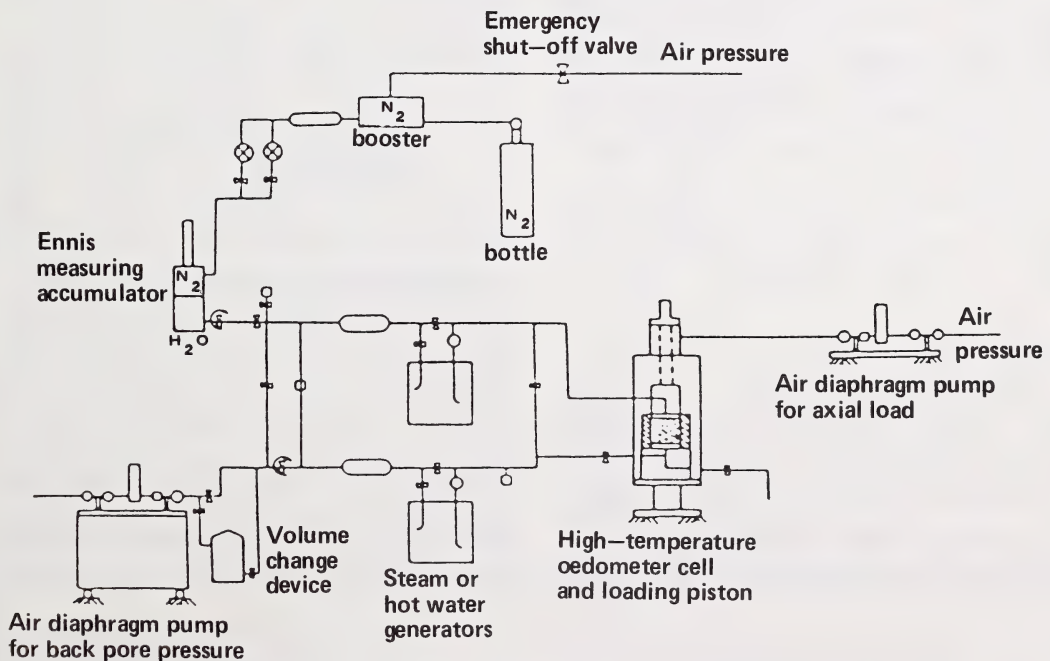

Figure 2. High-temperature oedometer system for measuring geomechanical properties.

Pore fluid pressure, vertical and lateral strains, and volume change of the specimen can be measured. Hot water or steam can be passed through the sample by the pressure injection system at pressures up to 20 MPa and temperatures up to 315°C to measure the permeability of the specimen or to flush bitumen out of the oil sands sample. Strain-controlled triaxial tests are run with a positive displacement pump applying the axial load. Stress-controlled tests are performed either with the same pump or with a servo power console unit.

The oedometer can be used to measure the compressibility of oil sands specimens at stresses up to 30 MPa and temperatures up to 315°C. Vertical compression, pore fluid pressure, and volume change of the test specimen can be measured. The pressure injection system can also be used with the oedometer to measure permeability or to remove bitumen.

The triaxial cell is equipped with an internal load cell mounted directly at the base of the test specimen during the triaxial testing. This permits a direct measure of load on the specimen, eliminating the uncertainty of piston friction. Similarly, internal axial strain and lateral strain measuring devices are used to measure the volumetric strain of the test specimen. In order to accurately trace the entire post-failure stress-strain curve the triaxial apparatus is equipped with a stiff loading frame (prestressed to 440 kN) with a small energy storage capacity. Post-peak stress-strain curves for specimens under high stresses are functions of energy release from the test frame. Pretensioning the frame results in the post-peak region being independent of the machine response and it therefore reflects the true oil sand properties.

Additional details on testing oil sands at elevated temperatures and pressures are given by Agar, Morgenstern, and Scott [9], and Agar [7].

DENSITY AND POROSITY

The ultimate objective of geotechnical testing is to determine material properties at in situ density or porosity. As noted previously, sample disturbance can adversely influence geotechnical properties in laboratory tests. The influence of sample disturbance on strength, compressibility, and stress-strain behavior has been discussed by Hardy and Hemstock [10], and Dusseault [1,11]

In general, in situ geophysical measurements provide a more reliable estimate of density, or porosity,

than direct measurements on samples. It is not uncommon for core recovery to be in excess of 100% when standard sampling techniques are cited. High-quality samples of the McMurray Formation tend to have porosities of about 35% and densities of 2.05 to 2.10 Mg/m^3. Mainland [12] cites an in situ porosity of 35% for Cold Lake oil sand.

Table 1 summarizes data on density and porosity from various sources and provides comments on sample quality as a guide. Data on recompacted oil sand are given for comparative purposes. It is not possible to reestablish the in situ porosity by recompaction alone, without pressure; nor is it possible to reestablish the interlocked fabric of oil sands by recompaction (Dusseault and Morgenstern [3]).

Additional geophysical information is available from borehole logs that enter the public domain through the Alberta Energy Resources Conservation Board.

STRENGTH CHARACTERISTICS

Stress path dependency

Laboratory determination of the geomechanical behavior of oil sands involves applying the history of stress representative of actual field conditions. Diagrams showing conventional stress paths followed in the laboratory or possible stress paths followed in the field are given in Figures 3a,b. The vertical axis is the major principal effective stress, σ'_1, and the horizontal axis is the minor principal effective stress, σ'_3, where $\sigma'_2 = \sigma'_3$. Some of the stress paths accessible in laboratory testing are shown in Figure 3a. Confined drained compression and confined undrained compression are the more common triaxial tests. They involve increasing the major principal total stress, σ_1, applied to the specimen while holding the intermediate and minor principal total stresses, σ_2 and σ_3, constant and equal. Prior to these conventional triaxial tests the sample is consolidated to approximate in situ stress conditions following an isotropic compression stress path ($K_o = 1$ where $K_o = \sigma'_3/\sigma'_1$). The specimen may also be consolidated following a confined compression stress path in an oedometer cell where lateral straining of the specimen is prevented and the minor and intermediate principal stresses increase at a lower rate than the major principal stress ($K_o < 1$).

A variety of stress paths are accessible in the triaxial test. Each test involves manipulating the principal effective stresses during the test to simulate the field

Table 1. Density and porosity of oil sands.

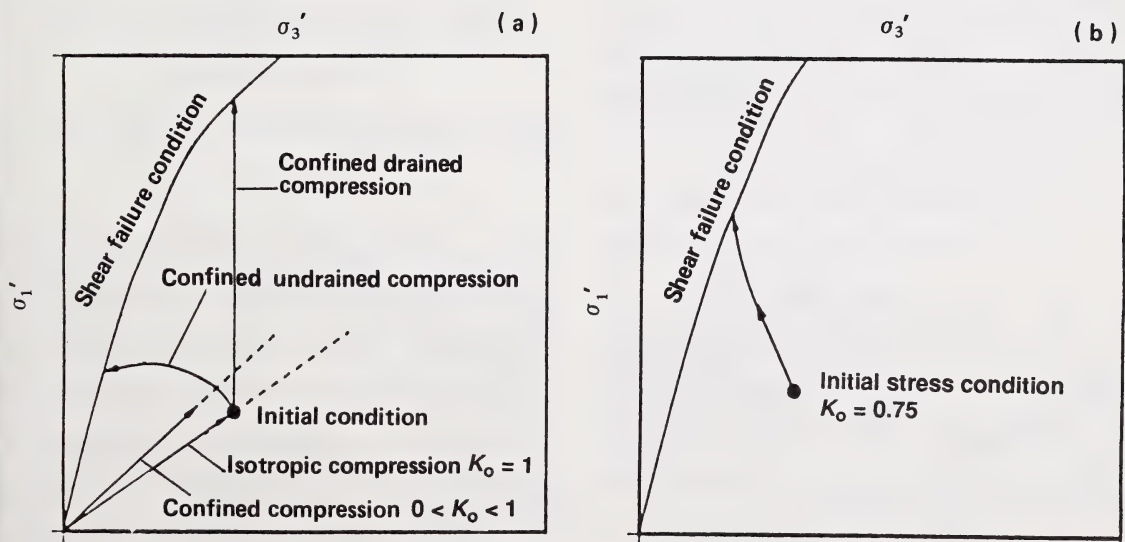| Source	Depth (m)	Bulk density (Mg/m³)	Porosity (%)	Sample quality (high, low, recompacted geophysical log)	Reference
Athabasca oil sands		1.96	39.2		[13]
		2.03–2.08	33.0–35.5		[13]
		1.75–2.09	34.0–46.0		[14]
		1.86–2.36	17.6–43.3	Geophysical Density log	[15]
	60	1.98–2.08	40.0		[15]
	300	2.10–2.19	34.0		[15]
		2.10–2.30			[16]
		2.04–2.40	16.0–35.0		[1]
		1.95–2.12	33.0–38.0	Disturbed	[7]
Cold Lake oil sands		1.96	38.3	Moderately disturbed	[7]

Figure 3. (a) Some laboratory stress paths in triaxial and oedometer tests. (b) Field stress path for steam injection.

stress path. The stress-strain response of the oil sand varies with the stress path followed, and therefore, the stress history applied during the test must be representative of the field condition. For simplicity, most triaxial cells operate with $\sigma_2 = \sigma_3$ although special cells which control all three principal stresses are available.

A possible field stress path for steam injection in a formation horizontally stratified with oil sands and shale layers is shown in Figure 3b. In this hypothetical bitumen recovery process, steam is injected at pressures higher than the in situ pore pressures but below the fracturing pressure. The formation is presumed to have a horizontal permeability much higher than the vertical permeability due to the stratification. During the early stages of steam injection, the vertical and horizontal effective stresses would be increased by thermal expansion of the reservoir matrix. Pore pressures would increase due to thermal expansion of pore fluids and the steam injection pressure. Because of the higher horizontal permeability, the net effect on the horizontal effective stress could be a reduction in stress. Due to the low vertical permeability and the small area heated, the net effect on the vertical effective stress could be an increase in stress. Such a stress path is shown in Figure 3b. As the stress conditions approach the shear failure envelope, shear deformations take place. If the stress changes are sufficient, shear failure occurs. This is only one of many scenarios that may place in the field. Variations in stress paths need to be considered when evaluating geotechnical properties.

Confined drained compression

The strength of ordinary sand under conditions of confined drained compression is a function of initial porosity or density and confining pressure. As illustrated in Figure 4, at low pressures dense sands dilate at peak shearing resistance, lose resistance with increased dilation, and then deform continuously in the fully dilated state. Loose sands contract during shear and then deform with no further change in resistance at the critical void ratio.

The principal stresses at failure are best described by the Mohr-Coulomb failure criterion:

$$\frac{\sigma_1' - \sigma_3'}{\sigma_1' + \sigma_3'} = \sin \phi$$

where σ_1' and σ_3' are the major and minor principal
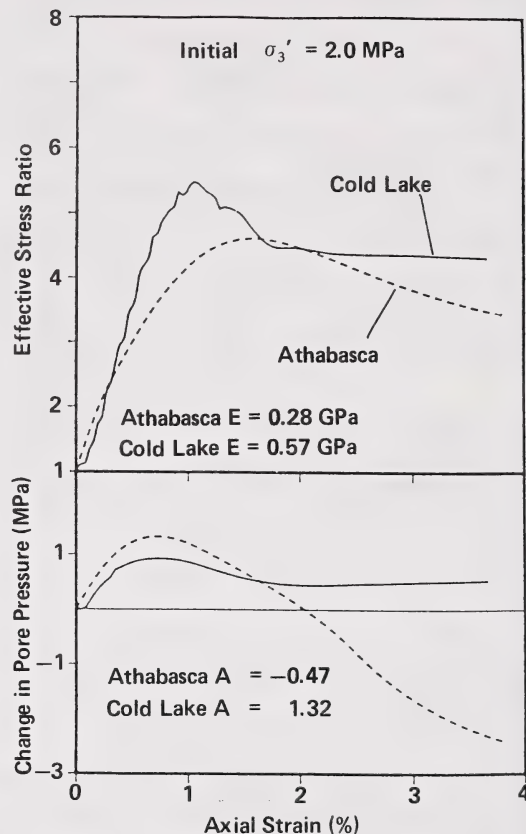
Figure 4. Confined undrained compression tests on oil sands.

effective stresses at failure respectively and ϕ denotes the angle of shearing resistance. At higher effective stresses, dilatancy is suppressed and crushing of grains occurs. This reduces the angle of shearing resistance, and the failure criterion often displays some nonlinearity.

Oil sands at low (surface mining) stresses are stronger than conventional dense sands, more dilatent, and more brittle. This difference has been attributed to their interlocked fabric and they have been called locked sands by Dusseault and Morgenstern [3]. The high frictional resistance at low stresses accounts for the substantial stability displayed by slopes in this otherwise uncemented material.

As shown in Figure 5, with increasing stress, dilation is suppressed, and the resistance envelope displays marked curvature. The shearing resistance of
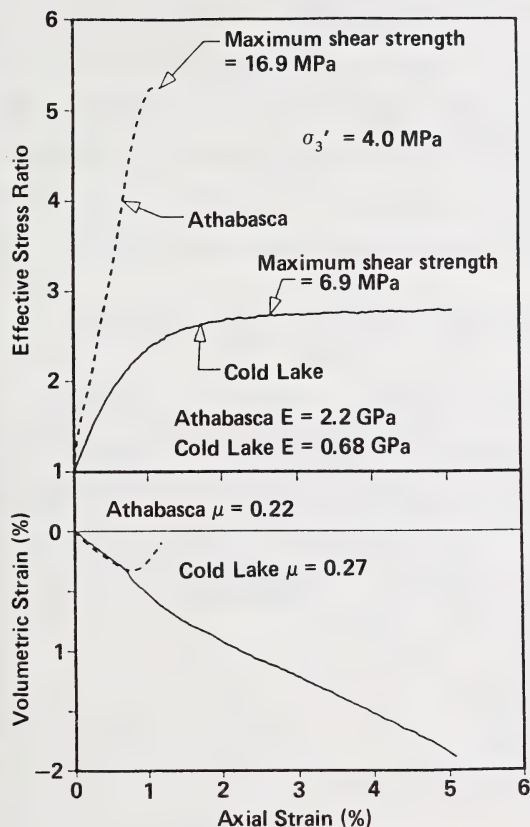
Figure 5. Confined drained compression tests on oil sands.

remolded oil sand is shown for comparison.

Agar [7] has shown that the confined drained shearing resistance of Athabasca oil sands is not influenced much by temperature. Results are given in Figure 6. As shown in Figure 5, Cold Lake oil sands are both weaker and more ductile than Athabasca oil sands.

Confined undrained compression

The stress-strain behavior of the particular samples from Cold Lake (Clearwater Formation) and Athabasca (McMurray Formation) oil sands for undrained compression under an initial effective confining stress of 2 MPa is shown in Figure 4. This stress path is also shown in Figure 3a. Both specimens display an increase in the pore fluid pressure at the beginning of the test due to compression of the sand matrix during the onset of
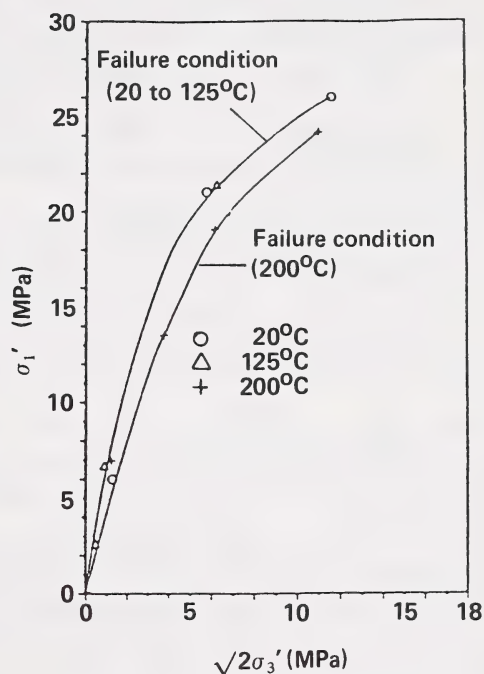
Figure 6. Effect of temperature on strength of oil sands.

straining. As the specimens reach their peak effective stress ratios, pore fluid pressures decrease since the sand matrix has a tendency to dilate under the reduced effective confining stress. The pore fluid pressure for the Cold Lake specimen stabilizes at about 2% axial strain and remains constant with a net pore pressure increase. Here the effective confining stress on the specimen becomes constant and the specimen achieves its maximum strength of 6.0 MPa. The pore fluid pressure of the Athabasca specimen, however, continues to fall below the initial back pressure in the sample resulting in a net increase in effective confining pressure of the specimen. The Athabasca specimen eventually reaches its maximum strength of 10.7 MPa at 8.7% axial strain (not shown in the figure) when the pore fluid pressure stabilizes.

The difference in maximum undrained shear strength of Cold Lake and Athabasca oil sands depends on the pore pressure response and the shearing resistance of the sand grain matrix. Athabasca oil sand has an undrained shear strength twice that of Cold Lake at 2 MPa initial effective confining stress, but requires very large strains to achieve the maximum failure

conditions. Cold Lake oil sand reaches its maximum strength failure conditions at low strains. The pore pressure parameter A at failure for Athabasca was –0.47 and was 1.32 for Cold Lake. The parameter is the ratio of the pore pressure change to the change in shearing stress. The negative value of A for Athabasca oil sands at failure indicates the very large decrease in pore fluid pressure during shear.

Table 2 summarizes the stress-strain properties determined for the Athabasca (McMurray Formation) and Cold Lake (Clearwater Formation) oil sands, including the influence of stress path and confining pressure. From these test results and others at different confining stresses, the following observations may be made:

• The stress path has a significant effect on the initial tangent modulus (Young's modulus) of Athabasca oil sands but a considerably lesser effect on that for Cold Lake oil sands.

• The maximum stress ratio for Cold Lake oil sands is highly dependent on the stress path but the stress ratio for Athabasca oil sands is only slightly affected.

• The maximum shear strength is strongly affected by the stress path for both the Athabasca and Cold Lake oil sands. For the Athabasca oil sands the undrained strength is considerably lower than the drained strength, while for the Cold Lake oil sands the undrained strength is higher than the drained strength.

• The strain-to-failure of the Athabasca oil sands is highly dependent on stress path while the strain-to-failure of the Cold Lake oil sands is only slightly dependent on stress path.

The strength of Athabasca (McMurray Formation) oil sands decreases somewhat at elevated temperatures as shown in Figure 6. The effect of temperature is to lower the effective strength 10% over a 200°C range of temperature. Temperature increase, however, also significantly increases the pore fluid pressure. Pore pressure dissipation must be included in the analysis of this class of problem to properly ascertain the effect of temperature. The decrease in strength of Cold Lake oil sand at elevated temperatures may be more significant than that of Athabasca oil sand since the former contains minerals that are more susceptible to physical breakdown at elevated temperatures and pressures.

DEFORMATION CHARACTERISTICS

Compressibility

The isotropic compressibilities of Athabasca (McMurray Formation) and Cold Lake (Clearwater Formation) oil sands specimens cycled over their in situ effective confining stress ranges are shown in Figure 7.
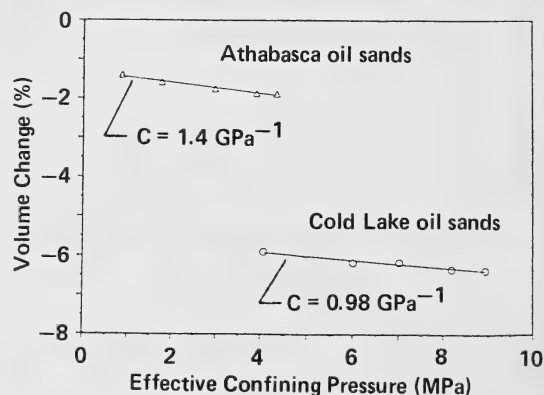
Figure 7. Compressibility of sand structure for oil sands

Table 2. Effect of stress path on stress-strain properties.

Stress path	Confined drained compression		Confined undrained compression	
	Athabasca	Cold Lake	Athabasca	Cold Lake
σ_3 (MPa)	4.0	4.0	2.0	2.0
E_i(GPa)	2.2	0.68	0.28	0.57
μ	0.22	0.27		
$[\sigma'_1/\sigma'_3]_{max}$	5.2	2.8	4.7	5.4
$(\sigma_1 - \sigma_3)$ (MPa)	16.9	6.9	10.7	6.0
$\varepsilon_{max\ ratio}$ (%)	1.1	2.5	1.6	1.1
ε_{peak} (%)	1.1	2.5	8.7	2.0

Cyclic compressibility tests performed on high-quality oil sands specimens provide a good indication of the in situ compressibility. The bulk modulus of compressibility, K, of Athabasca oil sands is 0.72 GPa, slightly greater than that of Cold Lake oil sands, 1.0 GPa. This difference in compressibility is due primarily to the difference in effective confining stresses in situ.

The compressibility of oil sands can be measured either by isotropic compression in the triaxial cell, as shown in Figure 7, or by confined compression in the oedometer. Figure 8 provides a comparison of the two methods for Cold Lake oil sands. In the confined compression test the specimen experiences both shear strain and volume change, whereas during isotropic compression the specimen does not undergo shear straining. As a result the stress path followed by the specimen in each test is different and a distinction must be made between constrained modulus, D, measured in the oedometer and the bulk modulus, K, measured during isotropic compression in the triaxial cell.

The compression of oil sand core is high upon initial loading but converges to low values after a loading and unloading cycle (Figure 8). This high initial compressibility reflects the amount of sample disturbance during coring. The confined and bulk moduli are measured based on cycling tests to give an indication of in situ compressibility. The repeatability of cycling results suggests the oil sand is behaving in an elastic manner over the stress range and that grain crushing is not occurring.

Table 3 shows the effect of stress path on compressibility. Conventional elastic theory has been used to compare the results of the isotropic compression stress path and the confined compression stress path. The following observations can be made from Table 3 and Figures 7 and 8.

- Athabasca oil sand is slightly more compressible than Cold Lake oil sand. This is probably due to the lower in situ confining stresses in the Athabasca deposit.
- The compressibility of Cold Lake oil sand during confined compression is only 60% of the compressibility during isotropic compression. Although not shown here, similar differences have been found for Athabasca oil sands.
- The initial decompression due to core disturbance is much less for Athabasca oil sands than for Cold Lake oil sands. This is probably because of the shallower depths of the Athabasca deposit and the resulting smaller decreases in confining stress and pore pressures when core is brought to the surface.
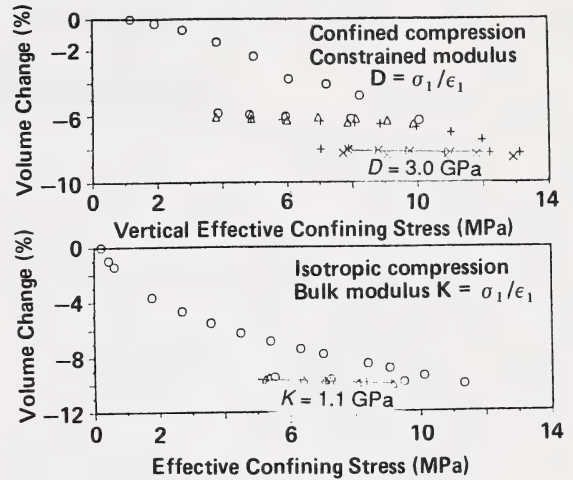
Loading cycle

o	First	+	Third
Δ	Second	x	Fourth

Figure 8. Consolidation of oil sands.

The compressibility of oil sands is also temperature dependent. Morgenstern [17] illustrated the effect temperature has on the confined compressibility of quartz sand. The compressibility of quartz sand increases significantly with temperature and is time dependent at high temperatures (Figure 9). This behavior results from particle degradation at high temperature. Quartz is the predominant mineral in
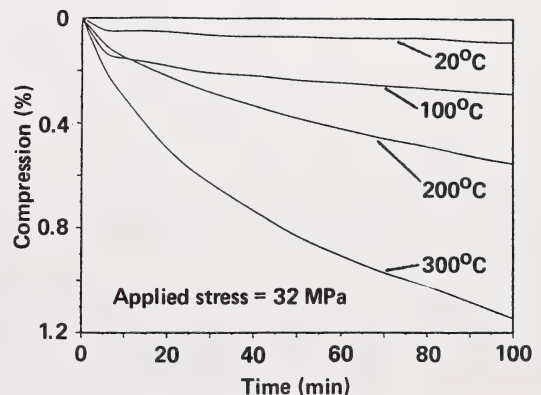
Figure 9. Compression of quartz sand under elevated temperature.

Table 3. Effect of stress path on compressibility.

Stress path	Isotropic compression		Confined compression	
	Athabasca	Cold Lake	Athabasca	Cold Lake
Stress range (MPa)	1 to 4.5	4 to 9	1.9 to 8.7[a]	6.9 to 15.5[a]
K or D (GPa)	0.72	1.0	1.4[b]	1.8[b]
$(\Delta V/V)_{\text{initial}}$	1.7%	6.2%		
Stress range (MPa)		5 to 9		8.6 to 15.5[a]
K or D (GPa)		1.1		1.9[b]
$(\Delta V/V)_{\text{initial}}$		10%		
Stress range (MPa)		4.1 to 7.5[a]		7 to 13
K or D (GPa)		1.7[b]		3.0
$(\Delta V/V)_{\text{initial}}$				8%

Stress range for isotropic compression is average effective principal stress, and for confined compression is vertical effective stress.

[a] Calculated from: $K_o = \dfrac{\mu}{1-\mu}$ [b] Calculated from: $K = \dfrac{D(1+\mu)}{3(1-\mu)}$

μ for Athabasca = 0.22
μ for Cold Lake = 0.27

Athabasca (McMurray Formation) oil sands. For the weaker-grained Cold Lake (Clearwater Formation) oil sand temperature-dependent grain breakage is significantly higher and may occur at lower temperatures and pressures.

Thermal volume change

The results of fully drained volumetric thermal expansion tests performed on Cold Lake (Clearwater Formation) and Athabasca (McMurray Formation) oil sands are shown in Figure 10. The thermal expansion tests were carried out under sufficient back pressure to prevent gas exsolution. Since the results of a fully drained thermal expansion test on oil sand is a measure of the volume change of both sand grains and soil structure, the abrupt decrease in the thermal volume change of the Cold Lake specimen at 75°C illustrates either a significant amount of temperature-induced grain breakage or a major rearrangement of the sand structure.

From the drained tests conducted on oil sand it is evident that a volume increase of <1% (Figure 10) is likely over the temperature range of 20 to 200°C, provided adequate back pore pressures are maintained to prevent gas exsolution. Thermal expansion tests

performed on oil sand under undrained conditions generate volume increases of the pore fluids as well as the mineral grains. Scott and Kosar [18] showed undrained heating of oil sand will result in a volume increase of about 6% over a 200°C temperature increase. Most of this increase, over 5%, is due to the pore fluids, water, and bitumen, with bitumen expanding slightly
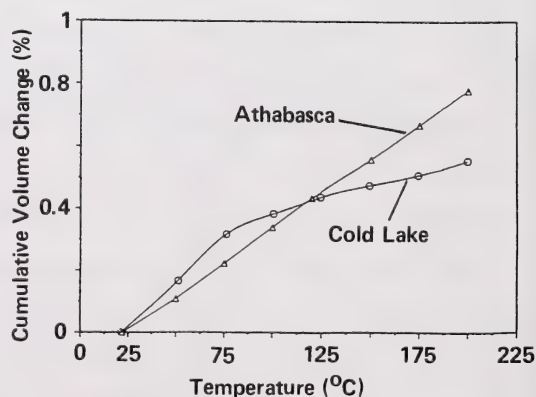
Figure 10. Volumetric thermal expansion of oil sands.

more than water. The remainder of the volume increase is due to the thermal expansion of the sand grains.

Quasi-elasticity

Linear theories of poroelasticity are often used to compute the interaction between pore fluid pressure changes, stresses, and deformations [5, 6]. Oil sands behave neither in a linear manner nor in an elastic manner and therefore the determination of poroelastic constants from laboratory tests is at best a crude approximation. When applied in practice, caution must be exercised to ensure that the laboratory test is at least consistent with the in situ stress path.

Laboratory measurements of the confined drained compression properties under an effective confining stress of 4 MPa for Cold Lake (Clearwater Formation) and Athabasca (McMurray Formation) oil sands are shown in Figure 5. The stress path for this test is shown in Figure 3a. The Athabasca oil sands specimen reaches its maximum shear strength at approximately 1% axial strain whereas the Cold Lake specimen does not reach maximum shear strength until the axial strain is well over 2%. The effective stress ratio, σ'_1/σ'_3 is plotted in the figure to normalize the effect of confining stress. The E values were determined from plots of $(\sigma_1 - \sigma_3)$ versus axial strain. The maximum shear strength and stress-strain modulus of Athabasca oil sands are about three times greater than those of the Cold Lake sands reflecting the difference in sand grain mineralogy, geological environment of deposition, and geological history. Athabasca oil sands consist of a uniformly graded predominantly quartz sand whereas Cold Lake oil sands consist mainly of much weaker minerals. Poisson's ratio for Athabasca and Cold Lake oil sands is seen to vary only slightly from 0.22 to 0.27. The influence of the mineralogy and stress history of the deposits appears to have little effect on the Poisson's ratio of the oil sands specimens. The Athabasca oil sands specimen displays a dilatant volume change at its maximum shear strength whereas the Cold Lake specimen continues to contract with increasing strain. The dilatant behavior of Athabasca oil sands under this effective confining stress, illustrates the strength of the quartz sand grains, which tend to ride up on each other during shear. In the Cold Lake specimen shearing occurs through the sand grains.

Based on curve fitting of experimental data, Agar et al. [19] suggest that a hyperbolic relationship may provide a useful empirical technique for modelling the nonlinear stress-strain behavior of oil sand up to about 80% of the peak shearing resistance.

IN SITU STRESSES

Origins

In situ stresses provide the context for material properties; they are not a material property in themselves. Changes in the in situ stress cause behavior governed by the geotechnical properties of the material. That behavior can in turn modify the stress state. For example, increases in pore pressure can cause material dilation that within the confinement provided by the ground leads to increased in situ stresses. This interaction between geotechnical properties and in situ stress dominates the behavior of in situ heavy oil recovery processes.

In situ stress magnitudes and orientations can change due to the engineering activities associated with thermal oil recovery. Pattern orientations and well spacings which were suitable for the stress field existing at the start-up of a small pilot, may not be suitable for the altered stress field which could exist during the expansion of a commercial project at the same location at a later date.

The knowledge of in situ stresses is essential for the proper interpretation of observation well, well diagnostic, and production data. This information also plays an integral role in the rational design of well patterns and spacing, and operating procedures for thermal recovery projects. The magnitude and orientation of the minimum in situ stress governs whether induced fractures or fracture-like features will be vertical, horizontal, or inclined. This orientation can be an important factor in the flow of heat and fluid in tar sand reservoirs.

By knowing the relationship between the vertical and horizontal stresses it is possible to predict the orientation of fractures induced in the reservoir during injection operations. Although hydraulic fractures can initiate at adverse orientations to the in situ stress field at the wellbore [20], as they propagate in the reservoir they will orient themselves to become perpendicular to the minimum in situ stress. Hence if the overburden stress is the minimum in situ stress, induced fractures will be horizontal in the reservoir. If one of the horizontal stresses is the minimum stress, induced fractures will be vertical.

The present-day state of stress acting at any point in the earth's crust is the summation of several components.

These include, but are not limited to, components due to the weight of the overburden, tectonic displacements, formation pore pressure, temperature, and residual stresses.

The component due to the overburden was estimated by Phillips [21], who suggested that by considering the gravitational forces acting on an elastic sphere, the vertical and horizontal stresses acting in the earth's crust could be approximated as follows:

$$\sigma_v = \int \rho\, g\, dz$$

$$\sigma_h = \frac{\upsilon}{(1-\upsilon)}\, \sigma_v$$

where σ_v and σ_h are the vertical and horizontal components of the in situ stress field, z is the depth, υ is Poisson's ratio and ρ is the mass density of the overburden; g is the acceleration due to gravity. Typical values of Poisson's ratio for most geological materials range from 0.2 to 0.33 while those for oil sands are limited to a narrower range. Following Phillips reasoning and using these values for Poisson's ratio, the ratio of the horizontal to vertical stress due to contributions from the overburden alone should range from 0.25 to 0.5. Results of in situ stress determinations performed around the world, including Western Canada, have shown that the ratios of the horizontal to vertical stresses can range from 0.5 to more than 1.0. The in situ stress state reflects contributions of more than one component. The variability of in situ stresses has been demonstrated by determinations in the Clearwater Formation near Cold Lake, Alberta which have shown that horizontal stresses can be less than, equal to, or greater than the vertical stress within an area of several square kilometres.

In general, due to the many factors which influence in situ stress fields, it is rarely possible to predict the present-day state of stress at a given location with any degree of certainty, other than in very shallow deposits. Nevertheless, it is possible to reliably determine some of the principal components of the in situ stress.

Determination

For purposes of this discussion it is assumed that the principal in situ stresses are oriented vertically and horizontally. Deviations in stress field orientation of up to 10° from the assumed orientations will have little impact on the results.

Of all the techniques that have been developed for in situ stress determinations to date (i.e. flat jacks, over-and undercoring, hydraulic fracturing, see Rocha et al. [22] Hooker et al. [23]) the technique that is most suitable for deeper heavy oil sand formations is the hydraulic fracturing technique discussed by Gronseth and Kry [24] and applied to low permeability gas sands by Kry and Gronseth [25].

In situ stress determinations by hydraulic fracturing can be performed either open-hole or through perforated casing. Open-hole stress determinations allow estimates to be made of the minimum and maximum stress acting perpendicular to the wellbore axis. As well, with the use of impression packers or borehole televiewers, they permit determination of the orientation of the maximum horizontal stress. For near-vertical wells, the third stress component can be inferred from integration of density logs of the overburden.

Cased-hole stress determinations can be performed in completed production wells prior to steam injection, which helps to minimize the costs associated with the test. With cased-hole stress determinations only the magnitude of the minimum horizontal stress can be determined from the hydraulic fracturing technique. For most applications this knowledge is sufficient to assess whether fractures induced during steam injection will be vertical or horizontal.

Hydraulic fracturing as a means of in situ stress determination was first suggested by Fairhurst [26] and Kehle [27], and has been used for that purpose since the early 1970s. It is similar to hydraulic fracturing for well stimulation purposes except that it is best performed using low flow rates ($<35L$/min) and small volumes (<2 m^3). Pressures measured during hydraulic fracturing well stimulation treatments will not generally produce reliable in situ stress data.

For either open- or cased-hole stress determinations the interval to be tested is isolated from the rest of the wellbore with packers. This interval is fractured by injecting fluid into the wellbore until the pressure is sufficiently high to induce a tensile fracture at the wellbore. The fracture is then extended by continued fluid injection. After several minutes of fracture propagation, fluid injection is terminated, and pressures are monitored for several minutes after pumping has ceased. The interval being tested is then repeatedly repressurized and shut-in until the value of the instantaneous shut-in pressure reaches a more or less constant value.

A pressure-time record and a flow-rate-time record of a stress determination in a newly drilled well completed in the Clearwater at Cold Lake is shown in Figure 11. The breakdown pressure, P_b, at nearly 11 MPa in Figure 11 is the pressure at which the fracture initiates. The fracture extension pressure, P_f, at 10.4 MPa for the first cycle and decreasing to 9.5 MPa for subsequent cycles, is the pressure required to extend the fracture in the formation. Finally, when fluid injection is discontinued for each cycle, the pressure rapidly drops to a value known as the instantaneous shut-in pressure, P_{isip}. The instantaneous shut-in pressure corresponds to a state of quasi-static equilibrium between fluid pressure holding the fracture open and the local stress normal to the fracture face closing it. In real situations, the pressure following shut-in will continue to decay until the wellbore pressure equilibrates with the formation pore pressure. P_{isip} cannot be determined from a figure such as Figure 11 because the time scale is too coarse. However, detailed inspection of the nature of the pressure-time record after shut-in for each cycle leads to a sequence of values of P_{isip}. For the test depicted in Figure 11, this sequence stabilized at 9.3 MPa for the final 4 cycles. This value is interpreted as the maximum stress acting perpendicular to the wellbore axis.

One of the key factors for successful in situ stress determinations by hydraulic fracturing is the proper interpretation of the instantaneous shut-in pressure. Gronseth and Kry [24] have shown that the instantaneous shut-in pressure when defined as the pressure after shut-in at the inflection point in the pressure-time record produces the best results. Judgement is required to infer the value of the minimum in situ stress from the measured instantaneous shut-in pressures. Experience has shown that uncertainty in stress values inferred from low volume, low rate cyclic hydraulic fracturing is less than 0.5 MPa. Uncertainty in integrated density logs is less than 0.1 MPa if log quality is sufficiently good.

Variability

In situ stresses vary with location due to the many natural factors influencing their origin. In oil sands one additional parameter influencing variability is the change associated with thermal oil recovery operations. Repeat stress determinations at Cold Lake have shown that the orientation of the maximum in situ stress can change from vertical at the start of steam injection to horizontal before the end of a steam injection cycle in a pad. They have also shown that over distances of a few kilometres at comparable depths, in situ stress states which favor horizontal fractures change to states favoring vertical fractures.

Figure 12 illustrates an example of the change caused by steam injection to nearby wells. This is the record of a stress test conducted after steam injection to a number of wells within 350 m of the test well. The stress determination record displayed in Figure 11 is the pre-steam-injection stress determination in the same well. Figure 12, for a stress test after nearby wells were steamed, is interpreted to represent the propagation of a fracture constrained by the wellbore to open against the minimum horizontal stress inferred to be 10.5 MPa. During cycle 6, the propagation of the fracture normal to the minimum in situ stress, the vertical stress, became dominant and the instantaneous shut-in pressure stabilized at 9.8 Mpa. The value of the original minimum in situ stress of 9.3 MPa is also indicated in
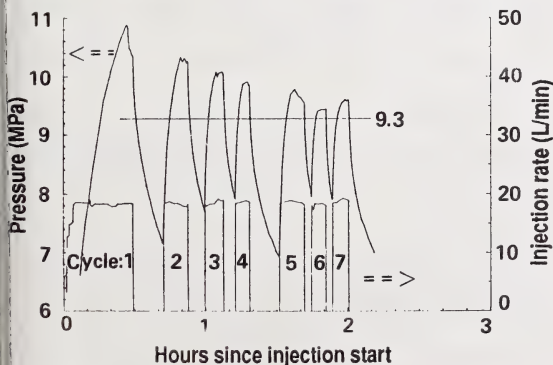

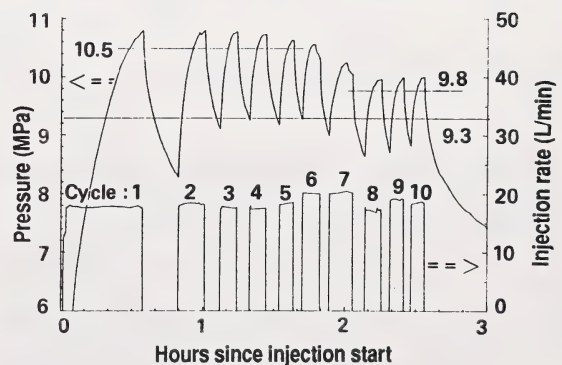**Figure 11.** Initial stress test results.

Figure 12. Steam-influenced stress test results.

Figure 12 to show that for this well, the preference for vertical fractures was changed to one for horizontal fractures by steaming of nearby wells.

Figure 13 shows the areal distribution of stresses over a region of reservoir before any steaming took place within 1 km of any of the wells tested. The data show that over this whole region, horizontal fractures would be expected and there would be no initial vertical tendency as shown in the preceding Figure 11. The minimum horizontal in situ stresses shown in Figure 13 were determined by the techniques illustrated in Figure 11. The vertical stresses were assessed by log integration. In several cases, P_{isip} varied as illustrated in Figure 12, with a decline to a value close to the log-integrated vertical stress. The cases illustrated with no estimate of the minimum horizontal stress were cases in which the P_{isip} sequence stabilized within 0.3 MPa of the log-integrated vertical stress estimate. In these cases it is speculated that fracture growth was very weakly constrained by the presence of the wellbore and even the small volume associated with the first few cycles of the stress test was enough to cause the favored propagation normal to the minimum in situ stress.
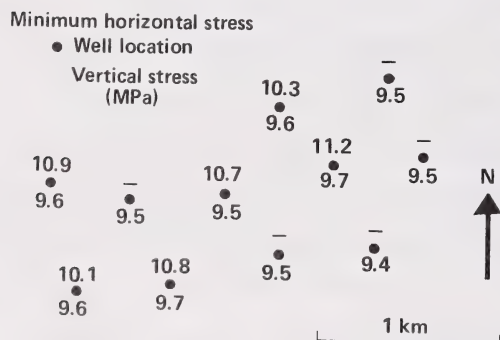
Figure 13. Areal distribution of stresses.

In situ stresses are fundamental determinants of the geotechnical behavior of an in situ recovery process. They have complex origins and can therefore not be predicted with sufficient accuracy at any arbitrary location. However, low volume, low rate cyclic hydraulic fracturing can be used to determine in situ stresses when it is necessary to have this information. As well as the natural influences giving rise to stress state variations, in situ recovery processes themselves change the state of stress. A complete understanding of an in situ recovery process requires knowledge of the interaction between the geotechnical behavior and changes in stress state in a reservoir.

REFERENCES

1. M.B. Dusseault, "The geotechnical characteristics of oil sands," Ph.D. thesis, Univ. of Alberta, Edmonton, (1977).
2. M.B. Dusseault and N.R. Morgenstern, Shear strength of Athabasca oil sands, Can. Geotech. J., 15 (1978) 216–238.
3. M.B. Dusseault and N.R. Morgenstern, Locked sands, Quarterly J. Eng. Geol., 12 (1979) 117–131.
4. A.E. Fair and E.R.F. Lord, Methods used to monitor and control block slides in oil sands at Syncrude's dragline operation in northern Alberta, Canada, Preprints of 37th Canadian Geotechnical Conference, Toronto (1984) 103–112.
5. J. Geertsma, Some rock-mechanical aspects of oil and gas well completion, Proc. European Offshore Petroleum Conference and Exhibition (1978) 301–310.
6. J.C. Jaeger and N.G. Cook, "Fundamentals of rock mechanics," 2nd. ed., Chapman and Hall, U.K.(1976).
7. J.G. Agar, Geotechnical behavior of oil sands at elevated temperatures and pressures, Ph.D. thesis, Department of Civil Engineering, Univ. of Alberta, Edmonton (1984).
8. K.H. Head, Manual of soil laboratory testing, Pentech Press, London (1980).
9. J.G. Agar, N.R. Morgenstern and J.D. Scott, Geotechnical testing of Alberta oil sands at elevated temperatures and pressures, Proc. 24th US Symposium on Rock Mechanics, Jun (1983) 795–806.
10. Hardy and R.A. Hemstock, Shearing strength characteristics of Athabasca oil sands, Alberta Research Council Information Series 45 (1963) 109–122.
11. M.B. Dusseault, The behavior of hydraulically induced fractures in oil sands, Underground rock engineering, CIM Special Vol. 22 (1980) 36–41.
12. G.G. Mainland, The development of in situ recovery technology at Cold Lake, Proc. 4th Annual Conf. on Advances in Petroleum Recovery Technology, Calgary, AOSTRA (1983).

13. S.M. Blair, The bitumen sands of Alberta, Alberta Research Council Report 18 (1950).

14. K.A. Clark, Bulk densities, porosities and liquid saturations of good grade Athabasca oil sands, Research Council of Alberta , Memo 22 (1957).

15. M.A. Carrigy, The physical and chemical nature of a typical tarsand: Bulk properties and behaviour, Proc. Seventh World Petroleum Congress, Mexico City, 3 (1967) 573–581.

16. E.W. Brooker, Tarsand mechanics and slope evaluation, Tenth Canadian Rock Mechanics Symposium, Kingston, Ont., 1 (1975) 409–446.

17. N.R. Morgenstern, Geotechnical engineering and frontier resource development, 21st Rankine Lecture, Geotechnique (1981) 305–365.

18. J.D. Scott and K.M. Kosar, Thermal expansion of oil sands, Proc. Forum on subsidence due to fluid withdrawal, U.S. Department of Energy and Republic of Venezuela Ministry of Energy and Mines, OK (1982) 46–57.

19. J.G. Agar, N.R. Morgenstern and J.D. Scott, Shear strength and stress-strain behavior of Athabasca oil sand at elevated temperatures and confining pressures, Can. Geotech. J., Feb, 24 (1987).

20. J.M. Gronseth and P.R. Kry, in situ stresses and the Norman Wells Expansion Project, 38th Annual Technical Meeting of the Petroleum Society of CIM in Calgary, Jun 7–10, 1987, Preprint no. 87-38-57 (1987).

21. D.W. Phillips, Tectonics of mining, Colliery Engineering, 25 (1948) 199–203, 278–82.

22. M. Rocha, Baptista J. Lopes and J. DaSilva, A new technique for applying the method of the Flatjack in the determination of stresses inside rock masses, Proc. 1st Cong. ISRM (Lisbon), 2 (1966) 57–65.

23. V.E. Hooker, J.R. Aggson, D.L. Bickel and W. Duvall, Improvement in the three component borehole deformation gage and overcoring technique, U.S.B.M. Rep. Inv. 7894, with appendix by Duvall on the undercoring technique (1974).

24. M. Gronseth and P.R. Kry, Instantaneous shut in pressure and its relationship to the minimum *in situ* stress, in: "Hydraulic fracturing stress measurements," M.D. Zoback and B.C. Haimson, Eds., National Academy Press, Washington D.C. (1983).

25. P.R. Kry and J.M. Gronseth, In situ stresses and hydraulic fracturing in the deep basin, J. Can. Pet. Tech., 22, no. 6 (1983) 31–35.

26. C. Fairhurst, Measurement of *in situ* rock stresses with particular reference to hydraulic fracturing, Rock Mechanics and Engineering Geology, 2 Ch.3–4 (1964) 129–47.

27. R.O. Kehle, Determination of tectonic stresses through analysis of hydraulic well fracturing, J. of Geophys. Res., 69 (1964) 259–273.
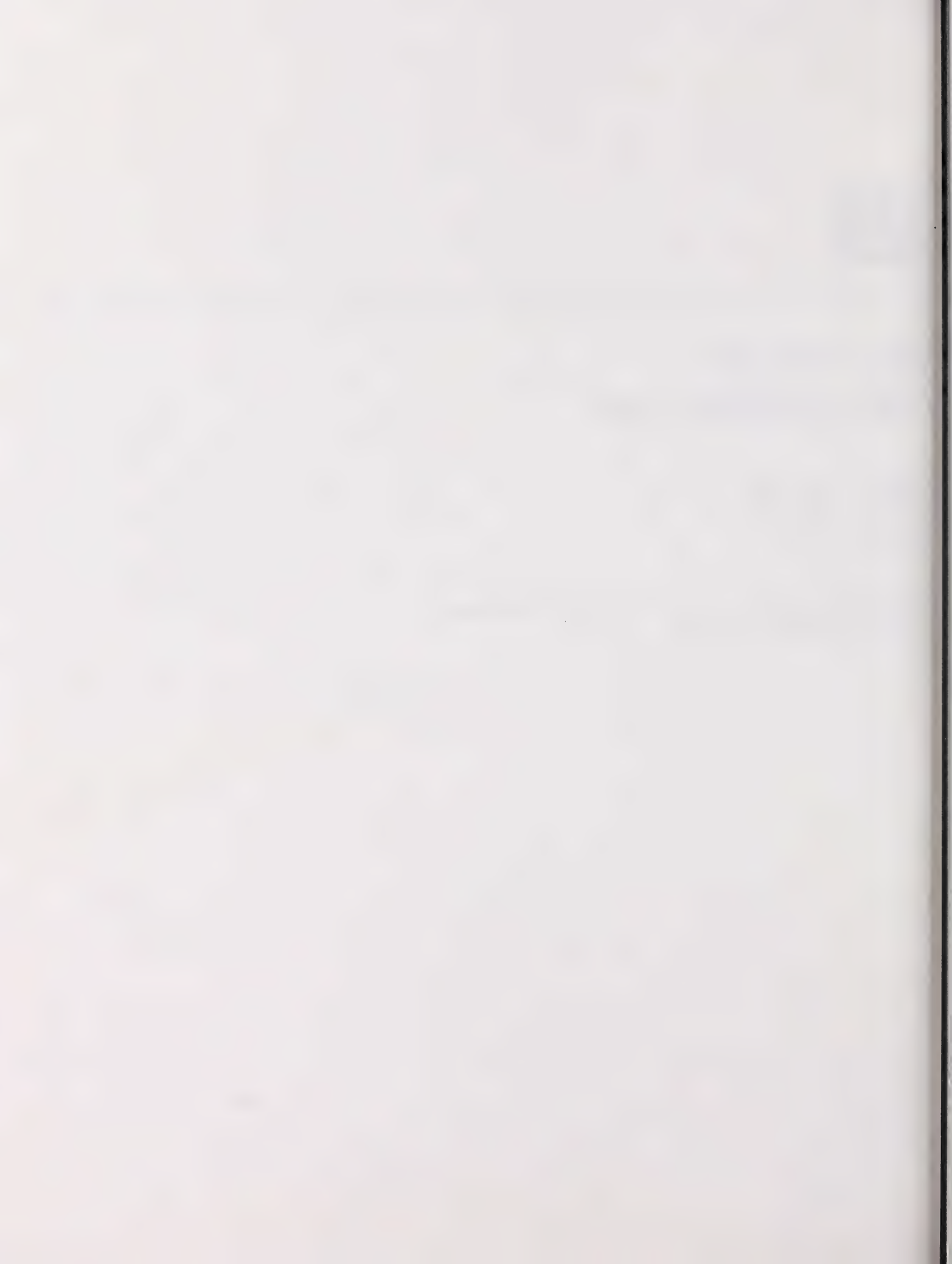
9
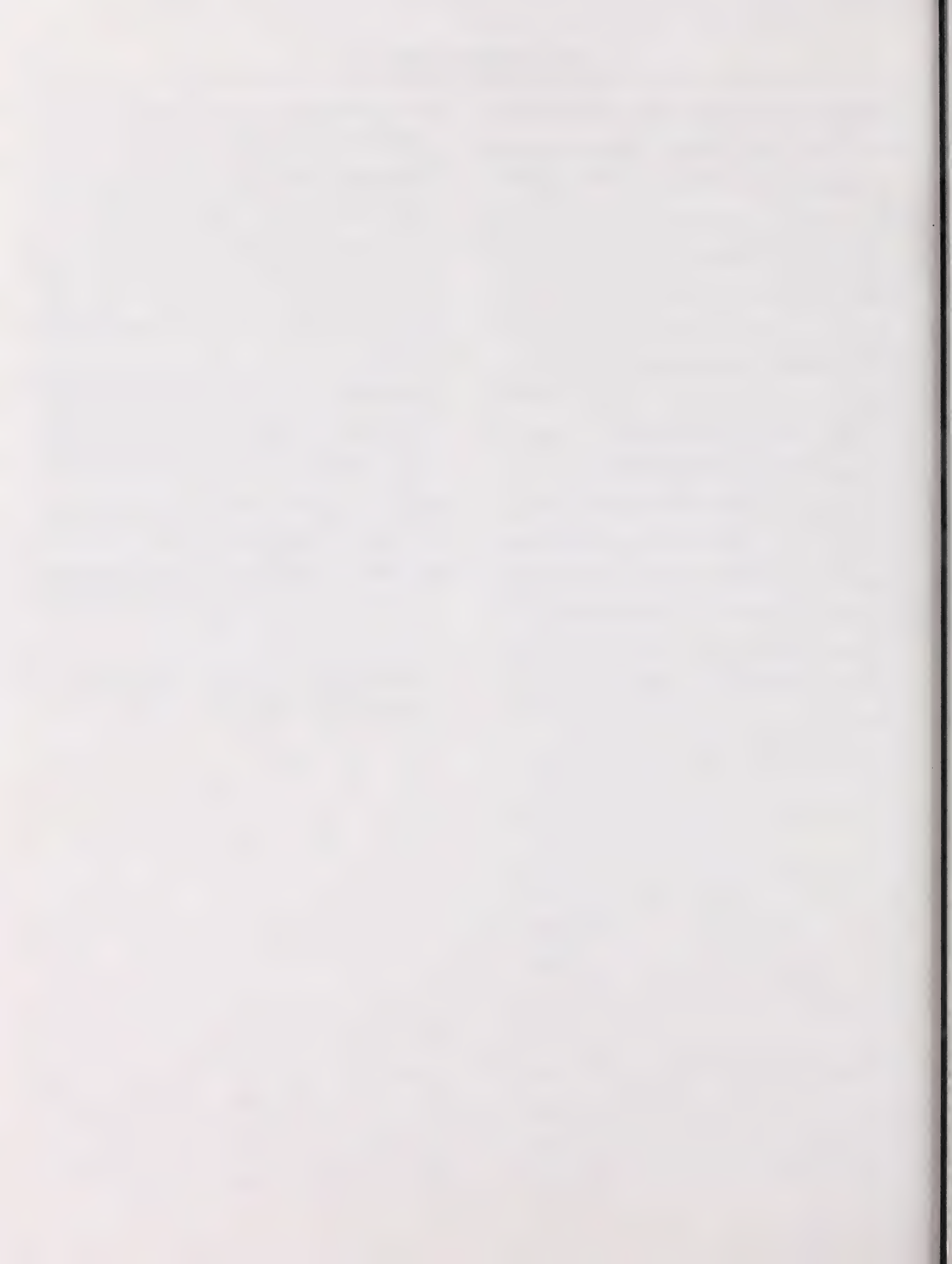
INORGANIC GEOCHEMISTRY

W. D. Gunter
G. W. Bird

Oil Sands and Hydrocarbon Recovery Department
Alberta Research Council

INTRODUCTION

An applied geochemical program must ultimately aim at identifying the causes of formation or well damage and developing treatment techniques that can be used to minimize, reverse, or in some specific cases, enhance the damage. Any proposed preventive or remedial techniques must be applicable with existing reservoir technology and must also be compatible with the reservoir geochemistry. This chapter consists of a brief description of the techniques that can be used to gather, evaluate, and interpret the geochemical processes that occur in thermal oil recovery. The techniques range from laboratory experiments in static autoclaves and flow systems to field fluid sampling at wellhead conditions.

The in situ heavy oil and tar sand recovery processes planned and tested in Alberta utilize heat from the injection of steam, hot water, or in situ combustion to lower the viscosity of the bitumen and enhance its recovery. Water-rock interaction is a factor that must be considered in designing an in situ production process. In situ recovery by steam injection is illustrated schematically in Figure 1. Surface water, ground water, or recycled water is converted to wet steam (less frequently dry steam or hot water) and injected into the reservoir at temperatures up to 350°C, sometimes with additives such as gases, surfactants, or solvents. The

cooling and condensation of the steam heat the reservoir, reducing the viscosity of the oil and pushing it towards the producing well (steam drive). Alternately, if no communication path exists between wells, the injected steam is allowed a soak period in the reservoir and then the mixture of oil, steam, condensed steam, and formation water is produced up the original injection well (steam stimulation or huff and puff).

The in situ combustion process is illustrated in Figure 2. The reservoir is ignited close to an air-water injection well and the combustion front moves away from the well. In the burn zone, air reacts with the fuel, producing mainly CO_2 and H_2O with lesser amounts of SO_2; temperatures in excess of 700°C can be reached. The high temperatures created by the transport of heat in front of the burn zone cause cracking of the hydrocarbons in the coking-vaporization zone and breakdown of many of the clay minerals. The lighter ends from the hydrocarbons move ahead into the steam zone while the residual coke left behind serves as fuel for the burn. Behind the combustion front is the post-burn zone consisting of sand and residual coke. The size of the steam zone depends on the mass of water injected. The water/steam ratio increases continuously until the water zone is reached where all the steam has condensed. The water zone contains injected water, formation water, and water from oxidation of the oil. Oil saturation is increased in the adjacent oil zone
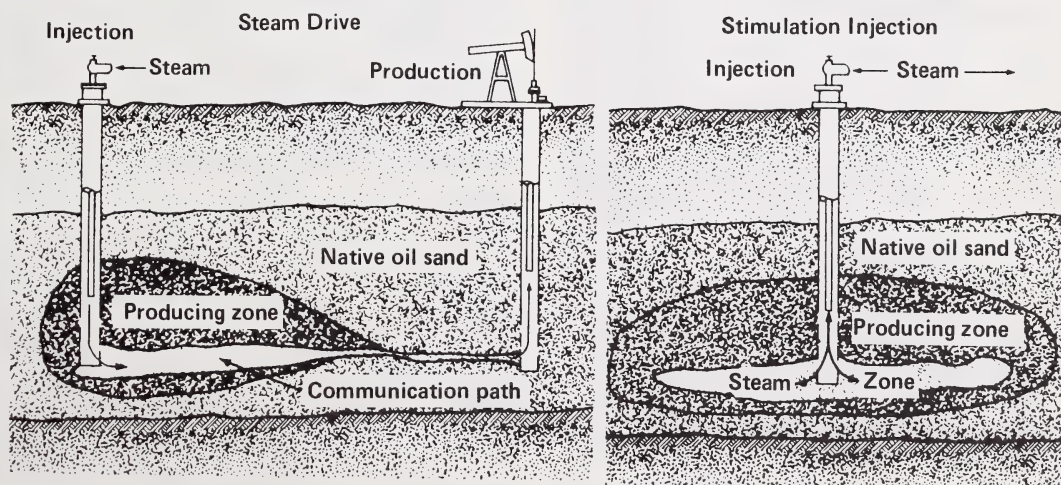

Figure 1. Thermal recovery; two modes of steam injection. Adapted from Gunter et al. [25].
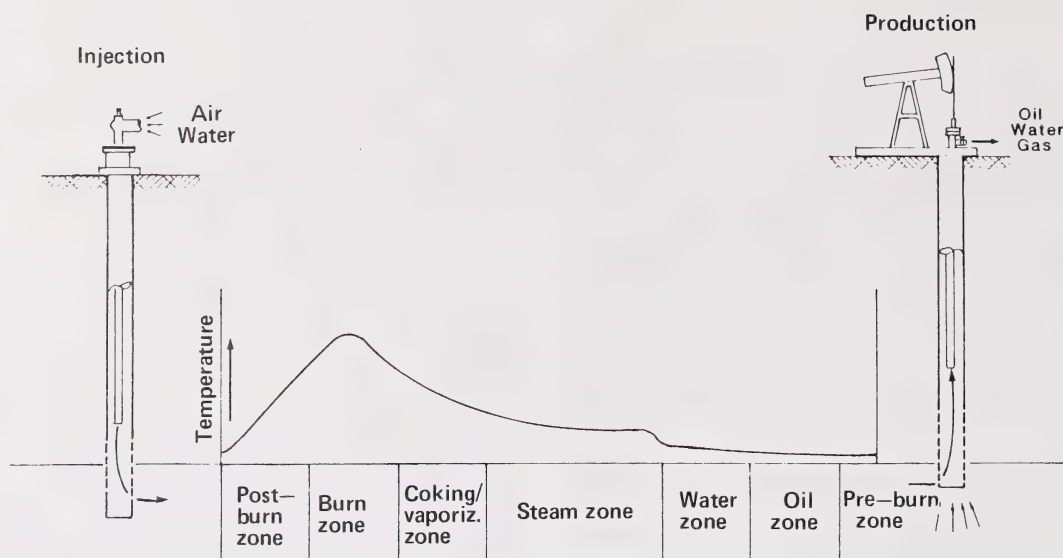
Figure 2. Thermal recovery; in situ combustion zones in a fire flood. Adapted from Gunter et al. [25].

because of displacement of oil from the water zone. Finally, the pre-burn zone abuts the oil zone. These zones sweep out towards the production well as the burn progresses.

Communication pathways that allow the steam and water to heat the oil and allow the viscous oil, once heated, to flow into the wellbore are essential to both steam and combustion processes. The high temperatures encountered during steam injection or fire floods greatly speed up the water-mineral reaction rates. Laboratory experiments using autoclaves, flow systems, and geochemical modelling can be used to determine what reactions are likely to occur as a result of the elevated temperatures. The reactions resulting from cooling and neutralization of the solutions as they move through the formation can be modelled or determined experimentally. In some reservoirs, geochemical reactions can cement an unconsolidated formation and, thus, be beneficial. In some of the more reactive formations, however, permeability can be drastically reduced either by formation damage or the precipitation of scales in the wellbore and production equipment. In some cases, lowering the permeability may help improve recovery by sealing off thief zones which are barren of oil but are heat sinks. Disposal of the produced water in the subsurface may plug up the disposal formation creating an injectivity loss.

Production fluid monitoring, that is, tracking the chemistry of the fluids, is a diagnostic tool that can be used to follow changes in the reservoir. Particular areas of use could include the prevention or prediction of formation damage, well scaling, or fines migration problems. Geochemistry can also be used to predict the in situ production of CO_2 from inorganic sources.

The surface properties of the bitumen and the minerals are affected by changes in pH and salinity of the reservoir fluids. Changes in the interfacial properties of the minerals, oils, or aqueous fluids can result in the dispersal of fines, altered wettability of the minerals, and altered relative permeability of the reservoir.

The chemical composition of the produced water can be used to estimate temperature changes in the reservoir. Geochemical tracers, either injected along with the steam or natural components of the reservoir fluid, may be used to determine the geometry of the reservoir and the source of the produced fluids. Geochemical computer programs can be used to back-calculate the chemical composition data obtained from samples taken at the surface to conditions in the reservoir. Theoretical thermodynamic calculations can be used to generate mineralogical phase diagrams for various reservoir physical conditions and fluid chemistries. The mineralogical composition of the formation and the composition of formation, injection,

produced water, and waste water form the basis for such calculations.

The extensive but not exhaustive reference list that has been compiled at the end of this chapter should serve to introduce the reader to the geochemical, geothermal, and petroleum literature relevant to thermally enhanced oil recovery. We trust that the information contained in this chapter will serve as a starting point to introduce the reader to the role of geochemistry in thermally enhanced recovery and provide the tools for a better understanding of the geochemical processes.

MINERALOGY

In Chapter 1, the variation in mineralogy and stratigraphy between the Athabasca, Wabasca, Peace River, and Cold Lake tar sand deposits in Alberta are described. The mineralogy varies from being simple in the Athabasca deposit to complex in the Cold Lake deposit. Bayliss and Levinson [1] have summarized the mineralogy of these unconsolidated tar sands. Quartz, potash-feldspar, plagioclase, calcite, dolomite, siderite, pyrite, kaolinite, muscovite, biotite, and glauconite were identified by X-ray diffraction of the bulk sand; kaolinite, illite, chlorite, smectite, and mixed-layer clays were found in the minus 2 μm sand fraction. The clay minerals can be <1% in the sands but up to 50% in the associated shales. The mineralogy of the rock fragments which can compose up to 30% of the sand is more complex.

The Devonian carbonate reservoirs include the bitumen-bearing rocks beneath the pre-Cretaceous unconformity which abuts the tar sands. The lithology is dominantly dolomite and dolomitic limestone with some calcareous shales. In contrast to the sandstones, aluminosilicate minerals including clays are much less abundant and are completely absent from the purer dolostones.

In addition to these native reservoir minerals, the high temperatures accompanying thermal recovery will cause many new minerals to be synthesized from reactions with the hot water and the sand. Table 1 lists the chemical compositions of minerals that may be present in the reservoir either before or after recovery. Composition of minerals not listed in the table may be obtained from Deer, Howie, and Zussman [2], Fleischer [3] or Klein and Hurlbert [4]. Their occurrence will be discussed later on in this chapter.

Table 1. Formulas for mineral phases.

Albite	$NaAlSi_3O_8$
Alunite	$KAl_3(SO_4)_2(OH)_6$
Anhydrite	$CaSO_4$
Amorphous silica	SiO_2
Analcime	$NaAlSi_2O_5(OH)_2$
Andalusite	Al_2SiO_5
Anorthite	$CaAl_2Si_2O_8$
Biotite	$K(Mg,Fe)_3(Al,Fe)Si_3O_{10}(OH)_2$
Boehmite	$AlO(OH)$
Brucite	$Mg(OH)_2$
Calcite	$CaCO_3$
Ca-smectite	$CaAl_{14}Si_{22}O_{60}(OH)_{12}$
Clinochlore	$Mg_5Al_2Si_3O_{10}(OH)_8$
Clinozoisite	$Ca_2Al_3Si_3O_{12}(OH)$
Diaspore	$AlO(OH)$
Dolomite	$CaMg(CO_3)_2$
Gibbsite	$Al(OH)_3$
Glauconite	$(K,Na)(Al,Fe,Mg)_2(Al,Si)_4O_{10}(OH)_2$
Gypsum	$CaSO_4 \cdot 2H_2O$
Hematite	Fe_2O_3
Kalsilite	$KAlSiO_4$
K-smectite	$K_2Al_{14}Si_{22}O_{60}(OH)_{12}$
Kaolinite	$Al_2Si_2O_5(OH)_4$
K-feldspar	$KAlSi_3O_8$
Laumontite	$CaAl_2Si_4O_8(OH)_8$
Lawsonite	$CaAl_2Si_2O_6(OH)_4$
Magnetite	Fe_3O_4
Melanterite	$FeSO_4 \cdot 7H_2O$
Mg-smectite	$MgAl_{14}Si_{22}O_{60}(OH)_{12}$
Muscovite (illite)	$KAl_3Si_3O_{10}(OH)_2$
Na-smectite	$Na_2Al_{14}Si_{22}O_{60}(OH)_{12}$
Nepheline	$NaAlSiO_4$
Paragonite	$NaAl_3Si_3O_{10}(OH)_2$
Phillipsite	$KAlSi_2O_6 \cdot 4H_2O$
Pyrite	FeS_2
Pyrrhotite	FeS
Pyrophyllite	$Al_2Si_4O_{10}(OH)_2$
Quartz	SiO_2
Sepiolite	$Mg_4Si_6O_9(OH)_{14}$
Serpentine	$Mg_3Si_2O_5(OH)_4$
Siderite	$FeCO_3$
Talc	$Mg_3Si_4O_{10}(OH)_2$
Wairakite	$CaAl_2Si_4O_{10}(OH)_4$
Wollastonite	$CaSiO_3$
Wustite	FeO

EXPERIMENTAL TECHNIQUES

Laboratory techniques

Reactor studies at conditions relevant to steam injection can be carried out in variety of static, stirred, or rocking pressure vessels depending on the nature of the solutions being studied and the pressure and temperature ranges of the experiments. The essential part of any reactor system is an autoclave. Commercial autoclaves with pressure ratings up to 50 MPa at temperatures to 450°C are available in a number of materials such as stainless steel, titanium, zirconium, and inconel in sizes ranging from 25 mL to several litres. A description of the many varieties of pressure vessels available is given in Ulmer and Barnes [5], Ulmer [6], and Edgar [7]. More details on experimental design for a specific type of reaction are given in Levenspiel [8].

Batch reactors

An example of the use of static autoclaves and a statistically designed matrix of experiments is described in detail in Boon and Hitchon [9]. For each autoclave run, a constant weight ratio of water to sand is used. All runs are made under saturated water vapor pressure conditions with or without the addition of gases such as CO_2. Complete experimental procedures can be found in Boon and Hitchon [9] who varied temperature, salinity, and pH, and controlled the presence and absence of bitumen to determine which factors were more important in water-rock reactions. At the end of each run, the fluid compositions were determined and the extent of mineral transformation was evaluated by X-ray diffraction.

Scanning electron microscopy (SEM) is also used as a diagnostic tool for identifying mineralogical changes that have occurred through reaction. A compilation of SEM microphotographs of naturally occurring minerals has been prepared [10]. Examples of hydrothermally synthesized minerals formed in autoclave runs are found in Hebner et al. [11] and Gunter et al. [12].

Reactions in autoclaves are often slow because of the slow rate of diffusion of components to and from the reacting sites. This problem can be overcome by using a stirred or rocking autoclave which keeps the reactants mixed during an experiment. A stirred reactor design for use with constant P_{CO_2} and with on-line sampling has been designed (Figure 3a) and is being used for determining the rates of carbonate mineral dissolution. This apparatus has a facility for isothermal and isobaric rapid quenching by removal of the reactants from the
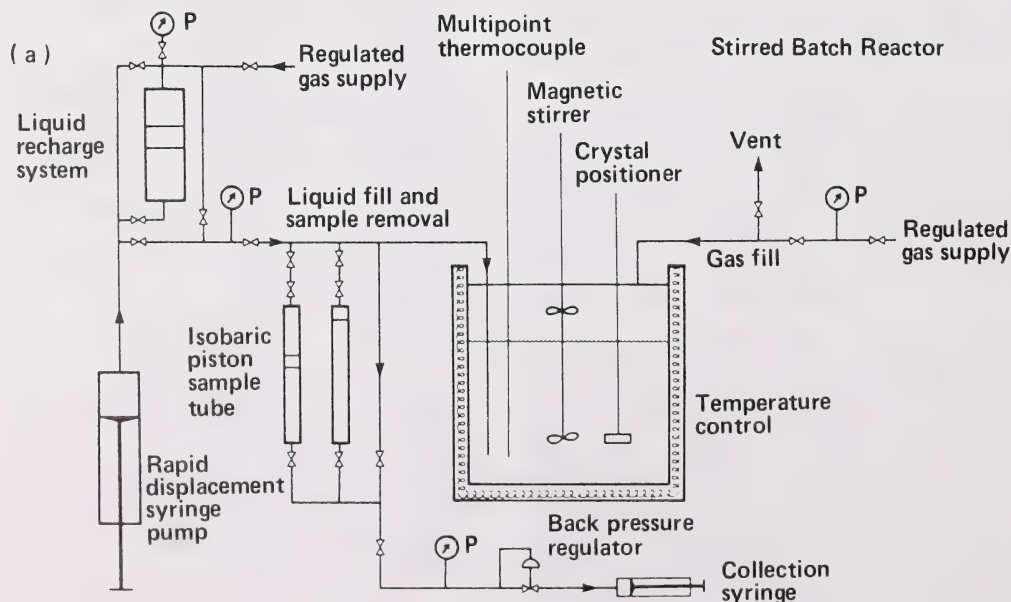
Figure 3a. Stirred batch reactor.

solutions. For more detail on this or other pressure vessel design and operation, the readers are referred directly to the technical literature or to standard textbooks such as that of Ulmer and Barnes [5] or Levenspiel [8].

Autoclaves can be adapted for on-line sampling when long-duration experiments are required and where the fluid composition is changing as a function of time. A example of such a "intermittent flow-through" system is described in Bird, Boon, and Stone [13] who used it to determine the rate of silica precipitation.

Flow reactors

A schematic design for a versatile flow system for hydrothermal studies is shown in Figure 3b. This flow system is designed so that an overburden pressure, generated by the saturated water vapor pressure at run conditions supplemented by N_2 pressure, can be imposed and maintained independently of the flow pressure. This system permits the injection of two fluids from accumulators; either singly or mixed together before entering the main pressure vessel.

The commercial autoclaves (Parr Instrument Co.)

used as the pressure vessels for the flow system, can hold cores up to 30 cm in length and 10 cm in diameter. These vessels will operate at pressures up to 12 MPa at temperatures up to 300°C. Other vessels with higher pressure and temperature ratings can be purchased or manufactured readily.

One of the constraints on the pressure and temperature rating of an overburden flow system is the ability to apply the overburden pressure at run conditions. We have used heat shrinkable teflon sleeves at temperatures up to 200°C and lead sleeves to slightly higher temperatures. For runs in the 250 to 300°C range thin-walled stainless steel or copper sleeves are manufactured by turning down the wall thickness of commercial copper or stainless steel tubing on a lathe and welding these to the end caps. Core sleeves with walls 0.4 mm thick will sustain an overburden pressure differential of up to 7 MPa at 300°C.

One advantage of the flexible, thin-walled metal sleeves is their ability to adapt to the shape of the unconsolidated core material inside. When the overburden pressure is applied, the sleeve collapses and transmits the pressure to the core material. Small ridges
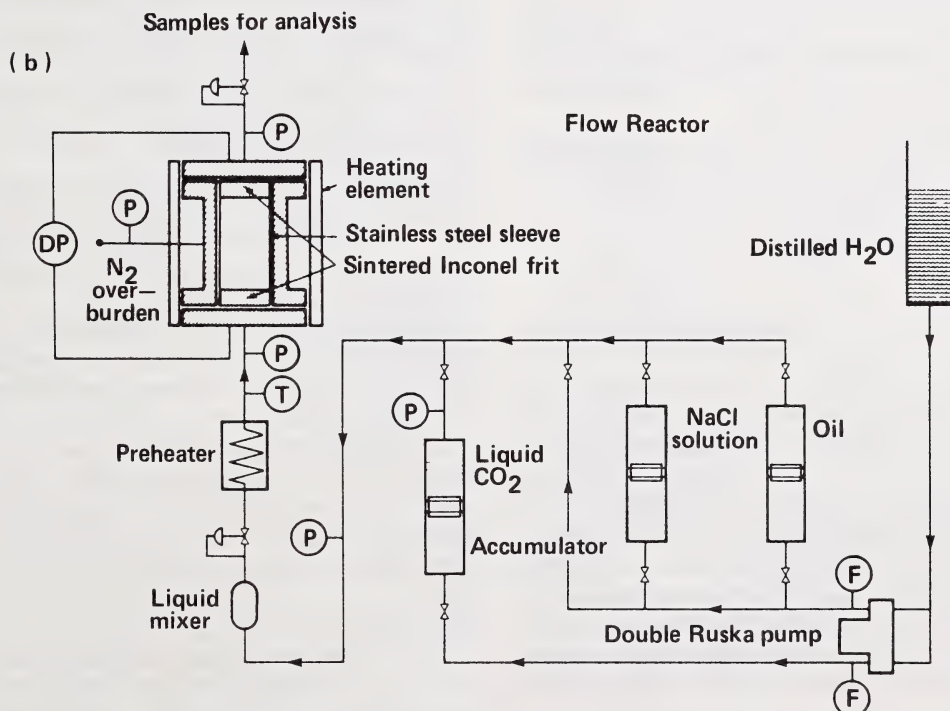
Figure 3b. Flow reactor.

form along the length of the core sleeve and the unconsolidated sand fills these ridges completely. Tracer tests have confirmed that these ridges do not constitute a high permeability zone [14].

The deformable sleeves are more difficult to use with consolidated cores as the core material cannot deform to the same shape as the core sleeve. One method that has been tested and found to work satisfactorily with consolidated core was to wrap the core in a thin lead sheet which is then machined to fit very closely inside the overburden sleeve. The core and blanketing lead are then inserted into the sleeve. When the overburden pressure is applied the lead sheet deforms to the same shape as the external surface of the core. At high temperature, the lead flows into the ridges of the external sleeve preventing fluid bypass.

Differential pressure gauges are placed in the pressure lines to measure the pressure drop as fluid flows through the core, and can be used to determine permeability at the temperature and pressure of the run.

Samples of the effluents are collected on the atmospheric pressure side of the final back-pressure regulator when only water is flowing through the core. For runs in which oil is injected, the flow system is modified by placing accumulators between the output end of the core and the final back-pressure regulator. The sampling accumulator prevents contamination of the back-pressure regulator by the oil and permits effluent sampling at run pressure.

The flow system described above has been used successfully to measure the amount and rate of CO_2 production from hydrothermal reactions and permeability changes resulting from such reactions [14,15] and for ambient and elevated temperature fines migration studies.

The system shown in Figure 3b can also be used for cleaning cores by the injection of solvents at ambient and elevated temperatures with the core confined by an overburden pressure. Toluene and methylene chloride have been used as solvents in this system without problems. If methylene chloride is used, however, caution must be taken to remove any residual solvent before applying heat as the methylene chloride can react with water to produce hydrochloric acid. The hydrochloric acid can attack the pressure tubing resulting in failure due to stress corrosion cracking.

References to other flow system designs can be found in the book by Ulmer and Barnes [5] and in the literature.

FIELD TECHNIQUES

Field sampling

There is no direct method for monitoring fluid-rock reactions in the subsurface. Water composition, however, is a sensitive indicator of the processes that are occurring as mixing of the injected and reservoir fluids modify the compositions of both water and gases that are in the reservoir. Furthermore, any changes in the mineralogy are also accompanied by changes in the composition of the co-existing liquid and gas phases. Since changes in ionic concentration of only a few milligrams per litre in the water can be measured by conventional analytical techniques, the water composition is a sensitive indicator of reaction progress. Careful collection and analysis of the injection and production water and gases accompanied by an appropriate technique for interpretation of the data should allow the operator of an oil recovery process to follow the progress of subsurface reactions in the immediate vicinity of the wellbore and in the formation, and correlate them with other process data.

A field fluid water monitoring program consists of four distinct components:

- Characterization of the reservoir mineral assemblages and formation water and gas before startup of the pilot.
- Representative sampling and chemical analyses of the injected and produced fluids at predetermined intervals over the life of the pilot.
- Interpretation of the analytical and physical data in terms of fines transport, mass balance, and solution-mineral equilibria to determine the extent and effects of reaction in the reservoir. Autoclave runs and core floods can be used to assist with the interpretation of the data.
- Prediction of future reservoir behavior is made from core floods, from history matching of fluid-rock reactions deduced, and from extrapolation using existing computer models.

Collection of analytical data is carried out to some extent by most operators. Interpretation of these data require geochemical expertise and can only be accomplished if the data collected are comprehensive and of a high quality.

Formation fluids

An oil sand reservoir could be considered to contain several different types of water which can differ substantially in composition. These are shown

schematically in Figure 4. Type 1 is bottom water, such as may be found at the base of the Peace River oil sand deposits. It is a formation water found within a zone or formation of high permeability and low to negligible oil saturation. Such a zone can have hydraulic continuity over substantial distances and may be recharged from a source beyond the reservoir. Consequently the bottom water composition need bear no relationship to the composition within the oil-saturated zones.

A second type of water (Figure 4) is that which occurs in isolated pockets of high water saturation within the oil-saturated zone. These pockets can produce some water if penetrated by a drill hole. Such water could be similar to the water within the oil-rich zones depending on whether the zones became isolated before or after the oil migration.

A third type of water is contained within shale beds. This water is trapped because of the low hydraulic conductivity of the shales. Water found in shales can differ substantially in composition from the water in other parts of the reservoir because of complex ion exchange phenomena associated with water migration through the shales. Shales have low hydraulic conductivities and are incapable of producing water in any significant quantity.

The shales can be present both as continuous beds of substantial areal extent and as stringers isolated from the main portions of the reservoir. The shale beds can be in hydraulic contact with water sources beyond the confines of the reservoir and for this reason may have water compositions that differ from the isolated shale stringers. For this reason, shale stringers are considered as containing a fourth type of water.

A fifth type of water is connate or irreducible water which was trapped within the oil-saturated zone (see Figure 4) at the time the oil migrated into the formation. In a good reservoir, connate water will make up the bulk of the water in the reservoir. Mossop [16] explains the characteristics of this connate water to be inherited from a sand which originally had its pores completely filled with water. During the emplacement of the bitumen most of the original water was displaced. The water left behind, known as the irreducible water saturation, is bound in the formation in three structural locations [17]: as adsorbed water on mineral surfaces, as bulk water trapped within the pore spaces, and as water trapped within clusters of fines by capillary forces (Figure 4, inset). The volume of adsorbed water is generally agreed to be less significant than that retained by capillary forces [17,18]. The adsorbed water and

trapped bulk water are different in chemical composition because of ion exchange phenomena on mineral surfaces.

Sampling of formation water types 1 to 4 is relatively straightforward because they all have a tendency to flow into the well when intersected by the drilling tool. Sampling connate waters in oil sands is more difficult because the high viscosity of the bitumen and the lack of hydraulic conductivity limit the amount of primary fluid production. Water layers that are penetrated by a well, by virtue of their hydraulic conductivity, are not likely to be original formation waters (connate waters). Water obtained from the reservoir by drillstem tests or bailing is unlikely to be connate water for the reasons discussed above. Moreover, drillstem or bailed samples are often contaminated by drilling fluids [19].

Analyses of connate, other formation waters, injection waters, produced waters, and gas separates, should commonly include subsets of the following chemical species:

Cations:
  H^+, Li^+, Na^+, K^+, Mg^{2+}, Ca^{2+}, Sr^{2+}, Ba^{2+}, Mn^{2+}, $Fe^{2+\&3+}$, Al^{3+}, Ti^{4+}

Anions:
  F^-, Cl^-, Br^-, I^-, NO_3^-, HCO_3^-, CO_3^{2-}, SO_4^{2-}, PO_4^{3-}

Other species:
  Inorganic carbon (TIC), SiO_2, B, NH_3, H_2S, alkalinity; organic carbon (TOC)

Gaseous species:
  H_2, NH_3, N_2, O_2, CO_2, SO_2, H_2S, CO, NO, COS, C_1–C_5 hydrocarbons

Other measurements:
  organic acids, conductivity, temperature, pressure, stable isotopes, Eh, charge balance

The exact species selected for analysis will depend on the end use for the chemical data. Oil sand reservoirs are typically undersaturated with gas and the process of removing the water will usually result in some further loss of the gas phase. The loss of the dissolved gases must be considered in chemical calculations applied to the results.

Drill core provides the most pristine source of connate water in the oil sands because the water is in
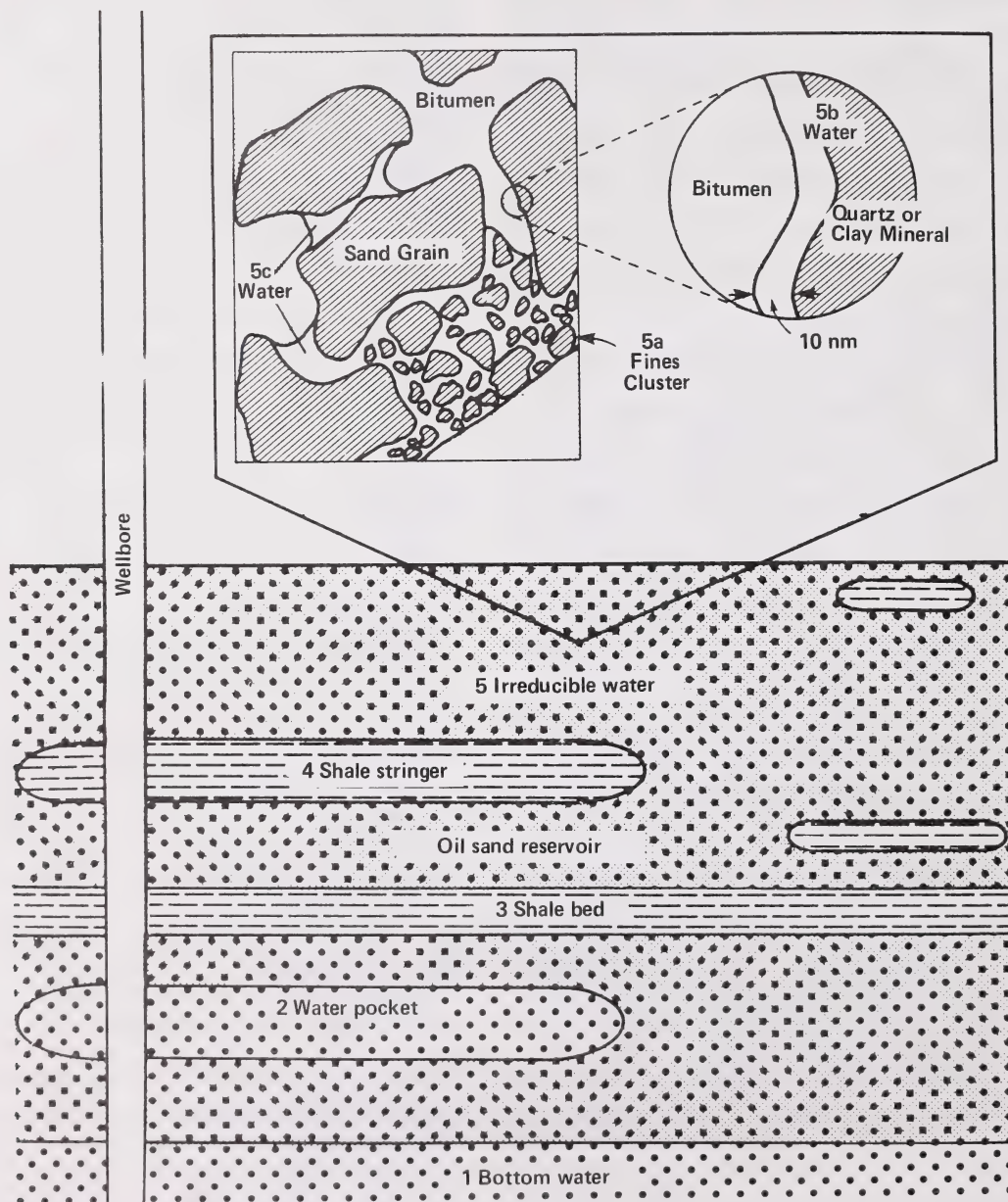
Figure 4. Formation water types. Adapted from Takamura [17].

isolated pockets surrounded by bitumen, and therefore protected from contamination. If the drill core has been fractured and contaminated with drilling mud or mud filtrate, the core cannot be used as a source of connate water. Commonly the core is preserved by freezing which results in an irreversible loss of dissolved materials such as Si and Al from the aqueous phase. If feasible, the core should be preserved at 2 to 3°C when water sampling is required.

Working with drill core requires working with small amounts of water. Oil sands of economic grade normally contain between 3 and 10 wt% water. Since only part of this water is extractable, relatively large volumes of core are required to recover sufficient water for analysis.

The chemical composition of the extracted water will vary depending on the method used to extract it from the drill core. The actual composition will depend on contributions from the bulk water, the adsorbed water, the oil, and ion exchange and dissolution reactions which occur between the water or other extracting medium and the minerals in the sand.

Four methods have been tested for extracting connate water from drill core [20]. The methods chosen were:

- hot water extraction [21] where boiling water is mixed with oil sand,
- cold water extraction, where cold water and an immiscible organic solvent are combined with the sand, shaken, and separated,
- solvent extraction, where an immiscible organic solvent is used to dissolve the bitumen and the formation water is displaced by centrifugation, and
- ultracentrifugation without the addition of solvent.

Carbon tetrachloride (CCl_4) was selected as the organic solvent because of its high density, high immiscibility with water, and nonpolar nature. No significant differences have been found in the chemistry of the connate waters collected using the centrifuge extraction techniques (last two methods above). However, several anomalies were found when water was used in the extraction process. Total inorganic carbon, propionate, aluminum, iron, silica, pH, and boron all show large increases in the connate water composition compared to that determined from the solvent extraction method (Table 2). The highest totals for dissolved solids and sodium were present in the connate water analysis from the hot water extraction; yet the highest chloride values were recorded from the connate water collected in the solvent extraction.

Normally, water can be considered as the only source for chloride in the oil sand. If this is the case, the concentration of chloride in the water samples extracted with solvent only, represents the limiting value for chloride. Then, chloride values for the solvent-plus-cold-water extraction and for the hot water extraction should be the same or lower depending on whether complete mixing of the distilled and bulk connate water took place during the extraction. Mixing was concluded to be incomplete in these examples because lower chloride values were found in all samples extracted with water (Table 2). Based on these results, any analyses of connate waters which involve addition of deionized water in the extraction procedure will contain significant errors because of leaching. Only organic solvent centrifuge or ultracentrifuge extractions are recommended for extraction of connate water from drill core.

Injected and produced fluids

Interpretation of chemical analyses of production waters can be used as a successful tool for monitoring subsurface chemical reactions, if the variations in the chemistry of the waters over a time period represent changes actually occurring in the subsurface and are not caused by inappropriate sampling procedures or errors in the chemical analysis. During the pilot operation, samples should be collected from both the injected and produced water. Samples of the produced gases and solids contained in the fluids should be taken at the same time and identified. The well should be sampled at regular intervals, initially to establish a baseline chemistry under stable operating conditions, and later to detect any fluctuations from the baseline which would indicate progressive formation damage or operational changes. The temperature, pressure, date, homogeneity of the sample (2-phase, 1-phase, etc.), and flow rate from the well, should be recorded for each sample. Both the injection and production history of the well must also be recorded, including (shut-in time, pressure, temperature, well kills, and blowdowns).

A representative sample must reflect the bulk chemistry of the three-phase water-oil-gas system. It is impossible to collect such a sample where laminar flow prevails because the three phases tend to stratify concentrically in the pipe. At the wellhead where the vertical conduit from the reservoir intersects the horizontal pipe in a "T" configuration, turbulent conditions exist and a representative sample can be taken (Figure 5). Even at this sampling point the gas-

Table 2. Connate water analyses of Clearwater Formation from homogenized Cold Lake core.

Units (mg/L)	Solvent only			Solvent plus water			Hot water		
	S1	S2	S3	SCW1	SCW2	SCW3	HW1	HW2	HW3
pH (25°C)	8.13	8.09	8.05	8.84	8.69	8.78	8.79	8.68	8.7
Lithium	<1	<1	<1	<2	<2	<2	NR	NR	NR
Sodium	2 650	2 550	2 625	3 498	3 529	3 354	3 907	3 654	3 251
Potassium	32	28	26	43	43	41	58.8	52.1	52.6
Magnesium	11	11	11	8.8	8.0	9.2	13.1	15.1	15.6
Calcium	18	18	17	10.5	11.2	11.7	14.0	15.1	14.8
Strontium	<1	<1	>1	<2	<2	<2	<2	<2	<2
Barium	<1	<1	<1	<2	<2	<2	<2	<2	<2
Manganese	<1	<1	<1	<2	<2	<2	<2	<2	<2
Iron	<1	<1	<1	33.4	31.3	35.2	57.7	72.2	64.1
Aluminum	<3	<3	<3	31.6	28.1	29.3	37.7	40.3	35.4
Fluoride	<20	<20	<20	19.7	18.4	18.3	21.7	21.4	21.9
Chloride	3 165	3 108	3 148	2 634	2 722	2 618	2 761	2 815	2 614
Bromide	<20	<20	<20	<18	<16	<17	<18	<17	<17
Nitrate	<20	<20	<20	<18	<17	<17	<18	<17	<17
Phosphate	<20	<20	<20	<18	<16	<16	<18	<17	<17
Sulfate	668	691	675	628	604	594	677	744	658
T. Si/SiO$_2$	<2/4.28	<2/4.28	<2/4.28	65.9/140	58.5/125	62.1/132	77.2/165	78.9/168	69.8/149
T. B/H$_3$BO$_3$	11/62.9	12/68.6	11/62.9	38.7/221	36.9/154	36.9/154	43.9/251	42.0/240	41.1/235
T. Inorganic carbon	56	61	60	643	657	633	834	824	806
Formate	<20	<20	<20	<18	19.8	20.7	<18	18.8	15.3
Acetate	<21	23.5	20	<18	20.2	17.2	19.3	20.7	16.9
Propionate	<20	<20	<20	126	121	119	173	164	162
Butyrate	<20	<20	<20	<18	<16	<17	<18	<17	<17
Calc. charge balance %	8.27	5.15	7.28	5.83	4.50	3.08	3.92	2.92	8.8

NR - Not reported.
T. - Total.

water-oil mass ratio will be different from that at the sand face because of the pressure drop in the tubing and gas production up the annulus. However, as long as the bulk chemistry of the mixture can be estimated from reservoir conditions based on production data (i.e. relative rates of flow in the annulus and tubing string), then the equilibrium distribution of species between the three phases at reservoir depth can be calculated if the pressure and temperature at the sand face are known [22]. Each of the three phases must be analyzed and their mass ratios determined in order to calculate this bulk chemistry.

At the wellhead of steam pilots, three-phase flow of oil, gas, and water is common. The temperatures at the sampling point range from 60 to over 200°C and the pressures from 0.1 to 10 MPa. Three types of wellhead samples can be distinguished — *isobaric-isothermal* samples, *isobaric* samples and *quench* samples [23]. In order to prevent flashing at the higher temperatures, sampling at constant pressure is recommended. The type of sample taken depends on the information needed. Collection of samples should include steps to prevent contamination and to preserve the samples for later analysis. Therefore it is essential to collect samples as near the wellhead as possible and to isolate them from the atmosphere.

Sampling Produced Fluids
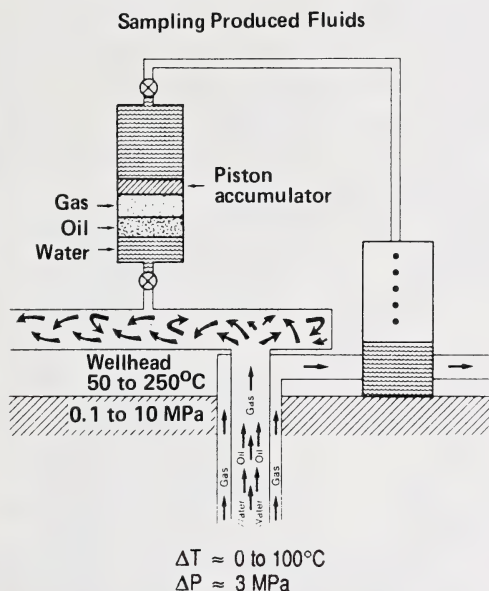
Figure 5. Isobaric sampling at the wellhead.

For accurate water analyses, several parameters must be measured in the field shortly after the sample has been collected, because certain chemical species are unstable when the sample is brought to the surface and exposed to a different environment. Lico et al. [24] recommended performing only those analyses in the field for which samples cannot be preserved for later laboratory analysis. Included in this category are hydrogen sulfide, alkalinity, pH, specific conductance, and ammonia. The procedures used for the field analyses closely followed those outlined by Lico et al. [24] and are outlined in Figure 6. The complete analytical procedure for the laboratory analyses is presented in a flow chart in Figure 7. Detailed procedures for sampling and chemical analysis of produced waters can be found in [19], [23], [25], and [26].

Analyses of the injection and production water and gas separates should be suitable for the purpose intended, and would commonly include some subset of the aqueous and gaseous components mentioned earlier. In addition to the common analyses (Na^+, Ca^{2+}, Mg^{2+}, alkalinity, Cl^-, SO_4^{2-}, and pH) performed by oil companies, dissolved carbon, aluminum, and silica are very important. It is extremely difficult to preserve
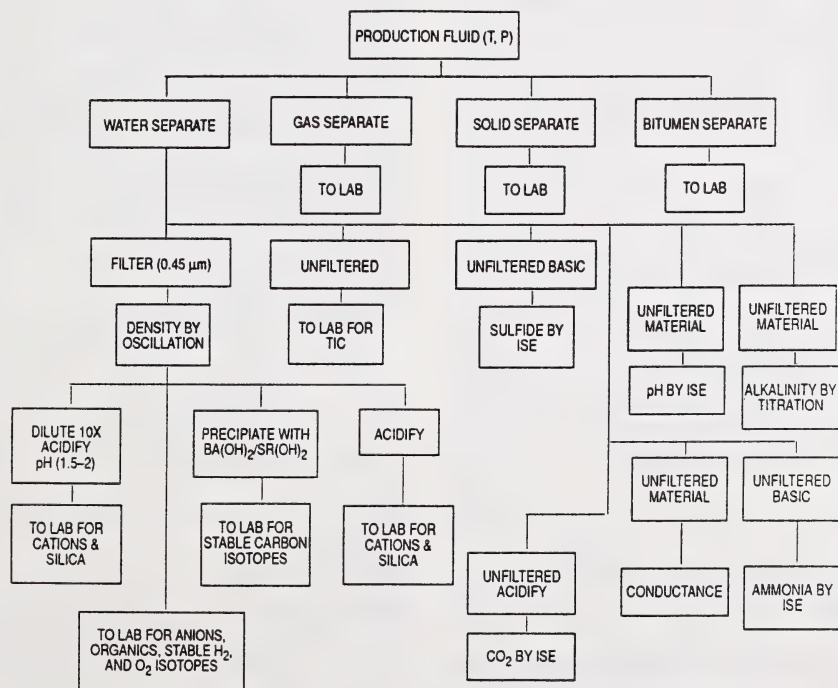
Figure 6. Sample preservation and chemical analysis completed at the sample site. Adapted from Gunter et al. [25].
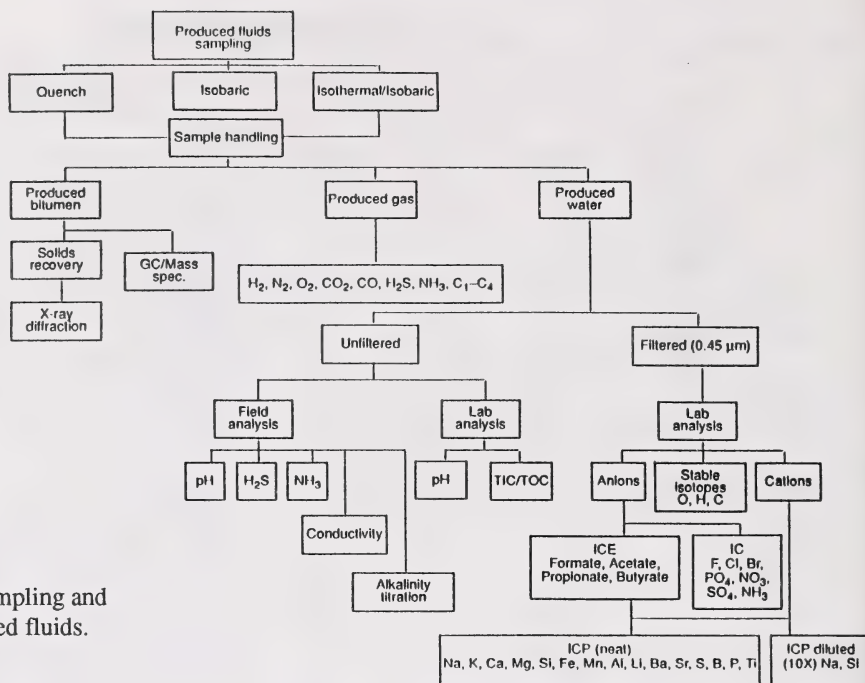
Figure 7. Flow chart for sampling and chemical analysis of produced fluids.

aluminum in the sample, and the low values of aluminum (50 µg/kg) in oil field waters cause problems in analysis. More reliable methods for aluminum analysis have to be developed if reactions between water and clay minerals are to be understood. Bicarbonate/carbonate should not be calculated from an alkalinity titration because other species such as boric and organic acids also contribute to the alkalinity. The bicarbonate/carbonate ratios can be calculated from the measured pH and a TIC measurement. Without dissolved silica, aluminum, and carbonate values, the saturation state of clay and carbonate minerals in the reservoir cannot be calculated. We recommend that K^+, SiO_2, and TIC be routinely determined in oil field waters, that dissolved aluminum be calculated from equilibrium considerations, and that an anion-cation charge balance be calculated for the more complete analyses to ensure that all the major ions have been detected.

GEOCHEMICAL COMPUTER MODELS AND PHASE EQUILIBRIA

Geochemical modelling of water-rock interactions in natural and artificial hydrothermal systems requires computer algorithms for a variety of complex chemical processes. Computer codes used for geochemical modelling of hydrothermal processes associated with enhanced oil recovery and deep waste disposal should have the capability to simulate the following processes:
- Mixing of formation and injection waters (and to predict the composition of the mixture and any mineral precipitation or dissolution which results).
- Gas separation by boiling or pressure drawdown and the effects on the water/steam or oil composition.
- Changes in water composition due to adsorption, desorption, and ion exchange on mineral surfaces.
- Mineral dissolution, and precipitation in and from water due to temperature and pressure gradients and water-rock reaction.
- Changes in porosity and permeability of the reservoir rocks as a result of water-rock interaction.

There are several computer programs presently available which model one or more of the above processes, but none incorporates all of them [27–29]. The most commonly used, publicly available programs are:
- PATHI and its later versions [30,31]
- EQ3/EQ6 [32]
- PHREEQE [33]
- GEOCHEM [34]
- SOLMINEQ and its later versions [35,36]
- WATEQ and its later versions [37,38]
- MINTEQ [39]
- BOILING [40,41]
- MINSOLV, CHILLER [42,43]
- GEO-CALC [44]

Geochemical models can be separated into three main types: *static closed system* models treat homogeneous chemical equilibria (i.e. reactions taking place in a single phase, water); *dynamic closed system* models or *mass transfer* models treat heterogeneous reactions between solid, liquid, and gas phases; and *dynamic open system* models or *mass transport* models treat heterogeneous reactions and add physical transport of material by adding flow equations to a static or mass transfer model. Very few geochemical models can treat mass transport and these for the most part are restricted to one-dimensional movement. Another failing of these models is that they assume equilibrium at all times between the aqueous fluid and the product minerals. All of the models listed above incorporate some aspects of mass transfer.

SOLMINEQ

Geochemical models are used by the petroleum industry primarily to determine the conditions of mineral precipitation in the near-well region. Since SOLMINEQ [35,36] is designed to consider water-rock reactions in oil reservoirs, we favor its application to oil sand problems. Consequently, the discussion which follows applies to SOLMINEQ, although several other programs in the above list can perform similar calculations.

Presently, the geochemical model SOLMINEQ is used mainly to calculate the saturation or scaling index (*SI*) of a mineral from a chemical analysis of a water sample taken at the wellhead. The *SI* is defined as the logarithm of thermodynamic activity product (*AP*) minus the logarithm of the equilibrium constant (K_{sp}) or the solubility product. SOLMINEQ calculates the activities of the appropriate aqueous species from the chemical analysis of the water sample and sums them to form log(*AP*). The relationship used is:

$$\log (AP) = \log (mP) + \log (\gamma P) \qquad (1)$$

where mP and γP are the concentration or molarity product and activity coefficient product respectively of the aqueous components representing the mineral composition. At low ionic strengths and low temperatures, $\gamma P \approx 1$ and the $AP = mP$. This approximation is not satisfactory at higher temperatures and/or high ionic strengths as displayed in Figure 8 for $CaSO_4$ (anhydrite).

The *SI* will be positive when the water is supersaturated with a mineral and negative when it is undersaturated. For example, the solubility of anhydrite
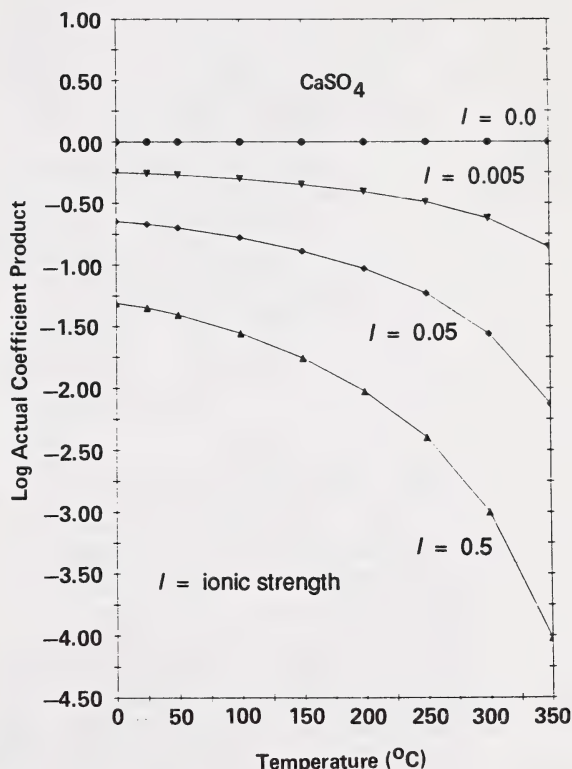
Figure 8. Activity coefficient product of calcium ion and sulfate ion versus temperature (*I* = ionic strength).

decreases rapidly with temperature as shown by the solid line labelled log (K_{sp}) in Figure 9. Consequently, in a thermal operation, even though the *SI* of anhydrite may be negative at the temperature of the wellhead, it could be positive at the higher temperature of the sandface. In Figure 9, the *AP* for dissolved anhydrite is plotted as a dashed line. Where it intersects the solid saturation (K_{sp}) line, *SI* = 0 and anhydrite is saturated in the water and will become supersaturated at any higher temperature (deeper in the well). The exact point of anhydrite accumulation will be determined by the degree of supersaturation required before precipitation is initiated, and the kinetics of the reaction once initiated. The conditions shown in Figure 9 are realistic for some thermal recovery operations and show that extrapolation of the chemical conditions determined at the surface or wellhead may not be adequate to predict scaling at other positions within the well or formation.

SOLMINEQ can be used to back-calculate the water
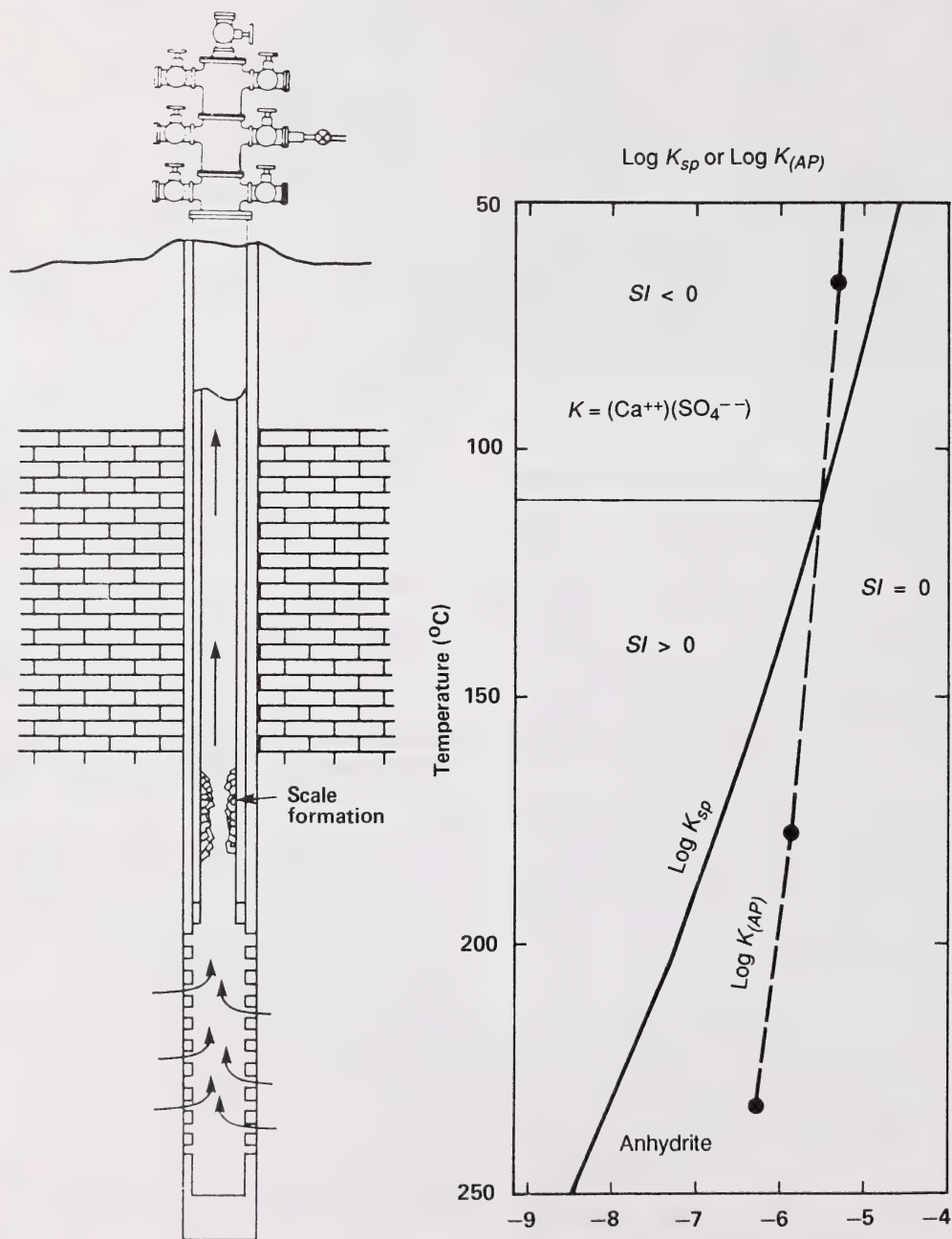
Figure 9. Saturation index *(SI)* for anhydrite. K_{sp} = solubility product or equilibrium constant for anhydrite. AP = activity product of the free calcium and sulfate ions. Log (AP) is plotted for a single specific water composition.

chemistry and *SI*s of a produced wellhead sample to the temperature and pressure conditions at the sandface or in the reservoir. Figure 10 is a flow chart illustrating the options in the program. The basic input data are from chemical analysis of a water sample at 25°C. The first step is to calculate the *SI*s at the elevated temperature of the wellhead and to estimate the temperature of the reservoir from geothermometers. A second temperature increment brings the water to the sandface or reservoir environment.

SOLMINEQ, by calculating *SI*s, can be used to predict potential scaling in complex multispecies chemical systems. The maximum amount of anhydrite or other scale that will precipitate from a 1000 g of water can also be calculated with SOLMINEQ by adjusting the *SI* to 0.

An option also exists in the SOLMINEQ program to calculate the effects of mixing two waters. If the chemical composition of the connate water is known, the program can be used to predict whether mixing of the injected water will result in supersaturation of any minerals.

The effect of gases must also be considered. Methane and CO_2, the dominant components of produced gas, are soluble in both water and bitumen. During three-phase flow in the reservoir, partitioning of gas between vapor, water, and bitumen occurs, and can affect the *AP*s of the minerals largely through pH control

of the water. This is mainly due to release of pressure as the fluids pass from the sandface to the surface causing boiling off of the gases. Carbon dioxide is usually the most active component although H_2S, SO_2, and NH_3 can also be important in specific situations. In order to be able to redistribute the gases between the water and bitumen, the mass ratios of oil, water, and gas must be measured at the surface and the physical conditions of the reservoir must be known. For this calculation, the solubilities of the gases in bitumen are based on idealized gas behavior, mainly because there are few data available and these vary considerably in quality. It is also assumed that the gases do not form any ionic or complex species with the bitumen. Consequently the solubility behavior in bitumen can be treated with simpler models than the corresponding solubilities in water. Figure 11 shows inverse Henry's law plots expressed as the solubility of CO_2 and CH_4 in bitumen and water at a partial pressure of 1 MPa. The solubility in bitumen is expressed as moles of gas per kilogram of bitumen (i.e. molality) similar to the scale used for the water. The solubility of CO_2 is similar in both water and bitumen, but CH_4 has a much higher solubility in bitumen (Figure 11). These Henry's law constants are used in SOLMINEQ to numerically titrate the noncondensible gases back into oil and water at a determined temperature and pressure. As well as estimating the change in pH, the partitioning of the gas
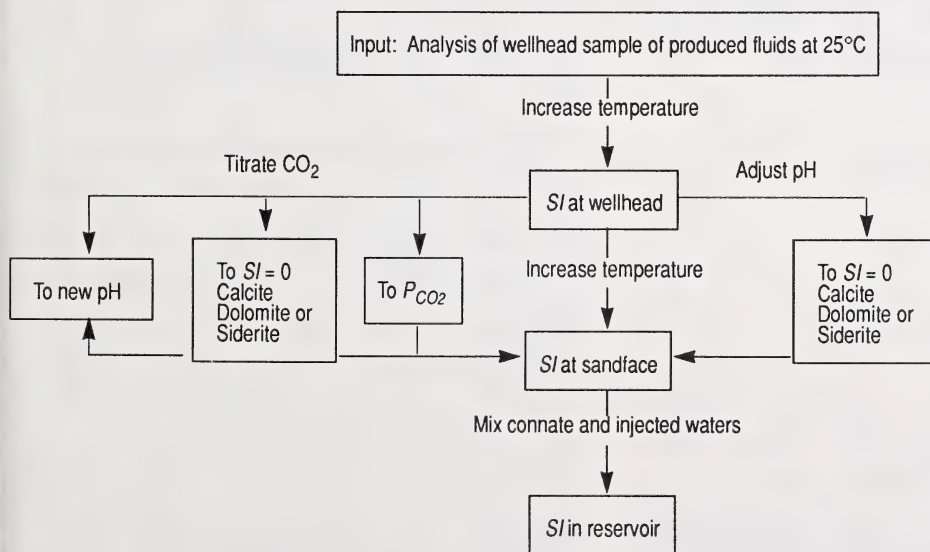
Figure 10. Flow Chart for some SOLMINEQ calculation paths of *SI* for a produced water and gas.

amongst the three fluids is calculated. Such a distribution for CO_2 and CH_4 in the reservoir is shown in Figure 12 for a steam pilot based on the sand face temperatures and produced fluids compositions measured at the midpoint of four successive cycles in a steam stimulation project. In the first cycle considered, the reservoir is undersaturated with gas. The reservoir becomes vapor dominated in all the succeeding cycles. In these later cycles, the quantity of gas produced per unit of oil is often higher than that in the original reservoir, perhaps because of gas override due to thermal effects and pressure release. If this is correct, it is undesirable because the oil remaining in the reservoir would become progressively less gas-saturated and more difficult to recover. Generation of gas from breakdown of the bitumen and/or carbonate minerals by water-rock reaction may also contribute substantially to the

production of excess gas. The source of the new gas formed can be estimated from stable isotopes as has been shown by Abercrombie and Hutcheon [45] and Cathles et al. [46].

Additives can be used in a thermal operation to enhance production. SOLMINEQ can be used to assess the effect of additives on the pH of the aqueous phase and on the *SI* of the minerals. The pH of a solution can be controlled and buffered by the addition of weak acids or weak bases and their salts to the solution. Some insight can be gained by plotting their dissociation constants as a function of temperature (Figure 13). The gases CO_2, SO_2, NH_3, and H_2S are all potentially useful in this context. Both H_2S and CO_2 when dissolved in water are weak acids; SO_2 is a strong acid and NH_3 is a weak base. Consequently the pH in the vicinity of a thermal well can be controlled by either injecting the
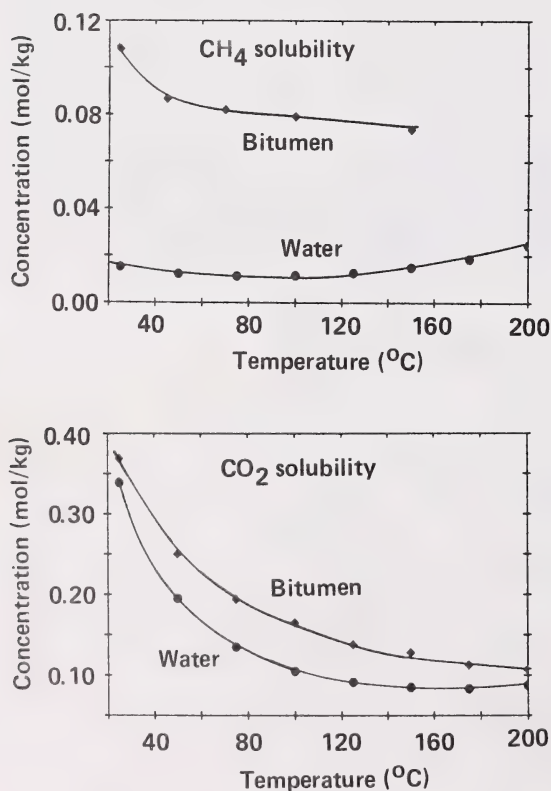
Figure 11. Solubility of CO_2 and CH_4 in water and bitumen at P = 1 MPa. Solubility of CO_2 in water does not include the aqueous bicarbonate and carbonate complexes.
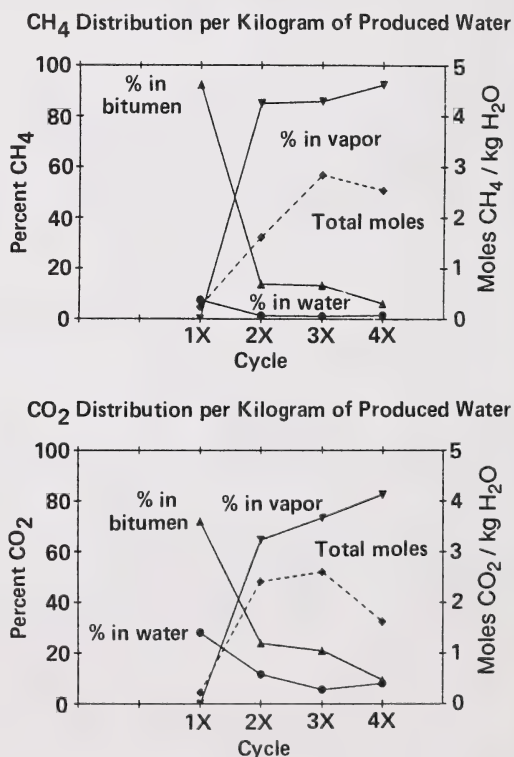
Figure 12. Production data and distribution for CO_2 and CH_4 at the midpoint of four consecutive steam cycles.

Dissociation constants at saturated water vapor pressures
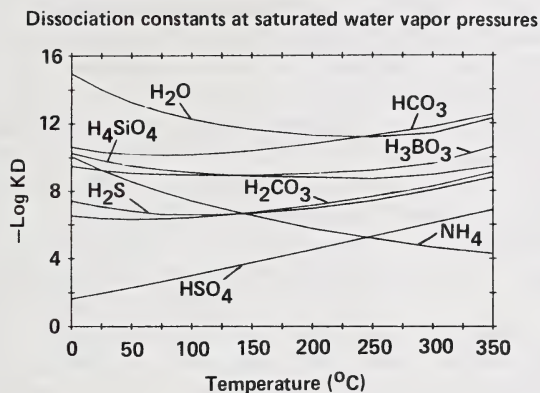
Figure 13. Variation with temperature of various acid dissociation constants along the steam saturation curve. Data base used is from SOLMNEQ.

volatile component directly into the steam or by adding the dissolved salts or the gases to the water fraction. Injecting SO_2 or H_2S into a well could pose both environmental and safety problems. In addition, SO_2 is a strong acid and strong oxidant and could cause severe corrosion problems. Consequently, CO_2 and NH_3, or salts of these gases are used to control pH in thermal recovery operations.

Watkins et al. [47] discuss some of the uses of NH_3 for pH control. Typically the water feed for steam boilers is high in bicarbonate (HCO_3^-), which can range to over 0.01 mol/kg. During boiling, HCO_3^- is converted to CO_2 which escapes into the steam fraction and OH^- which remains in the liquid water resulting in an increase in pH. The condensate pH can exceed 11 measured at 25°C compared to the boiler feed water pH of approximately 7. The high pH of the condensate enhances the solubility of silica and can cause rapid erosion of the gravel pack. Roberts and Tremaine [48] have shown that only small amounts of NH_3 are needed in the gas phase to effectively neutralize aqueous CO_2. Alternately adjustment of the pH can be made by adding a salt of a base. Both NH_3 gas and NH_4^+ salts can be used for pH adjustment in boilers and downhole. It is significant in this process that NH_3 and many of the ammonium salts such as NH_4HCO_3, $(NH_4)_2CO_3$, NH_4Cl, or NH_4NO_3 can be used in conjunction with superheated steam as these compounds have the unique property of decomposing into gases at the elevated temperatures and recombining to the equilibrium ionic species when the steam cools and condenses to water.

The extreme fractionation of the volatile species into the steam phase during boiling is illustrated in Figure 14a where the volatility ratios are plotted for reservoir gases. The volatility ratio is defined as the ratio of the concentration of the gas in the steam (i.e. moles of a gaseous component per 1000 g of steam) to the concentration of the gaseous component in the liquid phase, and can be calculated directly from the saturation pressure of steam and the Henry's law constants for the gaseous components (Figure 14b). The volatility ratios all decrease linearly with temperature and range from one million to one. SOLMINEQ bases its calculation for steam boilers on these ratios. At 300°C, CO_2 has a volatility ratio of 23 while NH_3 has a volatility ratio of 2. For example, a boiler operating at 300°C to produce

Volatility ratios

Figure 14. (a) Variation with temperature of the volatility ratios for selected produced gases. Data from Drummond [40]. (b) Variation with temperature of the Henry's law constants ($KH = P_{gas}/m_{gas}$) for selected produced gases. Data from Drummond [40].

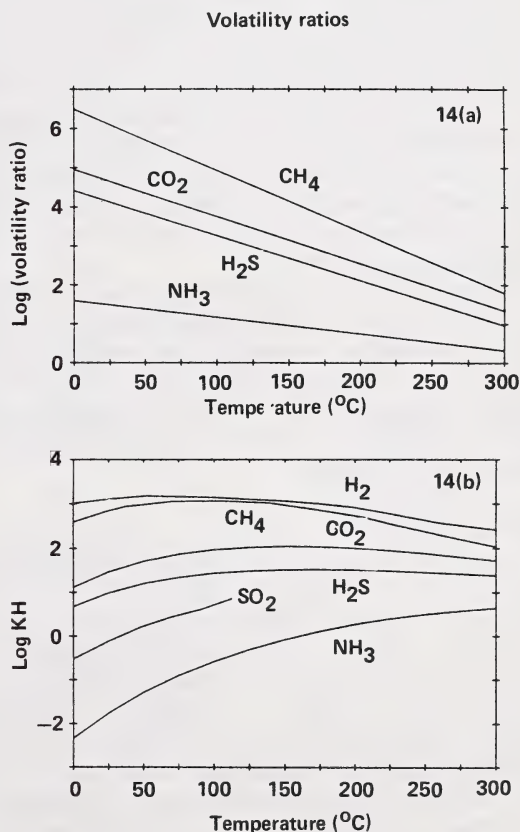80% quality steam using a boiler feed water containing 0.01 mol of $NaHCO_3$ per 1000 g of water at a pH of 8 at 25°C converts 80% of the original HCO_3^- in the feed water to CO_2 in the steam. The condensate has a pH of 9.9 at 300°C or a pH of 12.5 if quenched to 25°C. The condensate can be acidified by adding an equal amount of the salt of a base to the boiler feed water. The addition of 0.01 mol of NH_4Cl per kg of H_2O to the feed water causes 92% of the feedwater HCO_3^- to be converted to CO_2 in the steam fraction. The total CO_2 concentration remaining in the condensate is 0.0005 molal and the pH has fallen from 9.9 to 6.7. The aqueous NH_3 species concentrations are much higher than those of the CO_2 species because of the low volatility ratio for NH_3. A 1% increase in the NH_4Cl concentration to 0.0101 molarity has a large effect on the pH shifting it to 5.6. If the concentration of NH_4Cl is less than that of $NaHCO_3$ by 0.0001 mol, the pH increases to 8. The final pH is very sensitive to small changes in the concentration of either the basic or acidic salt when they are present in nearly equivalent concentrations. Consequently, an operator of a steam boiler would have to monitor the $NaHCO_3$ concentration of the feed water carefully if he hoped to control the pH of the boiler condensate by adding an equivalent amount of a basic salt such as NH_4Cl.

Programs such as SOLMINEQ require complete chemical analyses of the aqueous and gas phases, relative ratios of the oil/water/gas from production data, and the physical conditions at the time of sampling. If these data are available, a field fluid monitoring program can be a good tool to forecast scaling or chemical erosion near the wellbore.

Geothermometers

Temperatures in the reservoir can be calculated from geothermometers based on the produced water chemistry. Chemical geothermometers depend on the effect of temperature on the reaction between the minerals and the fluids in the reservoir. Most of the thermometers depend on a mineral assemblage equilibrating with the water in the reservoir before the water is produced to the surface. It is also assumed that the water composition is not altered during its journey to the surface. If this is true, then the composition of the water reflects the mineralogical composition and temperature of the reservoir, and can be used to supplement downhole thermocouple measurements.

The families of geothermometers that have proved most successful are based on the concentration of SiO_2 and the ratio of Na/K in the produced waters [49,50]. The SiO_2 family of geothermometers depends on the solubility of one of the solid silica polymorphs (quartz, chalcedony, cristobalite, or amorphous silica [51,52] controlling the amount of dissolved SiO_2. Each polymorph has a different solubility relationship with temperature (Table 3). In the tar sands, both quartz and chalcedony are present. Consequently, either quartz or chalcedony may control the concentration of SiO_2 in the produced water. Abercrombie and Hutcheon [45] have used the chalcedony geothermometer calibration of Arnorsson et al. [53] in Cold Lake oil sands successfully. However, both thermometers must be used with caution above 200°C because the waters become supersaturated with amorphous silica at surface temperatures; the silica can readily precipitate during ascent to the surface. Anomalously low temperatures would be calculated because of the loss of dissolved SiO_2. On the other hand, at high pHs, the solubility of the silica minerals increases greatly (Figure 15) and anomalously high temperatures would be determined unless the complexing of dissolved silica is taken into account. If there is any boiling during the passage of the water to the surface, the dissolved silica will also become more concentrated. If this is suspected an adiabatic calculation may be made instead of the conductive calculation where boiling is assumed not to occur. Computer programs such as SOLMINEQ which are designed to calculate and evaluate mineral saturations can handle these calculations easily.

The Na/K geothermometer supplements the SiO_2 geothermometer. In its simplest form it depends only on the ratio of Na/K in the produced waters, which is thought to be controlled by Na-K exchange with the alkali feldspars. Unlike the SiO_2 thermometer it is not affected by boiling because it is a univalent cation ratio (Table 3). However, the Na/K geothermometer does not work if the water contains appreciable Ca or Mg. In these cases another form of the Na/K thermometer is used which includes the effect of Ca and Mg (Table 3; References [54] and [55]). This version is sensitive to boiling because the equation describing the geothermometer is a mixture of divalent and monovalent cation ratios. Also, including Ca and Mg causes the thermometer to be more sensitive to quench reactions after the water exits the reservoir. For instance, precipitation of calcite will lower both the Ca and Mg in the water and make it impossible to use the Ca or Mg form of the thermometer. Fortunately the work by both Abercrombie and Hutcheon [45] and Saltuklaroglu [56]

Table 3. Equations for geothermometers modified from Kharaka and Mariner [50] and from Henley, Truesdell, and Barton [49].

Geothermometer	Equation[a]	Restrictions
1. Quartz-no steam loss (Fournier)	$t°C = \dfrac{1309}{5.19 - \log SiO_2} - 273$	$t = 0–250°C$
2. Quartz-no steam loss (Arnorsson et al.)	$t°C = \dfrac{1164}{4.90 - \log SiO_2} - 273$	$t = 180–300°C$
3. Quartz-maximum steam loss (Fournier)	$t°C = \dfrac{1522}{5.75 - \log SiO_2} - 273$	$t = 0–250°C$
4. Chalcedony (Fournier)	$t°C = \dfrac{1032}{4.69 - \log SiO_2} - 273$	$t = 0–250°C$
5. Chalcedony (Arnorsson et al.)	$t°C = \dfrac{1112}{4.91 - \log SiO_2} - 273$	$t = 25–180°C$
6. Amorphous silica (Fournier)	$t°C = \dfrac{731}{4.52 - \log SiO_2} - 273$	$t = 0–250°C$
7. Na/K (Fournier)	$t°C = \dfrac{1217}{\log(Na/K) + 1.48} - 273$	$t > 150°C$
8. Na/K (Truesdell)	$t°C = \dfrac{856}{\log(Na/K) + 0.857} - 273$	$t > 150°C$
9. Na/K (Arnorsson et al.)	$t°C = \dfrac{933}{\log(Na/K) + 0.993} - 273$	$t = 25–250°C$
10. Na-Li (Fouillac & Michard)	$t°C = \dfrac{1590}{\log(Na/Li) + 0.779} - 273$	$t = 0–350°C$
11. Mg-Li (Kharaka & Mariner)	$t°C = \dfrac{2200}{\log\left[(Mg)^{-2}/Li\right] + 5.47} - 273$	$t = 0–350°C$
12. Na-K-Ca (Fournier & Truesdell)	$t°C = \dfrac{1647}{\log(Na/K) + \beta\left[\log\left((Ca)^{-2}/Na\right) + 2.06\right] + 2.47} - 273$	$t < 100°C, B = 4/3$ $t > 100°C, B = 1/3$
13. $\Delta^{18}O(SO4^{=}\text{-}H_2O)$(McKenzie & Truesdell)	$1000 \ln \alpha = 2.88 (10^6 T^{-2}) - 4.1$ where $\alpha = \dfrac{1000 + \delta^{18}O\left(HSO_4^{=}\right)}{1000 + \delta^{18}O\left(H_2O\right)}$ and T is in K	

[a] Concentrations are in mg/L.
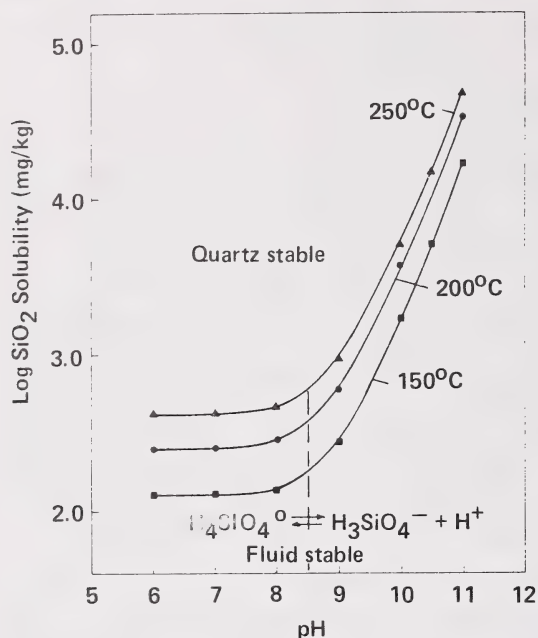
Figure 15. Variation with temperature and pH of the solubility of quartz.

supports the use of the simple Na/K form of the geothermometer in steam flooding of the Cold Lake tar sands.

Both the Na/Li [57] and Mg/Li [50] geothermometers may be applicable to the thermal recovery operations in the tar sands but they have not been tested because of the low concentrations of Li in the produced waters. Gas geothermometers [58] and isotope geothermometers [59] will probably not be useful because of the complexities added to their interpretation by the injection of steam.

Our work presented in Figure 16 also supports the use of mineral geothermometers. In Figure 16a, the quartz geothermometer based on SOLMINEQ calculations on the produced water chemistry are compared to wellhead and downhole thermocouple measurements at the midpoints of five successive cycles. The quartz geothermometer yields consistently higher temperatures. This may result from boiling due to the pressure drop across the perforations. It may also reflect the production of water from a higher-temperature zone some distance into the reservoir. In Figure 16b, the reservoir temperatures based on the Na/K and quartz geothermometers agree closely with each other. Over a complete production cycle, the temperature only drops

20°C. In contrast, the sandface temperature drops rapidly, being higher than the reservoir temperatures at the start of the production cycle but falling below the reservoir temperature as production continues.

Mineral-water phase diagrams

SIs as previously discussed are one way of monitoring potential scaling problems from chemical analysis of produced waters. An alternate approach is to plot mineral stability fields on aqueous activity diagrams [60]. To use these diagrams, a program such as SOLMINEQ is first used to convert the results of the chemical analysis from concentrations of dissolved ions
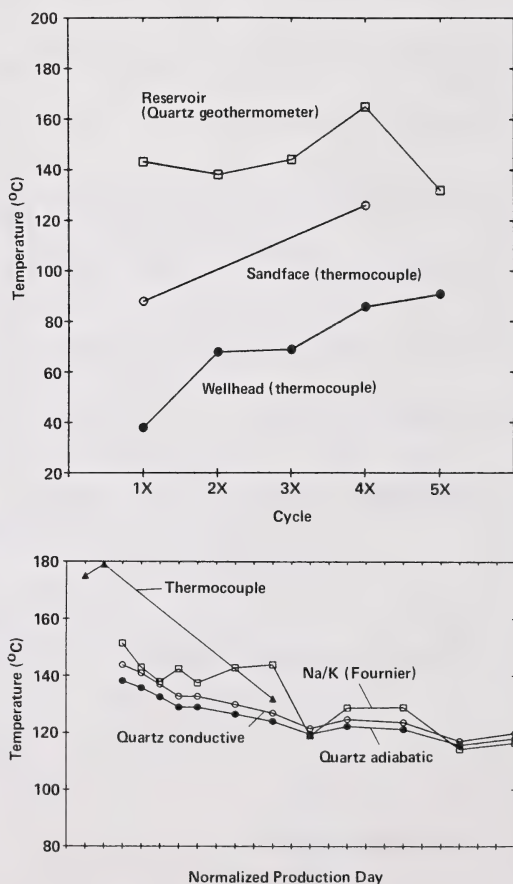
Figure 16. (a) Comparison of reservoir, sandface, and wellhead temperatures at the midpoint of five successive steam cycles. (b) Comparison of several geothermometer reservoir temperature predictions to direct thermocouple sandface temperature measurements over a single cycle.

at room temperature into thermodynamic activities at the temperature of the reservoir. Thermodynamic phase diagrams such as these provide an additional method of analyzing trends in sets of produced water chemistry both from laboratory experiments and produced field fluids. Such phase diagrams are calculated with the computer program GEO-CALC [61].

The most abundant mineral in the oil sands is quartz; in the carbonate trend, dolomite dominates. The solubility of quartz is controlled by two reactions as indicated in Figure 17. The total solubility of quartz is the sum of the concentrations of the aqueous silica complexes, H_4SiO_4 and $H_3SiO_4^-$. The concentration of the neutral complex, H_4SiO_4 dominates in acid and neutral solutions, while $H_3SiO_4^-$ dominates in basic solutions. The solubility of quartz increases with temperature (Figure 17) at a fixed pH. At lower temperatures, precipitation of quartz is so slow, that amorphous silica precipitation normally controls the maximum concentration of silica in the solution. Most of the reactions in the oil sands involve the aluminous clay minerals. *SI*s for these minerals can only be calculated if dissolved aluminum concentrations are known for the produced waters. As discussed earlier, aluminum is not normally measured in the produced fluids because the analytical methods used are not reliable. However, by writing reactions between aluminous minerals conserving aluminum, phase diagrams may be constructed that can be used for water analyses which are missing aluminum concentrations. Quartz and amorphous silica solubility (i.e. saturation surfaces) are superimposed on such an aluminosilicate, aluminum oxide/hydroxide stability diagram in Figure 18. The stabilities of these aluminosilicates are truncated by these saturation surfaces. Above 125°C, diaspore replaces gibbsite and at higher aqueous silica concentrations; kaolinite becomes stable succeeded by pyrophyllite. The upper thermal stability limit of kaolinite appears to be about 300°C at which point it breaks down to diaspore and pyrophyllite [62]. The aluminosilicate minerals, gibbsite, diaspore, kaolinite, and pyrophyllite, will form the basis from which we can move into the calcium, magnesium, potassium, and sodium systems.

In areas of the reservoir where high thermal gradients are encountered, the aqueous fluid may quickly become supersaturated with quartz. For this reason isothermal stability sections for the silicate minerals at temperatures of 25, 100, 200, and 300°C were drawn as a function of silica activity versus
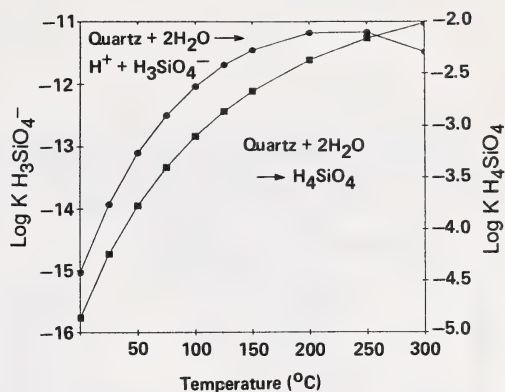
Figure 17. Quartz equilibria in aqueous solutions.
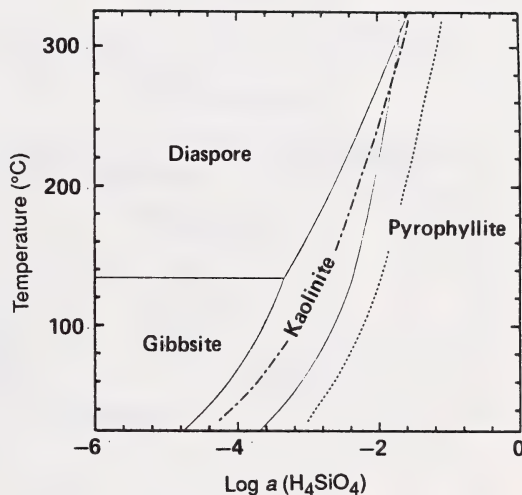
Figure 18. The stability fields of the aluminosilicates as a function of temperature and activity of silicic acid. The saturation surface for quartz is represented by the dash-dot line while the saturation surface for amorphous silica is the dotted line.

aK^+/H^+, aNa^+/aH^+, $aCa^{2+}/(aH^+)^2$, and $aMg^{2+}/(aH^+)^2$ in the aqueous phase (Figures 19 through 22) where a is the activity. The stability of these aluminosilicate minerals may be truncated by the saturation surfaces imposed by the nonaluminumous phases such as quartz and amorphous silica. The stable Na/K phases in the presence of quartz at low temperature are potassium feldspar, illite, paragonite, and analcime. At higher
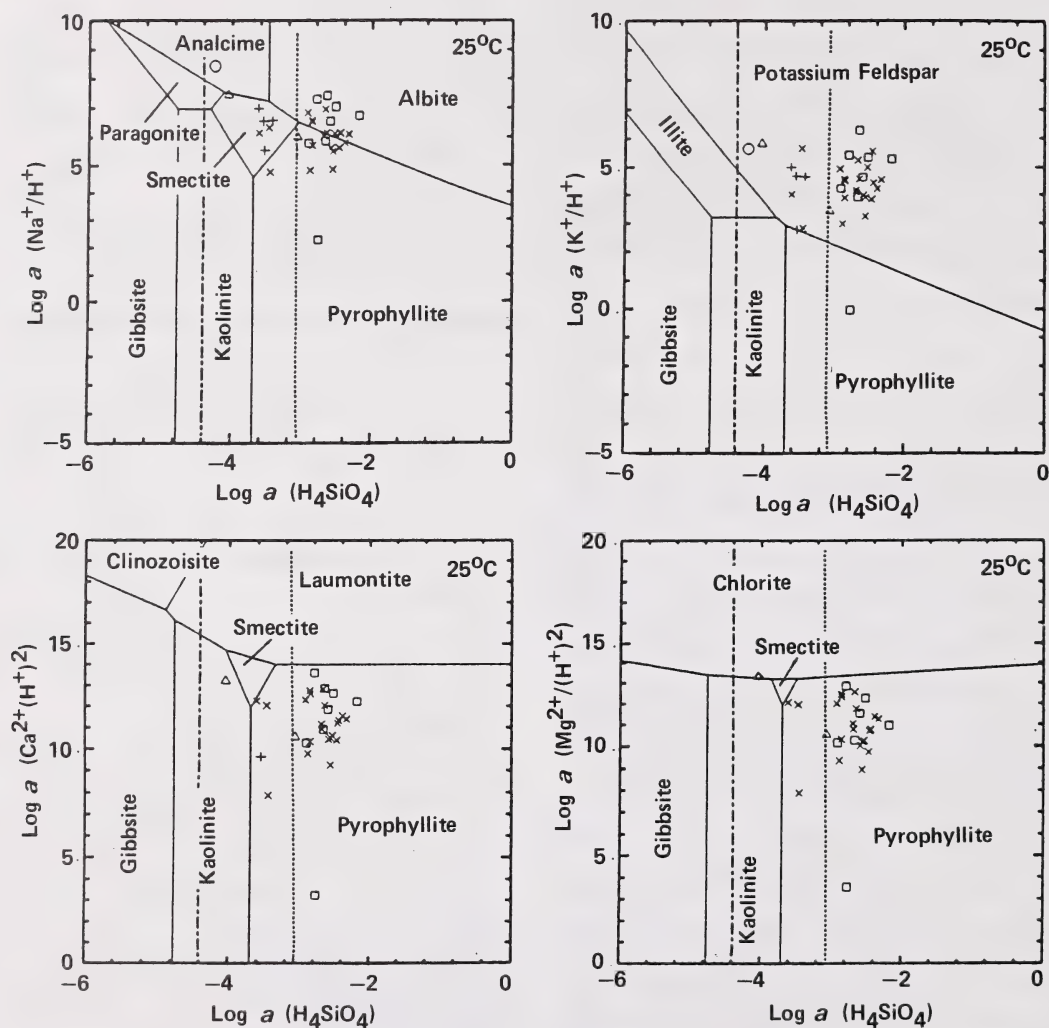
Figure 19. The stability fields of the Na, K, Mg, and Ca aluminosilicates calculated at 25°C as a function of the log activity ratios of various cations to hydrogen ion versus the log activity of silicic acid. The saturation surface for quartz is represented by the dash-dot line while the saturation surface for amorphous silica is the dotted line. Formation waters are plotted as triangles, boiler feed waters as pluses, boiler condensate as circles, production waters as squares, and waste waters as x's.
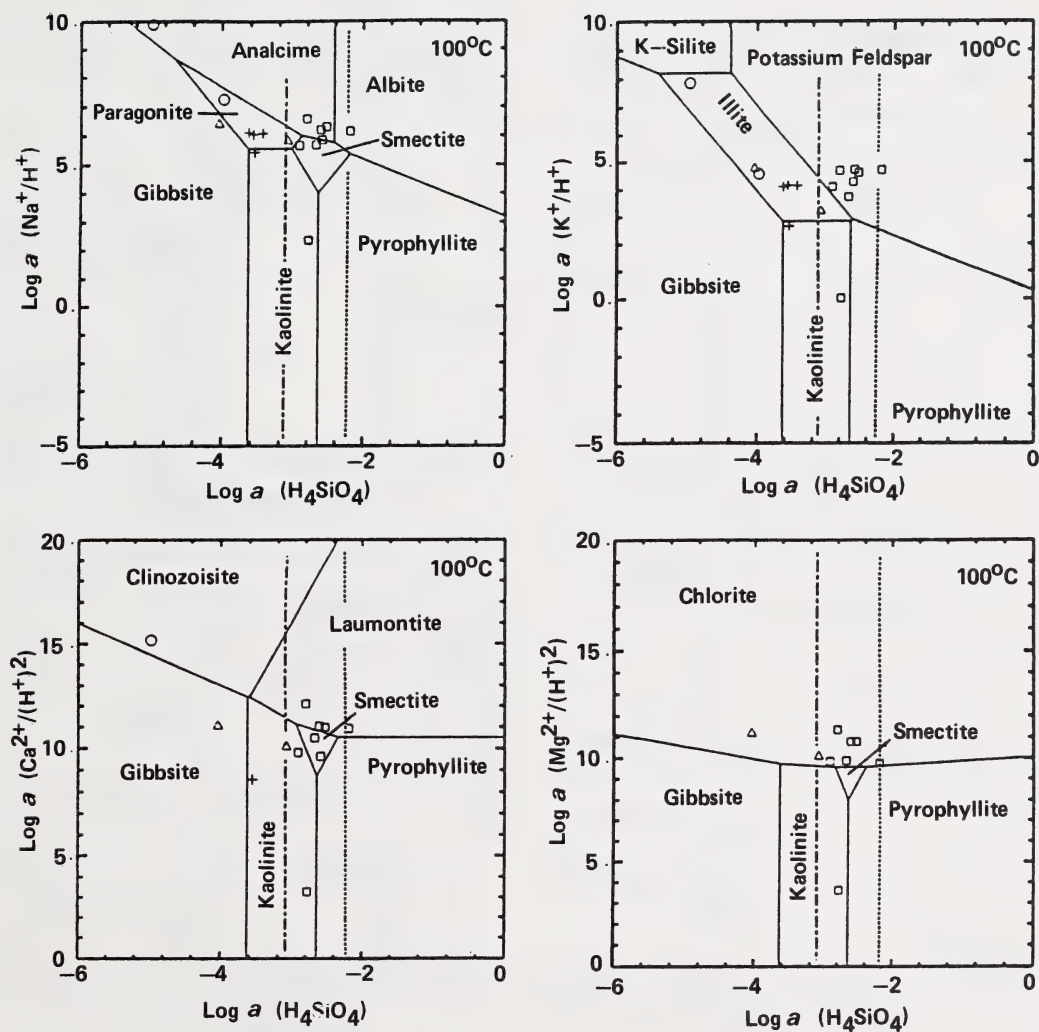
Figure 20. The stability fields of the Na, K, Mg, and Ca aluminosilicates calculated at 100°C as a function of the log activity ratios of various cations to hydrogen ion versus the log activity of silicic acid. The saturation surface for quartz is represented by the dash-dot line while the saturation surface for amorphous silica is the dotted line. Formation waters are plotted as triangles, boiler feed waters as pluses, boiler condensate as circles, and production waters as squares.
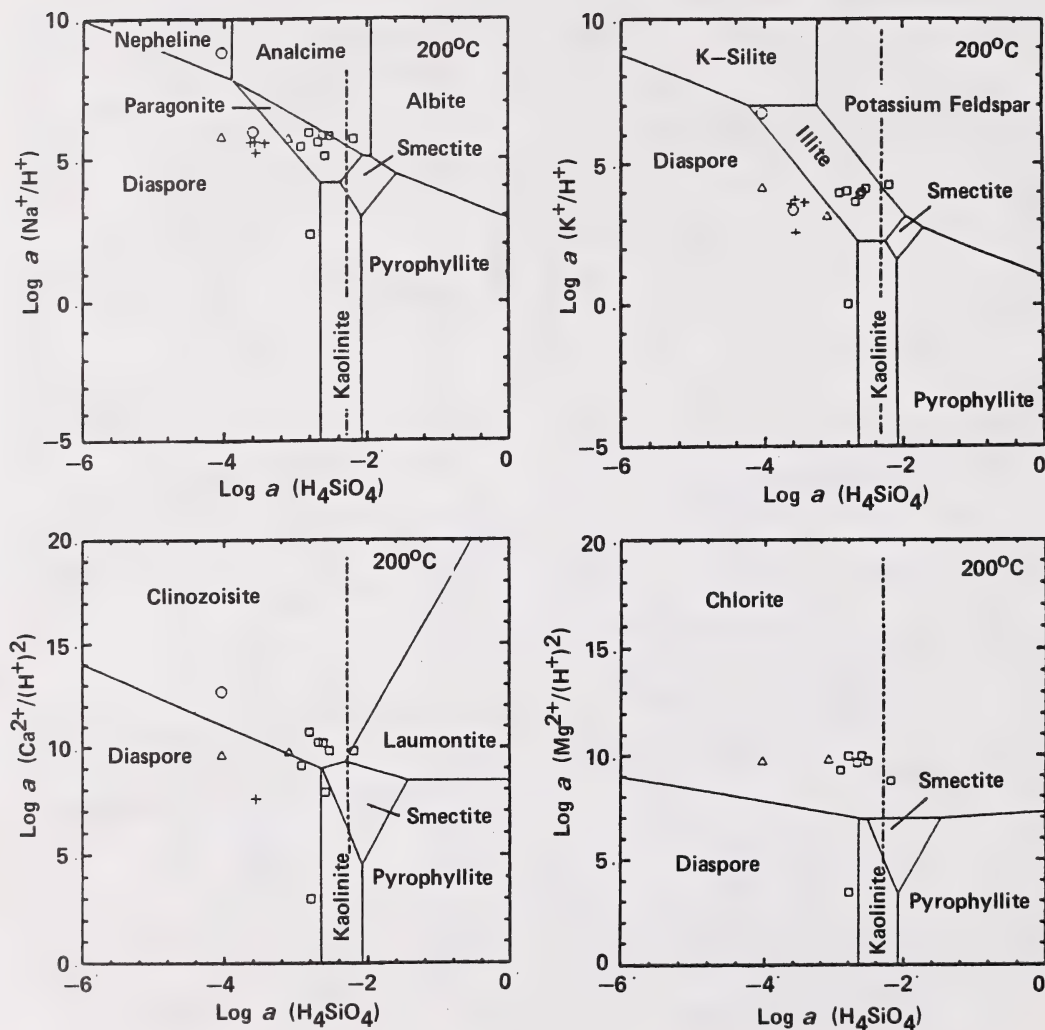
Figure 21. The stability fields of the Na, K, Mg, and Ca aluminosilicates calculated at 200°C as a function of the log activity ratios of various cations to hydrogen ion versus the log activity of silicic acid. The saturation surface for quartz is represented by the dash-dot line. Formation waters are plotted as triangles, boiler feed waters as pluses, boiler condensate as circles, and production waters as squares.
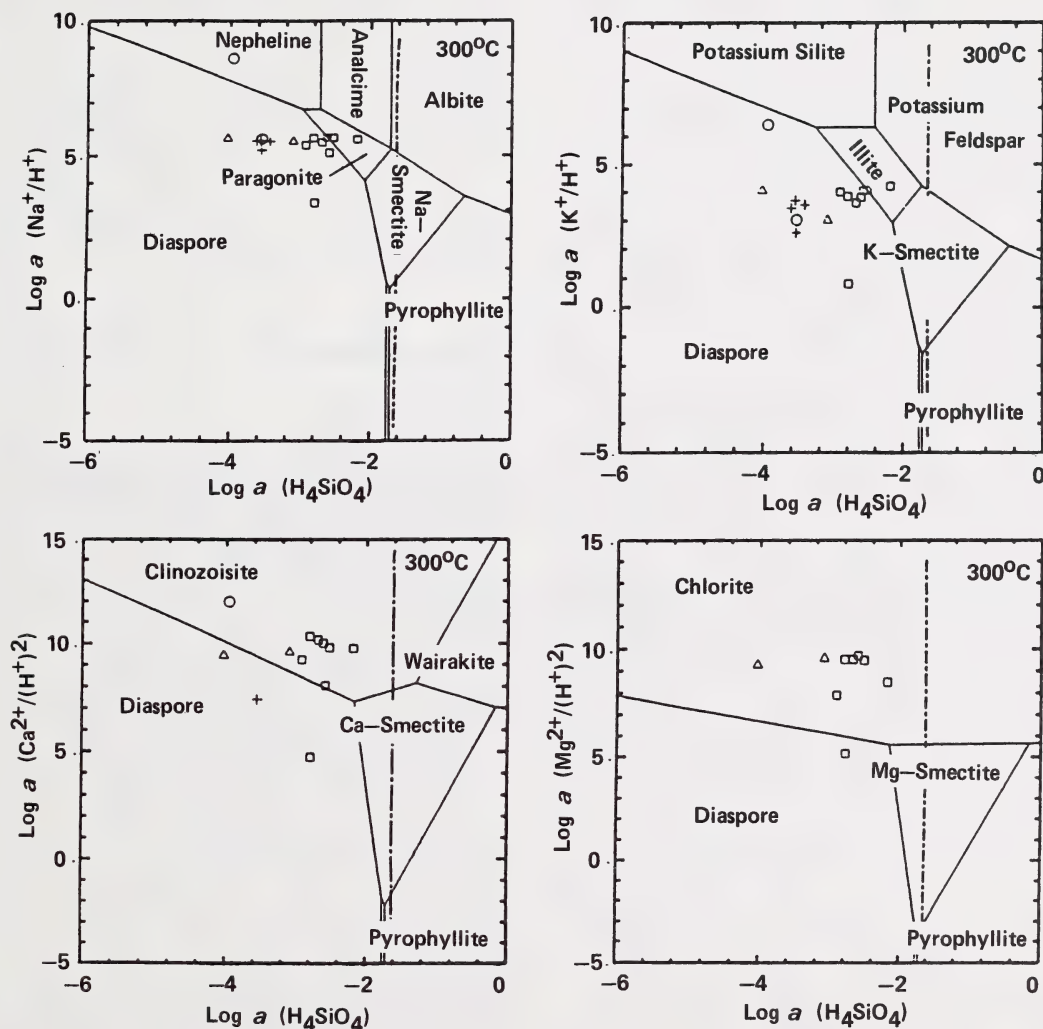
Figure 22. The stability fields of the Na, K, Mg, and Ca aluminosilicates calculated at 300°C as a function of the log activity ratios of various cations to hydrogen ion versus the log activity of silicic acid. The saturation surface for quartz is represented by the dash-dot line. Formation waters are plotted as triangles, boiler feed waters as pluses, boiler condensate as circles, and production waters as squares.

temperatures, the smectites displace illite and paragonite, and analcime reacts with quartz to form albite. At lower temperatures the potassium feldspar will be replaced by the potassium zeolite, phillipsite. Phillipsite does not appear on the diagram because of incomplete thermochemical data. Smectite and albite can be stable at all temperatures if the waters exceed quartz saturation. This is not true for the potassium analogue; smectite only appears above 100°C. At low temperatures, laumontite, zoisite, and the magnesian chlorite, clinochlore, are the stable Ca/Mg minerals coexisting with quartz, while at higher temperatures the smectites become important. If zoisite is kinetically inhibited from forming, anorthite will become stable at high temperatures with quartz present. The smectites are stable at all temperatures at higher silica concentrations but wairakite only appears at 300°C.

Only stoichiometric compositions are used for minerals plotted on these diagrams. In nature many of the phases form extensive solid solutions either between Na and K or Ca, Mg, and Fe. The smectites are highly variable in composition not only in the above elements but also in their Al/Si ratio. The smectite stability fields plotted on these diagrams are for the beidelite family based on the thermodynamic calculations of Nesbitt [63]. The locations of the smectite stability field boundaries are the most uncertain and the locations of the phase boundaries between such minerals are a band rather than a line. That is, the relative position of the mineral fields on the phase diagrams is correct but the width of the field is flexible depending on the extent of the solid solution. Consequently the interpretation of the water compositions plotted on these diagrams should be based on trends observed rather than single analyses.

Sulfides, oxides, and sulfates are common minerals found in oil sand reservoirs. Their relationship for the iron family (pyrite, pyrrhotite, wustite, magnetite, hematite, and melanterite) are plotted as a function of the pH, sulfate, and sulfide content in Figure 23. All phases are stable at all temperatures.

Siderite, calcite, and dolomite are the important carbonate minerals found both in the oil sands and the carbonate trend. Diagrams for calcite, dolomite, and siderite solubility as a function of temperature are presented in Figure 24. Four congruent dissociation reactions are considered; carbonate mineral to CO_3^{2-}, to HCO_3^-, to H_2CO_3, and to CO_2 gas. The carbonate minerals may be used to limit the stability of the aluminosilicate minerals if the P_{CO_2} is fixed through the last dissociation reaction. Dolomite readily breaks down

to calcite and silicate minerals. If there are no aluminosilicate minerals present, the magnesium released by the decomposition of dolomite will go to form magnesium silicates (talc, serpentine, or brucite) if quartz is present. Such reactions would be expected in the carbonate trend rocks where whole rock analyses show very low values for aluminum. Of course in the oil sands, the opposite is true.

Siderite and calcite are also common scale-forming minerals. If high-sulfate waters are encountered in the produced fluids, the dissolved calcium may form anhydrite or gypsum. The stabilities of anhydrite and gypsum are plotted as a function of temperature in Figure 25. Gypsum is stable to 50°C and is replaced by anhydrite at higher temperatures.

WATER CHEMISTRY

Formation waters

Hitchon et al. [64,65] have compiled extensive data on the formation water chemistry of the Cold Lake area. They report that the total dissolved solids (TDS) in the formation waters in and bounding the Clearwater Formation range from 60 000 mg/kg in the southern part of the Cold Lake area to <20 000 mg/kg in the northeast. The formation waters in Cold Lake are all dominantly of the NaCl type with appreciable amounts of bicarbonate and sulfate and pHs generally between 7 and 8. Unfortunately the Hitchon et al. compilation [65] contains no water analyses for the northeast part of the Cold Lake area where the richest oil sand deposits occur. In Table 4, formation water analyses from the Cold Lake area for samples from the Colony, Sparky, Clearwater, Cummings, and McMurray formations can be compared to analyses in Table 5. The connate waters from the Cold Lake area contain the lowest TDS. Takamura [17] in his study on the structure of the oil sand in the Athabasca deposits found that the Na^+ in the connate water based on the hot water extraction technique ranges from 700 to 2500 mg/kg. This is in the range of the values found for Na^+ in the Clearwater Formation connate waters recorded in Table 5. The other Cold Lake formation-water samples listed in Tables 4 and 5 were procured from drillstem tests or from separators after being produced from the tubing string, and were probably mostly bottom waters that would readily flow into the well. The one connate water sample cited in Table 5 from outside the Cold Lake area has extremely high TDS.
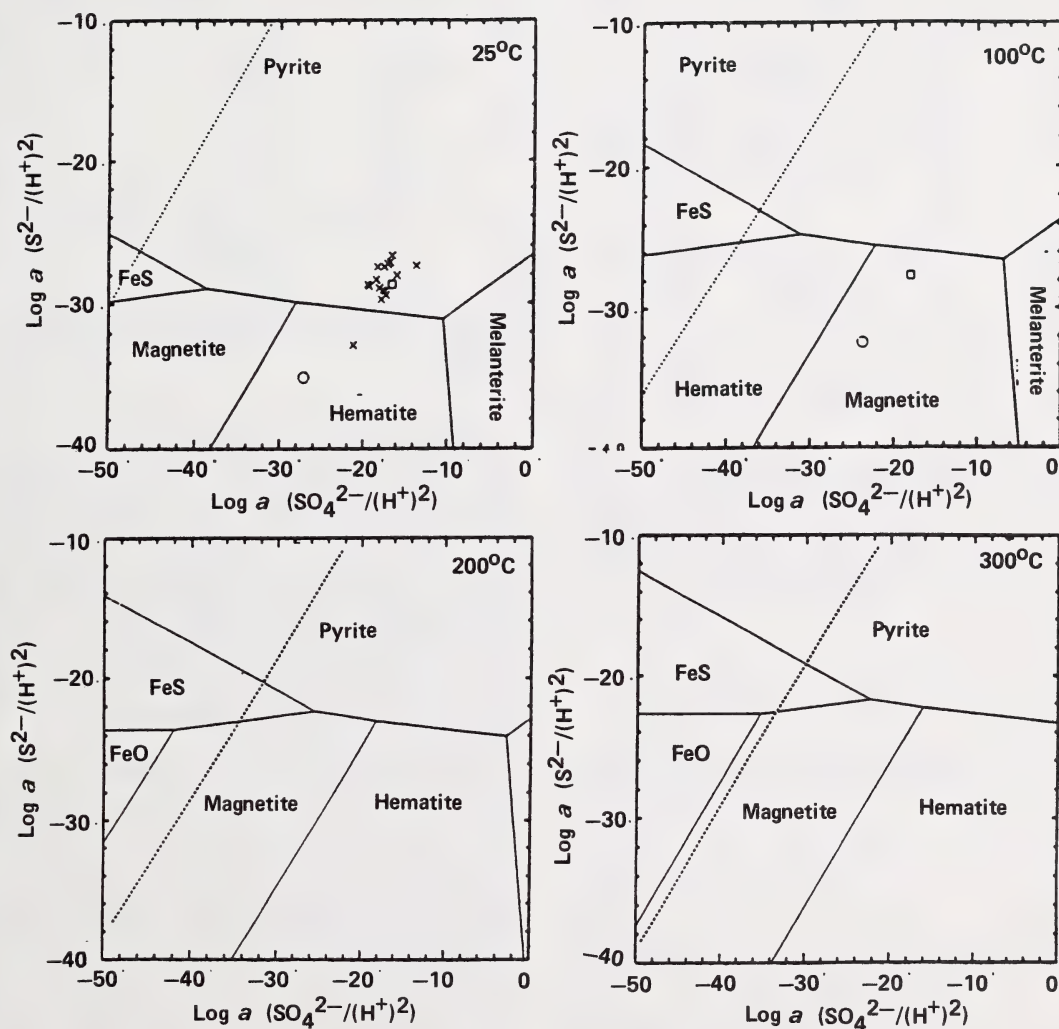
Figure 23. The stability fields of iron oxides, iron sulfates, and iron sulfides as a function of sulfate, sulfide, and hydrogen ions in water at 25, 100, 200, and 300°C. Boiler condensate are plotted as circles, production waters as squares, and waste waters as x's. The dotted line indicates the stability limits of water — to the upper left corner of this diagram, water breaks down.
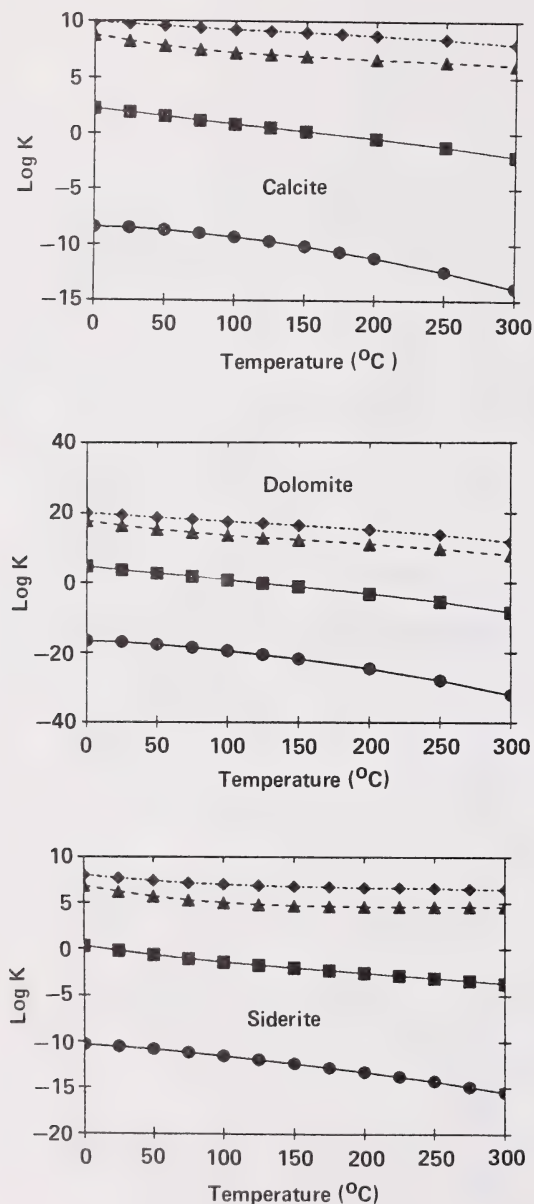
Figure 25. Variation with temperature of anhydrite and gypsum solubility. The equilibrium is: mineral = Ca^{2+} + SO_4^{2-} .

Thus in planning in situ projects, at least two types of formation water become important. The first type is the bottom water represented in Figure 4 which in the Cold Lake area is relatively high in TDS; and the other type is the connate or irreducible water of Figure 4 which is low in total dissolved solids. If the compositions of these two types of waters are known before the pilot is put in place, calculations may be made to determine the effects of mixing of both the bottom water and the connate water with the injection water or the effect of heating the waters.

The dissolved silica concentrations for two formation waters from Cold Lake are recorded in Table 5 and plotted as triangles in Figure 19. One is connate (the lower in silica concentration) from the Clearwater Formation and the other was collected by natural flow from the Grand Rapids Formation. The latter formation water is saturated with amorphous silica at 25°C which may be caused by contamination. Heating of these waters will decrease the saturation of silica. At 100°C and above both waters are undersaturated with quartz (Figures 20–22). Assuming that the waters equilibrate with quartz, the waters move from being in equilibrium with kaolinite and potassium feldspar or illite to the albite, smectite, zoisite, and clinochlore fields (Figures 19 through 22) during heating.

Figure 24. Calcite, dolomite, and siderite equilibria in water for various aqueous complexes. The equilibria are: mineral = cation + CO_3^{2-} (circles), mineral + H^+ = cation + HCO_3^- (squares), mineral + $2H^+$ = cation + H_2CO_3 (triangles), mineral + $2H^+$ = cation + $CO_{2(gas)}$ + H_2O (diamonds).

Table 4. Public domain Cold Lake formation water analyses.

Company:	Esso	Esso	Great Plains	Great Plains	Great Plains	Kissinger Glendon	Husky DH Ferriby
Formation: (mg/L)	Clearwater	McMurray	Cummings	Sparky	Colony	McMurray	Beaverhill Lake
pH (25°C)	7.3	7.6	7.55	7.99	8.0	7.1	7.6
Sodium	5 894	8 434	8 952	7 689	10 028	15 725	21 381
Magnesium	139	158	180	148	185	443	1 066
Calcium	277	83	280	252	512	801	2 453
Chloride	9 430	12 836	14 605	12 337	16 725	26 700	39 928
Sulfate	NR	646	11	106	absent	12	264
T. alk. (as HCO_3)	952	363	357	549	310	400	493
TDS	16 692	22 520	24 385	21 081	27 760	44 063	65 578
Reference	Esso (1979)	Esso (1979)	Samoil (1966)	Samoil (1966)	Samoil (1966)	C+GLL #F75–1047–3	ERCB #933–21251

NR - Not reported.
T. - Total.

Injection waters

Injection waters for steam injection and fire floods come from three main sources — river or lake water, subsurface aquifers, and recycled produced water [66]. The TDS of the produced water is normally too high to be directly used as boiler feed water and is usually blended with one of the other two sources. After blending, the water has to be further treated for oil, organics, hardness, suspended solids, iron, and oxygen [67]. The blended water is heated to enhance its treatment. Chlorination is used to break down the organics and oxidize any ammonia and hydrogen sulfide. Hardness, iron, and silica are reduced by lime softening and/or ion exchange. A large quantity of sludge is produced in lime soften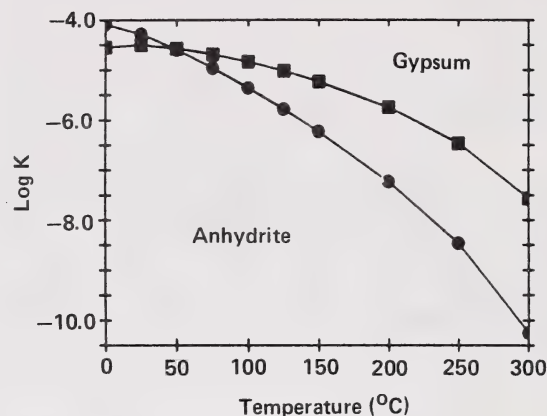ing, which must be disposed of. Oil and suspended solids are removed by filtration. Dissolved oxygen is removed by deaeration or reduction by sodium sulfite. Adjustment of the pH before the water enters the boiler or is injected down the well is normally required to prevent corrosion.

For most steam injection processes the quality of the steam is around 70 to 90% (that is, 70 to 90% dry steam with 30 to 10% steam condensate) and often the steam and condensate are injected together into the reservoir. This process results in a condensate phase which is a factor of five higher in TDS compared to the boiler feed water (Table 6). Both the feed waters and the condensate can be significantly supersaturated with quartz at 25°C (Figure 19 and Table 6) when the feed water is partially recycled water. Most of the feed waters are relatively high in bicarbonate which breaks down in the boiler to form carbon dioxide and hydroxide by the reaction:

$$HCO_3^- = CO_2 + OH^- \tag{2}$$

The acidic CO_2 partitions into the steam phase, driving the reaction to the right and resulting in a condensate pH in the range 10 to 12 as discussed in the section on computer models and phase equilibria. Hence it is possible that the injection fluid will separate in the formation into a basic water fraction overlain by acid steam. Assuming that the waters equilibrate rapidly with quartz, two different types of formation damage may develop: the acid fraction would favor stability of kaolinite while the basic fraction would promote smectite, clinozoisite (epidote), potassium feldspar, chlorite, or zeolite formation as seen in Figures 20–22. Several pilot operators separate the condensate and steam, and inject 100% steam down the hole in order to avoid basic alteration. Some pilot operators use additives such as NH_3 to try and suppress the formation of high-pH condensates which can cause formation damage or loss of gravel pack materials.

Table 5. Selected formation waters from oil sand and heavy oil reservoirs in Alberta.

	Connate waters					Other formation waters	
Area:	Cold Lake	Cold Lake	Cold Lake	Other	Cold Lake	Cold Lake	Other
Reservoir: (mg/L)	Clearwater	Clearwater	McMurray	McMurray	Clearwater	Grand Rapids	Mannville
pH (25°C)	8.50	8.25	8.22	7.62	8.42	6.55	8.98
Lithium	NR	<1	<1	2.7	<1	2.8	3.4
Sodium	2 623	2 510	4 010	16 000	2 250	9 626	3 870
Potassium	108	31	50	166	46	45	33.9
Magnesium	14.3	19	51	281	14	251	8.16
Calcium	19.5	24	25	160	14	450	8.3
Strontium	NR	1	4	224	1	41.5	1
Barium	0.4	<1	7	9.5	<1	16	2.3
Manganese	<0.1	<1	<0.1	0.2	<1	2.9	<0.1
Iron	4.5	<1	<0.1	0.18	<1	199	0.01
Aluminum	NR	<2	<2	<2	<1	4.5	<0.2
Fluoride	46	7.7	NR	NR	<2	26	NR
Chloride	3 655	2 840	5 130	26 600	2 190	16 480	2 300
Bromide	NR	NR	NR	NR	NR	144	NR
Nitrate	2.7	NR	NR	NR	NR	<0.1	NR
Sulfate	254	412	208	56	545	19	27
Phosphate	<0.5	NR	NR	NR	NR	NR	NR
T. Bicarbonate	569	575	1 411	136	861	1 098	5 240
T. Carbonate	32.01	18.1	53.4	3	36.6	1.9	981
T. Inorganic carbon	119	118	291	28.1	178	293	1 230
T. Si/SiO$_2$	2.6/5.56	2.1/4.28	3/6.42	6.1/13	2/4.28	21.5/46	6.6/14.2
T. B/H$_3$BO$_3$	12.6/72.0	9/51	7/40.	3.1/17.7	8/45.7	2.8/16.2	9.7/55.7
T. H$_2$S	NR	NR	NR	NR	NR	NR	<1
T. alk. (as HCO$_3$)	NR	NR	1 525	NR	NR	1 112	NR
TDS	7 410	6 492	10 990	43 547	6 006	28 482	12 556
T. Sulfur	NR	208	108	26	258	10.2	167
T. Phosphorous	NR	<1	<1	2.1	<1	NR	0.74
Formate	7.7	41	NR	NR	34	NR	<5
Acetate	18	<50	NR	NR	<50	NR	5.3
Propionate	<0.5	<50	NR	NR	<50	NR	<3
Butyrate	20	NR	NR	NR	NR	NR	<2
Calc. charge balance %	−0.38	12.4	4.35	−2.92	12.7	−4.62	2.82

NR - Not reported.

T. - Total.

Table 6. Selected boiler feed and boiler condensate waters for oil sand reservoirs in Alberta.

Area:	Boiler feed waters					Boiler condensates	
	Cold Lake	Cold Lake	Cold Lake	Cold Lake	Other	Cold Lake	Other
Reservoir: (mg/L)	Grand Rapids	Clearwater	Grand Rapids	Grand Rapids	Grosmont	Grand Rapids	Grosmont
Temperature fluid (°C)[a]	NR	NR	NR	19	10	60	40
pH (25°C)[b]	7.80	8.2	7.96	8.36	7.51	12.3	10.40
Lithium	0.8	<0.1	0.5	0.5	<0.1	2.9	<0.1
Sodium	1 600	363	1 140	1 180	275	6 400	305
Potassium	37	<0.1	23.5	21	0.8	109	0.8
Magnesium	<0.2	<0.1	<0.1	<0.2	<0.2	<2.	<0.2
Calcium	0.1	<0.1	<0.1	<0.1	<0.1	0.3	<0.1
Strontium	<0.1	<0.1	<0.1	<0.1	<0.1	<0.1	<0.1
Barium	<0.1	<0.1	<0.1	<0.1	<0.1	<0.1	<0.1
Manganese	<0.1	<0.1	<0.1	<0.1	<0.1	<0.1	<0.1
Iron	<0.1	0.1	<0.1	<0.1	<0.1	0.8	<0.1
Aluminum	<0.3	<0.1	<0.1	<0.3	<0.3	<0.3	<0.3
Fluoride	NR	0.28	<1	2	<2	<0.5	<2
Chloride	1 800	30	1 160	1 110	1.1	5 690	1.72
Bromide	NR	NR	52	6	<0.1	41	<0.1
Iodide	<1.5	NR	NR	<1	NR	<1	NR
Nitrate	0.9	NR	NR	6	0.19	6	1.34
Sulfate	106	140	192	420	<1	2 270	85.4
Phosphate	NR	1	22	<0.5	82.2	2	<1
T. Bicarbonate	53.8	728	61.1	230	674	0.16	169
T. Carbonate	0.43	9.02	0.62	6.03	1.59	99.7	237
T. Inorganic carbon	11	147	NR	47	141	20	99
T. Si/SiO_2	7.81/16.7	12.0/25.7	10.7/22.9	6.83/14.6	8.18/17.5	33.0/70.6	8.98/19.2
T. B/H_3BO_3	0.96/5.5	0.3/1.71	3.5/20.0	3.6/20.5	0.5/2.86	2.59/14.8	0.6/3.43
T. NH_3	NR	NR	NR	23	1.13	1.3	0.31
T. H_2S	NR	NR	NR	<0.02	<0.8	0.1	<0.8
T. alk. (as HCO_3)	NR	NR	90	283	591	1 387	418
TDS	3 675	1 383	2 680	3 040	1 101	15 559	951
T. Sulfur	170	46.4	100	155	58	795	96
T. Phosphorous	<0.1	0.41	90	0.4	0.5	1.9	0.2
T. Organic carbon	26	8.8	NR	37	10.5	144	107
Formate	NR	NR	NR	<1	<5	2	<5
Acetate	NR	43.3	NR	<1	<10	3	<10
Propionate	NR	NR	NR	<1	<10	2	<10
Butyrate	NR	NR	NR	<1	24.7	4	<5
Conductivity @ 25°C[c]	NR	1.23	4.40	4.65	0.999	22	1.1
Calc. charge balance %	23.9	−5.79	24.2	15.2	−8.29	13.8	−18.6

NR - Not reported.
T. - Total.
[a] - At collection point.
[b] - During measurement.
[c] - mmho/cm.

Produced waters

The injection waters have mixed with the formation waters and gas in the reservoir and reacted with the minerals before they are returned to the surface as produced waters at the wellhead. They have undergone extensive modification as can be seen from Table 7. Depending on the thermally enhanced recovery process used, the evolution of the waters may be completely different. Two extreme cases are found in steam stimulation and fire floods.

Most steam pilots start with cyclic steam stimulation until communication between wells is established and then switch to steam drive. During steam injection, water normally low in TDS is injected into the reservoir as a mixture of steam and condensate that then mixes with the connate water which is much higher in TDS. Further chemical changes are induced by reactions with the minerals. Upon backflow or production, this modified water mixture is produced back up the well. The waters are all high in silica (Figure 19) as a result of contacting the quartz sands in the reservoir at steam temperatures.

During the injection of air in a fire flood, sulfur in the oil or pyrite in the sand is oxidized and produces sulfuric acid. The sulfuric acid lowers the pH of the water drastically as well as producing a sulfate water. Consequently, although the initial water produced is connate, as the zones of a fire flood sweep towards the production well, the waters become increasingly acidic and high in sulfate. The gas signature of the fire flood is normally seen much earlier. The oxygen is consumed at the fire front but the nitrogen bypasses unaltered, and along with CO_2, replaces methane as the dominant components of the produced gas. Oxygen may appear later with the acid-sulfate waters.

The acid nature of fire flood waters results in a separation from those of the steam process plotted on Figures 19 through 22. The single fire flood water plots well down in the kaolinite field while the steam flood samples cluster just above the kaolinite field. Assuming the concentration of dissolved silica measured in the produced waters is inherited from equilibrium with quartz in the reservoir, the quartz geothermometer temperatures can be calculated. In Figure 26, these temperatures have been used to locate these waters on the appropriate phase diagrams. Again the single fire flood water plots well into the kaolinite field while the cyclic steam flood waters cluster around the illite-zeolite-potassium feldspar-smectite-chlorite phase boundaries. The fire flood waters are undersaturated

with calcite while steam flood samples are nearly always supersaturated. The boiling of CO_2 due to the release in pressure in the production well may be the reason for these observed supersaturations.

Chemical tracers may be injected into the reservoir to estimate reservoir sweep during recovery. A number of anions are commonly used in the liquid phase as these do not result in ion exchange on the minerals. Cooke [68] tested bromide and nitrate in a steam drive application. Heisler [69] used the radioactive tracers ^{57}Co, ^{60}Co and tritiated water (HTO) at the Peace River in situ project.

Some tracers are native to the virgin reservoir. Stable isotopes of carbon have been used by Cathles et al. [46] and Abercrombie and Hutcheon [45] to monitor the source of CO_2 production from bitumen and minerals. Chloride is one dissolved ion that is present in substantial quantity and that cannot be produced from the bitumen, minerals, or gases. Therefore, an increase in the chloride content in the produced water normally reflects an increase in the amount of connate or formation water being produced. In the production part of a cyclic steam cycle, the chloride content usually increases steadily with time (see Figure 27). The amount of mixing of connate and injected water can be estimated if the chloride concentration of the connate water is known. The estimated mass of connate water can be correlated with oil production. Generally, the ratio of connate water to produced oil is less than that in the reservoir due to the water-wet nature of the reservoir. Sudden breaks or changes in the rates of the chloride production can indicate condensate breakthrough from neighboring wells or from bottom water zones. Examples of the use of the chloride ion as a tracer are given in Gunter et al. [23] and Russell and Bird [70].

Waste waters

The composition of the waste water depends not only on the modifications of the source water prior to its injection into the reservoir and those that take place during its passage through the reservoir, but also on the produced water treatment carried out in the surface facilities.

A portion of the produced water cycle outside the reservoir is shown in Figure 28. On the production side of the reservoir, gas from the annulus is flared to atmosphere or burned as fuel depending on its composition. The water/oil mixture from the tubing string is mixed with that from other wells and sent to the main processing plant. The temperature is maintained

Table 7. Selected produced waters from steam and combustion projects from oil sand and heavy reservoirs in Alberta.

Area:	Produced waters						
	Cold Lake	Cold Lake	Cold Lake	Cold Lake	Cold Lake	Other	Other[d]
Reservoir: (mg/L)	Grand Rapids	Clearwater	Clearwater	Clearwater	Clearwater	Grosmont	Mannville
Temperature fluid (°C)[a]	NR	NR	88	68	54	99	48
pH (25°C)[b]	7.20	7.92	7.55	9.03	8.25	7.29	3.05
Lithium	5.1	5.5	8.7	NR	2.50	0.3	7.9
Sodium	7 300	4 140	4 150	990	722	875	5 700
Potassium	158	146	98	53	92	41.5	52
Magnesium	108	21.5	7.7	<0.2	0.20	2.4	435
Calcium	390	82	52	1.3	30.6	5.2	330
Strontium	23	3.4	NR	0.2	0.50	0.2	4.8
Barium	8.7	1.9	NR	<0.1	<0.10	0.3	<0.1
Manganese	3.5	0.2	NR	NR	<0.10	<0.1	38.5
Iron	22.5	0.5	<0.1	<0.1	<0.10	0.2	50
Aluminum	1	<0.5	<0.4	<0.3	<0.10	<0.3	1 360
Fluoride	NR	<2	0.78	NR	NR	2.4	NR
Chloride	9 080	5 880	6 370	909	1 160	588	5 700
Bromide	NR	20	NR	NR	NR	2	NR
Iodide	<1.5	NR	NR	NR	NR	NR	NR
Nitrate	<0.1	<2.5	NR	NR	NR	<0.5	NR
Sulfate	41	32	8.2	70.4	137	62	15 300
T. Bicarbonate	864	1 941	893	1 628	127	1 605	0.16
T. Carbonate	5.63	38.7	7.22	196	2.65	3.53	<0.001
T. Inorganic carbon	NR	397	185	360	25.7	347	38
T. Si/SiO$_2$	66/141	82.0/175	73.5/157	47.5/106	51.5/116	34.5/73.8	43/91.9
T. B/H$_3$BO$_3$	32/182	35.5/202	71.0/406	40.5/231	69.0/395	4.4/25	14.6/83.4
T. NH$_3$	NR	NR	29.3	54	110	NR	NR
T. H$_2$S	NR	<0.70	NR	<0.8	NR	2.3	NR
T. alk. (as HCO$_3$)	887	1 840	NR	2 639	NR	1 260	NR
TDS	18 566	13 016	1 213	4 727	2 888	3 437	29 837
T. Sulfur	30.5	18.7	7.5	25	43.6	91	5 300
T. Phosphorous	<0.1	1.80	NR	1.10	0.30	0.3	1.2
T. Organic carbon	NR	39.1	169	NR	202	140	1 960
Formate	NR	12	10	NR	NR	<5	NR
Acetate	NR	<10	64	NR	NR	<10	NR
Propionate	NR	<10	15	NR	NR	<10	NR
Butyrate	NR	65	<5	NR	NR	48	NR
Conductivity @ 25°C[c]	NR	19.60	NR	5.45	NR	3.70	27.70
Calc. charge balance %	23.6	−5.23	−3.87	6.41	7.5	−12.0	−0.31

NR - Not reported.
T. - Total.
[a] - At collection point.
[b] - During measurement.

[c] - mmho/cm.
[d] - Combustion pilot.
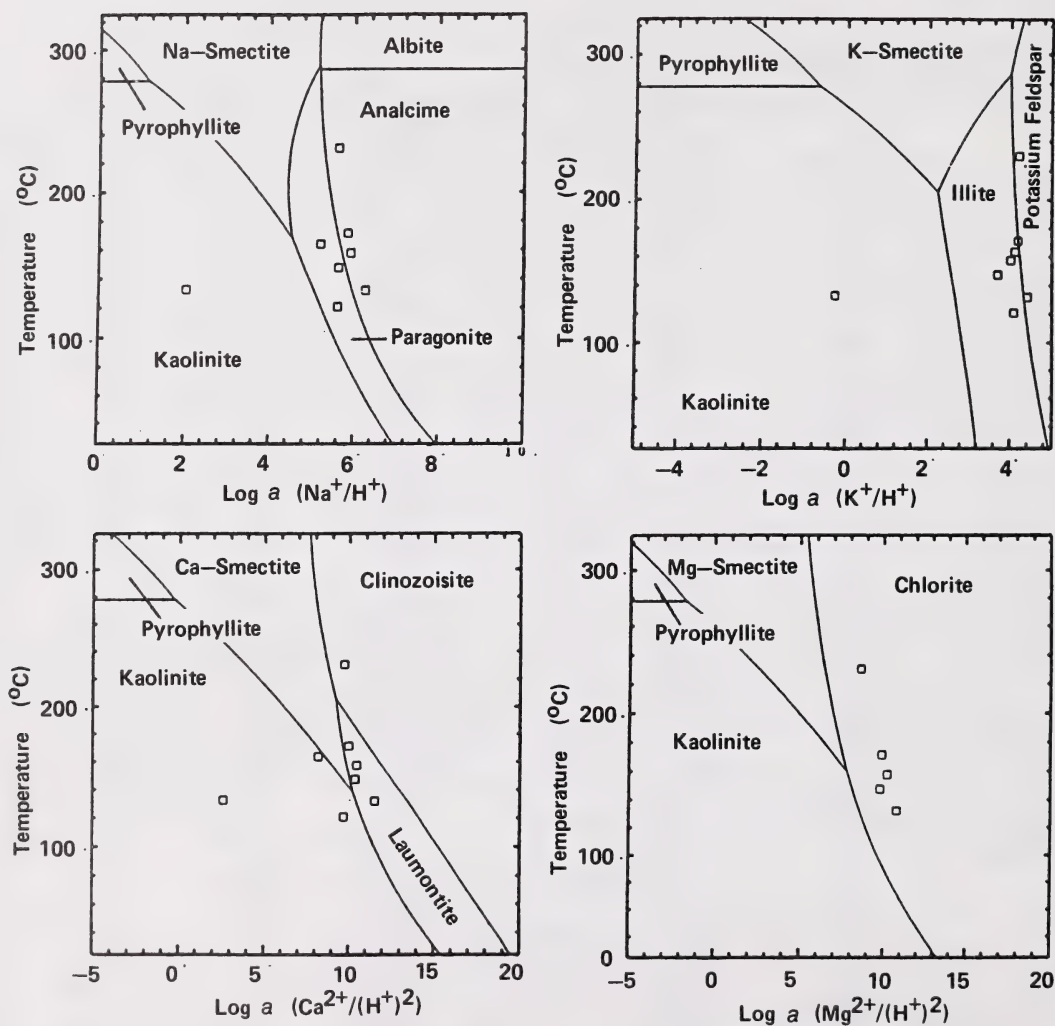
Figure 26. The stability fields of the Na, K, Mg, and Ca aluminosilicates as a function of the log activity ratios of various cations to hydrogen ion and temperature at saturated steam pressures. Aqueous silica is buffered by quartz. Produced water compositions are plotted as squares.
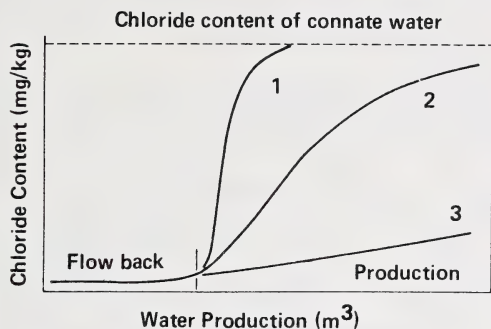
Figure 27. Typical Cl⁻ ion production curves for a single cycle in steam stimulation recovery. Curve 1 shows the expected pattern if water breakthrough from a bottom-water zone or aquifer has occurred. Curve 2 is the expected shape of a production curve where the injection water has remained in the production zone and mixed with the connate water. Curve 3 indicates production predominantly of steam condensate as could recur if a previously swept zone is the primary source of the production.

above 60°C. Usually primary separation of oil and water takes place in the free water knockout tank (Figure 28). From here the oily water stream goes to a heater treater or corrugated plate interceptor where the oil content is further reduced so that the water-rich fraction contains approximately 100 mg/kg oil [67]. This water moves on to a settling or skim tank where further separation takes place. A holding tank stores the water until it is needed for recycling or for disposal. The final step before disposal or recycling is filtration and possibly gas flotation. Each pilot has a different water treatment system but in general the above description applies.

Waste waters from 12 different oil sands and heavy oil field pilots representing the five main oil sands deposits (Athabasca, Cold Lake, Grosmont, Peace River, and Wabasca), as well as from the northern part of heavy oil area around Lloydminster, were analyzed for the inorganic components [25]. Many of the organic components in the samples were identified by GC/MS and are reported in Reichert et al. [71]. Most samples were collected near the disposal well pump (Figure 28) after all chemical and mechanical treatment of the produced fluids had occurred. The samples were predominantly produced water at about 60°C, from
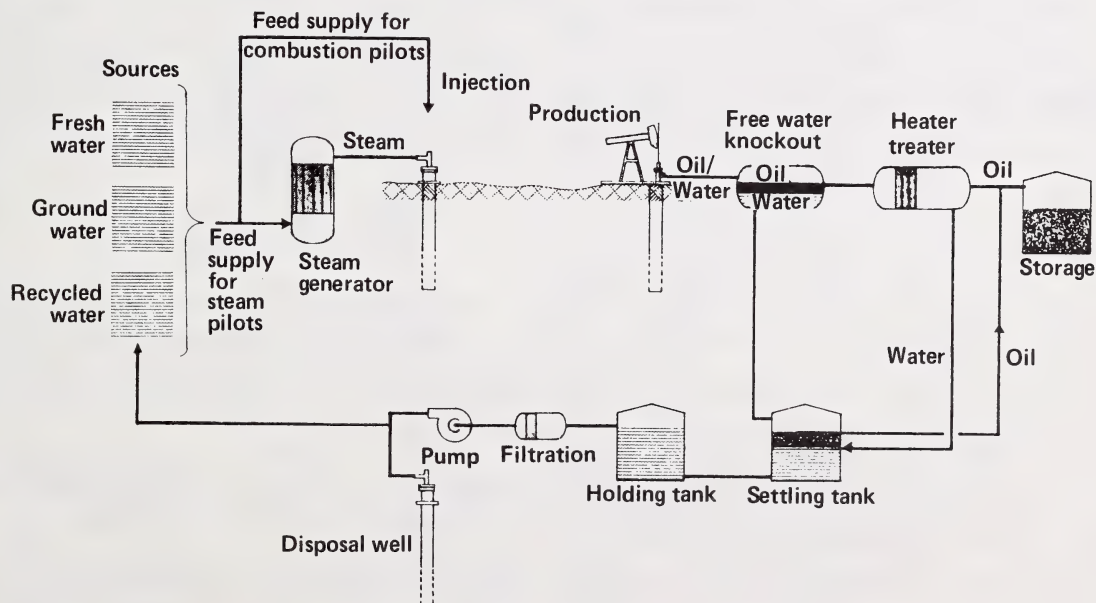
Figure 28. Water cycle in thermal recovery projects. Adapted from Gunter et al. [25].

steam or combustion, or combined steam-combustion pilots, although at one pilot, Site 5, a caustic hot water flood was in progress during sampling.

The chemical compositions of seven waste waters selected from the 12 sampling sites are listed in Table 8. Figure 29 shows the variation in TDS, pH, and temperature between the pilots. Temperatures of the water samples ranged from 20 to 90°C. The maximum in TDS (81 150 mg/kg) and minimum in pH (4.87) occurs for a combustion pilot. The highest pH (8.95) correlates with the lowest TDS (1133 mg/kg) and both correspond to the caustic hot water flood.

The saturation index for calcite has been exceeded for a number of the waste waters. The waters cluster in the pyrite field on the oxide-sulfide-sulfate stability diagram (Figure 23). The waste waters are all supersaturated with quartz and group around the produced waters (Figure 19) reflecting that they are composed dominantly of reservoir fluids having cooled substantially from their reservoir process temperature.

MINERAL-WATER REACTIONS

Steam injection

Saturation indices calculated from chemical analysis of produced waters have been discussed previously as one way of monitoring for potential scaling problems. This approach is most useful for the nonsilicate minerals for which the thermodynamic properties are known with reasonable accuracy. The silicate mineral saturations and reactions are more difficult to evaluate because the chemical composition of the solid phases can vary over wide ranges and there is a lack of accurate thermodynamic data at elevated temperatures. An alternate approach is to use a combination of autoclave and flow system studies in which the mineral reactions and the physical effects of these reactions can be determined, and combine the information from this source with thermodynamic calculations (see previous section on mineral-water phase diagrams) to extrapolate to other temperature, pressure, or chemical conditions.

The hydrothermal reactivity of oil-in-place and extracted sands from the Athabasca, Peace River, Cold Lake, and Wabasca deposits has been determined [72] using a statistical experimental design in which the formation minerals were subjected to steam condensate conditions in autoclaves. The major mineral reactions were identified. Dissolution of kaolinite and dolomite and the growth of analcime, calcite, chlorite, and

smectite are the major mineral reactions. Illite is also known to form in some of these reactions. Temperature and pH are the most important factors controlling the reaction rate.

Shales occur widely throughout the oil sand deposits as bands, lenses, or clay breccias. Boon and Hitchon [9,73] have completed a detailed study of water-bitumen-shale transformations under hydrothermal conditions. Their factorial experiment identified the main chemical processes, namely, cation exchange, the precipitation of two types of colloidal material (ferric hydroxide and aluminosilicates), the dissolution of quartz, the formation of smectite, and the dissolution of siderite. Colloidal silica and ferric hydroxide are potential causes of permeability damage [74].

Autoclave studies on pure mineral mixtures, Levinson and Vian [75] and Bayliss and Levinson [76] showed that calcite can react with kaolinite to yield smectite and CO_2 by:

$$\text{calcite + quartz + kaolinite =}$$
$$\text{Ca-smectite} + CO_2 + H_2O \qquad (3)$$
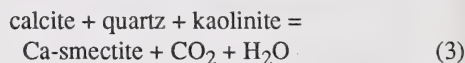
Reaction (3) was confirmed by Bird et al. [14] on oil sand core from the Grand Rapids Formation.

High-temperature core flood studies have been completed on Clearwater Formation samples by Boon et al. [77] and Kirk et al. [15]. Both of these studies showed that smectite synthesis occurred through a reaction that involved dolomite, kaolinite, and quartz. Kirk et al. showed that the reaction occurred very rapidly at a temperature of 265°C and that CO_2 gas was also a product of the reaction which is suggested to be:

$$\text{dolomite + quartz + kaolinite} + H_2O =$$
$$\text{Ca-Mg-smectite + calcite} + CO_2 \qquad (4)$$
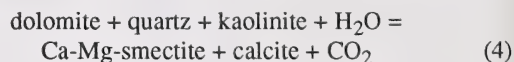
It was determined by electron microscopy that Na < Ca < Mg in the smectites produced during this study. Beidellite (dioctahedral smectite with substitution in the tetrahedral layer) with assumed Na:Ca:Mg = 1:1:2.5 could be formed by:

$$2.5MgCa(CO_3)_2 + 32H_4SiO_4 + 28Al_2Si_2O_5(OH)_4 + Na^+ =$$
dolomite   quartz   kaolinite

$$24Na_{1/24}Ca_{1/24}Mg_{5/48}Al_{7/3}Si_{11/3}O_{10}(OH)_2 + 1.5CaCO_3 +$$
smectite   calcite

$$3.5CO_2 + 95.5H_2O + H^+ \qquad (5)$$

Table 8. Selected waste waters from steam and combustion projects from oil sand and heavy oil reservoirs in Alberta.

	Waste waters						
Area:	Cold Lake	Other[d]	Other	Other	Other	Other	Other
Reservoir:	Grand Rapids	Lloydminster	Grosmont	Bluesky, Gething	Wabiskaw, McMurray	Wabiskaw, McMurray	Sparky
(mg/L)							
Temperature fluid (°C)[a]	68	20	30	62	85	68	75
pH (25°C)[b]	6.62	4.87	7.41	6.40	8.95	7.64	6.01
Lithium	2.7	18	0.1	0.2	0.2	0.7	1.9
Sodium	3 080	25 800	1 620	715	260	1 440	2 060
Potassium	87	550	20.5	17.9	8.7	515	90
Magnesium	21.5	1 350	114	18.1	0.2	33.5	52
Calcium	170	2 400	295	80	0.6	66	177
Strontium	6	140	3.6	0.8	<0.1	1.7	8
Barium	1.9	4	0.4	0.1	<0.1	0.2	3.2
Manganese	0.6	5	0.3	0.2	<0.1	0.1	0.3
Iron	0.1	215	0.1	<0.1	<0.1	<0.1	1.3
Aluminum	<0.3	<0.3	<0.3	<0.3	0.5	<0.3	<0.3
Fluoride	<2	<2	<2	<2	1	<2	<2
Chloride	4 850	49 500	3 230	845	200	1 640	3 580
Bromide	14	217	NR	0.5	15	3	12
Iodide	NR	NR	NR	NR	<1	NR	NR
Nitrate	5	<40	<2.5	13	0.7	<5	<5
Sulfate	78	378	123	55	83	355	54
Phosphate	NR	NR	NR	4	3	NR	4
T. Bicarbonate	494	98	620	509	76.1	1 357	173
T. Carbonate	0.51	0.01	4.91	0.2	4.91	10.4	0.04
T. Inorganic carbon	135	216	131	176	16.3	280	90
T. Si/SiO$_2$	91.9/196.7	7/15	31.3/67.1	36.5/78.1	69.2/148	9.35/20	75./160.4
T. B/H$_3$BO$_3$	23/131.5	27.5/157	0.9/5.15	5.2/29.7	9.37/53.6	7.2/41.1	19.1/109
T. NH$_3$	84.4	<1	6.4	11.1	9.7	11.1	25.6
T. H$_2$S	29.6	9.8	<1.6	95.6	0.005	74	3.6
T. alk. (as HCO$_3$)	479	227	554	573	132	1 530	210
TDS	9 603	81 150	6 097	2 627	1 133	5 924	6 795
T. Sulfur	516	345	93	1 320	46	1 340	270
T. Phosphorous	1.3	8.9	0.1	0.4	0.2	0.7	0.8
T. Organic carbon	216	696	120	369	302	309	214
Formate	<5	23	<5	<5	<1	<5	<5
Acetate	50	417	<10	70	7	300	29
Propionate	<10	<10	<10	19	38	<10	<10
Butyrate	17	<5	22	27	5	54	9
Conductivity	14.90	111	9.50	3.70	1.16	7.80	11.20
Calc. charge balance %	2.71	−2.12	−8.48	4.92	14.7	1.28	1.43

NR - Not reported.   c - mmho/cm.
T.   - Total.   d - Combustion pilot.
[a]   - At collection point.
[b]   - During measurement.
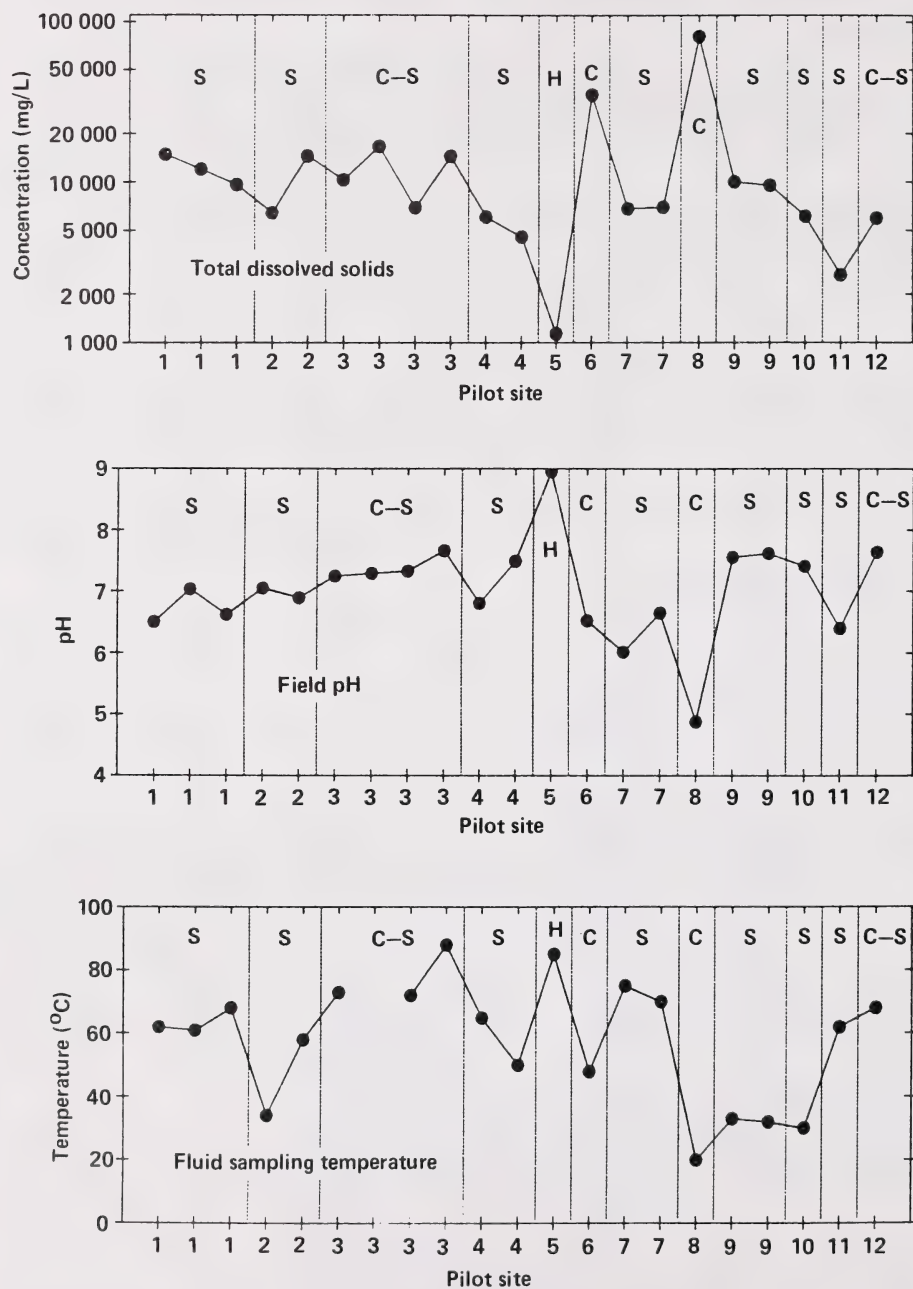
Figure 29. Variation of TDS, pH, and temperature for the waste water samples from 12 thermal recovery projects in the tar sands and heavy oil belt of Alberta. Adapted from Gunter et al. [25]. Note: S - Steam pilot; C - Combustion pilot; H - Hot water.

Montmorillonite (dioctahedral smectite with substitution in the octahedral layer) with assumed Na:Ca:Mg = 0.67:1:2.67 could be formed by:
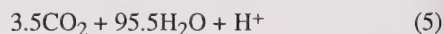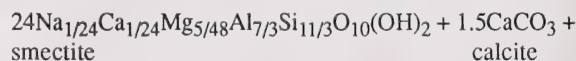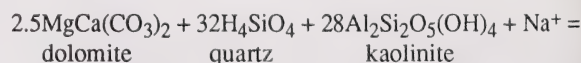
$$4MgCa(CO_3)_2 + 28H_4SiO_4 + 10Al_2Si_2O_5(OH_4) + Na^+ =$$
dolomite   quartz   kaolinite

$$12Na_{1/12}Ca_{1/8}(Al_{5/3}Mg_{1/3})Si_4O_{10}(OH)_2 + 2.5CaCO_3 +$$
smectite   calcite

$$5.5CO_2 + 63.5H_2O + H^+ \qquad (6)$$
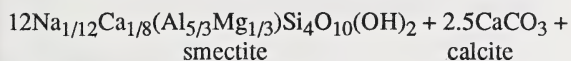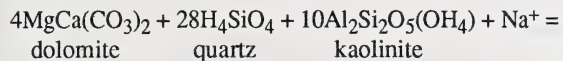
The production fluid analyses in the runs of Kirk et al. [15] showed that the greatest production of CO_2 occurred during the injection of the first two pore volumes of fluid (Figure 30) which implies that the reaction rates are very rapid. A mechanism for the smectite-forming reaction is given in Gunter and Bird [78].
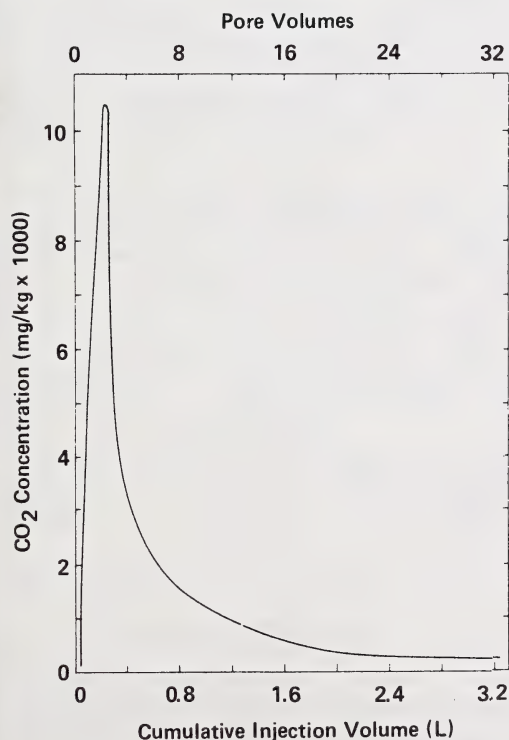
Figure 30. Carbon dioxide production from decomposition of dolomite in a core flood of Clearwater reservoir sand at 265°C. Adapted from Kirk et al. [15].

It is important to note that the presence of carbonate minerals in a formation is not required for smectite synthesis. Reactions such as

$$Na^+ + kaolinite + H_4SiO_4 =$$
$$Na\text{-smectite} + H_2O + H^+ \qquad (7)$$
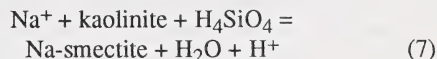
also take place.

Some preliminary scoping results have been reported for reaction (7) by Hebner et al. [11] who suggested that a high Na concentration coupled with a high pH will favor the formation of analcime over smectite by the reaction:

$$2\,Na^+ + kaolinite + 2\,H_2SiO_4 =$$
$$2\,analcime + 2\,H^+ + 2H_2O \qquad (8)$$
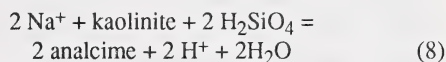
The Sedimentology Research Group [79] completed a field study of the Clearwater Formation and concluded that steam flooding was responsible for the reduction of porosity in the reservoir. They proposed reaction (7) as the mechanism for smectite formation during a steam flood of the Clearwater Formation.

Abercrombie and Hutcheon [45] and Cathles et al. [46], using carbon isotopes, confirmed that much of the CO_2 gas is formed by inorganic reactions. The production of free CO_2 gas from inorganic geochemical reactions has important implications for in situ thermal recovery. The produced gas is a potential source of gas drive in the reservoir and also can lower the viscosity of the bitumen substantially. At the same time, the pH of the water in the reservoir will be lowered which can alter the flow properties of the bitumen by neutralizing the effects of natural surfactants and altering the interfacial tension. It is also possible that thin carbonate-rich zones could provide a conduit for steam or water injection as the carbonate dissolves and reacts.

The reactions described above are compatible with the thermodynamic calculations on these silicate systems. The phase diagrams of Figures 19 through 22 show the stability fields of the aluminosilicate minerals at 25°C, 100°C, 200°C, and 300°C. Superimposed on these diagrams are the compositions of boiler feed and boiler condensates, formation waters, produced waters, and waste waters. The most striking feature of these diagrams is that the compositions plot over very narrow ranges of activity values, and the compositions of the produced fluids have tended to separate away from the boiler feed and condensates. All of the high-temperature

produced waters are supersaturated with quartz. The narrow range of chemical compositions in the produced waters indicates that the formation mineralogy has reacted with the injection fluids and has buffered the composition of the produced water, regardless of the extraction process. The scatter of the data most likely results from different temperature regimes in the reservoirs. The diagrams also show that increasing the temperature of the process will increase the stability regions of the smectite minerals and favor reactions which lead to the breakdown of kaolinite.

On the K/H_4SiO_4 diagrams, the illite field is prominent up to 200°C and the K-smectite only becomes significant at higher temperatures. In the Mg^{2+} system, chlorite is a prominent phase at all temperatures. The Na/H_4SiO_4 diagrams confirm that the analcime-forming reaction (reaction (8)) is favored by high Na and high pH. Figures 19 through 22 show that large analcime and small smectite fields are present at 100 and 200°C. The analcime field is compressed and the smectite field has grown much larger by 300°C. The high pH also favors a high concentration of dissolved silica (see Figure 15). It is possible that the analcime-forming reactions could also be favored by high Na and Si concentrations in formations containing highly soluble volcanic glass, such as are found in the Clearwater Formation throughout the Cold Lake area.

In situ combustion

The mineral-water reactions during in situ combustion are expected to be more complex than those occurring during steam flooding. This will be particularly true if the minerals have passed through all of the combustion zones in a reservoir (see Figure 2). The limited number of water analyses and post-fire core descriptions create additional problems interpreting the effects of fire flooding.

In a few cases, the mineralogy of the post-burn zone has been described. Hutcheon [80] found that chlorite was synthesized from kaolinite, siderite, and quartz. On the other hand, Lefebvre and Hutcheon [81] found illite forming in the post-burn zones containing coke and K–feldspar and hematite forming in the coke-free zones. Tilley and Gunter [82] examined a post-burn core and found that wet combustion of a sandstone has resulted in two distinct zones containing four mineralogical assemblages:

Zone B
    quartz–kaolinite–illite–smectite–alunite–hematite
    quartz–kaolinite–alunite–hematite–smectite

Zone C
    quartz–illite–vermiculite–kaolinite
    quartz–illite–smectite–kaolinite

The growth of smectite has occurred dominantly in the uppermost part of Zone B and the lowermost part of Zone C and is suggestive of steam-type conditions. The zone of combustion is indicated by red coloration and the growth of alunite and hematite in Zone B.

The compositions of the Zone C interstitial waters have been plotted in Figure 31, a phase diagram constructed for steam and quartz saturation at 300°C. The stability field for vermiculite is not represented but it would lie between those for smectite and chlorite. Both waters plot quite close to the smectite stability fields, but in the chlorite field. The same observation is true for 200°C.
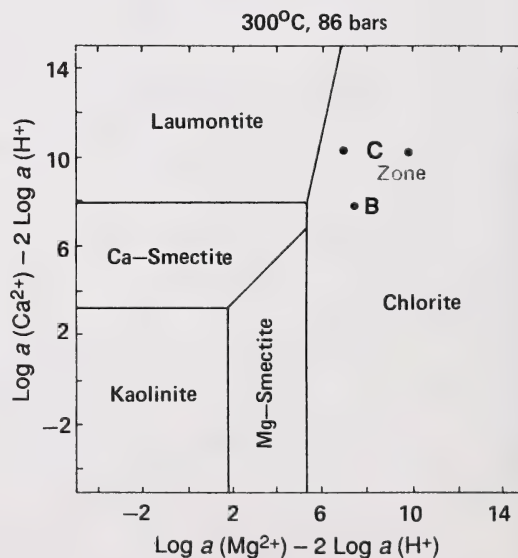
Figure 31. Mineralogical phase diagram for Ca and Mg aluminosilicates drawn at 300°C for quartz and steam saturation. Waters from Zones B and C are labelled. Adapted from Tilley and Gunter [81].
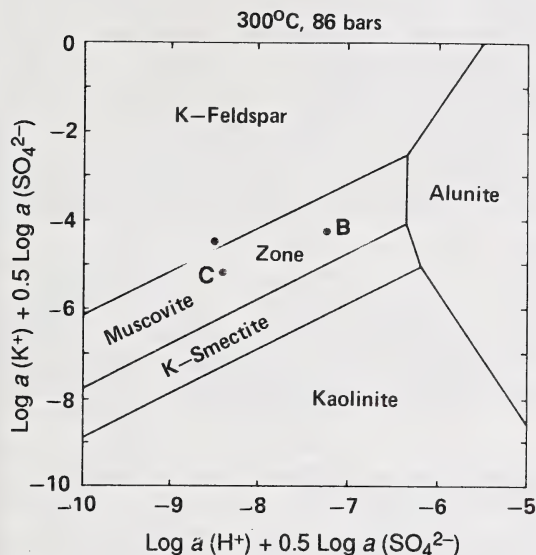
Figure 32. Mineralogical phase diagram for K-aluminosilicates and sulfates drawn at 300°C for quartz and steam saturation. Waters from Zones B and C are labelled. Muscovite is used as a proxy for illite. Adapted from Tilley and Gunter [81].

The compositions of waters from Zones B and C have been plotted in Figure 32 on a K^+–H^+–SO_4^{2-} phase diagram constructed for steam and quartz saturation at 300°C. All three waters plot close to or in the field of illite (muscovite). The Zone B water lies closest to the alunite stability field at 300°C, and in fact , the Zone B water lies in the alunite field at 200°C. Also, the Zone B water moves into the Ca/Mg-smectite stability field of Figure 31 between 200 and 300°C.

The absence of illite in the alunite-bearing sample suggests that the decomposition of illite might have been one source of K^+ for formation of alunite by a reaction:

$$\text{illite} + 4H^+ + 2SO_4^{2-} + 6H_2O = \text{alunite} + 3H_4SiO_4 \quad (9)$$
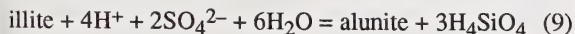
However, formation or injected waters may also have provided K^+.

The presence of alunite indicates a low pH, sulfate-rich environment [83]. Such conditions were probably produced by combustion of the oil, producing acid gases. These acid gases dissolve in the steam zone producing sulfate ions and lowering the pH. Hence, the synthesis of alunite will be controlled by the mass of acid gas formed during the burn. In Lefebvre and Hutcheon's study, either sulfate was too low or the pH was too high to form alunite, and illite formed instead (Figure 32), while in the case of Hutcheon [80], the pH was too high and chlorite formed (Figure 31).

Kinetics of mineral dissolution and precipitation

Quartz constitutes the major component in most oil sands formations and further dominates the chemistry because of its low molecular weight relative to other silicates. Dissolved silica is one of the most important species in determining the geochemistry of mineral dissolution, precipitation, and transformation. There has been much interest in silica thermodynamics in recent years and reliable data are known for the solubility as functions of temperature and pH [84,85]. Silica solubility is strongly pH dependent above pH 8 (see Figure 15) and large quantities of silica can be dissolved and moved through a reservoir when high-pH solutions are injected. The condensate cut that accompanies wet steam from once-through steam generators can have a pH of 10 to 12. Extensive gravel pack damage [86] and reservoir damage [87] have been observed in the field. This damage can be attributed to the high solubility of silica at elevated pH and temperature.

Bird et al. [13] reported new measurements and reviewed the literature on the dissolution and precipitation kinetics of quartz. They recommend the use of a kinetic equation:

$$k_- = k' \exp (E_A/RT) \quad (10)$$

where k_- is the precipitation rate constant in s^{-1}, $k' = 0.11$, $E_A = 51.4$ kJ/mol, R is the gas constant, T the temperature in kelvins, A is the surface area of the quartz and M is the mass of water in the system.

Stone et al. [88] incorporated the quartz dissolution and precipitation equation and silica mass transport into a numerical simulation of thermal recovery. They successfully predicted the silica production history of a number of large-scale displacement experiments such as that described above.

The silica transport model has been further developed to calculate the rate of silica dissolution from gravel packs and propped fractures in the vicinity of the well under elevated pH conditions. As kinetic parameters for silica dissolution and precipitation are unavailable for high pH, the neutral pH kinetics equation is used in this model. The results of the calculations provide estimates for the lifetime of gravel packs and

propped fractures that are in reasonable agreement with the results of field trials. An example of a durability calculation for a gravel pack is given in Table 9.

Table 9. Expected life of a gravel pack when high-pH steam condensate is injected. The calculations are based on the quartz precipitation results of Bird, Boon, and Stone and assume a radial gravel pack 1 m high, having a 0.140 m inner radius, a 0.406 m outer radius, and an injection rate of 125 m^3/d of 70% quality steam at a bottom hole temperature of 250°C.

pH of condensate	Expected life (d)
10.5	16
9.0	500
8.0	5 000

Kinetic data for mineral reactions between aluminosilicate minerals such as kaolinite, illite, chlorite, and smectite clays are not generally available for conditions relevant to steam injection or fire flooding. The kinetics and mechanisms of clay transformation such smectite to smectite/illite mixed-layer clays are known from the diagenetic patterns observed in deep basins and geothermal systems and were reviewed by Weaver [89]. In natural systems, the smectite to smectite/illite conversion begins in the 100°C temperature range with increasing temperature favoring the formation of smectite/illite mixed-layer clays and ultimately illite or muscovite.

The reaction trends observed in laboratory studies and field studies of steam flooding conditions show that the reactions proceed in the opposite direction to natural diagenesis: smectite is synthesized in the temperature range above 200°C. Moreover, the reaction rates observed in natural systems are many orders of magnitude slower than those found in core floods by Kirk et al. [15] who observed that decomposition of kaolinite and the production of CO_2 gas began before the flow system had reached a stable temperature (<2 h) and that the reaction was largely complete by the time a few pore volumes of fluid had passed through the core. Bird et al. [14] observed a similar rate of reaction in cores containing calcite as a starting material. Clearly, kinetics and metastable chemical equilibria must be considered in interpreting the rate and directions of hydrothermal reactions in thermal recovery projects.

Gunter and Bird [78] developed a mechanism and modelled reaction (3) using the computer program PATH.UBC [31]. Cathles et al. [46] presented a kinetic model based on field observations of a steam flood process at Buena Vista, CA. Both the Gunter and Bird [78] and Cathles et al. [46] models require a reaction of aluminosilicate phases with carbonates in order to generate the CO_2 gas that is produced. Although the reaction rates were not calculated, the laboratory core flood, field pilot observations, and kinetic models, require that the reactions proceed very rapidly. The rapid and large production of CO_2 gas during steam injection has to be considered in designing a process for the exploitation of heavy oil reservoirs containing both carbonate and aluminosilicate minerals.

FORMATION DAMAGE

Formation damage can be defined as a loss in permeability or well productivity resulting from some aspect of a field operation [74]. A number of factors can influence the permeability of the near-well region such as scale precipitation, fines transport and pore blockage, damage from drilling mud or injection fluid particulates, wettability alteration, and sludge formation from the bitumen itself. The effective drainage area for a well can be several tens of metres which must funnel into a zone of only a few centimetres diameter. For this
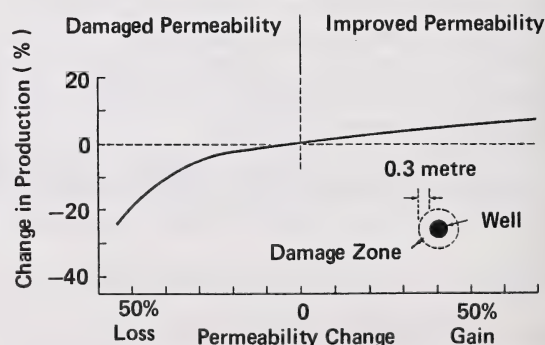

Figure 33. Permeability changes around a wellbore. Redrawn from Krueger [74]. This figure shows that a zone of reduced permeability of only a few centimetres radial thickness can reduce productivity to a fraction of its initial value. Removal of permeability damage can increase productivity substantially.

reason, the effect of permeability loss in the near-well region has a disproportionate effect on well productivity. This effect is illustrated in Figure 33 from Krueger [74].

In this section we are limiting the discussion of formation damage to the effects of inorganic geochemical phenomena or phenomena related to the inorganic geochemistry. For further discussion of formation damage, the reader is referred to the extensive reference lists in Krueger [74] and Donaldson et al. [90].

Wettability effects

Most reservoir rocks have been laid down in, or in the case of carbonates, precipitated from water. A thin film of water coats the surface of the minerals and fills the pore spaces. When the oil moves into the reservoir later, it fills the centres of the pores and is distributed as insular and funicular structures in enlargements in the pore network. In such a system the reservoir remains water-wet. In an oil-wet system the fluid distributions are reversed and the oil will coat the grains and be distributed as films and pendular rings. Alteration of the formation from strongly water-wet to strongly oil-wet can result in the production of high water cuts in the production fluids and physical damage from fines migration.

A number of factors can alter the wettability, resulting in mixed or heterogeneous wettability (see extensive series of reviews by Anderson, references [91–96]). Most oils contain a number of charged surface-active constituents that can partially dissolve in the water and then sorb on the surface of the minerals. The wettability can also be altered during the process of drilling and completing a well, as the fluids used in the operation can be quite different from the natural fluids in the reservoir. It is normal to attempt to tailor the properties of the completion fluids to maintain a highly water-wet system but this is not always successful and conditions of mixed wettability can exist in the well vicinity.

Organic sludges and scales can form by a number of processes including thermal degradation of the oils, incompatibility between the oil and various injection fluids, and by direct precipitation of ashphaltic materials if the water coating the mineral grains is evaporated by superheated steam or fire flood conditions. Acidization to remove inorganic scale has also been reported to cause organic sludge formation although the phenomenon is not well understood. The deposition of organic sludges or organic solids can decrease the porosity available to flow, and hinder the production of both oil and water.

A number of methods are available for alleviating oil-wet conditions and removing organic sludge. A solvent injection may help to redissolve the sludges so that they can be produced into the well or flushed into the formation. Injection of strong caustic solutions may re-water-wet the minerals and cause the oil-wet surfaces to become water-wet.

Injection of dry steam or creation of thermal conditions that flash all of the water to steam can deposit an organic coating directly on the mineral surfaces when the pendular water films are evaporated. In the case of ashphaltene-rich bitumens, the ashphaltenes can be deposited on the grains as a coke-like material which partially cements and consolidates the friable sands. It has been suggested that the caustic injection could be used to reestablish water-wet conditions after dry steam injection, and that this procedure could be accomplished without the loss of consolidation created by the organic precipitates [K. Takamura, personal communication].

The injection of wet steam from once-through boilers is often a water-wetting treatment in itself. The condensate cut of wet steam can be highly alkaline with pHs as high as 10 to 11 (see earlier sections on computer models and phase equilibria and interpretation of water chemistry). These high pHs can activate the natural surfactants present in the oils resulting in the formation of emulsions and the stripping of the organic films away from the mineral surfaces.

Fines transport

Fines transport has been recognized as a formation damage mechanism for some time and a vast literature exists on the subject. Standardized methods for evaluating a formation for susceptibility to fines transport have been developed [90,97].

The factors that control the tendency for fines to become loose and to migrate include the size and mineralogical composition of the fines, the salinity of the formation water, the compatibility of the formation and injection waters, the compatibility of the injection water with the fines, the physical nature of the flow path, the wettability of the fines, and the viscosity and flow rate of the transporting fluid. Until recently, it was considered that permeability damage from fresh water injection was largely a result of swelling of smectite clays. It is now established that salinity variations can also result in the dispersal and migration of kaolinite, illite, smectite, and silica fines because of surface chemistry effects [98–102]. The general conditions of

permeability damage from fines transport are shown in Figures 34a through 34c. High salinity stabilizes fines attachment while low salinity causes fines migration (Figure 34a). The pH effect is exactly the opposite; high pH causes dispersion while low pH favors stabilization or attachment.

Kaolinite is the clay mineral most susceptible to fines migration. This is largely due to the fact that kaolinite occurs in loosely attached booklets in the pore system (Figure 34b). These booklets can be entrained in the moving fluids and transported to pore constrictions where they lodge and block off the flow path with substantial loss in permeability. The physical effect can be aggravated by the use of an inappropriate chemistry which can both neutralize or reverse the colloidal forces attracting kaolinite grains to the other silicate minerals and disperse the plates which make up the booklet structures. Similar problems can occur with other mineral fines such as the illite and smectite clays.
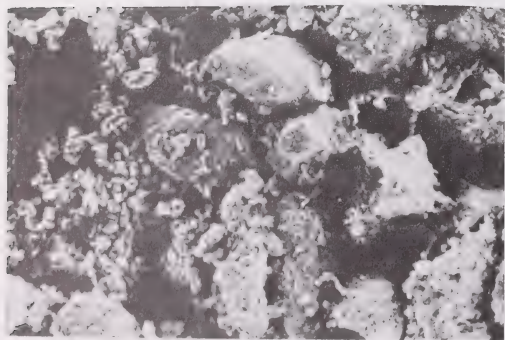
The engineering problems associated with illite result from its small grain size and fibrous nature. The fibrous nature of illite and its tendency to bridge pore structures results in an increased tortuosity of the flow paths. This decreases the permeability and increases the irreducible water saturation. Because of illite's fibrous nature and small cross sectional area, the fibres are fragile and easily disrupted during flow which can lead to serious fines migration problems.

Smectite has long been recognized for its tendency to cause problems resulting from osmotic swelling, migration, and pore blockage. Smectites also have extremely high surface areas and unique grain coating textures that can result in a large volume of microporosity. These factors combine to create high irreducible water saturations that can result in a high water-to-oil ratio in the production fluids.

The hydrodynamic forces acting on fines particles are proportional to the viscosity and velocity of the moving fluids, and some of the theory of fines mobilization has been worked out [98,103,104]. The conditions under which the hydrodynamic forces exceed the colloidal forces can be calculated for kaolinite and silica at temperatures up to about 90°C. It is not possible to make similar calculations for illite and smectite as the surface chemistry is not adequately defined. A schematic illustration of the hydrodynamic effects on clay migration appears in Figure 34c.
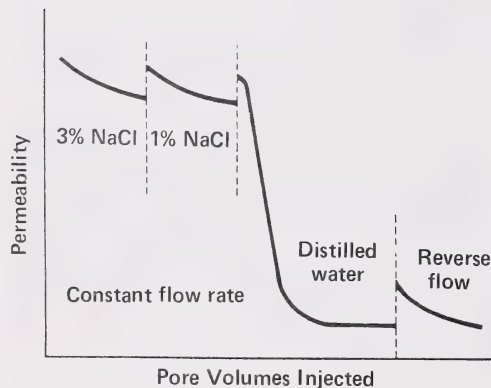

Figure 34a. Effect of salinity on fines migration.

Figure 34b. SEM photograph of kaolinite fines occluding porosity.
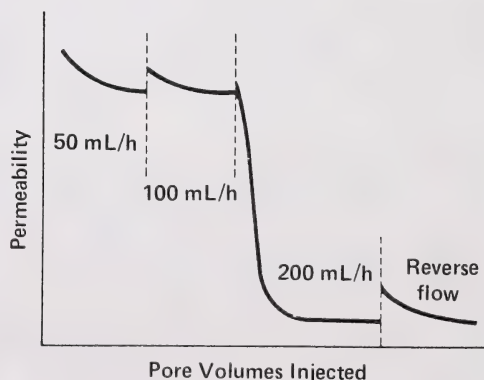

Figure 34c. Effect of hydrodynamic forces on fines migration.

Because of the complex interplay between the chemistry of the minerals, the oils, and the formation water at in situ recovery temperatures, it is necessary to determine the conditions of fines migration damage by a series of flow tests under realistic reservoir conditions. These tests are usually carried out in a flow system such as that described in the section on experimental techniques. Each test would consist of mounting a core in an overburden sleeve and injecting the relevant process fluids through the core at a series of increasing flow rates. Permeability is determined at each step and the flow rate is increased until permeability damage is noted or until the highest realistic field injection or production rates have been exceeded.

Under water-wet conditions, the fines are expected to be mobilized when water is being injected. If the fines are oil-wet or partially oil-wet, then some permeability damage can be observed when oil is flowing though the core. Generally, the oil is much more viscous than the water and the hydrodynamic forces from flowing oil are much greater. This means that damage from oil can occur at much lower flow rates than from water at the same temperature and pressure. This factor adds further importance to understanding the wettability effects of different injection fluids.

Many of the fines migration tests reported in the literature have been carried out using cores from which the oil or bitumen has been extracted with organic solvents, typically methylene chloride or toluene plus isopropyl alcohol. Some of the experiments carried out in our laboratory suggest that the extraction procedure can alter the oil- or water-wetting conditions of the core and limit our ability to interpret the results in terms of field conditions. We would recommend carrying out fines migration tests on unextracted core plugs at residual saturation of the immobile fluid phase. That is, a test for fines migration in water should be carried out using an unextracted core that has been taken to residual oil saturation at low flow rates before increasing the flow velocities to determine the rate dependence. The same core should also be tested for fines migration in the oil phase at residual water saturation.

An extensive literature exists on clay stabilizing agents. Chemical treatments with organic polymers [105], potassium hydroxide [106], hydrolyzable zirconium salts [107], hydroxy-aluminum solutions [108], and other formulations have been tested and recommended. No one chemical has yet been found that is universally effective, and the potential for fines migration and stabilization should be evaluated at the beginning of every thermal recovery project. Tests to determine the sensitivity of the formation to fines migration and the effectiveness of a clay stabilizing agents should also be run on virgin core and not extracted core material, and should be carried out under conditions as close as possible to the operating conditions of the project.

Hydrothermal reactivity

Formation damage from hydrothermal reaction will occur when new mineral phases are formed which lower the permeability of the formation. These reactions can include the synthesis of new silicate minerals such as smectite clays or the precipitation of nonsilicate minerals when ions are leached from the formation in sufficient quantity to exceed the solubility of any of a number of carbonate, sulfate, or oxide minerals.

Laboratory studies in the past have indicated the potential for permeability loss when hot fluids come into contact with a formation. The permeability of three cores was measured by Kirk et al. [15] and was found to have decreased by 50 to 98% in core floods of three weeks run duration. The greatest decrease in permeability was found in cores in which pH-11 fluids were injected. The percentage of fines, defined as the material passing through a 400–mesh standard sieve, was found to have doubled over the course of the runs. Boon et al. [9] also reported a permeability decrease but the magnitude was not quantified. Fines migration was reported in the core studied by Boon et al. who attributed the loss in permeability to this effect. Kirk et al. [15] found no evidence of fines migration and attributed the loss in permeability to the synthesis of smectite. SEM pictures of other laboratory experiments suggest that analcime growth (Figure 35b) may also cause pore blockage. Permeability loss due to mineral growth is a slow process (Figure 35a) compared to clay migration.

In addition to the direct loss of permeability from the newly synthesized clay, the synthesis of smectite (Figure 36b) may make the formation more susceptible to damage by other mechanisms such as osmotic swelling (Figure 36a), fines migration, and pore blockage.

In diagenesis, illite is known to form from reactions such as [109]:

$$\text{smectite} + K^+ = \text{illite} + Na^+ + Ca^{2+} + H_4SiO_4 + H_2O$$

$$(11)$$
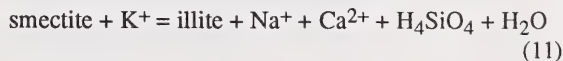
Synthesis of illite can occur by reaction (11) if both smectite and K^+ are present. The addition of K^+ or NH_4^+ ions to injection fluids has been suggested as a means of stabilizing water-sensitive smectite-bearing formations. Day et al. [110] suggested that NH_4^+ ions could be used to prevent the synthesis of smectite clays and to consolidate friable formations. Day et al. believed that the mechanism was the synthesis of NH_4^+-illites, nonexpandible NH_4^+-smectites and NH_4^+-feldspars. The results of Day et al. [110] are compatible with the phase relationships shown in Figures 19 through 22 (K/H_4SIO_4 sections) which show a wide stability field for illite up to 200°C. The presence of NH_4^+ ions in the injection fluids may place the composition in or near the illite stability field, and NH_4^+ substitution for K^+ may account for the stabilizing effects of NH_4^+ salts and the prevention of formation damage [106,110].

Chlorite is also known to form during hydrothermal reactions between kaolinite, carbonate minerals, and quartz [78]. The synthesis of chlorite can explained on the basis of the phase diagrams (Figures 19 through 22, Mg/H_4SiO_4 sections) as chlorite occupies a prominent stability field over most of the temperature range of steam-assisted recovery. One major engineering problem associated with chlorite is the precipitation of iron hydroxide gels after acidizing. These gels can create considerable loss of permeability and are difficult to remove once formed.
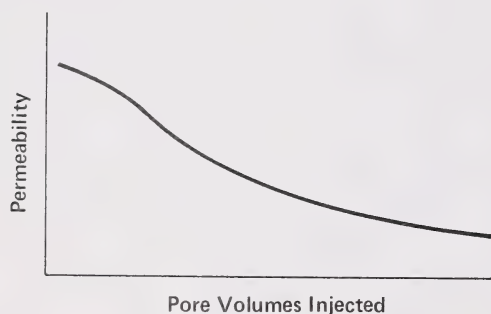
Figures 35a. Permeability change as a function of mineral growth.
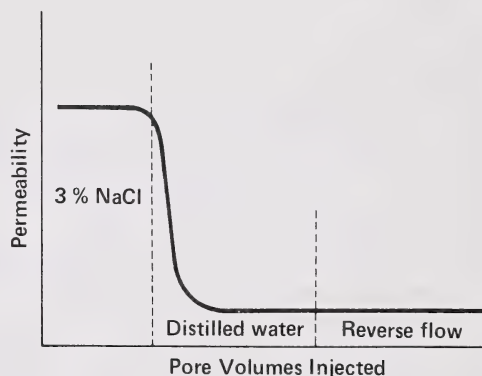
Figure 36a. Permeability change due to swelling clays: effect of salinity.
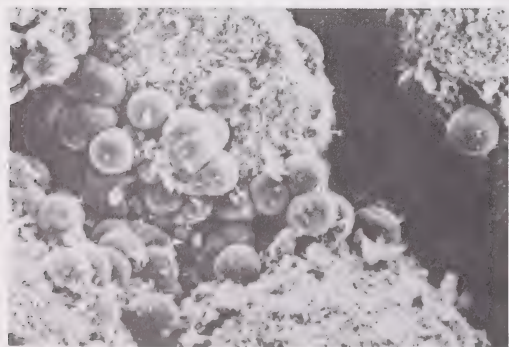
Figure 35b. Hydrothermally grown analcime blocking pore throats.
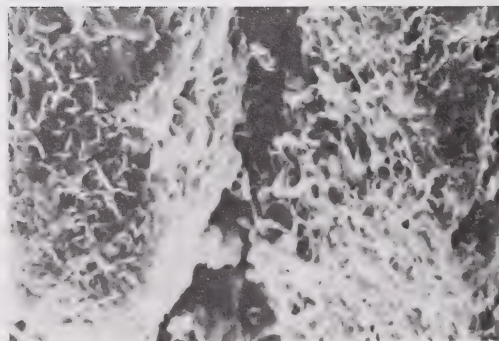
Figure 36b. Permeability change due to swelling clays: smectite coating sand grains and bridging porosity.

Water compatibility and scaling

Restrictions in injection or production can occur from inorganic scale formation within the wellbore itself or in the formation in the vicinity of the well. The significance of the precipitation of scale and small declines in permeability is illustrated in Figure 33. The conditions of precipitation of inorganic, nonsilicate scales can be calculated readily using computer programs such as SOLMINEQ as discussed in an earlier section. Calcite, anhydrite, barite, and siderite are some of the more common nonsilicate scale materials. The precipitation of insoluble phosphate minerals is a distinct possibility if the formation waters are rich in divalent cations and diammonium phosphate solutions are used with the drilling muds.

Potential scaling problems can be identified if water samples are collected and analyzed over the life of well. Phosphate and sulfate scale are difficult to treat by acidizing or other chemical methods, and anticipation of their formation and preventative treatment is more likely to be successful than remedial treatment by acidizing, EDTA, or other means. Scale inhibitors, widely marketed by oil service companies, vary widely in their success ratios.

Waste water and formation water compatibility are also a concern for the treatment and disposal of waste waters. After removal of the oil, the produced waters from oil sand steam pilots are either recycled through the boiler or are injected into a disposal formation. The waste water has been through a high-temperature cycle (100 to 700°C) and is still warm (20 to 90°C) when injected into a disposal formation whose temperature is close to 25°C. Consequently, precipitation from the waste water may occur by reaction with the minerals of the disposal formation, by mixing of the formation and waste waters, and by cooling of the waste water. These precipitates can reduce the permeability and porosity of the disposal formation and limit its suitability for disposal.

Computer programs such as SOLMINEQ can be used to determine whether the waste water is compatible with the disposal formation if the mineralogy and water chemistry of the disposal formation are known. Representative sampling of formation water is more difficult than that of waste water because the disposal formation is not directly accessible. Errors introduced by sampling procedures must be considered when comparing water analyses.

The McMurray and the Beaverhill Lake formations, both of which are used for waste water disposal can be used as examples. Two analyses were obtained of waters collected from these two formations and are listed in Table 4. The TDS content of the McMurray Formation water is about two-thirds that of the Beaverhill Lake Formation water. The Beaverhill Lake carbonate level is about the same as that in the McMurray, but its sulfate level is 20 times higher.

The computer program SOLMINEQ [35,36] was used to calculate the saturation state of mineral families at 25°C in the waste waters, the formation waters, and various mixtures of the two. By constructing *SI*-curves linking the formation water and waste water to the 50% mixture of the two, the tendencies for precipitation can be discerned. This can be considered a preliminary screening step in judging water compatibilities.

Two general types of *SI*-curves which lead to precipitation can be considered. In Case 1 (Figure 37a) the injection water has a positive *SI* and the slope of the *SI*-curve does not change sign between the injection and formation waters; therefore the 50% mix has an *SI* intermediate between the two. In Case 2 (Figure 37b), the injection water has a negative *SI* and the mixture has a larger *SI* than either the injection or formation water. An alternate of Case 2 would be if the *SI* of the waste water was positive. Precipitation occurs in that region of the curve above the line indicating an *SI* greater than zero. Mineral precipitation will occur directly from the waste water in Case 1, while in Case 2, precipitation is only possible from the mixture. Other cases can be envisioned but they will not lead to precipitation.
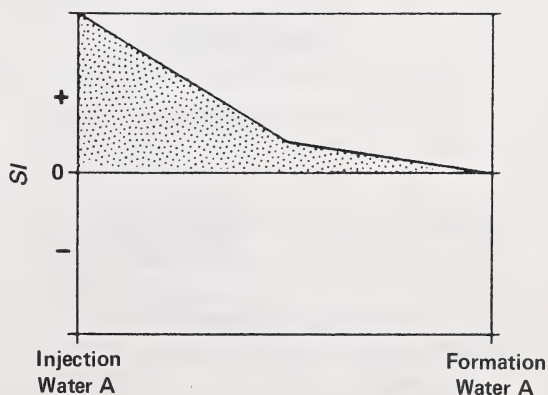
Figure 37a. Effect of mixing two incompatible waters on the stability of a hypothetical mineral. Adapted from Gunter et al. [25].
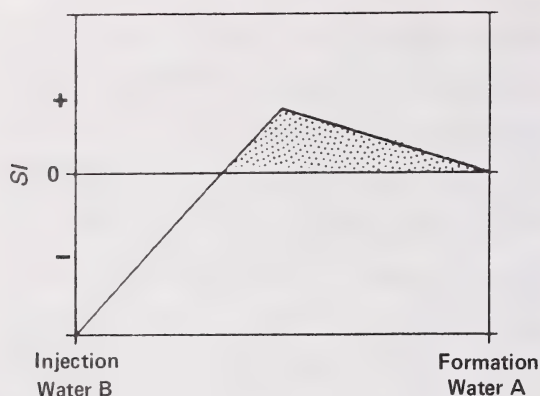
Figure 37b. Effect of mixing two incompatible waters on the stability of a hypothetical mineral. Adapted from Gunter et al. [25].

In Figure 38 the SIs for two representative mineral families have been plotted. Several assumptions about the concentrations of the dissolved species (e.g. SiO_2, Al, K, and Fe) had to be made, particularly because of the incomplete analyses of the formation waters (see reference [24] for more discussion).

Figure 38a illustrates an example of Case 1 in which the injection water is highly supersaturated with amorphous silica and the SI is decreasing as the formation water composition is approached. The high amorphous silica values in the waste waters are caused by reaction with reservoir minerals at high temperatures. Although the waste waters become supersaturated with quartz during the first few degrees of cooling from reservoir temperatures, the kinetics of quartz precipitation are unfavorable and little quartz is formed. Upon further cooling, the solution supersaturates with amorphous silica which precipitates more readily.
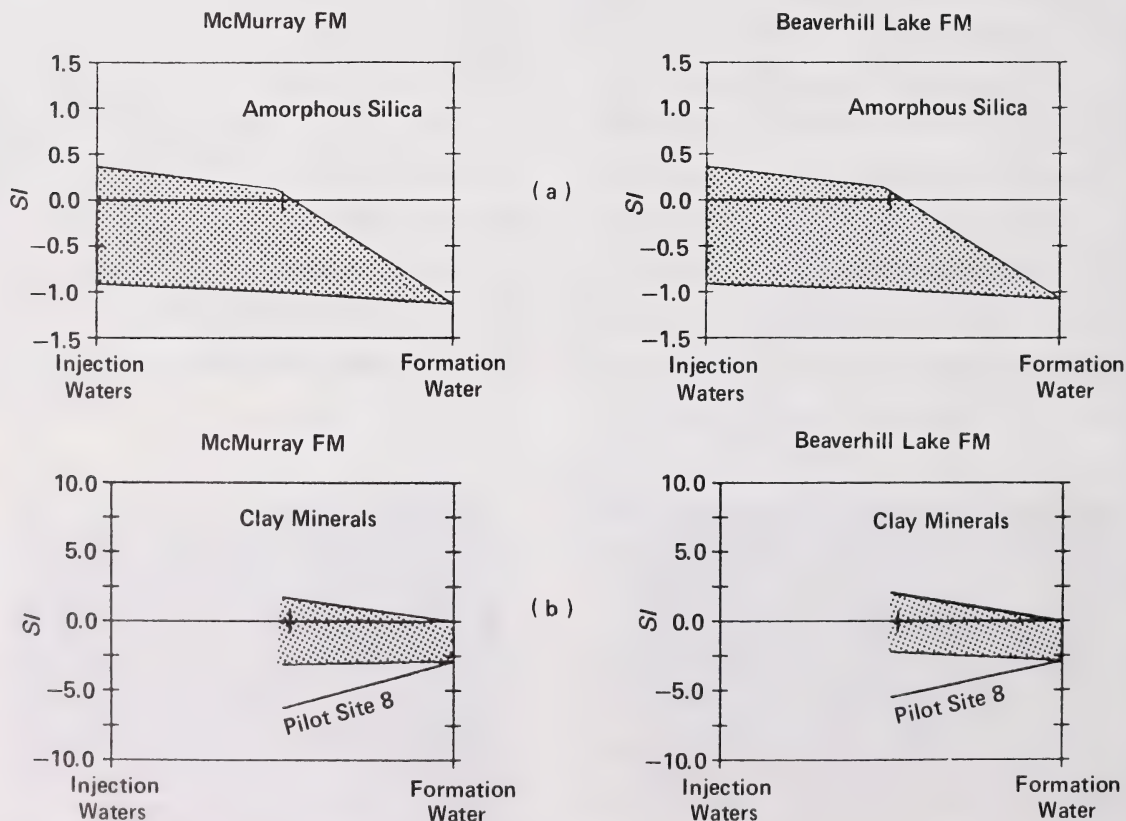
Figure 38. Stability of amorphous silca and clay minerals for mixing of formation waters from the McMurray sand and Beaverhill Lake carbonate with waste waters from 12 thermal recovery projects from the tar sands and heavy oil belt of Alberta. The shaded areas represent the variability in SI for the minerals based on the composition of all the waste waters. Adapted from Gunter et al. [25].

Amorphous silica is the solid most likely to control the concentration of silica in the disposal waters.

Figure 38b illustrates an example of Case 2. In this situation the mixture of waste and formation water has a larger *SI* than either the injection water or the formation water. Here the *SI* for the clay minerals is always greater than zero until 100% of formation water is reached.

The chemistry of the oil sand waste waters is quite variable (Table 8, Figure 29) but somewhat dependent on the type of thermal oil recovery technique used. Although the formation water compositions were not well characterized and the waste water samples were from a number of different processes and a wide geological and geographical area, several general conclusions were reached [24]. In no case, does the saturation of the 50% mix of the two waters appreciably exceed that of both end members (waste water and formation water). Consequently the mixing of the injection and formation water is relatively unimportant because it does not initiate any new precipitation events. Maintaining a satisfactory injectivity in the disposal formation may depend on the amount of precipitation of amorphous silica and calcite from the disposal waters during cooling. Precipitation of amorphous silica would lower the concentration of silica in solution and would significantly decrease the saturation indices of the other silicate minerals. Exactly where the amorphous silica precipitates depends on its kinetics and the rate of injection into the disposal formation. In the disposal formation, there is ample opportunity for heterogeneous nucleation, which may greatly increase the precipitation rates of amorphous silica. Rimstidt and Cole [111] have recorded such an example. Therefore, amorphous silica may accumulate in the disposal reservoir near the well bore if it is not flushed out in suspension or as a colloid.

ACKNOWLEDGEMENTS

REFERENCES

1. P. Bayliss and A.A. Levinson, Mineralogical review of the Alberta oil sand deposits (lower Cretaceous, Mannville group), Bull. of Can. Petroleum Geol., 24 (1976) 211–224.

2. W.S. Deer, R.A. Howie and J. Zussman, An introduction to the rock forming minerals, Longmans Pub., London (1966).

3. M. Fleischer, 1975 Glossary of mineral species, Mineralogical Record (1975).

4. C. Klein and C.S. Hurlbut, "Manual of mineralogy," 20th ed., John Wiley and Sons, New York (1985).

5. G.C. Ulmer, and H.L. Barnes, Eds., "Hydrothermal experimental techniques," Wiley Interscience Pub., New York (1987).

6. G.C. Ulmer, Ed., "Research techniques for high temperature and high pressure," Springer-Verlag, New York (1971).

7. A.D. Edgar, "Experimental petrology, basic principles and techniques," Claredon Press, Oxford (1973).

8. O. Levenspiel, "Chemical reactor engineering," 2nd ed., John Wiley & Sons, New York (1972).

9. J.A. Boon and B. Hitchon, Application of fluid-rock reaction studies to *in situ* recovery from oil sand deposits; Alberta, Canada – I. aqueous phase results for an experimental-statistical study of water-bitumen-shale reactions, Geochim et Cosmochim Acta, 47 (1983) 235–248.

10. J.E. Welton, "SEM petrology atlas," Am. Assoc. Pet. Geol., Tulsa(1984).

11. B.A. Hebner, G.W. Bird and F.J. Longstaffe, Fluid/pore mineral transformation during simulated steam injection: Implications for reduced permeability damage, J. Can Pet. Tech, 25 (1986) 1–6.

12. W.D. Gunter, P.K. Aggarwal, G.W. Bird and J. Leone, Modeling of smectite synthesis in reservoir sands: Comparison of PATH's predictions to autoclave experiments, Paper no. 29, Fourth UNITAR/UNDP International Conference on Heavy Crude and Tar Sands, Edmonton, Canada, Aug (1988).

13. G.W. Bird, J. Boon and T. Stone, Silica transport during steam injection into oil sands i. Dissolution

and precipitation kinetics of quartz: new results and review of existing data, Chemical Geology, 54 (1986) 69–80.

14. G.W. Bird, W.D. Gunter, F.J. Longstaffe and B. Wiwchar, The effects of steam condensate flooding of Grand Rapids Formation core from the Cold Lake area, Alberta, (manuscript in preparation).

15. J.S. Kirk, G.W. Bird and F.J. Longstaffe, Laboratory study of the effects of steam-condensate flooding in the Clearwater Formation: High temperature flow experiments, Bull. Can. Pet. Geol., 35 (1987) 34–47.

16. G.D. Mossop, Geology of the Athabasca oil sands, Science, 207 (1980) 145–152.

17. K. Takamura, Microscopic structure of oil sand, Can. J. Chem. Eng., 60 (1982) 538–545.

18. N.R. Morrow, The retention of connate water in hydrocarbon reservoirs, J. Can. Pet. Tech, 10 (1971) 38–55.

19. A.G. Collins, "Geochemistry of oilfield waters," Elsevier, Amsterdam (1967).

20. W.D. Gunter, B. Fuhr, G.W. Bird and L. Holloway, Formation water analyses from oil sands drill core, (abstr.) American Association of Petroleum Geologists Research Conference on Prediction of Reservoir Quality through Chemical Modeling, Park City, UT, Jun 21–26, Program and Abstracts (1987).

21. J.T. Bulmer and J. Starr, Eds., Syncrude analytical methods for oil sand and bitumen processing, Alberta Oil Sands Technology and Research Authority, Edmonton (1979).

22. E.H. Perkins and W.D. Gunter, Applications of SOLMINEQ.88 and SOLMINEQ.88 PC/SHELL to thermally enhanced oil recovery, 4th UNITAR/UNDP International Conference on Heavy Crude and Tar Sands, Edmonton, Canada, Aug (1988).

23. W.D. Gunter, E.H. Perkins, B. Young and G.W. Bird, Geochemical monitoring of oil field fluids, Paper no. 11, 4th UNITAR/UNDP International Conference on Heavy Crude and Tar Sands, Edmonton, Canada, Aug (1988).

24. M.S. Lico, Y.K. Kharaka, W.W. Carothers and V.A. Wright, Methods for collection and analysis of geopressured geothermal and oil field waters, U.S. Geological Survey Water Supply Paper 2194 (1982).

25. W.D. Gunter, B.J. Fuhr and B. Young, Composition of water in waste well disposal from oil sands and heavy oil field pilots of Alberta, Proc. 3rd Canadian/American Conf. on Hydrogeology, Hydrogeology of Sedimentary Basins: Application to Exploration and Exploitation, B. Hitchon, Ed., National Water Well Association, OH (1986) 233–249.

26. R.W. Hull, Y.K. Kharaka, A.S. Maest and T.L. Fines, Sampling and analysis of subsurface waters, a summary of current methodology, Proceedings of 1st Canadian/American Conference of Hyrogeology, Practical Applications of Groundwater Geochemistry, B. Hitchon and E.I. Wallick, Eds., National Water Wells Association, OH (1984) 117–126.

27. D.K. Nordstrom, L.N. Plummer, T.M.L. Wigley, T.J. Wolery, JJ.W. Ball, E.A. Jenne, R.L. Bassct, D.A. Crerar, T.M. Florence, B. Fritz, M. Hoffman, G.R. Holdren, G.M. Lafon, S.V. Mattigod, R.E. McDuff, F. Morel, M.M. Reddy, G. Sposito and J. Thrailkill, A comparison of computerized chemical models for equilibrium calculations in aqueous systems, in "Chemical modelling in aqueous systems," E.A. Jenne, Ed., American Chemical Society, Symposium series 93 (1979) 857–892.

28. EPRI (Electric Power Research Institute), Geo-hydrochemical models for solute migration, Volumes I and II, EPRI report EA-3417, Palo Alto, CA (1984).

29. D.K. Nordstrom and J.L. Munoz, "Geochemical thermodynamics," Blackwell, Palo Alto, CA (1985).

30. H.C. Helgeson, T.H. Brown, A. Nigrini and T.A. Jones, Calculation of mass transfer in geochemical processes involving aqueous solutions, Geochim. et Cosmochim. Acta, 24 (1970) 569–592.

31. E.H. Perkins, "A reinvestigation of the theoretical basis for the calculation of mass transfer in geochemical processes involving aqueous solutions," M.Sc. thesis, Dept. of Geological Sciences, University of British Columbia, Canada (1980) 149pp.

32. T.J. Wolery, Calculation of chemical equilibrium between aqueous solution and mineral: The EQ3//EQ6 software package, Lawrence Livermore Laboratory, report UCRL-52658 (1979).

33. S.L. Parkhurst, C. Thorstenson and L.N. Plummer, PHREEQE: A computer program for geochemical calculations, U.S. Geological Survey Report PB81-167801 (1980).

34. G. Sposito and S.V. Mattigod, A computer program for the calculation of chemical equilibria in soil solutions and other natural water systems, Report, Kearney Foundation of Soil Science, Univ. of California (1980).

35. Y.K. Kharaka, W.D. Gunter, P.K. Aggarwal, E.H. Perkins and J.D. De Braal, SOLMINEQ.88: A computer program for geochemical modeling of water-rock interactions, U.S. Geological Survey Water-Resources Investigation Report 88-4227 (1988).

36. P.K. Aggarwal, R.W. Hull, W.D. Gunter and Y.K. Kharaka, SOLMINEQF: A computer code for geochemical modeling, Proc. 3rd Canadian/American Conf. on Hydrogeology, Hydrogeology of Sedimentary Basins: Application to Exploration and Exploitation, B. Hitchon, Ed., National Water Well Association, OH (1986) 196–203.

37. A.H. Truesdell and B.F. Jones, WATEQ, A computer program for calculating chemical equilibria of natural waters, J. Res., U.S. Geological Survey, 2 (1974).

38. J.W. Ball, E.A. Jenne and M.N. Cantrell, WATEQ3: A geochemical model with uranium added, U.S. Geological Survey, Open File Report 81-1183 (1981).

39. A.R. Felmy, D. Girvin and E.A. Jenne, MINTEQ: A computer program for calculating aqueous geochemical equilibria, U.S. Environmental Protection Agency, Athens, GA (1984).

40. S.E. Drummond Jr., "Boiling and mixing of hydrothermal fluids: Chemical effects on mineral precipitation," unpublished Ph.D. thesis, Pennsylvania State Univ. (1981).

41. S.E. Drummond Jr. and H. Omoto, Chemical evolution and mineral deposition in boiling hydrothermal systems, Economic Geology, 80 (1984) 126–147.

42. M.H. Reed, Calculation of multicomponent chemical equilibria and reaction processes in systems involving minerals, gases and an aqueous phase, Geochim. et Cosmochim. Acta, 46 (1982) 513–528.

43. M.H. Reed and N. Spycher, Calculation of pH and mineral equilibria in hydrothermal waters with application to geothermometry and studies of boiling and dilution, Geochim. et Cosmochim. Acta, 48 (1984) 1479–1492.

44. E.H. Perkins, T.H. Brown and R.G. Berman, Software for the computation and graphical display of intensive variable phase diagrams, Proceedings Lawerence Livermore National Workshop in Geochemical Modelling, Fallen Leaf Lake, CA, Sep (1986).

45. H.J. Abercrombie and I.E. Hutcheon, Remote monitoring of water-rock-bitumen interactions during steam-assisted heavy oil recovery, 5th International Symposium on Water-Rock Interaction, Extended Abstracts. Int. Assoc. of Geochem. and Cosmochem. (1986) 1–4.

46. L.M. Cathles, M. Schoell and R. Simon, CO_2 generation during steam flooding: A geological based kinetic theory that includes carbon isotope effects and application to high-temperature steam floods; Society Pet. Eng. Paper 16267, presented at SPE Symposium on Oil Field Chemistry, San Antonio, TX, Feb (1987).

47. D.R. Watkins, L.J. Kalfayan, D.J. Watanabe and J.A. Holm, Preventing gravel pack and formation dissolution during steam injection, Soc. Pet. Eng. Paper 13660, presented at California Regional Meeting, Bakersfield, CA, Mar 27–29 (1985).

48. B.E. Roberts and P.R. Tremaine, Vapour liquid equilibrium calculations for dilute aqueous solutions of CO_2, H_2S, NH_3 and $NaOH$ to 300°C, Can. J. of Chem. Eng, 63 (1985) 294–300.

49. R.W. Henley, A.H. Truesdell and P.B. Barton Jr., Fluid-mineral equilibria in hydrothermal systems, Reviews in Economic Geology, Soc. of Ec. Geologists, Chelsea, MI, 1 (1984).

50. Y.K. Kharaka and R.H. Mariner, Chemical geothermometers and their application to formation waters from sedimentary basins, in S.E.P.M. Special Publication "Thermal history of sedimentary basins," N.D. Naeser and T.H. McCulloh, Eds., Springer, NY (1988) 99–117.

51. R.O. Fournier, Silica in thermal water: Laboratory and field investigations, in Proceedings of the International Symposium on Hydrogeochemistry and Biogeochemistry, Japan, 1970, The Clark Company, Washington, D.C., (1973) 122–139.

52. R.O. Fournier and J.J. Rowe, Estimation of underground temperatures from the silica content of water from hot water from hot springs and wet-steam wells, Am. J. of Sci, 264 (1966) 685–697.

53. S. Arnorsson, E. Gunnlaugsson and H. Svavarsson, The chemistry of geothermal waters in Iceland. III. Chemical geothermometry in geothermal investigation, Geochim. Cosmochim. Acta, 47 (1983) 567–577.

54. R.O. Fournier and A.H. Truesdell, An empirical Na-K-Ca chemical geothermometer for natural waters, Geochim. et Cosmochim. Acta, 37 (1973) 1255–1275.

55. R.O. Fournier and R.W. Potter II, A magnesium correction for the Na-K-Ca geothermometer, Geochim. et Cosmochim. Acta, 43 (1979) 1543–1550.

56. M. Saltuklaroglu, Monitoring reservoir temperature by means of produced water chemistry in steam based recovery processes, Pet. Soc. Can. Inst. Min., Paper no. 85-36-31 (1985).

57. C. Fouillac and G. Michard, Sodium/lithium ratio in water applied to geothermometry of geothermal reservoirs, Geothermics, 10 (1981) 55–70.

58. W.F. Giggenbach, Geothermal gas equilibria, Geochim. et Cosmochim. Acta, 44 (1980) 2021–2032.

59. A.H. Truesdell and J.R. Hulston, Isotopic evidence on environments of geothermal systems, in "Handbook of environmental isotope geochemistry, v. 1, the terrestrial environment," P. Fritz and J. Ch, Fontes, Eds., Elsevier, Amsterdam, (1980) 179–226.

60. T.S. Bowers, K.J. Jackson and H.C. Helgeson, "Equilibrium activity diagrams for coexisting minerals and aqueous solutions at pressures and temperatures to 5 kb and 600°C," Springer-Verlag, New York (1984).

61. T.H. Brown, R.G. Berman and E.H. Perkins, GEO-CALC: Software package for calculation and display of pressure-temperature-composition diagrams using an IBM or compatible personal computer, Computers and Geosciences 14 (1988) 279–289.

62. V.J. Hurst and A.C. Kunkle, Dehydroxylation, rehydroxylation and stability of kaolinite, Clays and Clay Minerals, 33 (1985) 1–14.

63. H.W. Nesbitt, Estimation of the thermodynamic properties of Na- Ca- and Mg- beidelites, Canadian Mineralogist, 15 (1977) 22–30.

64. B. Hitchon, Hydrogeology of the Cold Lake study area, Alberta, Canada, data base, Section I: Phanerozoic data, Alberta Geological Survey, Alberta Research Council (1985).

65. B. Hitchon, G.K. Billings and J.E. Klovan, Geochemistry and origin of formation waters in the Western Canadian Sedimentary Basin III. Factors controlling chemical composition, Geochim. et Cosmochim. Acta, 35 (1973) 567–598.

66. A.G. Collins and C.C. Wright, Enhanced oil recovery injection waters, in "Developments in petroleum science 17A, enhanced oil recovery, I. fundamentals and analyses," E.C. Donaldson, G.V. Chilingarian and T.F. Yen, Eds., Elsevier (1985) 151–221.

67. J. Kus and R. Card, Produced water reuse considerations for in situ recovery: A case development, J. Can. Pet. Tech., 23 (1984) 66–70.

68. R.W. Cooke, Aerial sweep efficiency determination in steam-drive projects utilizing chemical tracers, paper presented at international Symposium on Oilfield and Geothermal Chemistry, Denver, CO, Jun 1–3 (1983).

69. R.P. Heisler, Interpretation of radioactive tracer results in a steam drive project, SPE Reservoir Engineering, 3 (1988) 281–287.

70. B. Russell and G.W. Bird, Interpreting reservoir performance using produced water chemistry, Paper no. 72, 4th Unitar/UNDP International Conference on Heavy Crude and Tar, Edmonton, Aug (1988).

71. C. Reichert, B. Fuhr and M. Rawluk, Water soluble organics in waste waters from oil sand and heavy oil field pilot plants, 69th Canadian Chemical Conference, Saskatoon, Sask., Paper EN-E2-4 (1986).

72. J.A. Boon, An experimental-statistical study of mineral transformation during in situ recovery of bitumen from various oil sand deposits in Alberta, Canada, Proc. 3rd Int. Symp. Water-Rock Interaction, Edmonton, Alberta (1980).

73. J.A. Boon and B. Hitchon, Application of fluid-rock reaction studies to in situ recovery from oil sand deposits Alberta, Canada – II. mineral transformations during an experimental-statistical study of water-bitumen-shale reactions, Geochim. et Cosmochim. Acta, 47 (1983) 249–257.

74. R.F. Krueger, An overview of formation damage and well productivity in oilfield operations, J. Pet. Tech, 38 (1986) 131–152.

75. A.A. Levinson and R.W. Vian, The hydrothermal synthesis of montmorillonite group minerals from kaolinite, quartz and various carbonates, Am. Min., 51 (1966) 495–498.

76. P. Bayliss and A.A. Levinson, Low temperature hydrothermal synthesis from dolomite or calcite, quartz and kaolinite, Clays and Clay Minerals, 19 (1971) 109–144.

77. J.A. Boon, T. Hamilton, L. Holloway and B. Wiwchar, Reaction between rock matrix and injected fluids in Cold Lake oil sands — potential for formation damage, Paper 82-33-37 presented to Petroleum Society of C.I.M. at 33rd Annual Technical Meeting in Calgary, Jun 6–9 (1982).

78. W.D. Gunter and G.W. Bird, CO_2-production in tar sand reservoirs under in-situ steam conditions: reactive calcite dissolution, Chemical Geology, 70 (1988) 301–311.

79. Sedimentology Research Group, The effects of *in situ* steam injection on Cold Lake oil sands, Bull. Can. Petr. Geol., 29 (1981) 447–478.

80. I. Hutcheon, A review of artificial diagenesis during thermally enhanced recovery, Clastic Diagenesis: American Association of Petroleum Geologists Memoir 37, D.A. McDonald and R.C. Surdam, Eds., (1984) 413–429.

81. R. Lefebvre and I. Hutcheon, Mineral reactions in quartzose rocks during thermal recovery of heavy oil, Lloydminster, Saskatchewan, Canada: Applied Geochemistry, 1 (1986) 395–405.

82. B.J. Tilley and W.D. Gunter, Mineralogy and water chemistry of the burnt zone from a wet combustion pilot in Alberta, Bull. Can. Pet. Geol., 36 (1988) 25–38.

83. J.J. Hemley, P.B. Hostetler, A.J. Gude and W.T. Mountjoy, Some stability relations of alunite, Economic Geology, 64 (1969) 599–612.

84. R.O. Fournier and R.W. Potter II, An equation correlating the solubility of quartz in water from 25° to 900°C at pressures up to 10,000 bars, Geochim. Cosmochim. Acta, 46 (1982) 1969–1973.

85. R.H. Busey and R.E. Mesmer, Ionization equilibria of silicic acid and polysilicate formation in aqueous chloride solutions to 300°C, Inorganic Chem., 16 (1977) 2444–2450.

86. M.G. Reed, Gravel pack and formation sandstone dissolution during steam injection, Soc. Pet. Eng. Paper 8424 presented at 54th Annual Tech. Conf., Las Vegas, NV (1979).

87. L.L. McCorriston, R.A. Demby and E.C. Pease, A study of reservoir damage produced in heavy oil formations due to steam injection, 56th Annual Fall Tech. Conf. & Exhib., Soc. Pet. Eng. AIME, San Antonio, TX, SPE Paper 10077, Oct. (1981).

88. T. Stone, J. Boon and G.W. Bird, Modelling silica transport in large-scale laboratory experiments, J. Can. Pet. Tech., 25 (1985) 1–7.

89. C.E. Weaver, Geothermal alteration of clay minerals and shales: Diagenesis, Technical report to the Office of Nuclear Waste Isolation, Columbus, OH (1979).

90. E.C. Donaldson, G.V. Chilingarian and T.F. Yen, "Enhanced oil recovery 1. Fundamentals and analysis," Elsevier Science Publishers B.V., Amsterdam, The Netherlands, (1985).

91. W.G. Anderson, Wettability literature survey-Part 1: Rock/oil/brine interactions and the effects of core handling on wettability, J. Pet. Tech, 38 (1986) 1125–1144.

92. W.G. Anderson, Wettability literature survey-Part 2: Wettability measurement, J. Pet. Tech, 38 (1986) 1246–1262.

93. W.G. Anderson, Wettability literature survey-Part 3: The effects of wettability on the electrical properties of porous media, J. Pet. Tech, 38 (1986) 1371–1378.

94. W.G. Anderson, Wettability literature survey-Part 4: The effects of wettability on capillary pressure, J. Pet. Tech, 39 (1987) 1283–1300.

95. W.G. Anderson, Wettability literature survey-Part 5: The effects of wettability on relative permeability, J. Pet. Tech, 39 (1987) 1453–1468.

96. W.G. Anderson, Wettability literature survey-Part 6: The effects of wettability on waterflooding, J. Pet.Tech., 39 (1987) 1605–1622.

97. T.W. Muecke, Formation fines and factors controlling their movement in porous media, J. Pet Tech., Feb (1979) 144–150.

98. C.M. Cerda, Mobilization of kaolinite fines in porous media, Colloids and Surfaces, 27 (1987) 219–241.

99. K.C. Khilar, "The water sensitivity of Berea Sandstone," Ph.D. thesis, Univ. of Michigan, University Microfilms International (1981).

100. K.C. Khilar and H.S. Fogler, Permeability reduction in water sensitivity of sandstones, in "Surface phenomena in enhanced oil recovery," Plenum Publishing Co., New York City, Soc. Pet. Eng. and DOE, (1981).

101. K.C. Khilar and H.S. Fogler, Water sensitivity of sandstones, Soc. Pet. Eng. J., 23 (1983) 55–64.

102. K.C. Khilar, H.S. Fogler and J.J. Ahluwalia, Sandstone water sensitivity: Existence of a critical role of salinity decrease for particle capture, Chem.

Eng. Sci., 38 (1983) 789–800.

103. C. Gruesbeck and R.E. Collins, Entrainment and deposition of fines particles in porous media, Soc. Pet. Eng. J. 22 (1982) 847–856.

104. J. Happel, Viscous flow in multiparticle systems: Slow motion of fluids relative to beds of spherical particles, AIChE J., 4(2) (1958) 197.

105. H.C. McLaughlin, E.A. Elphingstone and B. Hall, Aqueous polymers for treating clays in oil and gas producing formations, Soc. Pet. Eng. Paper 6008, presented at 51st Annual Fall Technical conference and exhibition, Oct 3–6 (1976).

106. R.D. Syndansk, Stabilizing clays with potassium hydroxide, J. Pet. Tech., Aug (1984) 1366–1374.

107. F.W. Peters and C.M. Stout, Clay stabilization during fracturing treatments with hydrolyzable zirconium salts, J. Pet. Tech., Feb (1977) 187–194.

108. M.G. Reed, Stabilization of formation clays with hydroxy-aluminum solutions, J. Pet. Tech. (1972) 860–864.

109. J. Hower, Shale diagenesis, Chap. 4 in "Clays and the resource geologist," Mineralogical Assoc. Canada Short Course Handbook, Vol. 7, F.J. Longstaffe, Ed. (1981).

110. J.J. Day, B.B. McGlothlin and J.L. Huitt, Laboratory study of rock softening and means of prevention during steam or hot water injection, J. Pet. Tech., 19 (1967) 703–711.

111. J.D. Rimstidt and D.R. Cole, Geothermal mineralization i: The mechanism of formation of the Beowawe, Nevada, siliceous sinter deposit, Amer. J. Sci., 283 (1983) 861–875.

10

FLUID FLOW IN POROUS MEDIA

T.R. Heidrick
V.S.V. Rajan
M. Polikar*
C. Cerda**

Oil Sands and Hydrocarbon Recovery Department
Alberta Research Council

* Presently at BP Resources Canada Limited, Bonnyville, Alberta
** Presently at IRSST, Montreal, Quebec
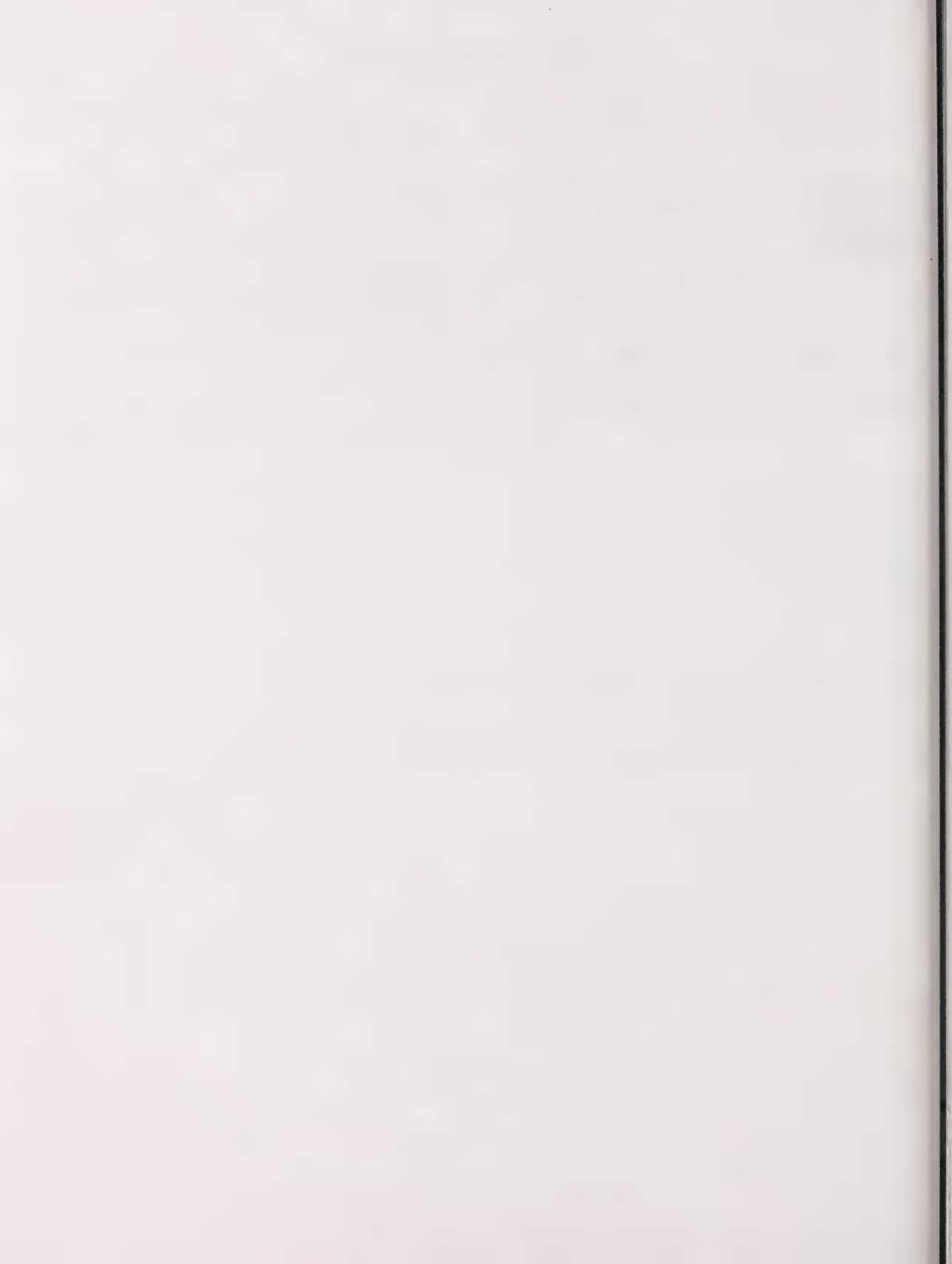
EQUATION OF MOTION (DARCY'S LAW) FOR SINGLE-PHASE FLOW

The equation generally used to describe the flow of a fluid through a porous medium is based on experiments conducted by the French engineer, Henry Darcy [1]. These experiments, conducted in a sand pack, are shown schematically in Figure 1.
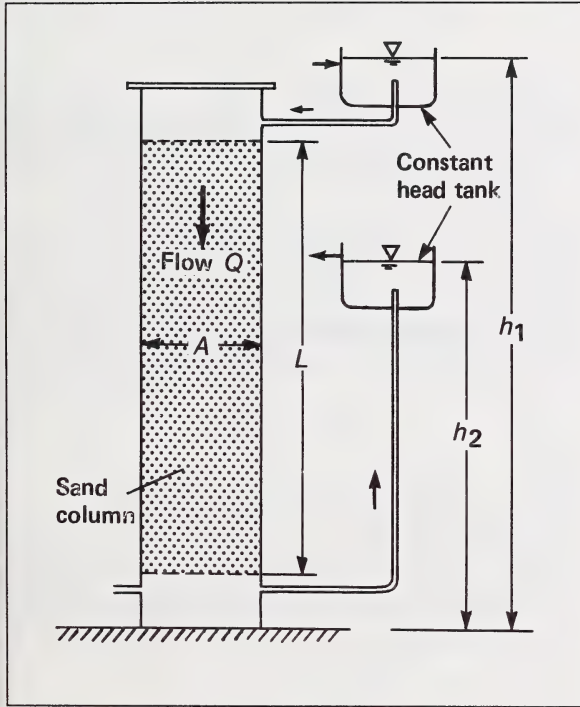
Figure 1. Darcy's experiment.

Darcy observed that

$$Q = K \frac{A\left(h_1 - h_2\right)}{L} \tag{1}$$

where K is a proportionality constant called the hydraulic conductivity, and the other terms are defined on the figure. In recent years, Darcy's law has been shown to be the averaged momentum balance equation in which the terms expressing inertia and internal friction in the fluid have been neglected. The hydraulic conductivity has been found to depend on both the physical properties of the flowing fluid and the structure of the pore space. Specifically,

$$K = \frac{k \rho g}{\mu} \tag{2}$$

where k is the permeability of the porous medium which is, in principle, a function of only the pore structure of the medium. It is independent of the nature of the flowing fluid, pressure gradient, and macroscopic dimensions of the medium.

For three-dimensional flow of a single-phase fluid of constant density, Darcy's law can be written as

$$U = \frac{\underline{\underline{K}}}{\mu} \cdot \nabla \Phi \tag{3}$$

For a fluid or gas that has a pressure-dependent density, $\rho = \rho(P)$, Darcy's law takes the form

$$U = -\frac{k \rho}{\mu} \cdot \nabla \Phi^* \tag{4}$$

where,

$$\Phi^* = g z + \int_{P_o}^{P} \frac{dP}{\rho(P)}$$

is called Hubbert's potential.

In the more general case, where $\rho = \rho(C,P,T)$ where C is the concentration of dissolved components and T is temperature, Darcy's law takes the form

$$U = -\frac{\underline{\underline{k}}}{\mu} \cdot \left(\nabla P + \rho g \nabla z\right) \tag{5}$$

The negative sign indicates that flow is in the direction of decreasing potential. For flow along an arbitrary direction s in an isotropic medium, the generalized Darcy's law becomes

$$U_s = \frac{-k}{\mu} \left(\frac{dP}{ds} + \rho g \frac{dz}{ds}\right) \tag{6}$$

The average fluid velocity vector through the pores, V can be calculated from

$$V = \frac{U}{\phi} \tag{7}$$

When the gravitational term is much smaller than the pressure term, a situation often encountered in reservoir engineering, Equation (6) reduces to

$$U_s = -\frac{k}{\mu}\frac{dP}{ds} \qquad (8)$$

Under such conditions, or in horizontal flow, this equation may be integrated, which for the linear case shown in Figure 2a yields

$$Q = \frac{-kA}{\mu}\left(\frac{\Delta P}{L}\right) \qquad (9)$$

(a) linear

(b) radial

Figure 2. Geometries for integrated forms of Darcy's law.

For the horizontal radial flow example illustrated in Figure 2b this integration yields

$$Q = \frac{-2\pi k h}{\mu}\frac{\Delta P}{\ln\left(r_1/r_2\right)} \qquad (10)$$

For a compressible fluid, Q varies with P. However, it may be assumed that

$$PQ = P_m Q_m = \text{constant} \qquad (11)$$

where P_m is the arithmetic average of P_1 and P_2, and, Q_m is the volumetric flow rate at P_m. With this definition, Equations (9) and (10) can be applied by replacing Q with Q_m.

Darcy's law in the various forms presented above is valid as long as the flow is laminar. Such conditions exist as long as the Reynolds number values are below about 10. For an unconsolidated porous medium, the particle Reynolds number is usually defined [2] as:

$$Re_p = \frac{dU\rho}{\mu\left(1-\phi\right)} \qquad (12)$$

Although Darcy's law is empirical, De Wiest [3] showed heuristically, that it can be derived from the Navier-Stokes equation. Alternatively, consider the capillary tube shown in Figure 3. The relationship between flow rate and pressure drop across the tube is given by

Figure 3. Capillary tube model of a porous medium.

Poiseuille's law for laminar flow by

$$Q_j = \frac{\pi r_j^4}{8\mu}\left(\frac{P_1 - P_2}{l_j}\right) = \frac{\pi r_j^4}{8\mu}\left(\frac{\Delta P}{l_j}\right) \tag{13}$$

$$Q_{x_j} = \frac{\pi r_j^4}{8\mu}\frac{\Delta P}{l_j}\frac{L}{l_j} = \frac{\pi r_j^4}{8\mu}\frac{\Delta P}{L}\left(\frac{L}{l_j}\right)^2 \tag{14}$$

Now, if we have n_j tubes of radius r_j, each having the same orientation and length, l_j, then the total component of flow in the x-direction attributable to these tubes is

$$Q_{x_j} = \frac{\pi}{8\mu}\, n_j r_j^4\left(\frac{L}{l_j}\right)^2 \frac{\Delta P}{L} \tag{15}$$

If there are N groups of tubes of different radii r_j, lengths l_j and orientations, then the total component of flow in the x-direction is

$$Q_x = \frac{\pi}{8\mu}\left(\sum_{j=1}^{N} n_j r_j^4\left(\frac{L}{l_j}\right)^2\right)\frac{\Delta P}{L} \tag{16}$$

However, from Darcy's law

$$k = \frac{\pi}{8A}\sum_{j=1}^{N} n_j r_j^4\left(\frac{L}{l_j}\right)^2 \tag{17}$$

Hence, as mentioned previously, permeability depends only on the pore structure. De Wiest's analysis, as outlined by Greenkorn [4], also tends to confirm this point.

PERMEABILITY

As outlined previously, permeability is a measure of the ability a porous medium to conduct fluids. It may be determined either from field tests (drillstem pressure buildup) or in the laboratory. For the latter, permeability is determined by means of an instrument called a permeameter, where flow through a small porous medium fully saturated with a fluid is considered. A constant head difference is applied across the sample

tested, producing a steady flow rate. Permeability is calculated from a direct measurement of all the variables appearing in Darcy's law (Equation (9)). These measurements are straightforward in the case of an incompressible fluid (water or oil). If a gas is employed for determining permeability, both the gas compressibility and the slip phenomenon (Klinkenberg effect) at very low pressures may have to be taken into account [5]. Detailed measurement procedures have been published by the American Petroleum Institute [6] (API). In the absence of direct measurement, several models are available that allow the permeability of a formation to be estimated, if some knowledge of the porosity and grain size distribution is available.

One of the most accepted models employs the concept outlined in the previous section. The pore space is envisaged as equivalent to a bundle of parallel capillaries with a common hydraulic radius and a flow area representing some average pore cross section. This model was first developed by Kozeny [7], refined by Carman [8] and independently derived by Fair and Hatch [9].

Kozeny [7] and Carman [8] give the following equation for estimating the permeability of a porous medium

$$k = \frac{1}{36\, c}\frac{\phi^3}{(1-\phi)^2}\, d^2 \tag{18}$$

This is similar to a model developed by Happel [10].

The general expression

$$k = f(\phi)\, d^2 \tag{19}$$

results where $f(\phi)$ is a function of porosity only. For polydisperse spheres, Equation (18) is written as

$$k = \frac{\dfrac{1}{180}\dfrac{\phi^3}{(1-\phi)^2}}{\sum\left(\dfrac{w_i}{d_i}\right)^2} \tag{20}$$

Figure 4 shows the similarity of this porosity function $f(\phi)$ for both the Happel and the Kozeny-Carman models. The Kozeny-Carman equation has been more widely used for predicting permeability of a porous medium.
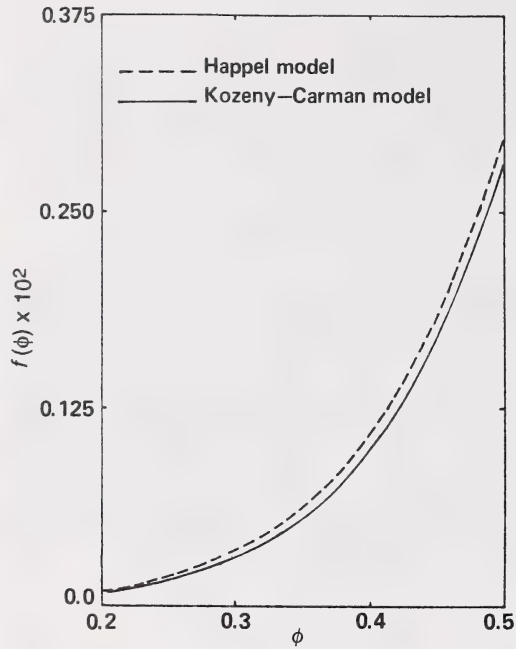
Figure 4. Porosity function $f(\phi)$.
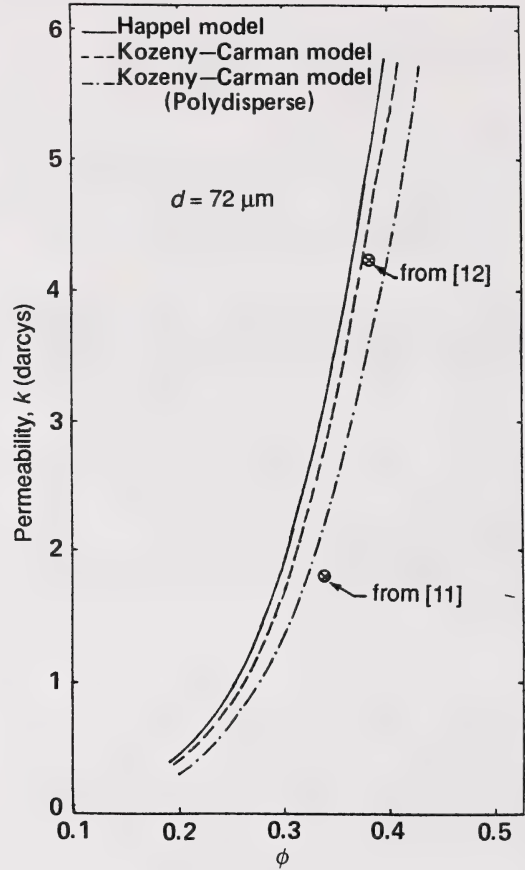
Figure 5. Permeability versus porosity.

Table 1. Particle size distribution of 200-mesh sand sample [11].

Particle size		Fractional weight
Mesh	Microns	(%)
170	88	40.1
200	74	21.8
230	62.5	9.9
270	53	23.9
325	44	1.4
400	37	1.4
400	< 37	1.5

Figure 5 shows the permeability as a function of porosity for the case of 200-mesh sand (mean size $d \sim 72$ μm) reported by Polikar et al. [11] using both the Happel and the Kozeny-Carman models. Also shown are data from Isaacs [12]. The measured porosity difference was due to different confinement pressures applied to the packing. As shown, the predicted values are higher than the actual, owing to the presence of finer fractions. However, with corrections to the model for the polydisperse case, utilizing the data given in Table 1 improves the predictions. In any case, these models appear capable of giving reasonable estimates of the permeability of porous media if both porosity and grain size distribution are known.

MULTIPHASE FLOW

Equations of motion

Oil sands contain two or more component fluids and hence an extension of Darcy's law to multiphase flow is required. This introduces the concept of effective permeability in an isotropic porous medium. Effective permeability to a fluid [13] is a measure of the ability of a porous medium to conduct that fluid when two or more fluid phases (such as oil, gas, and water) are present in the void space. It has been found to depend on the degree of saturation of each of the phases and on various rock and fluid properties [14]. By empirical analogy to Equation (6), Darcy's law for oil, gas, and water may be written for one-dimensional flow in the s-direction at constant densities in an isotropic porous medium:

$$U_o = -\frac{k_o}{\mu_o}\left[\frac{dP_o}{ds} + \rho_o g \frac{dz}{ds}\right] \qquad (21)$$

$$U_g = -\frac{k_g}{\mu_g}\left[\frac{dP_g}{ds} + \rho_g g \frac{dz}{ds}\right] \qquad (22)$$

$$U_w = -\frac{k_w}{\mu_w}\left[\frac{dP_w}{ds} + \rho_w g \frac{dz}{ds}\right] \qquad (23)$$

where k_o, k_g, and k_w are the effective permeabilities to oil, gas, and water, respectively. Effective permeabilities measured in the laboratory are usually normalized by the permeability of the porous medium

$$k_{ro} = \frac{k_o}{k} , \; k_{rg} = \frac{k_g}{k} , \; k_{rw} = \frac{k_w}{k} \qquad (24)$$

These normalized values are called *relative permeabilities*. Further, the concept of relative permeability is only valid for isotropic porous media.

Determination of relative permeability

The concept of effective permeability is an empirical extension of Darcy's equation from single- to multiphase flow through porous media. Since this extension is valid only under restrictive assumptions, great care must be exercised when attempting to extend its area of applicability. There are several methods of determining or estimating relative permeability. These range from analytical models to laboratory experiments to history matching of field production data. This section will primarily deal with the laboratory measurements of relative permeability.

Measurements of relative permeability have been performed since the mid-1930s. Wyckoff and Botset [15] described the relative permeability concept for oil, gas, and water flowing simultaneously through a porous medium. The flow was believed to be governed by fluid properties, the pressure gradient and saturation of each fluid, and the configuration of the medium itself.

Most of the concepts in the experimental approach for determining relative permeability were developed in the 1950s. Two methods, namely the *steady-state* method and the *unsteady-state* or *dynamic displacement* method, are commonly used for direct determination of permeability. Both methods have been extensively used to study two- and three-phase flow situations. Neither method has proven to be free of limitations. In most cases, the measurements are performed on small horizontal core samples.

The steady-state method provides flexibility in controlling changes in saturation and requires that the test specimen be homogeneous. The experiments are difficult because of the presence of end-effects and complications in obtaining accurate saturation measurements. The Penn State method [16] is among the best available. A fixed ratio of fluids is allowed to flow simultaneously through the core sample until saturation and pressure equilibria are established. The saturation distribution is measured with nonintrusive devices and the permeability is calculated from the pressure drop. Several fluid ratios are injected, until equilibrium is attained in the system in each case, to

cover the entire saturation range. With this approach, end- and intermediate-point relative permeabilities and saturations can be measured with confidence for the specific experimental conditions. However, it is a time-consuming method if one wants to obtain a complete set of relative permeability curves.

Dynamic displacement methods, on the other hand, are considered to be more representative of reservoirs where saturation changes may occur too rapidly for equilibrium to be attained. In these experiments, water or gas displaces the oil. Production and pressure drop are monitored continuously during the flooding operation. Although measurements are quick and simpler to make, their interpretation may be questionable under certain circumstances because of inhomogeneities in the porous medium, scaling requirements, and flow instabilities. These unsteady-state methods are based on the Buckley-Leverett [17] frontal advance theory that assumes negligible gravitational and capillary forces as compared to viscous forces. Capillary pressure effects can be minimized as high flow rates are used in displacement experiments.

Welge [18] first proposed a method to calculate the ratio of two-phase relative permeabilities from displacement experiments. He showed that the fractional flow of oil in the outlet stream, f_o, could be determined from the slope of the dimensionless cumulative production curve:

$$f_o = \frac{d(N_P)}{d(W_I)} \qquad (25)$$

When capillary and gravitational effects are negligible, f_o can also be expressed in terms of relative permeabilities

$$f_o = 1 - f_w = \left[1 + \frac{\mu_o\, k_{rw}}{\mu_w\, k_{ro}}\right]^{-1} \qquad (26)$$

The relative permeability ratio is then calculated by combining Equations (25) and (26) at any saturation, S_w, corresponding to

$$S_w = S_{wc} + N_P - W_I f_o \qquad (27)$$

Johnson et al. [19] extended Welge's technique to calculate individual phase relative permeabilities (JBN method). They introduced the concept of relative

injectivity, I_r

$$I_r = \frac{\left(\dfrac{Q}{\Delta P}\right)}{\left(\dfrac{Q}{\Delta P}\right)_{ref}} \qquad (28)$$

where the reference condition is taken as the irreducible water (initial oil) saturation condition. Then, from the slope of the injectivity function, it follows that

$$\frac{f_o}{k_{ro}} = \frac{d\left(\dfrac{1}{W_I I_r}\right)}{d\left(\dfrac{1}{W_I}\right)} \qquad (29)$$

The relative permeability to oil is calculated directly by combining Equations (25) and (29). The relative permeability to water is then calculated from Equation (26). In addition to the production history, the slope of the relative injectivity curve (which is inversely proportional to the pressure drop history) is required to decouple the permeabilities. The slopes are determined analytically from best statistical curve fits to the experimental data. More recently, Jones and Roszelle [20] developed a graphical technique as an alternative to the JBN method. Despite being easy to use, all of the unsteady-state methods apply only under negligible capillary pressure conditions. Therefore, results should be interpreted with great care. Because of these idealized assumptions, several workers [21,22] have resorted to an optimization technique for obtaining relative permeability curves by matching data from laboratory displacement experiments with predictions from a numerical reservoir model.

Limitations in the calculations and interpretation of relative permeability curves using either method cannot solely be attributed to experimental techniques and measurement difficulties. The exact shape of the curves not only depends on the geometry of the pore space occupied by each phase, but also on physical and chemical interactions that may result from the fluid-solid contacts. Relative permeability curves depend on the manner in which an experiment is performed. For a given distribution of fluids in the pore space, there are many possible ways in which the fluids can flow. The flow is known as *drainage* when the saturation of the wetting phase is decreasing and *imbibition* when the

saturation is increasing. The fluid saturation history affects the distribution of fluid phases and causes a hysteresis effect. The magnitude of this hysterisis depends on the degree of consolidation of the porous medium and the pore geometry. Trapping of the nonwetting fluid phase during imbibition also contributes to the hysteresis. The shape of the curves can also be a function of the method used to interpret the production data [21], because of the nonuniqueness of history matching techniques.

The relative permeability properties in a porous medium depend on saturation and saturation history hysteresis, pore size and geometry, and contact angle. These parameters control the capillary pressure characteristics for a given fluid-rock system and therefore the microscopic distribution of the fluids in the pore space. By means of the contact angle, which is a measure of the wettability of a rock surface, a direct dependence of the relative permeability on wettability can be established. Therefore, proper handling of core samples to ensure that wettability is maintained from the reservoir to the laboratory test apparatus is vital in obtaining representative relative permeabilities.

Craig [23] presented typical water-oil relative permeability curves for water-wet and oil-wet formations. These are shown in Figure 6. He also gave rules of thumb to show the differences in the flow properties (Table 2) that indicate the different wettability preferences, noting that rocks with intermediate wettability have some of the characteristics of both water-wet and oil-wet formations.

Morgan and Gordon [24], in their study on the influence of pore geometry on water-oil relative permeability, illustrated that these rock properties controlling pore geometry in a reservoir can also affect the relative permeability characteristics. Microscopic examination revealed that rocks with larger, well-interconnected pores have relative permeability curves of a characteristic shape. Characteristic curves were also determined for rocks with smaller pores. Morgan and Gordon concluded that rocks with large pores have a smaller irreducible water saturation because of the small surface area that leaves a relatively large amount of pore space available for the flow of fluids. This condition allows high end-points to exist and results in a large saturation change during two-phase flow. Rocks with small pores have larger surface areas and a higher irreducible water saturation which leaves little room for the flow of fluids. An initial low relative permeability to oil suggests that very small pores control the flow, and

this also causes saturation changes to be small during two-phase flow.

Relative permeability data for Alberta heavy oils and bitumens

Due to the experimental difficulties encountered in determining relative permeability, a suitable laboratory procedure that eliminates end-effects and resulting saturation gradients is generally used. Usually, the experimental conditions are idealized and simplified by the use of small core plugs, or reconstituted sand cores and refined oils, rather than native reservoir materials. Very few experimental data on relative permeability involving heavy oil or bitumen have been reported in the literature. Most of the data used in reservoir modelling studies were obtained from production data using history matching techniques. The need to establish uniqueness of the estimated relative permeabilities should be noted. Experimental work has been primarily performed at the Petroleum Recovery Institute in Calgary on Lloydminster heavy oils, and at the Alberta Research Council on Athabasca bitumen. More recently, some additional experimental data have been published [25–27] for the various Alberta deposits.

Polikar et al. [11,28] recently presented the results of relative permeability studies in reconstituted Athabasca oil sand cores. The earlier study showed that temperature did not affect the end-point relative permeabilities and saturations in the range of 125 to 250°C. The later work presented steady-state bitumen-water relative permeability curves. A single set of curves was obtained for the experiments performed, with no significant temperature dependence between 125 and 175°C. These curves are shown in Figure 7.

Hirasaki [29] found that the shape of the normalized relative permeability curves and the end-point mobility ratio, M_r, were important adjustable parameters during history matching of an oil displacement process. A graphical comparison of published data on Alberta heavy oil and water relative permeability used in reservoir simulation is presented in Figure 8, where all the curves were brought to the same scale by normalizing the water saturation, and the oil and water relative permeabilities. A wide variation was found, since most data were obtained by history matching the production performance of individual fields.

A similar comparison was also undertaken for experimentally determined heavy oil and water relative permeabilities. Figure 9 presents the published data along with the steady-state data obtained by Polikar et
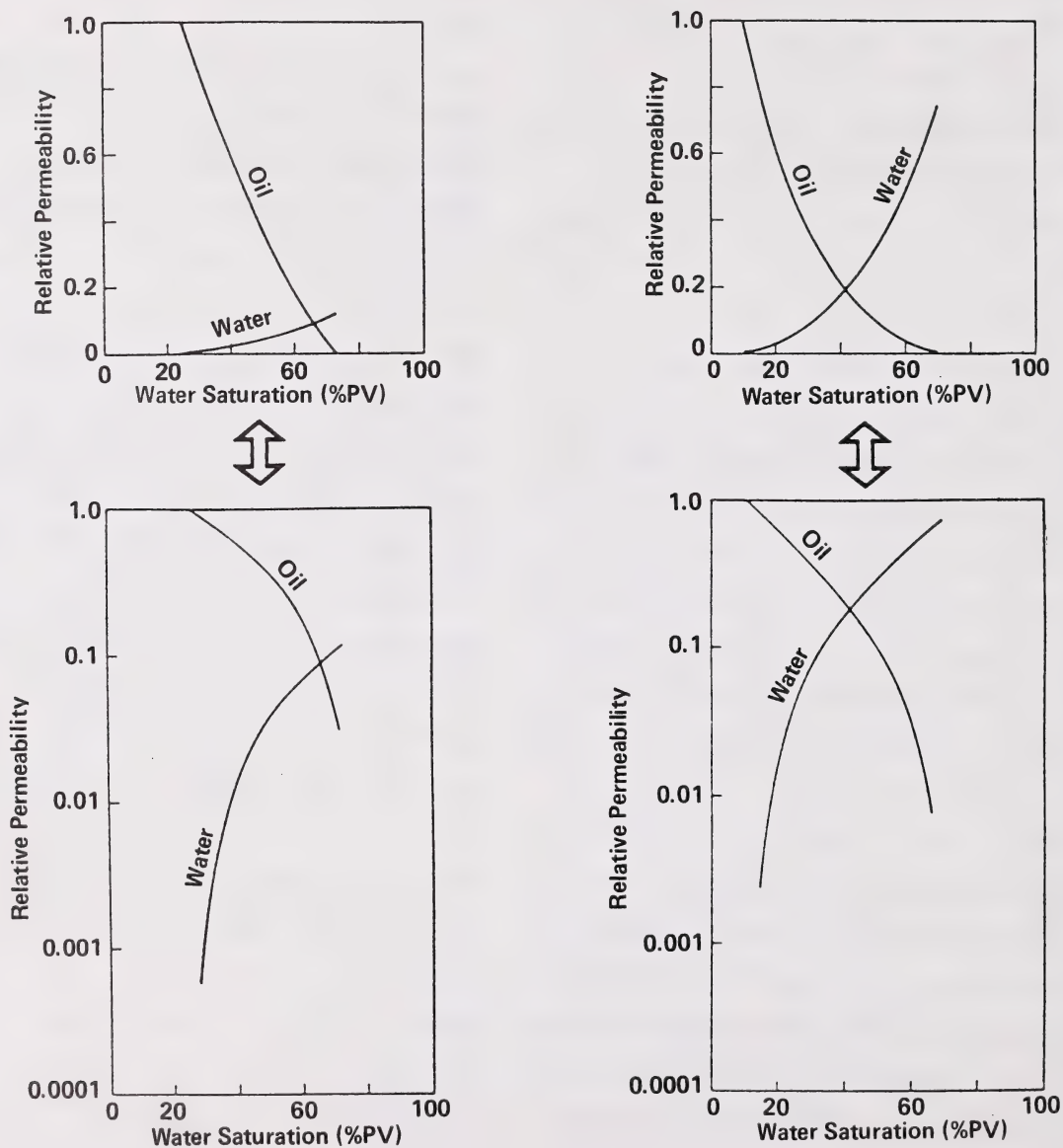
Figure 6. Typical relative permeability curves for strongly water-wet rock [23].

Table 2. Flow properties and associated wettability preferences.

| Flow property | Wettability preference | |
	Water-wet	Oil-wet
Connate water saturation	usually >20 to 25% pore volume	generally <15% pore volume, frequently <10%
Saturation at which oil and water relative permeabilities are equal	>50% water saturation	<50% water saturation
Relative permeability to water at maximum water saturation (flood-out)	generally <30%	>50% and approaching 100%
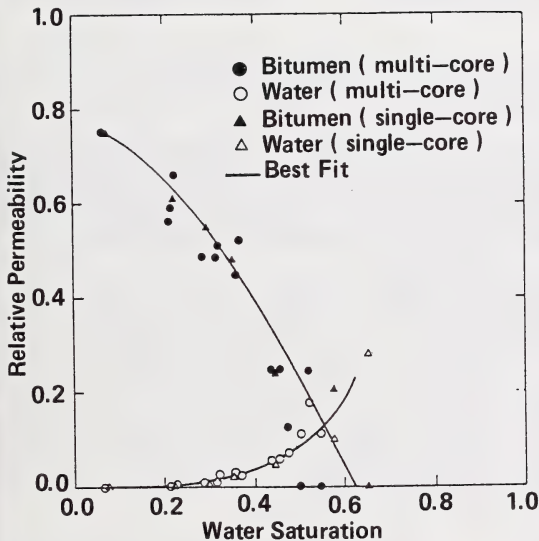
Figure 7. Bitumen-water relative permeability curves [28].
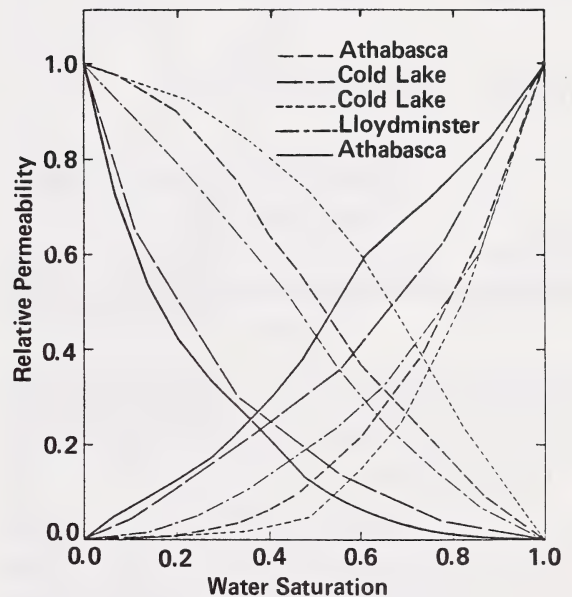
Figure 8. Normalized heavy oil-water relative permeability curves used in reservoir simulations [28].

al. [28] in a normalized form. One set of representative curves was chosen from each of the available published works. In this case also, there was a wide variation in the relative permeabilities for heavy oil and water systems. The range of this variation was very similar to that found for the reservoir simulation curves (see Figure 8). A common trend also emerges from these graphical comparisons: the higher the oil curve the lower the water curve, in most cases.

The relative permeability curves compared above were determined experimentally in clean, extracted or native sand cores, with heavy oil or bitumen and water

as the flowing fluids. In all cases the saturation range for the non-normalized curves never exceeded 0.5, indicating that final recovery under the experimental conditions would not reach 50% of the initial oil-in-place in a laboratory setting. The curves, however, differ considerably. The two heavy oil curves obtained by the steady-state method are the highest [28] and the lowest [25] and their corresponding water curves are the two lowest ones. Polikar used clean unconsolidated sand, whereas the other study used native sand. The oil-water curves that were obtained by history matching of laboratory displacement experiments make up the
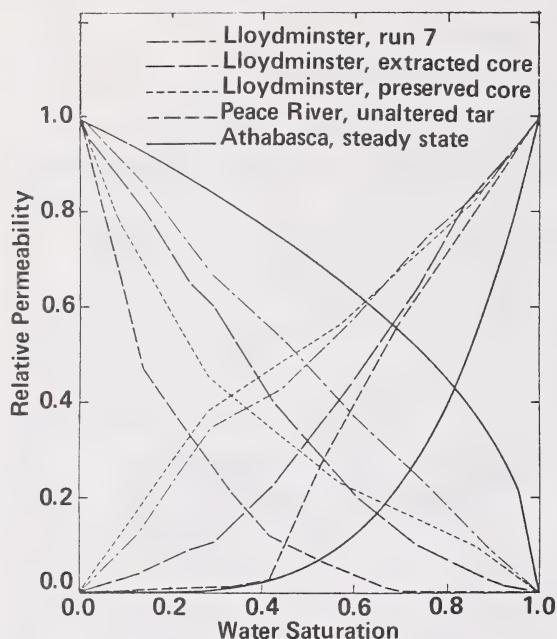
Figure 9. Normalized heavy oil-water relative permeability curves from experiments [28].

remaining portion of Figure 9. The shape of the latter curves was indicated by the history matching procedure, as concave-upward curves are the most commonly found curves in the literature.

As seen earlier, the relative permeability curves may have various shapes, depending on the dominant mechanisms controlling the multiphase flow through porous media. Due to reservoir heterogeneity and local interfacial effects, the dominating features may vary with the location. Therefore, a single set of relative permeability curves may describe a small homogeneous test core, but not an entire reservoir. A range of relative permeability curves may be necessary to describe the recovery of heavy oils, as indicated earlier in the comparative study for Alberta heavy oils and bitumens.

Three-phase relative permeability

While two-phase relative permeabilities are not easy to obtain experimentally, three-phase relative permeabilities are even more difficult to determine [30]. Stone [31] considered two-phase flow conditions to be limits of three-phase flow. He used two sets of two-phase data to predict the relative permeability of the intermediate wetting phase in a three-phase system by

the use of probability concepts and appropriate empirical definitions. In many reservoirs that involve three-phase flow, water-oil-gas flow will be bounded by water-oil flow in the lower portion and by oil-gas flow in the upper portion. The relative permeability to oil in a three-phase water-oil-gas system will therefore be a combination of the relative permeability to oil in a water-oil system and the relative permeability to oil in an oil-gas system. Water and gas three-phase relative permeabilities are, according to Stone, the same as their corresponding two-phase relative permeabilities. In his first model [31], Stone developed an expression relating the three-phase oil relative permeability to the oil saturation. He revised and improved this probability model to yield a new relationship known as Stone's second model [32]:

$$k_{ro} = \left(k_{row} + k_{rw}\right)\left(k_{rog} + k_{rg}\right) - \left(k_{rw} + k_{rg}\right) \quad (30)$$

These probability models strongly depend upon the assumption that there is only one mobile fluid in any channel, and may not account for the total physics of the process. Dietrich and Bondor [33] applied these models to published three-phase data and found them to be only partially successful. They found it necessary to modify Stone's second model for the case where gas-oil relative permeability was measured in the presence of irreducible water. Except for very low values of the oil relative permeability at irreducible water and zero gas saturation, they found their model to qualitatively match the curvature of isoperms of published three-phase flow experiments. Their model is:

$$k_{ro} = \frac{1}{k_{rocw}}\left(k_{row} + k_{rw}\right)\left(k_{rog} + k_{rg}\right) - \left(k_{rw} + k_{rg}\right) \quad (31)$$

This model tends to predict a high residual oil saturation and also, tends to give incorrect values for small k_{rocw}, since $k_{ro} \to \infty$ as $k_{rocw} \to 0$.

Yet another modification to Stone's model has been proposed [34]. This model does not have the restriction of Dietrich and Bondor model. The modified model is:

$$k_{ro} = k_{rocw}\left[\left(\frac{k_{row}}{k_{rocw}} + k_{rw}\right)\left(\frac{k_{rog}}{k_{rocw}} + k_{rg}\right) - \left(k_{rw} + k_{rg}\right)\right] \quad (32)$$

In summary, many models or equations have been proposed over the years for calculating three-phase

relative permeability. They either rely on the use of two-phase experimental data to synthesize three-phase relative permeabilities [32,33], or they directly calculate three-phase relative permeabilities using more easily determined variables such as irreducible water saturation or capillary pressure versus pore size distribution curves. Usually, the estimation is made using one of the following models: Brooks and Corey [35] equations for drainage, Naar et al. [36] equations for imbibition, Land [37] equations for both drainage and imbibition. Ideally, it is still considered advisable to measure two and three-phase relative permeabilities in the laboratory for use in reservoir engineering calculations.

DISPLACEMENT OF OIL

In this section, we will discuss the immiscible displacement of oil by water in a porous medium. This is pertinent to water flood processes for oil recovery. Analysis of this problem requires an understanding of multiphase flow in a porous medium. The concept of relative permeabilities discussed in the previous section will be applied to describe the immiscible displacement problem.

Consider a porous medium where the oil is displaced ahead of the advancing water. If it can be assumed that the region where an appreciable saturation gradient exists is small, the porous medium can be divided into two regions: one containing mainly oil with connate water and the other containing mainly water with immobile, residual oil. The boundary separating these two regions is represented mathematically as a front or discontinuity in saturation. Such immiscible displacement of one fluid by another is a moving boundary problem that has been solved in many ways. In reality, a sharp interface between the displaced and the displacing phases seldom exists, and instead, a distribution of saturations between the two regions described above exists. The first analysis to account for such a saturation distribution behind the flood front was made by Buckley and Leverett [17] who considered the one-dimensional isothermal flow of incompressible, immiscible fluids by neglecting the effects of gravitational and capillary forces. This problem has been discussed in detail by many authors — Bear [5], Craig [23], Collins [38], Scheidegger [39], and Bentsen [40].

Immiscible displacement flow equations

Consider the case of linear displacement in a thin tube of homogeneous, isotropic, porous medium inclined at an angle θ to the horizontal. The flow is upwards along the direction x. The radial pressure and saturation distribution are assumed to be uniform in the small tube cross section. The nonwetting oil phase is displaced by the wetting water phase. For stable, isothermal, incompressible flow, the two-phase flow continuity equation for each phase may be written as follows:

$$A\phi \frac{\partial S_w}{\partial t} + \frac{\partial Q_w}{\partial x} = 0 \qquad (33)$$

and

$$A\phi \frac{\partial S_o}{\partial t} + \frac{\partial Q_o}{\partial x} = 0 \qquad (34)$$

where the saturations are related by

$$S_o + S_w = 1 \qquad (35)$$

Adding Equations (33) and (34) and using Equation (35), the total flow rate is given by:

$$Q_o + Q_w = Q_t = \text{constant} \qquad (36)$$

From Darcy's law for the two phases.

$$Q_w = \frac{-k_w A}{\mu_w} \left(\frac{\partial P_o}{\partial x} + \rho_w g \sin\theta \right) \qquad (37)$$

and

$$Q_o = \frac{-k_o A}{\mu_o} \left(\frac{\partial P_o}{\partial x} + \rho_o g \sin\theta \right) \qquad (38)$$

where the phase pressures are related through the capillary pressure:

$$P_c \left(S_w \right) = P_o - P_w \qquad (39)$$

After some algebraic manipulation of Equations (37) and (38) using Equations (36) and (39), the equation for fractional flow rate of the displacing water phase is

given by:

$$f_w^* = \frac{Q_w}{Q_t} \frac{\left[1 + \frac{Ak_o}{Q_t \mu_o}\left(\frac{\partial P_c}{\partial x} - \Delta\rho\, g \sin\theta\right)\right]}{\left(1 + \frac{k_o \mu_w}{k_w \mu_o}\right)} \tag{40}$$

where,

$$\Delta\rho = (\rho_w - \rho_o) \tag{41}$$

Substituting f_w^* in Equation (33) for constant total flow rate Q_t,

$$-\left(\frac{\partial S_w}{\partial t}\right)_x = \frac{Q_t}{A\phi}\left(\frac{\partial f_w^*}{\partial x}\right)_t \tag{42}$$

Since the capillary pressure P_c is a function of the wetting phase saturation S_w only,

$$\left(\frac{\partial P_c}{\partial x}\right)_t = \left(\frac{dP_c}{dS_w}\right)\left(\frac{\partial S_w}{\partial x}\right)_t \tag{43}$$

Thus, f_w^* is a function of S_w and the gradient $(\partial S_w/\partial x)$ at any time.

Equation (42) is nonlinear and is not easily solved. It can be rewritten as:

$$-\left(\frac{\partial S_w}{\partial t}\right)_t\left(\frac{\partial x}{\partial S_w}\right)_t = \frac{Q_t}{A\phi}\left(\frac{\partial f_w^*}{\partial S_w}\right)_t \tag{44}$$

Since, the saturation S_w is a function of x and t only,

$$\frac{dS_w}{dt}\bigg|_{S_w} = 0 = \left(\frac{\partial S_w}{\partial x}\right)_t\left(\frac{\partial x}{\partial t}\right)_{S_w} + \left(\frac{\partial S_w}{\partial t}\right)_x \tag{45}$$

Combining Equations (44) and (45),

$$\left(\frac{\partial x}{\partial t}\right)_{S_w} = \frac{Q_t}{A\phi}\left(\frac{\partial f_w^*}{\partial S_w}\right)_t \tag{46}$$

The Eulerian form of the flow equation (42) has thus been expressed in the Lagrangian form in Equation (46) where a moving front of saturation S_w is observed as function of time t. This is the principle of the "method

of characteristics" solution of the nonlinear equation [39,42,43]. Numerical integration of Equation (46) with the appropriate boundary condition is employed [41]. Buckley and Leverett [17] in their original paper simplified the problem by neglecting the gravitational and capillary pressure terms. The fractional flow f_w^* is replaced by f_w:

$$f_w = \left(1 + \frac{k_o \mu_w}{k_w \mu_o}\right)^{-1} = \left(\frac{M}{M+1}\right) \tag{47}$$

For many cases of displacement in heavy oil reservoirs of interest, the two phases flow co-currently at very large pressure gradients and the buoyancy effects are small because of the small density difference $\Delta\rho$. Hence, the assumptions of Buckley and Leverett are not unreasonable except near the displacement front, where a large saturation gradient $\partial S_w / \partial x$ may exist. Although the capillary pressure gradient is neglected, it should be noted that the capillary effect in flow is implicit in the mobility ratio used in the flow equation. It is clear that f_w is a function of S_w only with the oil-water viscosity ratio as a parameter. Thus, Equation (46) can be written in a quasi-linear form

$$\frac{dx}{dt}\bigg|_{S_w} = \frac{Q_t}{A\phi}\left(\frac{df_w}{dS_w}\right) \tag{48}$$

Equation (48) can be integrated easily to give the location of the front

$$x(t)\bigg|_{S_w} - x(0)\bigg|_{S_w} = \frac{W(t)}{A\phi}\left(\frac{df_w}{dS_w}\right) \tag{49}$$

where

$$W(t) = \int_0^t Q_t\, dt \tag{50}$$

Equation (49) gives the saturation distribution at any time given the initial distribution and $f_w(S_w)$. This is usually done graphically, since the relative permeability function is available in graphical form unless approximate functional relationships are used.

In practice, most fractional flow curves exhibit two water saturations having the same slope df_w / dS_w. This is because of the maxima that occur in df_w / dS_w (see

Figure 10). The consequence is that two different saturations would exist at the same location and at the same time. This situation worsens when an initial saturation distribution exists prior to flooding, resulting in triple-valued saturation distribution over a length of the porous medium (see Figure 11). Buckley and Leverett recognized the unreality of this solution and suggested a discontinuous saturation distribution. From material balance considerations, the discontinuity location x_f is such that the shaded area between the unreal continuous solution and the discontinuous line are equal. They also suggested that including capillary pressure gradient (exceedingly large at the saturation discontinuity) in the fractional flow curve would result in the plane of saturation discontinuity being converted into a zone of more gradual transition in saturation. The nature of this transition zone would be dependent on the flow rate.

The critical or cutoff saturation at which discontinuity occurs, is determined as shown in Figure 10. The procedure involves drawing a tangent from the point $(0, S_{wc})$ to the $f_w(S_w)$ curve. As discussed earlier, this ensures that the shaded areas on either side of the discontinuity in Figure 11 are equal.

In the solution using the method of characteristics, triple-valued saturation profiles do not appear [41,42]. A thorough discussion of the meaning of the triple-value in noncapillary Buckley-Leverett theory has been given by Cardwell [42]. Bentsen [40] has also solved the fractional flow equation with capillarity.

Stability of displacement flow

We have so far discussed some aspects of frontal displacement in a stable flow situation. However, one important phenomenon associated with the frontal movement, which is very much dependent on the oil-water mobility ratio, is the frontal stability. This is usually associated with the formation of so-called viscous fingers. In a situation where the displacing fluid is more mobile and wetting than the displaced nonwetting fluid, a perturbation occurs when the frontal surface plane approaches a small more permeable region in a local microscopic heterogeneity of the porous medium. The displacing fluid will move more rapidly in this region. This gives rise to flow irregularities which grow rapidly in the form of fingers extending from the front. In general, the displacement front is stable if $M_r \leq 1$, while for $M_r \geq 1$, the front is unstable. Gravity tends to minimize the effect and has a stabilizing effect depending on the flow direction. The capillary forces act mainly normal to the fingers and tend to equalize saturations, thus having a stabilizing effect on the displacement front. This pore-scale or microscopic heterogeneity is a major factor in the onset of instability of immiscible displacement flows. Whether the fingers grow and cause flow instability depends on the balance between viscous, gravitational, and capillary forces. Figure 12 shows a schematic of the instability or viscous fingering phenomenon.

Viscous fingering and stability of immiscible displacement flows in porous media have been analyzed by Bear [5], van Meurs and van der Poel [44], Chuoke et

Figure 10. Fractional flow as a function of saturation of the wetting phase.
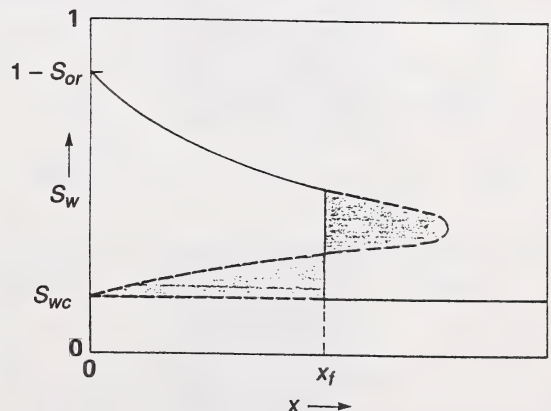
Figure 11. Buckley-Leverett solution for linear immiscible displacement equation and saturation discontinuity.

al. [45], and Bentsen [46]. Bentsen [46] has developed a criterion for stability as follows:

$$I_{sr} \leq \pi^2 \qquad (51)$$

where, I_{sr} = instability number, a function of capillary and buoyancy forces, mobility ratio, and geometry.

In a recent paper, Skaugen [47] gives an analytical model for viscous fingering. He also developed an expression for the stability criterion. He has shown that the critical flow rate for the onset of instability is:

$$Q_t > \frac{A}{(M_r - 1)} \frac{k_{rw}}{\mu_w} g \Delta\rho \sin\theta \qquad (52)$$

This shows that the displacement will always be unstable for horizontal flows if $M \geq 1$. In the Buckley-Leverett type of displacement with no shock front or saturation discontinuities (when $M_r \geq 1$), the saturation gradients along the length of the porous medium will decrease with time and the effects of capillary forces, $dP_c(S_w)/dx$ will also decrease.

A very brief introduction to viscous oil displacement by water and the stability of such flows has been given in this section. The cited references should give a more complete overview of this subject.
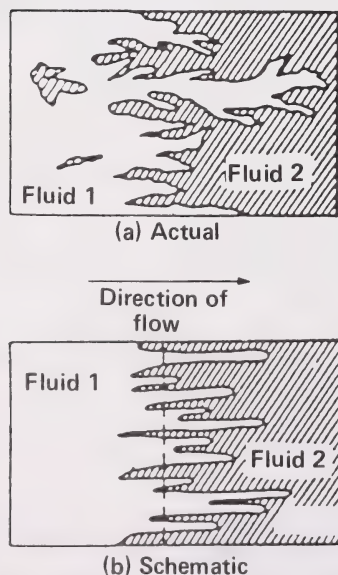
Figure 12. Instability at a moving interfaces.

STEAM DISPLACEMENT FRONTS

Bituminous oils have very high viscosities under reservoir conditions and will not flow through the reservoir sand porous matrix. Also, the oil deposit is too deep and can be efficiently mobilized and recovered only by in situ methods. These methods (thermal or nonthermal) involve reducing the viscosity of the oil in place. Thermal methods involve the use of steam, combustion, or electricity to heat the oil. Prats [48] has discussed the various thermal recovery methods in detail. This section deals with the use of steam in bitumen recovery.

Oil recovery methods with steam

Steam processes can be divided into two categories: cyclic steam stimulation (huff and puff) and steam flooding (steam drive). Figures 13 and 14 schematically show the mechanisms of the above two processes, respectively. In the former case, high pressure steam is
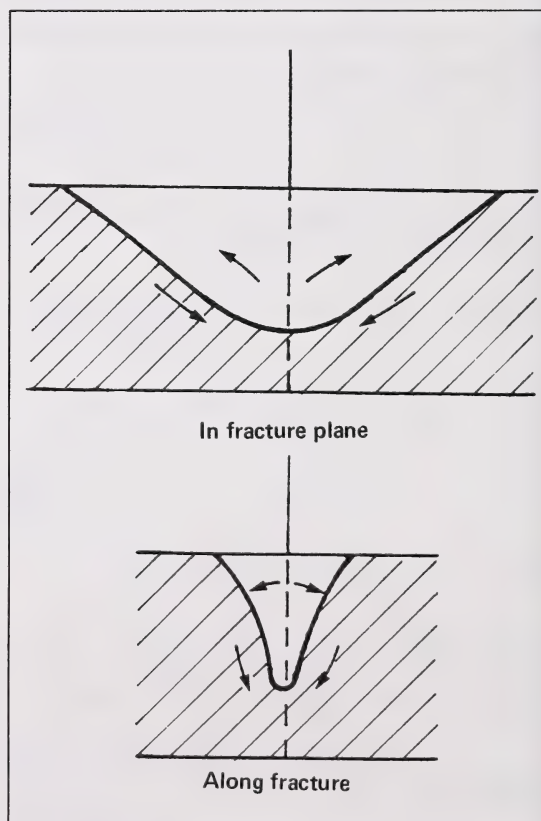
Figure 13. Cyclic steam stimulation [49].
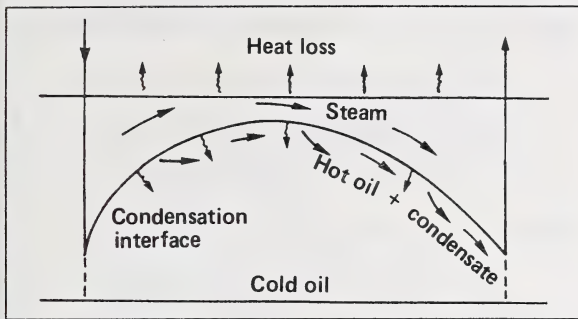
Figure 14. Steam flooding [49].

Figure 15. Gravity drainage concept [49].

injected into a reservoir well, soaked for a period of time and the same well is used for production. The initial steam injection fractures the reservoir, usually in a vertical plane. The injected steam heats the reservoir on either side of the fracture and mobilizes the oil. The thermal expansion of the oil also disrupts the sand and increases its permeability. During the production cycle, condensate water and mobilized oil drain below the steam saturated zone to the wellbore and are pumped to the surface. The steam zone expands and cools as the fluids are produced. The injection and production cycles are repeated. The steam chamber grows sideways and along the fracture plane with repeated cycles.

Steam flooding or drive uses separate wells for injection and production. The injected steam flows along a natural or artificial high-permeability path between the wells. The condensate water and steam carry the oil to the production well. Because of buoyancy effects, the steam tends to override the reservoir and leave the oil below resulting in low produced oil-to-steam ratio. Steam stimulation is used to obtain initial production and communication.

The steam processes have limited displacement efficiency. The flow rate of steam is generally high which can disperse the mobilized oil into droplets leaving a significant amount of oil behind. Since the oil and the hot fluids flow in a co-current fashion and since the other fluids (mainly hot water) are much less viscous than the oil, viscous fingering can also occur, lowering the displacement efficiency.

An alternate procedure for steam recovery is the steam or thermally assisted gravity drainage process discussed by Butler et al. [50]. Figure 15 illustrates this process. The mobilization of oil by steam heating
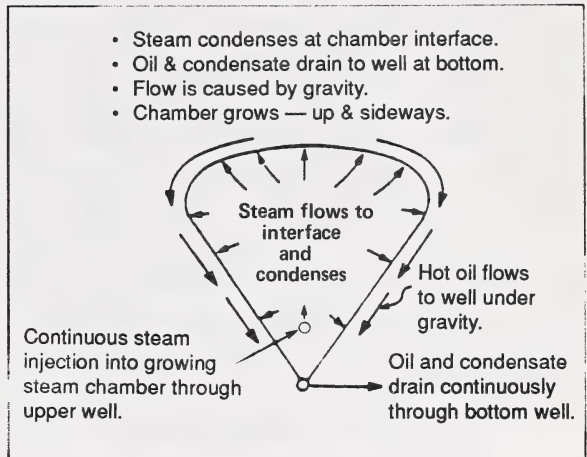
is the same as in the other steam process. The main feature is that the steam with expanding steam chamber rises upwards towards the periphery. The condensate and oil drain by gravity countercurrent to the rising steam towards the horizontal producer well near the base of the reservoir. Since the flow path of the oil and steam are separate, the displacement is slow. However, the fingering problem is eliminated, thereby improving the oil recovery efficiency. The steam chamber growth is limited by the upper and lateral boundaries of the reservoir. Multiple parallel horizontal wells can also be used to improve recovery efficiency (see Figure 16).
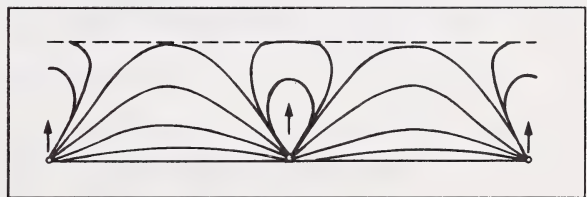
Figure 16. Steam chamber growth above adjacent horizontal wells [49].

Oil recovery models

We have seen that steam pressure cycling and gravity drainage are two mechanisms by which a steam front can advance in the immobile oil sand. In the steam drive process, the injected steam may tend

to override the oil zone and heat the formation from the top, causing displacement of oil (see Figure 17a). Even if steam gravity override does not occur, once steam breaks through at the producing well, the steam zone expands (from the initial communication path) perpendicular to the flow direction. In both these cases, the mobilized bitumen layer is dragged or ablated away by the steam condensate along the steam-oil interface. Kumar et al. [51] present a simple thermal conduction mechanism for the steam override model of a steam flooding process. The rate of downward movement (see Figure 17a) of the steam oil interface is given by:

$$\frac{dh_s}{dt} = \frac{Q_o(t)}{\phi \left(S_{oi} - S_{or} \right) A} \tag{53}$$

Using Darcy's law for flow through the heated zone from the injection to the production well,

$$Q_o(t) \propto \left(\Delta P_{i-p} \right) k_o \int_{h_s}^{h} \frac{dz}{\mu_o} \tag{54}$$

The proportionality constant to be used in Equation (54) depends on the configuration of the wells.

It is assumed that sufficient steam is injected to maintain a constant-temperature steam zone.

As stated earlier, the steam drive process is not as simple and is more an ablation rather than a displacement process, where the mobilized oil is eroded or dragged away from the interface by the steam and condensate towards the producer. Edmunds [54] has analyzed this problem in detail. Figure 17b shows the steam drag process. The production rate of oil is given by:

$$Q_o = h_s \sqrt{\frac{2\phi \left(S_{oi} - S_{or} \right) k_o \, \Delta P_{i-p} \, \alpha}{\mu_o m}} \tag{55}$$

where,

$$m = \ln \left(\frac{\mu_o(T_s)}{\mu_o(T)} \right) \tag{56}$$

Gravitational force tends to alter the shape of the steam zone or front.

References [53] through [57] deal with the analytical treatment of the gravity drainage process based on the analysis by Butler et al. [50]. Butler [58] analyzed the rise of interfering steam chambers from parallel horizontal wells. The expression for oil production rate by gravity drainage is very similar to that in Equation (55) except that the pressure drop ΔP_{i-p} is replaced by $g\Delta h_o$, where Δh_o is the change in the oil zone thickness. The approximate solution using Butler's "Tandrain" concept for the oil production rate as a function of time is given in a dimensionless form as follows:

$$Q^* = \sqrt{\frac{3}{2} - t^{*2} \sqrt{\frac{2}{3}}} \tag{57}$$

where Q^* and t^* are the dimensionless production rate and time respectively [53].
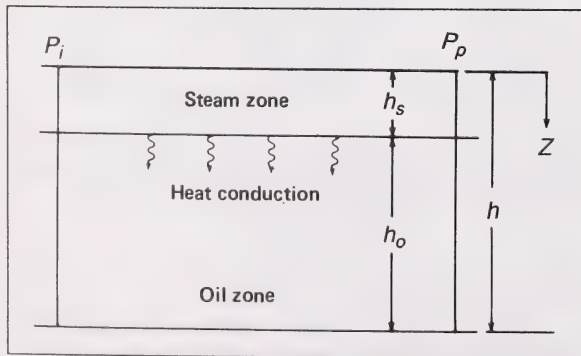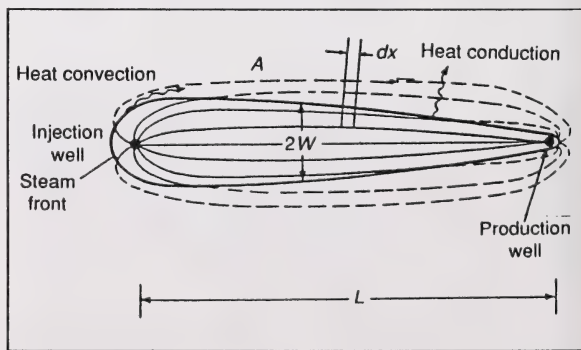
Figure 17. (a) A gravity override model of steam flooding [51]; (b) Steam flood in oil sands at breakthrough [52].

LIST OF SYMBOLS

A	area of cross section normal to flow (m^2)
A_j	area of cross section of capillary tube j (m^2)
c	Kozeny constant to Equation (18) = 5, (–)
C	concentration (kg/m^3)
d	particle diameter (µm)
d_i	particle diameter of class i (µm)
$f(\phi)$	function defined in Equation (19), (–)
f_w^*	fractional flow function = (Q_w/Q_t), (–)
f_w^*	modified fractional flow function defined in Equation (40), (–)
g	gravitational acceleration = 9.81 (m/s^2)
h_1, h_2	fluid head (m)
h	height (m)
I_r	relative injectivity defined in Equation (28), (–)
I_{sr}	instability number in Equation (51), (–)
$\underline{\underline{k}}$	permeability tensor of second order (m^2)
$\overline{k}$	permeability to a fluid (m^2)
k_r	relative permeability (–)
k_{row}	relative permeability to oil in oil-water system (–)
k_{rog}	relative permeability to oil in gas-oil system (–)
k_{rocw}	relative permeability to oil at connate water saturation (–)
k_{rwro}	relative permeability to water at residual oil saturation (–)
K	hydraulic conductivity (m/s)
l_j	length of capillary tube j (m)
L	length of porous medium along flow direction (m)
m	viscosity coefficient defined in Equation (56), (–)
M	mobility ratio = $(k_{rw} \mu_o / k_{ro}\mu_w)$, (–)
M_r	end-point mobility ratio = $(k_{rwro}\mu_o / k_{rocw} \mu_w)$, (–)
n_j	number of capillary tubes j (–)
N	total number of capillary tubes (–)
N_p	number of pore volumes (–)
P	pressure (Pa)
P_c	capillary pressure = $(P_o - P_w)$, (Pa)
Q	flow rate (m^3/s)
Q_j	flow rate in capillary tube j (m^3/s)
Q_{xj}	flow rate in capillary tube j along x-direction (m^3/s)
Q_x	net flow rate along direction x (m^3/s)
Q^*	dimensionless flow rate (–)
r_j	radius of capillary tube j (m)

Re_p	particle Reynolds number defined in Equation (12), (–)
s	flow direction (m)
S	fluid volumetric saturation (–)
S_{oi}	initial oil saturation (–)
S_{or}	residual oil saturation (–)
S_{wc}	connate water saturation (–)
t	time (s)
t^*	dimensionless time (–)
T	temperature (°C)
U	fluid velocity vector (m/s)
U	specific discharge rate (m/s)
U_s	fluid velocity along direction s (m/s)
V	mean fluid velocity vector in the pores (m/s)
w_i	weight fraction of particles of size d_i (–)
W	total fluid volume (m^3) or pore volumes
x,z	orthogonal directions (m); z is positive vertically upwards
x_f	location of displacement front (m)

Greek letters

α	thermal diffusivity of porous medium (m^2/s)
Δ	difference operator (–)
∇	gradient vector operator (–)
ϕ	porosity or void volume fraction (–)
Φ	energy per unit volume of fluid or flow potential (Pa)
Φ^*	Hubbert's potential = $(gz + \int dP/\rho(P))$ (m)
θ	inclination to horizontal (rad)
μ	fluid viscosity (Pa·s)
π	constant = 3.14159 (–)
ρ	fluid density (kg/m^3)
Σ	summation operator (–)

Subscripts

|	
g	gas phase
$i-p$	injection-production
I	injected
o	oil phase
p	particle
P	produced
ref	reference
s	steam
t	total
w	water phase

REFERENCES

1. H. Darcy, "Les fontaines publiques de la ville de Dijon," Victor Dalmont, Paris (1856).
2. R.B. Bird, W.E. Stewart and E.N. Lightfoot, in "Transport phenomena," John Wiley and Sons, New York (1960).
3. R.J.M. De Wiest, "Geohydrology," Wiley, New York (1965).
4. R.A. Greenkorn, "Flow phenomena in porous media," Marcel Dekker, Inc., New York (1983).
5. J. Bear, "Dynamics of fluids in porous media," American Elsevier Publishing Company, Inc., New York (1972).
6. American Petroleum Institute (API), "Recommended practice for determining permeability of porous media," API RP27, Issued by API (1952).
7. J. Kozeny, "Hydraulik," Sitz.-Ber. Wiener Akad., Abt. IIa, 136 (1927) 271-f.
8. P.C. Carman, "Fluid flow through granular beds," Trans. Inst. Chem. Eng. (London) 15 (1937) 150–166.
9. G.M. Fair and L.P. Hatch, Fundamental factors governing the streamline flow of water through sand, J. Amer. Water Works Assoc., 25 (1933) 1551–1565.
10. J. Happel, Viscous flow in multiparticle systems: Slow motion of fluids relative to beds of spherical particles, A. I. Ch. E. J., 4 (1958) 197–201.
11. M. Polikar, F. Ferracuti, V. DeCastro, V.R. Puttagunta and S.M. Farouq Ali, Temperature effects on bitumen-water relative permeabilities, Paper no. 85-36-14 presented at the 36th Annual Technical Meeting of the Petroleum Society of CIM, Edmonton, Alberta, Jun 2–5 (1985).
12. E.E. Isaacs and C. McCarthy, private communication (unpublished data).
13. M. Muskat, "The flow of homogeneous fluids through porous medium," J.W. Edwards, Ann Arbor, MI (1946).
14. M. Honarpour, L. Koederitz and A.H. Harvey, "Relative permeability of petroleum reservoirs," CRC Press Inc., Boca Raton, FL (1986).
15. R.D. Wyckoff and H.G. Botset, The flow of gas-liquid mixtures through unconsolidated sands, Physics, 7 (1936) 325–345.
16. R.A. Morse, P.L. Terwilliger and S.T. Yuster, Relative permeability measurements on small core samples, Oil and Gas J., 46, no. 16 (1947) 109, 113, 115–116, 119–120, 122, 125.
17. S.E. Buckley and M.C. Leverett, Mechanism of fluid displacement in sands, Trans. AIME, 146 (1942) 107–116.
18. H.J. Welge, A simplified method for computing oil recovery by gas or water drive, Trans. AIME, 195 (1952) 91–98.
19. E.F. Johnson, D.P. Bossler and V.O. Naumann, Calculations of relative permeability from displacement experiments, Trans. AIME, 216 (1959) 370–372.
20. S.C. Jones and W.O. Roszelle, Graphical techniques for determining relative permeability from displacement experiments, J. Pet. Tech., 30, no. 5 (1978) 807–817.
21. P.M. Sigmund and F.G. McCaffery, An improved unsteady-state procedure for determining the relative permeability characteristics of heterogeneous porous media, Soc. Pet. Eng. J., 19, no. 1 (1979) 15–28.
22. J.S. Archer and S.W. Wong, Use of a reservoir simulator to interpret laboratory waterflood data, Soc. Pet. Eng. J., 13, no. 6 (1973) 343–347.
23. F.F. Craig, Jr., "The reservoir engineering aspects of waterflooding," SPE monograph, vol. 3, Dallas, TX (1971).
24. J.T. Morgan and D.T. Gordon, Influence of pore geometry on water-oil relative permeability, J. Pet. Tech., 22, no. 10 (1970) 1199–1208.
25. P.J. Closmann, M.W. Waxman and C.T. Deeds, Steady-state tar/water relative permeabilities in Peace River cores at elevated temperature, Paper SPE 14227 presented at the 60th Annual Technical Conference and Exhibition of SPE, Las Vegas, NV, Sep 22–25 (1985).
26. B.B. Maini and J.P. Batycky, The effect of temperature on heavy oil/water relative permeabilities in horizontally and vertically drilled core plugs, Paper SPE 12115 presented at the 58th Annual Technical Conference and Exhibition of SPE, San Francisco, CA, Oct 5–8 (1983).
27. D.W. Bennion, R.G. Moore and F.B. Thomas, Effect of relative permeability on the numerical simulation of the steam stimulation process, J. Can. Pet. Tech., 24, no. 2 (1985) 40–44.
28. M. Polikar, V.R. Puttagunta, S.M. Farouq Ali and V.P. DeCastro, Relative permeability curves for bitumen and water in oil sand systems, Paper no. 86-37-03 presented at the 37th Annual Technical Meeting of the Petroleum Society of CIM, Calgary, Alberta, Jun 8–11 (1986).
29. G.J. Hirasaki, Sensitivity coefficients for history matching oil displacement processes, Soc. Pet. Eng.

J., 15, no. 1 (1975) 39–41.

30. D.N. Saraf, J.P. Batycky, C.H. Jackson and D.B. Fisher, An experimental investigation of three-phase flow of water-oil-gas mixtures through water-wet sandstones, paper SPE 10761 presented at the California Regional Meeting of the Society of Petroleum Engineers, San Francisco, CA, Mar 24–26 (1982).

31. H.L. Stone, Probability model for estimating three-phase relative permeability, J. Can. Pet. Tech., 22, no. 2 (1970) 214–218.

32. H.L. Stone, Estimation of three-phase relative permeability and residual oil data, J. Can. Pet. Tech., 12, no. 4 (1973) 53–61.

33. J.K. Dietrich and P.L. Bondor, Three-phase oil relative permeability models, Paper SPE 6044 presented at the 51st Annual Fall Technical Meeting, New Orleans, Oct 3–6 (1976).

34. K. Aziz and A. Settari, "Petroleum reservoir simulation," Applied Science Publishers Ltd., London (1979).

35. R.H. Brooks and A.T. Corey, Hydraulic properties of porous media, Hydrology Papers, no. 3, Colorado State University, Fort Collins, CO, Mar (1964).

36. J. Naar, J.H. Henderson and R.J. Wygal, Les ecoulements polyphases en milieux poreux consolides, Revue IFP, 18, no. 2 (1963) 196–214.

37. C.S. Land, Calculation of imbibition relative permeability for two- and three-phase flow from rock properties, Soc. of Pet. Eng. J., 8, no. 2 (1968) 149–156.

38. R.E. Collins, "Flow of fluids through porous materials," The Petroleum Publishing Co., Tulsa, OK, Ch. 6 (1976).

39. A.E. Scheidegger, "The physics of flow through porous media," Univ. of Toronto Press (1963) 224–229.

40. R.G. Bentsen, Conditions under which the capillary term may be neglected, J. Can. Pet. Tech., 17, no. 4 (1978) 24–30.

41. F.J. Fayers and J.W. Sheldon, The effect of capillary pressure and gravity on two-phase fluid flow in porous medium, Trans. AIME, 216 (1959) 147–155.

42. W.T. Cardwell, "The meaning of the triple value in noncapillary Buckley-Leverett theory," Trans. AIME, 216 (1959) 271–276.

43. V. Reitman, V.S.V. Rajan and T.R. Heidrick, The effect of injected fluid volume on heavy oil displacement in a porous medium, SPE Paper 15065, Proc. SPE Meeting, Oakland, CA, 1 (1986) 175–179.

44. P. van Meurs and C. van der Poel, A theoretical description of water-drive process involving viscous fingering, Trans. AIME, 213 (1958) 103–112.

45. R.L. Chuoke, P. van Meurs and C. van der Poel, The instability of slow, immiscible, viscous liquid-liquid displacements in permeable media, Trans. AIME, 216 (1959) 188–194.

46. R.G. Bentsen, A new approach to instability theory in porous media, Soc. Pet. Eng. J., 25, no. 5 (1985) 765–779.

47. E. Skaugen, Analytical model of viscous fingering including Buckley-Leverett type displacement, Proc. Conf. Fluid Flow in Porous Media, Rome, 1 (1985) 89–98.

48. M. Prats, "Thermal recovery," SPE monograph, Dallas, TX, 7 (1982).

49. R.M. Butler, Technical changes in the in-situ recovery of bitumen, Talk at the II District Five Meeting of CIM, Hinton, Alberta, Sep (1985).

50. R.M. Butler, G.S. McNab and H.Y. Lo, Theoretical studies on the gravity drainage of heavy oil during in situ steam heating, Can. J. Chem. Eng., 59 (1981) 455–460.

51. D. Kumar, H.N. Patel and E.S. Denbina, Use of gravity override model of steam flooding at Cold Lake, Paper 86-37-72, CIM Meeting, Calgary (1986).

52. N.R. Edmunds, An analytical model of the steam drag effect in oil sands, J. Can. Pet. Tech., 23, no. 5 (1984) 30–39.

53. R.M. Butler and D.J. Stephens, The gravity drainage of steam-heated heavy oil to parallel horizontal wells, Paper 80-31-31, CIM Meeting, Calgary (1980).

54. R.M. Butler, D.J. Stephens and M. Weiss, The vertical growth of steam chambers in the in situ thermal recovery of heavy oils, Proc. 30th Can. Chem. Eng. Conf., Edmonton (1980).

55. R.M. Butler, New interpretation of the meaning of the exponent in the gravity drainage theory for continuously steamed wells, AOSTRA J. Res., 2, no. 1 (1985) 67–71.

56. F.R.S. Ferguson and R.M. Butler, Steam assisted gravity drainage model incorporating energy recovery from a cooling steam chamber, Paper 86-37-25, CIM Meeting, Calgary (1986).

57. R.M. Butler, A new approach to the modelling steam-assisted gravity drainage, J. Can. Pet. Tech., 24, no. 3 (1985) 42–51.

58. R.M. Butler, Rise of interfering steam chambers, Paper 86-37-23, CIM Meeting, Calgary (1986).

11
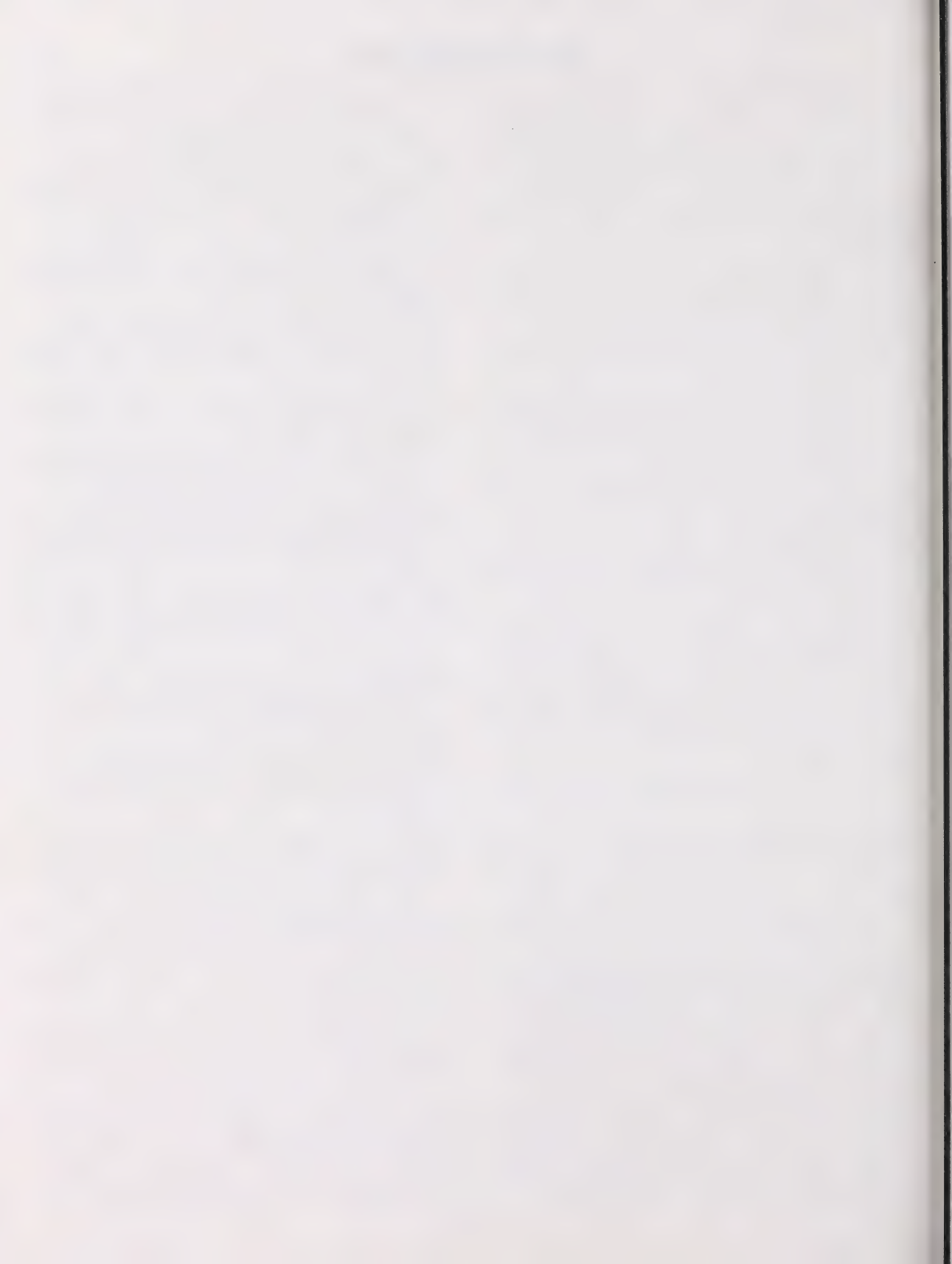
HEAT TRANSFER

J.D. Scott

Department of Civil Engineering
University of Alberta

INTRODUCTION

Heat transfer in a porous medium is a function of the thermal conduction and thermal convection processes in the porous medium. These processes are controlled by the physical properties of the solid matrix composing the formation, and the fluids in the pores of the matrix.

Considerable laboratory experimental work has been done on conduction heat transfer of the Athabasca oil sands of Alberta. The basic theories for thermal conductivity and thermal diffusivity are given in this chapter followed by an outline of laboratory test apparatus and test procedures. Measurements of thermal conductivity and thermal diffusivity are given, and the measurements are evaluated and interpreted. Much of this material has been obtained from Seto [1].

In contrast to thermal conductivity, little laboratory study of thermal convection has been attempted. The large number of physical properties of the solid matrix and pore fluids which control the thermal convection make it a site-specific property, not amenable to laboratory measurement. An overview of convective heat transfer in oil sands is given by Butler [2]. In this handbook, Chapter 10 on fluid flow and Chapter 12 on mass transfer provide much additional information on evaluating thermal convection processes in a formation. An important factor in heat transfer, the heat capacity of the materials composing an oil sands formation, is discussed in Chapter 4 on thermochemistry and thermodynamics.

FACTORS AFFECTING THERMAL PROPERTIES

Table 1 lists the major factors that affect three important thermal properties of oil sands: thermal conductivity, thermal diffusivity, and specific heat. As recognized by many investigators, the material itself (mineral grains, soil structure, and density), its degree of saturation, and the temperature, are significant factors controlling thermal conduction in oil sands. There is, however, uncertainty as to the effects of bitumen and water proportions on the thermal conduction. Some researchers suggest that there is no significant difference in thermal conductivity whether the nonwater phase in the pores is oil or air, while others argue that an oil-bitumen parameter should be included for proper correlation analysis. Little work has been done on the thermal property measurements on nonhomogeneous or possibly anisotropic oil sand specimens; the effects of nonhomogeneity and anisotropy on the thermal properties are therefore uncertain. The dependence of the thermal properties of uncemented sands and shales on the effective confining pressure is also not well known.

Table 1. Factors affecting thermal properties of oil sands.

	Factors	Thermal conductivity	Thermal diffusivity	Specific heat
Material	mineral grains	significant	significant	intermediate
	soil structure (grain size distribution)	significant	significant	low
	density (porosity)	significant	significant	intermediate
Saturation	bitumen/water proportions	uncertain	uncertain	significant
	degree of fluid saturation (presence of gas)	significant	significant	significant
Uniformity	homogeneity	uncertain	uncertain	low
	isotropy	uncertain	uncertain	low
Ambient conditions	confining pressure	uncertain	uncertain	low
	pore fluid pressure	low	low	low
	temperature	significant	significant	intermediate

CONDUCTIVE HEAT TRANSFER

Basic theory of heat conduction

The theory of heat conduction states that heat flows from the region of higher temperature to the region of lower temperature. The rate of heat flow is proportional to the temperature gradient. For an infinite and isotropic medium, the one-dimensional flow of heat by conduction, q, is given by

$$q = -kA \frac{dT}{dx} \qquad (1)$$

The proportionality constant, k, is known as thermal conductivity of the medium. The minus sign indicates that heat is transferred in the direction of decreasing temperature. A is the cross-sectional area for the flow and dT/dx is the temperature gradient. Equation (1) is also known as Fourier's law of heat conduction. For the three-dimensional case

$$q = -kA \left(\frac{dT}{dx} + \frac{dT}{dy} + \frac{dT}{dz} \right) \qquad (2)$$

Fourier's differential equation

Except in the special case of steady-state heat conduction, the heat flow will be associated with a change in temperature. The temperature, in an infinite and isotropic medium is given by

$$\frac{\partial T}{\partial t} = \frac{k}{\rho c} \left(\frac{\partial^2 T}{\partial x^2} \right) \qquad (3)$$

Another property related to the thermal conductivity is the thermal diffusivity α.

$$\alpha = \frac{k}{\rho c} \qquad (4)$$

where ρ is the density and c is the specific heat.
Using Equation (4), Equation (3) becomes

$$\left(\frac{1}{\alpha} \right) \frac{\partial T}{\partial t} = \left(\frac{\partial^2 T}{\partial x^2} \right) \qquad (5)$$

Equation (5) is the one-dimensional form of the more general Equation (6) which was first derived by Fourier in 1822:

$$\frac{\partial^2 T}{\partial x^2} + \frac{\partial^2 T}{\partial y^2} + \frac{\partial^2 T}{\partial z^2} = \frac{1}{\alpha} \left(\frac{\partial T}{\partial t} \right) \qquad (6)$$

There are two classes of solutions to this equation:
(1) Steady-state solutions where the term $\partial T/\partial t$ is zero.
(2) Non-steady-state solutions where temperature changes with time.

The first class of solutions pertains to problems such as the steady-state heat loss through insulation. The second class of solutions is more pertinent to thermal recovery problems. An example would be that of the heat loss from the upper surface of a heated reservoir to the overburden which is initially at some uniform low temperature. Solutions to this type of problem and other types of applications including the spreading and advancing of heat fronts, and heat loss from wellbores are discussed in detail by Butler [2].

Measurement techniques

The experimental techniques that have been used to measure the thermal conduction of oil sand are well described in the literature (after Seto [1], Lillico [3], Scott and Seto [4], Hanafi and Karim [5]). These thermal conduction test methods are generally divided into two categories: steady-state and transient-state techniques.

Theoretical basis of the steady-state method. Steady-state one-dimensional linear heat conduction in a uniform homogeneous medium is governed by the following Laplace's equation:

$$\frac{\partial^2 T}{\partial z^2} = 0 \qquad (7)$$

where $T(°C)$ is the temperature at any point z (m) from the origin.

Assuming that the temperature at $z = L_1$ is T_1 and at some other location, $z = L_2$, T_2, the solution to Equation (7) is:

$$T = \frac{T_2 - T_1}{L_2 - L_1} z + T_1 \qquad (8)$$

The rate of heat flow, q, is:

$$q = -k \frac{\partial T}{\partial z} A$$

or

$$q = -k \frac{T_2 - T_1}{L_2 - L_1} A \qquad (9)$$

Standard hot plate apparatus. The ASTM standard test method for steady-state thermal transmission properties of a material employs a guarded hot plate assembly (Figure 1).
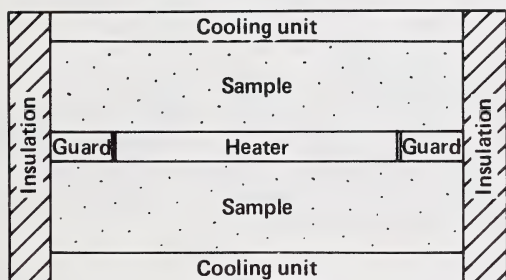
Figure 1. General features of the guarded hot plate apparatus.

The apparatus consists of a constant heat generating source at one surface of the test specimen and a constant cold surface maintained at the other. The outer boundaries of the heating and cooling units together with the specimen are well insulated so that one-dimensional heat flow is ensured across the bulk of the sample. Thermocouples are used to monitor temperatures at both surfaces of the specimen during the test until it is certain that thermal equilibrium of the system has been reached. With flow-rate of heat, q, specimen thickness, $L_2 - L_1$, cross-sectional area of the specimen, A, and steady-state temperature differential, $T_2 - T_1$, known, the thermal conductivity of the specimen can be evaluated from Equation (9). Many investigators have found that this test procedure is valid only for dry and homogeneous materials with low to medium conductivities.

Thermal comparator or divided bar apparatus. A schematic drawing of one type of comparator assembly

is shown in Figure 2. In this apparatus, a sample of unknown thermal conductivity is sandwiched between two standard reference samples of known conductivity. A thermal gradient across the stack of samples is created by the upper stack heater and the lower heat sink. Temperatures across the sample and the standard material are measured when thermal equilibrium of the system is achieved. Since the rate of heat flow in the stack arrangement is constant, the thermal gradients across the samples will vary according to their respective thermal conductivities. With the thermal gradients measured and the conductivity of the reference material known, the thermal conductivity of the test specimen may readily be determined by equating the rate of heat flow (Equation (9)) in the specimen with that across the reference material. Pyroceram glass ceramic, Code 9609 or fused quartz is generally used as the standard reference material.

The divided bar apparatus employs the same technique as that used by the thermal comparator except that two bars of a standard material (e.g. brass) are used to sandwich the test specimen (Figure 3). The metal bars are taken as the reference for thermal conductivity evaluation.

Coaxial thermal testing apparatus. The steady-state coaxial or cylindrical thermal testing apparatus employs
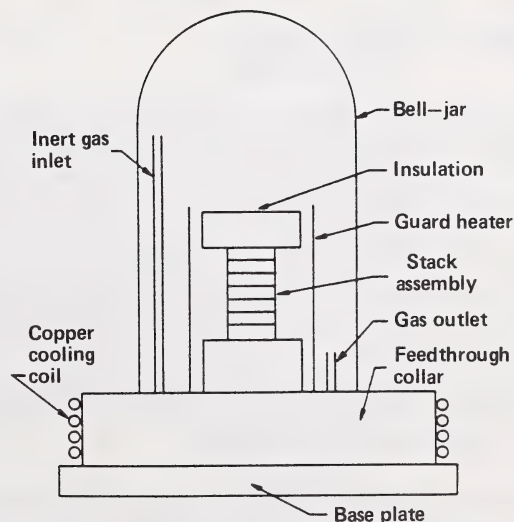
Figure 2. Schematic diagram of experimental setup for thermal comparator.

Figure 4. Steady-state coaxial thermal testing apparatus.

Figure 3. Divided bar apparatus.

A,B   — brass bar
R   — rock specimen
1–8   — thermojunctions
C   — heating coil
W   — dead weight (6 lb)

the theory of one-dimensional radial heat flow. Figure 4 depicts an example of the apparatus. A constant heat source generates heat along the inner core of the cylinder. The external surface temperature of the assembly is maintained by a constant-temperature fluid bath. Thermal equilibrium is established as heat moves radially outwards in a steady-state condition. The steady-state one-dimensional radial heat flow theory will not be detailed here, but the solution can readily be derived by applying the new boundary conditions and a cylindrical coordinate system to the governing differential equation, Equation (9).

Thermal conduction heat transfer cell. A heat transfer cell (Figure 5) developed by Lillico [3] measures the one-dimensional steady-state heat flux and temperature drop across a sample. Heat flux is found by measuring

the temperature drop across a known thickness of borosilicate glass for which the thermal conductivity is known. Thermal conductivity is measured by heating from above and cooling from below, thus suppressing convection. This heat transfer cell measures thermal conductivity to an accuracy of ± 7%.

Theoretical basis of the transient method. The partial differential equation that governs one-dimensional radial heat flow in an infinite homogeneous medium may be written as follows:

$$\frac{\partial^2 T}{\partial r^2} + \frac{1}{r}\frac{\partial T}{\partial r} = \frac{1}{\alpha}\frac{\partial T}{\partial t} \qquad (10)$$

where T = temperature, a function of r and t (°C)
   r = radial distance (m)
   t = time (s)
   α = thermal diffusivity of the medium (m²/s)

Depending on the boundary conditions imposed, Equation (10) will yield solutions that are useful in the determination of the thermal conductivity and diffusivity of a material.

As stated previously

$$\alpha = \frac{k}{\rho c}$$

Since the thermal conductivity and the thermal diffusivity of a material can be established experimentally and since the density is a measurable
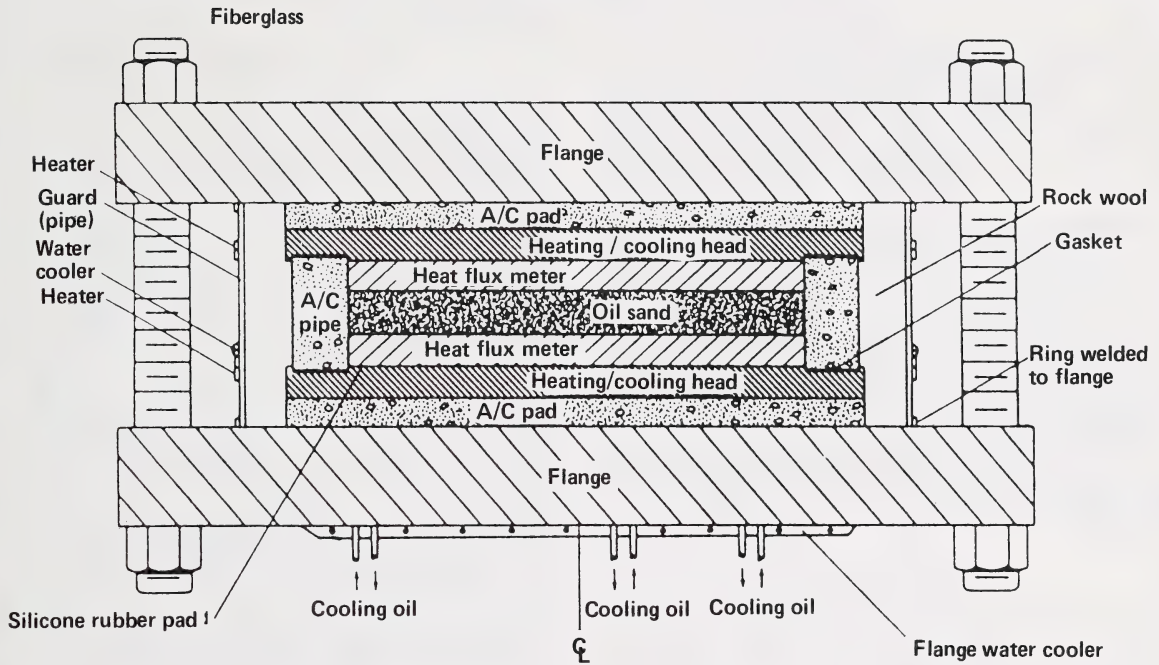
Figure 5. Thermal conductivity mode of heat transfer cell.

quantity, the specific heat of the material can be calculated from Equation (4).

The transient-state line-source technique of thermal conductivity determination generally assumes a uniform initial temperature throughout the medium and continuous heat source of strength, q_i, supplied instantaneously at the centre line at time, t, greater than zero (Figure 6).

The solution of Equation (10) for this set of boundary conditions can be obtained from Carslaw and Jaeger [9] and is stated as follows:

$$T = -\frac{q_i}{4\pi k}\exp_i\left(-\frac{r^2}{4\alpha t}\right) \qquad (11)$$

where T = temperature, a function of r and t ($°C$),
q_i = power input per unit length of line source (W/m),
k = thermal conductivity of the medium (W/m·K),
α = thermal diffusivity of the medium (m^2/s),
r = radial distance from line source (m),
t = time from start of power input (s).
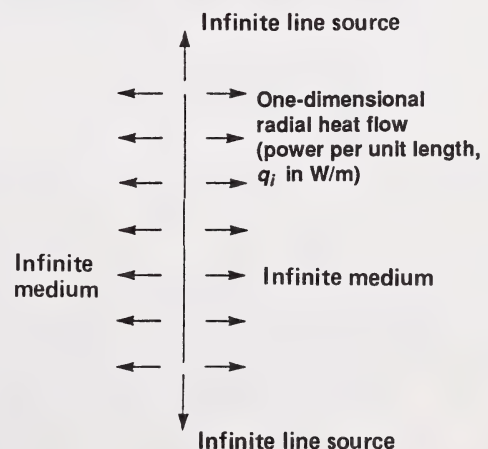
Figure 6. Transient-state one-dimensional radial heat conduction in a uniform homogeneous medium.

Also:

$$-\exp_i(-x) = \int_x^\infty e_u^{-u}\, du, \quad \text{for (x)} > 0$$

or

$$-\exp_i(-x) = -\gamma - \ln x - \sum_{n=1}^{\infty} \frac{(-x)^n}{n \cdot n!} \qquad (12)$$

where $\gamma = 0.577\,22$ (Euler's constant).

A plot of the exponential integral is shown in Figure 7. Nix et al. [10] have calculated for $r^2/4\alpha t < (0.16)^2$, the infinite summation term of Equation (12) may be reduced to the first two terms. Equation (11) may thus be approximated to better than 1% by the following expression:

$$T = \frac{q_i}{4\pi k}\left(\ln \frac{4\alpha t}{r^2} - \gamma\right) \qquad (13)$$

If the difference in temperature at two separate times of measurement is used, Equation (13) will yield:

$$T_2 - T_1 = \frac{q_i}{4\pi k}\ln \frac{t_2}{t_i} \qquad (14)$$

The above equation indicates a linear relationship between temperature and the natural logarithm of time. Therefore, thermal conductivity can ideally be calculated from the slope of a $T_2 - T_1$ vs $\ln(t_2/t_1)$ if the power input per unit length, q_i, is known.

However, typical plots of the $T_2 - T_1$ vs $\ln(t_2/t_1)$ relationships generally have shapes like the ones delineated by Wechsler [11] in Figure 8. As recognized by many researchers, the finite radius of the thermal conductivity probe, the thermal properties of the probe and the internal thermocouple, as well as the thermal contact resistance between the probe and the medium, together contribute to the initial curvature of the plots at region A. The linear portion of the curve obtained by a well-designed probe in region B is used for the evaluation of thermal conductivity. For large t_2/t_1, in region C, the experimental plots start to bend again. Wechsler [11] suggests that this is due to the loss of heat axially along the probe and/or the effects of finite sample diameter. If the curve is concave upward in region C, the deviation may be due to sample boundary
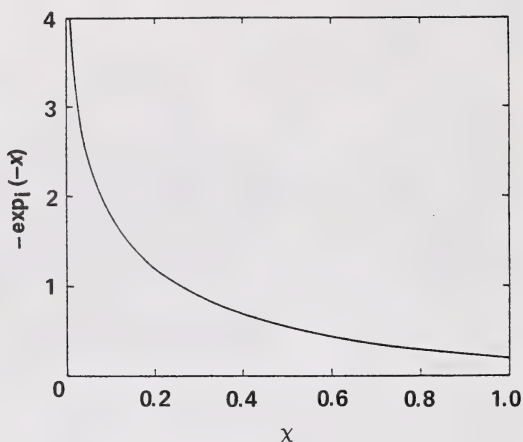
Figure 7. The exponential integral, $-\exp_i(-x)$.

Curve I	Ideal line heat source response
Curve II	Response of a well-designed probe
Curve III	Response of an unsuitable probe
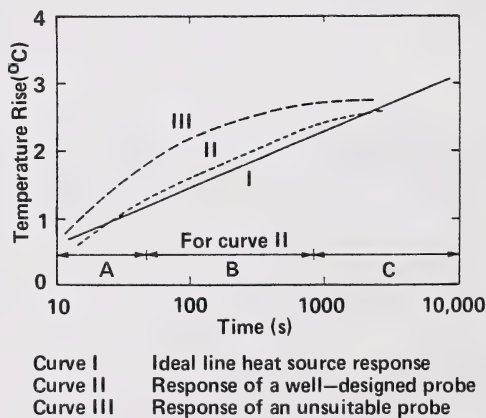
Figure 8. Typical probe temperature-time profiles.

effects, such as, heat reflection or boundary insulation. If the curve is concave downward, as in most cases, the deviation may be due to one or more of the two heat-loss effects mentioned above.

To fulfill the radial heat flow assumption, Blackwell [12] recommends that the length of the sample, L, be greater than $(4\alpha t/0.0632)^{1/2}$; and to minimize axial heat loss along the thermal conductivity probe, Blackwell [13] also suggests that the length-to-diameter ratio of the probe be greater than 25. Wechsler [11] suggests that the radius of the sample, R should be greater than or

equal to $(-4\alpha t \ln 0.02)^{1/2}$ in order to minimize the effect of finite sample size.

The transient-state thermal test cell. A drawing of the internal part of a transient state thermal test cell developed by Seto [1] is shown in Figure 9. The cell is enclosed in a triaxial compression cell which can be heated to 300°C and can hold a fluid at confining pressures up to 30 MPa. A constant heat source may be generated by a thermal conductivity probe or a heating jacket wrapped around the cylinder. Thermocouples are used to monitor the internal and external surface temperatures.

To perform a thermal conductivity experiment, the desired ambient temperature and effective confining pressure are first established. Cartridge heaters in the exterior triaxial cell wall are used if heating is required. When thermal equilibrium of the system is attained, the test is started by switching on the power supply to the central thermal conductivity probe. The rate of temperature rise at the probe heater, which is related to the thermal conductivity of the sample, is monitored by the internal thermocouple. The external temperature of the specimen is monitored to ensure that it does not

change during the experiment.

In the case of a thermal diffusivity experiment, the external sample temperature is incremented by about 20°C using the heating jacket. The temperature rise at the internal and external thermocouples are monitored for thermal diffusivity determination.

The transient-state effective thermal conductivity method. A transient method, developed by Hanafi and Karim [5], measures the transient temperature at the centre and the surface of a spherical sample when it is subjected to a convective fluid stream.

The temperature response when fed into relations obtained from the consideration of the transient conductive heat transfer within a sphere, can yield an average value for the thermal conductivity.

The transient response at the centre of an oil sand sphere subjected to a convective field can be expressed as

$$\frac{\left(T_f - T\right)}{\left(T_f - T_i\right)} = 2 \sum_{m=1}^{\infty} f(\alpha) e^{-a_m^2 \alpha t} \qquad (15)$$

where

$$f(\alpha) = \left[\cos\left(\alpha_m R\right) - \frac{k}{h_c R \left(\alpha_m R\right) \sin\left(\alpha_m R\right)} \right]^{-1}$$

$R =$ radius of the sphere and α_m's are the roots of the Eigenvalue equation.

$$\alpha_m R \cos\left(\alpha_m R\right) + \left(\frac{h_c R}{k-1}\right) \sin\left(\alpha_m R\right) = 0 \qquad (16)$$

Equation (15) can be simplified by examining the values of α_m under the specific conditions of the experiment. Also, for values of $h_c R / k$ similar to those used by Hanafi and Karim [5], the first root, α_1, of Equation (16) is usually less than 1.6 while all the other roots are larger than 4.0. Thus, in Equation (15), the terms containing $\alpha_2{}^2$, $\alpha_3{}^2$ will be decreasing in value rapidly and Equation (15) assumes the following simplified form:

$$\frac{\left(T_f - T\right)}{\left(T_f - T_i\right)} = \theta_n = e^{-\alpha_1^2 \alpha t}$$
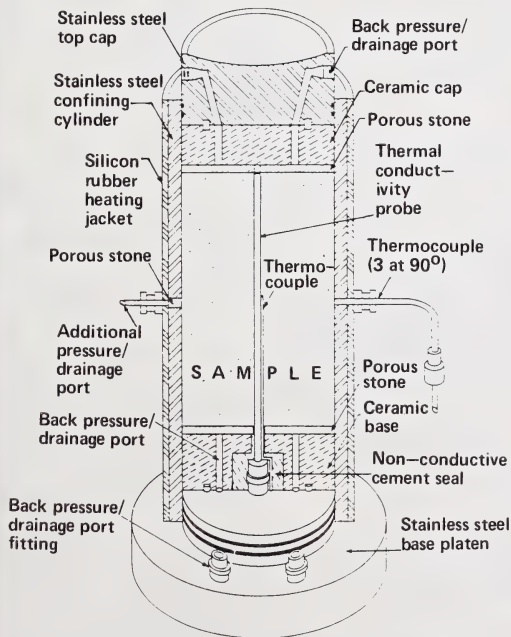
Figure 9. Transient-state thermal test cell.

Labels on figure:
Stainless steel top cap
Stainless steel confining cylinder
Silicon rubber heating jacket
Porous stone
Additional pressure/drainage port
Back pressure/drainage port
Back pressure/drainage port fitting
Thermocouple
SAMPLE
Back pressure/drainage port
Ceramic cap
Porous stone
Thermal conductivity probe
Thermocouple (3 at 90°)
Porous stone
Ceramic base
Non-conductive cement seal
Stainless steel base platen

or

$$\ln \theta_n = -\alpha_1^2 \, \alpha t \qquad (17)$$

Values of the oil sand thermal diffusivity obtained from Equation (17) were compared with values obtained from Equation (15) using ten terms. The maximum difference in the thermal diffusivity values obtained from both equations was 2%. Accordingly, by measuring the transient temperature response at the sphere centre, the relationship linking $\ln \theta_n$ with t can be established, and when used with Equation (17), the values of the thermal diffusivity can be obtained.

The process of finding the thermal conductivity k using this technique can be summarized as follows:

1. The temperature at the sphere centre is measured as a function of time.
2. The relationship linking $\ln \theta_n$ with t (Equation (17)) is then obtained and the slope is evaluated.
3. Knowing the convective heat transfer coefficient h_c on the sphere surface, and by assuming a suitable value for k, the Eigenvalue α_1 can be calculated from Equation (16).
4. The slope obtained in step 2 together with the calculated value of α_1 have to satisfy the relation:

$$\text{slope} = \alpha_1^2 \, \frac{k}{\rho c} \qquad (18)$$

Values of the density ρ are obtained from measuring the mass and the volume of representative samples. The specific heat is usually correlated with the percentage of oil, water and sand in the sample according to the following relationship [14,15]

$$c = x_x c_s + x_x c_w + x_o c_o \qquad (19)$$

Equation 18 is then used to calculate k.

5. The value of k obtained in step 4, and the one assumed in step 3, have to coincide within prescribed accuracy, which can be taken as 0.1% . Iterations of steps 3 and 4 are performed until convergence of k occurs.

The transient temperature response was also obtained at the sphere surface and at its centre simultaneously. This permits the use of the value obtained for k to calculate the transient response of temperature at the sphere surface. Comparisons of some of the measured and calculated temperature responses at the sphere surface were carried out to check the accuracy of the technique used. The calculated values of the surface temperature were usually from 1 to 3% higher than the corresponding measured values.

The transient temperature response was measured by Hanafi and Karim [5] both at the centre and the surface of spherical oil sand samples in a convective heated stream of air of moderate velocity, as well as above boiling liquid nitrogen at atmospheric pressure.

An electrically heated uniform-velocity stream of air was used with a fine wire mesh screen supporting the sample. Two thermocouples were inserted at the centre and the surface of a 19-mm diameter spherical oil sand fragment. A third thermocouple was located vertically with its bead 13 mm away from the sphere surface and at about one sphere radius above the screen. The three thermocouples were of Chromel-Alumel wires of 0.30 mm diameter, inserted within very thin quartz sheaths to preclude electrical contact inside the oil sand sample. The transient temperature response was recorded using a chart recorder that was checked against a high precision digital millivoltmeter. Generally, the samples were not subjected to the air stream long enough to attain steady state, minimizing the possible physical and chemical changes within the samples.

Theoretical basis of the thermal diffusivity test. Unlike the transient-state thermal conductivity measurement method in which a constant line source of heat is generated along the longitudinal axis, a thermal diffusivity experiment generally involves the heating or cooling of the cylindrical sample surface. One method of thermal diffusivity testing is immersing a sample with uniform initial temperature into a bath of constant temperature fluid and monitoring the time-temperature response of the sample. However, in the development of the general theory, an infinite cylinder is assumed so that radial heat flow in the uniform homogeneous medium is one-dimensional. Jaeger [16] has shown that the deviation in the diffusivity result is <10% (for $\tau_j < 0.2$; $\tau_j = 4\alpha t/d^2$) even if the length-to-diameter ratio (L/d) of the finite cylinder is only 1. The samples used by Seto [1] were trimmed to cylindrical shapes with L/d ≥ 2. Together with careful adjustments such that τ_j was <0.15, the accuracies of the diffusivity results were much better than 10%. Instead of having the sample immersed in a constant-temperature fluid bath, the thermal diffusivity test used a heating jacket to heat the external sample surface. Although the radial heat flow and infinite cylinder assumptions may be justified by the proper design of the apparatus, the surface temperature

rise cannot be taken as instantaneous. A constant surface temperature may not be achieved until some time has elapsed after the start of the test. Therefore, it is necessary to describe the boundary conditions as follows:

• Uniform initial temperature throughout the medium, except at the surface of the cylinder.
• Surface temperature is a function of time, $\phi(t)$.

The governing differential equation is still Equation (10), but the solution for the newly prescribed conditions is given by Carslaw and Jaeger [9] as follows:

$$T = \frac{2\alpha}{R} \sum_{n=1}^{\infty} e^{-\alpha\delta n^2 t} \frac{\delta_n J_0\left(r\delta_n\right)}{J_1\left(R\delta_n\right)}$$
$$\int_0^t e^{\alpha\delta n^2 \lambda} \phi(\lambda)d\lambda \qquad (20)$$

where T =   temperature as a function of r and t (°C)
        α =   thermal diffusivity of the medium (m^2/s)
        R =   external radius of sample (m)
        δ_n =   (n = 1,2,3, ...) positive roots of the function, $J_0(R_o\delta) = 0$ (dimensionless)
        t =   time (s)
        r =   radial distance from centre of cylinder (m)
   $J_0(x), J_1(x)$ =   Bessel function of order 0 and 1 respectively
        $\phi(t)$ =   surface temperature of sample as a function of time (°C).

Measurements of thermal conductivity and thermal diffusivity

Karim and Hanafi [17] studied the thermal conductivities of various natural and reconstituted Athabasca oil sand samples at temperatures ranging from 20 to 120°C. The apparatus used was a coaxial-type steady-state thermal testing assembly. Bitumen contents were adjusted during the preparation of different remolded samples. The findings are presented in Figure 10. There is no mention of the degrees of water saturation of the samples. The percentages given are for oil contents by mass.

Cervenan, et al. [18] used a steady-state hot plate apparatus for the determination of thermal conductivities of some reconstituted Athabasca oil sand samples at room temperature and atmospheric pressure. The dependence of thermal conductivity on water saturation is delineated by a curve shown in Figure 11.
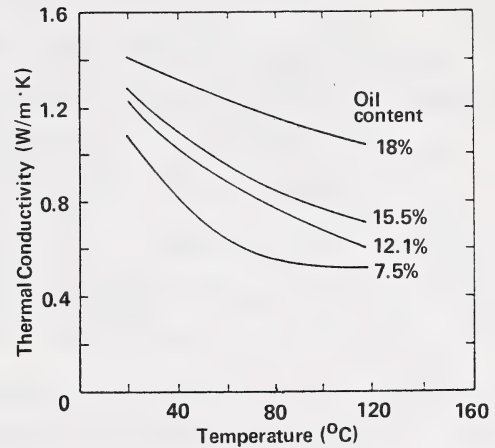
Figure 10. Thermal conductivity of Athabasca oil sands.
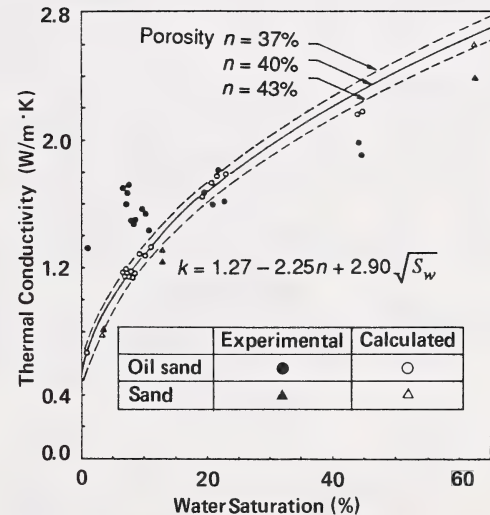
Figure 11. Correlation of thermal conductivity with water saturation of Athabasca oil sands.

Seki et al. [19] devised a transient-state thermal testing apparatus for thermal property determination. Thermal conductivity and specific heat values of specimens from a disturbed medium-grade Alberta oil sand sample were measured. From the ratios of thermal conductivity to heat capacity (the product of density and specific heat), thermal diffusivity values of the sample were derived. The variations of thermal conductivity,

heat capacity, and thermal diffusivity with temperature are depicted in Figure 12. It should be noted that the drastic drop of the thermal conductivity (and subsequently the diffusivity) value at about 100°C is due to vaporization of fluids in the specimen. There is no provision of a back-fluid pore-pressure system to prevent fluids from vaporizing at elevated temperatures.

Seto [1] performed transient-state thermal conductivity and diffusivity tests on remolded and undisturbed core samples of Athabasca oil sands. Physical properties of the oil sand specimens are given in Table 2. Changes in thermal conductivity and diffusivity with temperature for each of the samples are shown in Figures 13 through 22.

The remolded oil sand samples were first tested as prepared. The degree of liquid saturation as well as the proportions of water and bitumen were determined prior to the testing sequence. Therefore, these values are applicable to the air-water-bitumen saturated condition. As water was injected into the test system for full water-bitumen saturation of the sample, it was assumed that air inside the sample was displaced by water. Therefore,

Figure 13. Change in thermal conductivity with temperature, rich remolded oil sand.
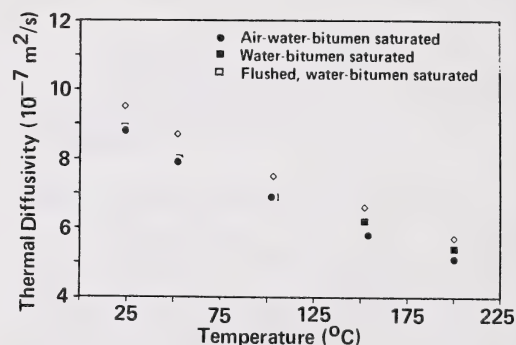
Figure 14. Change in thermal diffusivity with temperature, rich remolded oil sand.

Figure 12. Thermal properties of Athabasca oil sands (after Seki et al. [19]).
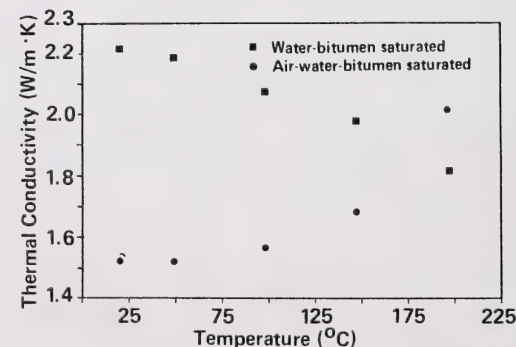
Figure 15. Change in thermal conductivity with temperature, lean remolded oil sand.
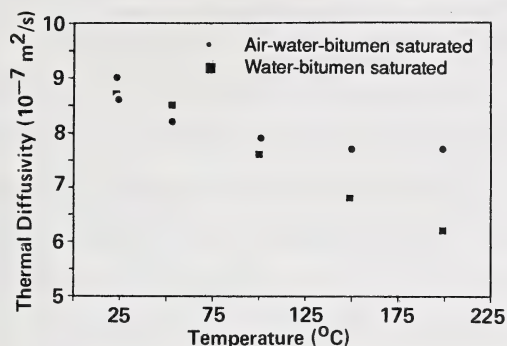
Figure 16. Change in thermal diffusivity with temperature, lean remolded oil sand.
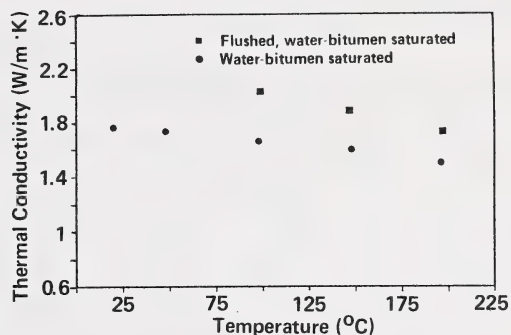
Figure 19. Change in thermal conductivity with temperature, rich undisturbed oil sand.
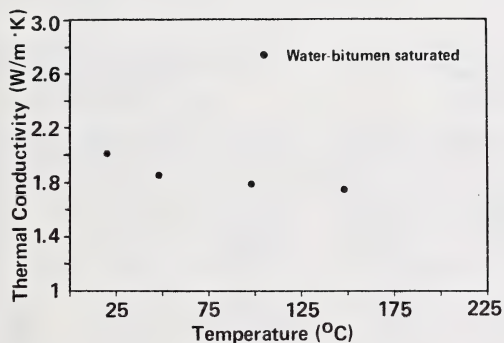
Figure 17. Change in thermal conductivity with temperature, medium undisturbed oil sand.
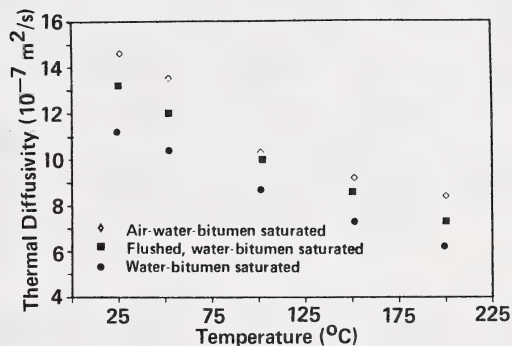
Figure 20. Change in thermal diffusivity with temperature, rich undisturbed oil sand.
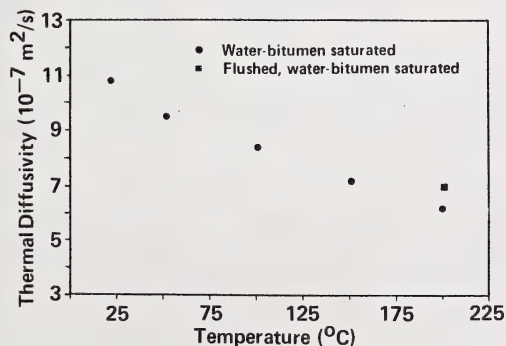
Figure 18. Change in thermal diffusivity with temperature, medium undisturbed oil sand.
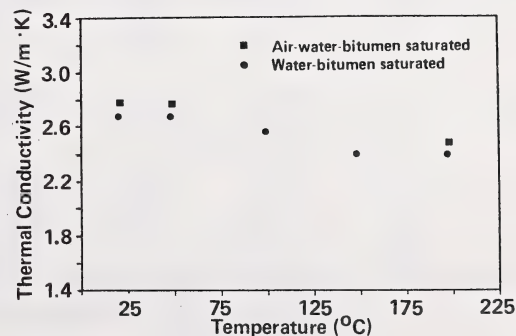
Figure 21. Change in thermal conductivity with temperature, lean undisturbed oil sand.
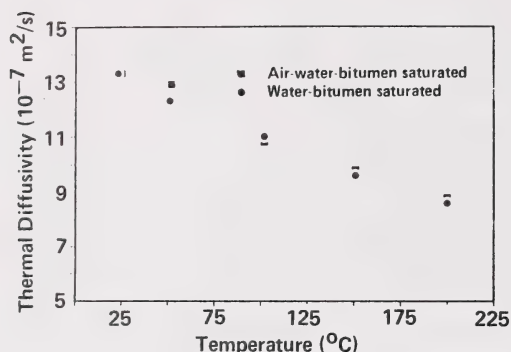
Figure 22. Change in thermal diffusivity with temperature, lean undisturbed oil sand.

the bitumen saturation did not change. Upon completion of the entire testing sequence, the water and bitumen contents of the sample were again measured. If the sample had been flushed with hot water to reduce the bitumen content for the final stage of testing, the saturations measured were assumed to apply to this last testing condition.

All undisturbed oil sand samples were fully saturated by displacing air with water prior to thermal property measurements. The initial air voids were assumed to be filled with water after saturation. Therefore, the water and bitumen contents of each specimen were known at the beginning of the testing sequence. Hot water flushing was employed to reduce the bitumen content for a second stage of testing of the rich oil sand specimen. Nitrogen was injected into the thermal test cell to displace some of the water at room

Table 2. Physical properties of oil sand samples.

Sample	Saturation code	Density (g/cm³)	Porosity (%)	Constituents (mass %)			Degree of saturation (%)		
				Solids	Bitumen	Water	Overall	Bitumen	Water
ROSR	A	1.797	44.0	82.5	16.5	1.0	71.3	67.5	3.8
	W	1.943	–	77.1	15.4	7.5	100.0	67.5	32.5
	F	1.933	43.4	77.5	10.1	12.4	100.0	45.0	55.0
ROSL	A	1.775	41.8	85.3	4.0	10.7	62.5	16.9	45.6
	W	1.929	39.6	79.9	3.7	16.4	100.0	18.4	81.6
UOSM	W	2.073	35.0	83.2	12.3	4.5	100.0	73.0	27.0
	F	2.062	34.9	83.2	7.2	9.6	100.0	42.6	57.4
UOSR	W	2.085	34.3	83.6	14.7	1.7	100.0	89.4	10.6
	F	2.085	34.3	83.6	6.6	9.8	100.0	40.3	59.7
	A	1.973	34.3	88.3	7.0	4.7	67.5	40.3	27.2
UOSL	W	2.137	31.1	85.5	3.1	11.4	100.0	31.4	78.6
	A	2.104	20.3	89.0	2.2	8.8	78.8	15.9	62.9
TS	D	1.700	35.1	100.0	0.0	0.0	0.1	0.0	0.1
	S	2.059	33.1	84.3	0.0	15.7	100.0	0.0	100.0

Saturation code: A = air-water-bitumen saturated. W = water-bitumen saturated.
F = flushed, water-bitumen saturated. D = dry.
S = water saturated.

temperature for the final stage of testing of this sample as well as the lean bitumen sample. It was assumed that the amount of bitumen expelled from the sample during nitrogen flushing was negligible because of the high viscosity of bitumen at room temperature. Hence, the measured bitumen content at the end of the test sequence was applied to the last two stages of the tests. This meant that bitumen contents of the undisturbed lean oil sand sample under full water-bitumen-saturated and nitrogen-flushed conditions should be the same before and after the testing sequence. Within the limits of experimental errors in the bitumen extraction procedures, the results shown in Table 2 indicate that this is true.

To determine the amount of water displaced by nitrogen during nitrogen flushing of a specimen, a measuring cylinder was used to collect water from the bottom drainage port of the high-temperature high-pressure cell.

Evaluation and interpretation of test procedures and measurements

Comparison of steady-state and transient-state tests. Results of steady-state and transient-state thermal conductivity measurements on dry and water-saturated quartz sand samples at room temperatures are compared in Table 3 (after Seto, [1]). The densities of the specimens are similar enough for a comparison of the results. Thermal conductivity values of the dry Ottawa sand samples are quite compatible. The higher measured conductivity of water-saturated sand under the steady-state testing condition may be attributed to moisture redistribution and convective effects in this type of test. It appears that steady-state hot plate tests should be used for dry specimens only. The

compatibility of measured thermal conductivity values of the dry Ottawa sand specimens suggests that reasonable accuracy may be obtained from transient-state testing.

As also noted by Combs et al. [20], thermal conductivities of moist materials as measured using a needle-probe (thermal conductivity probe) method are often less than those obtained using a steady-state method. They attribute the higher steady-state thermal conductivity values to the effects of convective heat transfer in the water fraction of the aggregates. Hutcheon and Paxton [21] have studied the effects of moisture migration in a closed guarded hot plate. The authors concluded that the thermal conductivity values obtained by testing moist materials in a hot plate may be of limited value when used in the usual heat flow equations for prediction of heat transmission. Since the transient-state thermal test cell was devised to minimize convective effects during a thermal conductivity test, results obtained using this apparatus may be more applicable to actual field conditions.

Factors affecting thermal conduction and thermal diffusivity of oil sands. Factors affecting the thermal properties of oil sands are given in Table 1. Based on his experimental results, Seto [1] made the following observations:

Temperature. The effects of temperature on the thermal properties of fluid-saturated oil sands have been studied extensively. Thermal diffusivity is found to decrease with increasing temperature. The decrease in diffusivity, for a temperature increase from 20 to 200°C, ranges from about 14% for the partially-saturated lean remolded oil sand to about 45% for the water-bitumen saturated rich undisturbed oil sand. It appears that the

Table 3. Thermal conductivity of quartz sand.

	Dry sand			Water-saturated sand		
	ρ (g/cm^3)	ϕ (%)	k (W/m $\cdot$ K)	ρ (g/cm^3)	ϕ (%)	k (W/m $\cdot$ K)
steady-state	1.800	32.0	0.43	2.134	32.0	4.03
transient-state	1.787	32.6	0.44	2.113	32.6	3.41

ρ = dry or total density
ϕ = porosity
k = thermal conductivity

higher the bitumen saturation of a specimen, the greater the percent drop of diffusivity value with increasing temperature.

Although Seki et al. [19] noted a slight rise in thermal diffusivity of their oil sand sample from about 20 to 80°C, a general trend of decreasing thermal diffusivity with increasing temperature can be observed from Figure 12. Since their test data were affected by vaporization of fluids at high temperatures, it is felt that their thermal diffusivity values may not be representative of the in situ oil sand conditions.

With the exception of the partially-saturated lean remoded oil sand specimen, all measured thermal conductivity values of oil sand samples were found to decrease with increasing temperature. The percent drop ranges from about 11% for the lean undisturbed sample to about 28% for the rich remolded sample from 20 to 200°C. Again, a larger decrease is noted for the rich oil sand samples with higher bitumen saturations. The increase in thermal conductivity of the lean remolded oil sand specimen with temperature may be attributed to a density increase due to load consolidation as well as heat consolidation during thermal testing.

The drop in thermal conductivity of oil sands with increasing temperature has also been observed by many investigators. Thermal conductivity of the Athabasca oil sand specimen (18% bitumen content) tested by Karim and Hanafi [17] decreases by about 25% from 20 to 120°C (Figure 10).The general trend of decreasing thermal conductivity with increasing temperature is also depicted in Figure 12 by Seki et al. [19].

Temperature dependence of the thermal conductivity of dry quartz sand shows an opposite trend. Thermal conductivity increases from 0.51 to 0.55 W/m·K for a temperature increase from 20 to 200°C. The density of the quartz sand sample is 1.74 g/cm^3. The same trend has been noted by other researchers. Flynn and Watson [8] showed an increase in the average thermal conductivity of their dry Ottawa sand sample (with density of 1.76 g/cm^3) from 0.37 to 0.44 W/m·K for a temperature rise from 25 to 200°C.

Bitumen/water proportions. Figures 23 and 24 display the changes in thermal conductivity and thermal diffusivity with bitumen saturation respectively. The data plotted represent oil sand specimens that are 100% saturated by water and bitumen. Therefore, the dependence of the thermal properties on water saturation may be visualized by simply reversing the horizontal axis from 100 to 0%.
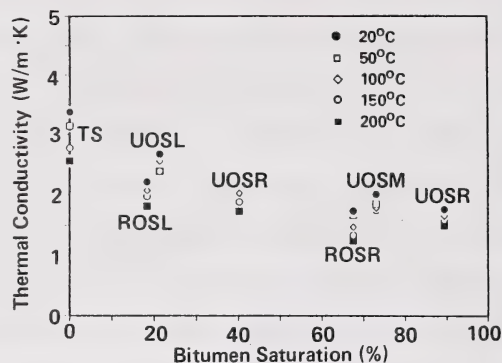
Figure 23. Change in thermal conductivity with bitumen saturation, saturated oil sand.
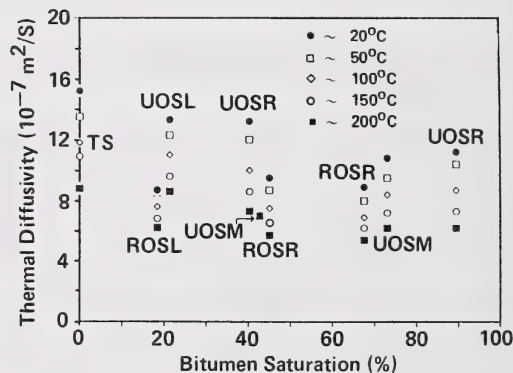
Figure 24. Change in thermal diffusivity with bitumen saturation, saturated oil sand.

As depicted in Figure 23, thermal conductivity of a fully saturated sample decreases with increasing bitumen saturation (or decreasing water saturation). Thermal conductivity values of undisturbed oil sand specimens are higher than those of the remolded ones at roughly the same bitumen saturation. It is believed that higher densities of the undisturbed specimens contribute to the difference. Thermal conductivity values of the oil sand specimens appear to drop quite sharply for a bitumen saturation change from 0 to near 20%. The reduction is about 60%. The rate of decrease in thermal conductivity then decreases at higher bitumen saturations.

Karim and Hanafi [17] (Figure 10) indicate that an increase in bitumen content increases the thermal

conductivity of oil sands. Cervenan et al. [18] show that, for the same degree of saturation, an increase in bitumen content decreases the thermal conductivity. From the observations made from thermal conductivity tests on the oil sand samples of varying bitumen/water proportions used by Seto [1], it appears that the latter trend is correct. The lack of control on the pore water contents in many of the test procedures causes the difference in test results obtained by some investigators. If little or no water is present in a sample, the increase in bitumen content may actually increase the thermal conductivity. However, samples in this state would generally not be reflecting in situ conditions during a thermal stimulation process.

Thermal diffusivity of saturated oil sand is shown to decrease with increasing bitumen saturation in Figure 24. However, more significant differences between thermal diffusivity values of undisturbed and remolded oil sand specimens at roughly the same bitumen saturation are observed. This indicates that thermal diffusivity is affected to a much greater degree by density difference than is thermal conductivity. It can also be observed that the decrease in thermal diffusivity of undisturbed samples with increasing bitumen saturation is gradual. A sharp drop in thermal diffusivity (30 to 70%) is observed for remolded oil sand specimens with bitumen saturations increasing from 0 to near 20%. At higher bitumen saturations, the change in thermal diffusivity is less pronounced.

Degree of saturation. The effects of degree of liquid saturation on thermal conductivity and thermal diffusivity of oil sands are shown in Figures 25 and 26 respectively. Both thermal conductivity and thermal diffusivity of oil sands are shown to increase with degree of saturation. Variations from the general trends are probably due to differences in density and bitumen/water proportions. Again, the significant influence of density on thermal diffusivity is illustrated in Figure 26. The undisturbed samples have higher thermal diffusivity values than those of the remolded ones.

Density. As mentioned during the discussion on the previous factors, density (or porosity) has a significant effect on the thermal properties of a material. The general trend of higher thermal conductivity and diffusivity values for the denser undisturbed samples can be seen in Figures 23 and 24. The effects of density difference on thermal diffusivity (about 21 to 53%) are
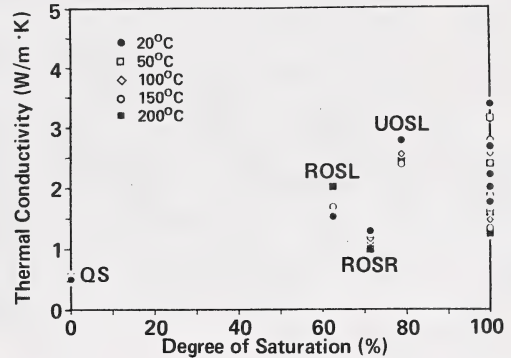
Figure 25. Change in thermal conductivity of oil sand with degree of saturation.
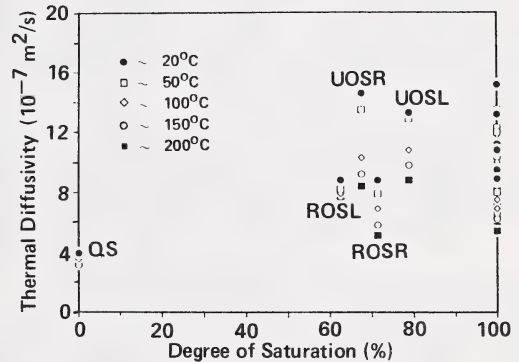
Figure 26. Change in thermal diffusity of oil sand with degree of saturation.

more pronounced than those on thermal conductivity (about 15 to 18%). Since it is impossible to recompact an oil sand structure back to its original "locked" state, a remolded oil sand specimen should have a higher porosity than that of the original sample. Therefore, in order to achieve more representative results that may be used in the field, undisturbed oil sand samples should be used for thermal property testing.

Mineral grains and soil structure. Oil sand samples from two different localities of the Athabasca deposits were tested by Seto [1]. A general comparison of the values indicates that the lean, silty oil sand specimens have higher thermal conductivities than the rich oil sand specimens under roughly the same conditions. The

difference may be partially attributed to the slight difference in mineralogy. The major source of variations stems from the difference in soil structure. With more fines in the void space between the crystalline grains in the soil matrix, greater contact areas are created for the better-graded lean oil sands. Heat conduction through the specimen is facilitated by the provision of more conductive flow paths. On the other hand, the number of surface contacts is smaller for a poorly-graded or uniform material. Assuming that the degree of saturation and fluid saturant proportions are the same, the poorly-graded material should exhibit lower thermal conductivity.

The same comparison is made for thermal diffusivity. The effects of mineralogy and soil structure are less prominent.

Comparison of thermal conductivity measurements. Thermal conductivity values of quartz sand and extracted oil sand samples obtained by various researchers are tabulated in Table 4.

It can be observed that thermal conductivity values (0.44 and 0.49 W/m·K respectively) of the dry quartz sand and tailings quartz sand specimens measured by Seto [1] in the transient-state thermal test cell are quite comparable to the other data. Thermal conductivities of

Table 4. Comparison of thermal conductivities of quartz sand.

Thermal conductivity (W/m·K)	Porosity (%)	Density (g/cm³)	Water saturation (%)	Reference and remarks
0.41	34	1.76	0.0	Kerstern [22], At 100°C, 20–30 Ottawa sand
0.627	–	–	0.0	Somerton [23], Fine sand
2.752	–	–	100.0	Fine sand
0.557	–	–	0.0	Coarse Sand
3.072	–	–	100.0	Coarse sand
0.257–0.314	37–41	–	0.0	Krupiczka [24]
0.38	–	1.76	0.0	Flynn and Watson [8], 20–30 Ottawa sand
0.26	–	1.57	0.0	
0.254–0.575	30–50	–	0.0	Somerton, Keese and Chu [25],
1.419–3.756	30–50	–	100.0	Brine–saturated
2.684 ± 0.032	–	–	–	Poulsen et al. [26]
0.337–0.446	31–45	–	0.0	Somerton, Keese and Chu [25]
2.080–2.460	28–37	–	100.0	extracted oil sands
0.80	45	–	3.3	Cervenan, Vermeulen, and Chute [18]; extracted oil
1.24	45	–	12.7	sands; water saturations given by % total mass
2.39	43	–	62.2	
0.44	33	1.787	0.0	Seto [1], 20–30 Ottawa sand
3.41	33	2.113	100.0	20–30 Ottawa sand
0.49	35	1.700	0.0	Oil sand tailings sand
3.38	35	2.059	100.0	Oil sand tailings sand

the water-saturated samples (3.88 and 3.41 W/m•K) appear to be on the high side of the range of published values. The difference could be due to differences in mineralogy, grain size distribution, and density.

Figure 27 illustrates thermal conductivity values of Athabasca oil sands determined by different investigators. Thermal conductivity values of the saturated-medium undisturbed oil sand specimen (with 12% bitumen by mass) and dry and water saturated quartz sand measured by Seto [1] are also plotted.
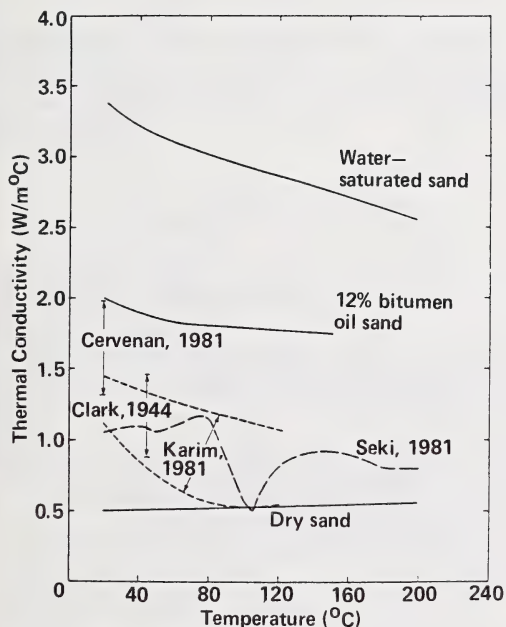
Figure 27. Comparison of thermal conductivity of medium Athabasca oil sand.

It is of interest to note from Figure 27 that none of the other published data fall above the line represented by the medium-grade oil sand. As discussed earlier, the higher the hydrocarbon content (or saturation) of a water-bitumen-saturated material, the lower is its thermal conductivity. Therefore, it is anticipated that at least some of the published data for water-bitumen-saturated, but leaner (lower bitumen saturation), oil sand samples would show higher thermal conductivities than those of the medium undisturbed oil sand. The main reason for this prediction not being realized is that the densities of the reconstituted or remolded oil sand specimens tested by other researchers are generally

lower than that of the undisturbed specimen used by Seto. The relatively intact soil structure of an undisturbed oil sand sample provides better contacts for heat conduction than the disrupted structure of a remolded sample. The inability to provide sufficient back pore-fluid-pressure to maintain gases in solution at high temperatures also accounts for some of the variations of results. The medium oil sand specimen was fully saturated while some of the other specimens prepared by the other researchers were only partially saturated. The differences in the degrees of saturation also contributed to differences in the thermal conductivities.

Variations in thermal conductivity of the water-saturated and dry quartz sand samples with temperature are also delineated in Figure 27 because they represent the upper and lower boundaries respectively of the thermal conductivity of Athabasca oil sands. Since the thermal conductivity of bitumen is lower than that of water but higher than that of air, all oil sands with different air-water-bitumen saturations will exhibit thermal conductivities between these boundaries. However, as the upper values are 5 to 7 times the lower values, the boundaries may not be taken as a guide to assist the determination of thermal conductivity. Nevertheless, the significant effect of air-water-bitumen saturation on thermal conductivity is illustrated by the quartz sand values.

The thermal conductivity data of fully liquid-saturated undisturbed oil sand samples are plotted in Figure 28 (after Seto, [1]). The upper and lower boundaries for water-saturated and dry quartz sands are also included in the figure. In keeping with the findings discussed earlier, oil sand specimens with high bitumen contents have lower thermal conductivities. The lower the bitumen content of a fully saturated sample, (the leaner the sample), the closer its thermal conductivity is to the upper boundary value.

Figure 29 illustrates thermal diffusivities of the fully liquid-saturated undisturbed oil sand samples. Calculated diffusivities from Seki [19] are also included. As observed previously, the higher the bitumen proportion of a water-bitumen-saturated oil sand sample, the lower its thermal diffusivity. The importance of testing undisturbed samples is again demonstrated, as the less dense disturbed oil sand specimen (9% bitumen) prepared by Seki [19] exhibits much lower thermal diffusivities than anticipated. Vaporization of fluids at about 100°C also complicated the thermal conduction process.
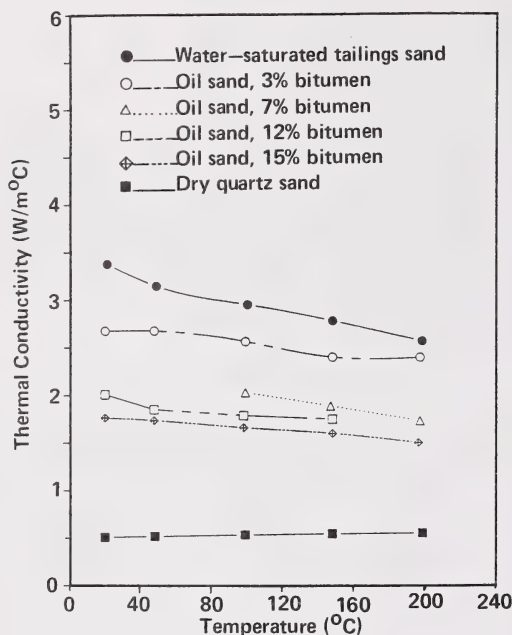
Figure 28. Comparison of thermal conductivities of saturated Athabasca oil sand samples.
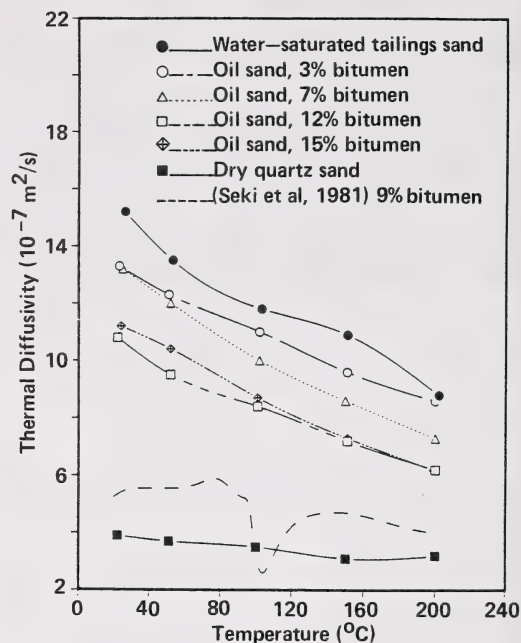
Figure 29. Comparison of thermal diffusivities of saturated Athabasca oil sand samples.

CONVECTIVE HEAT TRANSFER

Natural convection

Natural convection in oil sands is the movement of pore fluids throughout an oil sand layer under the influence of a density or concentration gradient.

The pore fluid of oil sands contains both water and bitumen, and the multifluid natural convection process in porous media is applicable to oil sand behavior.

The convection fluids in a horizontal layer of a porous medium can best be characterized by the Rayleigh number (Ra), which is the ratio of the buoyant to viscous forces (after Katto and Masuoka [27], and Lillico [3]) as follows:

$$Ra = \frac{K\rho_{fl}g\beta\Delta TH}{\eta\alpha} \qquad (21)$$

where g = local gravity acceleration constant (m/s^2)

β = coefficient of thermal volume expansion of the fluid (K^{-1})

ΔT = temperature difference across the layer (K)

K = absolute permeability of the fluid-saturated porous medium (m^2)

H = thickness of the layer (m)

η = dynamic viscosity of the fluid (Pa·s)

and

α = thermal diffusivity of the medium (m^2/s)

α = $k/\rho c$

where k = thermal conductivity of the saturated porous medium (W/m·K)

ρ = density (kg/m^3)

c = specific heat (kJ/K·kg).

When a fluid-saturated porous medium bounded by two horizontal impermeable surfaces is heated from below, convection does not occur until the buoyant forces overcome the viscous forces. Thus, until the Rayleigh number reaches a critical limit (Ra_c) no convection occurs. When Ra_c is exceeded, convection occurs and as Ra continues to increase, the heat transfer through the medium increases and the pattern of fluid motion can change. The value of Ra_c and the patterns of fluid motion depend on the thermal characteristics of the fluid and the shape of the layer, but for a single, constant-viscosity fluid, in an infinite layer Lapwood

[28] showed that $Ra_c = 4\pi^2$.

For a cylindrical reservoir heated from below where the ratio of the radius to the height of the reservoir approaches unity, the critical Rayleigh number also approaches the value of $4\pi^2$. A summary of the critical Rayleigh numbers for different boundary conditions and for heating from below is presented in Table 5. The Rayleigh number

$$Ra_q = \frac{K\rho_{fl}\beta g H^2 q''}{n\,\alpha k} \qquad (22)$$

is for problems with prescribed surface heat flow. The horizontal wave number at the onset of natural convection in a porous medium between parallel plates is given by

$$a = \left(\Delta^2 + \gamma_m^2\right)^{1/2} = \pi \qquad (23)$$

where γ_m and Δ are the wave numbers in the two horizontal directions.

Wooding [29] and Castinel and Combarnous [30] studied the effect of anisotropic permeability on the onset of natural convection in a geothermal reservoir. They found that the value of critical Rayleigh number was reduced when the ratio of the vertical permeability to the horizontal permeability decreased from unity.

Kassoy and Zebib [31] found the values of the critical Rayleigh number of a temperature-dependent viscosity was less than that of the constant value viscosity.

The coefficient of thermal expansion and density of water are also temperature dependent.

In many in situ thermal recovery methods, hot fluids such as hot water or steam are injected into the oil sand bed. A heat front is formed and moves through the oil sand bed towards the production wells, driving gases and the liquid fraction of the oil sand ahead of it. During this convective heating process, heat and mass transfer occur simultaneously. Latent heat exchange may also take place and phase change of the liquid may also occur. Thus, it is evident that the transport processes in oil sand beds or test cells are extremely complicated; the phenomena involved are not fully understood. In heat and mass transfer, complexity arises from the large number of variables involved. These variables include porosity, permeability, temperature, pressure, material composition, and the associated chemical and physical changes that may occur with time. In addition, limits on the amount of information available on the physical, chemical, and thermal properties of the oil sands have made the convective heat transfer study of oil sand more difficult.

Researchers including Kassoy and Zebib [31,36] and Straus and Schubert [37] have found that the value of the critical Rayleigh number based on the variable-property analysis was less than that based on the constant-property analysis. Thus, it is important that proper values of these variables such as porosity, permeability, temperature, and material composition should be used for each convective heat transfer study. Table 6 shows a qualitative evaluation of the factors which affect thermal conductivity in a reservoir.

Measurement techniques

Thermal convection cell. A thermal convection cell was designed by Burretta [38] to obtain measurements of natural convective heat transfer in a porous medium. The details of the convection cell are shown in Figure 30. The test section was cylindrical in shape. The porous medium was heated from below and cooled from above. Thermocouples were used for temperature measurements and temperature monitoring within the convective cell.
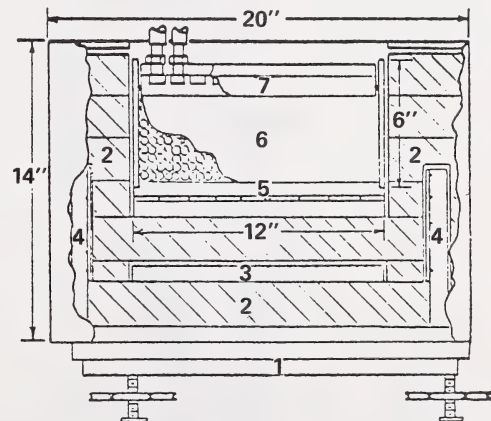
1 Levelling table
2 Urethane insulation
3 Base guard heater
4 Circumferential guard heater
5 Lower plate and heater
6 Porous layer
7 Liquid-cooled upper plate

Figure 30. Convection cell, after Buretta [38].

Table 5. Value of the critical Rayleigh numbers for onset of free convection in a porous medium.

Upper boundary conditions				Lower boundary conditions				$Ra = \dfrac{K\rho_{f}g\beta\Delta TH}{\eta\alpha}$	$Ra_{q} = \dfrac{K\rho_{f}g\beta q''H^{2}}{\eta\alpha k}$	a	References
Thermal		Hydrodynamic		Thermal		Hydrodynamic					
Constant temperature	Constant heat flux	Impermeable wall	Constant pressure	Constant temperature	Constant heat flux	Impermeable wall					
x		x		x		x		39.48 $(4\pi^{2})$		3.14 (π)	Lapwood [28]
	x	x		x		x			27.10	2.33	Nield [33]
	x	x			x	x			12.0	0	Nield [33]
x			x	x		x		27.10		2.33	Lapwood [28]
			x		x	x			17.65	1.75	Nield [33] Ribando and Torrance [34]
x			x	x		x			9.87 (π^{2})	1.57 $(\pi/2)$	Elder [35]
	x		x		x	x			3.0	0	Nield [33]

Table 6. Factors affecting convective heat transfer.

Factors[a]	Permeability	Viscosity	Coefficient of thermal expansion of fluid	Rayleigh numbers $Ra = K\rho_{fl}g\beta\Delta t\, H/\eta\alpha$
Material				
mineral grains	low	low	low	uncertain
soil structure	significant	low	low	significant
density (porosity)	significant	significant	low	significant
Saturation				
bitumen/water proportions	significant	significant	significant	significant
degree of fluid saturation (presence of gas)	significant	significant	significant	significant
Uniformity				
homogeneity	significant	low	low	significant
isotropy	significant	low	low	significant
Ambient conditions				
confining pressure	intermediate	low	intermediate	low
pore fluid pressure	low	low	intermediate	low
temperature	significant	significant	significant	significant

[a] The reservoir dimensions and geometry will also influence the critical Rayleigh number.

Convection heat transfer cell. This heat transfer cell was developed by Lillico [3] to investigate the onset of natural convection in oil sands. The cell was designed based on the Schmidt-Milverton principle. A layer of oil sand sample was heated from below and cooled from above, allowing the uniaxial steady-state thermal conductivity of the sample to be measured. The onset of convection was detected when the measurement of the oil sand system's steady-state effective thermal conductivity suddenly increased. The heat transfer cell in the convection mode is shown in Figure 31.

Forced convection

The fluid motion in an oil sand reservoir may be induced by the injection of hot fluids (hot water or steam) into the reservoir.

Convective heat transfer. Consider the one-dimensional flow of hot water within a reservoir with thickness, h, shown in Figure 32. It is assumed that there is no heat loss from the upper and lower horizontal bounds of the reservoir and that temperature is a function of only the horizontal distance, x, and time, t.
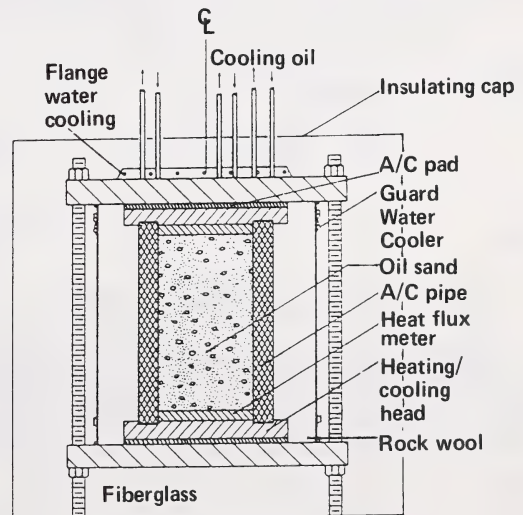
Figure 31. Natural convection mode of heat transfer cell, after Lillico [3].
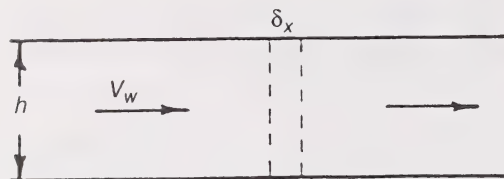
Figure 32. One-dimensional flow in reservoir, after Butler [2].

It is also assumed that the fluid saturations do not change during the process; for example, the oil saturation is at the residual oil level and the water saturation is constant.

The fluid flowing out of the differential element shown in the figure will, in general, be at lower temperature than that which is entering. The associated quantity of heat gain or loss will come from or go to the inventory of heat within the element. A heat balance about the differential element yields:

$$-hV_w \rho_w \, c_w \left(\frac{\partial T}{\partial x}\right)\delta x = h\rho_b c_b \left(\frac{\partial T}{\partial t}\right)\delta x \qquad (24)$$

where subscript w is for water and subscript b is for bulk or total;

heat in – heat out = accumulation.

This may be rearranged to:

$$\left(\frac{\partial T}{\partial t}\right) + \frac{V_w \rho_w c_w}{\rho_b c_b}\left(\frac{\partial T}{\partial x}\right) = 0 \qquad (25)$$

where

$$\rho_b c_b = (1-\phi)\,\rho_s c_s + \phi S_w \rho_w c_w + \phi S_o \rho_o c_o$$

Equation (26), which is the general solution of Equation (25) describes a heat front which moves along the bed at a velocity V_f. The solution is such that any existing temperature profile is moved unchanged along the bed.

$$T = f(x - V_f t)$$

where f is any function

$$V_f = \frac{V_w \, \rho_w c_w}{\rho_b c_b} \qquad (26)$$

Figure 33 depicts the movement of a heat front along the bed such as would be caused by suddenly raising the temperature of the injected water.
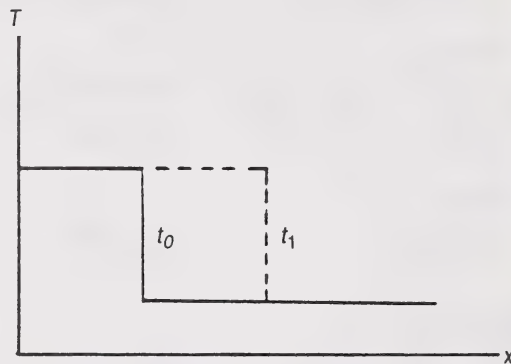
Figure 33. Movement of heat front through reservoir, after Butler [2].

There are many simplifications in the above derivation which are not realistic in actual operations. The vertical heat losses are neglected and the solid and fluid are assumed to have the same temperature at a particular location. The latter assumption is sometimes referred to as thermostatic equilibrium. It is probably reasonably realistic in reservoir-scale operations but it is often unrealistic in small process-type packed beds. If heat transfer resistances between the fluid and the bed are included in the theory, sharp fronts tend to become spread out with time.

Another phenomenon causing longitudinal dispersion is that of thermal conduction in the direction of the fluid flow.

Despite these various assumptions, the situation shown in Figures 32 and 33 has within it the basic concept of a heat front moving through a reservoir at a rate that is less than the fluid velocity.

Convective heat transfer including heat loss. The vertical heat losses were first considered by Lauwerier [39] for the situation shown in Figure 34. It was assumed that hot water was flowing in a water-saturated layer of thickness, h, within an oil sand reservoir. As the water flows through the water-saturated zone it loses

heat to the oil sand above and below. The derivation is also applicable to a sand heated by water, bounded above and below by impermeable strata. Figure 34 shows the situation modelled by Lauwerier.
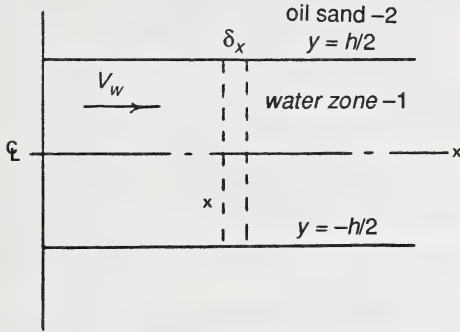
Figure 34. Flow of hot water through reservoir by Lauwerier, [2].

A heat balance about the differential region gives Equation (27). It is the same as Equation (23) with the addition of the last term which represents heat loss to the oil sand above and below.

$$-hV_w\rho_w c_w\left(\frac{\partial T}{\partial x}\right)\delta x =$$

$$h\rho_b c_b\left(\frac{\partial T}{\partial t}\right)\delta x - 2K_2\left(\frac{\partial T_2}{\partial y}\right)y = \frac{h}{2}\delta x \qquad (27)$$

The term $\rho_b c_b$ represents the volumetric heat capacity of the saturated water layer as given by:

$$\rho_b c_b = (1 - \phi)\,\rho_s c_s + \phi S_w \rho_w c_w + \phi S_o \rho_o c_o \qquad (28)$$

The conduction of heat within the oil sand is determined by Fourier's equation (29) where $\rho_2 c_2$ is the volumetric heat capacity of the oil sand determined by an equation similar to (28):

$$K_2\left(\frac{\partial^2 T_2}{\partial y^2}\right) = \rho_2 c_2\left(\frac{\partial T_2}{\partial t}\right) \qquad (29)$$

Substituting the dimensionless variables of Equation (30):

$$\xi = \frac{4K_2 x}{h^2 \rho_w c_w V_w}, \; \chi = \frac{2y}{h}$$

$$\tau = \frac{4K_2 x}{h^2 \rho_b c_b}, \; \theta = \frac{\rho_b c_b}{\rho_2 c_2} \qquad (30)$$

results in the system of equations

$$\text{For } |\chi| > 1, \; \theta\left(\frac{\partial^2 T^2}{\partial \chi^2}\right) = \left(\frac{\partial T_2}{\partial t}\right) \qquad (31)$$

$$\text{For } |\chi| = 1, \left(\frac{\partial^2 T^2}{\partial \tau}\right) + \left(\frac{\partial T_2}{\partial \xi}\right) - \left(\frac{\partial T_2}{\partial \chi}\right) = 0 \qquad (32)$$

and $T_1 = T_2$,

$$\text{for } \tau = 0, \; T_1 = T_2 = 1 \quad if \; \xi < 0$$
$$= 0 \quad if \; \xi > 0. \qquad (33)$$

These equations were solved by Lauwerier to give Equation (34) which expresses the temperature within the oil sand layer as a function of time and location.

$$T_2 = \left(\frac{\xi + |\chi| - 1}{2\left(\theta\left(\tau-\xi\right)\right)^{1/2}}\right) U\left(\tau-\xi\right) \qquad (34)$$

where $U(\tau - \xi) = 0$ if $\xi > \tau$
and $U(\tau - \xi) = 1$ if $\xi < \tau$.

Growing steam zone and related solutions. Marx and Langenheim [40] developed theoretical relations to describe the case of a growing steam zone which is limited in its growth rate by the loss of heat to the overburden and underburden and by the rate at which steam is introduced.

Mandl and Volek [41] considered the situation when the latent heat of the steam was completely consumed and heat was carried by the sensible heat. They

developed an equation to predict the critical time when the heat is transferred beyond the condensation front by the sensible heat of the condensate. A different expression was also formulated to describe the vertical heat loss from the steam zone for time greater than the Mandl and Volek critical time.

Myhill and Stegemeier [42] considered the effect of a nonvertical heat front on the vertical heat loss equation used by Marx and Langenheim.

Solutions to applications such as steam injection into a thin channel, a thin horizontal layer, or fracture are shown in Butler [2]. Besides hot water and steam flooding, fire flooding is another thermal recovery method. A convective heat transfer model was presented by Ward and Ward [43]. It describes the formation and advancement of convective fronts in fire flood operations.

LIST OF SYMBOLS

General

A	cross-sectional area (m^2)
a	wave number
c	specific heat kJ/(K•kg)
d	diameter (m)
g	local gravity acceleration constant (m/s^2)
H	distance or thickness (m)
h	height (m)
h_c	convective heat transfer coefficient (W/m^2•K)
K	absolute permeability (m^2)
k	thermal conductivity (W/m•K)
L	length (m)
q	heat flow (W)
q''	heat flux (W/m^2)
q_i	power per unit length (W/m)
R	radius (m)
Ra	Rayleigh number
S	saturation
r	radial distance (m)
T	temperature (°C)
t	time (s)
V_f	velocity of heat front (m/s)
V_w	velocity of water (m/s)
$x_{x,xo}$	mass fractions

Greek letters

α	thermal diffusivity (m^2/s)
β	coefficient of thermal expansion (°C^{-1})
δ_x	differential element
η	dynamic viscosity (Pa•s)
ρ	density (kg/m^3)
ϕ	porosity

Functions

$\exp_i$	exponential integral
e	exponential function
$f(a)$	function name
$J_0(x), J_1(x)$	Bessel function of order 0 and 1 respectively
$\ln$	natural log function
α_m	roots of an Eigenvalue equation
γ	Euler's constant = 0.577 22
Δ, γ_m	wave numbers
δ_n	(n = 1,2,3...) positive roots of the function, $J_0(R_0\delta) = 0$
θ_n	function name
$\phi(t)$	time function

Subscripts

c	critical
b	bulk or total
f	final
fl	fluid
i	initial
m	identification letter
n	nondimensional
o	oil
q	prescribed with surface heat flow
s	solid or sand grain
w	water

REFERENCES

1. A.C. Seto "Thermal testing of oil sands," M. Sc. thesis, Univ. of Alberta (1985) 320p.
2. R.M. Butler, Lectures on thermal recovery, Univ. of Calgary (1985) 416p.
3. D.A. Lillico, "Development of an oil sands heat

transfer cell," M. Sc. thesis, Univ. of Alberta (1986) 109p.

4. J.D. Scott and A.C. Seto, Thermal property measurements on oil sands, J. Can. Pet. Tech., Dec (1986) 70–77.

5. A. Hanafi and G.A. Karim, The thermal conductivity of oil sands using a transient method, J. Ener. Resour. Tech. Dec 108 (1986) 315–320.

6. J. DuBow, Simultaneous measurement of the thermal and electrical conductivity of Green River oil shales, U.S. Department of Energy, final report, TID-29381 (1977) 92p.

7. A.E. Benfield, Terrestial heat flow in Great Britain, Proc. of the Royal Soc. of London, Series A, 173 (1939) 428–450.

8. D.R. Flynn and T.W. Watson, High temperature thermal conductivity of soils, Proc. of the 8th Int. Conf. on Thermal Conductivity, C.Y. Ho and R.E. Taylor, Eds., Plenum Press, NY (1969) 913–939.

9. H.S Carslaw and J.C. Jaeger, "Conduction of heat in solids," Clarendon Press, Oxford, England (1959) 198–201, 261–262.

10. G.H. Nix, G.W. Lowery, R.I. Vachon and G.E. Tanger, Direct determination of thermal diffusivity and conductivity with a refined line-source technique, process in astronautics and aeronautics, vol, 20: Thermophysics of spacecraft and planetary bodies," G. Heller, Ed., Academic Press, New York (1967) 865–878.

11. A.E. Wechsler, Development of thermal conductivity probes for soils and insulations, U.S. Army Cold Regions Research Engineering Laboratory, Technical Report 182, Hanover, NH (1966) 83p.

12. J.H. Blackwell, A transient-flow method for determination of thermal constants of insulating materials in bulk, Part I–theory, J. App. Phys. (1954) 137–144.

13. J.H. Blackwell, The axial flow error in the thermal-conductivity probe, Can. J. Phys. (1956) 412–417.

14. J.E. Parrott and A.D. Stuckes, "Thermal conductivity of solids," Pion Limited, London (1975).

15. A. Hanafi, "Experimental and analytical studies of volatilization and burning of oil sand particles," Ph. D. thesis, Univ. of Calgary (1979).

16. J.C. Jaeger, The use of complete temperature-time curve for determination of thermal conductivity with particular reference to rocks, Australian J. Phys., 12 (1959) 203–217.

17. G.A. Karim and A. Hanafi, The thermal conductivity of oil sands, Can. J. Chem. Eng., 59 (1981) 461–464.

18. M.R. Cervenan, F.E. Vermeulen and F.S. Chute, Thermal conductivity and specific heat of oil sand samples, Can. J. Earth Sci., 18 (1981) 926–931.

19. N. Seki, K.C. Cheng and S. Fukusako, Measurements on thermal conductivity and thermal diffusivity of Alberta oil sands, Proc. of the 17th Int. Conf. on Thermal Conductivity, Plenum Press, NY (1981) 635–642.

20. J. Combs, S. Quiett and L.H. Axtell, Thermal conductivity measurement techniques for geothermal exploration heat flow surveys, Trans. Geothermal Resources Council, 1 (1977) 49–51.

21. N.B. Hutcheon and J.A. Paxton, Moisture migration in a closed guarded hot plate, ASHVE trans., 58 (1952) 301–320.

22. M.S. Kersten, Thermal properties of soils. Bull. no. 28, Univ. of Minnesota Institute of Technology Engineering Experiment Station (1949).

23. W.H. Somerton, Some thermal characteristics of porous rocks, Pet. Trans., AIME, 213 (1958) 375–378.

24. R. Krupiczka, Analysis of thermal conductivity in granular materials, Intl. Chem. Eng., 7, (1967) 122–144.

25. W.H. Somerton, J.A. Keese and S.L. Chu, Thermal behavior of unconsolidated oil sands, Soc. Pct. Eng. J., 14 (1974) 513–521.

26. K.D. Poulsen, S. Saxov, N. Balling and J.I. Kristiansen, Thermal conductivity measurements on Silurian limestones from the island of Gotland, Sweden, Geologiska Foreningen Stockholm Forhandl, part 3, 103 (1981) 349–356.

27. Y. Katto and T. Masuoka, Criterion for the onset of convective flow in a porous medium, Int. J. Heat and Mass Transfer, 10 (1967) 279–309.

28. E.R. Lapwood, Proc. Cambridge Philos. Soc., 44 (1948) 508–521.

29. R.A. Wooding, 2nd Workshop Geotherm Reservoir Eng. (1976) 339–345.

30. G. Castinel and M. Combarnous, Int. Chem. Eng., 17 (1977) 605–614.

31. D.R. Kassoy and A. Zebib, Phys. Fluids, 18 (1975) 1649–1651.

32. Geothermal heat transfer, Ch. 11 in "Handbook of heat transfer applications," W.M. Rohsenow, J.P. Hartnett and E.N. Ganie, Eds., 2nd ed., McGraw-Hill Book Company (1985).

33. D.A. Nield, Water resources res., 4 (1967) 553–560.

34. R.J. Ribando and K.E. Torrance, J. Heat Transfer, 98 (1976) 42–48.

35. J.W. Elder, J. Fluid Mech., 27 (1967) 29–48.

36. A. Zebib and D.R. Kassoy, Phys. Fluids, 20 (1977) 4–9.

37. J.M. Straus and G. Schubert, J. Geophys. Res.,82 (1977) 325–333.

38. R.J. Burretta, "Thermal convection in a fluid filled porous layer with uniform internal heat sources," Ph. D. thesis, Univ. of Minnesota (1972) 151p.

39. H.A. Lauwerier, The transport of heat in an oil layer caused by the injection of hot fluid, Appl. Sci. Res. A, 5 (1955) 145–150.

40. J.W. Marx and R.N. Langenheim, Reservoir heating by hot fluid injection, Pet. Trans. AIME, 216 (1959) 312–315.

41. G. Mandl and C.W. Volek, Heat and mass transport in steam drive processes, SPEJ, Mar (1969) 59–79.

42. N.A. Myhill and G.L. Stegemeier, Steam-drive correlation and prediction, JPT, Feb (1978) 173–182.

43. C.E. Ward and G.D. Ward, Heat transfer and oil displacement models for tar sands reservoirs, Soc. Pet. Engnrs. Reservoir Engineering, Nov, 2 (1987) 565–572.

12

MASS TRANSFER
BY DIFFUSION

T. Schmidt

Oil Sands and Hydrocarbon Recovery Department
Alberta Research Council
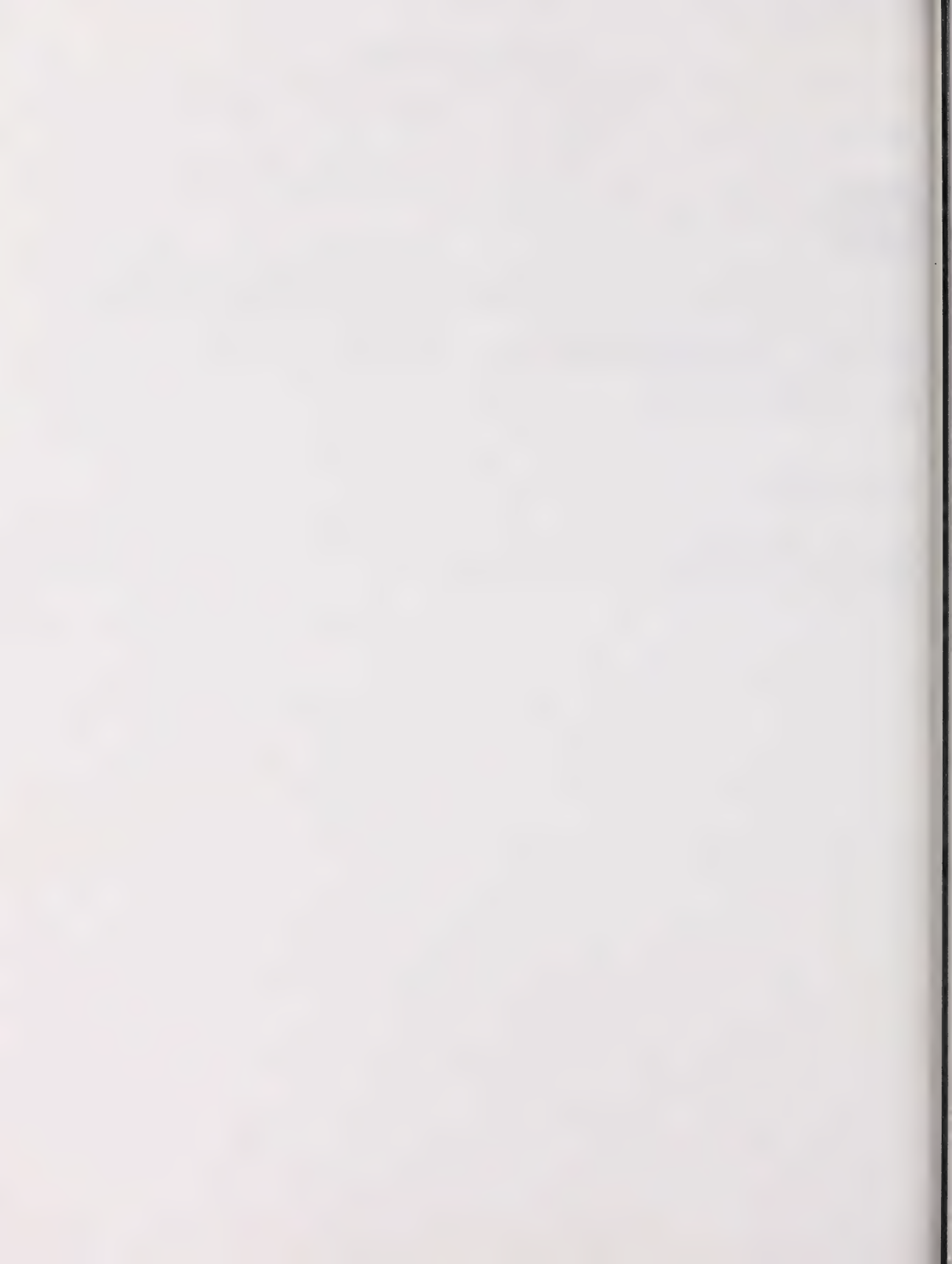
INTRODUCTION

This chapter deals with the migration of one substance through another under the influence of a concentration gradient. In oil recovery from tar sands, mass transfer occurs in many situations:

- Volatile components are transferred from the steam-heated liquid to the vapor (distillation).
- A soluble component, such as CO_2, is transferred from the gas phase to the liquid phase (absorption).
- A soluble component, such as the product of aquathermolysis reaction, is transferred from the liquid to the gas (stripping).
- Components, such as CO_2, are transferred between water and bitumen phases (liquid-liquid extraction).
- Bitumen can be considered as a solid being dissolved in a solvent (bitumen distillation).
- Chemicals injected into a formation are removed by adsorption on the surface of sand grains (adsorption).
- Supersaturated solutions of silica precipitate, causing permeability reduction (crystallization).

Two major factors control mass transfer: the distribution of components between phases at equilibrium (which can be calculated from thermodynamics), and the rate at which mass transfer occurs under the conditions prevailing in the reservoir. Before the mid-1980s, most reservoir simulation was limited to application of the first factor. The present chapter deals with the second factor, mass transfer rates.

Classical engineering approaches to mass transfer problems involving the complex intertwining of irregular flow geometrics and flow instabilities such as viscous fingers or density inversion, often make use of lumped characterization schemes involving dimensionless groups such as the Schmidt, Peclet, and Reynolds numbers. In some instances and depending on observation scale, mixing that results from effects other than molecular diffusion dominates the process [1]. On the other hand, laboratory experiments using a rocking cell apparatus take about 1 to 2 days to reach 95% equilibrium [2]. Hence, in numerical simulators it is questionable to assume equilibrium in all reservoir elements, and realistic mass transfer rates should be incorporated where necessary.

The first part of this chapter is a concise presentation of the fundamentals. Great effort has been made to be as brief as possible without sacrificing precision.

The second part of the chapter presents data and correlations. We must accept that predictive theories are far from complete (with the exception of dilute gases at low pressures), and available data are sparse. The correlations presented may be used to choose the functional form most appropriate for the computer representation of data.

Diffusion data are required for the estimation of the following parameters:

- Dispersion coefficient (usually given in dimensionless form as dispersivity divided by diffusivity).
- Mass transfer coefficient (usually correlated as the Sherwood number or Nusselt number for mass transfer).
- Schmidt number (ratio of kinematic viscosity to diffusivity).
- Lewis number (ratio of thermal diffusivity to diffusivity).
- Damkohler number (ratio of reaction rate constant times length to diffusivity).
- Peclet number for mass transfer (ratio of velocity times length to diffusivity).

FUNDAMENTALS

Fick's law

Fick's law of diffusion, together with Fourier's law of heat transfer, Ohm's law of electric current, and Newton's law of viscosity, belong to the group of linear laws of transport phenomena. The basic feature of these laws is that they all relate linearly the flux of the quantity of interest to the gradient of some intensive quantity (driving force) [3–5].

Fick's law for binary system in the barycentric description

It is generally agreed that the driving force for diffusion is the gradient of chemical potential [5]. The proportionality constant between diffusion velocity[a] and the driving force is called mobility. Mathematically:

$$V_A - V = -b_{AB} \nabla_T \, \tilde{\mu}_A \qquad (1)$$

The (–) sign indicates that the diffusion velocity is in the opposite direction of the isothermal gradient in chemical potential, $\tilde{\mu}_A$ is the chemical potential on a mass basis [10]. The inverse of the barycentric mobility is called barycentric friction coefficient, and has the dimensions of force per unit velocity:

---

[a] See Table 1 and Figures 1 and 2. Symbols are defined at the end of this chapter.

$$\nabla_T \, \tilde{\mu}_A \; = -k_{AB} \left(V_A \; - V \right) \qquad (2)$$

There is theoretical justification for Equation (1). In irreversible thermodynamics [16], the negative of the isothermal gradient is called the generalized force driving component A:

$$X_A \; = -\nabla_T \, \tilde{\mu}_A \qquad (3)$$

In the linear theory of irreversible thermodynamics the fluxes are assumed proportional to the forces. Hence

$$I_A \; = \; L_{AB} X_A \qquad (4)$$
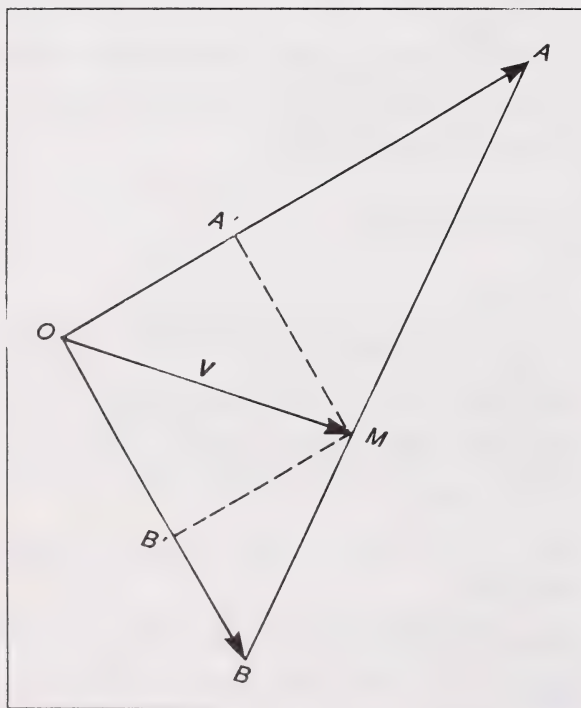
$$OA \; = \; V_A$$
$$OB \; = \; V_B$$
$$OM = \; V$$
$$OA \; = \; W_A V_A$$
$$OB \; = \; W_B V_B$$
$$AM \; = \; V_A - V$$
$$BM \; = \; V_B - V$$

Figure 1. Diffusion velocities in the barycentric description.

where I_A is the diffusion flux in barycentric coordinates (centre of gravity):

$$I_A \; = \; \rho_A \, (V_A \; - \; V) \qquad (5)$$

L_{AB} is called the barycentric phenomenological coefficient. Equation (5) is equivalent to the left-hand side of Equation (1), and Equation (3) to the right-hand side of Equation (1). Writing the gradient of chemical potential in the form

$$\nabla_T \tilde{\mu}_A \; = \; \left(\frac{\partial \tilde{\mu}_A}{\partial W_A} \right)_{T,P} \nabla W_A \qquad (6)$$

where W_A is the weight fraction of A, we get

$$I_A \; = \; -\rho D_{AB} \nabla W_A \qquad (7)$$

where

$$D_{AB} = b_{AB} \left(\frac{\partial \tilde{\mu}_A}{\partial \ln W_A} \right)_{T,P} \qquad (8)$$

Equation (7) is called Fick's law in the barycentric description. Equation (8) in the ideal case leads to the Planck-Einstein relation, hence, it may be called the generalized Planck-Einstein relation in the barycentric description.

Using the definitions of Tables 1 and 2 we can prove

$$I_A \; + \; I_B \; = \; 0 \qquad (9)$$

or using Fick's law

$$-\rho D_{AB} \nabla W_A + \rho D_{BA} \nabla W_A \; = \; 0 \qquad (10)$$

where we used $\nabla W_B = -\nabla W_A$. Hence

$$D_{AB} \; = \; D_{BA} \qquad (11)$$

Therefore, for a binary system there is only one diffusion coefficient. We have also proved

$$b_{AB} \; = \; b_{BA} \qquad (12)$$

and

$$L_{AB} \; = \; L_{BA} \, \frac{\rho_A}{\rho_B} \qquad (13)$$
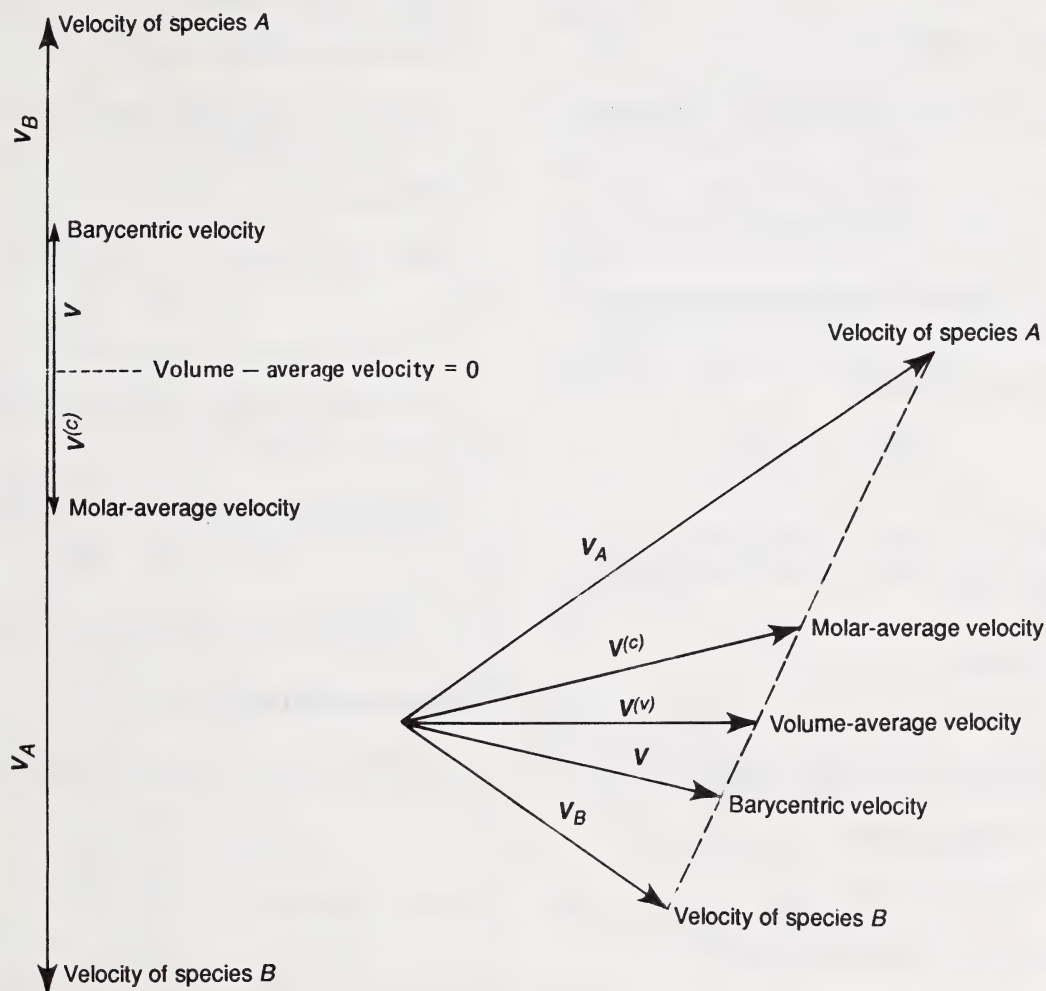
Figure 2. Barycentric velocity (V) and molar average ($V^{(c)}$) for a system containing 20 wt% A and 80 wt% B. Ratio of molecular weights $M_B/M_A = 4$. Ratio of partial molar volumes, $\bar{V}_B / \bar{V}_A = 2$.

Writing the barycentric velocity in terms of V_A, V_B, we get from Equation (5)

$$I_A = \rho W_A W_B (V_A - V_B) \qquad (14)$$

hence the diffusion velocity of A with respect B to is

$$\left(V_A - V_B\right) = -D_{AB} \frac{\nabla W_A}{W_A W_B} \qquad (15)$$

Other forms of Fick's law

If the partial specific volume of A is

$$\tilde{V}_i = \left(\frac{\partial V}{\partial m_i}\right)_{T,P, \quad Mj \neq 1} \quad i = A,B \qquad (16)$$

we can write the density as

$$\rho = \frac{1}{\tilde{V}_A W_A + \tilde{V}_B W_B} \qquad (17)$$

Table 1. Velocities.

Average velocity of a species

The arithmetic average of the individual velocities of the particles of that species:

$$V_A = \frac{1}{N_A} \sum_{i=1}^{N_A} V_i$$

where V_i is the velocity of the i-th particle of the specie i

Barycentric velocity

$$V = \frac{\left(m_A V_A + m_B V_B + \ldots\right)}{m}$$

where $m = m_A + m_B + \ldots$ is the total mass of the system and m_A, m_B, ... are the total masses of species $A, B, \ldots$

Alternatively

$$V = W_A V_A + W_B V_B + \ldots$$

where W_A, W_B, ... are weight fractions.

Molar-average velocity

$$V^{(c)} = X_A V_A + X_B V_B + \ldots$$

where X_A, X_B, ... are mole fractions.

Volume-average velocity

$$V^{(c)} = \phi_A V_A + \phi_B V_B + \ldots$$

where ϕ_A, ϕ_B ... are volume fractions.

Diffusion velocity of species A

- Barycentric description: $V_A - V$
- Molar-average description: $V_A - V^{(c)}$
- Volume-average description: $V_A - V^{(v)}$
- With respect to species B: $V_A - V_B$

Table 2. Fluxes (of species A).

With respect to stationary axes

- mass flux: $n_A = \rho_A V_A$
- molar flux: $N_A = C_A V_A$

Diffusion fluxes

- barycentric description: $I_A = \rho_A(V_A - V)$

$$J_A^{(m)} = C_A \left(V_A - V \right)$$

- molar-average description: $I_A^{(c)} = \rho_A \left(V_A - V^{(c)} \right)$

$$J_A = C_A \left(V_A - V^{(c)} \right)$$

- volume-average description: $I_A^{(v)} = \rho_A \left(V_A - V^{(v)} \right)$

$$J_A^{(v)} = C_A \left(V_A - V^{(v)} \right)$$

Relation between fluxes $I_A + I_B = 0$

$$M_A J_A^{(m)} + M_B J_B^{(m)} = 0$$

$$\frac{I_A^{(c)}}{M_A} + \frac{I_B^{(c)}}{M_B} = 0$$

$$J_A + J_B = 0$$

$$\tilde{V}_A I_A^{(v)} + \tilde{V}_B I_B^{(v)} = 0$$

$$\overline{V}_A J_A^{(v)} + \overline{V}_B J_B^{(v)} = 0$$

ϕ_i is the volume fraction, defined by $\phi_i = \tilde{V}_A \rho_A = \overline{V}_A C_A$

Relation between molar and mass flux

$I_A = M_A J_A$, in any representation.

and using the Gibbs-Duhem equation we can prove

$$\nabla \rho A = \rho^2 \tilde{V}_B \nabla W_A \qquad (18)$$

substituting in Equation (15)

$$\dot{\rho}_A \phi_B (V_A - V_B) = -D_{AB} \nabla \rho_A \qquad (19)$$

where ϕ_B is the volume fraction of B:

$$\phi_B = \rho_B \tilde{V}_B \qquad (20)$$

We can write the left side of Equation (19) as

$$\rho_A \phi_B (V_A - V_B) = \rho_A (\phi_B V_A - \phi_B V_B)$$
$$= \rho_A (V_A - \phi_A V_B - \phi_B V_B) \qquad (21)$$

where $\phi_B = 1 - \phi_A$. The volume-average velocity is defined

$$V^{(v)} = \phi_A V_A + \phi_B V_B \qquad (22)$$

and the corresponding diffusion flux is given by

$$I_A^{(v)} = \rho_A \left(V_A - V_B \right) \qquad (23)$$

Using Equations (21) to (23) in Equation (19) we get

$$I_A^{(v)} = -D_{AB} \nabla \rho_A \qquad (24)$$

which is Fick's law in the volume-fixed coordinate system.

There is a fundamental reason why the barycentric formulation (7) is preferable: continuity preserves mass, but not volume. Hence, only for fluids with constant density can we have a finite region where the net volume flux is zero:

$$I_A^{(v)} + I_B^{(v)} = 0 \qquad (25)$$

In many situations Equation (25) can only be satisfied along a plane perpendicular to the fluxes, that is, a region of zero thickness. The experimenter can have difficulties determining this plane. Theorists may incorrectly attempt to use Equation (25) to simplify the continuity equation (setting the volume velocity equal to zero).

The ambiguities that arise when volume-fixed coordinates are used have been thoroughly investigated and reported in Crank [3].

Other forms of Fick's law can be obtained, and each has its particular merits. Tables 1 through 5 summarize the results. The diffusion coefficient has the same value in the barycentric, the volume-fixed, and the mole-fixed formulations.

It must be stressed that understanding the theory is not important for experimenters only: application of the wrong form of Fick's law will lead to incorrect predictions.

The continuity equation in binary mixtures

In the absence of chemical reactions, the continuity equations for each of the species A, B are

$$\frac{\partial \rho_A}{\partial t} = -\nabla \cdot \rho_A V_A \qquad (26)$$

$$\frac{\partial \rho_B}{\partial t} = -\nabla \cdot \rho_B V_B \qquad (27)$$

Adding, we get

$$\frac{\partial \rho}{\partial t} = -\nabla \cdot \rho V \qquad (28)$$

which is called the overall continuity for total mass. Notice that the velocity is the barycentric velocity.

For isobaric, isothermal systems we can use

$$I_A = \rho_A (V_A - V) = -\rho D_{AB} \nabla W_A \qquad (29)$$

and

$$d\rho_A = \rho dW_A + W_A d\rho \qquad (30)$$

to get

$$\frac{DW_A}{Dt} \equiv \frac{\partial W_A}{\partial t} + V \cdot \nabla W_A = \frac{1}{\rho} \nabla \cdot \rho D_{AB} \nabla W_A \qquad (31)$$

where we used Equation (28) to simplify the extra terms. The operator D/Dt is called substantial derivative.

If we write the species continuity Equations (26) and (27) in terms of moles, the steps are similar, but the velocity that appears in the overall continuity is not the barycentric velocity but the velocity of the centre of moles:

$$\frac{\partial C_A}{\partial t} = -\nabla \cdot C_A V_A \qquad (32)$$

$$\frac{\partial C_B}{\partial t} = -\nabla \cdot C_B V_B \tag{33}$$

$$\frac{\partial C}{\partial t} = -\nabla \cdot CV^{(c)} \tag{34}$$

$$\frac{DX_A}{Dt} = \frac{\partial X_A}{\partial t} + V^{(c)} \cdot \nabla X_A = \frac{1}{C} \nabla \cdot CD_{AB} \nabla X_A \tag{35}$$

Notice that the substantial derivative is different in the centre-of-moles description from the substantial derivative in the barycentric description. Since the substantial derivative operator is represented by the same symbol in both cases this can be a source of confusion.

To completely determine the system, an additional equation is needed, which in the barycentric formulation is the density

$$\rho = \frac{1}{\bar{V}_A W_A + \bar{V}_B W_B} \tag{36}$$

and in the centre-of-moles description the concentration

$$C = \frac{1}{\bar{V}_A X_A + \bar{V}_B X_B} \tag{37}$$

Simplifications of the continuity equations

If $\tilde{V}_A = \tilde{V}_B$, then ρ is constant and Equation (31) reduces to

$$\frac{\partial W_A}{\partial t} + V \cdot \nabla W_A = \nabla \cdot D_{AB} \nabla W_A \tag{38}$$

and the overall continuity equation reduces to

$$\nabla \cdot V = 0 \tag{39}$$

Similarly, if $\bar{V}_A = \bar{V}_B$, then C is constant and Equation (35) reduces to

$$\frac{\partial X_A}{\partial t} + V^{(c)} \cdot \nabla X_A = \nabla \cdot D_{AB} \nabla X_A \tag{40}$$

with overall continuity in the form

$$\nabla \cdot V^{(c)} = 0 \tag{41}$$

Notice that Equations (39) and (41) mean two different things. If $\tilde{V}_A = \tilde{V}_B$, then

$$V = V^{(v)} \tag{42}$$

that is, the barycentric velocity equals the volume-fixed velocity. If $\bar{V}_A = \bar{V}_B$, then

$$V^{(c)} = V^{(v)} \tag{43}$$

that is, the mole-fixed velocity equals the volume-fixed velocity.

Equations (38), (39), and (42) are satisfied by liquid mixtures that do not change density with composition.

Equations (40), (41), and (43) are usually satisfied for gases at low pressures.

Table 6 presents the continuity equation in the barycentric and molar descriptions.

Fick's second law
Assume:
(a) D_{AB} is constant
(b) $\tilde{V}_B = \tilde{V}_B$ for all concentrations
(c) the only solution of $\nabla \cdot V = 0$ is $V = 0$
Equation (31) then reduces to

$$\frac{\partial W_A}{\partial t} = D_{AB} \nabla^2 W_A \tag{44}$$

Similarly, if we assume:
(a') D_{AB} is constant
(b') $\bar{V}_A = \bar{V}_B$ for all concentrations
(c') the only solution of $\nabla \cdot V^{(c)} = 0$ is $V^{(c)} = 0$
then Equation (35) reduces to

$$\frac{\partial X_A}{\partial t} = D_{AB} \nabla^2 X_A \tag{45}$$

Notice that under the assumptions (b) and (b') we can write Equations (44) and (45) as

$$\frac{\partial \rho_A}{\partial t} = D_{AB} \nabla^2 \rho_A \tag{46}$$

$$\frac{\partial C_A}{\partial t} = D_{AB} \nabla^2 C_A \tag{47}$$

respectively.

Table 3. Fick's law (species A).

Barycentric description

$$I_A = -\rho D_{AB}\nabla W_A$$

Molar-average description

$$J_A = -CD_{AB}\nabla X_A$$

Volume-average description

$$I_A^{(v)} = -D_{AB}\nabla \rho_A$$

$$J_A^{(v)} = -D_{AB}\nabla C_A$$

With respect to stationary axes

$$n_A = -\rho D_{AB}\nabla W_A + \rho_A V$$

$$= -D_{AB}\nabla \rho_A + \rho_A V^{(v)}$$

$$N_A = -CD_{AB}\nabla X_A + C_A V^{(c)}$$

$$= -D_{AB}\nabla C_A + C_A V^{(v)}$$

Relation between fluxes

$$V_A - V_B = \frac{I_A}{\rho W_A W_B} = \frac{J_A}{CX_A X_B}$$

$$= \frac{I_A^{(v)}}{\rho_A \rho_B \tilde{V}_B} = \frac{J_A^{(v)}}{C_A C_B \tilde{V}_B}$$

Table 4. Thermodynamics.

Thermodynamic driving force

If G is the free energy of the system, chemical potential on a *molar* basis is defined

$$\mu_A = \left(\frac{\partial G}{\partial N_A}\right)_{T,P,N_B,\ldots}$$

Using the *mass* of A instead of moles

$$\tilde{\mu}_A = \left(\frac{\partial G}{\partial m_A}\right)_{T,P,m_B,\ldots}$$

The relation between the two is $\mu_A = M_A \cdot \tilde{\mu}_A$

In terms of standard states

$$\tilde{\mu}_A = \tilde{\mu}_A + \tilde{R}_A T \ln\frac{f_A}{f_A^\circ}$$

$$\mu_A = \mu_A^\circ + RT \ln\frac{f_A}{f_A^\circ}$$

where $R = M_A \tilde{R}_A$ is the same for all substances, while $\tilde{R}_A$ depends on the substance. The fugacities are the same in the molar and mass descriptions.

Gibbs-Duhem equation in molar and in mass descriptions

From $dG = VdP - SdT + \Sigma \mu_i dN_i$

and $dG = d\Sigma \mu_i N_i = \Sigma \mu_i dN_i + \Sigma N_i d\mu_i$

it follows $Vdp - SdT = \Sigma N_i d\mu_i$;

hence, at constant T and P $\Sigma N_i d\mu_i = 0$,

or, by dividing by $N = \Sigma N_i$, $\Sigma X_i d\mu_i = 0$.

On a mass basis, from $dG = VdP - SdT + \Sigma \tilde{\mu}_i dm_i$

and $dG = \Sigma \tilde{\mu}_i dm_i + \Sigma m_i d\tilde{\mu}_i$, $\Sigma m_i d\tilde{\mu}_i = 0$

or dividing by $m = \Sigma m_i$, $\Sigma W_i d\tilde{\mu}_i = 0$.

Table 5. Transport coefficients.

Mobility

- barycentric description $V_A - V = -b_{AB}\nabla_T \tilde{\mu}_A$

- molar-average description $V_A - V^{(c)} = -b_{AB}\nabla_T \mu_A$

Phenomenological coefficient in barycentric description

$$L_{AB} = b_{AB}\rho_A = b_{AB}C_A$$

Diffusivity

- barycentric description $D_{AB} = b_{AB}\left(\dfrac{d\tilde{\mu}_A}{d\ln W_A}\right)_{T,P}$

- molar-average description $D_{AB} = b'_{AB}\left(\dfrac{d\mu_A}{d\ln X_A}\right)_{T,P}$

Friction coefficient

- barycentric description $k_{AB}\left(V_A - V\right) = -\nabla_T \tilde{\mu}_A$

- molar-average description $k'_{AB}\left(V_A - V^{(c)}\right) = -\nabla_T \mu_A$

Relationships between transport coefficients

$$b'_{AB} = \frac{b_{AB}}{\left(M_A W_B + M_B W_A\right)}$$

$$D_{AB} = D_{BA}$$

Table 6. Continuity equations.

Barycentric description (centre of gravity)

$$\frac{\partial W_A}{\partial t} + V \cdot \nabla W_A = \frac{\left(\nabla \cdot \rho D_{AB}\nabla W_A\right)}{\rho}$$

$$\frac{\partial \rho}{\partial t} = -\nabla \cdot \rho V$$

where

$$\rho = \frac{1}{\left(\tilde{V}_A - \tilde{V}_B\right)W_A + \tilde{V}_B}$$

and V is the barycentric velocity.

Molar description (centre of moles)

$$\frac{\partial X_A}{\partial t} + V^{(c)} \cdot \nabla X_A = \frac{\left(\nabla \cdot C D_{AB}\nabla X_A\right)}{C}$$

$$\frac{\partial C}{\partial t} = -\nabla \cdot C V^{(c)}$$

where

$$C = \frac{1}{\left(\overline{V}_A - \overline{V}_B\right)X_A + \overline{V}_B}$$

and $V^{(c)}$ is the velocity of the centre of moles.

Either pair of equations, (44) and (45) or (46) and (47), is called Fick's second law.

Mathematically they are identical to the heat equation. In many places they are called the diffusion equation or the heat-diffusion equation.

Some comments on the solutions

Classical solutions of the diffusion equations. If D_{AB} is constant and either $\bar{V}_A = \bar{V}_B$ or $\overline{V}_A = \overline{V}_B$ we are lead to linear equations, unless the boundary conditions introduce nonlinearities. Linear equations can be solved by the superposition of simpler problems. In this section we consider only cases where $V = 0$.

As an example, suppose we want to solve

$$\frac{\partial W}{\partial t} = D \frac{\partial^2 W}{\partial x^2} \tag{48}$$

subject to nonhomogeneous initial conditions

$$W(0, x) = f(x) \tag{49}$$

and the nonhomogeneous boundary conditions

$$\frac{\partial W}{\partial x}(t, 0) + A W(t, 0) = g(t) \tag{50}$$

$$\frac{\partial W}{\partial x}(t, 1) + B W(t, 1) = h(t) \tag{51}$$

To solve, let $W = W_1 + W_2 + W_3$, where each W_i satisfies Equation (48) with homogeneous conditions, with these exceptions:
for W_1

$$W_1(0, x) = f(x) \tag{52}$$

for W_2

$$\frac{\partial W_2}{\partial t}(t, 0) + A W_2(t, 0) = g(t) \tag{53}$$

for W_3

$$\frac{\partial W_3}{\partial x}(t, 1) + B W_3(t, 1) = h(t) \tag{54}$$

Particular cases are obtained when $A = B = \infty$ (Dirichlet boundary conditions) and $A = B = 0$ (Neumann boundary conditions).

The Dirichlet problem and the general problem (boundary conditions of the form in Equations (50) and (51)) always have a unique solution. The Neumann problem has unique solutions up to an arbitrary constant, that is, one must specify the value of W at an additional point.

For stationary solutions ($\partial W/\partial t = 0$) one obtains Laplace's equation

$$\nabla^2 W = 0 \tag{55}$$

which has an unique solution for Dirichlet and mixed boundary conditions.

For Neumann conditions (gradient prescribed on the boundary) it is required that

$$\oint F \cdot dS = 0 \tag{56}$$

where F is the gradient of W evaluated at the boundary and dS is an element of area of the boundary. If Equation (56) holds, the solution of Equation (55) is unique up to an additive constant.

The convection-diffusion equation. Let us assume V is not zero. Then if D_{AB} is constant and either or $\tilde{V}_A = \tilde{V}_B$ or else $\overline{V}_A = \overline{V}_B$, we are lead in general to the equation

$$\frac{\partial W}{\partial t} + V \cdot \nabla W = D_{AB} \nabla^2 W_A \tag{57}$$

which is called the convection-diffusion equation. The velocity field must satisfy

$$\nabla \cdot V = 0 \tag{58}$$

and usually can be obtained from a suitable potential or stream function. Many solutions are available in Skelland [4], Kays [5], and Levich [6].

Equation (57) shows that it is not necessary to have time as an independent variable to get an equation analogous to the heat equation. Suppose $\partial W_A / \partial t = 0$, $V = U_i$, and $\nabla^2 W_A = \partial^2 W_A/\partial y^2$. Substituting, we get

$$U \frac{\partial W_A}{\partial x} = D_{AB} \frac{\partial^2 W_A}{\partial y^2} \tag{59}$$

which is the same equation as (48) with $D = D_{AB}/U$ and x corresponding to t.

Nonlinear cases. Most other cases that arise when the

simplifications mentioned above (constant D_{AB}, $V_A = V_B$, etc.) cannot be made, lead to nonlinear equations. The main cases are:

- Cases where the density is a function of concentration.
- Cases where the diffusivity is a function of concentration.
- Cases where the velocity is a function of concentration, as for example, with concentration-dependent viscosity.
- Cases where reactions are present and their order is not zero or one.
- Moving boundary problems.
- Nonlinear boundary conditions, as example, complex dissolution kinetics.

In these cases one cannot use any of the classical solution methods described above.

Multicomponent systems. For systems with more than two components there is very little that can be said with some degree of certainty, and that can be used in practical applications. Most work done so far has only academic importance (to check Onsager's relations, for example), and is restricted to ideal situations (ideal gases, principally) and dilute solutions (where volume changes are negligible).

As an introduction to multicomponent diffusion the reader may consult Hirschfelder et al. [7], p. 516–519, 715–717, and 751; Lightfoot et al. [8]; Hsu and Bird [9]; and Slattery [10], p. 475–485. For a short overview, Bird et al. [11] is highly recommended. Use of an average diffusion coefficient for multicomponent systems must be done with care because it can lead to erroneous results in some cases.

In multicomponent diffusion the following phenomena may occur:

- The diffusion flux of a component may be zero, even though there is a concentration gradient of that component.
- The diffusion flux of a component may not be zero, even though the concentration gradient of that component is zero.
- The direction of the flux may be opposite that predicted by the concentration gradient (flux from low concentration toward high concentration).

These are called, respectively, presence of a diffusion barrier, osmotic diffusion, and reverse diffusion.

For multicomponent systems it seems the calculation of diffusion in reservoirs will have to rely on empirically-determined diffusivities in a pseudo-binary system for the time being. This must be done carefully since the approach has severe limitations.

DATA AND CORRELATIONS

Partially because diffusion is more complicated than viscous flow or heat conduction, there is a limited amount of reliable diffusivity data. Close examination shows that some experimenters do not clearly specify the reference velocity or are unaware of diffusion-driven convection. Other times, comparison of data from different sources shows considerable discrepancy.

While it is better to use experimental values, the above considerations necessitate the calculation of estimated or extrapolated values of diffusivity.

The following sections present useful correlations for gases and liquids. For more extensive treatment, we recommend the monographs by Reid et al. [12] and Bretsznajder [13] as the most complete sources of data and correlations for gases and liquids, and the extensive article by Marrero and Mason [14] for gases.

Available bitumen data and correlations are presented in the last section of this chapter.

Diffusivity in gases

Predictive theories of diffusion are highly developed for dilute gases. A very simplified statistical mechanical theory such as that described in the first pages of Hirschfelder et al. [7] immediately gives most of the facts. According to the simplified theory, the diffusivity (cm^2/s) is given by

$$D_{AB} = 2.6280 \times 10^{-3} \frac{\left(\frac{T^3}{2M_{AB}}\right)^{1/2}}{P\delta_{AB}^2} \quad (60)$$

where the reduced molecular weight M_{AB} is

$$M_{AB} = \frac{M_A M_B}{M_A + M_B} \quad (61)$$

and the average collision diameter (Å) is

$$\sigma_{AB} = \frac{\sigma_A + \sigma_B}{2} \quad (62)$$

The pressure P is given in atmospheres.

The following main features follow from Equation (60):

- In gases, the binary diffusivity increases with temperature, roughly as $T^{3/2}$.

- Diffusivity depends on the molecular weight of both species.
- Diffusivity depends on the size of the molecules, given in terms of the collision diameter (Equation 62), squared. This is proportional to the cross area $\pi\sigma^2_{AB}$ of a sphere having diameter equal to $\sigma_A + \sigma_B/2$. Then if V is the volume of such a sphere, the diffusivity is inversely proportional to $V^{2/3}$.
- Diffusivity is inversely proportional to pressure.

The accurate theory as developed in Chapter 8 of Chapman and Cowling [15] leads to the following expression for the first approximation to D_{AB}:

$$D_{AB} = 0.0026280 \ \frac{\left(\dfrac{T^3}{2M_{AB}}\right)^{1/2}}{P\sigma^2_{AB}\, \Omega^{(1,1)*}_{AB}\left(T^*_{AB}\right)} \tag{63}$$

$$T^*_{AB} = \frac{kT}{\varepsilon_{AB}} \tag{64}$$

$$\varepsilon_{AB} = (\varepsilon_A \varepsilon_B)^{1/2} \tag{65}$$

and the collision integral $\Omega^{(1,1)*}_{AB}(T^*_{AB})$ is calculated using some model for the intermolecular potential. For the Lennard-Jones potential the integral is tabulated in Table I–M of Hirschfelder et al. [7]. See also Table 7. Higher-order approximations can be calculated, but for Lennard-Jones potentials the improvement is minimal ($< 3\%$). The first approximation can be easily programmed for computer use. The equation for the first approximation

$$\Omega^{(1,1)*}_{AB} \ \text{is} \ \Omega^{(1,1)*}_{AB} = 1.075\left(T^*_{AB}\right)^{-0.1615}$$

$$- 2\left(10\, T^*_{AB}\right)^{-0.741\,\log\,(10T^*_{AB})}$$

The force constants σ_i and ε_i/k are given in Table 8 for a selected list of substances. More extensive tables are available in Hirschfelder et al. [7] and Bird et al. [11]. For unlisted force constants one may use the approximations

$$\frac{\varepsilon_i}{k} = 0.75T_{ci} \tag{66}$$

$$\sigma_i = \frac{5}{6}\left(V_{ci}\right)^{1/3} \tag{67}$$

where T_{ci}, V_{ci} are the critical temperature and pressure of substance i, respectively. Other equations for gases are given in Table 9.

The dependence of the diffusion coefficient in the composition of a mixture is usually slight. However, experiments carried out by Sigmund [16] in the methane-propane system show that at pressure above 100 atm the diffusion coefficient can change up to a factor of four with methane concentration going from zero to one mole fraction.

Diffusivity in liquids

Predictive theories of diffusion are not as well developed for liquids as they are for gases. However, a starting point can be made if we assume the soluble molecules are large compared with the solute and use the Stokes equation for the force acting on a sphere of radius immersed in a fluid.

Diffusivity at infinite dilution. For dilute solutions of spheres in Newtonian fluids the force acting on N spheres moving with velocity U with respect to fluid of viscosity μ is

$$F_A = 6\pi\mu_B rUN \tag{68}$$

where $6\pi\mu_B rU$ is the force acting on one sphere. If M_A is the mass of N particles, the velocity per unit force acting on a unit mass of A is then

$$\frac{U}{F_A/M_A} = \frac{M_A}{6\pi\mu_B rN} \tag{69}$$

The left-hand side is the mobility defined by Equation (1). Substituting in Equation (8) and rearranging

$$\frac{D_{AB}\mu_B}{T} = \frac{RM_A}{6\pi rN\left(M_A W_B + M_B W_A\right)}$$

$$= \frac{k}{6\pi r}\left(\frac{M_A}{M_A W_B + M_B W_A}\right) \tag{70}$$

where k is Boltzmann's constant.

Table 7. Values of the collision integral calculated with Lennard-Jones potential.

T_{AB}^*	$\Omega_{AB}^{(1,1)*}$	T_{AB}^*	$\Omega_{AB}^{(1,1)*}$	T_{AB}^*	$\Omega_{AB}^{(1,1)*}$
0.30	2.662	1.65	1.153	4.0	0.883 6
0.35	2.476	1.70	1.140	4.1	0.878 8
0.40	2.318	1.75	1.128	4.2	0.874 0
0.45	2.184	1.80	1.116	4.3	0.869 4
0.50	2.066	1.85	1.105	4.4	0.865 2
0.55	1.966	1.90	1.094	4.5	0.861 0
0.60	1.877	1.95	1.084	4.6	0.856 8
0.65	1.798	2.00	1.075	4.7	0.853 0
0.70	1.729	2.1	1.057	4.8	0.849 2
0.75	1.667	2.2	1.041	4.9	0.845 6
0.80	1.612	2.3	1.026	5.0	0.842 2
0.85	1.562	2.4	1.012	6	0.812 4
0.90	1.517	2.5	0.996	7	0.789 6
0.95	1.476	2.6	0.987 8	8	0.771.2
1.00	1.439	2.7	0.977 0	9	0.755 6
1.05	1.406	2.8	0.967 2	10	0.742 4
1.10	1.375	2.9	0.957 6	20	0.664 0
1.15	1.346	3.0	0.949 0	30	0.623 2
1.20	1.320	3.1	0.940 6	40	0.596 0
1.25	1.296	3.2	0.932 8	50	0.575 6
1.30	1.273	3.3	0.925 6	60	0.559 6
1.35	1.253	3.4	0.918 6	70	0.546 4
1.40	1.233	3.5	0.912 0	80	0.535 2
1.45	1.215	3.6	0.905 8	90	0.525 6
1.50	1.198	3.7	0.899 8	100	0.513 0
1.55	1.182	3.8	0.894 2	200	0.464.4
1.60	1.167	3.9	0.888 8	400	0.417 0

From: J.O. Hirschfelder et al. [7], p.1126, 1127.

The Stokes solution is valid when there are very few spheres. Hence, the equation will be correct when $W_A \to 0$, $W_B \to 1$. Substituting, we get the Einstein-Stokes relation

$$\frac{D_{AB}^o \mu_B}{T} = \frac{k}{6\pi r} \qquad (71)$$

where the symbol D^o_{AB} means diffusivity of A in B at infinite dilution. Equation (71) applies when the fluid sticks to the surface of the sphere (no slip boundary condition). If some slip is allowed, the solution to the Stokes problem [73] leads to

$$\frac{D_{AB}^o \mu_B}{T} = \frac{k}{6\pi r} \left(\frac{\beta r + 3\mu_B}{\beta r + 2\mu_B} \right) \qquad (72)$$

where β is the coefficient of slip. If $\beta = \infty$ we are led to Equation (71) and if $\beta = 0$ we get

$$\frac{D_{AB}^o \mu_B}{T} = \frac{k}{4\pi r} \qquad (73)$$

Equation (73) is applicable when the diameters of solute and solvent molecules are of the same order of magnitude, while (72) is applicable when the diameter

Table 8. Values of the collision integral calculated with Lennard-Jones potential.

Gas	M	$\sigma(\text{Å})$	$\varepsilon/k(\text{K})$
Air	28.8	3.711	78.6
CCl_4	153.823	5.947	322.7
CH_3OH	32.042	3.626	481.8
CH_4	16.043	3.758	148.6
CO	28.01	3.69	91.7
CO_2	44.01	3.941	195.2
C_2H_4	28.054	4.163	224.7
C_2H_6	30.07	4.443	215.7
C_2H_5OH	46.069	4.530	362.6
C_3H_8	44.097	5.118	237.1
$n–C_4H_{10}$	58.124	4.687	531.4
$iso–C_4H_{10}$	58.124	5.278	330.1
$n–C_5H_{12}$	75.151	5.784	341.1
C_6H_6	78.114	5.349	412.3
H_2	2.016	2.827	59.7
H_2O	18.015	2.641	809.1
H_2S	34.08	3.623	301.1
NH_3	17.031	2.900	558.3
N_2	28.013	3.798	71.4
O_2	31.999	3.467	106.7
SO_2	64.063	4.112	335.4

Source: [7], p. 1110–1111.

of the solute molecules is much larger than the solvent diameter.

If the diameter of the solute is estimated from

$$2\,r = \left(\frac{V_A}{N_o}\right)^{1/3} \qquad (74)$$

where V_A is the molar volume and N_o is Avogadro's number, Equation (73) leads to

$$\frac{D_{AB}^o \, \mu_B}{T} = \frac{k}{2\pi}\left(\frac{N_o}{V_A}\right)^{1/3} \qquad (75)$$

Wilke and Chang [17] plotted the logarithm of $T/D_{AB}\mu$ versus the logarithm of the solute molar volume and observed that the slope of the curve was not 1/3 but 0.6. They also followed the same approach to find the dependence on molecular weight of solvent. Using a substantial number of experimental data they were able

to correlate within 10% using the expression

$$D_{AB}^o = 1.4 \times 10^{-8}\left(\frac{\left(\xi M_B\right)^{1/2}\,T}{\mu_B V_A^{0.6}}\right) \qquad (76)$$

where ξ is an empirical constant, called the association parameter ($\xi =1$ for nonassociated, $\xi = 2.6$ for water). See Table 10 where other correlations are also presented.

Since viscosity has been found to satisfy Andrade's equation in a restricted temperature range

$$\mu = A \exp (B/T) \qquad (77)$$

one may try to eliminate the viscosity term in the correlations, using an exponential dependence of diffusivity, say

$$D = A' \exp (B'/T) \qquad (78)$$

Table 9. Equations for diffusivity in gases.

Equation (D_{AB} in cm^2/s)	Notes and references
$$D_{AB} = 2.628 \times 10^{-3} \frac{\left(\dfrac{T^3}{2M_{AB}}\right)^{1/2}}{P\,\sigma_{AB}^2}$$	Simplified kinetic theory, Hirschfelder et al. [7], p. 14
$$D_{AB} = 2.628 \times 10^{-3} \frac{\left(\dfrac{T^3}{2M_{AB}}\right)^{1/2}}{P\sigma_{AB}^2\,\Omega_{AB}^{(1,1)*}}$$	Chapman-Engskok theory, Hirschfelder et al. [7], p. 539
$$D_{AB} = \frac{0.00100\,T^{7/4}}{P\left(V_A^{1/3}+V_B^{1/3}\right)^2}\left(\frac{M_A+M_B}{M_A M_B}\right)^{1/2}$$	Fuller et al. The volumes V_A and V_B are given as the sum of given diffusion volume increments: C, 16.5; H, 1.98; O, 5.48.
$$D_{AB} = \frac{0.0150\,T^{1.81}}{P\left(T_{CA}T_{CB}\right)^{0.1405}\left(V_{CA}^{0.4}+V_{CB}^{0.4}\right)^2}\left(\frac{M_A+M_B}{M_A M_B}\right)^{1/2}$$	Chen and Othmer [32]
$$D_{AB} = 2.52 \times 10^7\,\mu_{air}^{2.74}\,\frac{\left(\dfrac{1}{M_A}+\dfrac{1}{M_B}\right)^{0.615}}{\left(V_{CA}^{0.4}+V_{CB}^{0.4}\right)^{2.46}}$$	Othmer and Chen [33]
$$D_{AB} = \frac{B\,T^{3/2}}{P\sigma_{AB}^2\,\Omega_{AB}^{(1,1)*}}\left(\frac{M_A+M_B}{M_A M_B}\right)$$	Wilke and Lee [34]. B is given by $B = 0.00214 - 0.000492\,(M_a + M_b\,/\,M_a M_b)^{1/2}$.
$$D_{AB} = \frac{100\mu V_m}{0.122M-1.3}$$	Suggested by Ibrahim and Kuloor for use with air only (B = air). μ, V_m, and M are the viscosity, molar volume, and molecular weight of gas A.

Table 10. Equations for diffusivity in liquids at infinite dillution.

Equation (D_{AB} in cm²/s, volumes in mL)	Notes and references
$$\frac{D^o_{AB}\,\mu_{AB}}{T} = 7.4 \times 10^{-8}\,\frac{\left(\xi M_B\right)^{1/2}}{V_{bA}^{0.6}}$$	Wilke and Chang [17]. $\xi = 1$ for non-associated solvents, 1.5 for ethanol, 1.9 for methanol, 2.6 for water.
$$\frac{D^o_{AB}\,\mu_B^{0.93}}{T^{0.93}} = 5.4 \times 10^{-8}\left(\frac{M_B^{0.5}\,\Delta\tilde{H}_B}{V_{bA}^{0.5}\,\Delta\tilde{H}_A}\right)^{0.93}$$	Sitamaran et al. [36]. $\Delta\tilde{H}_A\,\Delta\tilde{H}_B$ are the latent heats of vaporization in cal/g.
$$\frac{D^o_{AB}\,\mu_B}{T} = 4.4 \times 10^{-8}\left(\frac{V_{bB}}{V_{bA}}\right)^{1/6}\left(\frac{\Delta H_B}{\Delta H_A}\right)^{1/2}$$	King et al. [37].
$$\frac{D^o_{AB}\,\mu_B}{T} = 8.93 \times 10^{-8}\left(\frac{V_A}{V_B^2}\right)^{1/6}\left(\frac{P_B}{P_A}\right)^{2}$$	Tyn and Calus [38]. P_A, P_B are the parachors of A and B, respectively.
$$\frac{D^o_{AB}\,\mu_B^{0.92}}{T^{1.29}} = 1.55 \times 10^{-8}\,\frac{P_B^{0.5}}{V_B^{0.23}\,P_A^{0.42}}$$	Hayduk and Minhas [39]. P_A, P_B are the parachors of A and B respectively.
$$\frac{D^o_{AB}\,\mu_B^{0.907}}{T} = 9.89 \times 10^{-8}\,\frac{V_B^{0.265}}{V_A^{0.45}}$$	Siddiqui and Lucas [40].
$$\frac{D^o_{AB}\,\mu_{AB}}{T} = 0.88\,\frac{R}{V_o}\left(\frac{V_{BC}^2}{N_o V_{AC}}\right)^{2/3}$$	Shridhar and Potter [41]. $V_o = 0.31\,V_{BC}$, N_o is Avogrado's number, R is the universal gas constant.
$$\frac{D^o_{AB}\,\mu_{AB}}{T} = 8.52 \times 10^{-8}\left(\frac{1.4 V_{bA}^{2/3} + V_{bB}^{2/3}}{V_{bA}^{5/3}}\right)$$	Lusis and Ratcliff [42].
$$D^o_{AB} = \frac{1.4 \times 10^{-5} L_A}{\mu_B^o V_{AB}^{0.6}\,\mu_w^{1.1}\,L_w}$$	Thakar and Othmer [43]. L_A = latent heat of vaporization of air. L_W = latent heat of vaporization of water.
$$\frac{D^o_{AB}\,\mu_B}{T} = \frac{1}{\zeta_A}\left[\frac{N_o}{V_B}\right]^{1/3}\left[\frac{M_B}{M_A}\right]^{1/2}\exp\left[\frac{E_{\mu B}-E_{DAB}}{RT}\right]$$	Akgerman and Gainer [16]; apply to gases in liquids. $\zeta_A = 6\,[V_A/V_B]^{1/6}$.
$$D^o_{AB} = 2.75 \times 10^{-8}\,\frac{T}{\mu_B}\left[\frac{R_B}{R_A^{2/3}}\right]$$	Umesi and Danner [21]. R = radius of gyration.
$$\frac{D^o_{AB}\,\mu_B}{T} = 0.088\,\frac{V_{CB}^{4/3}}{N_o^{2/3}}\,\frac{R}{V_B C_A^{2/3}}$$	Potter and Shridar, reported by Umesi and Danner [21] as a private communication of the authors [41]. Compare with Shridar and Potter, above.

The theoretical justification for this is found in Eyring's theory of transition states, which gives

$$D^o_{AB} = \left(\frac{V_B}{N_o}\right)^{2/3} \left(\frac{kT}{h}\right) \exp\left(\frac{\Delta S}{R} - \frac{\Delta H}{RT}\right) \qquad (79)$$

for the diffusivity of A in B. According to the transition states theory, Equation (71) at the molecular level is

$$\frac{D^o_{AB}\,\mu_B}{kT} = \frac{\lambda_1}{\lambda_2\,\lambda_3} \qquad (80)$$

where λ_1 = distance between liquid layers,
λ_2 = distance between adjacent molecules in the direction of diffusion, and
λ_3 = distance between adjacent molecules in the direction perpendicular to diffusion.

Similar expressions are obtained in the Hole theory.

The original formulation has been found unsuitable for predictions. Akgerman and Gainer [18] have obtained the modified form

$$D^o_{AB} = \frac{kT}{\zeta_A \mu_B} \left(\frac{N_o}{V_B}\right)^{1/3} \left(\frac{M_B}{M_A}\right)^{1/2} \cdot$$

$$\exp\left(\frac{E_{\mu B} - E_{DAB}}{RT}\right) \qquad (81)$$

where

$$\zeta_A = 6\left(\frac{V_A}{V_B}\right)^{1/6} \qquad (82)$$

and $E\mu_B$, E_{DAB} are the activation energies for viscosity and diffusion, respectively. Equation (81) is recommended for diffusion of gases in liquids.

Hildebrand [19] is a very strong opponent of activation of energy theories. He clearly states that diffusivity should not be plotted as $\ln D$ vs $1/T$, but simply D vs T, and has presented results that approximate quite effectively a straight line. Very little work on liquid diffusion data has been reported using Hildebrand's approach.

Diffusivity in concentrated solutions. While for gases

the diffusion coefficient is independent of composition at low pressures, in liquids concentration dependence is observed at all pressures. Hence, rigorously speaking, in liquids one cannot apply Fick's second law (Equation (44)). If the concentration is very low, one may use Equation (44) using for D_{AB} the value at infinite dilution, D^o_{AB}. This symbol requires some explanation, because it will be used frequently in this section.

The symbol D^o_{BA} means the diffusivity of B in A at infinite dilution of B (concentration of B going to zero). It should not be confused with D^o_{AB}, since in general

$$D^o_{AB} \neq D^o_{BA} \qquad (83)$$

(compare with Equation (11)).

Hence, for infinite dilution of we define D^o_{AB}:

$$D^o_{AB} = D_{AB}\big|_{X_A \approx 0} = D_{BA}\big|_{X_A \approx 0} \qquad (84)$$

and for the infinite dilution of B

$$D^o_{BA} = D_{BA}\big|_{X_B \approx 0} = D_{AB}\big|_{X_B \approx 0} \qquad (85)$$

All the equations of Table 10 apply to infinite dilution of A.

It has been observed that in some cases one can simplify the interpretation of diffusion data if one writes the diffusion coefficient as the product of kinetic part and a thermodynamic part

$$D_{AB} = D_{AB,\,kin}\left(\frac{\partial \ln a_A}{\partial \ln x_A}\right)_{T,P} \qquad (86)$$

$D_{AB,kin}$ is called the kinetic diffusion coefficient or activity-corrected diffusivity and generally varies linearly with concentration; however, this is not universally true and $D_{AB,kin}$ may actually be more concentration dependent than D_{AB}.

In Table 11 we present equations for the calculation of binary diffusion coefficients in concentrated solutions. In the absence of data at infinite dilution required for the equations of Table 11 one can use the equations of Table 10. Obviously, the possibilities are many (for the references given we have 84 possibilities) and most have not been tested. Garg et al. [20] recommend the Umesi-Danner [21] correlation for carbon dioxide in bitumen at infinite dilution. For

Table 11. Equations for binary diffusivity in concentrated liquids.

Equation	Notes and references
$$D_{AB} = D_{AB}^o \left(1 + \frac{d \ln \gamma_A}{d \ln x_A} \right) \frac{\mu_B}{\mu_{AB}}$$	Gordon [44], James et al. [45]. Use in aqueous solutions.
$$\frac{D_{AB} \mu_{AB}}{T} = \left(\frac{D_{BA}^o \mu_A}{T} - \frac{D_{AB}^o \mu_B}{T} \right) X_A$$ $$+ \frac{D_{AB}^o \mu_B}{T} X_A$$	Powell et al. [46], Wilke [47]. For nonideal solutions.
$$\frac{D_{AB} \mu_{AB}}{T} = \left[\left(\frac{D_{BA}^o \mu_A}{T} - \frac{D_{AB}^o \mu_B}{T} \right) X_A \right.$$ $$\left. + \frac{D_{AB}^o \mu_B}{T} \right] \left(1 + \frac{d \ln \gamma_A}{d \ln X_A} \right)$$	Powell et al. [46], Wilke [47]. For nonideal solutions.
$$D_{AB} = \left(D_{AB}^o \right)^{X_B} \left(D_{BA}^o \right)^{X_A} \left(1 + \frac{d \ln \gamma_A}{d \ln X_A} \right)$$	Vignes [48]. Not recommended for n-alkanes.
$$D_{AB} \mu_{AB} = \left(D_{AB}^o \mu_B \right)^{X_B} \left(D_{BA}^o \mu_A \right)^{X_A} \left(1 + \frac{d \ln \gamma_A}{d \ln X_A} \right)$$	Leffler and Cullinan [49]. Not recommended for n-alkanes.
$$D_{AB} = \mu_{AB} \xi' \left(\frac{D_{AB}^o}{\mu_A} \right)^{X_A} \left(\frac{D_{AB}^\infty}{\mu_B} \right)^{X_B}$$	Asfour and Dullien [50]. D_{AB}^o = diffusivity at infinite dilution of A. D_{AB}^∞ = diffusivity at infinite dilution of B. $$\xi = \frac{\left(V_{fm}^{2/3} \right)}{\left(V_{fA}^{2/3} \right)^{X_A} \left(V_{fB}^{2/3} \right)^{X_B}} \cdot \left(\frac{M_A^{X_A} M_B^{X_B}}{M_m} \right)$$ m means mixture and V_f is free volume.
$$D_{AB} = X_A D_{BA}^o + X_B D_{AB}^o$$	Caldwell and Babb [51].

concentrated solutions they use the complicated equation derived by Teja [22] which is based in the corresponding states theory.

For systems where viscosity is strongly a function of concentration an exponential coefficient may be useful. If we use the following expression for the viscosity of mixtures

$$\ln \mu_{AB} = X_A \ln \mu_A + X_B \ln \mu_B \qquad (87)$$

and assume the following expression is constant

$$\frac{D_{AB}\,\mu_{AB}}{T} = B \qquad (88)$$

we get

$$D_{AB} = S_1 \exp(-S_2) \qquad (89)$$

where

$$S_1 = \frac{B}{\mu_B} \qquad (90)$$

$$S_2 = \ln \mu_A / \mu_B \qquad (91)$$

and B is the constant of Equation (88). In the molar-fixed description with no bulk flow we obtain

$$\frac{\partial X_A}{\partial t} = S_1 \frac{\partial}{\partial X}\left[e^{-S_2 X_A} \frac{\partial X_A}{\partial X} \right] \qquad (92)$$

The solution of (92) is relatively simple and is given in Crank [3], p.112. No correlation has been developed for this type of concentration dependence using experimental data, but this approach may prove very useful in bitumen systems.

Data and correlations for bitumen

Diffusivity of gases in bitumen. At the time of this writing there was only one paper in the published literature reporting the diffusivity of carbon dioxide in bitumen [23]. Hence, for comparison purposes we present in Table 12 some published data for diffusivity of carbon dioxide in other hydrocarbon systems.

The results obtained at the Alberta Research Council under sponsorship of AOSTRA are reported in [24]. The most recent data on the system CO_2-Athabasca bitumen are presented in Table 13. These results update and complete the results reported by Schmidt et al. [23].

The values reported in this table are obtained by assuming a constant diffusion coefficient and are therefore a weighted average of the true diffusivity. All measurements were made at 5 MPa and cover the range from room temperature to 200°C.

Measurements of the effective diffusivity $\hat{D}_{AB}$ of carbon dioxide in bitumen/Ottawa sand and in simulated Ottawa sand (Athabasca bitumen in water-saturated Ottawa sand) give values which are about two-thirds the diffusivity in pure bitumen. These values are about twice those expected when using the expression

$$\hat{D}_{AB} = \frac{\varepsilon D_{AB}}{\tau} = \frac{\phi D_{AB}}{\tau} \qquad (93)$$

and may be due to instabilities caused by surface tension gradients (Marangoni effect), or swelling.

The penetration of methane and ethane in bitumen were also determined using a diffusion model. Average diffusivities of methane and ethane in Athabasca bitumen at different temperatures and 5 MPa are presented in Table 14.

Caution must be used when using average values of diffusivity since an average diffusivity will yield an error function curve while the true curve may be very different. Figures 3 and 4 illustrate the profiles for carbon dioxide and ethane diffusion in bitumen.

The activation energy of diffusion is not constant over the wide temperature range of the experiments. In Figure 5 we present the Arrhenius plot of carbon dioxide
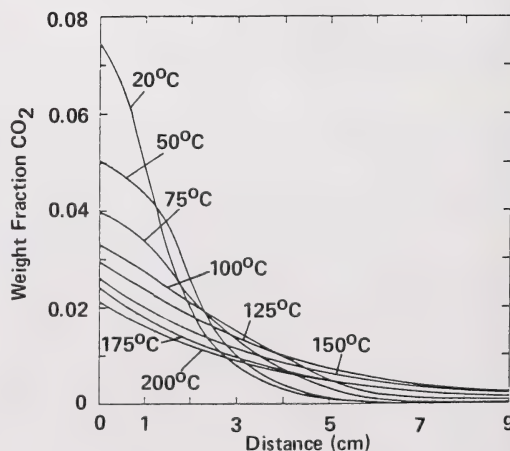
Figure 3. Experimental concentration profiles for CO_2 diffusing in Athabasca bitumen at 5 MPa after 192 h.

Table 12. CO_2-hydrocarbon systems.

System		Temp (°C)	Pressure (MPa)	Diffusivity ($10^{-9} m^2/s$)	Reference
Mole fraction CO_2 (X_A)	B				
saturation	Maljamar crude ($\mu_B = 2$ mPa•s)	25	5.2	$\overline{D}_{AB} = 2.1$	[52]
0.3	n-heptane ($X_B = 0.7$)	20	1.9	$D_{AB} = 5.6$	[53]
0.6	n-heptane ($X_B = 0.4$)	20	3.5	$D_{AB} = 4.6$	[53]
0.9	n-heptane ($X_B = 0.1$)	20	5	$D_{AB} = 5.0$	[53]
≈ 0	iso-octane	25	0.1	$D^o_{AB} = 6.34$	[54]
≈ 0	n-octane	25	0.1	$D^o_{AB} = 6.0$	[55]
≈ 0	white spirit	25	0.1	$D^o_{AB} = 2.11$	[55]
≈ 0	gas oil, BP 200-300°C ($\mu_B = 3.9$ Pa•s)	25	0.1	$D^o_{AB} = 1.95$	[55]
≈ 0	gas oil, BP 300-400°C ($\mu_B = 26.5$ Pa•s)	25	0.1	$D^o_{AB} = 0.73$	[55]
saturation	toluene	25	0.1	$D^o_{AB} = 4.6$	[56]
saturation	decahydronaphtalene	25	0.1	$\overline{D}_{AB} = 2.33$	[56]
saturation	tetradecane	25	0.1	$\overline{D}_{AB} = 2.95$	[56]
saturation (gravity 0.865)	stock tank oil ($\mu_B = 3$ Pa•s)	75	15	$\overline{D}_{AB} = 8.5\text{–}9.2$	[57]
saturation (gravity 0.985)	stock tank oil ($\mu_B = 290$ Pa•s)	66	15	$\overline{D}_{AB} = 3$	[57]
saturation	stock tank oil ($\mu_B = 570$ Pa•s)	80	15	$\overline{D}_{AB} = 4.6$	[57]

Table 13. Diffusivity of carbon dioxide in Athabasca bitumen at 5 MPa.

Temperature (°C)	Average diffusivity ($10^{-9} m^2/s$)	Pure bitumen viscosity (Pa•s)
20	0.279	361.7
50	0.500	8.36
75	0.710	1.01
100	0.920	0.221
125	1.15	0.072 2
150	1.41	0.003 12
175	1.55	0.001 65
200	1.75	0.001 00

Table 14. Diffusivity of gaseous hydrocarbons in Athabasca bitumen at 5 MPa.

Gas	Temperature (°C)	Average diffusivity ($10^{-9} m^2/s$)	Pure bitumen (Pa•s)
methane	50	between 0.4 and 0.75	8.36
ethane	20	0.175	361.7
ethane	50	0.174	8.36
ethane	75	0.337	1.01
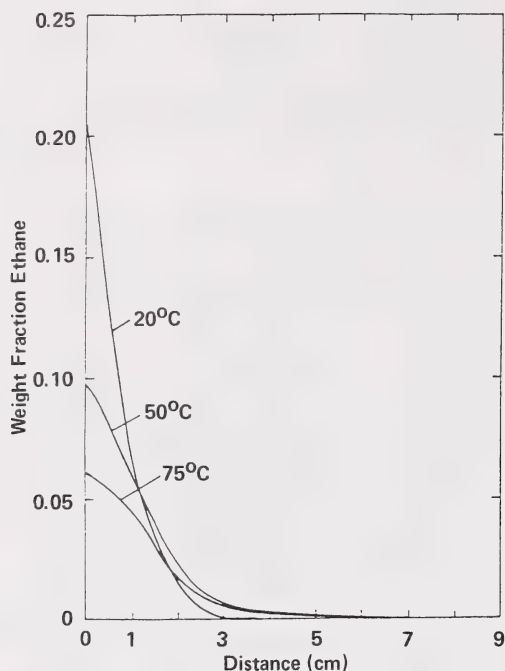
Figure 4. Experimental concentration profiles for ethane diffusing in Athabasca bitumen at 5 MPa after 192 h.

Figure 5. Arrenius plot of diffusivity of carbon dioxide in Athabasca bitumen.

diffusivity versus temperature (plot of $\ln D_{AB}$ vs $1/T$). It is observed that the average diffusivity is not as strong a function of temperature as one might expect.

If $\bar{D}_{AB}$ represents the average diffusivity, the expression

$$\frac{\bar{D}_{AB}\,\mu_B^{0.16}}{T} = 2.04 \times 10^{-12} \qquad (94)$$

correlates the experimental values of diffusivity with the pure bitumen viscosity over six decades of viscosity values (see Figure 6).

Experimental data for liquid-bitumen systems. There are several reported studies on diffusion in bitumen-liquid systems. The oldest are the measurements made by Hopper [25] and Haliburton [26], who measured the diffusivity at infinite dilution of Athabasca bitumen in carbon tetrachloride and benzene, respectively. More recently, Fu and Phillips [27] measured the overall diffusivity of several liquid hydrocarbons in Athabasca bitumen. The most recent work is by Oballa and Butler

[28], who measured the diffusivity of Suncor coker-feed bitumen and toluene over the entire concentration range. The results are given in Table 15 (pages 12–22).

The results of Fu and Phillips should be viewed with caution since their diffusivities are about a hundred times the values usually found in liquid systems. In the same category are the results obtained by Baltus and Anderson [29] which we report at the bottom of Table 15. They measured the diffusivity of asphaltenes in tetrahydrofuran using microporous membranes. The asphaltenes were extracted from a Kuwait atmospheric bottom. Thrash and Pildes [30] report much lower diffusivities for Middle East asphaltenes in toluene.

The data of Oballa and Butler [28], Hopper [25], and Haliburton [26] appear more reasonable. The effect of concentration is easily appreciated in Figures 7 and 8 which are reproduced from [28]. Figures 9 and 10 present the plot of concentration (in terms of volume function) as a function of Boltzmann's variable $x/(T)^{1/2}$. The close grouping of the experimental points indicates the excellent precision of the measurements.

Table 15. Bitumen-liquid systems.

System		Temp (°C)	Pressure (atm)	Diffusivity[a] $(10^{-9}\text{m}^2/\text{s})$		Reference
A	*B*					
Athabasca bitumen	carbon tetrachloride	25	1.0	$D_{AB}^o =$	1.1	[25]
Athabasca bitumen	benzene	25	1.0	$D_{AB}^o =$	0.59	[26]
pentane	GCOS bitumen	23	1.0	$\overline{D}_{AB} =$	146	[27]
hexane	GCOS bitumen	23	1.0	$\overline{D}_{AB} =$	107	[27]
heptane	GCOS bitumen	23	1.0	$\overline{D}_{AB} =$	69.8	[27]
isohexane	GCOS bitumen	23	1.0	$\overline{D}_{AB} =$	70.1	[27]
2-2' dimethyl butane	GCOS bitumen	23	1.0	$\overline{D}_{AB} =$	28.2	[27]
cyclohexane	GCOS bitumen	23	1.0	$\overline{D}_{AB} =$	30.1	[27]
benzene	GCOS bitumen	23	1.0	$\overline{D}_{AB} =$	81.9	[27]
toluene	GCOS bitumen	23	1.0	$\overline{D}_{AB} =$	77.8	[27]
octane	GCOS bitumen	23	1.0	$\overline{D}_{AB} =$	66.4	[27]
toluene	bitumen[b]	20	1.0	$D_{AB}^o =$	0.05	[28]
toluene (20% vol.)	bitumen[b] (80% vol.)	20	1.0	$D_{AB} =$	0.13	[28]
toluene (40% vol.)	bitumen[b] (60% vol.)	20	1.0	$D_{AB} =$	0.44	[28]
toluene (60% vol.)	bitumen[b] (40% vol.)	20	1.0	$D_{AB} =$	0.19	[28]
toluene (80% vol.)	bitumen[b] (20% vol.)	20	1.0	$D_{AB} =$	0.105	[28]
toluene	bitumen[b]	20	1.0	$D_{AB}^o =$	0.1	[28]

Asphaltenes

asphaltene (MW 200-400)	tetrahydrofuran	25	1.0	$\overline{D}_{AB} = 1\,610$		[29]
asphaltene (MW400-800)	tetrahydrofuran	25	1.0	$\overline{D}_{AB} = 1\,310$		[29]
asphaltene (MW 800-1 600)	tetrahydrofuran	25	1.0	$\overline{D}_{AB} =$	885	[29]
asphaltene (MW 1 600-3 200)	tetrahydrofuran	25	1.0	$\overline{D}_{AB} =$	524	[29]
asphaltene (MW 3 200-6 400)	tetrahydrofuran	25	1.0	$\overline{D}_{AB} =$	271	[29]
asphaltene	toluene	25	1.0	$\overline{D}_{AB} =$	0.45	[30]

[a] Refer to list of symbols.
[b] Suncor coker-feed bitumen.

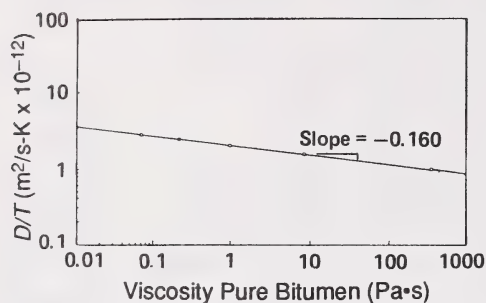**Figure 6.** Logarithmic plot of $\overline{D}_{AB}/T$ vs viscosity of pure bitumen.

Figure 9. Concentration dependence on $y/t^{1/2}$ for bitumen-toluene system.

Figure 7. Concentration-distance curves for bitumen-toluene, run 13, [28].
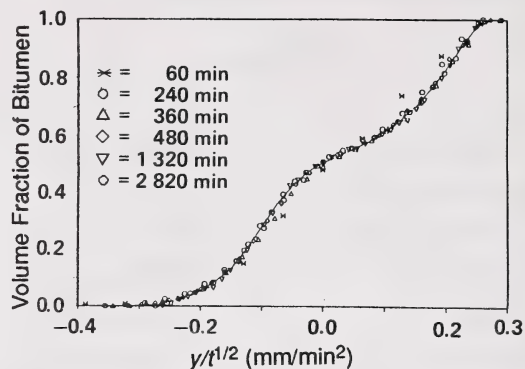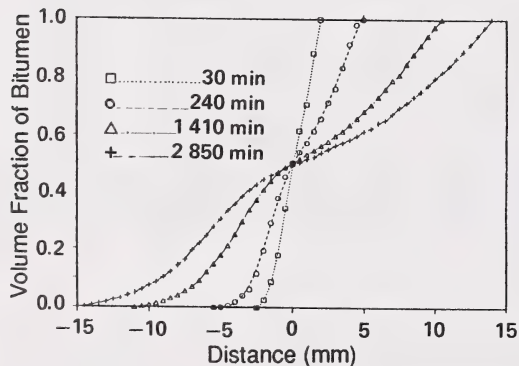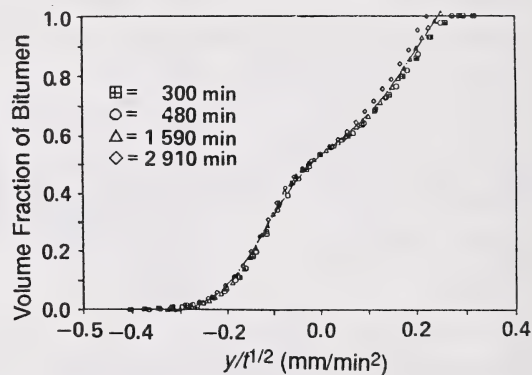

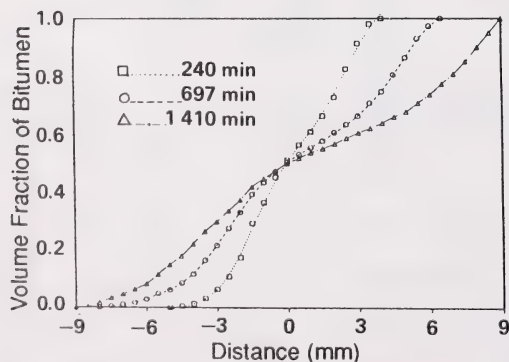**Figure 10.** Concentration dependence on $y/t^{1/2}$ for bitumen-toluene system.

Figure 8. Concentration-distance curves for bitumen-toluene, run 14, [28].

LIST OF SYMBOLS

a_A	activity of A
A	pre-exponential term in Andrade viscosity equation
A'	pre-exponential term in Arrhenius diffusivity equation
B	activation energy for viscosity in Andrade equation
B'	activation energy for viscosity in Arrhenius expression
b_{AB}	mobility in barycentric description
b'_{AB}	mobility in fixed description
C	total concentration, moles per unit volume
$C_A, C_B, ...$	concentration of $A, B, ...$ in moles per unit volume
D_{AB}	binary diffusion coefficient
D^o_{AB}	binary diffusion coefficient at infinite dilution of A
$\overline{D}_{AB}$	average diffusion coefficient
$\hat{D}_{AB}$	effective diffusion coefficient
$E_{\mu A}, E_{\mu B}$	activation energy for viscosity of species $A, B, ...$
E_{DAB}	activation energy for diffusivity for solute A in solvent B
G	Gibbs free energy
I	mass flux in mass units per unit area per unit time
H	enthalpy
i	unit vector in x-direction
J	molar flux in moles per unit area per unit time
I_A, I_B	mass flux of $A, B, ...$ in barycentric coordinates
$I^{(v)}_A, I^{(v)}_B$	mass flux of $A, B, ...$ in volume-fixed coordinates
$I^{(c)}_A, I^{(c)}_B$	mass flux of $A, B, ...$ in mole-fixed coordinates
J_A, J_B	molar flux of $A, B...$ in molar-fixed coordinates
$J^{(m)}_A, J^{(m)}_B$	
$J^{(v)}_A, J^{(v)}_B$	molar flux of $A, B, ...$ in barycentric coordinates
	molar flux of $A, B, ...$ in volume-fixed coordinates
k	Boltzmann constant
k_{AB}	friction coefficient
L_A, L_W	latent heat of vaporization of A, of water, ...
L_{AB}	phenomenological coefficient in barycentric description

M_{AB}	reduced molecular weight $= (M_A \cdot M_B) / (M_A + M_B)$
M_w	molecular weight
$M_A, M_B, ...$	molecular weight of $A, B, ...$
m	total mass $= M_A + M_B + ...$
$m_A, m_B, ...$	total mass of species of $A, B, ...$
N_o	Avogadro's number
$N_A, N_B, ...$	number of particles of $A, B, ...$
N_A	molar flux with respect to stationary axes
n_A	mass flux with respect to stationary axes
P	pressure
R	universal gas constant
$\overline{R}$	radius of gyration
r	radius
S	entropy
S_1, S_2	constants
T	absolute temperature
T^*_{AB}	kT/ε_{AB}
t	time
$\overline{V}, \overline{V}_m$	molar volume $= 1/C$
V_{CA}, V_{CB}	critical volume of $A, B, ...$ (mL)
V_b	molar volume at boiling point (mL)
$\overline{V}_A, \overline{V}_B$	partial molar volume of $A, B ...$
V	barycentric velocity
$V^{(v)}$	volume-average velocity
$V^{(c)}$	molar-average velocity
$V_A, V_B, ...$	velocity of species $A, B, ...$ with respect to stationary coordinates
$\tilde{V}_A, \tilde{V}_B, ...$	partial specific volume of $A, B, ...$
$\tilde{V}$	specific volume $= 1/\rho$
$W_A, W_B, ...$	weight fraction of $A, B, ...$
$X_A, X_B, ...$	generalized force acting on species $A, B, ...$
x	distance coordinate
$X_A, X_B, ...$	mole fraction of $A, B, ...$

Greek symbols

∇_T	isothermal gradient
ε	cross area available for diffusion
ε_{AB}	$= \varepsilon_A \varepsilon_B$
$\varepsilon_A, \varepsilon_B, ...$	energy parameters
μ_A	chemical potential of A per mole
μ_A	viscosity of pure A
μ_{AB}	viscosity of mixture of A and B
$\tilde{\mu}_A$	chemical potential of A per unit mass
ρ	density
ξ, ξ'	constants
$\Omega^{(1,1)*}_{AB}$	collision integral for A and B

$\phi_A, \phi_B, \ldots$ volume fraction of $A, B, \ldots$
ϕ porosity
ζ constant

REFERENCES

1. P.M. Sigmund – personal communication, Feb (1988).
2. C.T. Fu – personal communication, Feb (1988).
3. J. Crank, "The mathematics of diffusion," 2nd ed., Oxford University Press (1975).
4. A.H.P. Skelland, "Diffusional mass yransfer," John Wiley & Sons, New York (1974).
5. W.M. Kays, "Convective heat and mass transfer," McGraw-Hill Book Co., New York (1966).
6. V.G. Levich, "Physicochemical hydrodynamics," Prentice Hall, Englewood Cliffs, NJ (1962).
7. J.O. Hirschfelder, C.F. Curtiss and R.B. Bird, "Molecular theory of gases and liquids," corrected printing, John Wiley & Sons (1964).
8. E.N. Lightfoot, E.L. Cussler and R.L. Rettig, A.I.Ch.E. J., 8 (1962) 708–710.
9. Hsu, Hhsien-wen and R.B. Bird, A.I.Ch.E. J., 6 (1960) 516–524.
10. John C. Slattery, "Momentum, energy and mass transfer in continua," 2nd ed., Robert E. Kriegger Publishing Co., Huntington, New York (1981).
11. R.B. Bird, W.E. Stewart and E.N. Lightfoot, "Transport phenomena," Wiley (1960).
12. R.C. Reid, J.M. Prausnitz and T.K. Sherwood, "The properties of gases and liquids," 3rd ed., McGraw-Hill Book Company, New York (1977).
13. S. Bretsznajder, "Prediction of transport and other physical properties of fluids," Pergmon Press (1971).
14. T.R. Marrero and E.A. Mason, J. Phys. Chem. Ref. Data, 1, no. 1 (1972) 3.
15. S. Chapman and T.G. Cowling, "The mathematical theory of non-uniform gases," Cambridge Univ. Press (1960).
16. P.M. Sigmund, "Binary molecular diffusion in dense gas mixtures: The methane-nitrogen systems," Research Report RR-21 Petroleum Recovery Research Institute, Calgary, Alberta, Jun (1973).
17. C.R. Wilke and P. Chang, A.I.Ch.E. J., 1 (1955) 264.
18. A. Akgerman and J.L. Gainer, I&EC Fundamentals, 11 (1972) 373–379.
19. J.H. Hildebrand, Science, 174 (1971) 490–493.
20. A. Garg, A. Mehrotra and W. Svercek, "Prediction of infinite dilution and mutual diffusion coefficient for carbon dioxide/bitumen systems," AOSTRA University Research Program – Agreement 318B, Summer student report, Aug (1986).
21. N.O. Umesi and R.P. Danner, Ind. Eng. Chem. Process Dev., 20 (1981) 662–665.
22. A.S. Teja, Ind. Eng. Chem. Fundam., 24 (1985) 39–44.
23. T. Schmidt, T.H. Leshchyshyn and V.R. Puttagunta, "Diffusivity of carbon dioxide in Athabasca bitumen," Petroleum Society of CIM, Paper no. 82–33–100 presented at the 33rd Annual Technical Meeting in Calgary, Alberta, Jun 6–8 (1982).
24. T. Schmidt, E. Jossy and V.R. Puttagunta, "Mass transfer studies," final report of project 188, Alberta Research Council, Dec (1986).
25. D.A. Hopper, "Liquid diffusion in porous media, referring in particular to the Athabasca tar sands," Master of Applied Science thesis, Univ. of British Columbia (1945).
26. J. Haliburton, "Liquid diffusion in porous media with specific reference to the Athabasca tar sands," Master of Applied Science thesis, Univ. of British Columbia (1947).
27. C.H.B. Fu and C.R. Phillips, Fuel, 58 (1979) 557–560.
28. V. Oballa and R.M. Butler, "An experimental study of diffusion in the bitumen-toluene system," paper presented at the CIM meeting, Calgary, Alberta, Jun 7–10 (1987).
29. R.E. Baltus and J.L. Anderson, Chem. Eng. Sci., 38 (1983) 1959–1969.
30. R.J. Thrash and R.H. Pildes, "The diffusion of petroleum asphaltenes through well characterized porous membrane," paper presented at the Symposium on Residuum Upgrading and Coking of the American Chemical Society, Atlanta meeting, Mar 29–Apr 3 (1981).
31. E.N. Fuller, P.D. Schettler and J.C. Giddings, Ind. Eng. Chem., no. 5, 58 (1966) 19–27.
32. N.H. Chen and D.F. Othmer, J. Chem. Eng. Data, 7 (1962) 37.
33. D.F. Othmer and N.H. Chen, Ind. Eng. Chem. Process Des. Dev., 1 (1962) 249–254.
34. C.R. Wilke and C.Y Lee, Ind. Eng. Chem., 47 (1955) 1253.
35. S.H. Ibrahim and N.R. Kuloor, Brit. Chem. Eng., 6 (1961) 862.

36. R. Sitamaran, S.H. Ibrahim and N.R. Kuloor, J. Chem. Eng. Data 8 (1963) 198–201.

37. C.J. King, L. Hsueh and K.W. Mao, J. Chem. Eng. Data, 10 (1965) 348–350.

38. M.T. Tyn and W.F. Calus, J. Chem. Eng. Data, 20 (1975) 106.

39. W. Hayduk and B.S. Minhas, Can. J. Chem. Eng., 60 (1982) 295.

40. M.A. Siddiqui and K. Lucas, Can. J. Chem. Eng., 64 (1986) 839.

41. T. Shridhar and O.E. Potter, A.I.Ch.E. J., 23 (1977) 590.

42. M.A. Lusis and G.A. Ratcliff, Can. J. Chem. Eng., 46 (1968) 385–387.

43. N.S. Thakar and D.F. Othmer, Ind. Eng. Chem., 45 (1953) 589.

44. A.R. Gordon, J. Chem. Phys., 5 (1937) 522.

45. J.J. James, J. Hollingshead and A.R. Gordon, J. Chem. Phys., 7 (1939) 89.

46. R.E. Powell, W.E. Roseveare and H. Eyring, J. Appl. Phys., 12 (1941) 669.

47. C.R. Wilke, Chemical Engineering Progress, 45 (1949) 218–224.

48. A. Vignes, Ind. Eng. Chem. Fundam., 5 (1966) 189–199.

49. J. Leffler and H.T. Cullinan, Ind. Eng. Chem. Fundam., 9 (1970) 84.

50. Abdul-Fatah Asfour and F.A.L. Dullien, Chem. Eng. Sci., 14 (1986) 1891–1894.

51. C.S. Caldwell and A.L. Babb, J. Phys. Chem., 60 (1956) 51.

52. A.T. Grogan, V.W. Pinczewski, G.J. Ruskauff and F.M. Orr, "Diffusion of carbon dioxide at reservoir conditions: Models and measurements," paper presented at the SPE/DOE Fifth Symposium on EOR, Tulsa, OK, Apr 20–23 (1986).

53. H. Saad and E. Gulari, J. Phys. Chem., 88 (1984) 136–139.

54. B.H.C. Chen and S.H. Chen, Chem. Eng. Sci., 40 (1985) 1735–1741.

55. G.A. Davies, A.B. Ponter and K. Craine, Can. J. Chem. Eng., 45 (1967) 372–376.

56. W.T. McManamey and J.M. Woollen, A.I.Ch.E. J., 19 (1973) 667–669.

57. L. Denoyelle and C. Bardon, "Diffusivity of carbon dioxide in reservoir fluids," paper presented at the 86th Annual Meeting, Canadian Institute of Mining and Metallurgy in Ottawa, Apr (1984).

13
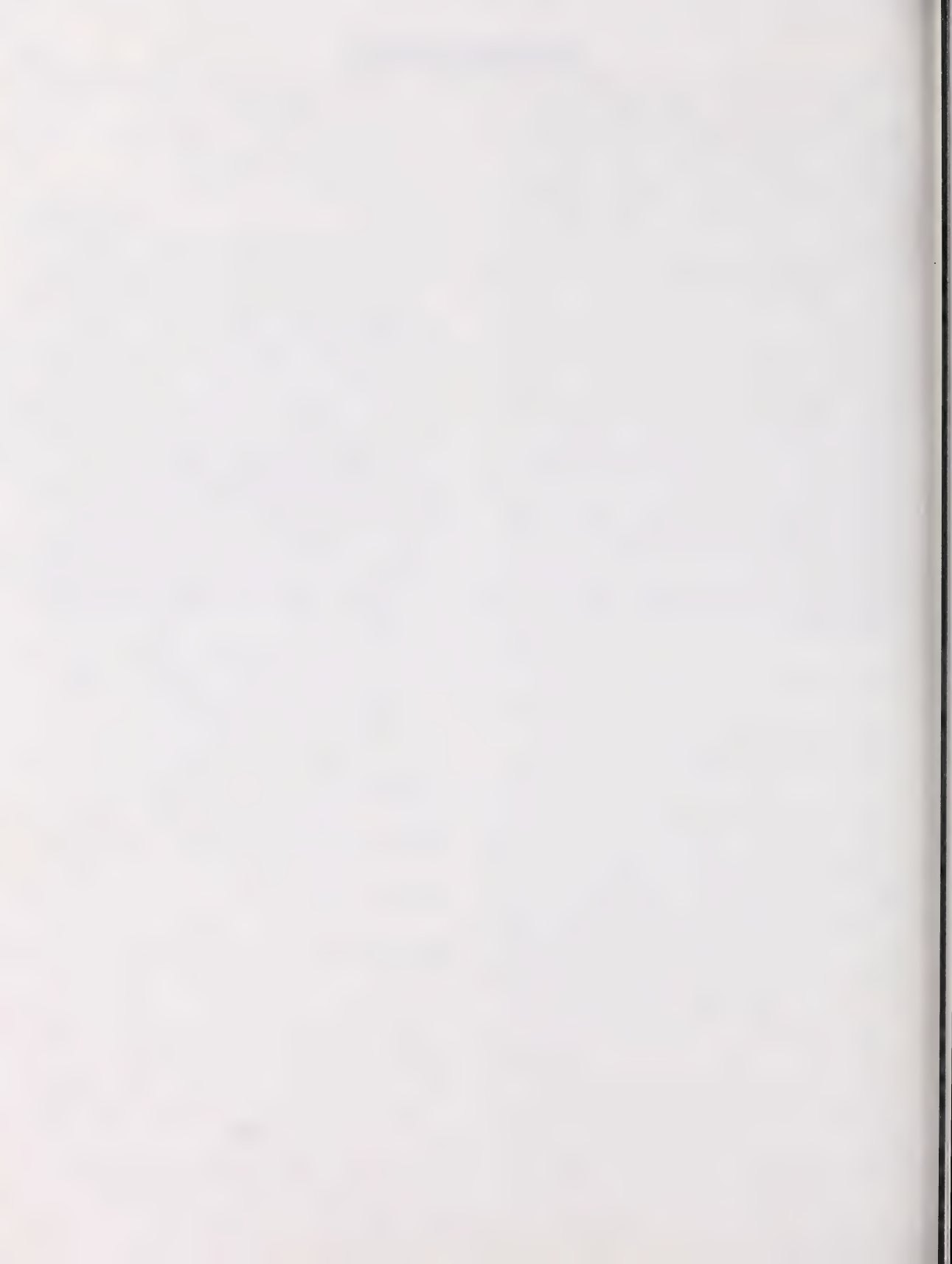
ELECTRICAL HEATING
OF RESERVOIRS

F.S Chute
F.E. Vermeulen

Department of Electrical Engineering
University of Alberta

ELECTROTHERMAL PROCESSES IN OIL SAND

Introduction

Thermal recovery methods in general, as applied to oil sand and heavy oil deposits, have the common objective of raising the formation temperature to reduce the viscosity of the bitumen or heavy oil to the point where it can be swept from the formation. Transferring electromagnetic energy to the deposit is proving to be a possible and effective means of supplying the necessary heat. These electrothermal processes convert electromagnetic energy to heat deep within the formation using a system of excitor electrodes to induce currents to flow through the deposit. By proper choice of operating frequency and excitor spacing, considerable control can be effected over the path taken by the currents and hence over the temperature profiles that will develop in the deposit. Electrothermal processes are virtually free of problems related to very low initial formation injectivity, poor heat transfer, and the near impossibility of adequately controlling the movement of injected fluids and gases. Such problems have plagued other thermal recovery processes including steam soaking, steam flooding, and fire flooding [1,2].

The current densities and heating rates induced within the formation by the excitor electrodes decrease with distance from any individual excitor. The resulting heating is generally nonuniform, with overheating occurring near the electrodes. However, at low frequencies (such as the common power frequency, 60 Hz) currents can be forced to penetrate great distances into the formation. In these cases uniform heating of selected portions of the formation can then be achieved by electrode placements that utilize highly-electrically-conductive shale and water bearing zones within the formation to distribute the current widely [3,4]. At frequencies above a few hundred kilohertz where currents are rapidly absorbed and penetrate only small distances from an individual excitor (see the following section on electrical properties), the most direct way of obtaining heating over large formation volumes is to decrease the spacing between excitor wells. Several high-frequency methods using transmission-line arrays of electrodes to transport the electromagnetic energy to deep within the formation have been described [1,5,6].

Most proposed electrothermal processes have been related to the development of power-frequency systems where the oil sand acts as a resistive heating element between the various electrode wells. At this low frequency, current flow in the formation is primarily via ionic conduction through the water-saturated portion of the interconnected pore spaces throughout the reservoir. Unless considerable care is taken, the water in the immediate vicinity of the electrodes vaporizes and the continuous water path between electrodes is broken. Once contact between the formation and the electrode surface is lost, current flow and heating cease. The design and subsequent operation of power-frequency electrodes that can pass the large currents (up to 1000 A) necessary to heat the bulk of the formation in a reasonable time (1 to 2 y), without vaporizing the formation water surrounding the electrodes, has proven to be a difficult task. However, practical solutions are emerging [4,7].

Power-frequency electrothermal processes can be implemented with as few as one well every 0.8 ha (2 acres) in a typical Athabasca oil sand, and offer the advantage of utilizing a readily available commercial source of power [8]. They are generally preferable to high-frequency methods in situations when:

- the desired temperatures to be reached in the formation are lower than the in situ steam temperature, or
- when the formation contains sufficient water that the interwell resistances are low enough to permit acceptable heating rates at excitation voltages of less than a few thousand volts.

On the other hand, a high-frequency electrothermal scheme should be considered if:

- the formation is to be heated to temperatures exceeding the steam temperature, as might be desirable if recovery is to be effected solely by gravity drainage assisted by autogenously developed steam and hydrocarbon vapors, and/or if
- the formation to be heated contains very little initial moisture, such as is generally the case with the oil sands of Utah, for example.

At frequencies above a few megahertz oil sands generally exhibit sufficient electrical conductivity (see next section on electrical properties) that acceptable heating rates can be achieved without excessive voltages in the surface generating equipment, even with all the moisture removed from the deposit. There are instances where it might be desirable to operate at a low frequency until water has been evaporated and then to switch to a higher frequency to continue heating the formation electromagnetically [9,10]. However, it must be borne in mind that a high-frequency process will require costly frequency conversion equipment that may not be commercially available at the power levels required.

Reviews of some of the various electrothermal processes, which range in operating frequency from a fraction of a hertz to microwave frequencies of several gigahertz have been prepared by Chute and Vermeulen [10,11] and by Haston [12]. There have been a few field tests of some of these schemes.

The electric preheat steam drive process

The electrothermal process that currently offers the greatest promise for in situ recovery of bitumen from the moist oil sands of the Athabasca region is known as the electric preheat steam drive (EPSD) process. It involves completing an array of vertical wells into the formation, some of which act solely as electrodes while the remainder are completed for dual service as either electrode/steam-injectors or as electrode/producers. The electrodes are excited at power frequency and the formation acts as a resistive heating element between the wells. Separate electrode structures may be installed at the bottoms of the wells or the wells may be completed in such a way that the lower portions of the well casing serve as the electrodes. The rate of power dissipation is controlled so that the pore water is not vaporized and a conductive path through the formation is maintained. After a period of time that can vary from several weeks to many months, the viscosity of the bitumen or heavy oil along prespecified channels between injector and producer wells will be reduced to the point where it can be displaced by injection of steam (or by sequential injection of hot water and steam). The driving fluid introduces substantial additional thermal energy to further heat the oil sand deposit. Electrical energy is thus used to supply only a fraction of the thermal energy requirement for the recovery process.

The electrode configuration for a particular implementation of the EPSD process in the Athabasca deposit is illustrated in Figures 1 and 2. The wells are arranged in rows spaced so that every fourth electrode well also serves as either an injector or producer in an inverted 7-spot production pattern. Alternate rows are excited at 60 Hz with the polarities shown. The electrodes in rows labelled "high" are completed in the average oil sand while the "low" electrodes are completed in the underlying shale. Current is forced to flow through the rich oil sand at the bottom of the pay zone in the manner suggested in Figure 2. The underlying shale layer and the average oil sand layer exhibit substantially greater electrical conductivities than the rich oil sand and therefore act to distribute the current more uniformly throughout the rich sand.
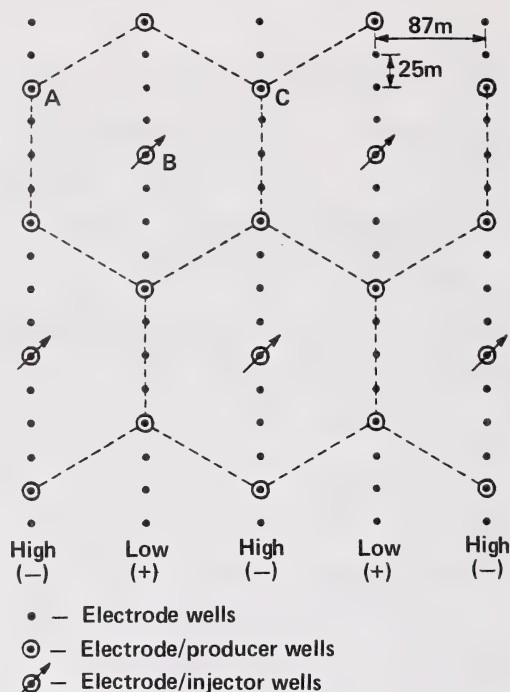
Figure 1. Possible areal pattern for EPSD process.
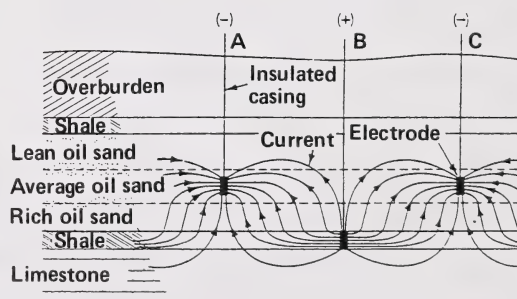
Figure 2. Staggered electrode placement for a possible implementation of the EPSD process.

Current is conducted to each of the electrodes along the well bore casings which are in turn electrically insulated from the surrounding formation. The casing insulation for the "high" electrodes may be removed and the casing directly grounded resulting in significant cost savings with little effect on the temperatures developed in the rich oil sand. The electrodes are assumed to be cooled

by circulating brine from the surface to ensure that the near-wellbore temperatures do not exceed the in situ steam temperature.

Numerical simulations using this configuration have shown [13,14] that at the end of an 18-month preheating period, at a current level of 400 A per well, the temperature in the rich oil sand midway between wells in adjacent rows can be raised from 15 to 50°C. Figure 3 shows the resulting temperature contours indicating a heated channel between the electrodes approximately 15 m in depth and extending the full width of the array.

The bitumen in this heated channel was shown to be sufficiently mobile to permit recovery by a hot-water and steam drive using the inverted 7-spot patterns shown in Figure 1 [14]. Simulation results indicated that approximately 70% of the original oil in place can be recovered before steam breakthrough to the producers, at an overall oil/steam ratio of 0.44 which includes the steam equivalent of the electrical preheat energy.

The Alberta Oil Sands Technology and Research Authority (AOSTRA) undertook a complete economic analysis of the EPSD configuration described above,
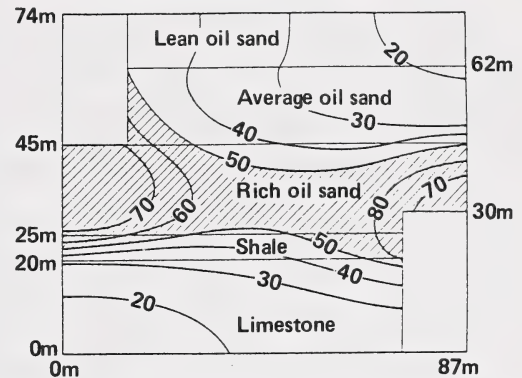
Figure 3. Temperature contours showing heated channel after 18 mo. of electric preheating.

based on a commercial-scale facility producing 2500 m^3 per calendar day of raw bitumen [14]. The supply cost breakdown for bitumen in 1984 dollars discounted at 10% is shown in Table 1. Significantly, the cost of electricity is only about 12% of the total supply price. It

Table 1. Design case supply price at 10% real discount rate [14].

	$/m^3	% of total
Capital costs [$44.83/m^3]		
Wells	31.34	28.85
Site preparation	3.96	3.65
Satellites	0.68	0.62
Distribution lines	1.77	1.63
Electrical facilities	0.68	0.63
Bitumen treating	1.82	1.67
Water treating	2.80	2.58
Steam facilities	1.78	1.64
Operating costs, excluding energy [$22.03/m^3]		
Wells	12.69	11.68
Steam facilities	4.10	3.78
Hot water injection	0.36	0.33
Water treating	3.39	3.12
Bitumen treating	1.50	1.38
Energy costs [$41.74/m^3]		
Fuel gas	28.28	26.04
Electricity	13.46	12.39
Total supply price	$108.61	100.0%

is worth noting that after this study was completed, an alternate well configuration was developed [8] that required electrode wells only at the locations of the injectors and producers shown in Figure 1. This reduction in the number of wells potentially decreases the well costs by nearly a factor of four and the supply price to less than $85/m^3 (1984 dollars).

Petrotech Systems Inc. [15] have also estimated the supply costs for producing bitumen with an electric preheat steam drive, based on a plant operating over 16 years (beginning in 1985) at a capacity of 250 m^3/d for 320 stream-days per year. The results discounted at 20% gave a capital cost of $32.46/m^3 and an operating cost of $45.00/m^3, figures that are somewhat less than those obtained by AOSTRA. However, the proposal called for electrode wells on 25 m x 10 m spacing with a probable cost for each well of $7655, resulting in a net electrode-well capital cost approximately one third that assumed in the AOSTRA study. Apparently it has been assumed that closer electrode spacing reduces the overheating near the electrodes to the point where circulating cooling fluid is not required, permitting the use of a less costly electrode configuration. Well costs were based on open-hole completions with electrodes connected to the surface by insulated (uninsulated in the case of ground-return electrodes) power cables sealed into the hole with grout.

The PCEJ electric preheat pilot

A version of the electric preheat steam drive process has been successfully tested on a small scale on a 150-acre site near Stoney Mountain (8-26-85-9-W4M) south of Fort McMurray, Alberta, by the PCEJ group [16,17], with Petro-Canada acting as operator. The electric preheat phase operated from approximately April 1981 to April 1982 with the steam drive operation completed in May 1983.

The pilot consisted of four electrode/producer wells at approximately 30 m spacing as shown in Figure 4. In addition, eight observation wells were completed and equipped to monitor temperature and electrical potential profiles. There were minor differences between actual well locations as completed in the field and the ideal array layout depicted in Figure 4. The wells were all completed at the base of the McMurray Formation at a depth of approximately 450 mKB, so as to pass current primarily horizontally between electrodes. Each electrode was approximately 15 m in length and extended from about 439 to 454 mKB. The electrodes consisted of sections of slotted liner about 15 m in
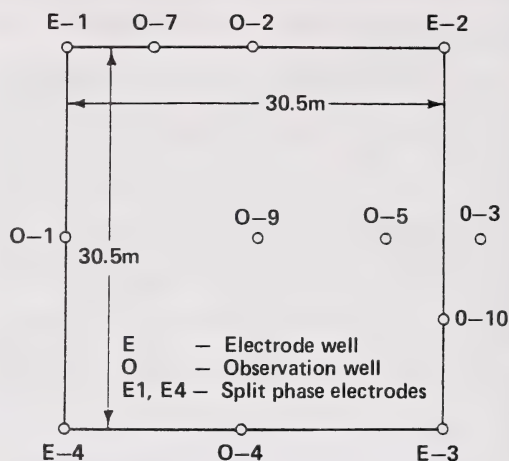
Figure 4. PCEJ pilot well layout, adapted from [17].

length surrounded by an under-reamed gravel-packed region, saturated with brine to maintain ohmic contact with the formation. It is assumed that current was delivered to the electrodes via the insulated wellbore casing which has proven to be an efficient method of delivering current downhole [18,19]. However, even though Khosla and Towson [17] indicate a 95% efficiency level, they imply that it was necessary during pilot operation to circulate cooling fluid to keep the casing temperature within structurally safe limits.

The bitumen-rich formation units above and below the electrode interval exhibited lower average electrical conductivity than those in the electrode interval. PCEJ felt that this conductivity contrast would constrain the current to flow in a predominantly horizontal manner, thereby establishing a communications channel lying between the bitumen-rich layers. Figure 5 shows a resistivity profile developed from log and core data from the site, and indicates the relative position of the electrodes.

The surface facilities included systems for electrical power delivery, steam generation, production handling, wellbore cooling, utilities, and process monitoring and control. The power source consisted of a 2500 KVA three-phase transformer fed from the Alberta Power grid. The maximum current level was 1000 A and the voltage output was variable in 130-V steps from 0 to 4200 V. The steam facilities were capable of providing 80 m^3/d of 80%-quality, 16-MPa steam. A PDP-1134 computer provided process control and monitored the progress of the pilot.
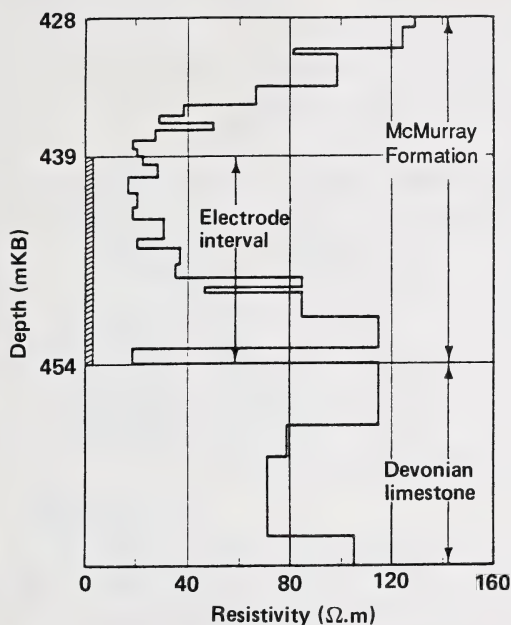
Figure 5. Resistivity model for PCEJ pilot site, adapted from [17].

The pilot wells were initially excited in a four-well split-phase scheme whereby electrodes 1 and 4 were excited from the same phase while wells 2 and 3 were excited from the two remaining phases. Thus, for a period of approximately 75 days, wells 1 and 4 carried about half of the current delivered to wells 2 and 3.

Three-well, three-phase operation began July 5 and continued for the remainder of the pilot test. The main electric preheat test terminated after 296 days of heating, and pilot operation was then tested at higher current levels. The field-measured line current versus time is indicated for electrode well E-1 in Figure 6. The dotted line represents the current predicted using PCEJ's electric preheat model (EPM) to numerically simulate pilot operation. The calculated current was not more than 23% in error. It should be noted that the current scale on Figure 6 was estimated from the stated maximum current capacity of the surface facilities (actual values have yet to be publicly released by PCEJ). However, numerical simulations using the electrothermal simulator MEGAERA at the University of Alberta to model the evolution of temperature (as reported by Towson [16]) for observation well O-7 indicates that this current scale is accurate. On this basis then it is surmised that when averaged over the entire 296-day preheat period the electrode current was approximately 550 A, and that the pilot was successfully operated at a current level of about 900 A during the "post electric preheat tests."

After about six months of heating, temperatures in the near-electrode region were found to exceed the in situ steam temperatures and formation water was flashed to steam. In some cases the flashing was severe enough to temporarily halt pilot operation while the electrodes were cooled by injecting an electrolyte solution. Periodic electrolyte injection apparently maintained ohmic contact with the formation and heating was
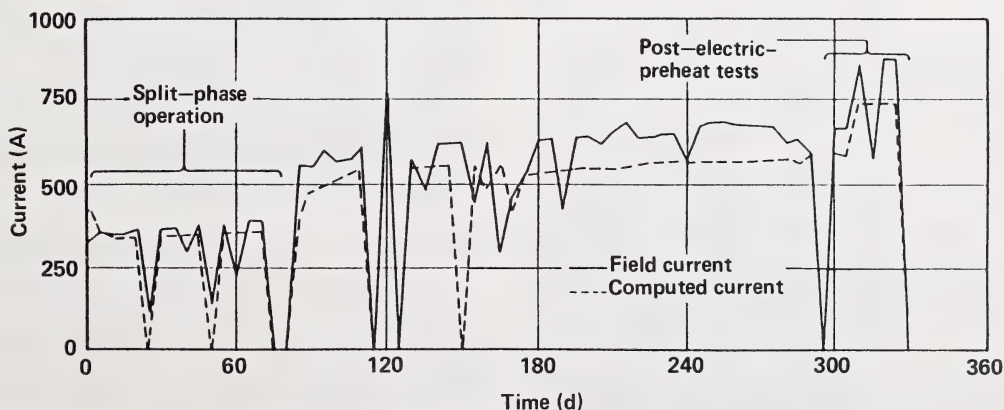
Figure 6. Current versus time for electrode well E–1, adapted from [17].

possible with a better than 80% stream factor.

Figures 7 and 8 illustrate the evolution of temperature for the first five months of operation as indicated by measurements made in observation wells O-2 and O-7. Referring to Figure 4 it is seen that O-2 is about midway between E-1 and E-2 while O-7 is about
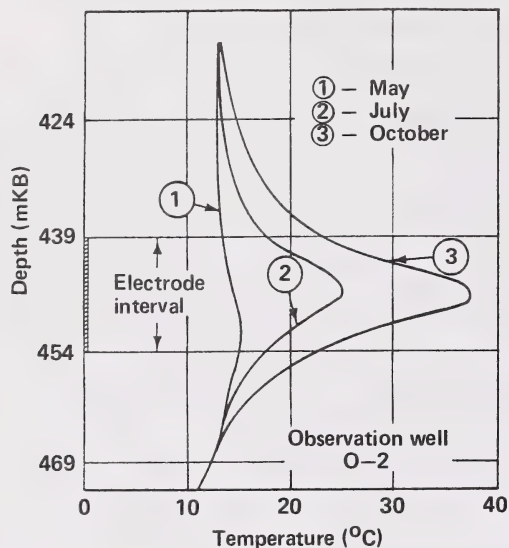
Figure 7. Evolution of vertical temperature profile at PCEJ pilot site in well O-2, adapted from [16].
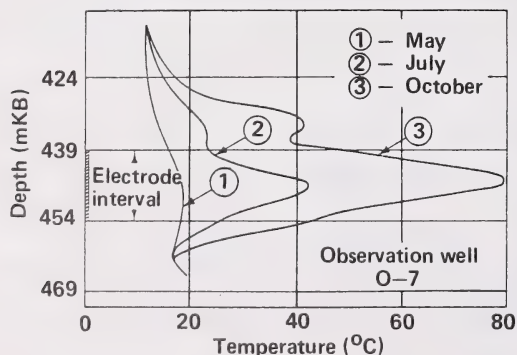
Figure 8. Evolution of vertical temperature profile at PCEJ pilot site in well O-7, adapted from [16].

midway between E-1 and O-2. Figure 9 shows a comparison between the temperature profile predicted by the numerical simulator and the field temperatures
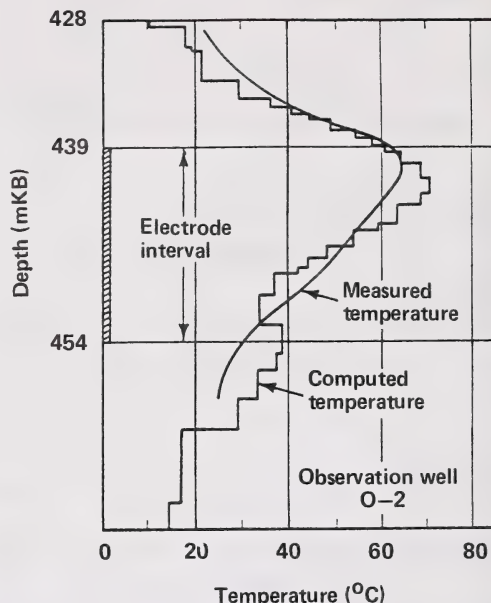
Figure 9. Comparison of measured and computed vertical temperature profiles in well O-2 at day 296 of electric preheat, adapted from [17].

for well O-2 after 296 days of electric preheating. A heated channel in which temperatures exceeded 65°C was established by the electric preheat. It is obvious that the heated channel developed in a predictable manner. Indeed Khosla and Towson note that predicted temperatures were generally within 15% of all corresponding field data.

While no actual values for power and energy consumption during pilot operation have been publicly released, they can be estimated in a rather straightforward manner from an approximation of the resistance between each pair of wells. Assuming the pilot electrodes represented a reasonably balanced three-phase load on the power supply,

$$P = \frac{3}{2} \cdot I^2 R_{2w} \qquad (1)$$

where P is the power in watts, I is the line current and R_{2w} is the resistance between two wells. The resistance between any two wells can be estimated, using the resistivity profile given in Figure 5, by approximating the resistance in terms of the theoretical resistance of

two long cylinders embedded in a layered medium. Evaluation of R_{2w} in this manner, however, requires an estimate of the effective radius of the PCEJ electrodes. It is reasonable to assume that this radius was between about 0.5 and 2 m, based on typical gravel pack dimensions and the fact that some of the electrolyte used to saturate the gravel pack would have at least partially invaded the formation region surrounding the electrodes. In this case the actual interwell resistances between wells at the PCEJ site are estimated to have been between about 1 and 1.5 Ω before heating was initiated. Thus, initial power levels most probably were in the range of 450 to 680 kW. Assuming an average current of 550 A, this range of power corresponds to a line-to-neutral voltage between about 270 and 410 V. It is evident that pilot operation did not entail any significant hazard due to high voltage levels in the surface equipment.

As the formation heats, the electrical conductivity is known to decrease, and correspondingly, R_{2w} must decrease. Thus, it would be expected that, since Khosla and Towson indicate the pilot was excited at substantially constant voltage, the input current and power should both increase with time. On the other hand, it was observed that in the field the input current and power levels were virtually constant. No explanation has been offered for this anomalous behavior. In any event, since the observed input power was approximately constant, the total electrical energy absorbed by the formation during operation of the pilot can be estimated as the product of the initial power and the heating time. Hence, on this basis, it can be surmised that the PCEJ pilot consumed electrical energy of the order of 4 GW•h.

Although no data have been released to the public with respect to the steam drive phase of the pilot operation, it has been stated [20] that bitumen recovery was disappointing due to geological factors in the reservoir. Khosla and Towson state that the numerical simulation of the process correctly predicted the communication time between hot electrode wells during steam injection.

The PCEJ pilot has established that hot interwell communication channels can be developed in a predictable manner using electric current to selectively heat the desired portions of the deposit. The notable agreement between numerical simulation results and actual field performance should be considered as a major indication of the ability of reservoir engineers to accurately forecast the performance of electric preheat steam drive processes in oil sand.

The electrothermic process

The Electrothermic Co. of Corpus Christi, TX, has developed an electrothermal process operating at power frequency termed the "electrothermic process" [19]. Although use of the process with a multi-electrode array has been envisaged, it has been used in a single-well configuration in most cases. The system is depicted schematically in Figure 10, which shows an open-hole completion wherein current is returned to the surface via the overburden. Current flows through the steel production tubing to an electrode formed by packing steel shot into a specially under-reamed section at the bottom of the well. The production tubing is electrically insulated with a concentric string of fiberglass pipe. Production and heating occur simultaneously.
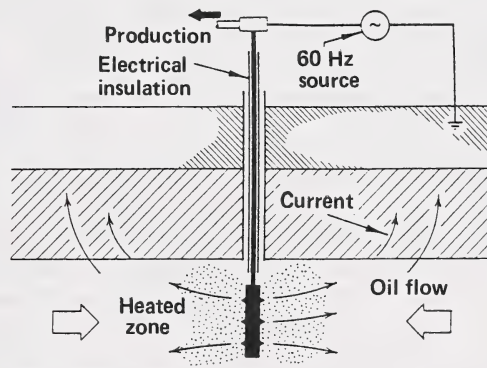
Figure 10. Schematic representation of the heating circuit for a typical electrothermic process, adapted from [19].

Current disperses into the formation beyond the heated zone and as indicated returns to the surface to complete the circuit. The viscosity of the oil in a zone extending several tens of feet from the electrode is reduced and will flow to the well if the reservoir has sufficient drive energy. Thus, this process may not be immediately applicable to immobile deposits such as the Athabasca oil sands. However, in cases where the heated zone can be brought to sufficiently high temperatures, there will be significant recovery via gravity drainage, and the electrothermic process could be used to initiate recovery by cyclic steam injection.

Perhaps the most important facet of the technology developed by the Electrothermic Co. relates to the successful design and completion of downhole electrode

systems for high current, high power applications. The electrodes used typically handle several hundred amperes at a few hundred volts for single well-power levels of up to 200 kW. Several well completion methods have been developed for formations of various depths, thicknesses, and oil viscosities [7,14,19]. The electrothermic process has been used to enhance production in viscous oil deposits since 1969, with some notable successes. Typical results are illustrated in Table 2.

Eddy current heating

The use of eddy currents induced by a coil excitor was suggested as early as 1929 [21] for processing mined hydrocarbons. More recently eddy currents have been advocated by F.T. Fisher's Sons Ltd. of Montreal, in a series of proposals dating back to 1976 [22]. They envisage a network of shafts and tunnels throughout the formation, through which is run copper-clad steel piping bedded in crushed gravel saturated with brine. These conductive pipe strings are interconnected to form a coil surrounding a large portion of the deposit. When excited at 60 Hz the magnetic field produced by the coil is presumed to induce eddy currents that circulate in closed loops within the deposit, heating the formation in much the same way as metals and semiconductors are routinely heated in induction furnaces.

However, analytic and experimental studies by Vermeulen and Chute [22] of such induction coils buried in contact with lossy media have indicated that eddy current heating will be negligible for the single loop, double loop, and toroidal loop configurations suggested by F.T. Fisher's Sons Ltd. Rather, current will tend to flow directly from the high potential end of the coil system to the low potential end, concentrating heating along this path. The zones that are effectively heated are illustrated in Figure 11. Note that only the series-connected spaced-loop configuration (Figure 11a) provides substantial heating of the bulk of the material enclosed by the system of conductors. While such heating would be effective, the high cost of the extensive tunnel and shaft access required to implement the scheme must be considered when comparing this approach to other electrothermal methods.

Table 2. Electrothermic process field results [19].

Location	Electrical power (kW)	Original production (bbl/d)[a]	Production after electrical heating (bbl/d)[a]	Oil gravity (°API)	Depth (m)
Southwest Texas	150 12	0	76 6–10	11 –	1 000
Eastern Utah	60	4	50	22	900
Mexico	–	6	283 max 65 avg	19	500
South-central Oklahoma	56–100	20[b]	80	11	2 400

[a]   1 bbl, 159 L.
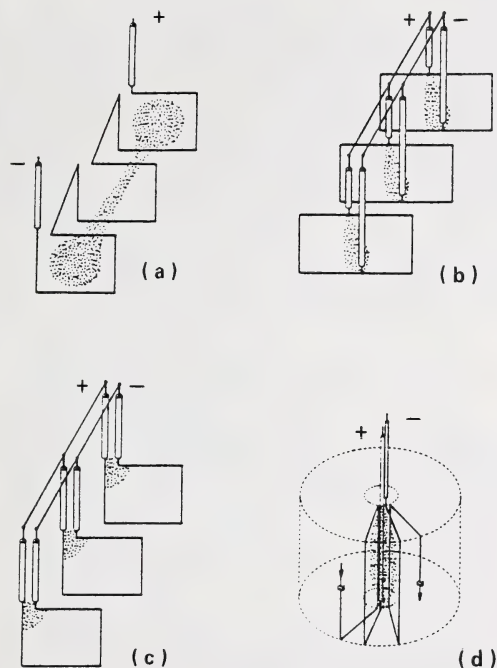[b]   Required daily injection of 40–80 bbl, 36° API blend oil.

Figure 11. Uninsulated buried coil configurations with insulated feed wires (a) series-connected loops (b) Fisher's parallel-connected double loops, (c) parallel-connected single loops, (d) toroid of series-connected loops. The dotted regions are those that are most intensely heated.

Electromagnetic flooding

Electromagnetic flooding [5,23] refers to an electrothermal process based on horizontal wells drilled several hundred metres into an oil sand formation. The wells are arranged in pairs consisting of one well completed near the base of the oil-bearing zone and a second well placed vertically above and parallel to the first. These wells could be placed into the formation from the surface using directional drilling techniques or from an underground mine. Each pair of wells is excited at one end by a high-frequency power source connected between the upper and lower wells so that electromagnetic energy will be propagated along the well-pairs (or, more practically, several pairs of wells may be excited in parallel from a single source). The operating frequency and well spacings depend upon the electrical properties of the deposit; the former is expected to range from about 100 kHz to several MHz. Power levels of about 100 to 200 kW per well-pair

would typically be required.

When power is first applied to a well-pair the electromagnetic energy is absorbed in the interwell region immediately adjacent to the source. The temperature of this region is rapidly increased to the point where formation water will be flashed to steam. Steam will first form adjacent to the wellbores where the current densities are the largest. As time progresses a virtually nonconducting (or at least, very resistive) region forms around each well, extending a few metres along the wells from the power source. At power frequency this zone need only be a few millimetres in diameter to effectively stop all current flow between wells, and to therefore terminate the heating prematurely. However, at high frequencies, the high-resistivity gap that initially forms can be capacitively bridged by the current. Heating between the wells continues, albeit only in the region within several metres of where the wells enter the formation.

Temperatures in the interwell region will continue to rise and the highly resistive zone grows as progressively more moisture is evaporated from the vicinity of the wells. In time this gap becomes large enough that it cannot be effectively bridged and the interwell current in this region is sharply reduced. The power being dissipated is likewise reduced. In effect, the current supplied by the source is shunted farther along the well-pair to where the insulating gap has not yet been formed around the wells, and heating of this more remote region begins. This process is continuous and an advancing heat front is observed to sweep gradually along the well-pair in a manner akin to a steam or fire flood. Such floods in tests on bench-sized physical models have been observed to proceed at rates that would correspond in the field to values ranging from 50 to 75 m per year. It has been further demonstrated that when the lower well of each pair is completed as a producer, recovery can be effected by simultaneous gravity drainage, assisted by autogenously generated steam and hydrocarbon vapors [24].

The IITRI single-well radio-frequency stimulation process

Radio-frequency heating at frequencies ranging from a few hundred kilohertz to microwave frequencies has long been advocated [25] as a means of single-well stimulation similar to the electrothermic process described above. Monopole or dipole-like antenna structures are completed downhole and electromagnetic energy is radiated away from the excitor into the pay

zone. The depth to which these waves can penetrate a moist oil sand formation is quite limited and heating is generally confined to the near-wellbore region. However, heating can be continued even after the water in the formation near the well has flashed to steam. In this way the heated zone will gradually advance radially outward with time in a manner analogous to the electromagnetic flooding techniques developed by McPherson et al. [5,23].

The IIT Research Institute of Chicago, Illinois has further refined and developed the RF single-well stimulation process and has undertaken a shallow well test near Ardmore, OK. The test was conducted by Uentech Corp. of Tulsa, OK in a 45 to 50 ft thick unconsolidated oil sand reservoir approximately 300 ft deep. A single well was drilled and cased to the top of the pay zone. A specially designed cylindrical antenna excitor of copper-clad steel was installed downhole. The bottom portion of this excitor served as the producer and consisted of a stainless steel screen in direct contact with a gravel pack. The antenna was powered by a 6.78 MHz, 40 kW transmitter. The well showed no significant initial production and RF stimulation was commenced in mid-December 1984. By January 1985 the initial temperature of 18°C had been raised so that near the excitor it was about 100°C. At 4.5 ft from the wellbore antenna the temperature was 65°C and 15 ft away it was 33°C. Production of 6° API oil was reported to be steadily increasing as of that date [26].

ORS Development Corporation (Oil Recovery Systems) of Tulsa, OK are currently testing the IITRI single-well stimulation process near Wildmere in the Lloydminster heavy oil field of eastern Alberta. The near-wellbore temperature has reportedly been raised from 24 to 35°C and production rates have increased threefold. EOR Ltd. of Calgary holds an exclusive license for this technology in Canada and Europe and is in the process of installing several more wells.

The IITRI Utah field test of radio-frequency heating of oil sand

Based on extensive analytic work and experimental studies using bench-sized physical models the IIT Research Institute has developed an electrothermal method that uses a simulated parallel plate transmission line to guide electromagnetic energy into the deposit. It consists of parallel rows of electrodes placed into the oil-bearing zone in the manner illustrated in Figure 12 and is referred to as a tri-plate line. Sresty et al. [6] indicate that typically, spacing between rows will be

about 2.5 times the spacing between wells in the same row. The outside rows are grounded and the output of the RF generator is connected to the centre row of electrode wells. The operating frequency, well spacings, and electrode lengths are selected so that the formation enclosed by the tri-plate line is exposed to as uniform a heating rate as possible.
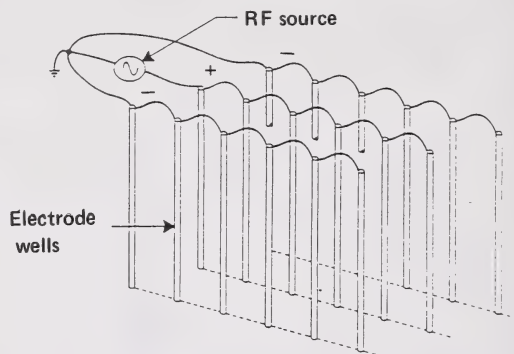
Figure 12. IITRI parallel electrode well configuration.

IITRI tested the process in 1981 in the Asphalt Ridge deposit near Vernal, Utah [6,27]. Three rows of electrode wells were drilled vertically into a surface outcrop to a depth of approximately 6 m. A total of 38 electrodes were placed: 10 in the middle row and 14 in each outer row. The heated volume of oil sand was about 25 m^3 which implies extremely close electrode spacings. A 12x12x8 ft collection room was mined out under the electrode array to provide for bitumen collection. This access made it possible to control standing wave effects on the tri-plate line by adjusting the terminal impedance. About 60 thermocouples were placed inside the electrodes on the inside surfaces facing the heated volume. Additional liquid-filled thermometers were used to monitor the temperatures between rows. The tri-plate line was excited from a 200 kW FRT-86 RF transmitter. During the field test the input power ranged from 40 to 75 kW. The operating frequency was 2.2875 MHz until evaporation of the formation water was completed, at which time the frequency was raised to 13.5 MHz in order to maintain a high heating rate. Other electrical equipment included appropriate matching networks, coaxial feeder cables (15.6 cm diameter) and auxiliary cooling equipment. The product recovery and handling equipment consisted of oil collection and pumping equipment, heat exchangers, and so on.

After 20 days of heating, at which time the RF source was disconnected, the average formation

temperature had risen to about 200°C. It peaked after 14 days and decreased somewhat after that due to changes made in the RF input power. About 8 barrels (1270 L) of bitumen were collected by gravity drainage and distillation during the field test. This recovery represents about 35% of the total bitumen content originally held within the oil sand test volume. Recovery of such a large percentage of the total bitumen in place in just over 20 days of operation must be viewed as encouraging. Figure 13 summarizes the temperature and production
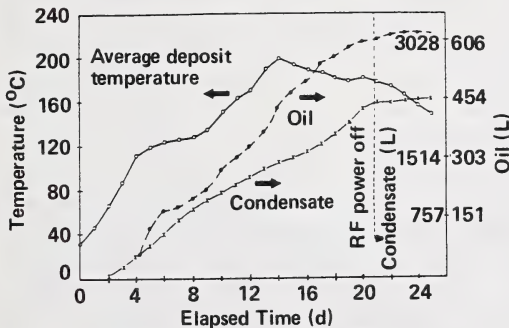
Figure 13. Temperature and production history for IITRI Utah field test of radio frequency, adapted from [6].

history of the test. Figure 14 shows a vertical profile of bitumen content in the test volume before and after the test, as determined by core analysis. The redistribution of bitumen saturation by gravity drainage is evident.

IITRI has conducted an economic analysis of the process based on a 1590 m^3/d commercial operation in an oil sand such as the Sunnyside deposit in Utah [6]. The project was assumed to extend for 20 years and all costs were discounted at 15% per annum. A pay zone about 20 m thick was assumed with electrode row spacings of 10 m. The distance between wells in the same row was taken as 4 m. The deposit was assumed to have an average bitumen content of 9.4% of which 70% was assumed to be recovered. Energy was purchased at 4¢/kW•h. Capital costs included mining, site preparation, surface facilities, working capital, project engineering, and management. Capital and operating costs (in mid-1981 dollars) are illustrated in Table 3 as a function of final heating temperature.

The IITRI tri-plate process has also been field tested on a very small scale in oil shales [28]. Oil shale volumes of about 1 m^3 were heated in a tri-plate line placed horizontally into an outcrop in Avintaquin
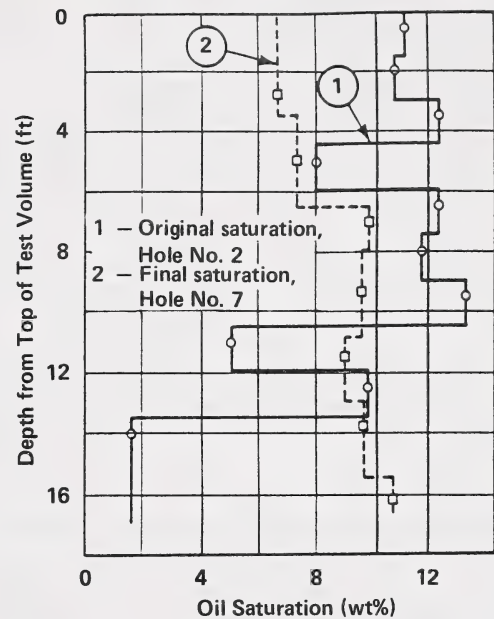
Figure 14. Oil saturation profiles for IITRI Utah field test of radio-frequency heating, adapted from [6].

Canyon, Utah during the period January to March 1980. Each array was connected to a 40 kW radio transmitter via rigid coaxial cable and a variable matching network. For the test, RF power levels ranged from 5 to 20 kW. The operating frequency was 13.56 MHz. Temperatures of between 340 and 400°C were achieved in the formation and up to 30% of the oil content of the shale was recovered.

Electrocarbonization

Electrocarbonization [11,29] (electrolinking or electrofracturing) involves completing at least two wells into the formation. Electrodes are lowered into the wells to make contact with the deposit. High voltages (up to 15 000 V for well spacings from 9 to 30 m) at power frequency are applied. Initially, large currents can be carried through the ion-rich pore water, and rapid heating results. As the moisture around the electrodes flashes to steam, current flow is generally observed to decrease. However, if the applied voltage is above some critical value, the current again begins to increase with time, apparently due to a slow decomposition of hydrocarbons that forms a growing carbon conduction path between electrodes. This carbonized path commences at one electrode and grows towards the

Table 3. IITRI supply price estimates [6].

Process temperature (°C)	Capital costs[a] ($/m^3)	Operating costs[a] ($/m^3)	Total costs[a] ($/m^3)
100	21.73	35.27	57.0
150	24.64	48.04	72.68
300[b]	0.61	76.07	106.68

[a]   Mid–1981 dollars.
[b]   These costs are offset by lower upgrading costs.

other electrode via a tortuous route along the line of least resistance. The paths are generally many-branched and often exhibit dead-end branches. Once a complete carbon link has been established between electrodes the resistance between wells drops dramatically and large currents can be passed at greatly reduced voltage levels. Using this carbon link, the formation can then be heated to the point where oil and gas are produced, by maintaining a high current flow between electrodes. During this phase the zone of carbonization gradually enlarges. This process has been shown in laboratory tests to be effective for Green River oil shale and Athabasca oil sands [29]. During the early stages of carbonization the evolution of steam creates an extensive system of fractures throughout the formation which have been observed to provide interwell communication.

Electroosmosis

Electrical forces at the interface between sand grains and pore water in a typical oil sand formation give rise to a diffuse layer of excess cations near the interface to compensate for the generally negatively charged mineral surfaces. These cations are free to move under the influence of an applied external electric field so that, when a DC potential difference is maintained between two electrodes completed into an oil-bearing formation, the cations migrate towards the cathode. The positively charged liquid layer near sand-water interfaces is thus drawn towards the cathode and draws with it water molecules from the bulk of the pore water because of viscous drag. The resulting decrease in effective water

saturation causes an increase in oil saturation and relative permeability to oil, so that the oil flow rate is likewise increased. Thus electroosmosis can be used to drive water away from the vicinity of a producing well in order to increase the flow of oil into the well as the relative permeability to oil increases. Electroosmosis has also been combined with resistive heating [11,30].

Microwave retorting

Oil has been successfully recovered from oil sand and oil shales by subjecting the material to microwave radiation in a pressure vessel. The sands and shales were heated to temperatures in the range 500 to 650°C where decomposition and distillation of the bitumen and kerogen occurred. As much as 86% of the original oil in place has been recovered in laboratory tests where small samples have been irradiated for 10 to 15 min at power levels of up to a few hundred watts, at a frequency of 2 450 MHz. Net energy ratios as high as 6 have been reported for this retorting process. In situ applications of microwave heating have also been considered [11,31–33].

Electrochemical effects

The passage of current at power frequency between a system of electrode wells completed so as to force current through the oil-bearing zone has been observed to greatly increase the formation pressure. Field tests at 120 kW with a two well single-phase system are reported to have resulted in the elevation of formation pressures by more than 2.07 MPa (300 psi) over an areal extent of about 400 ha (1000 acres) [34]. Pressure

increases were noted in wells up to 1830 m (6000 ft) from the electrode installation. The pressure increases are assumed to be related to the following observed electrochemical phenomena taking place in the heated oil-water system through which the current is passed:

- A limited reduction of viscosity is believed to occur because of current-induced changes in the molecular structure of the oil.
- Laboratory tests have shown that an oil and brine mixture produces large volumes of free hydrogen, carbon dioxide, and free oxygen, as well as methane and other hydrocarbon vapors, when alternating currents are passed through the mixture. The volumes of gas produced appear to be substantially greater than can be explained on the basis of release of gases in solution.
- Passage of current through an oil sand and brine mixture is known to cause gravity separation of the sand, water, and oil fractions.
- It is believed that exothermal reactions are promoted thus releasing heat to the formation through which current is passed.

Little work has been done in this area and more research into the possible electrochemical phenomena would seem warranted.

ELECTRICAL PROPERTIES OF OIL SAND

Introduction

The response of an oil sand reservoir to electrical excitation can be characterized in terms of an effective electrical conductivity σ_e, and an effective permittivity $\varepsilon_e = \varepsilon_o \varepsilon_R$, where ε_R is the relative dielectric constant and $\varepsilon_o = (1/36\pi) \times 10^{-9}$ F/m. There would seem to be no evidence to suggest that oil sands exhibit any magnetic behavior and it is generally accepted that the magnetic permeability is the same as that of a vacuum, $\mu_o = 4\pi \times 10^{-7}$ H/m. Knowledge of these electrical parameters is essential to the design and optimization of any electrical heating scheme. They will dictate the electrode or antenna sizes, shapes, and spacings, as well as the operating voltage, current, and power levels. Moreover, they will determine heating rates, system operating efficiencies, and overall electrical energy requirements.

No single method is available for the determination of the electrical properties of oil sand over the complete range of frequencies required to characterize the deposits. At frequencies below about 10 MHz, where all

samples are small compared to wavelength, an oil sand sample is typically held in a parallel plate or coaxial capacitor cell and the impedance of the loaded cell is determined using commercially available impedance bridges and vector voltage/current meters. At higher frequencies, up to and including the microwave range, measurements are based on a variety of transmission line, resonant-cavity perturbation, and time-domain reflectometry methods. An extensive review of appropriate measuring techniques existing prior to 1974 has been given by Lytle [35] who includes references to some 79 technical articles covering both laboratory and in situ methods for determining σ_e and ε_e. Radio frequency techniques before 1967 are discussed by Bussey [36]. A survey of more recent technology was undertaken by Iskander and duBow [37]. The literature also includes references to the design and construction of several specific systems for determining the electrical properties of consolidated and unconsolidated dielectric materials that are directly applicable to oil sand measurements [38–50].

While a number of logging tools and other methods permit a direct in situ determination of the electrical parameters, examination of the dependencies of these parameters on frequency, temperature, and moisture content is most conveniently conducted on oil sand samples that have been reconstituted from core material or mined oil sand. However, the relative distribution of σ_e and ε_e values within the formation is of fundamental importance to the design and implementation of an electrical heating scheme and is best obtained by collecting extensive log data from the proposed site. Currently, the best available data with respect to the absolute in situ values of low-frequency conductivity of oil sand formations are obtained from logging tools such as the Schlumberger Dual Induction-SFP log.

The bulk of available data on oil sands have been obtained from measurements on samples reconstituted from mined oil sand and held under conditions of temperature, pressure, and moisture content intended to represent the formation as closely as possible. Measurements on such samples typically exhibit variations of up to 20% even when the samples are prepared with substantially the same density from oil sand with virtually the same moisture content. These variations have been attributed to the inherent differences in the reconstituted pore geometry from sample to sample. Thus, any one data point may not be representative of the electrical properties of the

formation from which the sample was obtained. However, the average or mean values of the measurements of many such samples have been assumed to characterize a volume of the formation much larger than an individual sample, in which such differences in pore geometry and texture occur naturally [40].

Unless otherwise noted, the data and observations presented in the following sections relate to the Athabasca oil sands.

Variation of electrical conductivity and permittivity with frequency

Figures 15, 16, and 17 show the frequency-dependent nature of σ_e and ε_R over the frequency range 60 Hz to 1 GHz for Athabasca oil sand samples reconstituted from mined sand obtained from the Suncor site at Fort McMurray, Alberta [11,40]. The individual data points relate to samples with different densities and moisture contents and the range of values is indicated on each figure.

The effect on σ_e and ε_R of reduced water content is

illustrated in Figures 18 and 19 [42]. Successive samples were prepared from mined oil sand that had been spread and left exposed to air for extended periods of time. Moisture contents were determined by Dean-Stark analysis. Also shown in Figures 18 and 19 are the results for several samples of extracted bitumen. (No significant differences were observed for the response of bitumen obtained by hot water extraction or by Dean-Stark extraction.)

Table 4 lists some relative dielectric constant values obtained for Athabasca oil sand at microwave frequencies [43].

Based on these data the following observations can be made:

• The effective conductivity varies slowly with frequency and is virtually constant up to a frequency of about 10^6 to 10^7 Hz. The magnitude of σ_e ranges between 10^{-1} to 10^{-4} S/m, increasing with increasing moisture content.

• Above about 10^7 Hz there is a substantial linear increase in σ_e with frequency.

Figure 15. Conductivity and relative dielectric constant versus frequency at 24°C for Athabasca oil sand.
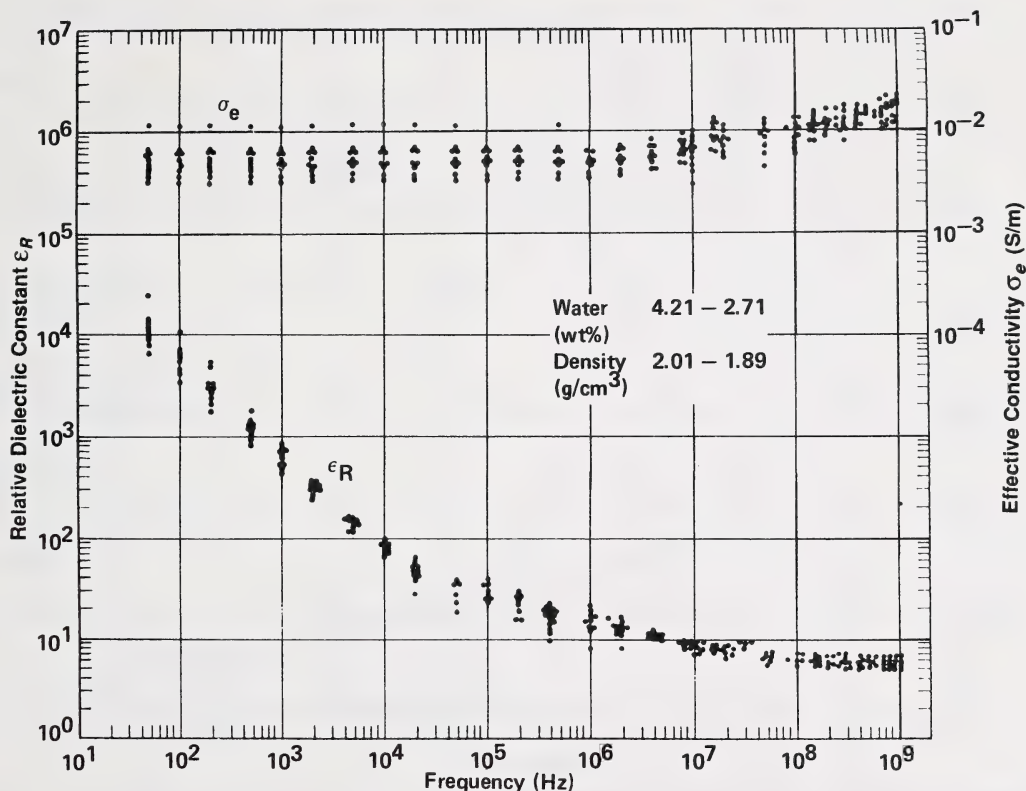
Figure 16. Conductivity and relative dielectric constant versus frequency at 24°C for Athabasca oil sand.

- At frequencies below about 10^3 to 10^4 Hz the effective permittivity increases approximately linearly with decreasing frequency. Values of relative dielectric constant in excess of 10^5 can be obtained.
- At higher frequencies the permittivity asymptotically approaches a constant value that depends on moisture content. At microwave frequencies the relative dielectric constant rarely exceeds a value of about 5.
- Dried samples exhibit conductivities that vary approximately linearly with frequency over the entire frequency range above about 10^3 Hz. The conductivity of extracted bitumen also exhibits a linear dependence even at frequencies below 10^3 Hz. This suggests that the departure from a linear relationship for dried oil sand samples may be due to a small amount of adsorbed water forming interconnected paths through the supposedly dry oil sand sample, or to a significant contribution to the low-frequency conductivity from the mineral and clay matter in the sample.

- The relative dielectric constant rarely exceeds approximately 10 at low frequencies for dry samples and is of the order of 3 at microwave frequencies which is comparable to the values for the host rock and bitumen.

Similar frequency-dependent behavior has been observed for virtually all moist earth materials. It has been suggested [51] that σ_e and ε_e can be represented as

$$\sigma_e = \sigma'(\omega) + \omega\,\varepsilon''(\omega) \qquad (2)$$

$$\varepsilon_e = \varepsilon'(\omega) + \frac{\sigma''(\omega)}{\omega} \qquad (3)$$

where ω is the angular frequency $2\pi f$. For oil sand $\sigma'(\omega)$, $\sigma''(\omega)$, $\varepsilon'(\omega)$ and $\varepsilon''(\omega)$, which are generally functions of frequency, are essentially constants.
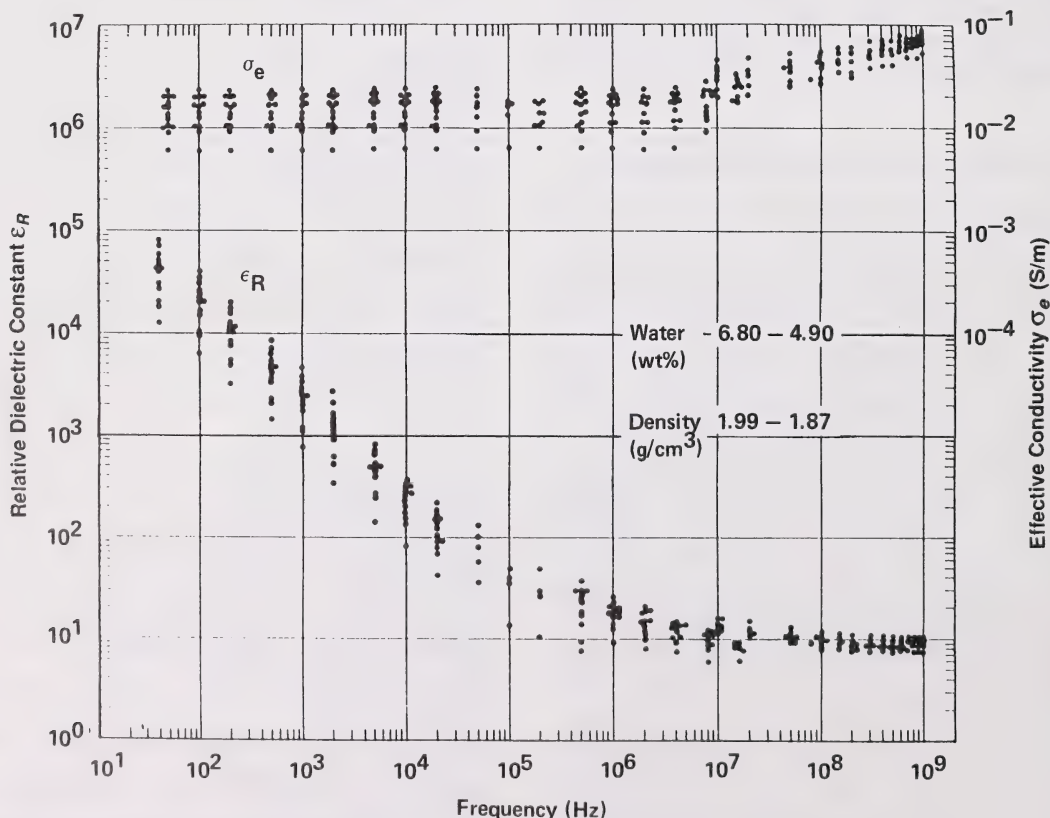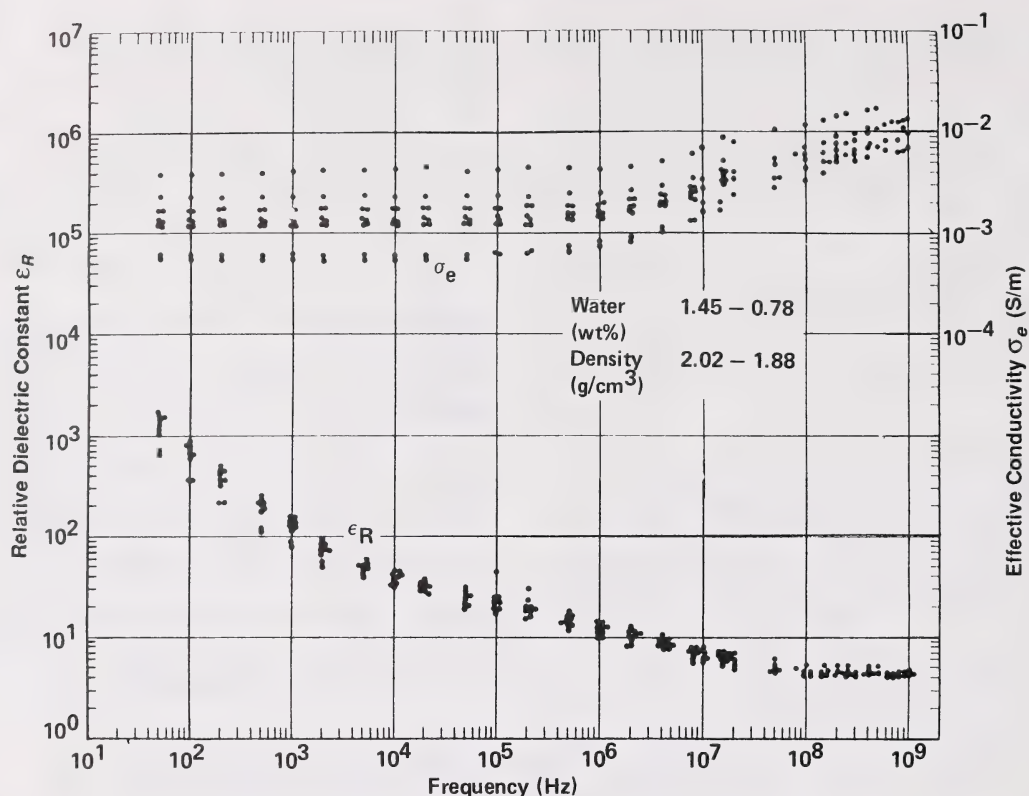
Figure 17. Conductivity and relative dielectric constant versus frequency at 24°C for Athabasca oil sand.
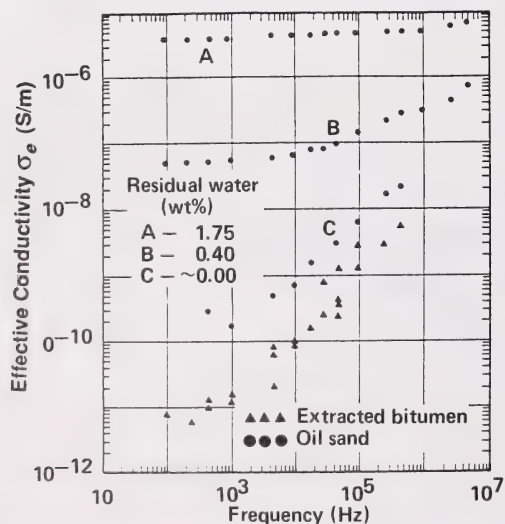
Figure 18. The effect of air drying on the frequency dependence of the electrical conductivity of a sample of Athabasca oil sand with an original bitumen content of 12.1 wt%.
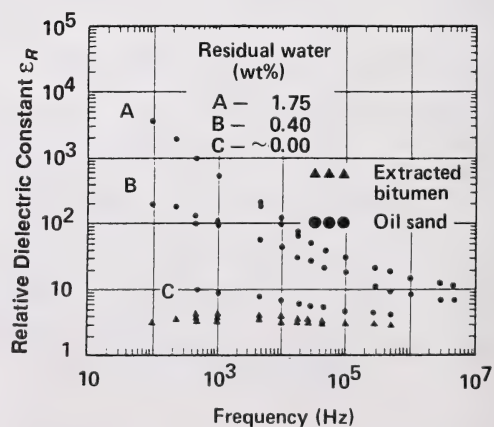
Figure 19. The effect of air drying on the frequency dependence of the relative dielectric constant of a sample of Athabasca oil sand with an original bitumen content of 12.1 wt%.

Table 4. Relative dielectric constant at microwave frequencies [43].

Material	Frequency (MHz)				
	2 270	2 700	2 870	3 300	4 000
Extracted sand (Dean-Stark)	2.4	2.37	2.41	2.32	2.49
Extracted bitumen (Dean-Stark)			2.58		
Sand/bitumen mixture (17% bitumen by weight)	3.23	3.2	3.22	3.24	3.26
Oil sand 1[a] (18% bitumen by weight)			3.43		
Oil sand 2[b]		5.14	5.21	5.35	5.35
Oil sand 2[c]	3.62	3.63	3.59	3.63	3.67

[a] Wt% water unknown.
[b] Composition unknown but water content estimated to be 5 wt%.
[c] After 8 weeks of air-drying.

The first term in the conductivity expression, σ', is the asymptotic value that σ_e approaches at frequencies below about 10^6 Hz. It can be related to the transport of free charges through the ion-rich water that partially saturates the complex pore structure of the oil sand. On the other hand, the second term is associated with variations in time of the distribution of bound charges at the atomic or molecular level that are not free to drift through the material. The value of ε'' can be obtained from the measured effective conductivity at a frequency sufficiently high that $\sigma' \ll \omega\varepsilon''$ (usually a frequency of the order of 1 GHz for oil sand).

The value of ε' in Equation (3) is the measured permittivity at microwave frequencies and is related to well-known polarization mechanisms in dielectric materials. The σ'' term, which accounts for the apparently anomalously high values of permittivity at low frequencies, can be determined from the measured value of ε_e at frequencies below about 10^3 Hz. Most recently this term has been related to the flow of diffusion currents in the ionic double layer surrounding sand and mineral grains and to the concentration and distribution of thin plate-like clay particles in the pore spaces of the formation [52].

In situ electrical heating techniques must be adapted to the electrical properties of the formation to be heated. Generally, it is desired to heat large volumes of the formation quickly, within a few weeks or several months, uniformly, and using as few electrodes (or antennas, etc.) as possible. A typical spacing between electrodes may be of the order of 50 to 100 m. The parameters that play the determining role in the selection of a heating scheme are the volumetric heating rate $\dot{Q}$ the loss tangent $\sigma_e/\omega e_e$, the wavelength λ, and the depth of penetration Δ.

The rate at which the electrical energy delivered to the formation is converted to heat within a unit volume of the formation is given by

$$\dot{Q}, = \sigma_e E^2 = \sigma' E^2 + \omega \varepsilon'' E^2, \ (\text{W/m}^3) \quad (4)$$

where E = rms electric field intensity (V/m).

At frequencies below about 10^6 Hz the first term dominates and the heating is derived from the transfer of kinetic energy to the bulk of the pore water from free charge carriers that have been accelerated by the applied electric field. The surrounding bitumen and the sand matrix are then heated indirectly by thermal conduction. However, this conductive heat transfer is sufficiently rapid that, for electrical current densities that can typically be established in situ, a macroscopic volume element is observed to heat uniformly. At frequencies above 10^7 Hz the situation changes: the second term of Equation (4) dominates, and the bitumen, sand, and water are heated directly at the atomic or molecular level by transfer of kinetic energy from bound charges oscillating in the applied electric field.

It should be noted that in situations where the moisture content of the formation is low, whether this is due to little water content in the formation to begin with, or because water has been driven off by heating above the steam point, heating is due primarily to the $\omega\varepsilon''$ term at all frequencies. In these cases the effective conductivity approaches that of the bitumen and sand components (see Figure 18). The conductivity may then be so small that at low frequencies practical heating rates are unattainable without dramatic increases in the applied electric field. The required field could be large enough to initiate dielectric breakdown within the material or to create hazardous conditions in the vicinity of the surface generating equipment because of high source voltage requirements. However, the effective conductivity can be increased approximately linearly with increasing frequency, and oil sand formations under such low moisture conditions can be satisfactorily heated by operating at frequencies above about 10^6 Hz.

The loss tangent $\sigma_e/\omega\varepsilon_e$ determines whether propagating electromagnetic waves can exist in a heating scheme operating at some given frequency, or whether all electromagnetic fields are attenuated in a distance comparable to or less than a wavelength. The range of loss tangents illustrated in Figure 20 indicates that significant wave propagation in oil sand takes place only at frequencies higher than several tens of megahertz, where loss tangents are less than unity.

Wavelength λ and depth of penetration Δ are indicative of the uniformity with which a formation can be heated for given electrode dimensions, electrode spacings, and operating frequency. They can be

calculated from σ_e and ε_e as

$$\lambda = \frac{2\pi}{\omega\left(\frac{\mu_o\varepsilon_e}{2}\left[\left[1+\left(\frac{\sigma_e}{\omega\varepsilon_e}\right)^2\right]^{1/2}+1\right]\right)^{1/2}} \quad (5)$$

and

$$\Delta = \frac{1}{\omega\left(\frac{\mu_o\varepsilon_e}{2}\left[\left[1+\left(\frac{\sigma_e}{\omega\varepsilon_e}\right)^2\right]^{1/2}-1\right]\right)^{1/2}} \quad (6)$$
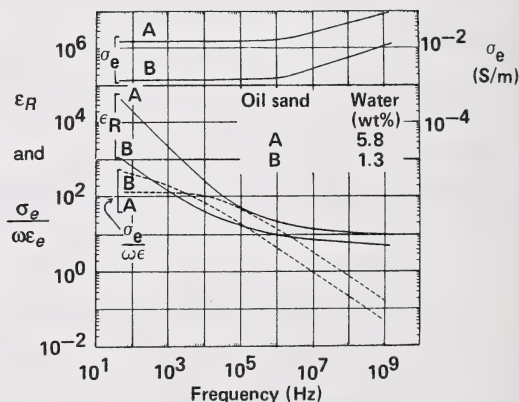
Figure 20. Average conductivity, relative dielectric constant and loss tangent as a function of frequency for typical Athabasca oil sands.

The ranges of wavelengths and depths of penetration depicted in Figure 21 show that, for electrode spacings of the order of 100 m, heating at frequencies greater than a few hundred hertz will lead to the appearance of wavelength effects and to a depth of penetration that is not much more than the interelectrode spacing. For such electrode spacings a frequency below about 10^3 Hz must be chosen in order to achieve uniform heating throughout the oil sand formation. Alternatively, higher frequencies could be used provided the spacing between excitors was suitably reduced.
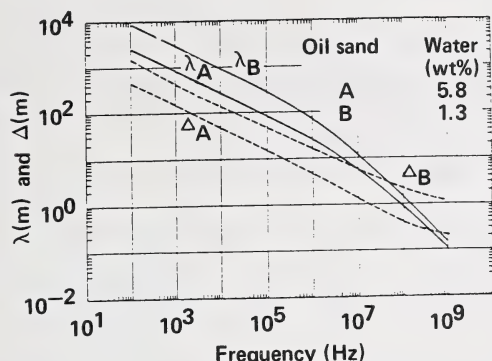
Figure 21. Average wavelength and depth of penetration as a function of frequency for typical Athabasca oil sands.

Variation of electrical conductivity and permittivity with temperature

As oil sand is heated above in situ temperatures the effective electrical conductivity increases in a complex manner that depends on the salinity of the pore water, the pore pressures, and the amount and distribution of clay fines in the formation. It also depends on the operating frequency and on the thermal history. Currently available data are insufficient to permit complete characterization of the temperature response, especially at temperatures in excess of 250°C and at frequencies other than power frequency.

At frequencies below about 10^6 Hz the conductivity increases with temperature in a manner that, for moist oil sands, is closely related to changes in the conductivity of the ion-rich pore water that permeates the formation. Figure 22 illustrates behavior typical of samples prepared using mined oil sand from the Suncor site at Fort McMurray, Alberta [4,11,40,44]. The conductivity of each sample, normalized with respect to its conductivity at 24°C, has been plotted versus temperature over the range 24 to 250°C. The measurements were obtained by gradually raising the sample temperature over a period of approximately 5 h. Also shown in the figure is the normalized conductivity of a 100-mM NaCl brine solution.

It is apparent that at temperatures of less than about 120°C sample conductivities increase approximately linearly at a rate that is virtually the same for all samples, independent of moisture and bitumen content. Further, this rate is not substantially different from that of a 100-mM NaCl solution [53], which is representative of Athabasca brines [54]. In this temperature range the
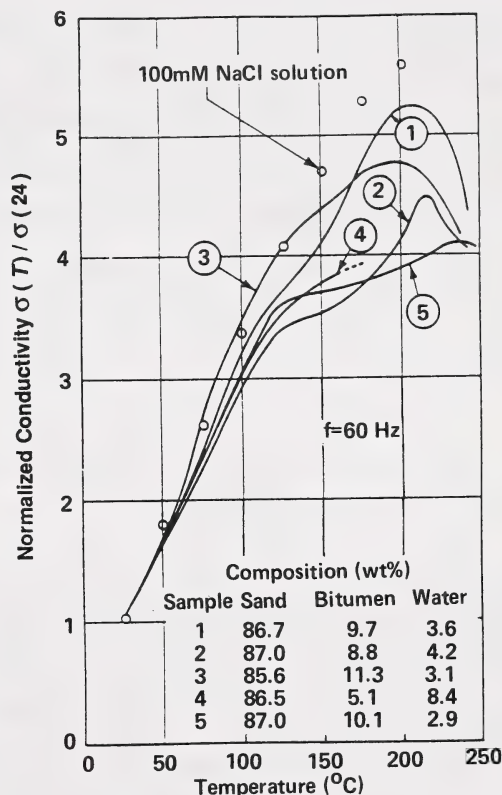
Figure 22. Normalized conductivity versus temperature for several typical samples of mined Athabasca oil sand.

increase in conductivity can be explained by the rapid decrease in pore water viscosity and the associated increase in ionic mobilities [55,56]. At temperatures below about 120°C the conductivity can be expressed as

$$\frac{\sigma(T)}{\sigma(24)} = \left[1 + \alpha_t (T - 24) \right] \qquad (7)$$

for $T \leq 120°C$

and $f \leq 10^6$ Hz

where $\sigma(T)$ is the conductivity at temperature $T(°C)$, $\sigma(24)$ is the conductivity at a temperature of 24°C and α_t is the temperature coefficient for electrical conductivity. Hiebert [44] has established an average value for α_t of 0.026/°C based on measurements of 25 reconstituted oil sand samples with moisture contents

ranging from 2.75 to 9.5 wt% and with bitumen contents ranging from 4.6 to 13.4 wt%. Actual values of α_t varied from sample to sample over a range of 0.019 to 0.033/°C. Equation (7) is applicable at temperatures below about 120°C and for operating frequencies less than about 10^6 Hz. It should be noted that no samples of very rich oil sand were included in the above measurements and anomalous results have been reported for samples with bitumen content over 14 wt% [44].

Recent measurements [57] have indicated that the electrical conductivity at power frequency, of oil sand samples reconstituted from mined sand or core, can be represented by a third-order polynomial of temperature of the form

$$\frac{\sigma(T)}{\sigma(24)} = 1 + \left(\alpha_1 \Delta T\right) + \left(\alpha_2 \Delta T\right)^2 + \left(\alpha_3 \Delta T\right)^3, \quad (8)$$
$$0 < T < 250°C$$

where $\Delta T = T-24$ and T is in °C. The electrical conductivity of shale samples from the Athabasca deposit was shown to exhibit similar behavior. Typical values for the temperature coefficients α_1, α_2, and α_3 for rich and lean oil sands and shales from the Athabasca deposit are given in Table 5. They were obtained by curve fitting data averaged from a number of samples at fixed temperatures between 24 and 240°C. Figure 23 shows the averaged data and the fitted curves using the coefficients given in Table 5.

The two expressions given above for the electrical conductivity of oil sand as a function of temperature indicate that the conductivity at power frequency can be considered to increase linearly with temperature up to about 120°C. It has been indicated [11] that, even

though conduction in the oil sand is increasingly dominated by polarization losses at frequencies above 10^6 Hz, the measured conductivity at higher frequencies also increases approximately linearly with temperature
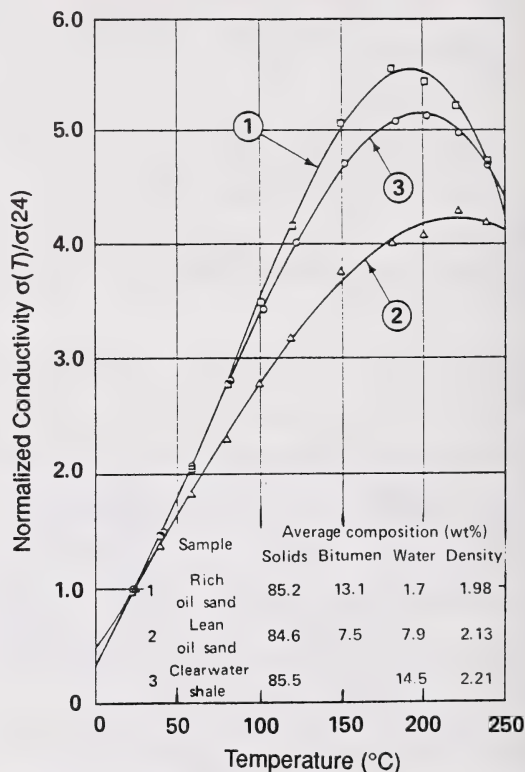
Figure 23. Averaged electrical conductivity data fitted by curves of Equation (8) . The coefficients α_1, α_2, and α_3 are given in Table 5.

Table 5. Temperature coefficients for the electrical conductivity of Athabasca oil sands and shale.[a]

$\sigma(T)/\sigma(24) = 1+(\alpha_1\Delta T) + (\alpha_2\Delta T)^2 = (\alpha_3\Delta T)^3; T = T-24(°C)$

Sample	α_1 (x 10^{-3} °C^{-1})	α_2	α_3
Rich oil sand	26.04	13.12	−9.97
Lean oil sand	26.59	j 3.60	−5.70
Shale	30.13	8.42	−8.47

[a] Based on unpublished data provided by the Applied Electromagnetics Laboratory at the University of Alberta.

[40]. The temperature coefficient of electrical conductivity, however, is generally somewhat smaller. Table 6 lists values of α_t for several frequencies. The high-frequency results were based on measurements on a large number of samples with moisture and bitumen contents ranging from 0.8 to 6.4 wt% and 7.4 to 16 wt% respectively.

At temperatures above about 100 to 125°C the conductivity at a frequency of 60 Hz is observed to increase at a generally slower rate than at lower temperatures, and to exhibit large variations from sample to sample. Above 200°C the conductivity actually begins to decrease. Noting that the electrical conductivity of clean sand and brine mixtures did not exhibit this type of response, Hiebert [44] concluded that complex hydrothermal reactions in the clay-water-bitumen system at high temperatures were responsible for the observed variations in sample conductivities above 125°C. He further noted that when oil sand samples were held at fixed temperatures in excess of 100°C for extended periods of time, the electrical conductivity decreased significantly. Typical results are shown in Figure 24 which illustrates the decrease in conductivity of several samples over a period of 180 h at fixed temperatures of 150 and 200°C. The sample conductivities are shown normalized with respect to the conductivity at the beginning of each of the constant temperature tests.

While Hiebert's data are insufficient for a quantitative description of oil sand conductivity at elevated temperatures, the following observations can be noted:

- At temperatures below about 100°C no significant changes in electrical conductivity were observed over periods of time in excess of 500 h.
- At 150°C the electrical conductivities remained relatively constant for the first 24-h period and thereafter decreased slowly to a stable value after some 80 to 150 h.
- The magnitude of the conductivity decrease at 150°C depended on the moisture content of the samples, being largest for high-moisture-content samples and varying between 10 and 20%. This result is consistent with the view that the decrease is related to hydrothermal reactions in the clay-water-bitumen system since in the Athabasca deposit a high clay and fines content is generally associated with high moisture content. Further, Hiebert [44] observed that the conductivity of clean (clay-free) sand and brine mixtures remained constant over periods in excess of 160 h even at temperatures of 200°C.
- At 200°C, the electrical conductivities decreased much more rapidly than at 150°C and generally reached stable values within 24 h. The decreases were also somewhat greater than at 150°C and ranged from about 15 to 30%. The largest decreases were again associated with high-moisture-content samples.
- At 240°C conductivity decreased even more rapidly than at 200°C and the amount of the decrease was greater. However, insufficient data were available to establish any consistent relationship between moisture content and conductivity decrease.
- The changes in electrical conductivity in all cases were not immediately reversible; it was noted upon

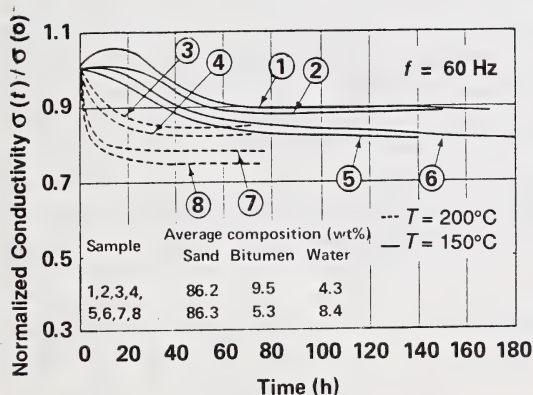**Figure 24.** Normalized conductivity versus time at 150 and 200°C for typical samples of mined Athabasca oil sand.

Table 6. Temperature coefficient for electrical conductivity of Athabasca oil sand samples [40].

	α_t			
Frequency (Hz)	<10^6	10^7	10^8	10^9
$\alpha_t(10^{-2}°C^{-1})$	2.6	2.07	1.93	1.78

cooling the samples that the conductivities were consistently lower at corresponding temperatures than they had been during the original heating of the sample. Clean sand and brine mixtures exhibited no such hysteresis during heating and cooling cycles.

There is little information available on the temperature dependence of the relative dielectric constant of oil sand. Chute et al. [11] indicate that at frequencies greater than about 10^6 Hz, the dielectric constant varies only slightly with temperature. In the range 4 to 150°C they noted a nearly linear increase of the form

$$\frac{\varepsilon_R(T)}{\varepsilon_R(24)} = \left[1 + k_t(T-24)\right] \qquad (9)$$

$$T \leq 150°C$$

$$f \geq 10^6 \, Hz$$

where $\varepsilon_R(24)$ is the relative dielectric constant at 24°C and k_t is the temperature coefficient of dielectric constant. The value of k_t was always at least an order of magnitude smaller than the temperature coefficient of conductivity, α_t. The observed values of k_t are presented in Table 7.

The marginal dependence of ε_R on temperature in the range 40 to 150°C is to be expected since at higher frequencies the polarization mechanisms are predominantly molecular, ionic, or electronic and are not significantly temperature dependent. However, at frequencies below 10^6 Hz, where interfacial effects contribute more strongly to the effective dielectric constant, substantial temperature dependence can be expected especially with high-moisture-content samples. It has been suggested that in such cases the increase with

temperature will be approximately linear and k_t will nearly equal α_t [58].

Das et al. [59] observed that even with very low moisture-content oil sand samples the dielectric constant varied dramatically with temperature at low frequencies. They have reported measurements of relative dielectric constant and loss tangent, at several frequencies, at temperatures up to 550°C, for a number of "dry" oil sand samples from Athabasca and from the Unita Basin and Circle Cliffs regions of Utah. The origin and average compositions of the samples are given in Table 8.

Typical results are shown in Figures 25 and 26 for samples from the northwest Asphalt Ridge region in the Unita Basin of northeastern Utah. Similar results were obtained for the other samples. At frequencies above about 50 kHz the dielectric constant and loss tangent are virtually independent of temperature, in agreement with the reported results of Chute et al. [11,40]. At lower frequencies the dielectric constant showed increasing temperature sensitivity, and at 200 Hz was observed to increase in a sharply nonlinear manner at temperatures above about 120°C. The anomalous behavior exhibited at about 400°C has been attributed to the creation of mobile charges due to thermal decomposition and fragmentation of the oil sand bitumen [59]. The loss tangent was also observed to increase substantially with increasing temperature above 120°C, indicating the conductivity at these temperatures increases more rapidly with temperature than does the dielectric constant (in other words, $\alpha_t > k_t$). Typical low-frequency behavior for the various samples listed in Table 8 is depicted in Figures 27 and 28.

The indicated behavior for the Athabasca sample (sample 1) in Figures 27 and 28 should not be considered typical. The apparent dielectric constant and conductivity of this sample are about an order of

Table 7. Temperature coefficient k_t for dielectric constant of Athabasca oil sand samples [40].

Moisture content	k_t (10^{-2} °C^{-1})			
	Frequency (Hz)			
(wt%)	10^6	10^7	10^8	10^9
4.9–6.8	<0.1	0.3	0.3	<0.1
2.7–4.2	0.6	0.4	0.4	<0.1
0.8–1.5	0.6	0.7	0.3	<0.1

magnitude less than exhibited by most Athabasca samples with similar moisture contents. Indeed, the measured values for this sample are typical of the results obtained for air-dried samples and indicate the possibility that the water phase was not continuous throughout the reconstituted sample.

Table 8. Average composition and origin of oil sand samples of Das et al. [59].

Sample number	Origin	Composition by wt%		
		Sand	Bitumen	Water
1	Athabasca	84.5	14.4	1.1
2	P.R. spring	88.6	11.2	0.2
3	NW Asphalt Ridge	86.7	13.1	0.2
4	NW Asphalt Ridge	92.1	7.8	0.1
5	Circle Cliffs	95.7	4.1	0.2

Figure 25. Relative dielectric constant versus temperature for oil sand samples from NW Asphalt Ridge, UT, at several frequencies, adapted from [59].

Figure 27. Relative dielectric constant versus temperature for several oil sand samples at low frequency, adapted from [59].

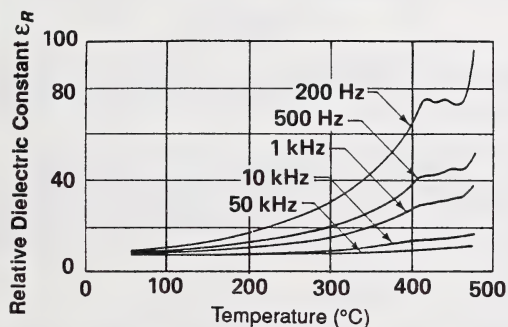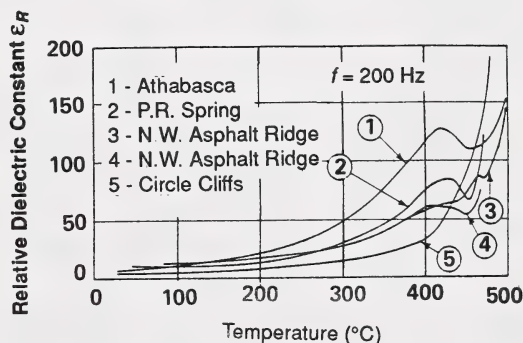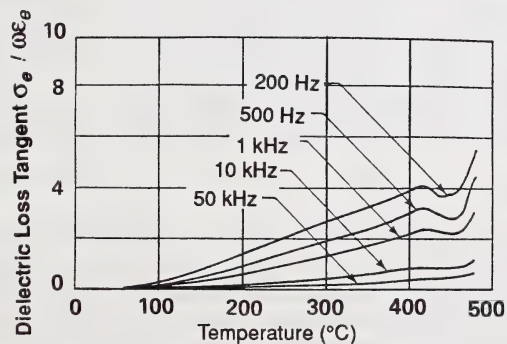**Figure 26.** Loss tangent versus temperature for oil sand samples from NW Asphalt Ridge, UT, at several frequencies, adapted from [59].
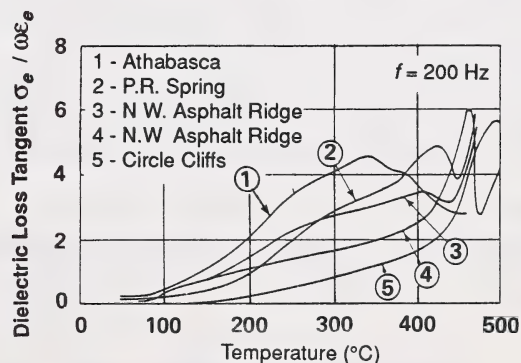

Figure 28. Loss tangent versus temperature for several oil sand samples at low frequency, adapted from [59].

Variation of electrical conductivity and permittivity with moisture content

In oil sands containing more than approximately 1 wt% water, the conductivity at frequencies below about 1 MHz is related to the transport of free charges through the ion-rich water that partially saturates the oil sand. The pore volume is usually occupied by water and bitumen, and gas saturations are negligible. The effective conductivity generally depends on both the salinity and the distribution of this water through the sand matrix. The range of observed conductivities in the Athabasca region is shown in Figure 29 (adapted from Hoekstra et al. [60]) which also indicates values for the overburden and underburden materials.
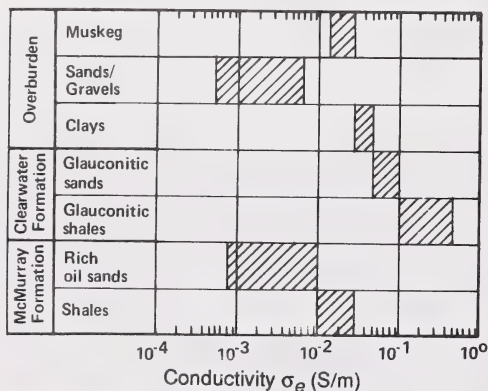
Figure 29. Conductivity ranges for different formation units encountered in the Fort McMurray area, adapted from [60].

Measurements made on oil sand samples reconstituted from mined oil sand from the Suncor site at Fort McMurray have shown that the conductivity is closely correlated with the weight percent of water held in the sample. A typical least-squares polynomial correlation at a frequency of 100 Hz and a temperature of 24°C is shown in Figure 30. The water contents were determined by Dean-Stark analysis of the individual samples. The results of many such correlations at various frequencies less than about 1 MHz indicated that the effective conductivity (S/m) of these reconstituted samples can be expressed as

$$\sigma_e \cong A W_w^2 \ (S/m), W_w \geq 0.01, f \leq 1\,MHz \qquad (10)$$

where W_w is the fractional weight of water in the sample and A is a constant that increases approximately linearly

with increasing density of the sample as $A \approx 12.7D - 18.5$, where D is the sample density.
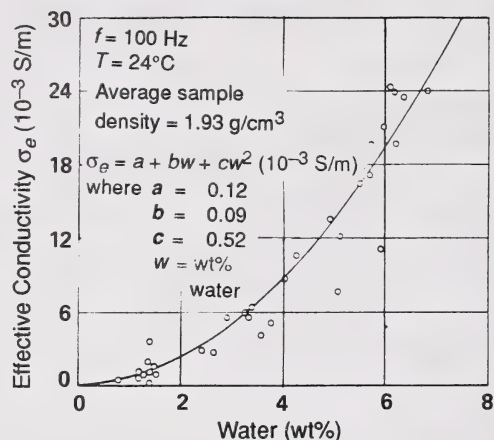
Figure 30. Conductivity versus weight percent water at 24°C and 100 Hz.

The porosity of these reconstituted samples was typically some 25% larger than could be expected in situ and the pore space was only partially saturated with water and bitumen. Gas saturations generally were of the order of 0.25. The observed increases of the conductivity with density can likely be attributed to changes in the orientation of the sand grains leading to changes to the shapes of the pore spaces as well as to decreases in the total pore volume upon compaction, and to the redistribution of water into previously gas-saturated portions of the pore volume.

Chute et al. [11] further observed that the conductivity data at frequencies between 1 MHz and 1 GHz could also be approximated by a second-order polynomial and that for water contents above about 2 wt% the square law term dominated. However, in these cases the constant A increased with increasing frequency by a factor of about 3 over the range from 1 MHz to 1 GHz.

It was also observed that the relative dielectric constant of the samples could be approximated with a second-order polynomial at frequencies below about 100 kHz. A typical correlation is shown in Figure 31 for $f = 10$ kHz and $T = 24°C$. For water contents in excess of about 2 wt% the dielectric constant was found to be satisfactorily approximated by

$$\varepsilon_R \cong B W_w^2, \ W_w \geq 0.02, \ f \leq 100\,kHz \qquad (11)$$

where the value of B was frequency dependent and varied from about 7.3×10^6 at 100 Hz to about 7×10^4 at 10 kHz.
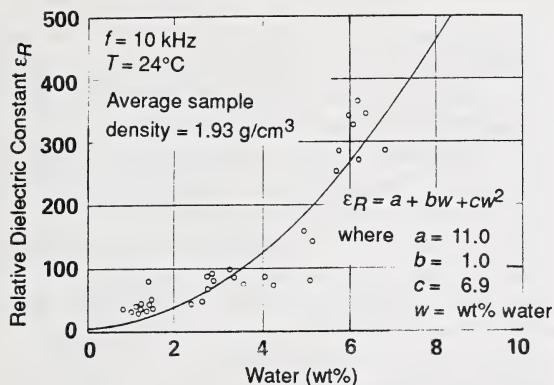
Figure 31. Relative dielectric constant versus weight percent water at 24°C and 10 kHz.

The data for ε_R at frequencies above about 1 MHz indicated a linear increase of dielectric constant with increasing water content of the form

$$\varepsilon_R = a + bW_w, \quad f \gtrsim 1\,\mathrm{MHz} \tag{12}$$

The values of the coefficients a and b for several frequencies are given in Table 9. They decrease as the frequency increases and the value of ε_R becomes less sensitive to the moisture content of the oil sand.

The conductivity correlations discussed above are inadequate for developing a numerical model of an electric preheat steam drive recovery process where movement of fluids results in continuous changes in pore water saturations and salinities, as well as in

porosity changes due to the thermal expansion of the sand matrix and possible swelling of the clay component. A large body of experimental evidence suggests that the conductivity of the oil-bearing formation at low frequencies can be expressed [61–64] as

$$\sigma_e = \sigma_w \frac{\phi^m S_w^n}{a} \tag{13}$$

where σ_w is the conductivity of the pore water, ϕ is the volume fraction of the formation not occupied by solids (the porosity), and S_w is the fraction of the pore space actually occupied by water. The parameters a, m, and n are usually experimentally selected so that the equation fits a particular set of data. It should be noted that measurements made on individual samples usually do not agree closely with this simple expression because of the significant scatter in the data as the result of textural differences from sample to sample. However, as more and more data are collected the average conductivities are observed to follow the form of Equation (13).

The value of the parameter a is generally somewhat less than 1 in sandstone and unconsolidated sand formations while the cementation index, m, is usually close to 2. The saturation exponent, n, is also approximately 2 in most cases where there is sufficient water so that it exists as a continuous phase throughout the formation and the water-wet nature of the individual sand grains is maintained. At water contents below this level the saturation exponent can be as high as 4 or 5. It is likely that the saturation exponents could be substantially greater than 2 for oil sands with moisture contents less than about 1 wt%.

To obtain satisfactory quantitative results based on Equation (13) a knowledge of the conductivity of the pore water is required. In general this conductivity exhibits both areal and vertical variations. For example,

Table 9. Coefficients of the linear approximation for the relative dielectric constant of Athabasca oil sand samples [11].

		$\varepsilon_R = a + bW_w$		
Frequency (MHz)	1	10	100	1000
a	10.0	3.7	3.3	3.3
b	170	160	100	82

Hackbarth and Nastassa [65] indicate that total dissolved solids in the groundwater of various lithological units in the McMurray Formation range from 5 000 to 10 000 mg/L in the oil sand. Values generally increase to the west and north of Fort McMurray. Corresponding values of σ_w based on NaCl equivalents range from 0.67 to 1.25 S/m at 15°C. Takamura [54] on the other hand suggests that the pore water is equivalent to a 30 to 100 mM NaCl brine with corresponding conductivities ranging from 0.25 to 0.83 S/m at 15°C.

While this expression has been successfully used in the log interpretation of many clean (clay-free) petroleum deposits it is generally recognized that a correction for shaliness should be applied [47,66,67]. Such a correction often takes the empirical form [47]

$$\sigma_e = \sigma_w \frac{\phi^m S_w^n}{\alpha\left(1 - V_{sh}\right)} + \sigma_{sh} V_{sh} S_w \qquad (14)$$

where σ_{sh} is the conductivity of the shale or clay component and V_{sh} is the volume fraction of the clay present in the formation. Many other corrections exist, some of which express the correction in terms of the cation exchange capacity of the clays [66].

Table 10 lists some of the formulas that have been used or proposed for the conductivity of oil sands.

Only limited data currently exist on the dependence of ε_R on water salinity, water saturation, and porosity. Bibhas [41] suggests that the complex refractive index of a formation can be empirically calculated as the volume average of the complex refractive indices of the sand, oil, and water components. Thus, since the complex refractive index is proportional to the square root of the complex relative dielectric constant defined as

$$\varepsilon_{RC} \stackrel{\Delta}{=} \varepsilon_R - j \frac{\sigma_e}{\omega \varepsilon_o} \qquad (15)$$

it follows that

$$\varepsilon_{RC}^{1/2} = \phi \; S_w \; \varepsilon_{RCW}^{1/2} + \phi \, (1 - S_w) \, \varepsilon_{RO}^{1/2} + (1 - \phi) \, \varepsilon_{RS}^{1/2} \qquad (16)$$

It has been assumed that the oil and sand components are essentially without loss and ε_{RO} and ε_{RS} represent respectively the relative dielectric constants of the bitumen and of the sand matrix. Calculation of ε_{RC} (and hence of ε_R and σ_e) from this relationship requires a knowledge of the complex relative dielectric constant of water ε_{RCW} at the operating frequency, which in turn requires a knowledge of the temperature and salinity of the pore water. This expression has been shown to approximately match measured values of ε_R for brine-saturated Berea sandstone (porosity 0.19, salinity 18.5 g/kg) at frequencies above about 20 MHz. Satisfactory values of σ_e were not obtained. At frequencies above 1 GHz (the microwave range) the term $\sigma_e/\omega\varepsilon_o$ is negligible in a typical oil sand as well as in water, and the relative dielectric constant can be calculated as

$$\varepsilon_R = [\phi \, S_w \, \varepsilon_{RW}^{1/2} + \phi \, (1 - S_w) \, \varepsilon_{RO}^{1/2} + (1 - \phi) \, \varepsilon_{RS}^{1/2}]^2 \qquad (17)$$

$$f \gtrsim 1 \, \text{GHz}$$

It is easily shown that this expression leads directly to the water saturation formula used to interpret data obtained with the Schlumberger electromagnetic propagation log (EPT) [67]. No comparable expression for ε_R is currently available for low frequencies.

Table 10. Formulas for the electrical conductivity of oil sand samples at low frequency.

Location	Formula	a	σ_W/a(S/m)	σ_W(S/m)
Shaly oil sands[a]	$\sigma_e = \sigma_w \dfrac{\phi^2 S_w^{1.6}}{a\left(1-V_{sh}\right)^2} + \sigma_{sh} V_{sh} S_w$	0.8	–	–
Shaly oil sands[b]	$\sigma_e = \sigma_w \phi_{EPT}^2$ [c]	–	–	–
Shaly oil sands[d]	$\sigma_e = \sigma_w \dfrac{\phi^2 S_w^2}{a\left(1-V_{sh}\right)} + \sigma_{sh} V_{sh} S_w$	–	–	–
Clean oil sands[d]	$\sigma_e = \sigma_w \dfrac{\phi^2 S_w^2}{a}$	0.81	–	–
Athabasca[e]	$\sigma_e = \sigma_w \dfrac{\phi^{1.8} S_w^{1.8}}{a}$	–	1.0 – 2.27	1.42 – 5.0[f]
Athabasca[g]	$\sigma_e = \sigma_w \dfrac{\phi^{1.5} S_w^{1.5}}{a}$	–	2.0	2.0 – 2.5[h] 1.1 – 3.3[i] 2.85[j]
Athabasca[k]	$\sigma_e = \sigma_w \dfrac{\phi^{1.78} S_w^n}{a}$	–	–	–
Cold Lake[l]	$\sigma_e = \sigma_w \dfrac{\phi^{2.15} S_w^2}{a}$	0.62	–	0.81[m]
NW Asphalt Ridge[n]	$\sigma_e = \sigma_w \dfrac{\phi^{2.15} S_w^2}{a}$	– –	– –	2.2 – 4.8[o] 1.0 – 2.2[p]
Athabasca[q]	$\sigma_e = \sigma_w \dfrac{\phi^{1.37} S_w^2}{a}$	0.88	–	0.33 – 1.35[r]
Athabasca[s]	$\sigma_e = \sigma_w \dfrac{\phi^{1.99} S_w^{1.99}}{a}$	–	1.38	–

a R.C. Sah et al. [68].
b J.M. Delano and R.P. Wharton [67].
c ϕ_{EPT} is the porosity recorded with the Schlumberger EPT logging tool.
d Schlumberger log interpretation vol. 1 — principles [47].
e H.N. Collins [69]; based on 6 wells.
f Based on resistivity measurements in basal water zones.
g R. Woodhouse [70]; based on 90 wells.
h Based on measurements of bottom water which was observed to contain 3 000–17 500 mg/L of dissolved solids.
i Estimated from SP logs
j Expected values based on resistivity measurements in adjacent water-bearing sands.

k T.J. Griffin and D.C. Bush [71].
l D. Minken [72]; based on 413 wells.
m Expected value based on resistivity measurement in adjacent water-bearing sands.
n L.J. Fahy et al. [73]; based on 8 wells.
o Estimated.
p Estimated from SP logs.
q A.D. Hiebert [44]; based on 30 reconstituted samples.
r Based on conductivity measurements on reconstituted samples of mined oil sand at 24°C.
s Based on a least-squares approximation of conductivity measurements on 78 reconstituted samples of mined oil sand at 24°C, using data from Chute et al. [11], Hiebert [44].

PHYSICAL AND NUMERICAL MODELLING OF ELECTROTHERMAL PROCESSES

Introduction

Cost and time considerations make it impractical to rely exclusively on field tests to evaluate and optimize electrothermal processes. Analytical calculations have been used to evaluate the performance of certain heating configurations at 60 Hz [74,75] and at radio frequencies [76]. While results thus obtained can provide much insight, they pertain to highly idealized situations and are, therefore, of limited value. Information about phenomena associated with electrothermal processes may be extended beyond the range of theoretical analysis by the use of small-scale physical models to simulate the full-scale system. For electromagnetic systems this approach was initially developed for geophysical studies and the analysis of antenna systems [77,78]. At the expense of reducing the number of degrees of freedom available to the model developer, the technique has been extended by Vermeulen et al. [79] to include thermal phenomena so that it can be applied to electrothermal processes over a wide frequency range. Numerical simulators provide an alternative method for studying electrothermal processes. These have been developed for two-dimensional problems in cartesian and cylindrical coordinates at 60 Hz [80,81,26] and at radio frequencies [26], as well as for three-dimensional problems at 60 Hz without simultaneous fluid flow [17,44], and with simultaneous fluid flow [82,83,44].

Physical scale modelling of electromagnetic heating

Physical scale modelling is a versatile tool for investigating in situ electromagnetic heating [84]. A physical model observes reality itself and, therefore, reflects the fundamental processes that actually occur. A numerical model, on the other hand, simulates only those physical processes that are built into it, and models a scenario that is preconceived. Electromagnetic phenomena are generally complex, and phenomena thought to be minor or entirely absent, may, in fact, dominate [22]. It is clear then, that a dual approach to the solution of electromagnetic heating problems may be mandatory: physical modelling to identify the inherent nature of the process, and subsequent numerical modelling to simulate those phenomena that physical modelling has identified to be of importance. Completely scaled physical models of an electromagnetically assisted recovery process can seldom be constructed because of the large number of conflicting scaling conditions that must be met. However, partially scaled and even unscaled elemental models of a process can yield valuable information about the physical processes. Comparisons between models of different size as well as analytical and numerical investigations can help delineate the relative importance of scaling criteria that have been ignored in such models.

Scaling criteria for modelling recovery processes that involve the electromagnetic heating of the reservoir can be formally obtained by dimensional analysis or by inspection of the differential equations describing the physical processes, namely the electromagnetic field equations (Maxwell's equations) [85] and the mass and energy conservation equations for multiphase viscous fluid flow in a porous medium [86,87]. Maxwell's equations and the equations governing the flow of heat and the motion of fluids through the reservoir are coupled only through the addition of the electrical heating source term, $\sigma_e E^2$, to the energy equation. The following discussion will focus primarily on the presentation of those scaling criteria that arise from the consideration of this coupling. These scaling groups are introduced by considering the relative magnitudes of various electrical and thermal phenomena present in the formation. Of course, many additional scaling groups are required to properly model convective transfer of heat, gravitational and capillary forces, relative permeabilities, fluid saturations, the injection of steam and/or other substances into the reservoir, and so on. These other scaling groups have been extensively summarized by Farouq Ali et al. [88] for a number of the more common enhanced oil recovery processes.

The steady-state electromagnetic response of a lossy system driven by a voltage or current source varying sinusoidally with time can be characterized by the wavelength, λ, and by the depth of penetration, Δ, in accordance with Equations (5) and (6). The wavelength is the distance a plane electromagnetic wave will travel through the material (the reservoir) during a time interval equal to the reciprocal of the operating frequency. The depth of penetration may be interpreted as the distance a plane electromagnetic wave travels as absorption by the medium reduces its amplitude by the factor e (Naperian base). The quantity $\sigma_e/\omega\varepsilon_e$ appearing in these expressions is the ratio of conduction to displacement current, the two components of electrical current flow in any lossy material. The conduction current, which is proportional to the product of the electrical conductivity, σ_e, and the electric field

intensity, is that part of the current that flows in time phase with the electric field (as in a resistor). The displacement current, which is proportional to the product of angular frequency, ω, effective permittivity, ε_e, and the electric field intensity, is that portion flowing in time quadrature with the electric field (as in a capacitor).

A necessary condition for constructing a geometrically similar model that will properly predict the electromagnetic response of a full-scale system is that the ratio of these two components of electrical current be equal in both the full-scale and model systems. Thus, the first electromagnetic scaling group (a) is given by

$$\frac{\sigma_e}{\omega \varepsilon_e} \qquad (a)$$

Further, for proper scaling of the propagating electromagnetic waves it is necessary that the ratio of the wavelength to any characteristic system dimension, L, be invariant. Thus,

$$\frac{\lambda}{L} \qquad (b)$$

is a second scaling group. In such an electromagnetic model homologous times are then defined by the group

$$\omega t \qquad (c)$$

where t = elapsed time. Groups (a) and (b) may be combined (using the expression for λ) to show that the group

$$L \sigma_e \left(\frac{\mu_o}{\varepsilon_e}\right)^{1/2} \qquad (d)$$

must also be in variant. It may, therefore, be noted that if all the electrical properties of the full-scale and model systems are given, then the physical dimensions of the model and the frequency at which it must be driven are completely determined by these electrical properties.

When scaling groups (a) and (b) are invariant, the ratio of the depth of penetration to any characteristic system dimension is likewise invariant. Since this ratio is representative of the spatial distribution of electrical

energy deposition in the reservoir, it is evident that the conversion of electromagnetic energy to heat will now occur in homologous fashion in the full-scale and model systems.

However, to achieve thermal similitude it is also necessary that in homologous volumes the ratio of electrical energy converted to heat, in homologous times, to the energy stored as heat be equal in the full-scale and model systems. This requirement leads to the scaling group

$$\frac{Pt}{M \Delta T L^3} \qquad (e)$$

where P = electrical power converted to heat
       M = volumetric heat capacity of the reservoir
       ΔT = temperature change.

Further, in both systems, in homologous volumes, the ratio of electrical power converted to heat, to the rate at which thermal energy is gained by thermal conduction, must be the same at homologous times. This condition leads to the scaling group

$$\frac{P}{LK\Delta T} \qquad (f)$$

where K = thermal conductivity of the reservoir (W/m•K)

Groups (e) and (f) are usually combined to yield the group

$$\frac{tD}{L^2} \qquad (g)$$

where D = thermal diffusivity of the reservoir (m²/s), and thermal similitude is ensured by requiring the invariance of groups (f) and (g), rather than (e) and (f).

Since P, the electrical power converted to heat, is the volume integral of the volumetric heating rate $\sigma_e E^2$, and since dimensionally the electric field is the ratio of voltage to distance, group (f) may be rewritten in terms of the system source voltage, V, as

$$\frac{V^2 \sigma_e}{K \Delta T} \qquad (f')$$

Alternatively, since terminal current, I, is dimensionally equivalent to electrical power divided by voltage, group

(f) may be expressed as

$$\frac{I^2}{\sigma_e K \Delta T L^2} \qquad \text{(f'')}$$

Many proposed processes for the electromagnetically assisted recovery of bitumen from oil sand use electrical energy to preheat the formation before actual recovery of bitumen by more conventional means. For such processes the effects of fluid movement during the preheat phase are generally negligible and the scaling groups introduced above are sufficient to define an accurately scaled electrothermal model. Indeed, only five of these groups can be considered independent and the most common selection is

$$\frac{\sigma_e}{\omega \varepsilon_e}, \quad \frac{\lambda}{L}, \quad \omega t, \quad \frac{P}{L K \Delta T}, \quad \frac{tD}{L^2}$$

The thermal response time of most systems is many orders of magnitude greater than the period of oscillation of the electromagnetic fields and the group ωt is usually ignored. Physically, this is equivalent to considering just the time-averaged (over one cycle of oscillation) value of the electrical heating term $\sigma_e E^2$, which is independent of ωt It should be noted that when the group ωt is ignored, the short-term temporal variations of the electromagnetic field quantities on a time scale comparable to the period of oscillation, do not scale with time t. However, time t does predict the long-term temporal variations of the electromagnetic field quantities that occur due to changes in the electrical properties of the formation as it heats. Thus, groups (a), (b) or (d), (g) and either (f) or (f ') or (f '') form a necessary and sufficient set for scaling electrothermal processes where fluid flow is initially of secondary importance.

However, even in these cases, selection of suitable materials and fluids for a model of a multilayered reservoir is not straightforward. It is usually necessary that the full-scale system and model be geometrically similar with respect to electrical and thermal properties, and that this similarity be maintained throughout the entire simulation. The electrical and thermal properties of each layer are different, and in particular, the electrical conductivity σ_e and the effective permittivity ε_e may vary by several orders of magnitude. Of major concern are the pronounced variations of σ_e and ε_e with

temperature. Since the scaling groups must be invariant not only initially, but also as heating progresses, the functional dependences of σ_e and ε_e on temperature in the model must virtually duplicate the variations in the actual reservoir. When such is not the case, or for those cases where the two systems are not completely geometrically similar, it may still be possible to get useful quantitative information, but interpretation of the model results must be done with considerable care. Ideally, the porous medium and the fluids used in the model should be the reservoir materials themselves. Such a choice is not generally possible since the invariance of group (d) would imply that no scale reduction is possible. However, in many important cases useful partially scaled models can be constructed.

Case I:

$$\frac{\sigma_e}{\omega \varepsilon_e} << 1 \text{ or } \frac{\sigma_e}{\omega \varepsilon_e} >> 1,$$

λ and Δ >> largest system dimension

Here either conduction or displacement current greatly dominates the current flow through the reservoir and the group $\sigma_e/\omega \varepsilon_e$ need not be scaled. Also the group λ/L need not scale since the system is electrically small. Thus, the model operating frequency and physical size, as well as the model materials, can be selected arbitrarily providing only that *geometric similarity is preserved* and that the restrictions defining Case I are also satisfied in the model. Thus, the groups

$$\frac{P}{L K \Delta T}, \frac{tD}{L^2}$$

are sufficient to define the scale model. Generally the model is constructed from actual reservoir materials and powered so that at homologous times identical temperature changes are observed at homologous locations throughout the system. An example is the modelling of current flow in oil sand at power frequencies, where generally $\sigma_e/\omega \varepsilon_e$ >> 1. Another example is the modelling of current flow at radio frequency near an in situ electrode, for the case where moisture has almost completely evaporated from the oil sand and the formation has been rendered an extremely poor conductor, so that $\sigma_e/\omega \varepsilon_e$ << 1.

Case II:

λ and Δ >> largest system dimension

Here both conduction current and displacement current are significant but the system can be considered electrically small. Group (a) must be invariant but group (b) can be ignored. *Geometric similarity is required* and the physical size of the model and the model materials must be selected so that, at the model operating frequency dictated by the invariance of group (a), the model dimensions are much less than the wavelength and the depth of penetration. Thus, the groups

$$\frac{\sigma_e}{\omega \varepsilon_e}, \frac{P}{LK\Delta T}, \frac{tD}{L^2}$$

are sufficient to define the scale model. An example is the modelling of current flow at power frequency through oil sand from which a significant amount of moisture has evaporated so that $\sigma_e/\omega\varepsilon_e$ has been reduced from its initial value and is no longer much greater than one.

Case III:

$$\frac{\sigma_e}{\omega \varepsilon_e} \gg 1$$

Here the operating frequency is such that conduction currents dominate and the system dimensions are comparable to or greater than the wavelength and depth of penetration. The system is no longer electrically small. Group (a) can be ignored and wavelength group (b) can be expressed as

$$L(\omega \mu_\circ \sigma_e)^{1/2}$$

Thus, the groups

$$L(\omega \mu_\circ \sigma_e)^{1/2}, \frac{P}{LK\Delta T}, \frac{tD}{L^2}$$

are sufficient to define the scale model provided that current flow in the model is also dominated by conduction current. Geometric similarity is required and scaling is usually accomplished so that identical changes in temperature are observed in homologous volumes at homologous times. A suitable scaling strategy in this case is to first select the physical scale reduction for convenience, and to then select model materials (fluids and porous matrix) and model frequency so that the wavelength group is invariant. These selections must also ensure that current flow in the model is dominated by conduction currents. Group (f) is then used to set the power level and homologous times are defined through group (g). It should be noted that because of the complex frequency dependencies of σ_e and ε_e for oil sand, shale, and limestone, substantial scale reductions are usually not possible when actual reservoir materials are used in the model. Artificial porous media with carefully tailored electrical conductivity must be used. Models constructed from sand packs saturated with various brine solutions have been used with considerable success [3]. An example of such scaling is the modelling of radio frequency heating of oil sand, such as might be produced by an antenna placed in a borehole [26] or by horizontal wells excited to produce an EMF as described earlier [23].

Case IV:

$$\sigma_e/\omega\varepsilon_e \ll 1$$

Here the operating frequency is such that displacement currents dominate and again the system dimensions are such that in relation to wavelength it cannot be considered electrically small. Group (a) can be ignored and the wavelength group (b) can be rewritten as

$$L\omega(\mu_\circ\varepsilon_e)^{1/2}$$

However, in so doing, it is implied that system dimensions are much smaller than the depth of penetration since in this case signal attenuation has been ignored. Thus, the groups for scaling these situations are just

$$L\omega(\mu_\circ\varepsilon_e)^{1/2}, \frac{P}{LK\Delta T}, \frac{tD}{L^2}$$

Modelling strategies are similar to those discussed for Case III. The modelling of high-frequency waves travelling through a formation region of low moisture content could fall in this category.

It should be noted that for any of the above cases groups (f) and (g) can be replaced by group (e) whenever redistribution of heat due to thermal conduction can be neglected. Then either the power level or the heating time can be selected independently.

For many electromagnetic processes in oil sand or heavy oil formations, no definitive categorization is possible. A case in point is the development of a scaling strategy for modelling an electromagnetic flooding operation between vertical pairs of horizontal wells whereby bitumen is recovered by gravity drainage to the lower wells [23]. A highly resistive region forms around the upper well as fluids drain toward the lower well and it becomes progressively more difficult to cause electrical current to pass through this drained region. It has been observed that the current flowing through the formation is shunted along the horizontal well pair, progressively bringing more of the formation into production. Conditions in the immediate vicinity of the wells may result in a negligible flow of conduction current through this region and model development based on the groups identified for Case IV would be indicated. On the other hand, conduction currents may dominate in the bulk of the formation suggesting a model satisfying the scaling conditions outlined for Case III. To adequately model this situation requires that a model be constructed for which the group $L\omega(\mu_\circ\varepsilon_e)^{1/2}$ is invariant in the vicinity of the upper well while the group $L(\omega\mu_\circ\sigma_e)^{1/2}$ must be simultaneously invariant in the remainder of the reservoir.

Further, since fluid production and electromagnetic heating occur at the same time in this process, the model must preserve the main features of the gravity drainage, in order to permit evaluation of the effects on bitumen recovery of varying power levels, operating frequencies, and well spacings. It is of particular concern to model the gradual decoupling of the electromagnetic currents flowing between wells as fluids are depleted from the regions around the upper wells. This decoupling, as well as the convective transfer of heat, will be adequately modelled providing that homologous volumes of the reservoir are drained in identical fashion in homologous times. One could assume that the same fluids (so that respective fluid densities and viscosities are invariant) and the same porosities and saturations are present in field and model, and further that the ratios of fluid heat

capacities to rock heat capacities are also invariant. Then, neglecting capillary effects and assuming Darcy's law represents the average velocity of the draining fluids, homologous volumes will be drained in homologous times providing the Darcy group

$$\frac{\rho g k k_r t}{\hat{\mu} L} \qquad (h)$$

is invariant for each fluid, where

ρ = fluid density
k = absolute permeability
k_r = relative permeability
$\hat{\mu}$ = bitumen viscosity.

Thus, the following five groups provide the basis for the development of a partially scaled model of an electromagnetically assisted gravity drainage process:

$$L\omega(\mu_\circ\varepsilon_e)^{1/2}, \; L(\omega\mu_\circ\sigma_e)^{1/2}, \; \frac{P}{LK\Delta T},$$
$$\frac{\rho g k k_r t}{\hat{\mu} L}, \; \frac{tD}{L^2}$$

A possible modelling strategy would be to eliminate time from the fourth and fifth groups above, and to use the resulting group to set the physical size reduction by selecting a coarser matrix and greater absolute permeability for the model than are present in the field. Scaling of time is then defined by the fifth group. The power level in the model is now obtained from the third group above, it generally being assumed that identical temperatures are established in field and model in homologous times. Finally, the first and second groups set the model frequency and electrical conductivity, where the latter is determined by the salinity of the formation water used in the model. Field behavior can now be inferred from the model data under the assumption that the relative permeabilities of the model are representative of those in the field.

Scaled physical models of this and other electrothermal processes have been used extensively to indicate field performance [3,4], and also to evaluate the performance of numerical simulators [81]. The development by PCEJ of an electrode well design, preliminary operating strategies, pilot configurations, and numerical simulators was in part supported by physical models [17]. A broad fundamental assessment

by Vermeulen and Chute [22] of the viability of in situ heating by use of large underground induction coils was based extensively on physical model studies. IITRI used a scaled physical model to assist in a feasibility study of 60 Hz in situ electrical heating of oil sands [89]. Scale-up criteria were applied by IITRI to laboratory measurements to obtain information on electrical and product recovery equipment design for a field test of in situ heating of oil sand at 2.2875 and 13.56 MHz in the Asphalt Ridge deposit near Vernal, UT [6]. IITRI also used a scaled physical model to obtain experience for a field test on electromagnetic stimulation of a heavy oil well near Ardmore, OK; excitation of the model at 200 MHz was equivalent to the actual excitation frequency of about 6.8 MHz [26].

Numerical models of electrothermal processes

The development to date of numerical models for electrothermal processes has primarily provided the ability to simulate heating at power frequencies. Such numerical models can be used when excitation of the formation is at frequencies other than 60 Hz, provided that the system dimensions are much smaller than the wavelength and the depth of penetration, and provided $\sigma_e/\omega\varepsilon_e$ is much greater than unity. While some existing numerical models are proprietory, several are in the public domain, and examination of one of these can provide helpful initial orientation for the design of subsequent models.

EPEIOS, written by Hiebert [44] of the Applied Electromagnetics Laboratory at the University of Alberta, is a three-dimensional finite difference solver of the resistive heating and heat conduction equations. The problem domain in EPEIOS is subdivided into variably sized rectangular grid blocks, each of which is assigned appropriate electrical properties (the grid block can be electrically conducting, insulating, or be part of an electrode) and appropriate thermal properties (the grid block can be thermally conducting, insulating, or at constant temperature). Electrical conductivity may be anisotropic in three directions; its variation with temperature may be specified by a piece-wise linear function or by a third-order polynomial. The outer boundaries of the problem domain are nominally no-flow electrical and no-flow thermal surfaces, and may be placed coincident with planes of symmetry in the field configuration.

Multiphase excitation by means of a multiplicity of electrodes is possible at either constant voltage or constant power, or else the current of one electrode may

be held constant. Electrodes may be cooled and wellbore resistances may be specified.

A conservative, block-centered, seven-point, three-dimensional formulation is used to difference the current continuity equation

$$\nabla \cdot (\sigma_e \nabla \psi) = 0 \qquad (18)$$

to arrive at the algebraic finite difference equations for the potential ψ. These equations are solved for ψ using the Point-wise Successive Over-Relaxation method (PSOR) [90] which includes automatic, adaptive relaxation parameter selection.

Multiphase excitation of electrodes is achieved by solving sequentially for the potential distribution ψ_1 due to excitation by the real parts of the electrode voltages, and the potential distribution ψ_2 due to excitation by the imaginary parts of the electrode voltages. The complete potential distribution within the problem domain is then given by $\psi = \psi_1 + j\psi_2$.

A conservative, block-centred, seven-point, three-dimensional formulation is also used to difference the heat conduction equation. The resulting finite difference equations are solved with the Douglas-Rachford Alternating Direction Implicit Method (ADIP) [91]. The heat conduction equation is solved explicitly, by using the electrical conductivities and heating rates calculated at the beginning of each time step.

At each time step EPEIOS permits an incremental and cumulative energy comparison by providing the energy input at the electrodes, and the sum of the energies dissipated in each grid block, as well as the sum of the energies in each grid block due to temperature changes.

EPEIOS has been extensively tested against electrical, thermal, and electrothermal problems with known analytical solutions. Excellent agreement between numerical and analytical solutions was obtained in all cases.

While EPEIOS does not simulate fluid flow or fluid expansion, a more versatile numerical simulator TCTM–EPEIOS written by Hiebert [44], does model fluid flow and expansion. This simulator is an implicitly coupled combination of the Alberta Research Council's Two-Component Thermal Model (TCTM) [92] and EPEIOS. TCTM is a highly implicit finite difference model that approximates the material balance and energy equations for three-phase fluid flow with steam

and a nonvolatile oil component. In the combined code TCTM solves the material balance and energy equations, where the latter includes heat conduction. TCTM then passes values of temperature, water saturation, and porosity for each grid block to EPEIOS, which uses these values, as well as the electrical conductivity of connate water, to calculate formation electrical conductivities from Archie's law and a temperature function. Heating rates are then calculated and passed back to TCTM and are entered as a source term in the energy balance. TCTM-EPEIOS can simulate fluid production and the loss of moisture that may occur in high-temperature regions near electrodes. It cannot simulate the movement of saline concentration within the reservoir and, therefore, while electrical heating takes place, can simulate fluid injection only if the conductivity of the injected fluid is equal to that of the connate water.

The calculated values of electrical heating rates depend on the square of the spatial derivates of potential. They are, therefore, more sensitive to spatial truncation errors caused by a limited number of grid blocks, than the calculation of fluid flow. TCTM-EPEIOS permits optimal selection of grid structures as it will accept a finer grid structure for solving the electrical equations than for solving the fluid flow equations.

To examine the importance of fluid flow and fluid expansion during electrical preheating, several test cases of electrical preheating followed by steam injection have been simulated. These cases included a homogeneous two-dimensional reservoir with vertical electrodes, a two-dimensional two-layer reservoir with horizontal wells, and a three-dimensional five-spot pattern with top-bottom electrodes in a multilayer reservoir. In all cases fluid, rock, and rock-fluid properties were typical of Athabasca oil sand reservoirs. The electrical preheat phases, which lasted from 180 to 379 d, were in all cases simulated first without fluid flow by EPEIOS, and then with fluid flow by TCTM-EPEIOS. Due to thermal expansion, higher reservoir pressures prevailed at the end of the preheat phase when simulated on TCTM-EPEIOS than when simulated on EPEIOS, however, the variation of interelectrode resistance, temperature at the end of the preheat phases, and cumulative oil production during the steam drive, very closely equalled each other. This indicates that fluid flow and thermal expansion during the electrical preheat phase may be neglected in some electric preheat processes, provided no fluid injection takes place during the preheat phase.

Killough and Gonzales at ARCO Oil and Gas Co.

[83] have developed a fully implicit, finite difference, three-dimensional numerical simulator, EEOR, to model the electrically enhanced oil recovery process. The general capabilities of this simulator are similar to those of TCTM-EPEIOS, in that EEOR models multiphase electrical heating and fluid flow. EEOR treats formation resistivity as a function of temperature, water saturation, and salinity, and models the movement of saline concentration within the reservoir. The multicomponent, multiphase reservoir simulation follows that of Coats [93]. EEOR utilizes a curvilinear, radial, or cartesian coordinate system. Unlike TCTM-EPEIOS, no indication is given that EEOR can use grid structures of different sizes for the electrical and fluid flow problems, nor that it can model anisotropic electrical conductivity. Validation of EEOR was accomplished by comparing numerical results against analytical and experimental data.

Khosla and Towson at Petro-Canada Resources [17] describe a three-dimensional electric preheat model, EPM, capable of handling the electric preheat process for a multiwell, multiphase electrical excitation with no fluid flow. EPM models the oil sand formation and overburden and underburden as networks of interconnected electrical resistances and interconnected thermal resistances. Near the wellbores the networks are two-dimensional and radial. These networks, in turn, are linked to three-dimensional networks in the remainder of the reservoir. Numerical modelling begins at the wellhead power transformer and electrode well behavior is simulated. EPM was initially calibrated with results from laboratory testing and from rudimentary physical models. It is operated in tandem with Intercomp's Steam Model (1979 version), and was ultimately used for history matching and performance prediction of the PCEJ Electric Preheat/Steam Drive Pilot test carried out in the Athabasca-McMurray reservoir during 1981 to 83 [16].

Todd and Howell of ARCO [82] have reported on an RZ electrothermic model, RZ EM, a reservoir simulator developed to model electrical heating and production of fluids from a formation. This simulator was developed for two geometries. A radial, two-dimensional, one-wellbore model was developed to study in detail the heating near the wellbore. A three-dimensional model was also developed. This model has larger grid blocks than the two-dimensional wellbore model, and hence gives less detail of heating near the wellbore. Current distribution and heat removal from the radial model (which provides for wellbore cooling) are input to the

three-dimensional model to compensate for lack of definition in the latter near the wellbores. The three-dimensional model is able to simulate three-phase electrical excitation of electrodes. RZ EM was interfaced with Intercomp's Steam Model (1976–77 version) and enhanced to study multiphase power application, thermal expansion of reservoir fluids and their production, and leakage of electrode well coolant into the formation and its effect on heating rate. Much of the experience gained from RZ EM was later applied to the development of EPM, described earlier [17].

Bridges et al. at IITRI [26] report on the evolution of several two-dimensional numerical electromagnetic models to estimate the spatial distribution of heat for selected types of electromagnetic excitors. One approach used the method of moments, originally developed by Harrington [94]; the second method, R–NET, simply modelled the earth media as a network of interconnected resistors. R–NET, however, did not consider high-frequency effects and the method of moments was cumbersome with anything but the simplest geometries. Z–NET, based on the work of Krone [95], was subsequently developed. This two-dimensional model in cylindrical coordinates is suitable for the study of single-well stimulation and allows consideration of all electromagnetic factors within the reservoir either at low or high frequencies. The outputs of Z–NET include the spatial distribution of the heat input around the borehole for either wet or dry reservoirs, the input impedance of the antenna-like excitor, and power delivery system losses. In conjunction with the above, a finite difference simulator in two-dimensional cylindrical coordinates, based on the work of Coats et al. [96] and Grabowski et al. [97], was developed at Texas A&M University to model the flow of oil, water, and steam, and the thermal aspects of an oil reservoir when an electromagnetic source is applied. The numerical model was used to provide design data for the Ardmore, OK single-well stimulation pilot project.

El–Feky [80] and Harvey and El–Feky [98] at the University of Missouri-Rolla have described a two-dimensional, two-phase (oil and water) numerical simulator which includes electrical heating at 60 Hz. The simulator was used to study improvements in sweep efficiency and oil recovery in water floods due to electrical formation heating. The movement of saline concentration is modelled. The mathematical model used contains several simplifying assumptions. The reservoir modelled was horizontal, uniform in thickness, and homogeneous in porosity and permeability. No gas

saturation was included in the model. The electrical current was confined to the reservoir (the overburden and underburden were modelled as much more resistive than the reservoir), and the electrodes contacted the entire reservoir. The simulator was used with uniform grid spacing to model one quadrant of a five-spot pattern, and results obtained were compared to measurements on laboratory-scale models with good agreement.

REFERENCES

1. M.A. Carrigy, Thermal recovery from tar sands, J.Pet. Tech., 35 (1983) 2149.
2. D.A. Redford, In-situ recovery from the Athabasca oil sands – past experience and future potential, 35th Annual Technical Meeting of the Petroleum Society of CIM, Calgary, Jun 10–13 (1984) 1057.
3. F.E. Vermeulen, F.S. Chute, M.R. Cervenan and J. Fearn, Physical modelling of the electrical heating of the oil sand deposits, final report AOSTRA agreement no. 58, Jun (1982).
4. F.S. Chute, F.E. Vermeulen, R.G. McPherson, A.D. Hiebert and J. Fearn, Electromagnetic heating of oil sands, final report AOSTRA agreement no. 296, Jun (1985).
5. R.G. McPherson, F.S. Chute and F.E. Vermeulen, The electromagnetic flooding process for in-situ recovery of oil from Athabasca oil sand, J. of Microwave Power, 21 (1986) 129.
6. G.C. Sresty, H. Dev, R.H. Snow and J.E. Bridges, Recovery of bitumen from tar sand deposits with the radio frequency process, SPE Reservoir Engineering, 1 (1986) 85.
7. Anon., A.C. current heats heavy oil for extra recovery, in World Oil (1970) 83.
8. loc. cit. (4), 104.
9. loc. cit. (4), 217.
10. F.S. Chute and F.E. Vermeulen, Present and potential applications of electromagnetic heating in the *in-situ* recovery of oil, AOSTRA J. Res., 4 (1988) 19.
11. F.S. Chute, F.E. Vermeulen and M.R. Cervenan, Physical modelling of the electrical heating of the oil sand deposits, final report AOSTRA agreement no. 31, Oct (1978).
12. J.A. Haston, Electrical heating applications in oil sands production, AOSTRA internal report, Jul (1982).
13. loc. cit. (4), 26.

14. F.S. Chute, N.R. Edmunds, T.E. Evans, M.E. McCormack, L.G. Stevens, F.E. Vermeulen and J.A. Haston, Electric preheat pilot studies (EPPS), AOSTRA internal report (1984).

15. J.S. Broz, W.T. Savery, J.E. Bridges and G.C. Sresty, Results from a preliminary feasibility study of electromagnetic hot waterflooding for tar sands and heavy oil, 20th Intersociety Energy Conversion Engineering Conference, Miami Beach, FL,18–23 Aug (1985).

16. D. Towson, The electric preheat recovery process, 2nd International Conference on the Future of Heavy Crude and Tar Sands, Caracas, Venezuela, 7–17 Feb (1982) 869.

17. A. Khosla and D.E. Towson, Application of computer modelling to the PCEJ electric preheat/steamdrive Athabasca pilot, 36th Annual Technical Meeting of the Petroleum Society of CIM, Edmonton, Alberta, 2–5 Jun (1985).

18. loc. cit. (3), 54.

19. H. Gill, The electrothermic system for enhancing oil recovery, J. Microwave Power, 18 (1983) 107.

20. loc. cit. (2), 1060.

21. I.W. Henry, Process and apparatus for the production, from hydrocarbon material, of gases or liquids of changed molecular weight, U.S. Pat. no. 321, 910, 18 Nov (1929).

22. F.E. Vermeulen and F.S. Chute, The induction heating of fossil fuels in-situ by electric and magnetic fields, Can. Elect. Eng. J. 10 (1985) 147.

23. R.G. McPherson, F.S. Chute and F.E. Vermeulen, Recovery of Athabasca bitumen with the electromagnetic flood process, J. Can. Pet. Tech., 24 (1985) 44.

24. loc. cit. (4), 253.

25. H.W. Ritchey, Radiation heating, U.S. Pat. no. 2, 757, 738, 7 Aug (1956).

26. J.E. Bridges, G.C. Sresty, H.L. Spencer and R.A. Wattenbarger, Electromagnetic stimulation of heavy oil wells, 3rd International Conference on Heavy Crude and Tar Sands, UNITAR/UNDP Information Centre for Heavy Crude and Tar Sands, Long Beach, CA, 22–31 Jul (1985).

27. G.C. Sresty, R.H. Snow and J.E.Bridges, The IITRI RF process to recover bitumen from tar sand deposits — a progress report, 2nd International Conference on the Future of Heavy Crude and Tar Sands, Caracas, Venezuela, 7–17 Feb (1982) 871.

28. J.E. Bridges, J.J. Krstansky, A. Taflove and G. Sresty, The IITRI in-situ RF fuel recovery process, J. Microwave Power, 18 (1983) 3.

29. T.W.W. Hill, Electro-thermal recovery of petroleum, Producers Monthly, 16 (1952) 14.

30. S. Levine and A. Sacuta, Electrokinetic flow in a parallel-plate channel containing bitumen and water: A model for oil sands, AOSTRA J. Res., 1(1985) 255.

31. W.E. Dumbaugh, W.N. Lawless, J.W. Malmandier and D.R. Wexell, Extraction of oil from oil shale and tar sand, Canadian Pat. no. 1, 108, 081, 1 Sep (1981).

32. V. Balint, A. Pinter and G. Mika, Process for the recovery of shale oil, heavy oil, kerogen or tar from their natural sources, U.S. Pat. no. 4, 419, 214, 6 Dec (1983).

33. A.C. Milan, "In-situ extraction of bitumen from Alberta's tar sand by microwave heating," B.A.Sc. thesis, Univ. of Windsor (1978).

34. N.L. Carpenter, Method For secondary recovery of oil, U.S. Pat. no. 4, 037, 655, 26 Jul (1977).

35. R.J. Lytle, Measurement of earth medium electrical characteristics: Techniques, results and applications, IEEE Trans. on Geoscience Electronics, 12 (1974) 81.

36. H.E. Bussey, Measurement of RF properties of materials — a survey, Proceedings of the Institute of Electrical and Electronic Engineers, 55 (1967) 1046.

37. M.F. Iskander and J.B. duBow, Time-and frequency-domain techniques for measuring the dielectric properties of rocks: A review, J. Microwave Power, 18 (1983) 55.

38. H.P. Schwan and C.D. Ferris, Four electrode null techniques for impedance measurement with high resolution, Review of Scientific Instruments, 39 (1968) 481.

39. F.S. Chute, M.R. Cervenan and F.E. Vermeulen, Simple cell for the measurement of the radio frequency electrical properties of earth materials, Review of Scientific Instruments, 49 (1978) 1675.

40. F.S. Chute, F.E. Vermeulen, M.R. Cervenan and F.J. McVea, Electrical properties of Athabasca oil sands, Can. J. Earth Sci., 16 (1979) 2009.

41. R. De Bibhas, Measurement and analysis of broadband dielectric properties of brine saturated rocks, Proceedings of SPWLA Twenty-Sixth Annual Logging Symposium, Jun 17–20 (1985).

42. F.J. McVea, "Electrical properties of the Athabasca tar sands," M.Sc. thesis, Univ. of Alberta, Edmonton, Alberta, Jun 12 (1978).

43. G. Walker, Microwave measurements on tarsand in the region of 2 to 4 GHz, Applied Electromagnetics Laboratory, Univ. of Alberta, internal report, Jun (1979).

44. A.D. Hiebert, "Modelling of the electric preheat process," Ph.D. thesis, Univ. of Alberta, Edmonton, Alberta, Jun (1986).

45. R.N. Rau and R.P. Wharton, Measurement of core electrical parameters at ultra-high and microwave frequencies, Can. J. of Pet. Tech. (1982) 2689.

46. A.M. Nicholson and G.F. Ross, Measurement of the intrinsic properties of materials by time-domain techniques, IEEE Trans. of Instrumentation and Measurement, 19 (1970) 377.

47. Schlumberger[R] Log Interpretation, Vol. 1-Principles (1972).

48. J.R. Wait, "Electromagnetic probing in geophysics," Golem Press, Boulder, CO (1971).

49. G.V. Keller and F.C. Frischknecht, "Electrical methods in geophysical prospecting," Pergamon Press, Oxford, England (1970).

50. G.R. Ahoeft, Initial report of the petrophysical laboratory, U.S.G.S. Geological Survey Circular (1979) 789.

51. B.D. Fuller and S.H. Ward, Linear system description of the electrical parameters of rock, Inst. of Electrical and Electronics Engineers Trans. on Geoscience Electronics, 8 (1970) 7.

52. P.N. Sen and W.C. Chew, The frequency dependent dielectric and conductivity response of sedimentary rocks, J. of Microwave Power, 18 (1983) 95.

53. H. Ucok, I. Ershaghi and G.R. Olhoeft, Electrical resistivity of geothermal brines, J. Pet. Tech., 32 (1980) 717.

54. K. Takamura, Microscopic structure of Athabasca oil sand, Can. J. Chem. Eng., 60 (1982) 538.

55. A.S. Quist and W.L. Marshall, Electrical conductances of aqueous sodium chloride solutions from 0 to 800° and at pressures to 4000 bars, J. Phys. Chem., 72 (1968) 684.

56. loc. cit. (4), 301.

57. F.E. Vermeulen, F.S. Chute and E. Sumbar, Electrical conductivity of Clearwater shale and rich oil sand as measured in the laboratory, final report AOSTRA agreement no. 296A, Jun (1987).

58. J.W. Kern, W.A. Hoyer and M.M. Spann, High temperature electrical conductivity of shaly sands, SPWLA Eighteenth Annual Logging Symposium, Jun 5–8 (1977).

59. M. Das, R. Thapar, K. Rajeshwar and J. du Bow, Thermophysical characterization of oil sands: 3. Electrical properties, Can. J. Earth Sci., 18 (1981) 742.

60. P. Hoekstra, J.D. Henderson and A.A. Kaufman, Geophysical surveys for oilsands exploration, Applied Oil Sands Geoscience Conference, Jun 11–13 (1980), Edmonton, Alberta.

61. G.E. Archie, Electrical resistivity — An aid in core analysis interpretation, Bull. of Amer. Assoc. Pet. Geol., 31 (1947) 350.

62. W.O. Winsauer, H.M. Shearin Jr., P.H. Masson and M. Williams, Resistivity of brine-saturated sands in relation to pore geometry, Bull. Amer. Assoc. of Pet. Geol., 36 (1952) 253.

63. S.J. Pirson, "Handbook of well log analysis," Prentice Hall, Englewood Cliffs, NJ, (1963).

64. E.I. Parkhomenko, "Electrical properties of rocks," Plenum Press, New York (1967).

65. D.A. Hackbarth and N. Nastassa, The hydrogeology of the Athabasca oil sands area, Alberta, Alberta Research Council Bulletin 38 (1979).

66. M.H. Waxman and E.C. Thomas, Electrical conductivities in shaly sands — I. The relationship between hydrocarbon saturation and resistivity index; II. The temperature coefficient of electrical conductivity, J. Pet. Tech. (1974) 213.

67. J.M. Delano Jr., and R.P. Wharton, An EPT interpretation procedure and application in freshwater, shaly oil sands, J. Pet. Tech. (1984) 1763.

68. R.C. Sah, A.E. Chase and L.E. Wells, Evaluation of the Alberta tar sands, 49th Annual Fall Meeting of Society of Petroleum Engineers of AIME, Houston, TX, 6–9 Oct (1974).

69. H.N. Collins, Log-core correlations in Athabasca oil sands, 49th Annual Fall Meeting of the Society of Petroleum Engineers of AIME, Houston, TX, 6–9 Oct (1974).

70. R. Woodhouse, Athabasca tar sand reservoir properties derived from cores and logs, 17th Annual Symposium SPWLA, Denver, CO, 9–12 Jun (1976).

71. T.J. Griffin and D.C. Bush, Core analysis in unconsolidated reservoirs using an improved consolidation technique, 36th Annual Technical Meeting of the Petroleum Society of CIM, Edmonton, Alberta, 2–5 Jun (1985).

72. D. Minken, The Cold Lake oil sands: Geology and a reserves estimate, Canadian Society of Petroleum

Geologists Oil Sand Symposium, Calgary, Alberta, 5–7 Sep (1973).

73. L.J. Fahy, C.G. Mones and N.W. Merriam, Northwest Asphalt Ridge tar sand deposit well logging and coring comparison, Synthetic Fuels From Oil Shale and Tar Sands Symposium, Louisville, KY, 17–19 May (1983).

74. A.H. Harvey and M.D. Arnold, Estimation of heat distribution in selective electric reservoir heating, J. Pet. Tech. (1980) 965.

75. A.H. Harvey, Influence of adjacent conductive formations on the selective electric reservoir heating process, Soc. Pet. Eng. J., 22, no. 5 (1982) 750.

76. E.R. Abernethy, Production increase of heavy oils by electromagnetic heating, J. Can. Pet. Tech., 15, no. 3 (1976) 91.

77. D.W. Strangway, Electromagnetic scale modelling, in "Methods and techniques in geophysics," Interscience, New York (1966) 1.

78. G. Sinclair, Theory of models of electromagnetic systems, Proc. Institute of Radio Engineers, 36 (1948) 1364.

79. F.E. Vermeulen, F.S. Chute and M.R. Cervenan, Physical modelling of the electromagnetic heating of oil sand and other earth-type and biological materials, Can. Elec. Eng. J., 4, no. 4 (1979) 19.

80. S.A. El–Feky, "Theoretical and experimental investigation of oil recovery by the electrothermic technique," Ph.D. thesis, Univ. of Missouri-Rolla (1977).

81. A.D. Hiebert, F.E. Vermeulen, F.S. Chute and C.E. Capjack, Numerical simulation results for the electrical heating of Athabasca oil sand formations, SPE Reservoir Engineering, Jan (1986) 76.

82. J.C. Todd and E.P. Howell, Numerical simulation of in situ electrical heating to increase oil mobility, The oil sands of Canada-Venezuela, CIM special volume 17, (1977) 477.

83. J.E. Killough and J.A. Gonzalez, A fully-implicit model for electrically enhanced oil recovery, Paper no. 15605, 61st Annual Technical Conference and Exhibition of the Society of Petroleum Engineers, New Orleans, Oct 5–8, (1986).

84. F.E. Vermeulen and F.S. Chute, Electromagnetic techniques in the in-situ recovery of heavy oils, J. Microwave Power, 18, no. 1 (1983) 15.

85. S. Ramo, J. Whinnery and T. Van Duzer, "Fields and waves in communication electronics," John Wiley and Sons Inc., New York (1967).

86. J. Geertsma, G.A. Croes and N. Schwartz, Theory of dimensionally scaled models of petroleum reservoirs, Trans. AIME, 207 (1956) 118–127.

87. A. Klinkenberg and H.H. Mooy, Dimensionless groups in fluid friction, heat, and material transfer, Chem. Eng. Progress, 44 (1948) 17.

88. S.M. Farouq Ali, D.A. Redford and M. Rafiqul Islam, Scaling laws for enhanced oil recovery experiments, China-Canada Heavy Oil Technology Symposium, Zhuo Zhou, China, Oct (1987).

89. J.E. Bridges, G.C. Sresty and H. Dev, In-situ RF heating for oil sand and heavy oil deposits, vol. II, Third International Conference on Heavy Crude and Tar Sands, Long Beach,CA, 22–31 Jul (1985) 1.

90. L.A. Hageman and D.M. Young, "Applied iterative methods," Academic Press (1981).

91. B. Carnahan, H.A. Luther and J.O. Wilkes, Ch. 7 in "Applied numerical methods," John Wiley and Sons Inc. (1969).

92. G.S. Reddy, D.R. Prowse and D.A. Redford, Physical modelling and numerical simulation of in-situ recovery of bitumen from oil sands by steam injection, 31st Annual Technical Meeting of the Petroleum Society of CIM, Calgary, Alberta (1980).

93. K.H. Coats, In-situ combustion model, Soc. Pet. Eng. J., 20 (1980) 533.

94. R. Harrington, "Field computations by the method-of-moments," MacMillan, New York (1968).

95. G. Krone, Equivalent circuit of the field equations of Maxwell, Proceedings of the Institute of Radio Engineers, May (1944) 289.

96. K.H. Coats, W.D. George, C. Chu and B.E. Marcum, Three-Dimensional simulation of steam flooding, Soc. Pet. Eng. J., Dec (1974).

97. J.W. Grabowski, P.K. Vinsome, R.C. Lin, A. Behie and B. Rubin, A fully implicit general purpose finite-difference thermal model for in situ combustion and steam, Soc. Pet. Eng. no. 8396 (1979).

98. A.H. Harvey and S.A. El–Feky, Selective reservoir heating could boost oil recovery, The Oil and Gas J., Nov 13 (1978) 185.